PNNL-23387

Pacific Northwest NATIONAL LABORATORY

Proudly Operated by Battelle *Since 1965*

NDE Techniques Used in PARENT Open Round Robin Testing

November 2014

RM Meyer

Prepared for the U.S. Nuclear Regulatory Commission
under a Related Services Agreement with the U.S. Department of Energy
CONTRACT DE-AC05-76RL01830

U.S. DEPARTMENT OF ENERGY

PACIFIC NORTHWEST NATIONAL LABORATORY
operated by
BATTELLE
for the
UNITED STATES DEPARTMENT OF ENERGY
under Contract DE-AC05-76RL01830

Printed in the United States of America

Available to DOE and DOE contractors from the
Office of Scientific and Technical Information,
P.O. Box 62, Oak Ridge, TN 37831-0062;
ph: (865) 576-8401
fax: (865) 576-5728
email: reports@adonis.osti.gov

Available to the public from the National Technical Information Service,
U.S. Department of Commerce, 5285 Port Royal Rd., Springfield, VA 22161
ph: (800) 553-6847
fax: (703) 605-6900
email: orders@ntis.fedworld.gov
online ordering: http://www.ntis.gov/ordering.htm

This document was printed on recycled paper.

(9/2003)

PNNL-23387

NDE Techniques Used in PARENT Open Round Robin Testing

RM Meyer

November 2014

Prepared for
the U.S. Nuclear Regulatory Commission
under a Related Services Agreement
with the U.S. Department of Energy
Contract DE-AC05-76RL01830

Pacific Northwest National Laboratory
Richland, Washington 99352

Summary

This report documents the nondestructive evaluation (NDE) techniques used in the open testing portion of the Program to Assess the Reliability of Emerging Nondestructive Techniques (PARENT), which is comprised of approximately 170 inspections performed on 19 test blocks by 23 teams from Japan, Europe, South Korea, and the USA. The teams examined dissimilar metal weld (DMW) and bottom-mounted instrumentation (BMI) test blocks. The goal of the open portion of PARENT is focused on evaluating the capability of novel and emerging NDE techniques from various entities including both industry and academia. The NDE techniques used in the open testing are broadly categorized as ultrasonic techniques, eddy current techniques, and other techniques. Motivations for developing many of the open NDE techniques can be characterized as addressing one or more of the following challenges: (1) to more accurately characterize large defects, (2) to enable inspections of difficult-to-access regions, and (3) to improve detectability of small defects. Information about the techniques was collected from teams participating in PARENT open testing and is included in the appendices of this report. The information in these appendices is referenced in the main body of the report, which includes brief overview descriptions of the NDE techniques used.

Acknowledgments

This report was jointly sponsored by the U.S. Nuclear Regulatory Commission (NRC); the Nuclear Regulatory Authority (NRA), Japan; the Korea Institute of Nuclear Safety (KINS); the Swedish Radiation Safety Authority (SSM); the Swiss Federal Nuclear Safety Inspectorate (ENSI); and the Technical Research Centre of Finland (VTT). The guidance and support provided by NRC personnel Iouri Prokofiev (project manager) and Stephen Cumblidge (technical advisor) is acknowledged and greatly appreciated. The author appreciates the assistance of Kay Hass in the formatting and organization of this report. Appreciation is also extended to the regional invigilators, Tommy Zetterwall (Europe), Ichiro Komura (Japan), and Kyung-cho Kim (South Korea) for their communication between team members and the author and for their roles in collecting the information that forms the basis of this report. The author also acknowledges contributions to the open testing portion of PARENT from the following organizations:

- Japanese Organizations
  - Ultrasonic Materials Diagnosis Laboratory (UMDL)
  - Institute of Nuclear Safety System, Incorporated (INSS)
  - Tohoku University
  - Nagoya University
  - Toyama University
  - Japan Power Engineering and Inspection Corporation (JAPEIC)
  - Mitsubishi Heavy Industries (MHI)

- European Organizations
  - Swiss Association for Technical Inspections, Nuclear Inspectorate (SVTI)
  - VTT Technical Research Center of Finland
  - Alstom [Switzerland]
  - Swiss Federal Laboratories for Materials Science and Technology (EMPA)
  - Chalmers Institute of Technology [Sweden]
  - Paul Scherer Institute (PSI) [Switzerland]

- Korean Organizations
  - Korea Atomic Energy Research Institute (KAERI)
  - Korea Research Institute of Standards and Science (KRISS)
  - Pusan National University (PNU)
  - Sungkyunkwan University (SKKU)
  - Hanyunag University (HYU)

- USA Organizations
  - IHI Southwest Technologies and Southwest Research Institute (SwRI)
  - AlphaSense
  - Pacific Northwest National Laboratory (PNNL)

Contributions by these organizations include descriptions of the NDE techniques they used in open testing and this material is included in the appendices of this report and referenced throughout the main body.

Acronyms and Abbreviations

3D SAFT-UT	three-dimensional synthetic aperture focusing technique
AECT	advanced ECT technique
BMI	bottom-mounted instrumentation
CAN	contact acoustic nonlinearity
CE-ECT	controlled excitation eddy current
CT	compact tension
DMW	dissimilar metal weld
EP-ECT	exciter-pickup eddy current techniques
FFT	Fast Fourier Transform
FSH	full screen height
GUW	guided ultrasonic wave
HHUT	higher harmonic ultrasonic technique
ID	inner diameter
IR	infrared
ISI	inservice inspection
LASH	large amplitude excitation subharmonic
LUV	laser ultrasound visualization
MNFM	microwave near field microscope
NDE	nondestructive examination
NRUS	nonlinear resonant ultrasound spectroscopy
OC-ECT	orthogonal coil array eddy current technique
OD	outer diameter
PA-ATOFD	phased array asymmetrical beam time-of-flight diffraction
PA-TP	phased array twin probe
PA-UT	phased array ultrasonic techniques
PARENT	Program to Assess the Reliability of Emerging Nondestructive Techniques
PE	pulse-echo
PE-ECT	pulsed excitation eddy current technique
PINC	Program for the Inspection of Nickel Alloy Components
PZT	piezoelectric transducer
SAFT	synthetic aperture focusing technique
SAW	surface acoustic wave
SHPA	subharmonic phased array
SPACE	subharmonic phased array for crack evaluation
TOFD	time-of-flight diffraction
TR	transmit-receive

TRT	time reversal technique
UIRT	ultrasound infrared thermography
UT	ultrasonic testing
UT-P/C	ultrasonic testing – pitch/catch

Contents

Figures

1.0 Introduction

The Program to Assess the Reliability of Emerging Nondestructive Techniques (PARENT) is a follow-on to the cooperative international Program for the Inspection of Nickel Alloy Components (PINC). PARENT is conducted to continue the work from PINC on evaluation of various nondestructive examination (NDE) technologies for detection and characterization of primary water stress corrosion cracks in dissimilar-metal welds (DMWs) and bottom-mounted instrumentation (BMI) penetrations and to incorporate lessons learned from PINC. Testing performed under PARENT consists of two main portions: (1) Blind testing and (2) Open testing. The blind portion of PARENT will evaluate the performance of established techniques using only qualified inspectors and qualified procedures, while the open portion of PARENT is focused on evaluating the capability of novel and emerging NDE techniques from various entities including both industry and academia. This report documents the techniques used in the open NDE testing portion of PARENT.

Approximately 220 inspections were performed on 19 test blocks for the open testing portion of PARENT by 23 teams from Japan, Europe, South Korea, and the USA. Four of the open test blocks are BMIs (P5, P7, P21, and P22) and 15 are DMWs (P1, P4, P12, P23, P24, P28, P29, P30, P31, P32, P37, P38, P41, P42, P46). A total of 13 inspections were performed on BMI test blocks and 205 inspections were performed on DMWs. The NDE techniques used in the open portion of study are broadly categorized as ultrasonic techniques, eddy current techniques, and other techniques. Motivations for developing many of the open NDE techniques can be characterized as addressing one or more of the following challenges: (1) to more accurately characterize large defects, (2) to enable inspections of difficult-to-access regions, and (3) to improve detectability of small defects.

The rest of this report is organized such that brief overview descriptions of ultrasonic techniques are provided in Section 2.0, while brief overview descriptions of the eddy current techniques used in the open testing are included in Section 3.0. Overview descriptions for other techniques are provided in Section 4.0, which includes descriptions for microwave near-field microscopy (MNFM) and radiographic techniques. More specific descriptions of the NDE techniques used in the open testing were collected from the open testing participants in the form of short power point overviews or in the form of more detailed multi-page descriptions. These descriptions are provided in the appendices and are referenced throughout the report to link the brief overview descriptions with specific implementation details.

2.0 Ultrasonic Techniques

This section documents ultrasonic techniques employed in the open testing portion of PARENT by providing brief overview descriptions of the techniques. This section is roughly organized by first providing the description for a variant of conventional ultrasonic testing involving single-element transducers, then by providing the description for phased array and other array transducer-based techniques. This is followed by overview descriptions for non-linear ultrasonic techniques, and overview descriptions for long-range or stand-off ultrasonic inspection techniques are provided last.

2.1 Through Transmission of Longitudinal Waves

A specific variant of conventional ultrasonic testing was assessed during the open testing based on a pitch/catch-type transducer arrangement for transmission and reception of longitudinal waves (UT-P/C). Mechanized scanning and encoding of transducer position and data was used to enhance flaw characterization ability. Identical angle beam (40° to 45°) transducers are used for both transmission and reception. Like most conventional ultrasonic techniques, the transducers are mounted on the outer surface of the component under inspection. A single reflection off of the backwall is required to direct the sound beam to the receiver located on the outer surface. The distance between the transmitter and receiver is such as to optimize this received signal. As the pair of transducers is scanned linearly over a flaw, shadowing of the transmitted signal by the flaw will result in a drop in the signal received (see Figure 2.1). Flaw characterization can be performed by analyzing C-scan images of the data like Figure 2.2. The dimensions of the flaws can be determined from C-scan images. The depth of flaws can be determined from the C-scans as shown in Figure 2.2 with the aid of the formula in Figure 2.1. A detailed description of how the UT-P/C technique was implemented in PARENT can be found in Appendix B.1. As reported in Appendix B.1.5, this technique is relatively insensitive to flaw surface roughness and to flaw orientation. In addition, material grain boundaries introduce very low noise, enabling the use of higher frequencies. However, inspection results can be heavily influenced by the presence of cladding and the technique can be difficult to implement when the ID surface is not parallel with the OD surface.

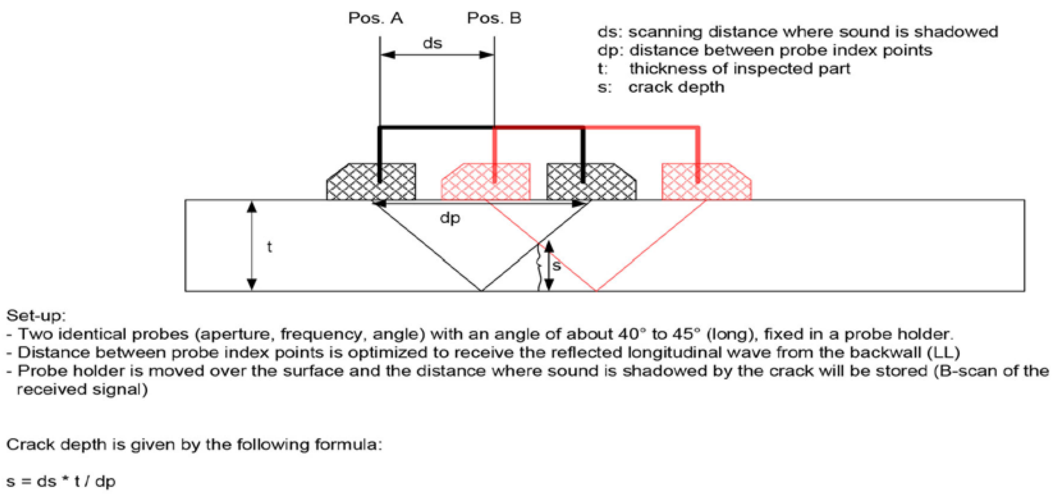

Figure 2.1. Illustration of Mechanized Scanning Through-Transmission Longitudinal Pitch/Catch Technique

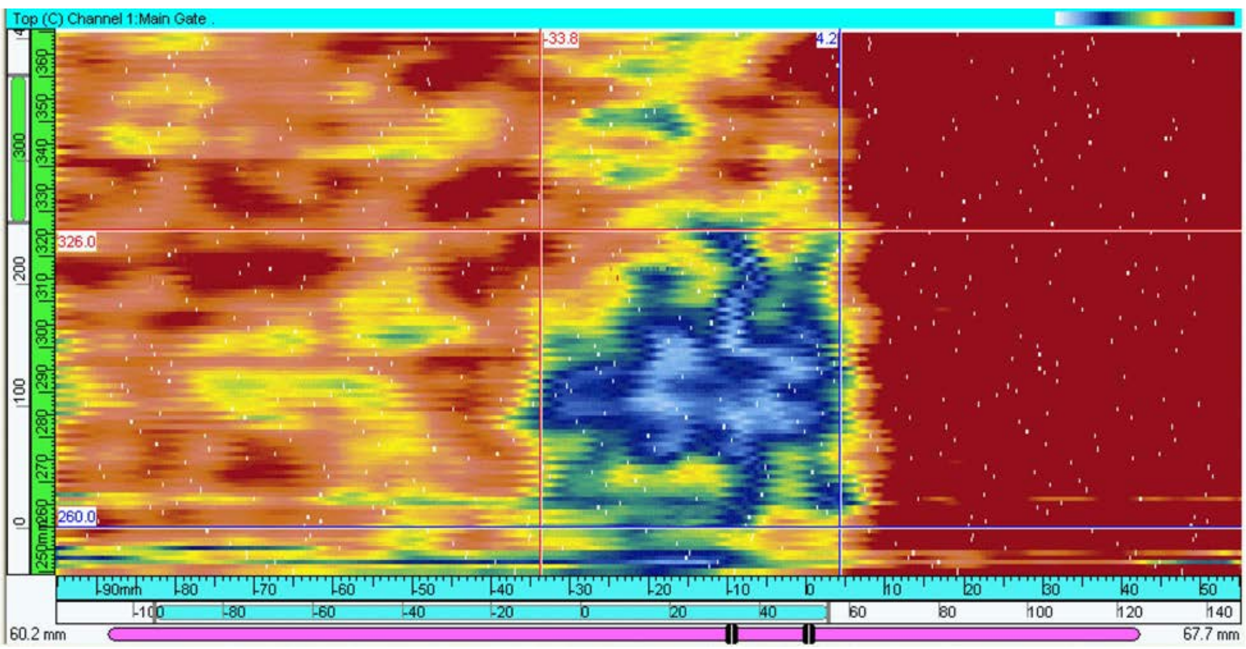

Figure 2.2. The Lower C-scan Shows the Received Amplitude Color Coded (0% FSH [white] to 100% FSH [red]). The Upper C-Scan Shows the C-scan after using a 6 dB Drop Filter (0% to 50% FSH [white] and 50% to 100% FSH [red]). On the left side of the C-scans, the influence of the cladding is visible. The attenuation caused by the cladding is a limiting factor and if it is too high, it can make inspection impossible.

2.2 Phased Ultrasonic Array

Phased array ultrasonic techniques (PA-UT) have been gaining increased acceptance for performing inservice inspection (ISI) of nuclear power plants. PA-UT uses a transducer consisting of multiple piezoelectric or piezocomposite elements in contrast to conventional UT, which uses transducers with only a single-element. Electronic beam steering and focusing is achieved by careful time delay sequencing of excitation signals to the individual elements in the PA-UT transducers to create complex constructive and destructive interference patterns to intensify the sound field in a desired location (see Figure 2.3). PA-UT data is often presented in A-scan, B-scan, C-scan, and D-scan image form for analysis. In this way, the linear dimensions of a flaw are characterized based on image analysis. Figure 2.4 shows an example of PA-UT data representation as A-scan, C-scan, and D-scan images. A PowerPoint overview of how several PA-UT techniques were implemented in PARENT can be found in Appendix A.3 while a more detailed description of how the techniques were implemented can be found in Appendix B.2–B.5.

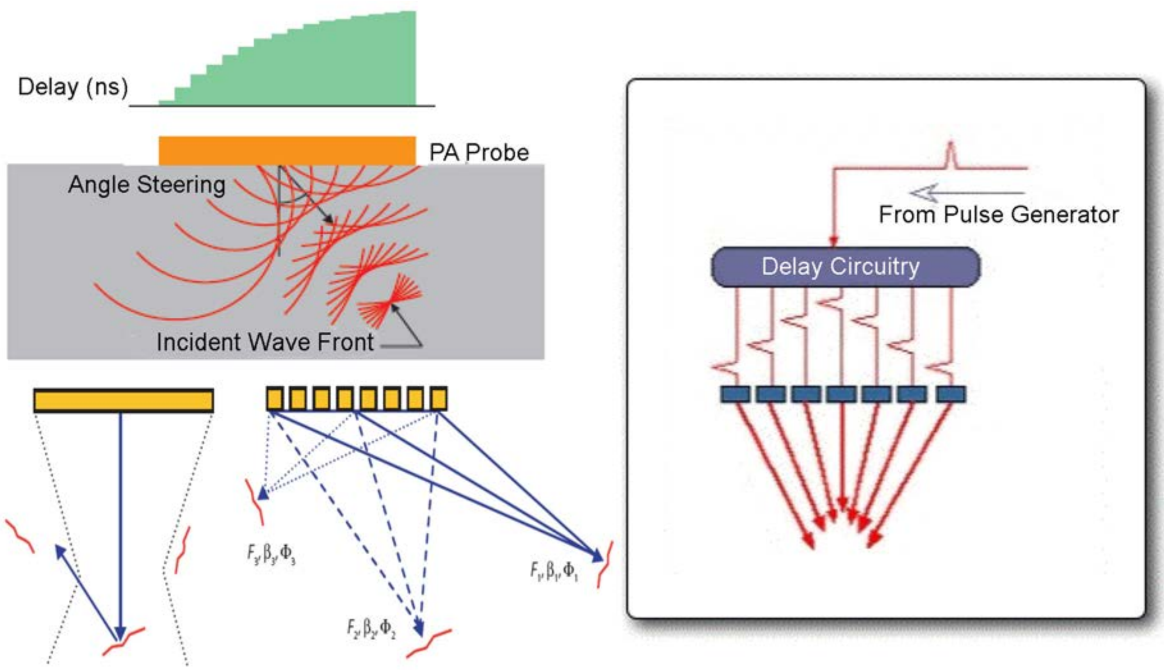

Figure 2.3. Illustration of Time Delay Sequencing of Excitation of PA-UT Transducer Elements to Achieve Beam Steering and Focusing

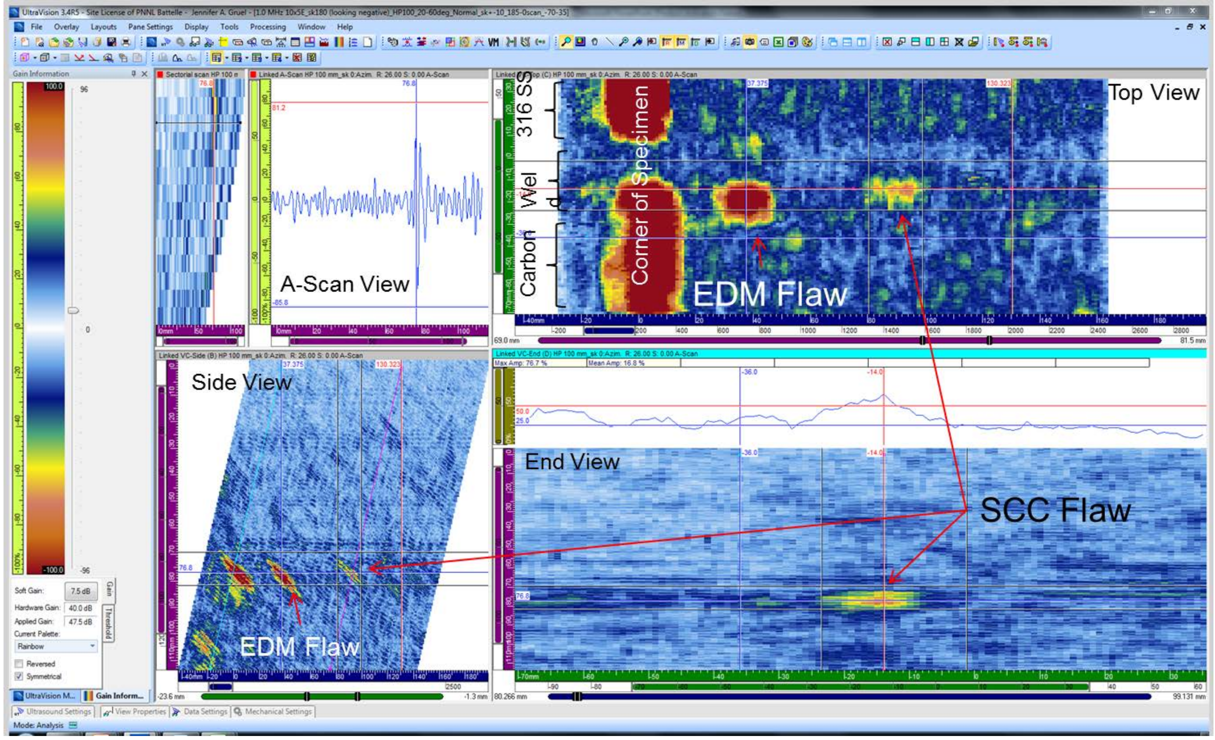

Figure 2.4. PA-UT Data Represented as A-scan (top left), C-scan (top right), and D-scans (bottom images)

There are many parameters to consider in tailoring PA-UT to a specific application including the size, number, and orientation of elements in a PA-UT transducer as well as frequency. In addition, probes for PA-UT may operate in pulse-echo mode or include separate arrays for transmitting and receiving. Like conventional UT, PA-UT can be implemented with automated and encoded or can be performed manually. The significant advantage of PA-UT over conventional UT is that it enables rapid examination of flaws from multiple angles resulting in more accurate and complete flaw characterization. However, the equipment (including the transducers, excitation electronics, and signal processing equipment) is more complex and costly in comparison to equipment for conventional UT exams. This increased complexity also requires a greater amount of personnel expertise to implement.

2.3 Three-Dimensional Synthetic Aperture Focusing Technique

Synthetic aperture focusing technique (SAFT) is a signal processing technique to correct for distortions in scanning images as a result of transducer focusing distortion, to obtain images with improved resolution. Similar to PA-UT, SAFT enables electronic control over transducer focus and can greatly improve inspection performance compared to conventional UT. However, with SAFT, this control is implemented through post-processing of collected data versus time delay sequencing of excitation signals. The basis for SAFT is easiest to illustrate for the 2D scenario, as shown in Figure 2.5.

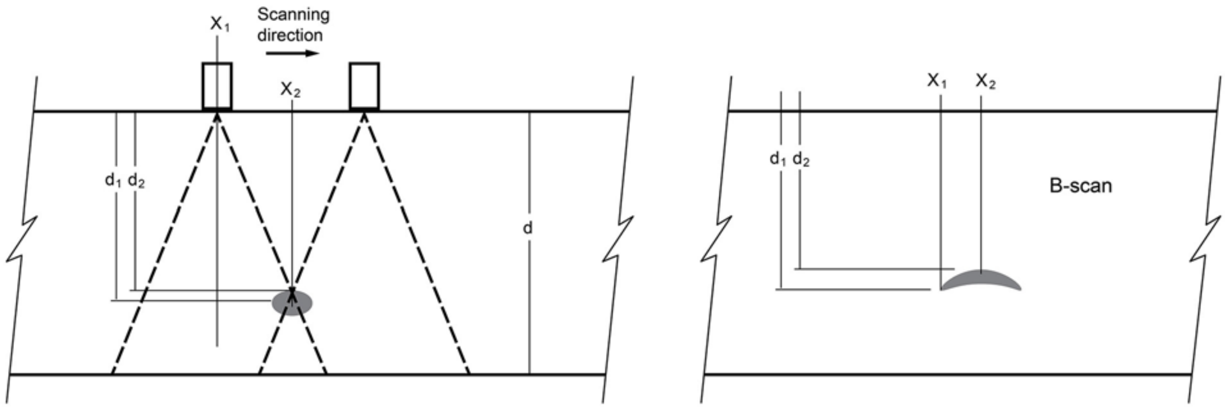

Figure 2.5. 2D Illustration of SAFT Correction for Focusing Distortion in Ultrasonic Inspections (left); B-scan Illustrating Distortion Caused by Beam Focusing Effects (right)

In this figure, an unfocused transducer located at x_1 transmits a signal and receives an echo from the defect located at x_2. As the transducer is scanned along x over the location of the defect, the B-scan image is created illustrating the distortion of the actual defect as a result of poor focusing. This distortion can be corrected for with knowledge of the incident beam width and path traveled by ultrasound through the test piece (Elbern and Guimaraes 1999),

$$d_2 = \left[d_1^2 - \left(x_1 - x_2 \right)^2 \right]^{1/2} . \qquad (2.1)$$

SAFT can also be implemented with a transducer array in which each element in the transducer can be individually excited in sequence while all elements "listen" for echo signals. Using a matrix array transducer allows SAFT imaging to be performed in 3D (see Figure 2.6). An obvious advantage of implementing SAFT with array transducers is that it enables flaws to be characterized much faster and without mechanical scanning of the transducer. However, mechanical indexing may still be required if the target inspection volume is very large. Data from 3D-SAFT can be presented in the form of a variety of images including A-scans, B-scans, C-scans, and D-scans. Thus, analysis procedures are similar to those for PA-UT. A PowerPoint overview of how the 3D-SAFT technique was implemented in PARENT can be found in Appendix A.2, while a more detailed description of how the 3D-SAFT technique was implemented in PARENT can be found in Appendix E.2.

3D-SAFT is a powerful technique in that it enables near arbitrary focusing and rapid characterization of defects through post processing of data. Similar to PA-UT, 3D-SAFT requires the use of sophisticated probes and data recording and processing equipment.

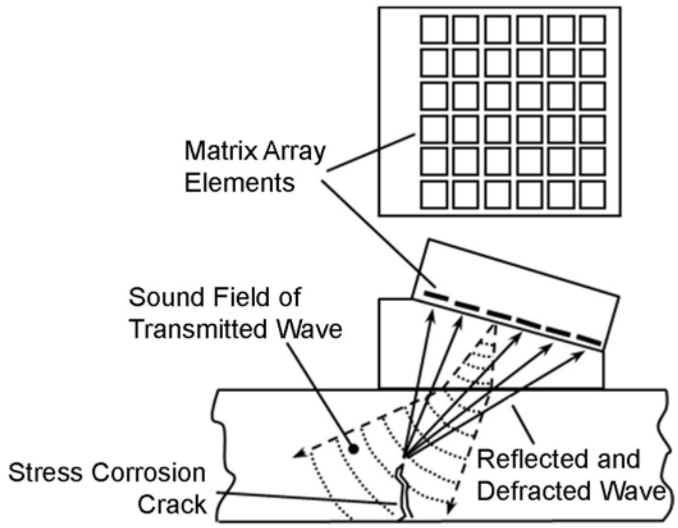

Figure 2.6. Implementation of 3D SAFT Using a Matrix Array Transducer. Individual elements are excited in sequence, while all elements "listen" for echoes.

2.4 Time Reversal Technique

The time reversal technique (TRT-UT) is a means for transmitting electronically focused ultrasonic energy through even non-homogenous media (Fink 1992; Fink 1999). TRT-UT is an iterative technique in which the reflection of ultrasonic energy from a target is interpreted as the emission of a weak ultrasonic signal from the target, which is detected by an array transducer. Under this interpretation, the target acts as a localized source and the sound field spreads as it propagates away from the target towards the array transducer. After digitization and recording of the signals at the transducer, they are time reversed and re-transmitted to generate a sound field that becomes more focused as it travels from the array transducer back to the target (see Figure 2.7). As the process is repeated, the focusing of the sound field improves. Formally, the basis for TRT-UT lies in the reciprocity property of the wave equation. A PowerPoint overview of how TRT-UT was implemented in PARENT can be found in Appendix A.1 and a more detailed description of how TRT-UT was implemented in PARENT can be found in Appendix C.6.

A significant advantage of TRT-UT is its ability to adaptively focus in non-homogenous media. In contrast to SAFT, knowledge of the actual path that ultrasonic signals travel through the test material is not required. Similar to SAFT and PA-UT, TRT-UT requires relatively sophisticated equipment and expertise for data recording and processing, in comparison to conventional UT. The techniques should be capable of performing both inner diameter (ID) and outer diameter (OD) inspections.

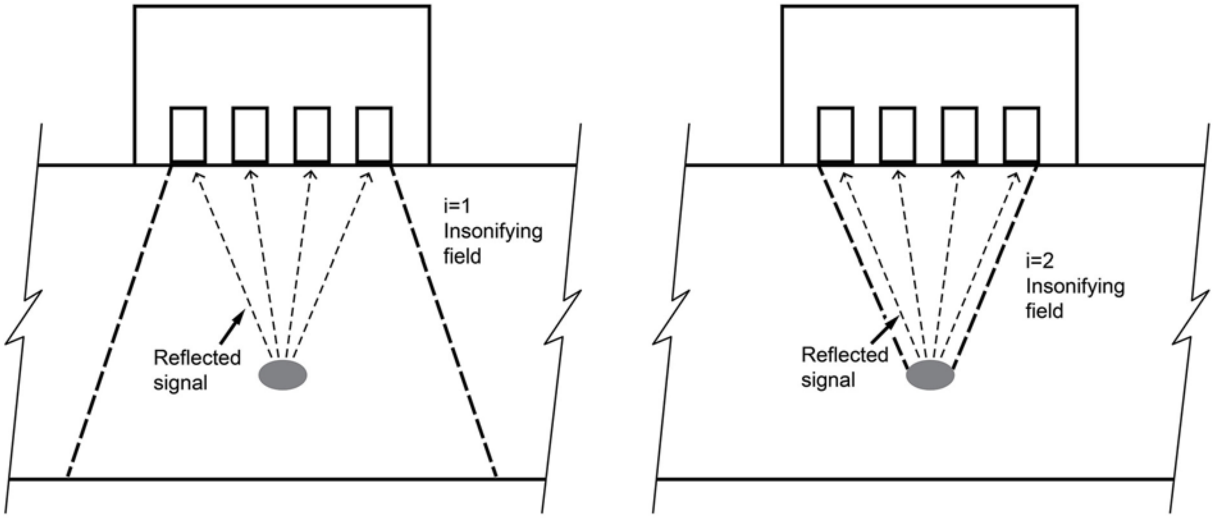

Figure 2.7. Illustration of the Time Reversal Technique (TRT) Concept for Focusing Ultrasonic Energy

2.5 Phased Array Asymmetrical Beam Time of Flight Diffraction

The phased array asymmetrical beam time-of-flight diffraction (PA-ATOFD) technique is implemented using a pair of 2D matrix array probes, with one probe serving as the transmitter and the other probe serving as the receiver (Ishida and Kitasaka 2013). Each probe is mounted on opposite sides of the flaw under investigation, similar to a regular time-of-flight diffraction (TOFD) configuration. However, the PA-ATOFD technique is based on the direct insonification of the crack tip as opposed to listening for the crack tip response when the base of the crack is insonified. With PA-ATOFD, the scan angle and focal depth of the transmitting and receiving probes may be arbitrarily adjusted, as indicated in Figure 2.8, to obtain the tip echo of the flaw from multiple scan angles. This enables improved discrimination of tip echo signals from sources of noise through synthesis (by the method named Multi-angle Synthesis Method (MA Method)) of the data from multiple scan angles and depths of focus as illustrated in Figure 2.9. A PowerPoint overview of how the PA-ATOFD technique was implemented in PARENT can be found in Appendix A.2, and a more detailed description of how PA-ATOFD was implemented in PARENT can be found in Appendix E.1.

In principle, the PA-TOFD technique could be applied on the component OD or ID and could handle geometrical complexities such as weld crowns or unlevel surfaces, although this would likely complicate the analysis. The PA-TOFD technique focuses on detecting crack tip signals and, thus, should be very accurate at depth sizing. The disadvantages of this technique include its large footprint with two matrix array probes, which may make it difficult to implement for certain components. Also, the technique could take a significant amount of time to implement as one must systematically scan through multiple depths of focus to identify the crack tip signal. However, if the technique is implemented in tandem with PA-UT or conventional UT for initial flaw detection and rough sizing, it is possible that the scan volume could be significantly reduced.

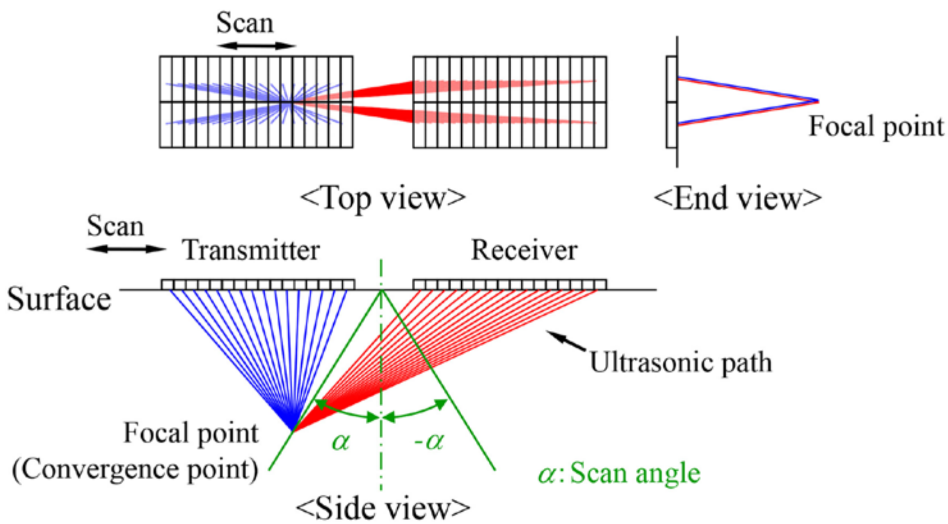

Figure 2.8. Schematic Illustration of the PA-ATOFD Technique

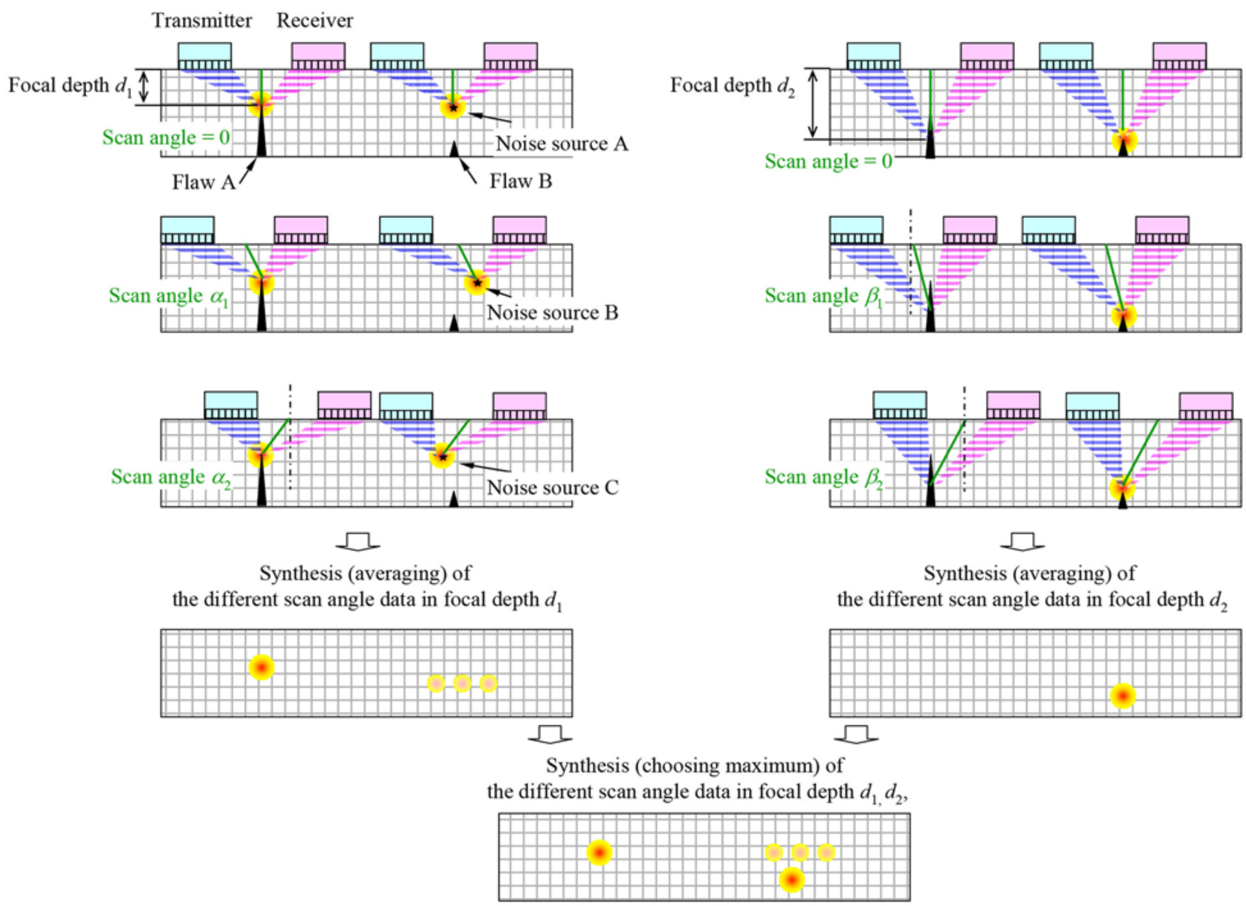

Figure 2.9. Data from Multiple Scan Angles and Depths of Focus are Synthesized in PA-ATOFD to Help Discriminate Crack Tip Signals from Noise

2.6 Phased Array Twin Probe

The phased array twin probe (PA-TP) method is very similar to the PA-ATOFD method except that both the transmitter and receiver are oriented in the direction perpendicular to the scan direction as opposed to parallel to the scan direction for the PA-ATOFD technique. An illustration of the PA-TP technique is provided in Figure 2.10. With PA-TP, the scan angle and focal depth of the transmitting and receiving probes may be arbitrarily adjusted to enable improved discrimination of tip signals from sources of noise through synthesis (by MA method) of the data from multiple scan angles and depths of focus as illustrated Figure 2.11. It is not immediately clear what advantages PA-TP may have over PA-ATOFD, or vice-versa, in terms of performance, but it is conceivable that geometry considerations could limit the use of one technique versus the other. For example, for inspection scenarios in which only single-side access to a weld is possible, the PA-TP could be implemented whereas PA-ATOFD could not. A PowerPoint overview of how the PA-TP technique was implemented in PARENT can be found in Appendix A.2, and a more detailed description of how PA-TP was implemented in PARENT can be found in Appendix E.1.

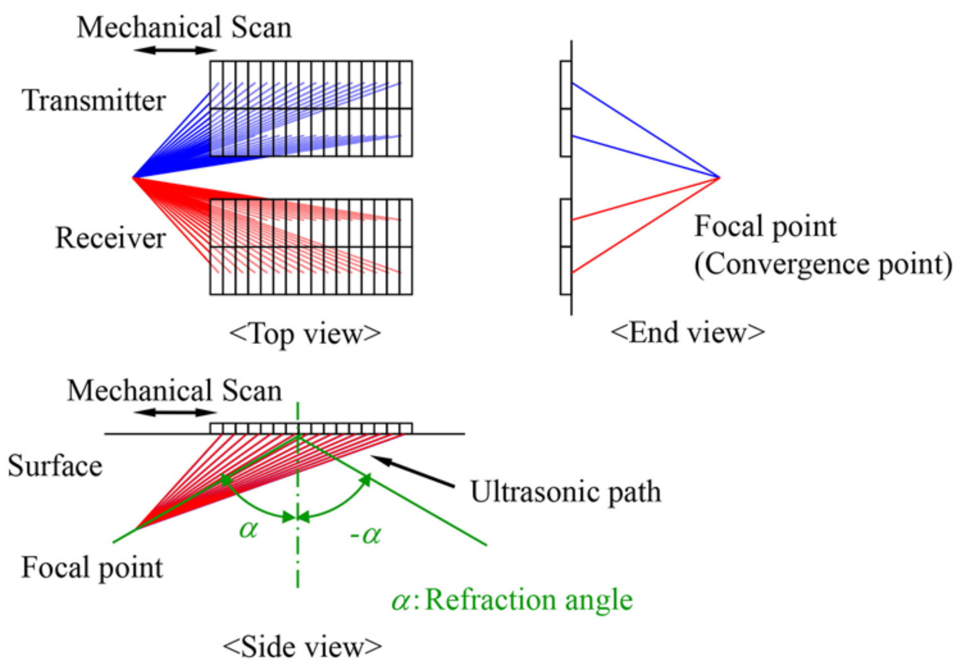

Figure 2.10. Schematic Illustration of the PA-TP Technique

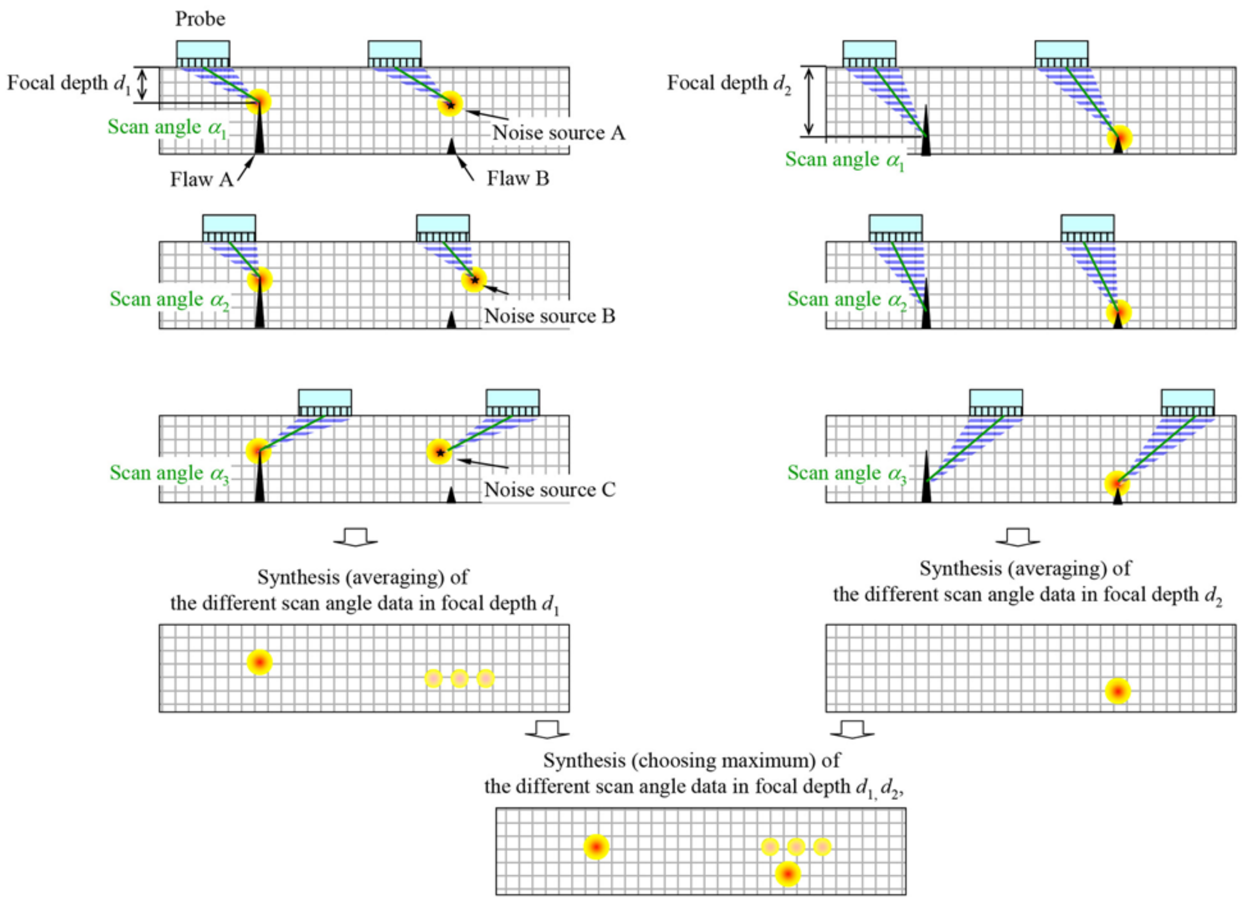

Figure 2.11. Data from Multiple Scan Angles and Depths of Focus are Synthesized in PA-TP to Help Discriminate Crack Tip Signals from Noise

2.7 Subharmonic Phased Array

Subharmonic phased array (SHPA), or subharmonic phased array for crack evaluation (SPACE), is an advanced ultrasonic testing technique that is based on the observation of nonlinear acoustic responses from material damage and phased array imaging techniques. More specifically, for crack evaluation, SHPA is based on the periodic contact (clapping) of the faces of tight cracks during the compressional period of an applied elastic wave, also referred to as contact acoustic nonlinearity (CAN). In this case, the clapping can occur if the amplitude of the elastic displacement is greater than the crack face separation (see Figure 2.12). In comparison to observations of higher harmonic generations, observations of subharmonic responses exhibit better selectivity to closed cracks (Ohara et al. 2008).

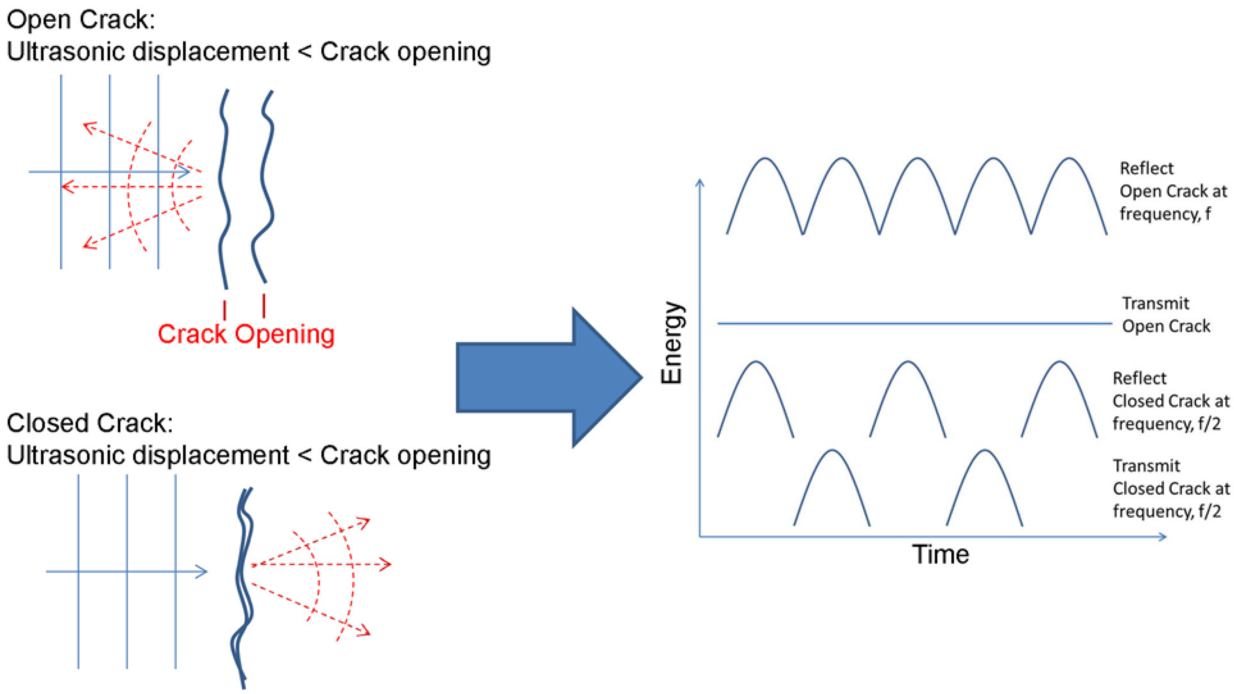

Figure 2.12. Illustration of the Crack Face "Clapping" Phenomena that is the Basis for Subharmonic Generation when Elastic Waves are Applied to Tight Cracks

SHPA provides fundamental array images at fundamental frequency f and subharmonic array images at the subharmonic frequency f/2, visualizing the open and closed parts of cracks, respectively. In PARENT, SHPA was implemented in a surface acoustic waves (SAW) mode to assess flaw detection and length sizing capability and in a bulk wave mode to assess flaw depth sizing capability (see Figure 2.13). As the figure shows, SAW mode requires mounting of the transducer on the same surface as the flaw's surface-breaking feature, while bulk wave mode is implemented similar to the way conventional UT and PA-UT would typically be performed in the field with the transducer mounted on the component OD surface.

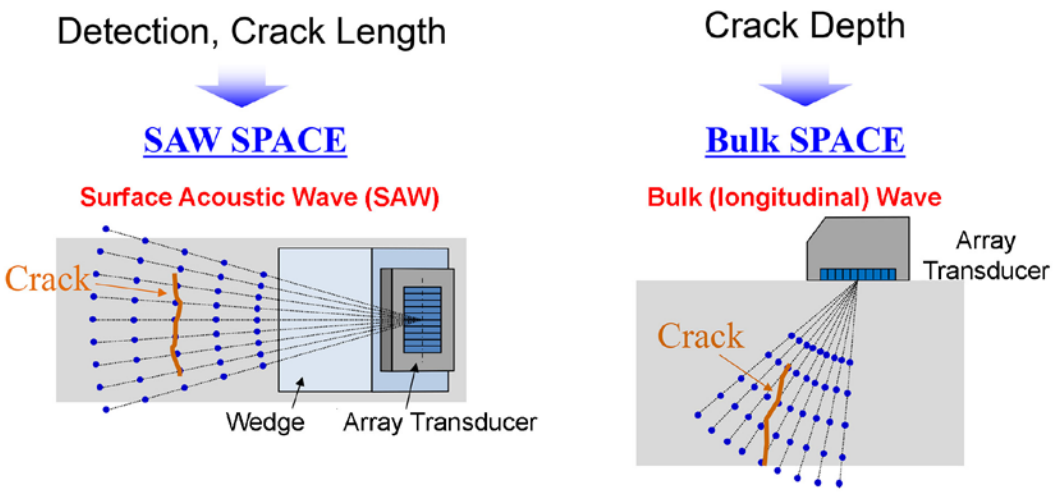

Figure 2.13. Illustration of SPACE Implementation in SAW Mode to Assess Detection and Length Sizing Capability and in Bulk Wave Mode to Assess Depth Sizing Capability

For PARENT, SHPA was implemented using a single phased array transducer for transmitting and receiving and using short burst waves for excitations. SHPA data analysis can be performed in a similar fashion to data analysis for regular phased array examinations. That is, through examination of A-scan data and image analysis of B-scans, C-scans, and D-scans (see Figure 2.14).

As noted, SHPA is particularly selective to closed or tight formed cracks but would not be useful for characterizing open cracks. Thus, characterization of both closed and open portions of cracks must be performed by analyzing images of data at the fundamental frequency, f (like regular phased array), in addition to the subharmonic image analysis. Otherwise, SHPA may be performed very similarly to regular phased array (PA-UT) examinations, with similar equipment requirements and data analysis procedures. A variant of SHPA, referred to as large amplitude excitation subharmonic UT (LASH), described in the next subsection, uses a large amplitude excitation pulse to enable characterization of flaws with larger crack openings using subharmonic data. A PowerPoint overview describing how the SHPA technique was implemented for PARENT can be found in Appendix A.2, and a more detailed description of how SHPA was implemented in PARENT can be found in Appendix E.3.

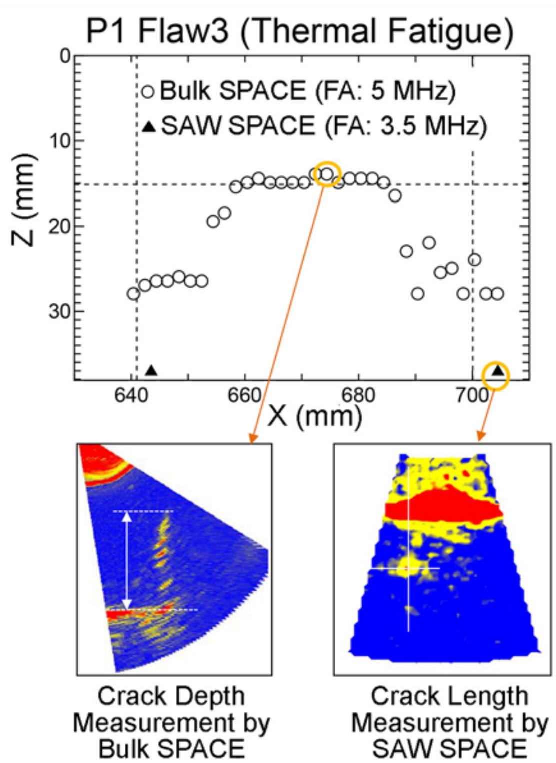

Figure 2.14. Illustration of SHPA Data Analysis for Length and Depth Sizing of Flaws

2.8 Large Amplitude Excitation Subharmonic

Large amplitude excitation subharmonic UT (LASH) is a variant of SHPA, described in the previous subsection, utilizing a large amplitude excitation pulse to generate elastic waves with larger displacement so that selectivity for flaws with crack openings relevant to field conditions can be obtained. Implementation of LASH differs in comparison to the implementation described for SHPA in the last subsection in that a transmit/receive arrangement is used to facilitate use of separate high-voltage transducer for excitation of elastic waves with large displacement. Data analysis can be performed similar to SHPA and PA-UT through analysis of A-scans, B-scans, C-scans, and D-scans.

As shown in Figure 2.15, this variant of LASH requires a separate high-voltage transducer for excitation in addition to the array transducer for signal reception. However, development of high-voltage array transducers could eliminate the need for the extra transducer for excitation. A PowerPoint overview of how LASH was implemented in PARENT can be found in Appendix A.2, and a more detailed description of how LASH was implemented in PARENT can be found in Appendix E.4.

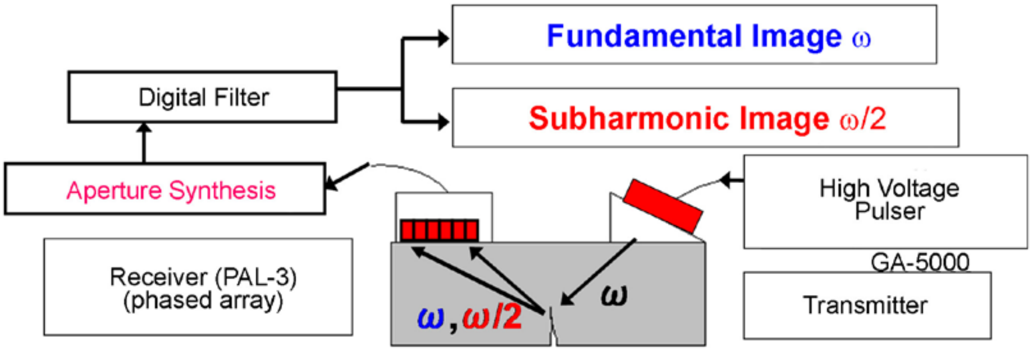

Figure 2.15. Depiction of the LASH Technique Implementation

2.9 Higher Harmonic Ultrasonic Technique

The higher harmonic ultrasonic technique (HHUT) for crack detection is also based on the phenomenon of CAN, as illustrated in Figure 2.12. Higher harmonics are generated, in addition to subharmonics, because of the nonlinearity induced in signals as they interact with the crack faces (illustrated in Figure 2.16). As a result, the acoustic waveform becomes distorted and the higher harmonic frequency components are generated in the transmitted wave or in the reflected wave from the crack.

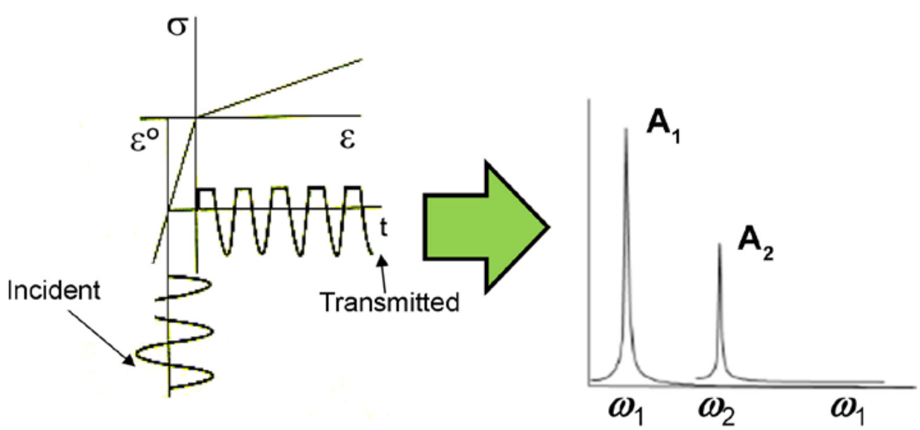

Figure 2.16. Illustration of Higher Harmonic Generation Because of the CAN Phenomenon

Thus, it would be possible to detect closed cracks by monitoring the magnitude of the higher harmonic frequency component generated in the transmitted or the reflected wave. The classical approach to describe the nonlinearity of a homogeneous elastic media is based on Taylor expansion of the dependence between the stress and strain tensors in the material and considers the coefficients of this expansion as the parameters of nonlinearity. In a simple example of one-dimensional longitudinal deformations in an isotropic solid, this expansion can be taken in a scalar form:

$$\sigma = \rho 0\, \mathrm{cl}^2 \left(\varepsilon + \beta\varepsilon^2 + \gamma\varepsilon^3 + \ldots \right), \tag{2.2}$$

where ρ0 and cl are the density and the longitudinal sound speed in the medium, respectively; σ is the stress, ε is the strain; and β, γ, are the non-linear parameters, which characterize, respectively, the quadratic and cubic non-linearity of the medium. Usually, the relative nonlinear parameter (β′) defined by the ratio of the second order harmonic frequency magnitude to the power of the fundamental frequency magnitude is used as the monitoring parameter (Jhang 2000), although the generation of higher order harmonics can provide useful monitoring parameters as well. Overviews of how HHUT was implemented in PARENT can be found in the Appendices A.1 and A.2. More detailed descriptions of how HHUT was implemented in PARENT can be found in Appendices C.7 and E.5.

HHUT can be implemented in pulse-echo (PE) or transmit-receive (TR) modes as shown in Figure 2.17. The technique could be implemented on the component ID or OD. To ensure sufficient interaction with the crack faces, the transducers should be mounted at an angle with respect to the crack faces, or perpendicular to them. The advantage of this technique compared to conventional UT is its sensitivity to closed cracks. However, compared to the subharmonic techniques described previously, higher harmonics are not as selective for closed cracks, although this may not necessarily be viewed as a drawback for all applications. A disadvantage of HHUT is that physical understanding of the technique is incomplete. As a consequence, quantitative characterization of flaws by HHUT will be difficult with a single measurement and may require relative comparison to responses obtained from already well characterized flaws.

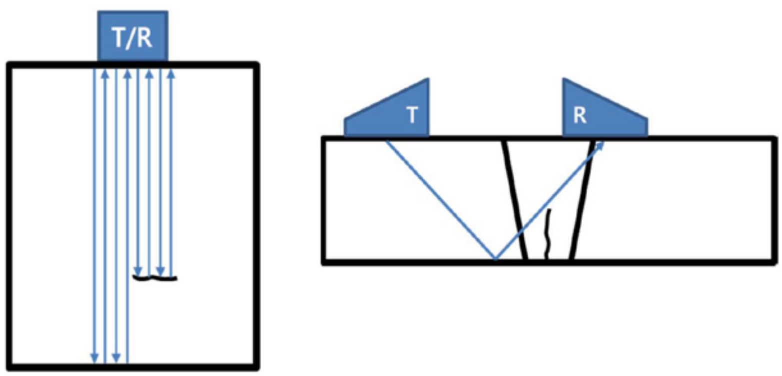

Figure 2.17. Illustration of HHUT Implementation in PE (left) and TR (right) Modes

2.10 Nonlinear Resonant Ultrasound Spectroscopy

Nonlinear resonant ultrasound spectroscopy (NRUS) is another acoustic technique, in addition to the SHPA, LASH, and HHUT techniques described earlier, in which material characterization or damage assessment is based on the observation of nonlinear acoustic/ultrasonic responses. With NRUS, signals are applied over a wide frequency sweep to specimens to observe material nonlinearity as a result of damage manifested as a shift in resonant frequency and damping of the resonant peak amplitude as the excitation signal amplitude increases. An illustration of this for cyclic fatigue crack growth in a compact tension (CT) is shown in Figure 2.18.

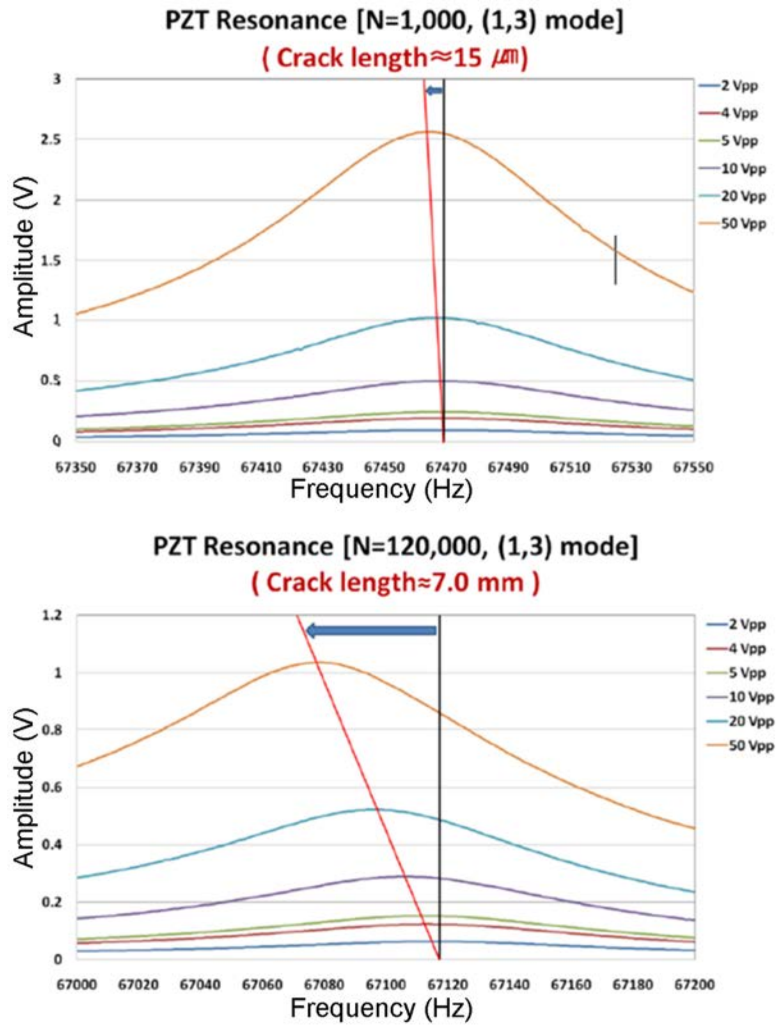

Figure 2.18. Resonance Frequency Shift in a CT Specimen in the Early Stage of Crack Initiation (top) and a CT Specimen with Crack Length of 7.0 mm (bottom)

NRUS can be implemented by permanent mounting of piezoelectric sensors on specimen surfaces, as illustrated in Figure 2.19. Resonant peaks can be generated through application of swept frequency excitation and the resonant modes can be identified with an iterative solver that matches observed spectra with predicted spectra. A PowerPoint overview of how NRUS as implemented in PARENT can be found in Appendix A.1 and a more detailed description of the implementation can be found in Appendix C.1. An advantage of NRUS is that it can be sensitive to very early stages of degradation like other nonlinear acoustic/ultrasonic techniques. Another advantage is that it is suitable for continuous monitoring and can monitor damage progression over an extended region without scanning of the sensors. However, physical models of nonlinear elastic responses in materials are incomplete at this stage; thus, it may be difficult to characterize damage based on a single measurement. In addition, because NRUS may be implemented to monitor over an extended region, it may be difficult to precisely locate the detected damage by NRUS.

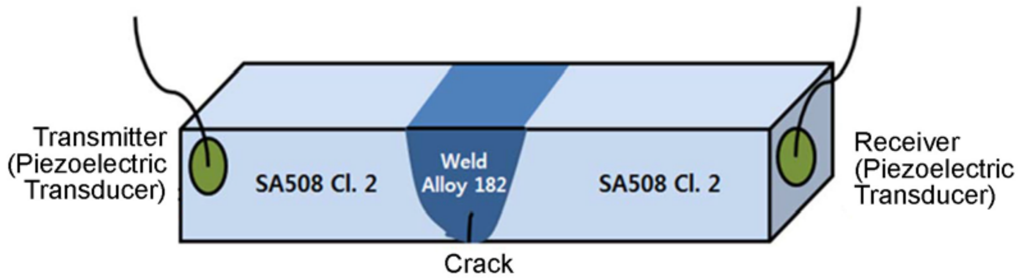

Figure 2.19. Schematic Drawing of Possible Piezoelectric Sensor Configuration

2.11 Guided Ultrasonic Waves

Guided ultrasonic waves (GUW) refers to an emerging class of techniques based on the propagation of low frequency acoustic/ultrasonic signals through materials. Analogous to the propagation of electromagnetic waves in bounded media, guided ultrasonic waves are formed when the dimensions of the test material and wavelength are on similar order of magnitude or when the dimensions of the test material are much less than the wavelength of the probing acoustic/ultrasonic energy. In this regime, the interactions of the waves with material boundaries is very significant and the multiple reflecting waves constructively and destructively interfere such that new modes of propagation are generated with velocity that is dependent on component geometry, dimensions, and frequency (see Figure 2.20). This is in contrast to bulk ultrasonic wave propagation in which only two modes (longitudinal and shear) propagate through materials with a velocity that is independent of the component geometry, dimensions, and frequency. The topic of GUW is treated in multiple textbooks including the book by Rose (1999).

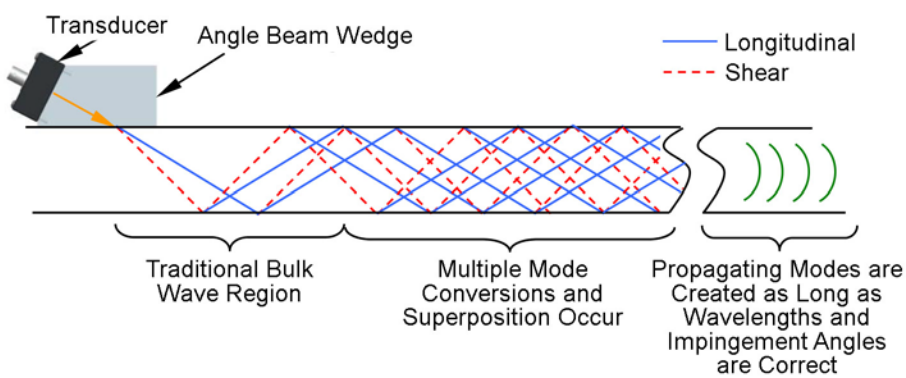

Figure 2.20. Illustration of GUW Formation and Propagation in Test Material

The dependence of GUW mode velocity on frequency is a phenomena known as dispersion. The design of GUW inspection procedures and the analysis of GUW data is greatly assisted by the calculation of dispersion curves for a given applications. The dispersion curves show the relationship between the phase velocity and group velocity for several modes as a function of frequency, as illustrated in Figure 2.21. Like conventional UT, it is possible to implement GUW techniques in pulse-echo (PE) or pitch/catch (PC) mode and it can also perform both ID and OD inspections. A PowerPoint overview of how GUW was implemented in PARENT can be found in Appendix A.1 while a more detailed description of its implementation can be found in Appendix C.5.

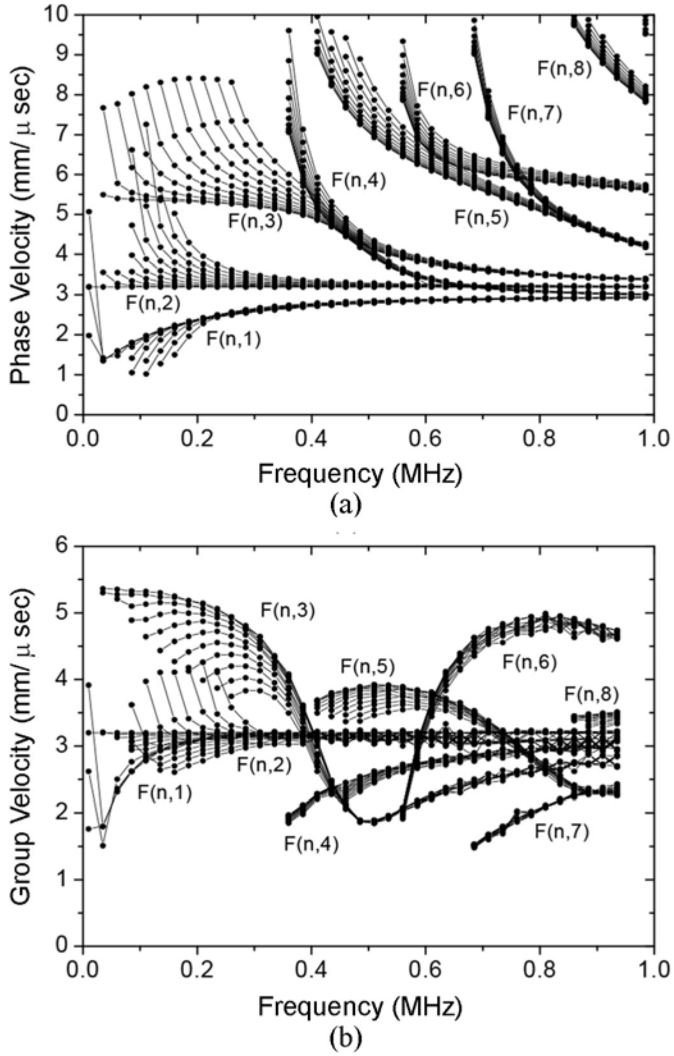

Figure 2.21. Guided Wave Dispersion Curves on Cylindrical Coordinate: (a) phase velocity dispersion curve; (b) group velocity dispersion curve

The first widespread application of GUW for NDE was in the long-range inspection of petrochemical pipelines for corrosion (Lowe et al. 1998). Since then, the number of GUW applications has increased, and in the nuclear power industry, GUW have been given serious consideration for the inspection of buried pipelines (EPRI 2008). These applications highlight the major benefits of GUW, which is the ability to perform fast inspections over a large distance in test materials, and the ability to inspect regions that may be inaccessible by conventional NDE equipment. However, GUW can be complex to implement in practice, often requiring systems tailored for specific applications. In addition, the analysis of GUW signals can be complicated, especially if multiple modes are propagated in the test material simultaneously.

2.12 Laser Ultrasound Visualization

Laser ultrasound is a technique in which ultrasound is transmitted and/or received in a material, similar to a traditional piezoelectric transducer (PZT). However, laser ultrasound allows the ultrasound to be transmitted and received from a distance, and without actual physical contact with the component under testing. A laser can be used to introduce the ultrasound via thermoelastic or ablative effects in the material surface (Rose 1984; Murray and Wagner 1999). A laser system can also be used to detect ultrasound via interferometry, photo electromotive force (photo-emf) detectors, or the optical beam deflection technique (Murfin et al. 2000). The laser ultrasound visualization (LUV) technique implemented in PARENT uses PZT sensors mounted on the component at discrete locations for signal detection. A laser is raster scanned over the surface of the test component and the received signals can be mapped with the laser ultrasound generated at different points. After a complete scan, the data can be processed and displayed as a movie clip for evaluation (see Figure 2.22). A more detailed description of the proposed LUV technique can be found in Appendix D.4.

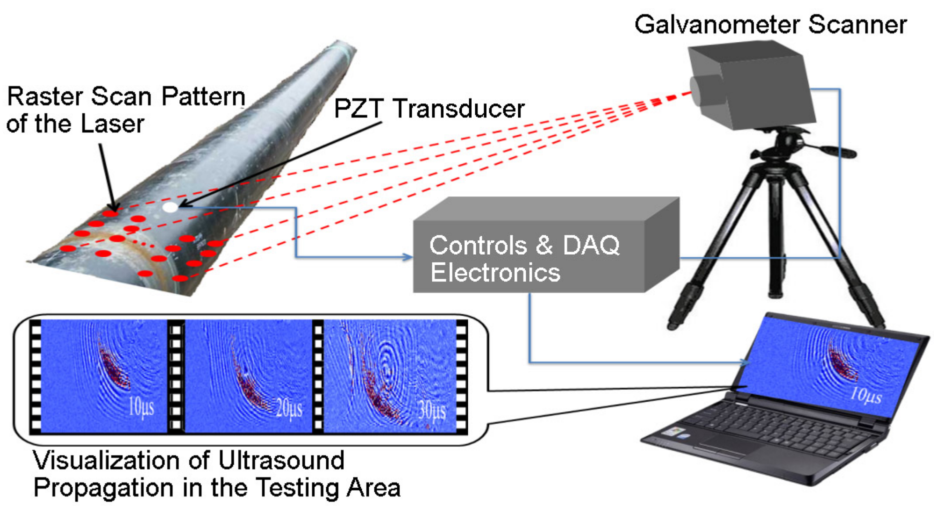

Figure 2.22. Schematic of the Envisioned LUV System

The obvious advantage of LUV is the stand-off mode of ultrasound generation, which can enable inspection of components that are otherwise difficult to access by more conventional means. Enhanced visualization schemes promise to make detection and characterization easier. Laser ultrasound techniques, in general, can be used to detect cracks that break the illuminated surface. However, depth sizing with laser ultrasound is more difficult and the ability of laser ultrasound to do so is undetermined. LUV is most suited for OD applications.

2.13 Ultrasound Infrared Thermography

Ultrasound infrared thermography (UIRT) is based on the detection of thermal energy generated when elastic energy is absorbed by a defect and converted to thermal energy through thermo elastic effects. An illustration of the general concept is provided in Figure 2.23. The result is an infrared image in the test specimen to which standard image analysis techniques may be applied to characterize defects based on temperature differences (see Figure 2.24). The main UIRT techniques include pulsed, phase lock-in, or a combination of both (Dillenz et al. 2000; Maldague 2001). A PowerPoint overview of how UIRT was implemented in PARENT can be found in Appendix A.1, while a more detailed description is provided in Appendix C.4.

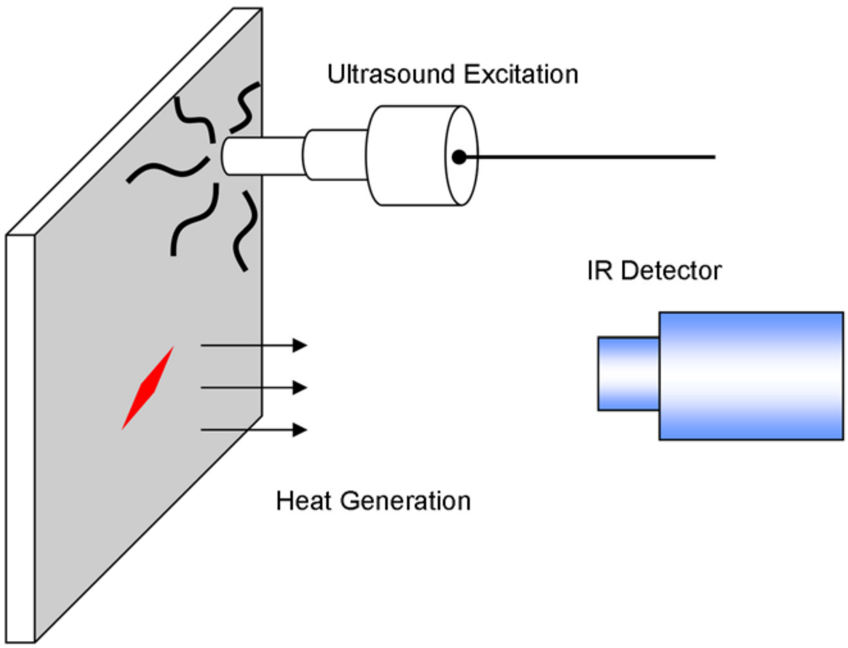

Figure 2.23. Illustration of the UIRT Concept

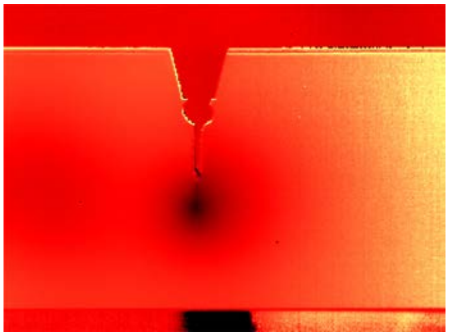

Figure 2.24. UIRT Image of a Test Specimen with Crack

With lock-in phase UIRT, amplitude and phase information about the thermal waves emitted from the specimen is preserved for several frequencies. The advantage of this is that it enables characterizing the depth of a source of thermal emissions within the test component. With pulsed phase lock-in thermography, broadband thermal signals arriving at each pixel of an infrared (IR) detector camera are analyzed using Fast Fourier Transform (FFT) analysis. The advantage of UIRT is that it potentially enables more rapid examination of large areas based on camera images in contrast to techniques that would require a point-by-point raster scan. The technique could be used to perform both OD and ID inspections. The potential disadvantage of the technique is that it requires a low thermal noise background so that flaws could be imaged reliably.

3.0 Eddy Current Techniques

Overview descriptions for eddy current techniques employed in the open testing portion of PARENT are provided in this section including a description of exciter-pickup eddy current techniques (EP-ECT), which refer to eddy current techniques that employ a coil for generating an excitation field and separate sensor to detect perturbations in the field because of flaws. This contrasts with conventional ECT in which the same coil may be used for both field excitation and detection. The controlled excitation eddy current technique (CE-ECT) is also a variant of PE-ECT but is described separately here because the probe is configured specifically to enhance its ability for characterizing deep flaws. Finally, overview descriptions for the orthogonal coil eddy current technique (OC-ECT) and pulsed excitation eddy current technique (PE-ECT) is included. In addition to CE-ECT, PE-ECT can be distinguished from conventional ECT in that it is often implemented for the purpose of characterizing flaws in the depth dimension.

3.1 Exciter-Pickup Eddy Current Techniques

In practice, an eddy current probe consists of one or more coils with the axis alignment most often perpendicular or parallel to the inspection surface normal. An alternating current source is applied to the one or more coils, generating magnetic fields. These magnetic fields induce eddy currents in the conducting materials when the probe is positioned nearby (see Figure 3.1). Flaws and defects in the test material impede the flow of eddy currents manifesting as a change in the measurable eddy current coil impedance. An important parameter for eddy current testing is the skin depth,

$$\delta = \sqrt{\frac{1}{\pi f \sigma \mu}}, \tag{3.1}$$

which provides a measure of the depth to which eddy current fields can penetrate in a test material. As can be seen from Eq. (3.1), this quantity depends on the coil frequency, f, and electrical conductivity, σ, of the test material (μ is the magnetic permeability). Thus, in metal components, the depth of penetration is usually small and the eddy current technique is often limited to surface examinations. Multi-coil techniques include separate coils for the generation of eddy current fields in the test material and for detection of the fields at the surface, as illustrated in Figure 3.2. These types of probes may also be referred to as reflection probes, driver-pickup, exciter-pickup, or send-receive probes. This contrasts with conventional ECT in which the same coil is used for both field generation and for signal reception. In PARENT, two teams applied basic multi-coil techniques. A PowerPoint overview of how one of the techniques was implemented in PARENT can be found in Appendix A.4, while a more detailed description can be found in Appendix D.1. A PowerPoint overview of how the second technique (referred to as the advanced ECT technique [AECT]) was implemented can be found in Appendix A.2, and a more detailed description of how AECT was implemented in PARENT can be found in Appendix E.7.

The advantage of eddy current techniques over ultrasonic techniques is that they are usually more sensitive to small defects and the probes do not require coupling to the test material surface. As noted, a significant disadvantage of eddy current techniques is that they are often relegated to surface inspections and are not very useful for characterizing the depth of flaws. In addition, the increased sensitivity of ECT can make it more prone to false calls from the pick-up of signals from superficial surface imperfections (such as scratches) and ECT techniques can be sensitive to lift-off variations and variations in material conductivity.

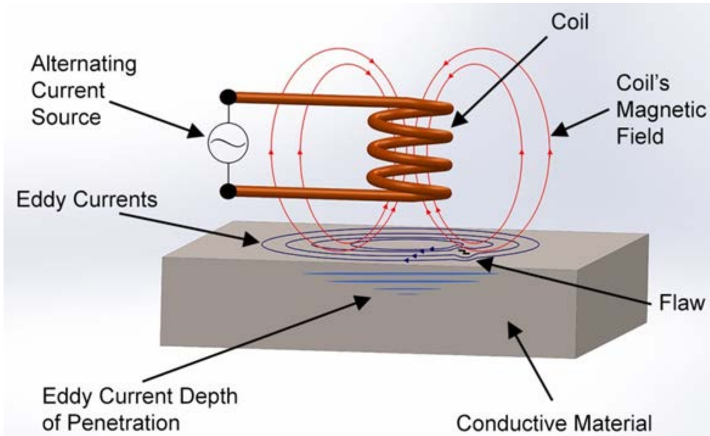

Figure 3.1. Depiction of a Single Coil Eddy Current Probe with an Alternating Current Excitation, Induced Magnetic Fields, and Induced Eddy Currents. Disturbance of eddy current flow can be caused by existence of a defect.

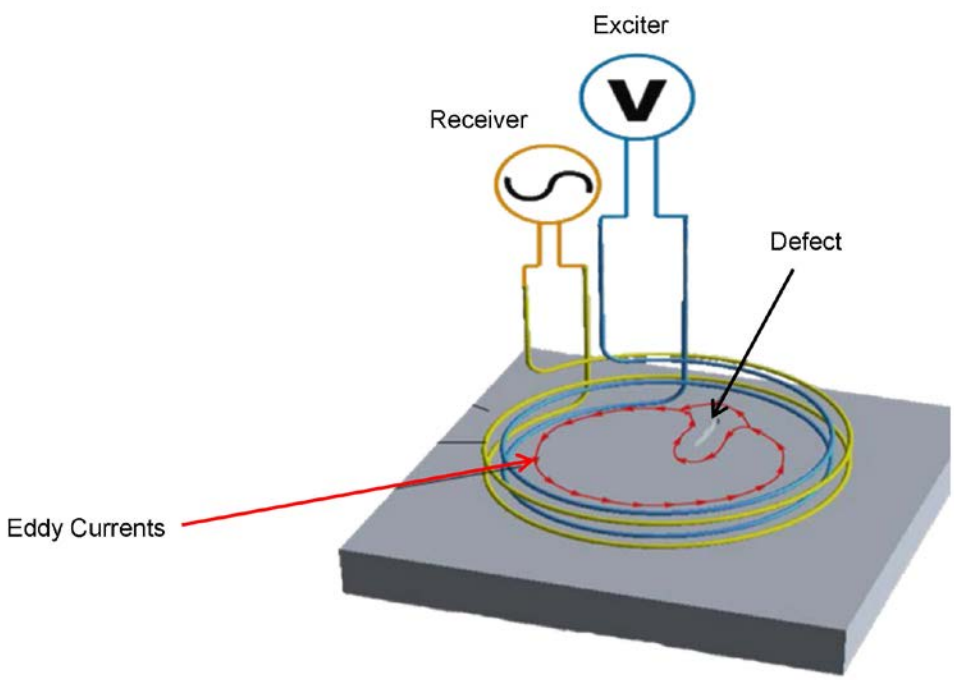

Figure 3.2. Schematic Illustration of an Eddy Current Probe with Separate Coils for Field Excitation and for Signal Detection

3.2 Controlled Excitation ECT

Controlled excitation eddy current (CE-ECT) is another type of exciter-pickup technique with coils configured so that eddy current response can be correlated with crack depth, even for deep cracks. In particular, the probe is designed such that the phase response shows correlation with depth for deep cracks, as illustrated in Figure 3.3. A schematic of the particular CE-ECT probe implementation for PARENT is provided in Figure 3.4. This particular probe has two exciter coils oriented with their axes perpendicular to the test surface normal and a pick-up sensor is located between the two exciter coils. A PowerPoint overview of CE-ECT and how it was implemented in PARENT is included in Appendix A.2, and a more detailed description of its implementation can be found in Appendix E.8.

The phase response of the CE-ECT to deep cracks is a significant advantage of CE-ECT over other eddy current techniques. However, the phase response is also dependent on other flaw parameters such as length, cross section, etc. More information is needed to fully understand the effects of other flaw parameters on the phase response. In addition, the footprint of the CE-ECT can be quite large, because the pick-up sensor must be separated sufficiently from the exciter coils. This may limit the ability to deploy the technology on component regions with poor accessibility.

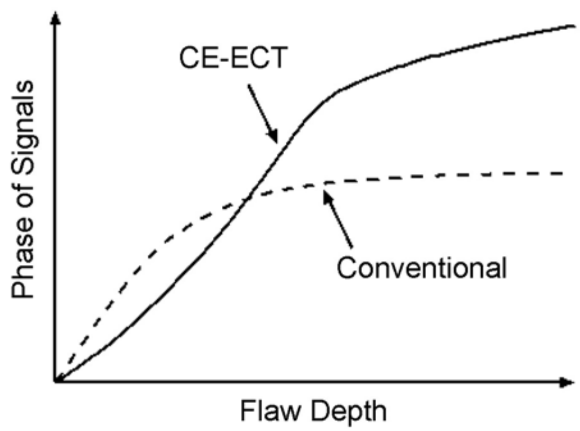

Figure 3.3. Illustration Showing that the Phase Response of CE-ECT has a Significant Correlation to Flaw Depth over a Large Range of Flaw Depth Values, Including for Deep Cracks

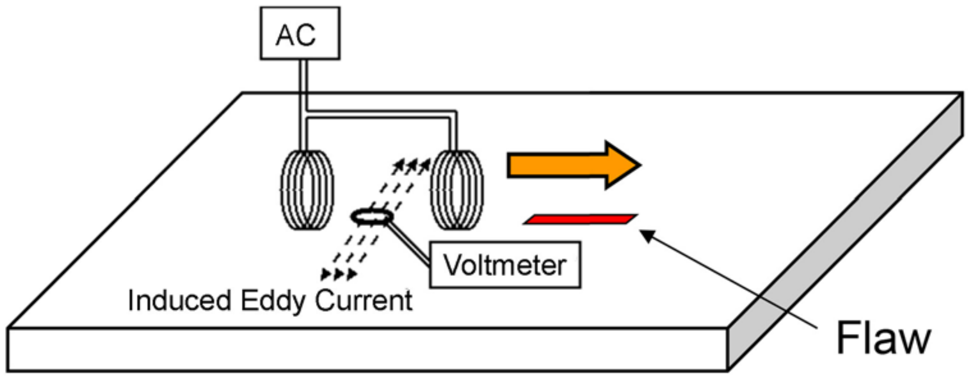

Figure 3.4. Illustration of the CE-ECT Probe for Measuring the Depth of Flaws

3.3 Orthogonal Coil Array Eddy Current Technique

The orthogonal coil array eddy current technique (OC-ECT) was implemented in PARENT using a commercial eddy current probe with an array of orthogonal coil pairs. The single orthogonal coil pair configuration has also been referred to as "plus-point" because when viewed from the test piece the intersecting orthogonal coils look similar to a plus sign (Figure 3.5). The OC-ECT technique is a differential eddy current technique meaning that the output of one coil is referenced to the output of the other coil. Differential eddy current probes are typically less sensitive to lift-off and surface irregularities. One advantage of OC-ECT is that it has directional sensitivity to flaws, making it possible to distinguish between axial and circumferential defects. The orthogonal coil configuration helps minimize the influence of flaw orientation with respect to the probe performance as defects that are parallel to the current flow can be missed. Rotation of the OC-ECT probe can also be performed to further minimize the influence of flaw orientation. A PowerPoint overview of how OC-ECT was implemented in PARENT can be found in Appendix A.2, and a more detailed description of its implementation can be found in Appendix E.6.

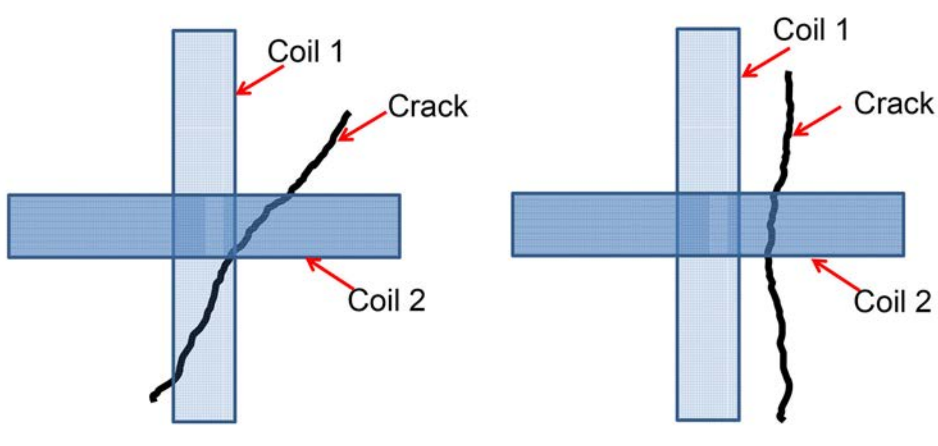

Figure 3.5. Illustration of Orthogonal Coil Pair and Relative Orientation to Surface Crack Profiles

3.4 Pulsed Excitation Eddy Current Technique

Pulsed excitation eddy current technique (PE-ECT) is an eddy current technique that relies on low duty cycle pulse excitations (Lebrun et al. 1997). This contrasts with most ECT concepts, which are based on continuous sinusoidal wave excitation at a single frequency (see Figure 3.6). The low duty cycle pulse results in a wide frequency band excitation field that allows deeper penetration into a test component owing to the lower frequency components (up to 30 mm) (Lee et al. 2012). The penetration depth can be tuned by changing the duty cycle of these pulses, with wider pulses containing stronger low-frequency components (Abidin et al. 2009). Besides the ability to penetrate significant depth, PE-ECT has other advantages over conventional ECT techniques such as lower power consumption and the ability to generate a richer set of data. However, the instrumentation used to drive pulsed sources can be more complex than for a conventional ECT system. In addition the interpretation of PE-ECT signals can require considerable expertise. A PowerPoint overview describing how PE-ECT was implemented in PARENT can be found in Appendix A.1. A more detailed description of how PE-ECT was implemented in PARENT can be found in Appendix C.2.

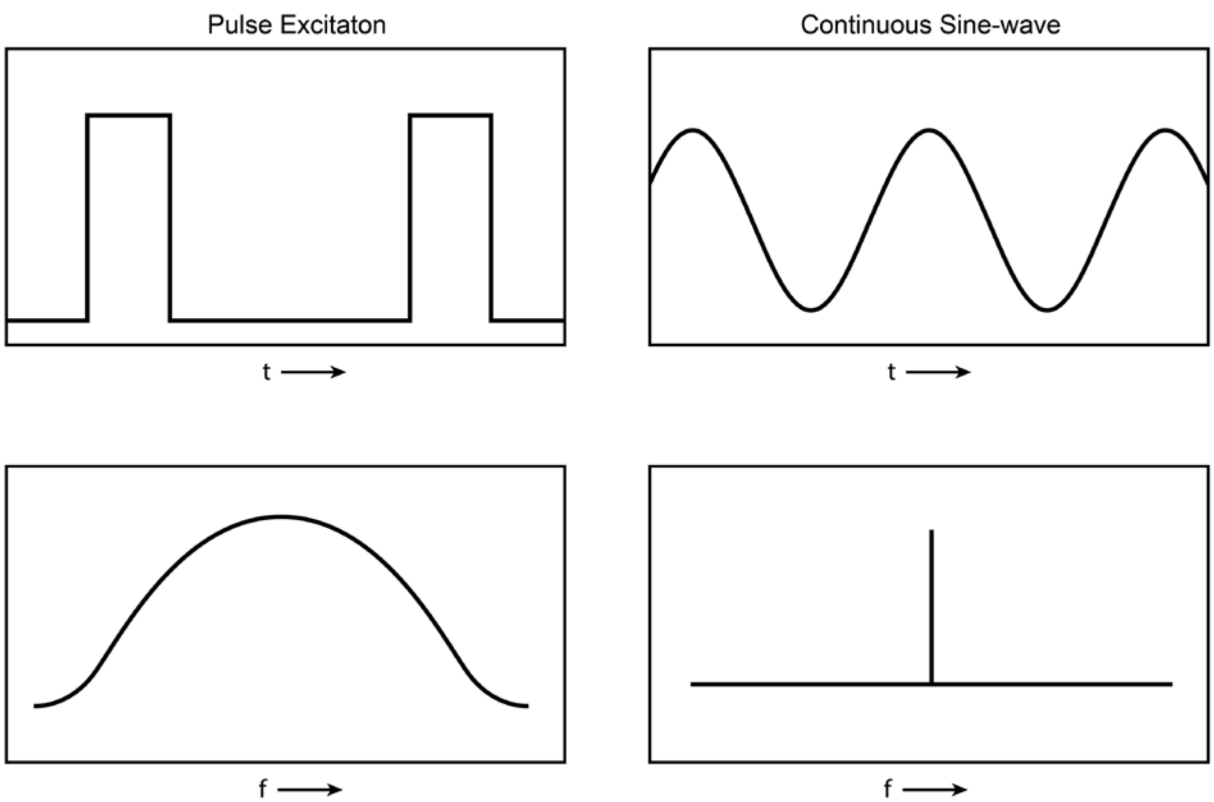

Figure 3.6. Comparison of Pulsed Excitation for PE-ECT (right) to Continuous Sine-Wave Excitation for Conventional ECT (left) and Illustration of the Frequency Spectrum Associated with Each Type of Excitation Source

4.0 Other Techniques

The section describes other techniques implemented in the open testing portion of PARENT and includes the microwave near field microscopy technique and radiographic techniques.

4.1 Microwave Near Field Microscope

Microwave near field microscope (MNFM) is an electromagnetic NDE technique that is based on sensing impedance changes as a result of the obstruction of surface excitation currents from discontinuities. In this respect, MNFM is similar to ECT, but operates at much higher frequencies such that the electromagnetic field does not penetrate the surface. Whereas ECT may operate approximately from 0.1 to 10 MHz, MNFM may be performed in a frequency range from approximately 1 GHz to over 100 GHz (Zoughi and Kharkovsky 2008). MNFM sensing is based on open-ended waveguides in which the standing wave pattern in the waveguide will change in response to the terminating impedance. Thus, when the tip of an MNFM probe is placed near a conducting surface and a surface-breaking discontinuity disrupts the flow of currents, it represents a change in the terminating impedance and will alter the standing wave pattern (see Figure 4.1).

Zoughi and Kharkovsky (2008) describe two types of interactions through which MNFM can not only indicate crack detection, but also provide information about crack width and depth. In dominant mode interaction (for instance, transverse electromagnetic mode), MNFM is performed primarily by observing the perturbations in the dominant mode as a result of interactions with surface-breaking discontinuities. In addition to affecting the dominant mode, the presence of cracks will result in the generation of higher order modes. Thus, MNFM can be used to characterize flaws based on both the analysis of dominant mode perturbations and higher order mode generations. MNFM is able to detect very tight cracks and is able to sense cracks that may be masked by layers of paint or corrosion products. Similar to conventional ECT, MNFM is primarily a surface inspection technique, although its ability to characterize the width and depth of flaws sets it apart from conventional ECT. A PowerPoint overview of how MNFM was implemented in PARENT is provided in Appendix A.2, and a more detailed description of its implementation can be found in Appendix E.9.

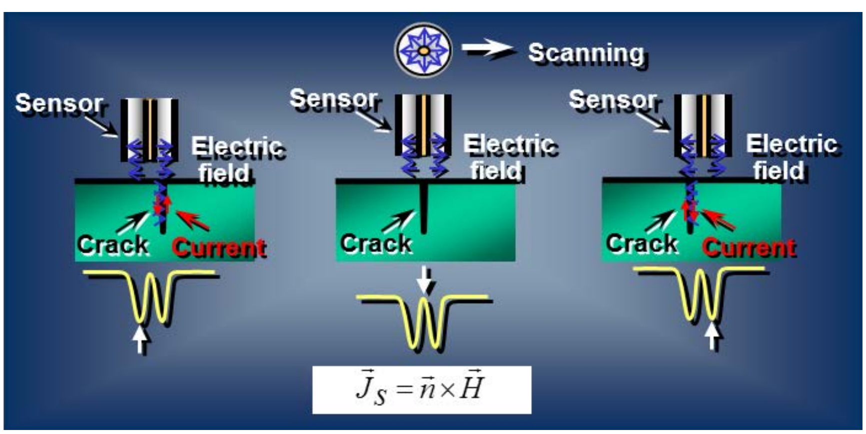

Figure 4.1. Illustration of the MNFM Technique for Crack Detection

4.2 Radiography Techniques

A radiographic inspection system uses a source of radiation (x-rays or gamma rays) to irradiate the specimen under test. X- or gamma rays penetrate the specimen, and are absorbed, scattered or otherwise attenuated when passing through the material. A detector of some form is used to collect and record the transmitted rays as illustrated in Figure 4.2. Several different sources are available (with different energy levels) (Halmshaw 1987) enabling the inspection of specimens with different thicknesses. The inspection itself requires a balance between the source energy, source-to-specimen distance, source-to-detector distance, and exposure time. Conventional radiographic inspection requires access to both sides of the specimen, with the source and detector placed on either side of the test specimen. The quality of the radiographs is usually determined through the use of image quality indicators (IQI) or penetrameters. Details on radiographic inspection, along with information on the choice of IQI devices, may be found in several publications, for instance Cartz (1995).

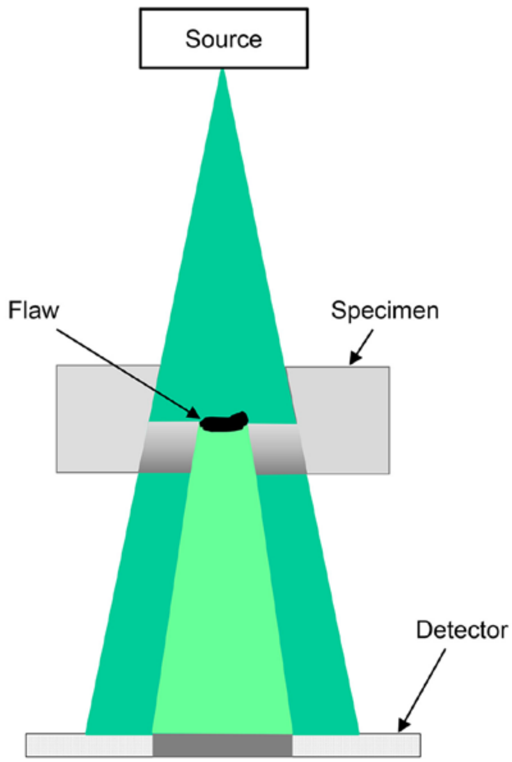

Figure 4.2. Illustration of a Radiographic Examination and Interaction of Source X-rays with Density Discontinuities such as Flaws

In conventional radiography, the location and orientation of the specimen is fixed relative to the source and detector location. The result is a radiograph where the orientation of any flaws is fixed with respect to the source and detector locations. The effectiveness of conventional radiography techniques for inspection of planar flaws is especially sensitive to the flaw orientation (see Figure 4.3). An alternative approach is to subject each region on the specimen to multiple radiographic inspections. Each inspection is performed with the specimen oriented at a different angle relative to the source and/or detector. While this technique improves the information on flaws (potentially enabling better detection and through-wall sizing), the approach tends to have higher costs. A common variation on this approach is computed tomography (CT), where multiple view angles are used, and the resulting two-dimensional data combined to create three-dimensional (3D) images of the specimen. Typically, CT scans require a computer-controlled scanner system to obtain precision control of view angles (Ewert et al. 2007). A description of how radiography techniques were implemented in PARENT can be found in the Appendices B.6 and B.7.

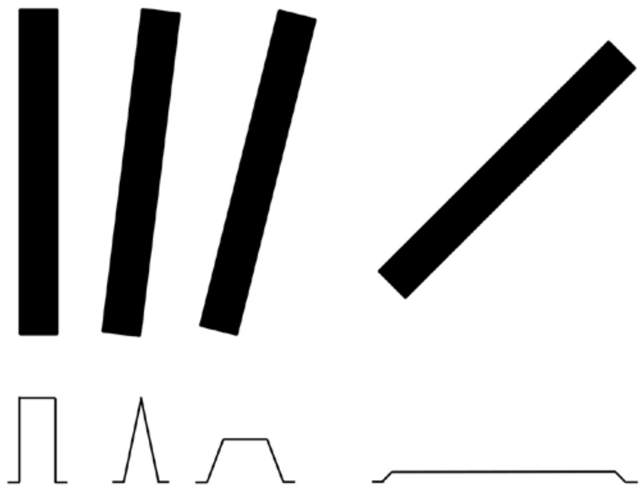

Figure 4.3. Illustration Depicting the Sensitivity of Conventional Radiography Signal to Planar Flaw Orientation

5.0 Closing

This report documents the NDE techniques utilized in the open testing portion of PARENT. A detailed description and discussion of the test blocks and the testing results will be provided in the final open testing report, which is scheduled for completion in summer of 2015. Conclusions regarding the performance of each NDE technique will be withheld until the analysis of open test data is completed and the conclusions will be documented in the final report.

6.0 References

Abidin IZ, C Mandache, GY Tian and M Morozov. 2009. "Pulsed Eddy Current Testing with Variable Duty Cycle on Rivet Joints." *NDT & E International* 42:599-605.

Cartz L. 1995. *Nondestructive Testing*. ASM International, Materials Park, Ohio.

Dillenz A, D Wu, K Breitruck and G Busse. 2000. "Lock-in Thermography for Depth Resolved Defect Characterisation." In *15th World Conference on Nondestructive Testing*. October 15-21, 2000, Rome, Italy. The Italian Society for Nondestructive Testing and Monitoring Diagnostics.

Elbern AW and L Guimaraes. 1999. "Synthetic Aperture Focusing Technique for Image Resaturation." In *International Symposium on NDT Contribution to the Infrastructure Safety Systems (NDTISS'99)*. November 22-26, 1999, Torres, Brazil. UFSM, Santa Maria, RS, Brazil.

EPRI. 2008. *Recommendations for an Effective Program to Control the Degradation of Buried Pipe*. Report No. 1016456, Electric Power Research Institute (EPRI), Palo Alto, California.

Ewert U, G-R Jaenisch, K Osterloh, U Zscherpel, C Bathias, M Hentschel, A Erhard, J Goebbels, H Hanselka, J Nuffer and W Daum. 2007. "Performance Control and Condition Monitoring." In *Springer Handbook of Materials Measurement Methods*, eds: H Czichos, T Saito and L Smith. Ch. 16.

Fink M. 1992. "Time Reversal of Ultrasonic Fields. I. Basic Principles." *IEEE Transactions on Ultrasonics, Ferroelectrics and Frequency Control* 39(5):555-566.

Fink M. 1999. "Time-Reversed Acoustics." *Scientific American* November:91-97.

Halmshaw R. 1987. "X-ray Real-Time Imaging for Weld Inspection: IIW 3rd Progress Report." *British Journal of Nondestructive Testing* 29(6):426-428.

Ishida H and J Kitasaka. 2013. "Development of a Phased Array TOFD UT Method to Measure the Depth of SCCs in Dissimilar Metal Weld." In *9th International Conference on NDE in Relation to Structural Integrity for Nuclear and Pressurized Components*, pp. 754-762. May 22-24, 2012, Seattle, Washington. NDT.net, Rheintalstr, Germany. http://www.ndt.net/article/jrc-nde2012/papers/120.pdf.

Jhang K-Y. 2000. "Applications of Nonlinear Ultrasonics to the NDE of Material Degradation." *IEEE Transactions on Ultrasonics, Ferroelectrics and Frequency Control* 47(3):540-548.

Lebrun B, Y Jayet and J-C Baboux. 1997. "Pulsed Eddy Current Signal Analysis: Application to the Experimental Detection and Characterization of Deep Flaws in Highly Conductive Materials." *NDT & E International* 30:163-170.

Lee KH, MK Baek and IH Park. 2012. "Estimation of Deep Defect in Ferromagnetic Material by Low Frequency Eddy Current Method." *IEEE Transactions on Magnetics* 48:3965-3968.

Lowe MJS, DN Alleyne and P Cawley. 1998. "Defect Detection in Pipes Using Guided Waves." *Ultrasonics* 36(1–5):147-154.

Maldague X. 2001. *Theory and Practice of Infrared Technology for Nondestructive Testing*. John Wiley and Sons, New York.

Murfin AS, RAJ Soden, D Hatrick and RJ Dewhurts. 2000. "Laser-Ultrasound Detection Systems: A Comparative Study with Rayleigh Waves." *Measurement Science and Technology* 11:1208-1219.

Murray TW and JW Wagner. 1999. "Laser Generation of Acoustic Waves in the Ablative Regime." *Journal of Applied Physics* 85(4):2031.

Ohara Y, S Yamamoto, T Mihara and K Yamanaka. 2008. "Ultrasonic Evaluation of Closed Cracks Using Subharmonic Phased Array." *Japanese Journal of Applied Physics* 47(5):3908-3915.

Rose JL. 1999. *Ultrasonic Waves in Solid Media*. Cambridge University Press, Cambridge, United Kingdom.

Rose LRF. 1984. "Point-source Representation for Laser-generated Ultrasound." *Journal of the Acoustical Society of America* 75(3):723-732.

Zoughi R and S Kharkovsky. 2008. "Microwave and Millimetre Wave Sensors for Crack Detection." *Fatigue & Fracture of Engineering Materials & Structures* 31:695-713.

Appendix A

Technique Summaries

Appendix A

Technique Summaries

A.1 Korean Techniques

11.1 NRUT

❑ Nonlinear Resonance Frequency Shift

Resonance frequency shifts downward and the normalized amplitude decreases as the driving voltage increases for the case of cracked specimen.

al 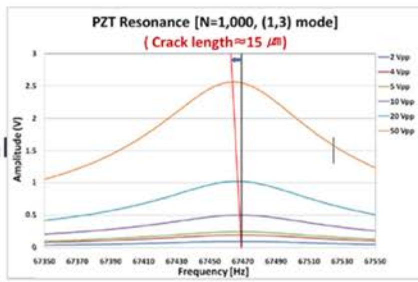

d 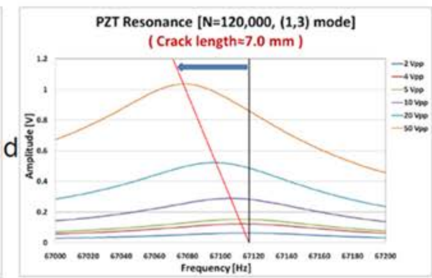

Slide - 3/116-

11.1 NRUT

❑ Nonlinear Resonance Ultrasonic Spectroscopy

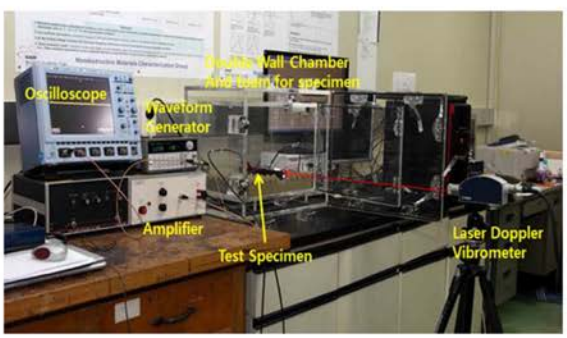

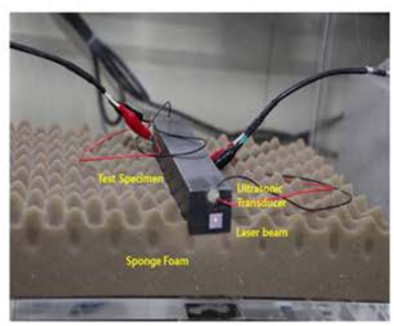

Configuration No. 1 for PARENT TEST SPECIMEN (P28, P29, P30)
(Both piezoelectric Transducers are located on the end of the specimen)

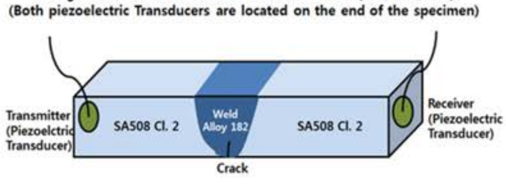

Slide - 4/116-

Overview

- Test Blocks Types Examined: ENSI Blocks
- NDE Technique: Nonlinear Resonance Ultrasonic Spectroscopy
- Measures: Detection of Surface Breaking Flaws
- Data Acquisition: Both Piezoelectric Transducer are located on the end of specimen
- Access: Outside and Side Surface of Blocks
- Measurement Instrument: Oscilloscope, Waveform Generator, Amplifier
- Probe: Piezoelectric transducer
- Signal Analysis/Interpretation: Manual

Slide - 5/116-

11.2 PECT

Eddy Current Test (ECT)

Sine-Wave Excitation ECT ⟺ Pulse Eddy Current Test (PECT)

Sine-Wave EC testing methods have served as the primary NDE method in the Nuclear and air-craft industry for more than 50 years.

- Single frequency , continuous excitation.
- Limited by the depth of penetration of fields or skin depth.

PECT is emerging technological approach which is principally developed for the detection of surface and sub surface defects.

- Large bandwidth.
- Information at low frequencies relevant for detecting deeper defects.

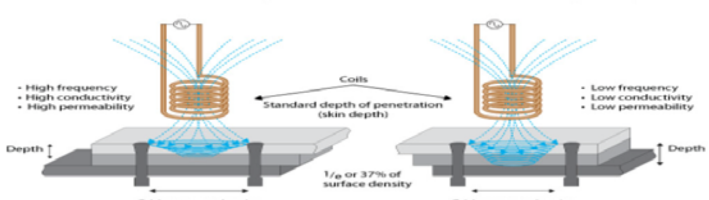

Slide - 6/116-

11.2 PECT

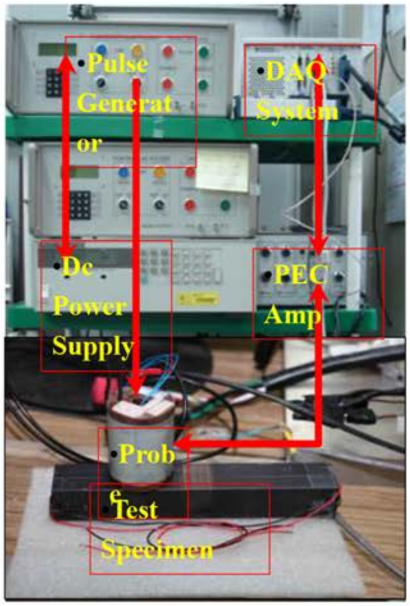

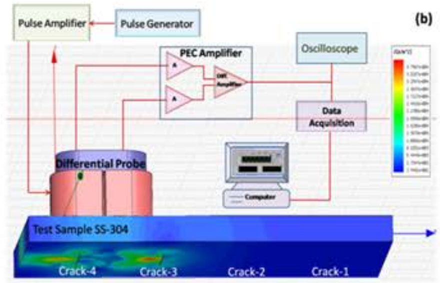

➢PEC testing is one of the most effective methods, which has been demonstrated to be capable of tackling different inspection tasks, such as sub-surface defect detection in complex structures.

➢The PECT system consists of a pulse amplifier, the probe having a driving coil and magnetic field detecting sensor, a sensitive PEC differential amplifier, and a computer with signal processing software.

Slide - 7/116-

11.2 PECT

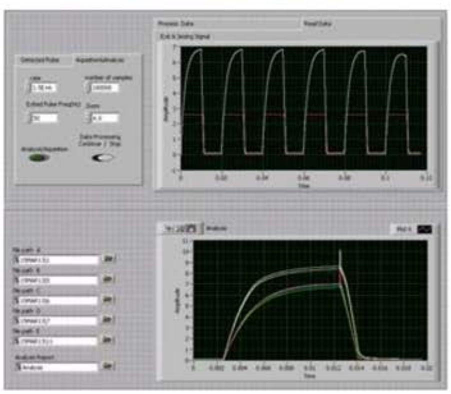

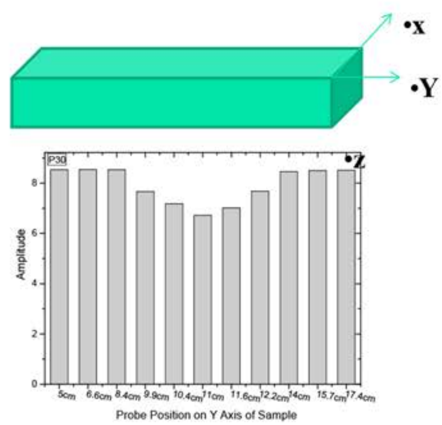

- A short duration high current Pulse is applied to Excitation Coil, corresponding e response from the sample is detected by the hall sensor and is recorded in the computer.
- If the probe placed on the sample in such a position that the Hall-sensor comes above the crack, then typical response signal like above figure is induced in the Hall-sensor from the test block.

•At the ferromagnetic material region, the height of pulse amplitude is nearly constant, and minimum amplitude is observed at the defect position. The crack is positioned in the neighborhood of y coordinate 11 cm, which shows the minimum PEC signal amplitude.

Slide - 8/116-

11.2 PECT

- PEC amplitude change with different sample and sample position. The data is obtained in the ide and opposite side of crack

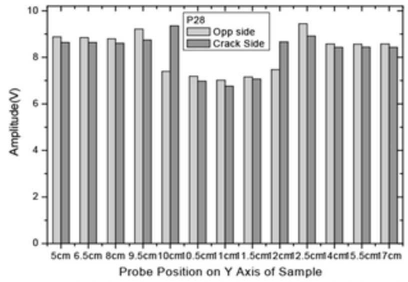

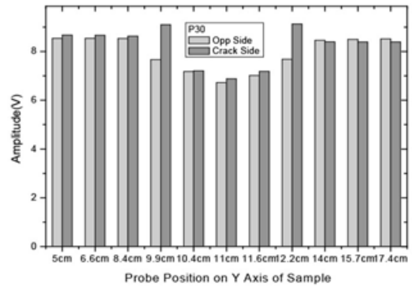

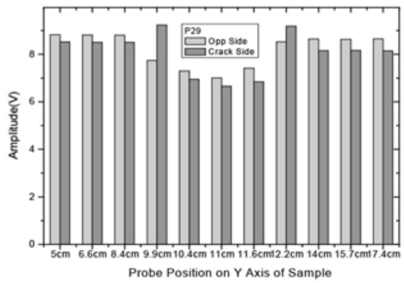

- **The nondestructive evaluation (NDE) to detect the sub surface crack using PEC under the thick plate using the PARENT round robin sample has been tried. The PEC amplitude measured in the ferromagnetic part is higher than that of the nonmagnetic part.**
- **The crack is positioned in the neighborhood of y coordinate 11 cm, which shows the minimum PEC signal amplitude.**

Slide **- 9/116-**

Overview

- **Test Blocks Types Examined: ENSI Blocks**
- **NDE Technique: Pulsed Eddy Current**
- **Measures: Location of Surface Breaking Flaws**
- **Data Acquisition: X-Y Scanners**
- **Access: Outside Surface of Blocks**
- **Measurement Instrument: Pulse Generator, PEC Amplifier, DAQ**
- **Signal Analysis/Interpretation: Manual**

Slide **- 10/116-**

20.1 PAUT

- **PAUT (Phased Array Ultrasonic Testing)**
- **Ultrasonic beam can be focused dynamically or steered by controlling the time delay for individual element of phased array ultrasonic transducer**
- **The position and size of defect can be visualized**

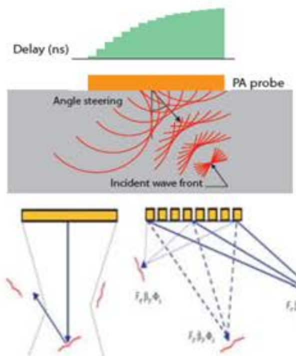

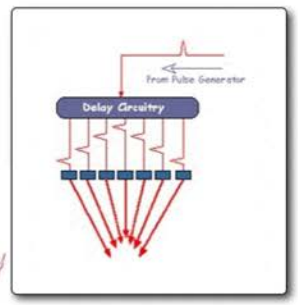

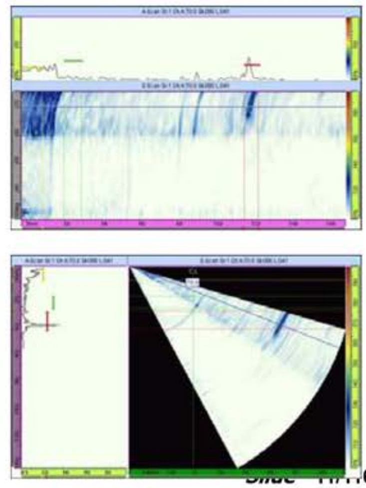

20.1 PAUT

- **The curved wedge for pipe and compensation algorithm for its focal point**

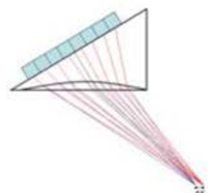

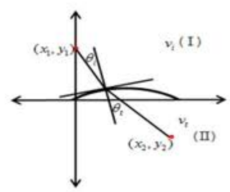

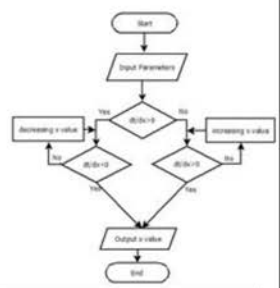

- **Test results for DMW specimen**

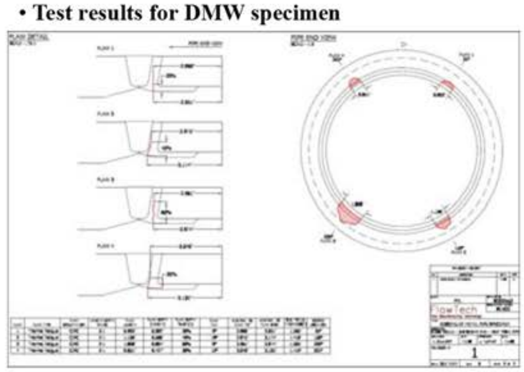

	Location (Deg.)		Length (mm)		Depth (mm)	
	실제값	측정값	실제값	측정값	실제값	측정값
Flaw 1	35	34.7	22.9	22	7.67	7.8
Flaw 2	150	148.3	28.9	31	14.4	14.8
Flaw 3	220	221.9	45.9	>41	23.0	17.5
Flaw 4	325	320.7	21.6	32	10.8	10.4

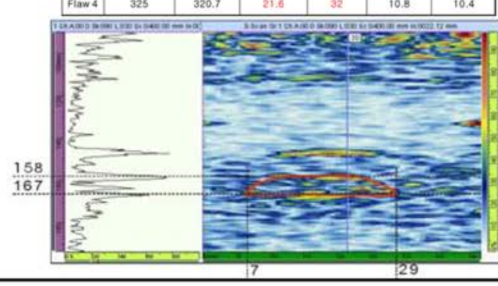

Overview

- Test Blocks Types Examined: DWM and ENSI Blocks
- NDE Technique: Phased Array UT
- Measures: Location/Length /Depth of Surface Breaking Flaws
- Data Acquisition: Manual Scans
- Access: Outside Surface of Blocks
- Measurement Instrument: Olympus-OmniScan MXU
- Probe:
  - Phased Array Probe, 64 elements, 2.25 MHz, and 53/29/35 (mm) (Length/Width/Pitch)
- Signal Analysis/Interpretation: Manual

Slide - 13/116-

20.2 UIRT

- UIRT (Ultrasound Infrared Thermography)
- Heat energy is generated from the crack when the external excitation (20-100 kHz) is applied into the test specimen
- Heat source is measured by the infrared thermography camera to detect defects.

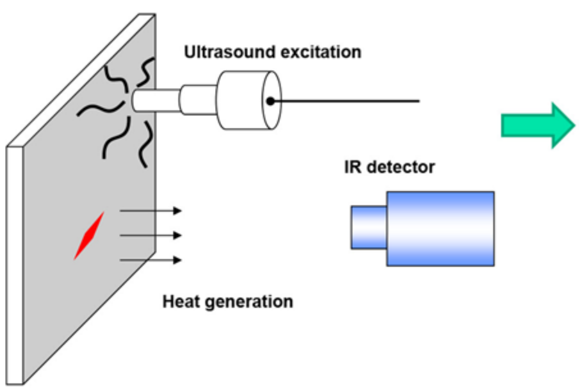

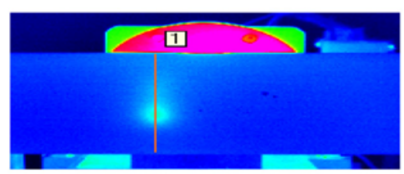

Infrared thermography

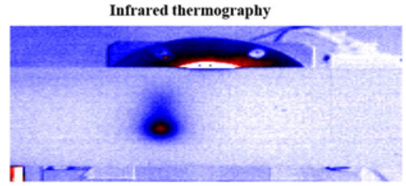

Lock-in phase infrared thermography

IR result from the inner crack of pipeline

Slide - 14/116-

20.2 UIRT

• The angle of 0 ° up to 270° was rotated by 90° step respectively

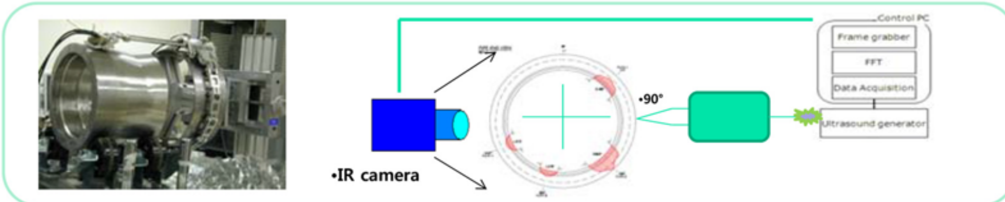

• Infrared camera rotates 360 ° with 45 ° angle of inclination

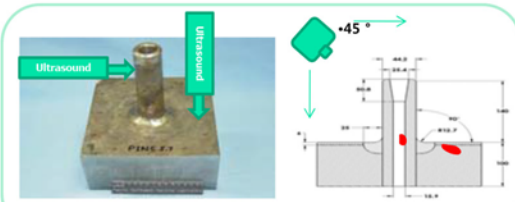

Ultrasound Exciter point

• Contact with the ultrasound horn on each side

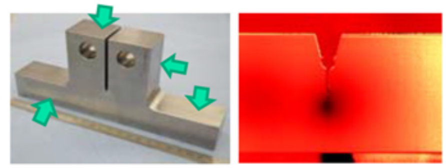

Ultrasound Exciter point

Image of thermography

Slide - 15/116-

20.2 UIRT

❖ Specimen : SBDMW Reference block P28,29,30,31,32,38

❖ Technical ID : UIR (Ultrasound Infrared Thermography)

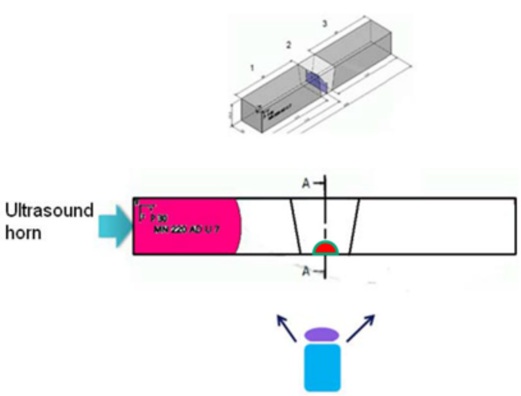

IR Camera

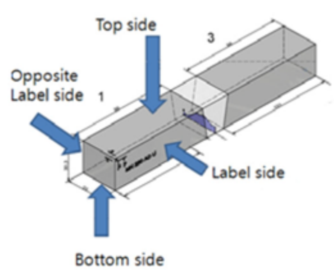

View-plane of Detection

Slide - 16/116-

20.2 UIRT

❖ Specimen : P30

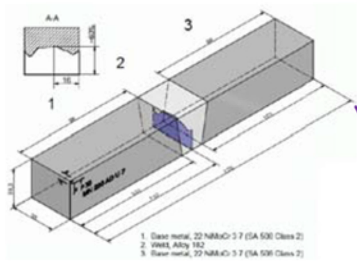

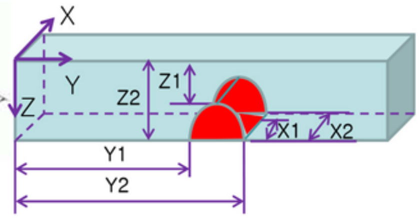

Defect No:	X1 (mm)	X2 (mm)	Y1 (mm)	Y2 (mm)	Z1 (mm)	Z2 (mm)	Defect max Tem(℃)	Defect min Tem(℃)	Surface breaking	Comments
1	0.00	35.02	98.56	115.72	10.12	30.32	44.97	18.77	Yes	UIR

Label : Front side (Y,Z)

Bottom side(X,Y)

Label: Back side (Y,Z)

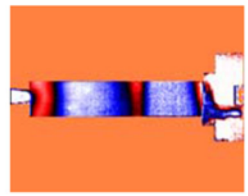

Top side (X,Y)

Slide - 17/116-

Overview

- **Test Blocks Types Examined: ENSI Blocks**
- **NDE Technique: Ultrasound Infrared Thermography**
- **Measures: Location/Length/Depth of Surface Breaking Flaws**
- **Data Acquisition: Manual Scans**
- **Access: Top side, Label Side, Opposite Label Side, Bottom Side of Blocks**
- **Measurement Instrument :**
  - **Ultrasound generator by UlTec–SEE2 Sonic**
  - **Infrared thermography by FlirCedip siver480**
- **Signal Analysis/Interpretation: Manual**

Slide - 18/116-

21 GW

❑ Guided wave

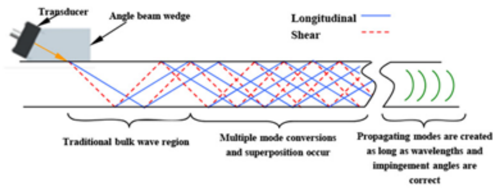

•Guided wave dispersion curve

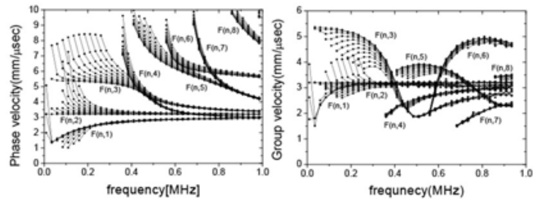

•Guided wave mode identification

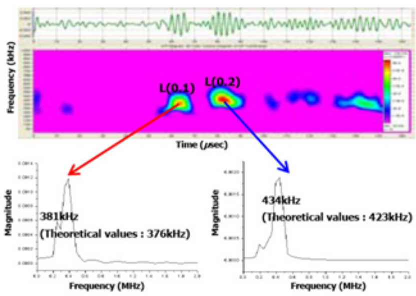

•Guided wave long distance inspection signal

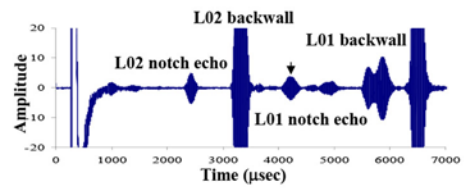

Slide - 19/116-

21 GW

❑P4

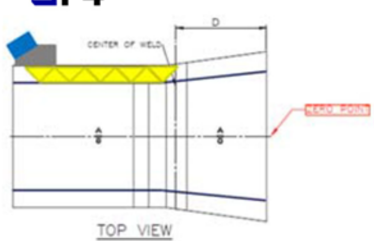

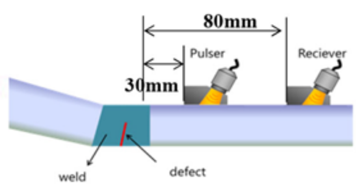

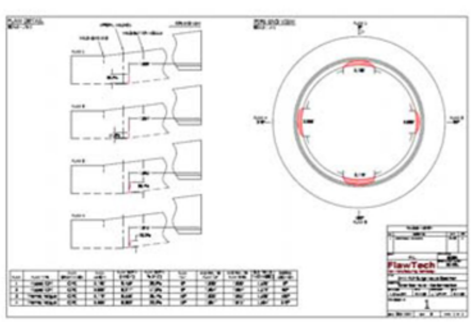

➢ **Guided wave inspection method**

1. P4: At the distance of defect, guided waves propagate axial direction of specimen and receive the signal from the defects.

2. With volume coverage, it is possible to detect ID defects access from OD.

Slide - 20/116-

21 GW

❑P5

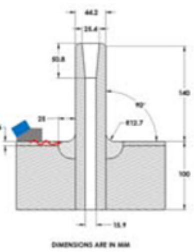

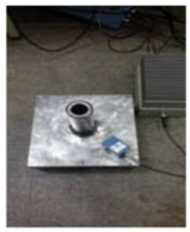

Top view

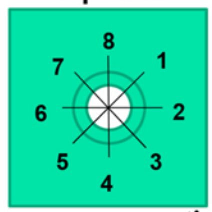

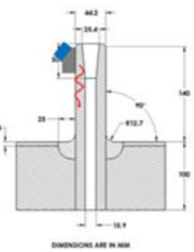

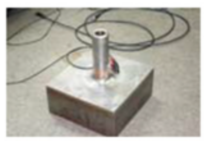

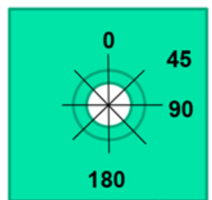

• Guided wave propagates along the surface of BMI specimen and BMI nozzle.

Slide - 21/116-

Overview

- Test Blocks Types Examined: DMW and BMI Specimens
- NDE Technique: Guided Wave UT
- Measures: Location of Surface Breaking Flaws
- Data Acquisition: Manual
- Access: J-Groove Weld Surface, BMI Surface of Blocks
- Measurement Instrument:
  - Ritec–Ritec RPR 4000 instrument with high power voltage
  - LeCroy Wave Surfer 42Xs, Sampling rate is 2.5GS/s
- Probe:
  - Frequency (500kHz, 1MHz, 1.5 MHz, 2.25 MHz)
  - Wedge (20° ~ 70°)
- Signal Analysis/Interpretation: Manual

Slide - 22/116-

22 Time Reversal Technique

❑ Time reversal technique

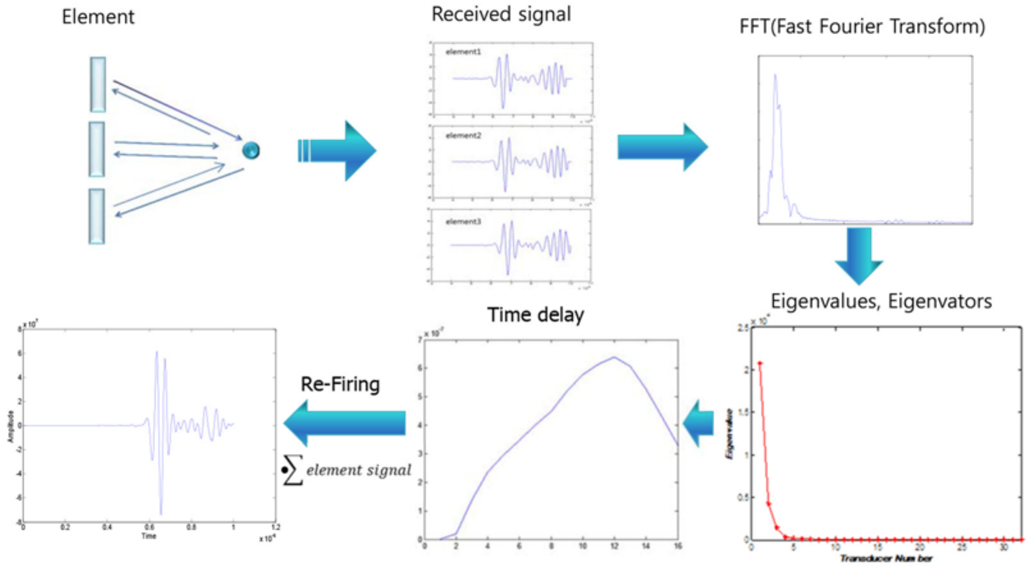

Slide - 23/116-

22 Time Reversal Technique

• **Inspection Equipment**

➢ Name : R/D TECH TomoScan FOCUS LT

➢ S/N : FLJ-1026

❖ Transducer : OLYMPUS 5L64-A2

❖ Wedge : P-45, SV-55 Wedge

❖ References Block

➢ 명칭 : ASTM E164 FTW TYPE CALIBRATION BLOCK

➢ S/N : No. A14457

• **Specimens for OPEN RRT**

➢ P29 specimen : fatigue crack

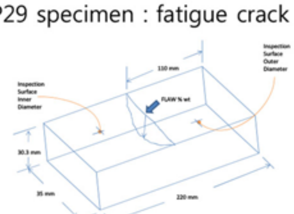

Flaw Position Relative to Weld	Center
End Reference to Flaw Base (Y)	110 mm
End Reference to Flaw Tip (Y)	110 mm
Flaw Depth (Absolute)	10 mm
Flaw Depth (Relative)	35%
X-Position at max. Flaw Depth	12 mm

Slide - 24/116-

22 Time Reversal Technique

- Synthetic Aperture Focusing Technique Results

Longitudinal Wave **Shear Wave**

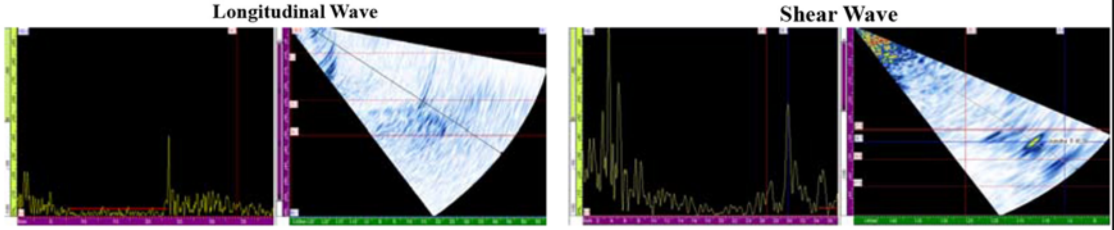

- Time Reversal Technique

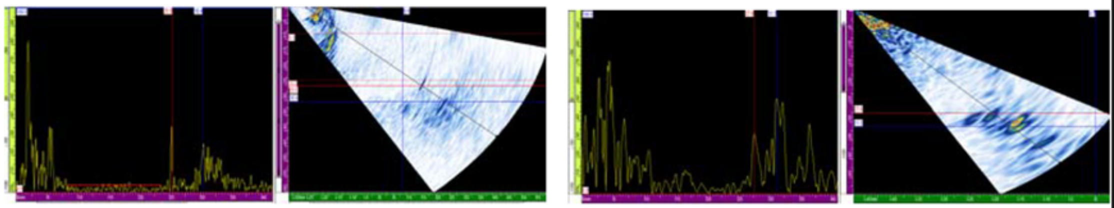

8.4mm **10mm**

Slide - 25/116-

Overview

- Test Blocks Types Examined: ENSI Blocks
- NDE Technique: Phased Array UT
- Measures: Location/Length/Depth of Surface Breaking Flaws
- Data Acquisition: Manual Scanner
- Access: Outside Surface of Blocks
- Measurement Instrument: Olympus TomoScan Focus LT
- Probe:
  - 5MHz 32Channel Olympus Phased array Ultrasonic Probes
- Signal Analysis/Interpretation: Manual

Slide - 26/116-

30 HHUT

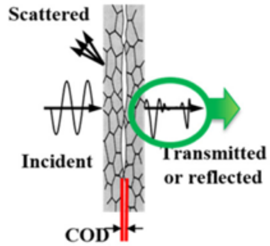

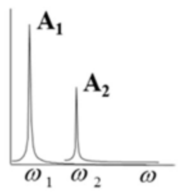

- The basic principle of the crack inspection by using higher harmonic UT (HHUT) is the contact acoustic nonlinearity (CAN)
- CAN effect is the phenomenon that generates harmonic component, which is caused by mainly two reasons as follows:
  - the waveform distortion when the crack is temporarily clamping
  - the nonlinear relationship between pressure and displacement at the contact interface
- The relative nonlinear parameter (β')

$$\beta' = \frac{A_2}{A_1^2} \qquad A_1\text{: fundamental freq.} \quad A_2\text{: second harmonic freq.}$$

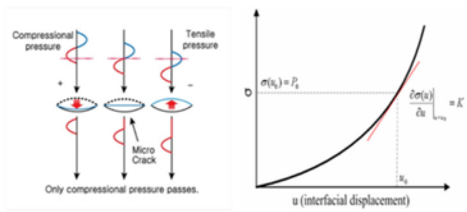

Basic principle of contact acoustic nonlinearity

Slide - 27/116-

30 HHUT

• CT Specimen (Al6061 fatigue crack) measurement using HHUT

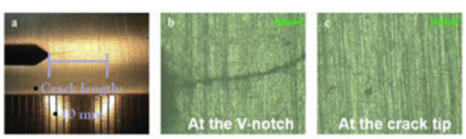

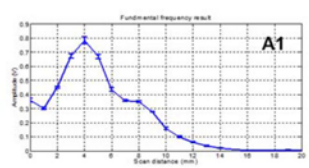

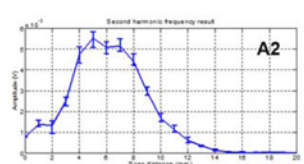

- The magnitudes of the fundamental frequency(A1) and the second harmonic frequency(A2) at different measuring positions along the crack direction from notch
- The maximum magnitude of the A1 appears at 4 mm, and the crack length was measured by 6.5 mm with 6dB drop (only open portion was detected)
- A2 shows the maximum value at 5 mm as well as has large value until 9 mm, which is close to the real size of the crack
- HHUT is able to detect the closed crack and it can improve the performance of crack sizing

Slide - 28/116-

30 HHUT

•Contact Acoustic Nonlinearity Imaging

•at Solid-Solid Contact Specimen

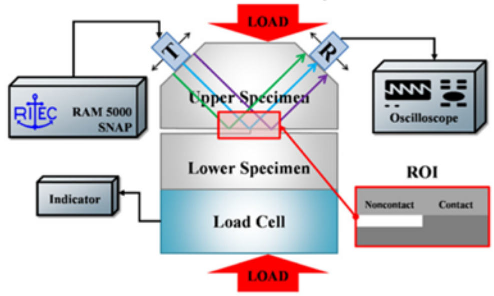

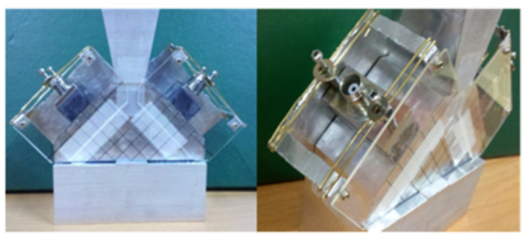

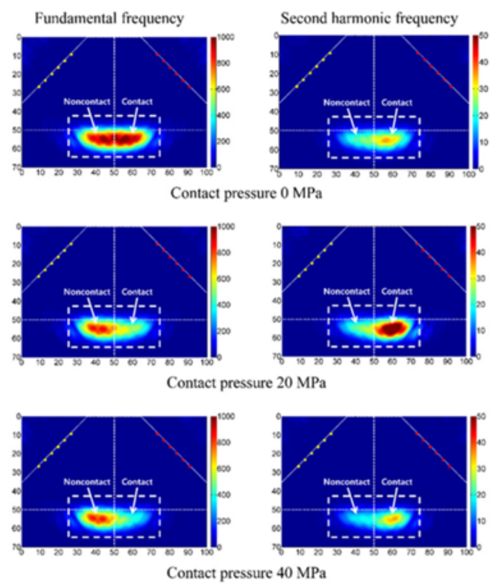

Slide - 29/116-

Overview

- Test Blocks Types Examined: ENSI Blocks
- NDE Technique: Higher Harmonic Ultrasonic Technique
- Measures: Location/Depth of Surface Breaking Flaws
- Data Acquisition:
  - Manual : PE(X-axis), VS
  - Auto : PE(Z-axis)
- Access: Outside Surface of Blocks
- Measurement Instrument:
  - High power pulser-receiver (RAM-5000 SNAP)
  - Pulser-receiver (5077PR)
- Probe:
  - 5MHz 0.375 Ultrasonic Transducer
  - 45˚ 2MHz, MBW 45-2/ 45˚ 4MHz, MBW 45-4
- Signal Analysis/Interpretation: Manual

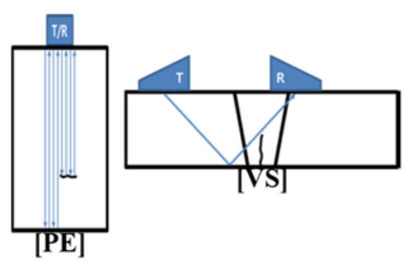

Slide - 30/116-

A.2 Japanese Techniques

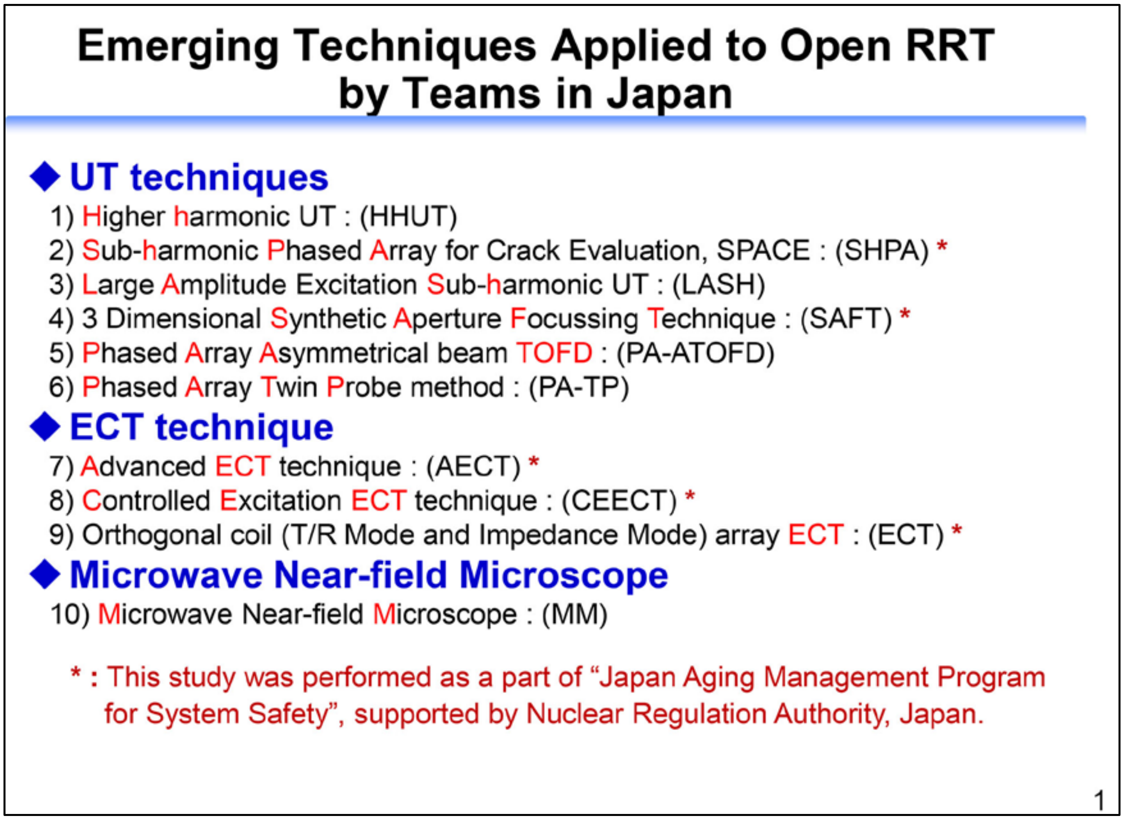

◆ Higher Harmonic UT: HHUT (1)

Basic concept of nonlinear ultrasonics (higher harmonic imaging)

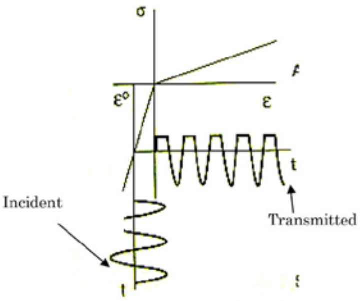

Fig. 1 Waveform distortion of the incident sine wave at SCC interface.

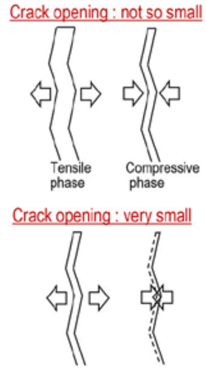

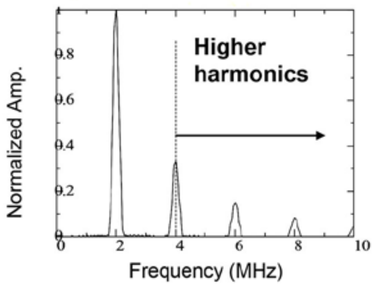

Fig. 2 Extraction of higher harmonics using analog high pass filter.

1 Stress strain response of SCC with narrow gap exhibits nonlinearity as shown in Fig.1.
2 Lower stiffness in tensile phase result in severe waveform distortion of incident sinusoidal tone-burst wave shown in Fig. 1.
3 This waveform distortion is expressed by higher harmonics in frequency domain as shown in Fig. 2.
4 Higher harmonics are extracted by analog high-pass filter.
5 Higher harmonic amplitude is mapped for scanned area.

2

◆Higher Harmonic UT: HHUT (2)

Immersion higher harmonic imaging. Experimental set-up.

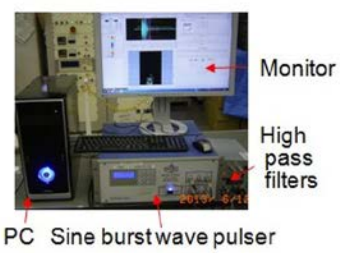

Fig.3 Higher harmonic imaging system.

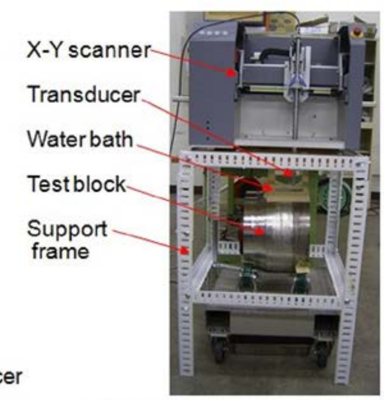

Fig. 4 Measurement set-up for normal incidence.

Fig. 5 Measurement set-up for angular incidence.

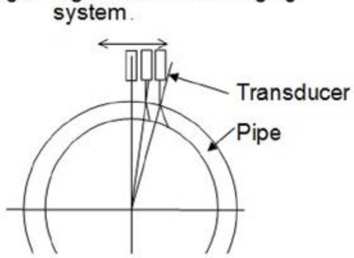

Fig. 6 Malfunction of in-plane scanning for pipes. Ultrasonic beam is deflected outwards at off-centered incidence.

Fig. 7 Experimental set-up for P28~P32,P38, P42 and P46

3

◆ Higher Harmonic UT: HHUT (3)

Higher harmonic images for P41.

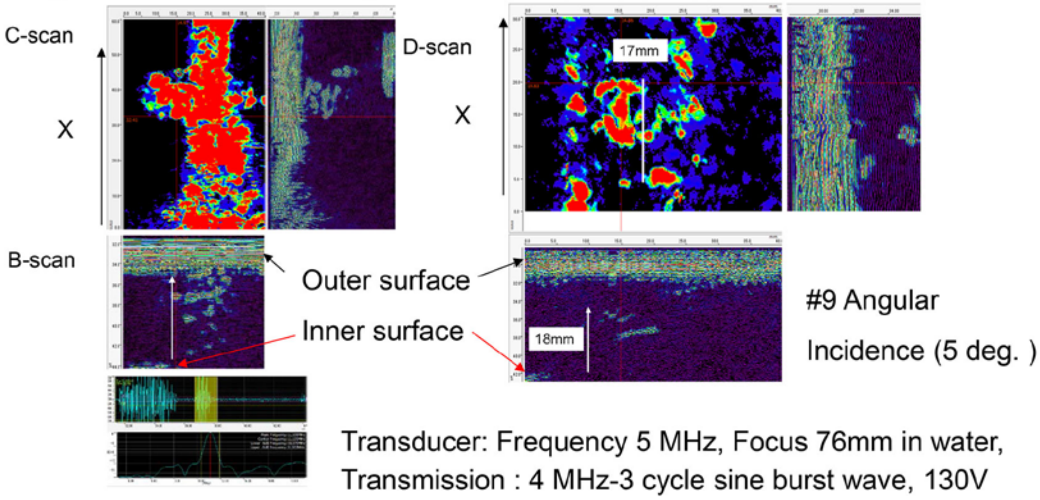

#6 Angular incidence (5 deg.)

Transducer: Frequency 5 MHz, Focus 76mm in water,
Transmission : 4 MHz-3 cycle sine burst wave, 130V
Reception: 8 MHz high-pass filter, gain 54 dB
Third Harmonic amplitude is mapped.
Depth is evaluated by B-scan image.

4

◆ Higher Harmonic UT: HHUT (4)

Higher harmonic images for P28 & 32.

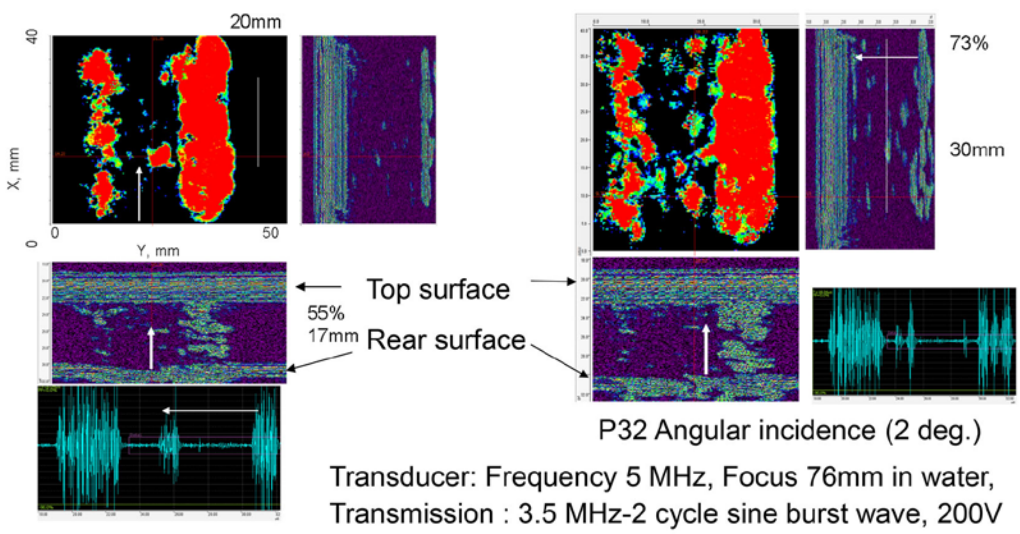

P28 Angular incidence (2 deg.)

P32 Angular incidence (2 deg.)

Transducer: Frequency 5 MHz, Focus 76mm in water,
Transmission : 3.5 MHz-2 cycle sine burst wave, 200V
Reception: 10MHz high-pass filter, gain 56 dB
Third Harmonic amplitude is mapped.
Depth is evaluated by B-scan image.

5

◆ Subharmonic Phased Array for Crack Evaluation(SPACE) : SHPA (1)

SPACE is a novel imaging method using the subharmonic generation by short-burst waves and a phased algorithm with frequency filtering.

SPACE provides fundamental array (FA) images at frequency *f* and subharmonic array (SA) images at the frequency *f*/2, visualizing the open and closed parts of cracks, respectively.

Detection, Crack Length → **SAW SPACE**

Crack Depth → **Bulk SPACE**

Surface acoustic wave (SAW)

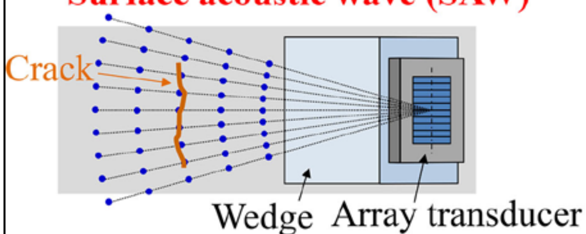

Bulk (longitudinal) wave

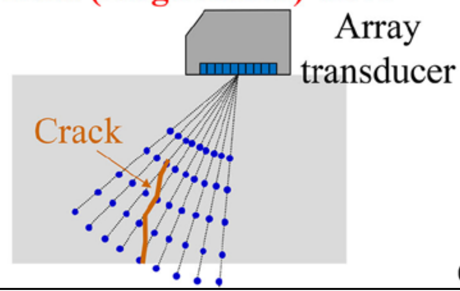

6

◆ Subharmonic Phased Array for Crack Evaluation(SPACE) : SHPA (2)

SAW SPACE : Detection, Crack Length

Surface acoustic wave (SAW)

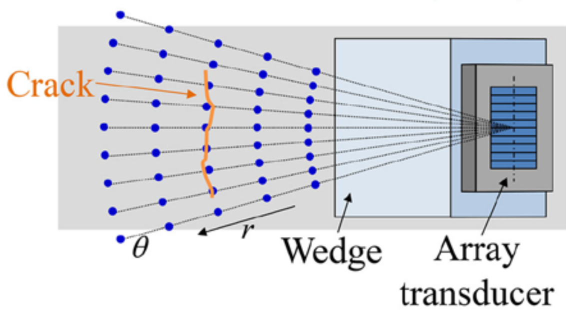

Specimen

SCC(SUS304, HAZ, High temperature pressurized water)

Array transducer

5 MHz, 32 elements, 0.5 mm pitch

Input condition

2 MHz, 3 cycle

θ=−14° ∼15° (1° step)

r =39.5 mm, 44.5 mm

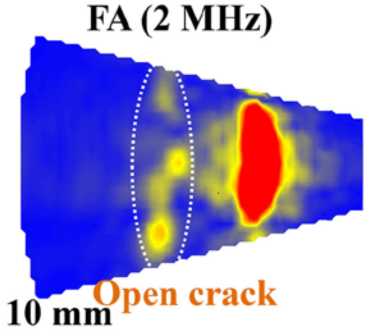

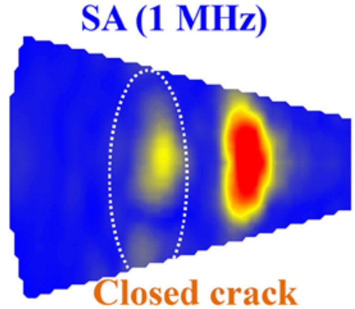

7

◆ Subharmonic Phased Array for Crack Evaluation(SPACE) : SHPA (3)

Bulk SPACE : Crack Depth

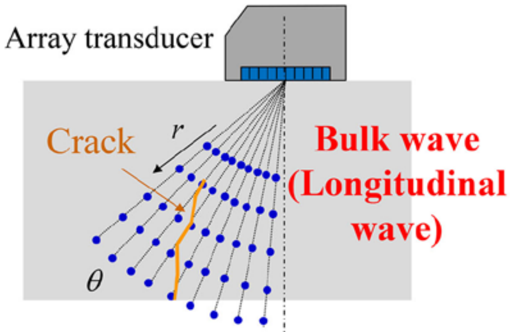

Specimen
SCC(SUS304, HAZ, High temperature pressurized water)

Array transducer
5 MHz, 32 elements, 0.5 mm pitch

Input condition
7 MHz, 3 cycle
θ=12° ∼71° (1° step)
r=12 mm∼42 mm (7.5 mm step)

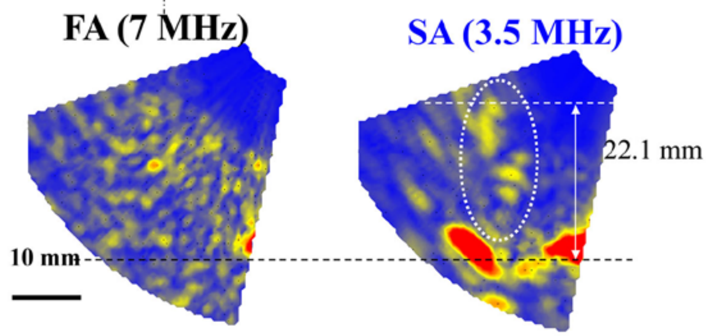

◆ Sub-harmonic Phased Array for Crack Evaluation(SPACE) : SHPA (4)

Fatigue Crack (SUS316L)

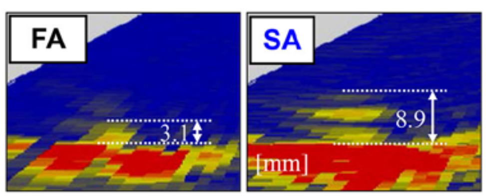

(a)Fundamental array (b)Subharmonic array

SCC (Sensitized SUS304)

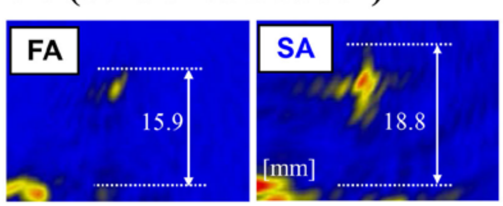

(a)Fundamental array (b)Subharmonic array

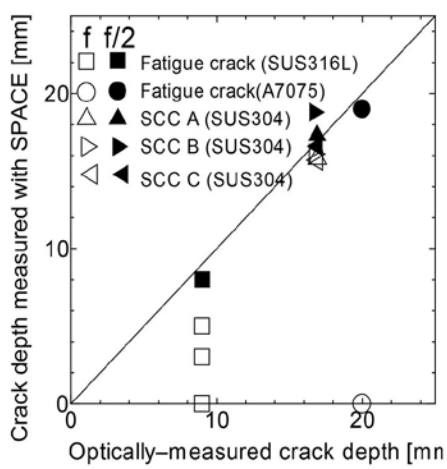

Depth of closed crack is precisely evaluated by the (b) subharmonic array (SA) images at frequency f/2.

◆ Subharmonic Phased Array for Crack Evaluation(SPACE) : SHPA (5)

SAW SPACE

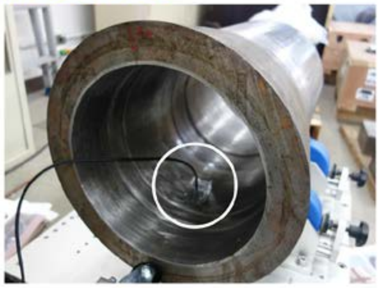

Bulk SPACE

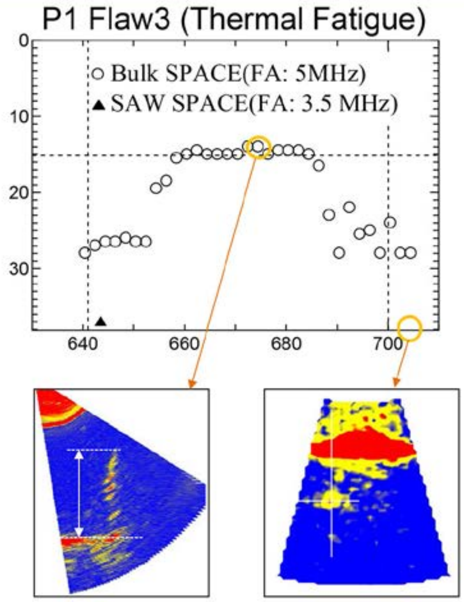

Crack Depth Measurement by Bulk SPACE

Crack Length Measurement by SAW SPACE

This study was performed as a part of "Japan Aging Management Program for System Safety", supported by Nuclear Regulation Authority, Japan.

◆ Large Amplitude Excitation Sub-harmonic UT : LASH (1)

Conventional Subharmonic imaging system called SPACE

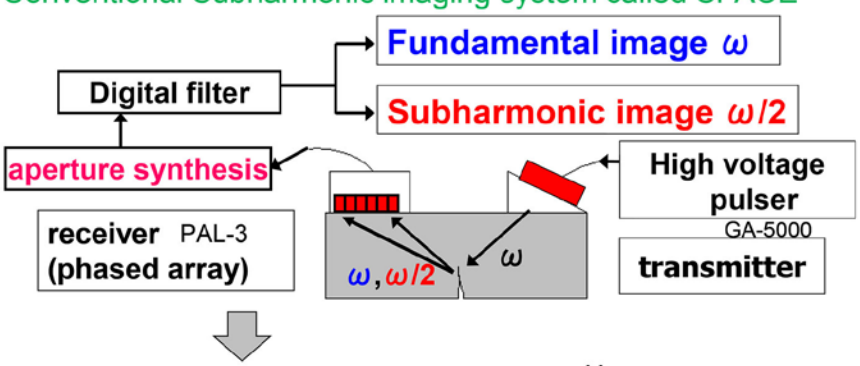

Advantage of Subharmonic Imaging system

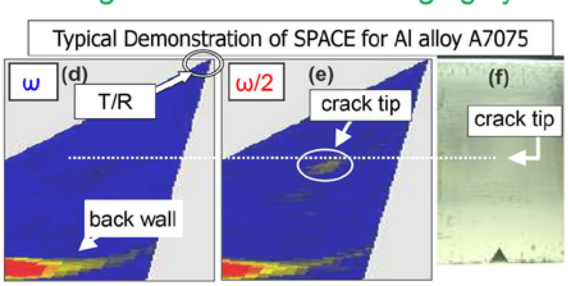

However,

Limitation of present SPACE

- Subharmonic wave generate only at closed cracks
- SPACE is not effective for most of the industrial open cracks

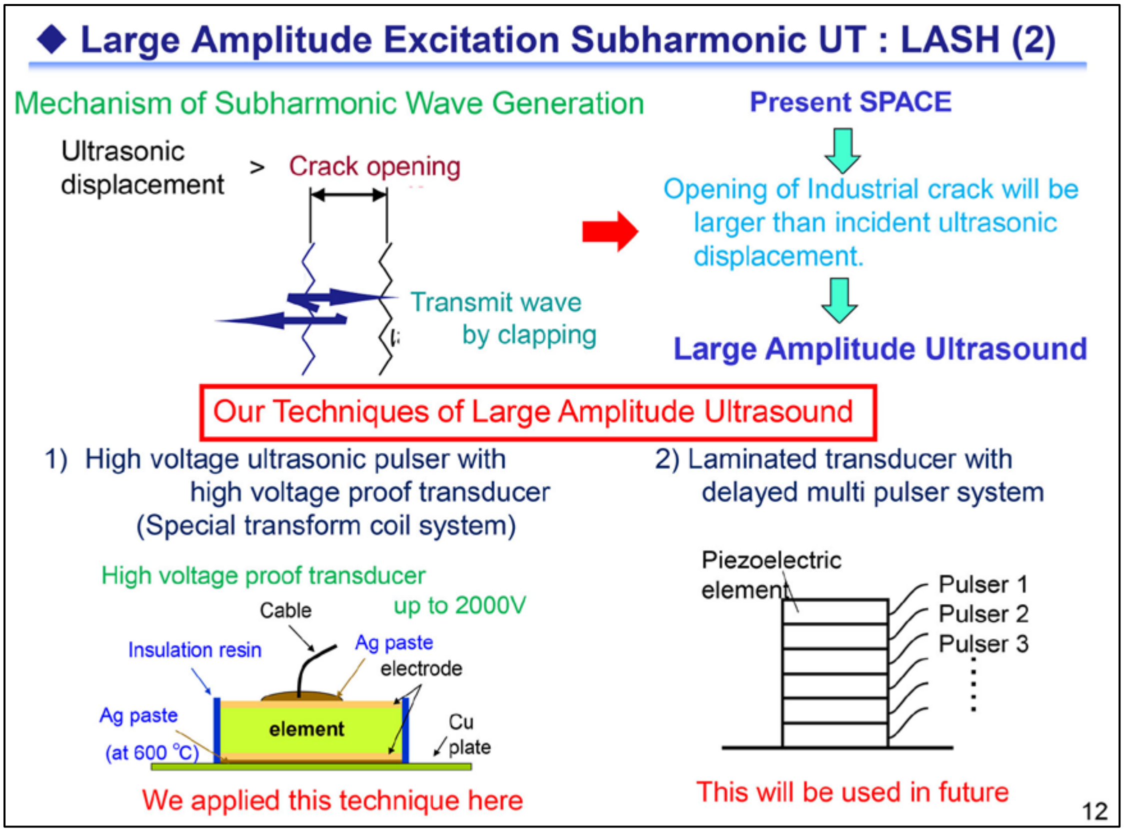
◆ Large Amplitude Excitation Subharmonic UT : LASH (2)
Mechanism of Subharmonic Wave Generation
Ultrasonic displacement
>
Crack opening
Transmit wave by clapping
Present SPACE
Opening of Industrial crack will be larger than incident ultrasonic displacement.
Large Amplitude Ultrasound
Our Techniques of Large Amplitude Ultrasound
1) High voltage ultrasonic pulser with high voltage proof transducer (Special transform coil system)
2) Laminated transducer with delayed multi pulser system
High voltage proof transducer
Cable
up to 2000V
Insulation resin
Ag paste
electrode
Ag paste
(at 600 ℃)
element
Cu plate
Piezoelectric element
Pulser 1
Pulser 2
Pulser 3
We applied this technique here
This will be used in future
12

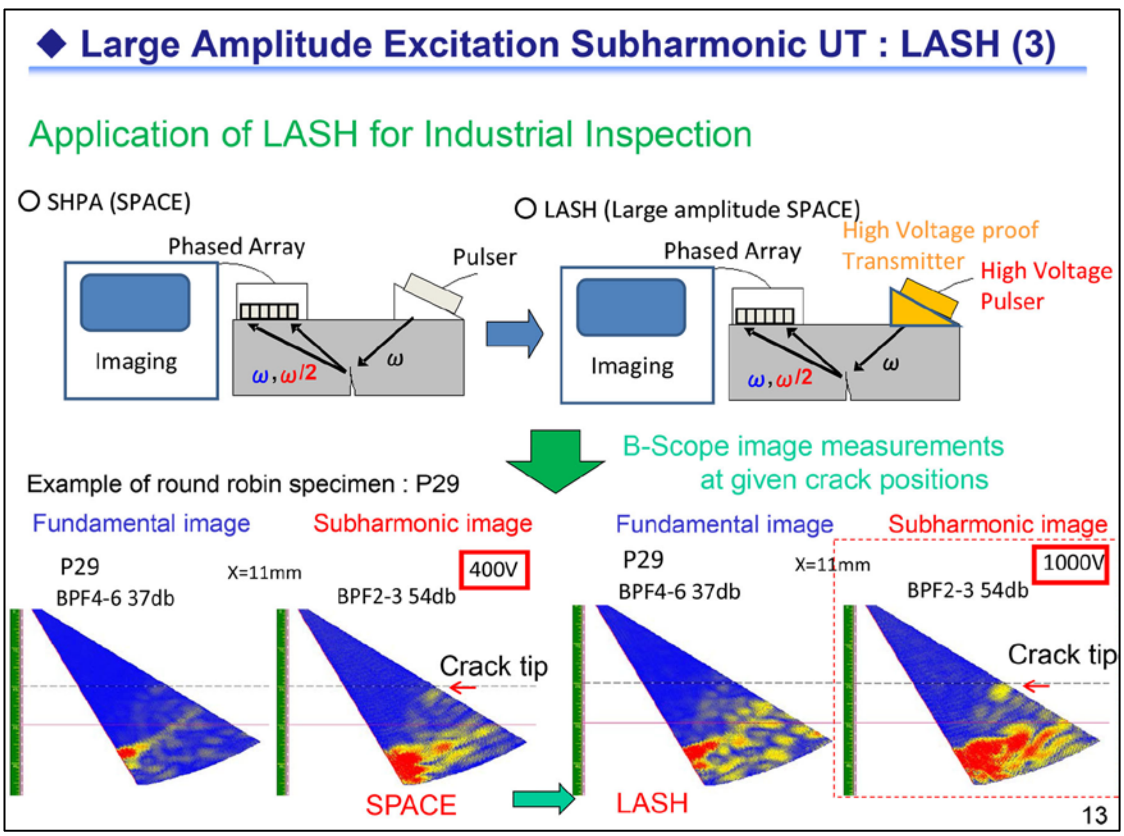
◆ Large Amplitude Excitation Subharmonic UT : LASH (3)
Application of LASH for Industrial Inspection
○ SHPA (SPACE)
Phased Array
Pulser
Imaging
ω, ω/2
ω
○ LASH (Large amplitude SPACE)
Phased Array
High Voltage proof Transmitter
High Voltage Pulser
Imaging
ω, ω/2
ω
B-Scope image measurements at given crack positions
Example of round robin specimen : P29
Fundamental image
Subharmonic image
P29
BPF4-6 37db
X=11mm
400V
BPF2-3 54db
Crack tip
SPACE
Fundamental image
Subharmonic image
P29
BPF4-6 37db
X=11mm
1000V
BPF2-3 54db
Crack tip
LASH
13

◆ Large Amplitude Excitation Subharmonic UT : LASH (4)

Only for the cracks in which crack tips can be observed in subharmonic B-scope images, three dimensional B-scope image were applied using the encoder system.

Three Dimensional B-Scope Image Measurement
(Optional measurement)

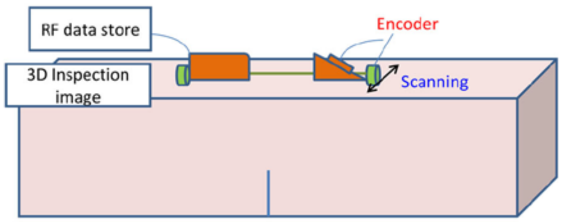

1) Several B-scope images were measured at parallel positions along the weld line.
2) Three dimensional images were reconstructed using the stored B-scope images.

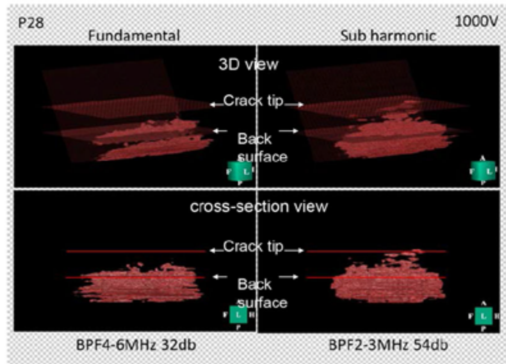

LASH technique could be improved S/N ratio of crack tip echo especially in subharmonic image for P-28, P-29 and Flaw-2 in P1.

14

◆ 3 Dimensional Synthetic Aperture Focussing Technique: SAFT (1)

3D-SAFT UT

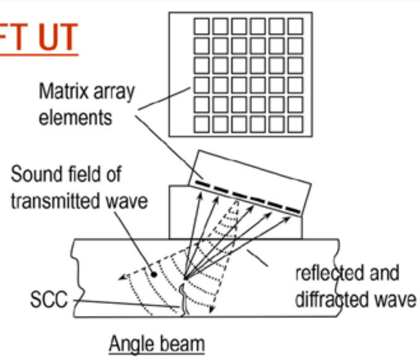

UT beams from many matrix array elements are transmitted into the objectives, and the reflected or diffracted waves from different directions are used for the SAFT processing

Typical examples of 3D-SAFT UT imaging of SCC

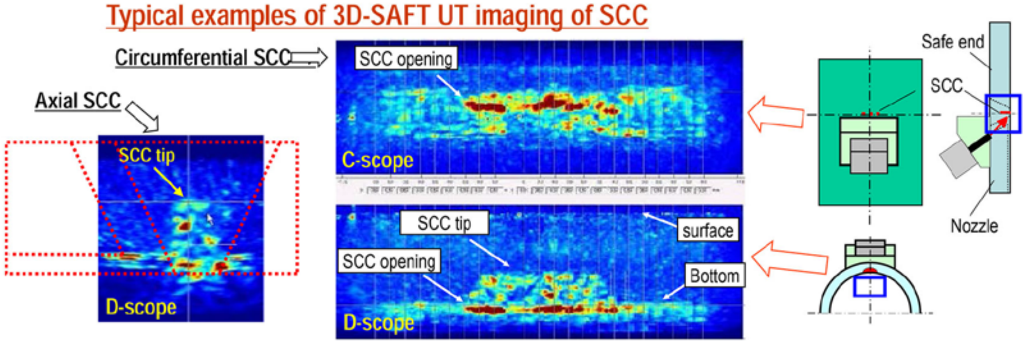

15

◆ 3 Dimensional Synthetic Aperture Focussing Technique: SAFT (2)

Application to Ni alloy weld inspection

Accuracy of SCC depth sizing

(safety valve)

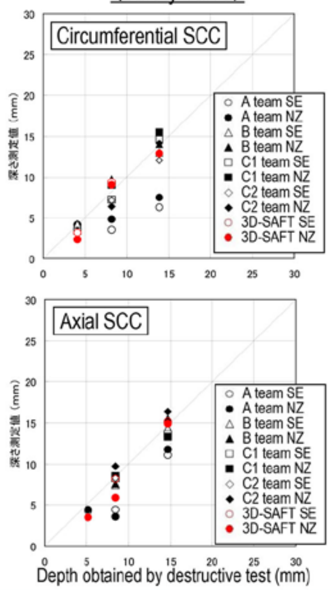

3D-SAFT has good accuracy of depth sizing.

Inspection capability from offset position

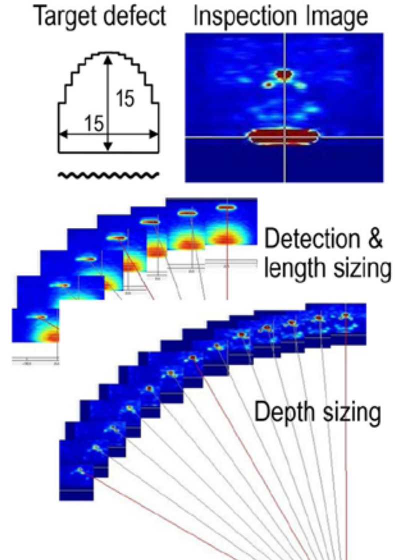

Good result of length & depth sizing are obtained between 0～60° offset direction.

16

◆ 3 Dimensional Synthetic Aperture Focussing Technique: SAFT (3)

	ℓ	a	b
ENSI block	42.5	45	50
Large bore	80	100	120
Small bore	43	80	70

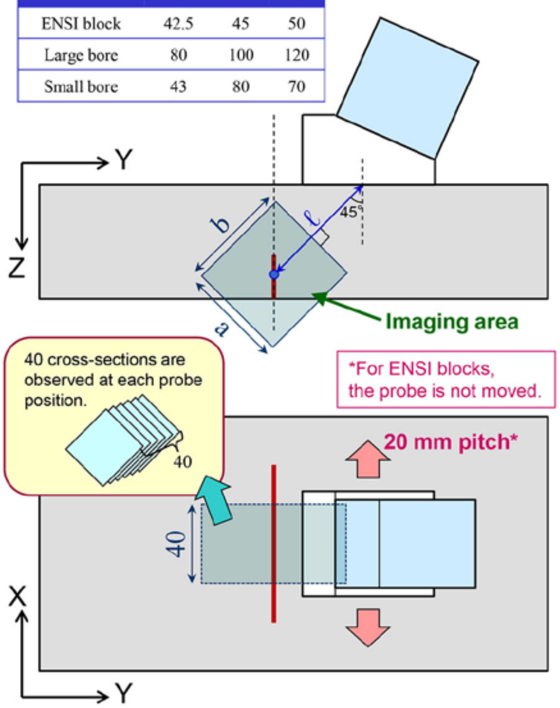

Probe

Frequency: 2 MHz

Channel: 256ch (16×16)

Probe wedge

Refracted angle (longitudinal wave): 45°

The contact surface is respectively contoured

- to match the curvature of both axial and circumferential inspection of SBDMW
- to match the curvature of both axial and circumferential inspection of LBDMW

Accumulated images

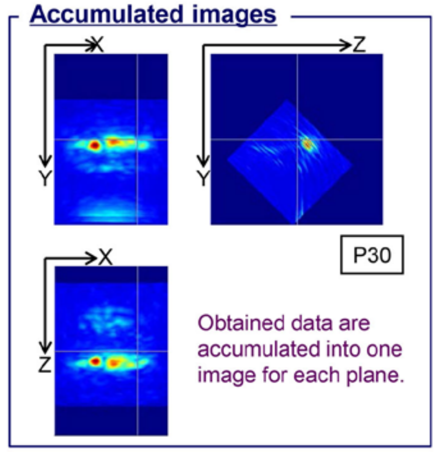

Obtained data are accumulated into one image for each plane.

17

◆ 3 Dimensional Synthetic Aperture Focussing Technique: SAFT (4)

Measurement

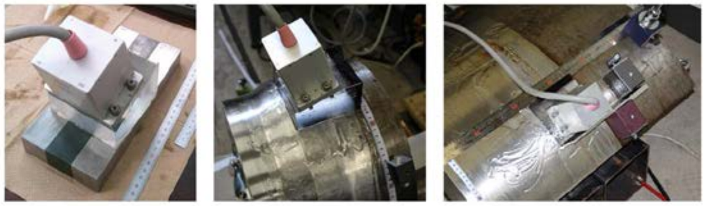

ENSI block — Small bore — Large bore

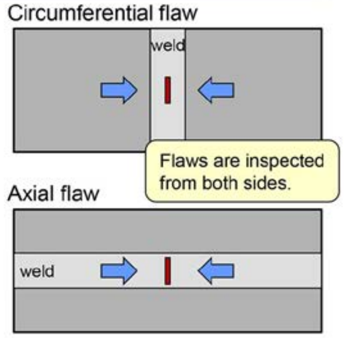

Sizing method

Binarized image

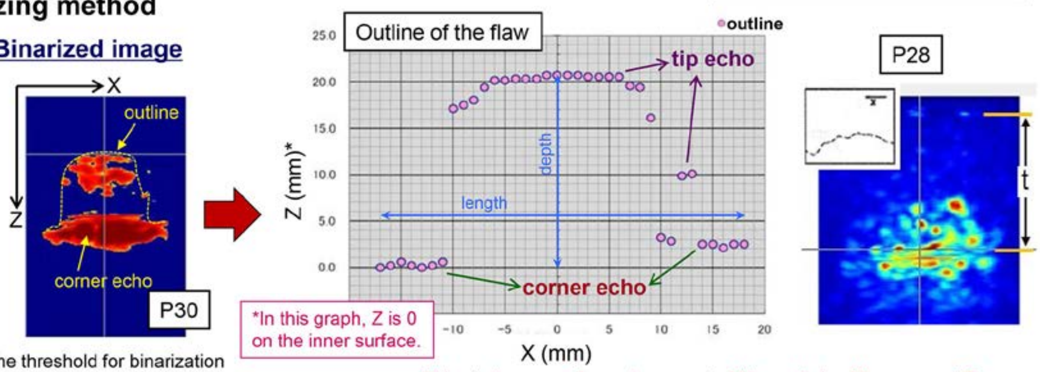

The threshold for binarization is the noise level.

This study was performed as a part of "Japan Aging Management Program for System Safety", supported by Nuclear Regulation Authority, Japan.

18

◆ Phased Array Asymmetrical Beam TOFD : PA-ATOFD (1)

➢Schematic diagram

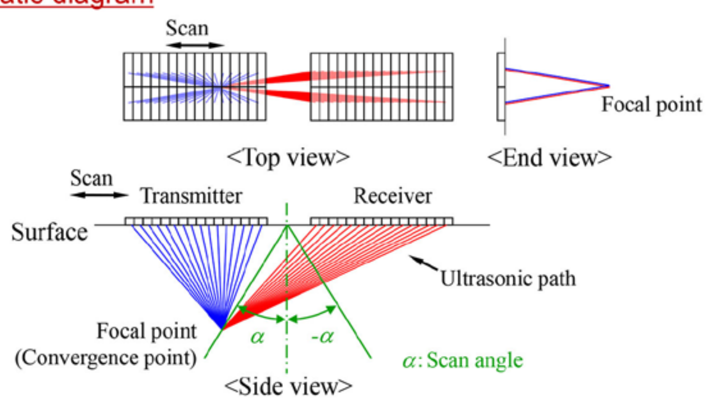

Two array probes for transmitter and receiver parallel to the scan direction

Ultrasonic beams with different scan angles and path lengths of the transmitter and receiver

⇩

Acquire the tip echo of the flaw with different scan angles

19

◆ Phased Array Asymmetrical Beam TOFD : PA-ATOFD (2)

Array probe

2.25MHz, 2x16 matrix array

2.25MHz, 4x8 matrix array

2MHz,10x25 matrix array

Setting

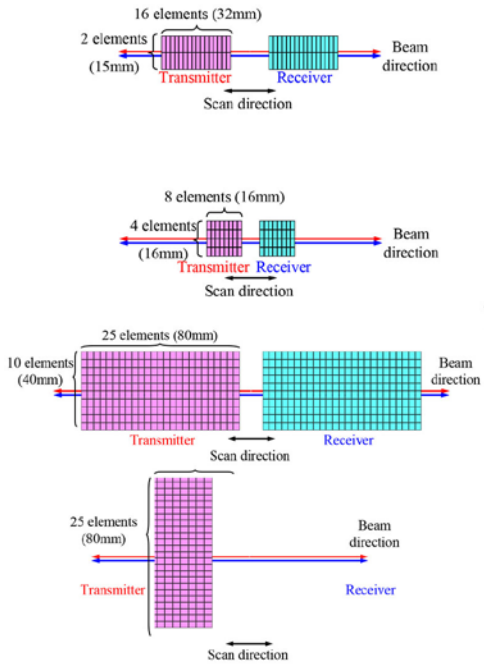

Apply to the inner surface (near crack side)

LB
P12, P23, P24, P37
Test block
P28, 29, 30, 31, 32, 38, 42, 46

Example of array probes and wedge

Apply to the outer surface (far crack side)

LB
P12, P23, P24, P37
SB
P1, 41

◆ Phased Array Asymmetrical Beam TOFD : PA-ATOFD (3)

➢ Data synthesis method

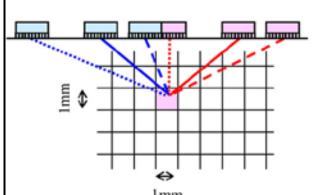

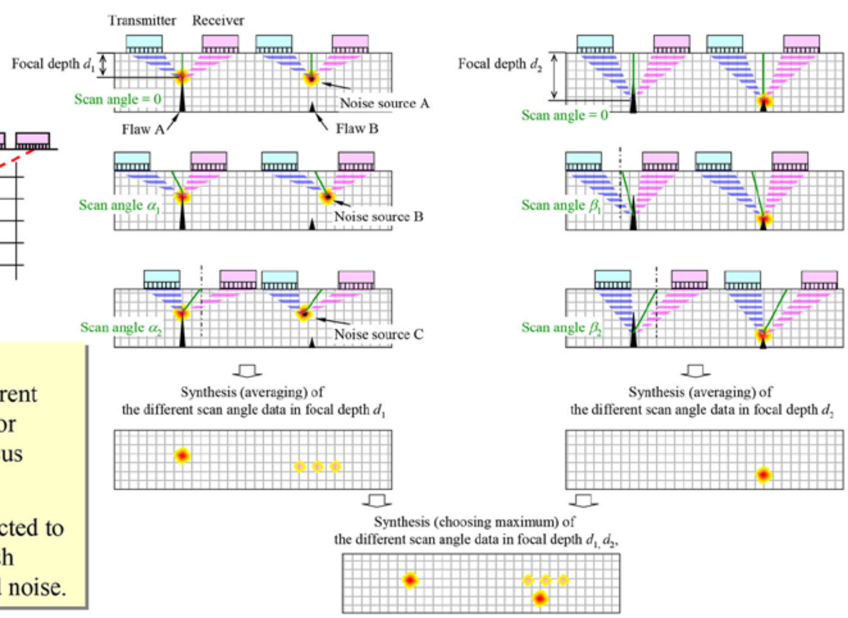

Scanning data are synthesized with different refraction angles and/or different depths of focus point.

This synthesis is expected to enable us to distinguish easily the tip echo and noise.

◆ Phased Array Twin Probe Method : PA-TP (1)

➢Schematic diagram

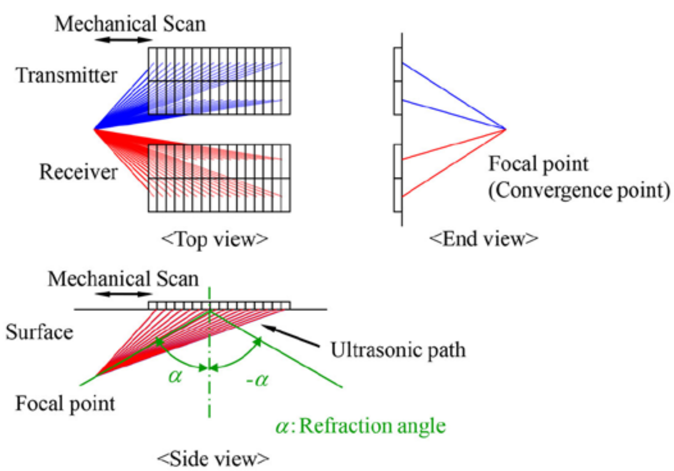

Array probe

2MHz, 10x25 matrix array

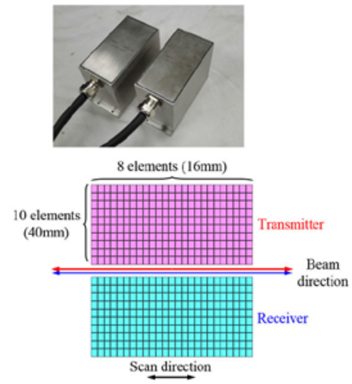

Apply to the outer surface
(far crack side)

LB
P12, P23, P24, P37
SB
P1, 41

Two array probes for transmitter and receiver perpendicular to the scan direction

Ultrasonic beams with different scan angles on the both side of the normal

⇩

Acquire the tip echo of the flaw with different scan angles

◆ Phased Array Twin Probe Method : PA-TP (2)

➢Data synthesis method

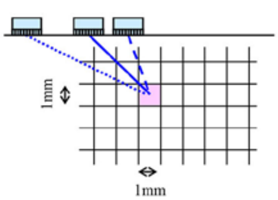

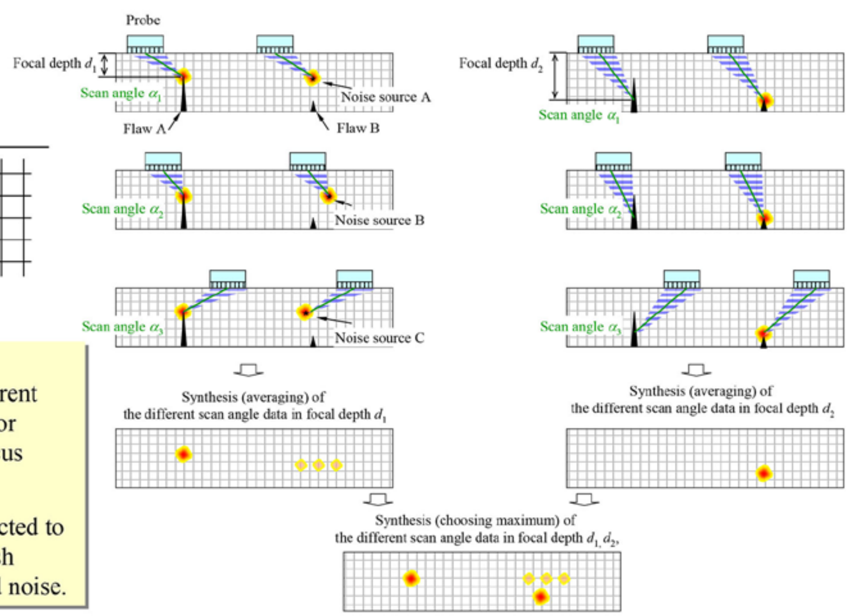

Scanning data are synthesized with different refraction angles and/or different depths of focus point.

This synthesis is expected to enable us to distinguish easily the tip echo and noise.

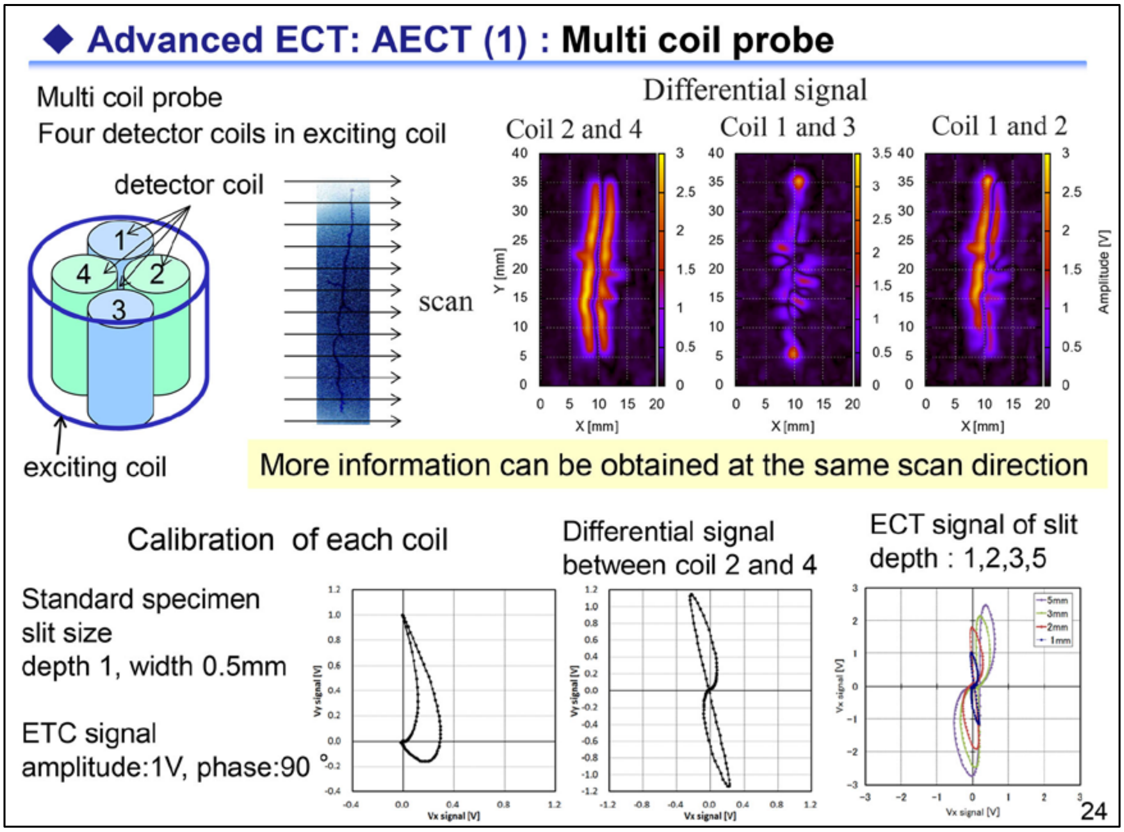
Advanced ECT: AECT (1) : Multi coil probe
Multi coil probe
Four detector coils in exciting coil
detector coil
1
2
3
4
exciting coil
scan
Differential signal
Coil 2 and 4
Coil 1 and 3
Coil 1 and 2
Y [mm]
X [mm]
Amplitude [V]
More information can be obtained at the same scan direction
Calibration of each coil
Standard specimen
slit size
depth 1, width 0.5mm
ETC signal
amplitude:1V, phase:90 °
Differential signal
between coil 2 and 4
ECT signal of slit
depth : 1,2,3,5
5mm
3mm
2mm
1mm
Vy signal [V]
Vx signal [V]
24

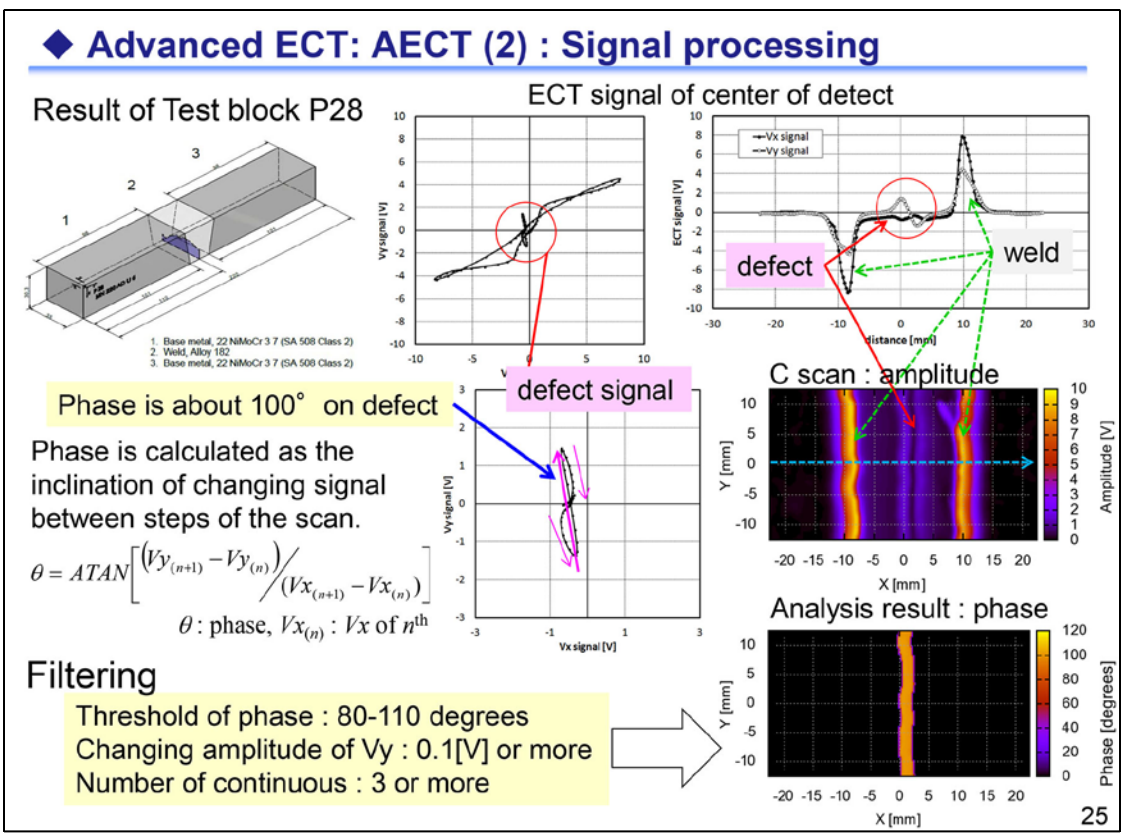
Advanced ECT: AECT (2) : Signal processing
Result of Test block P28
1. Base metal, 22 NiMoCr 3 7 (SA 508 Class 2)
2. Weld, Alloy 182
3. Base metal, 22 NiMoCr 3 7 (SA 508 Class 2)
ECT signal of center of detect
Vx signal
Vy signal
ECT signal [V]
distance [mm]
defect
weld
defect signal
Phase is about 100° on defect
Phase is calculated as the
inclination of changing signal
between steps of the scan.
$\theta = ATAN\left[\left(Vy_{(n+1)} - Vy_{(n)}\right) / \left(Vx_{(n+1)} - Vx_{(n)}\right)\right]$
θ : phase, $Vx_{(n)}$: Vx of n^{th}
Vy signal [V]
Vx signal [V]
C scan : amplitude
Amplitude [V]
Analysis result : phase
Phase [degrees]
Y [mm]
X [mm]
Filtering
Threshold of phase : 80-110 degrees
Changing amplitude of Vy : 0.1[V] or more
Number of continuous : 3 or more
25

◆ Advanced ECT: AECT (3) : Results of test block P12

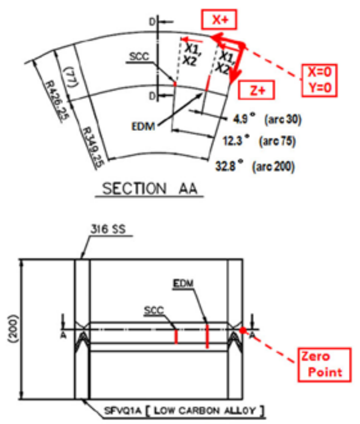

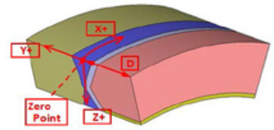

Flaw Dimension

Flaw	X1	X2	Y1	Y2
EDM	36.6	36.6	-27.0	7.0
SCC	91.5	91.5	-20.0	0.0

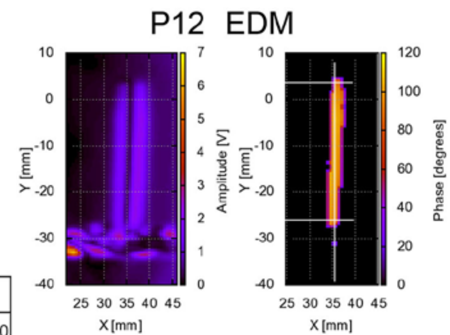

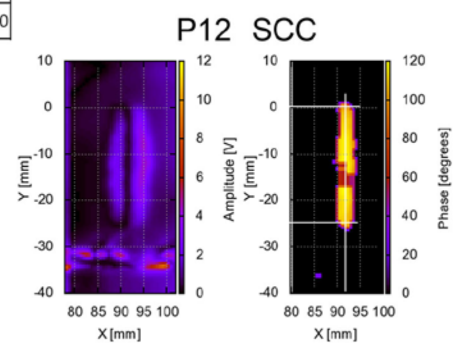

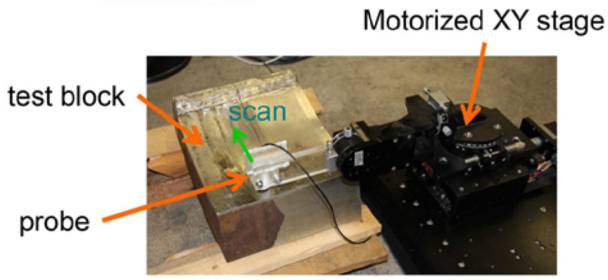

◆ Advanced ECT: AECT (4) : Results of test block P41

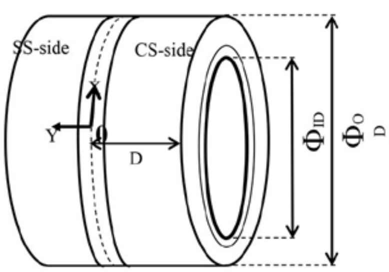

D	Φ_{ID}	Φ_{OD}
215 mm	222 mm	286 mm

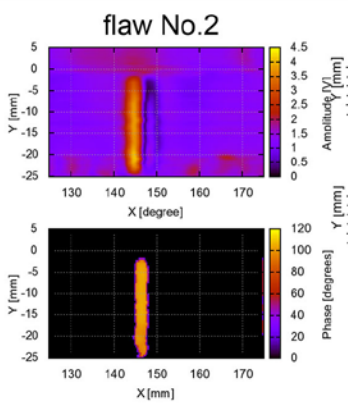

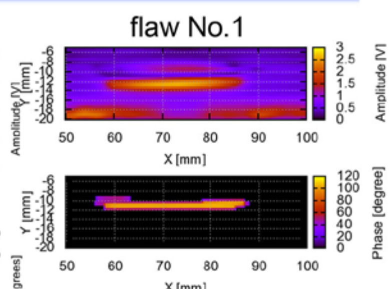

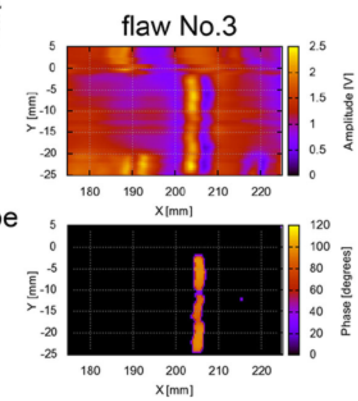

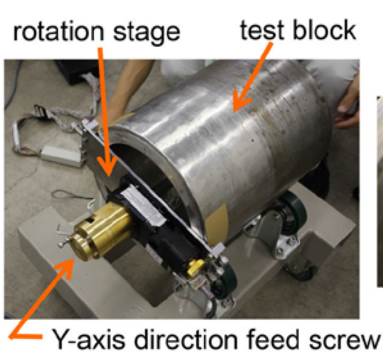

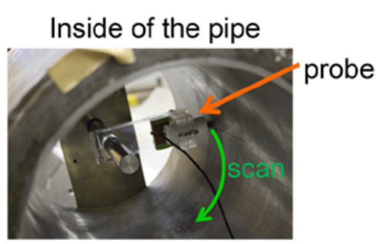

This study was performed as a part of "Japan Aging Management Program for System Safety", supported by Nuclear Regulation Authority, Japan.

◆ Controlled Excitation ECT: CEECT (1)

Problem of Conventional Eddy Current Testing

It is difficult to evaluate the depth of a flaw by ECT because the depth of a flaw does not provide a big difference in the ECT signal when the depth of a flaw is more than a certain value (In other words, the ECT signal saturates).

CEECT shows a difference in the signal phase even if the depth of a flaw is big.

Probe Configuration of CEECT

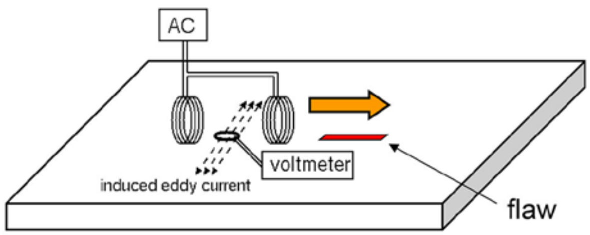

Two vertical exciters and one horizontal detector located away from the exciters.

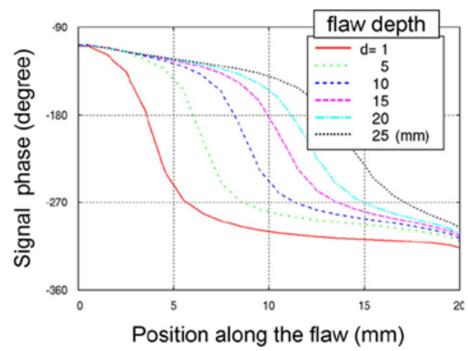

◆ Controlled Excitation ECT: CEECT (2)

Experimental results

Signals due to rectangular artificial slits of 40 mm in length on 316L austenitic stainless steel. Measured from near-side with an exciting frequency of 100 kHz.

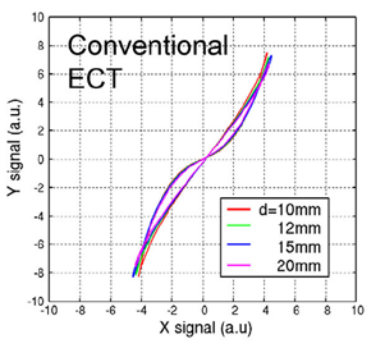

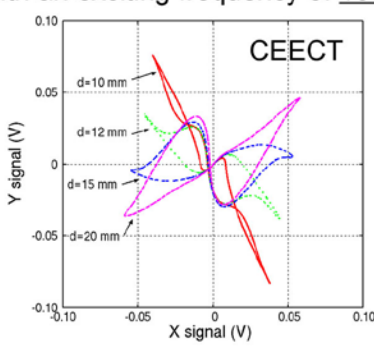

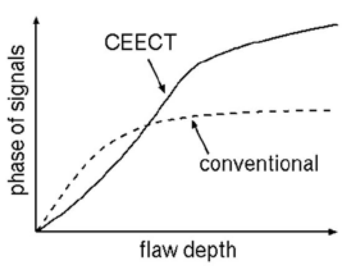

CEECT shows a difference in the signal phase even if the depth of a flaw is big.

◆ Controlled Excitation ECT: CEECT (3)

Disadvantages of CEECT

- Obtained signals have a complicated dependency on flaw parameters. Not only the depth but also the length (probably cross-sectional profile and electrical resistance as well) has a large effect on signals, which has not been quantitatively revealed yet.
- If the length of a flaw is shorter than approximately 20 mm, the change in signals with respect to the depth of a flaw becomes quite similar to that of conventional ECT (no superiority over conventional ECT).
- Since the detector needs to be located away from the exciters, the probe becomes quite large.

30

◆ Controlled Excitation ECT: CEECT (4)

Results of P12 inspection:

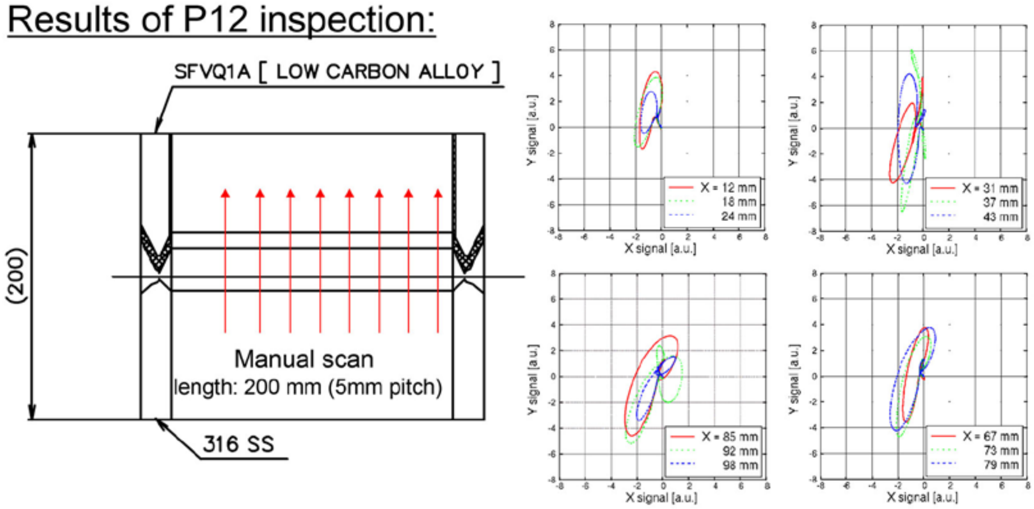

An 8-shaped loop: Flaw signal
Non 8-shaped loop: Noise

⇨ Flaw indications were confirmed at X=37 and 92 mm (same with the specification).

This study was performed as a part of “Japan Aging Management Program for System Safety”, supported by Nuclear Regulation Authority, Japan. 31

◆ Eddy Current : ECT (1)

The system is commercially available.

Instrument: R/D Tech MS5800

Probe: BMI probe (E342024D)

Coil: Ortho 3 mm

Number of coils: 24

Frequency: 200 kHz

Probe

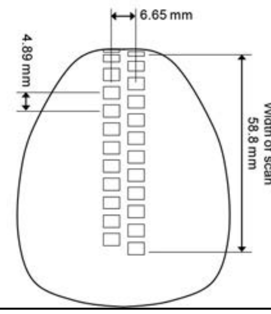

◆ Eddy Current : ECT (2)

Orthogonal coil (T/R Mode and Impedance Mode)

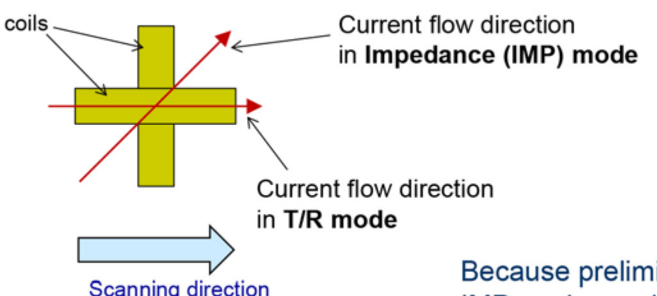

Because preliminary experiments showed IMP mode provided better results than TR mode, only IMP mode is used.

Advantages

- Orthogonal coils offer directional sensitivity
- Clear separation of circumferential and axial indications by 180° phase change
- Self compensation configuration (less sensitive to lift-off and conductive change)

Limitations

- Low sensitivity to defects parallel to current flow
- Complex signal interpretation is required for multidirectional cracks

◆ Eddy Current : ECT (3)

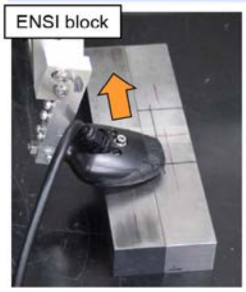

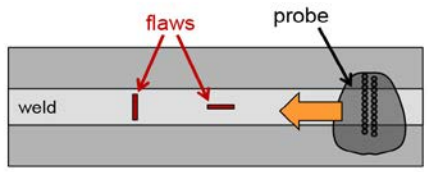

Only one path is scanned for each test block.

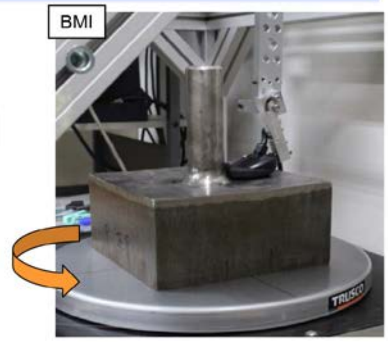

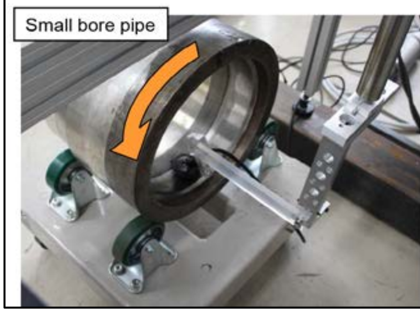

◆ Eddy Current : ECT (4)

Example of signal distribution

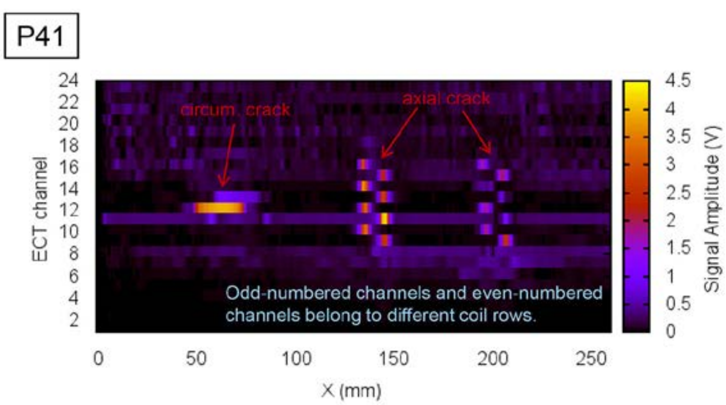

35

◆ Microwave Near-field Microscope : MM (1)

Quantitative evaluation of fatigue crack

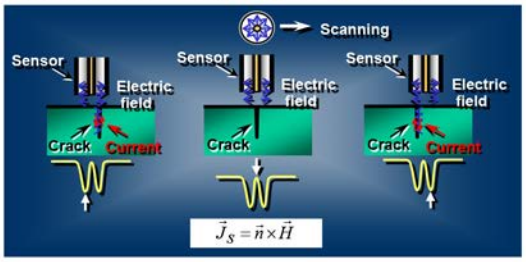

Mechanism of the detection of small crack using microwave

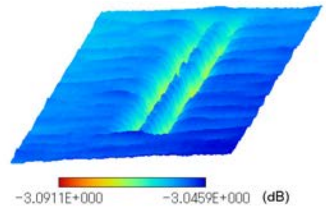

Microwave image of a 3-D fatigue crack

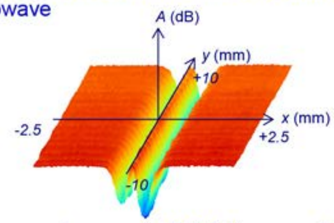

Microwave image of a 2-D fatigue crack

$$d = \frac{\Delta A(f_1) - \frac{G(f_1)}{G(f_2)}\Delta A(f_2)}{S(f_1) - \frac{G(f_1)}{G(f_2)}S(f_2)} \quad (1)$$

$$I = \Delta A'(f_1, y_s) - \frac{G'(f_1, y_s)}{G'(f_2, y_s)}\Delta A'(f_2, y_s) \quad (2)$$ [1]

$$\left.\begin{aligned} I_c(y_s) &= C_1 + C_2 \log\sqrt{\alpha^2 + \beta^2} \\ \alpha &= \frac{1}{M}\sum_{i=0}^{M}\frac{1}{\sqrt{kr}}\cos\left\{2kr\left(i\frac{\pi}{M}\right)\right\} \\ \beta &= \frac{1}{M}\sum_{i=0}^{M}\frac{1}{\sqrt{kr}}\sin\left\{2kr\left(i\frac{\pi}{M}\right)\right\} \end{aligned}\right\} \quad (3)$$

[1] Y. Ju et al., *NDT & E Int.*, 38, 726, (2005)

1

◆ Microwave Near-field Microscope : MM (2)

Measurement by manual scanning

Distribution of the electric and magnetic field at the sensor aperture

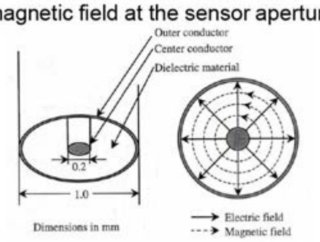

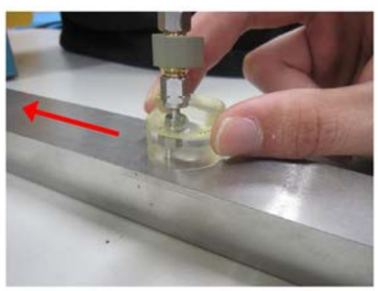

Detection of closed fatigue crack
(Frequency: 67 GHz)

Manual scanning

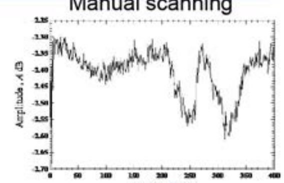

Automated scanning

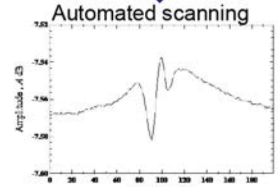

detection result of P23

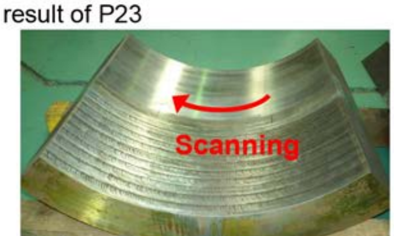

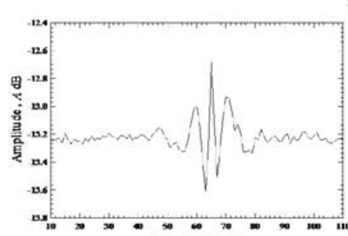

EDM slits on the curved surface were detected.

2

◆ Microwave Near-field Microscope : MM (3)

Measurement by automated scanning

Photograph of network analyzer

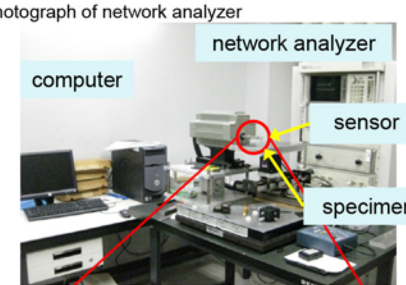

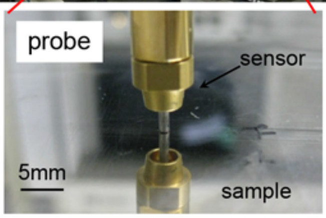

Test parameters

Frequency: 110GHz
Standoff distance : 60 mm
Scan direction pitch : 0.04 mm
Step direction pitch : 1 mm

P28 Detection result

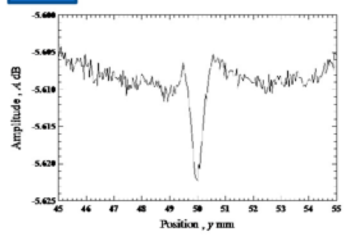

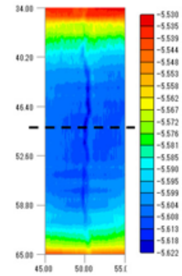

Visualization of crack
by two-dimensional imaging

Evaluation equation for crack depth sizing

$$d = \frac{\Delta A}{\eta_0 \eta_1 (40 \log_{10} e)\alpha}$$

d: crack depth
ΔA: amplitude difference
α: Attenuation constant
η_0, η_1:Constants of loss and irradiation of microwave

3

A.3 European Techniques

Technique Descriptions for 114-PA1, 122-PA1 & 122-PA2

PARENT-8, 20 December 2013
Esa Leskelä
VTT Technical Research Centre of Finland

VTT's Open Test Teams and Test Blocks

Team 1:
114-PA1

P1, P4, P41,
P28, P29
P29, P31
P32, P38
P42, P46
} ENSI Blocks

Team 3:
122-PA1 &
122-PA2

P28, P29
P29, P31
P32, P38
P42, P46
} ENSI Blocks

Techniques
114-PA1, 122-PA1 & 122-PA2

- Phased array ultrasonic technique
- All the techniques use the same 1.5 MHz probes
  - Dedicated probes for circumferential flaw inspection
  - Dedicated probes for axial flaw inspection (only 114-PA1)
- Shear wave (SW) and longitudinal wave (LW)
- T/R configuration
- OD access, manual encoded scanning from both sides of the weld

Technique 114-PA1

- Circumferential flaws:
  - Detection, characterization and length and height sizing of inner surface breaking circumferential flaws
- Axial flaws:
  - Detection, characterization and height sizing of inner surface breaking axial flaws but no length sizing

Techniques 122-PA1 & 122-PA2

- Techniques were developed for more accurate height sizing of flaws in the ENSI blocks but are easily applicable to real piping inspections.
- Goal was also to compare the performance of linear and sectorial scan in flaw height sizing and crack tip detection.
- Manual encoded scanning was used because of practical reasons (large probe in relation to small ENSI test blocks) – otherwise an automated scanner is used.

Equipment 114-PA1 & 122-PA1

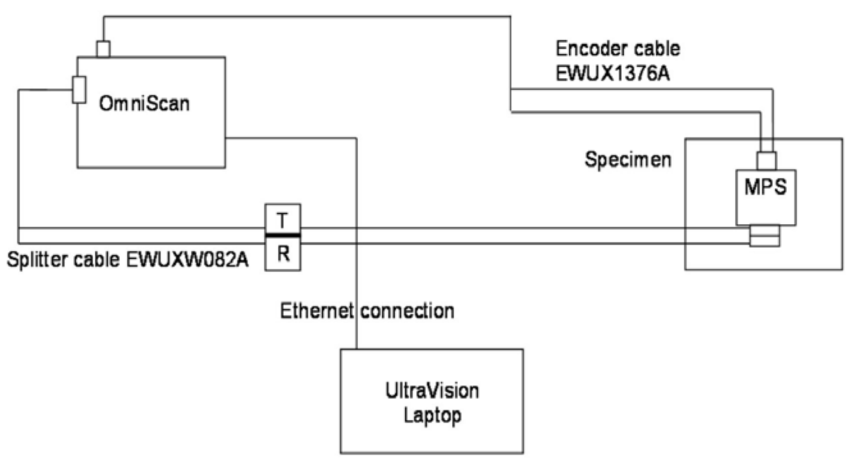

Equipment 122-PA2

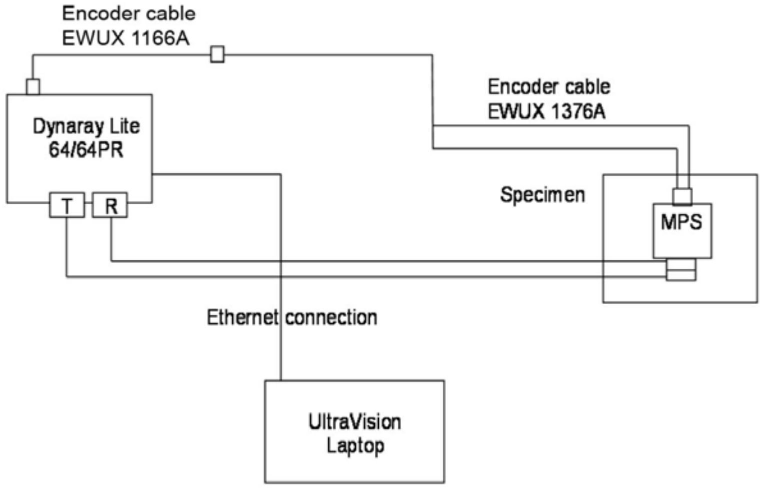

Techniques 114-PA1, 122-PA1 & 122-PA2

Technique	Technology	Access	Scanning Mode	Wave Mode	Frequency	Equipment	Scan Type	Flaw Type	Array Configuration	Refracted Angles	Skew Angles	Length Sizing	Height Sizing
114-PA1	PAUT, commercial procedure	OD	Manual encoded scanning	LW+SW	1.5 MHz	OmniScan & UltraVision	Linear T/R raster scan	CIRC + AXIAL	1D linear for circ. flaws, 2D matrix for axial flaws	LW for circ. flaws: 30°, 45°, 60°, 70° SW for circ. flaws: 45°, 60° LW for axial flaws: 25°, 35°, 45°, 55° SW for axial flaws: 35°, 45°, 55°	Only for axial flaws −22.5° … +22.5°, step 2.5°	Full amplitude drop	Crack tip or conservative measurement using the upper extent of the flaw image
122-PA1	PAUT, non-commercial procedure							CIRC	1D linear	LW 45°, 50°, 55°, 60°, 65° SW 45°, 50°, 55°, 60°	N/A	N/A	Crack tip or -6 dB drop
122-PA2						Dynaray Lite	Sectorial T/R one line scan			Sectorial 40° – 70°, step 1°			

Techniques 122-PA1 and 122-PA2

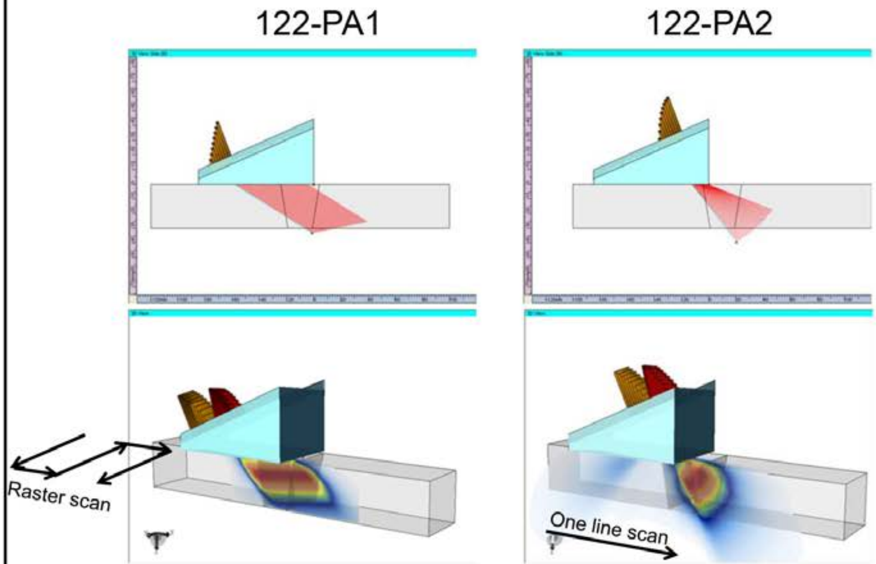

Techniques 122-PA1 and 122-PA2

- End views of test block P46 without flaw
- Linear scan with 122-PA1: high resolution, good SNR
  - ➔ good sizing performance expected
- Sectorial scan with 122-PA2: lower resolution, stronger metallurgical and mode converted signals

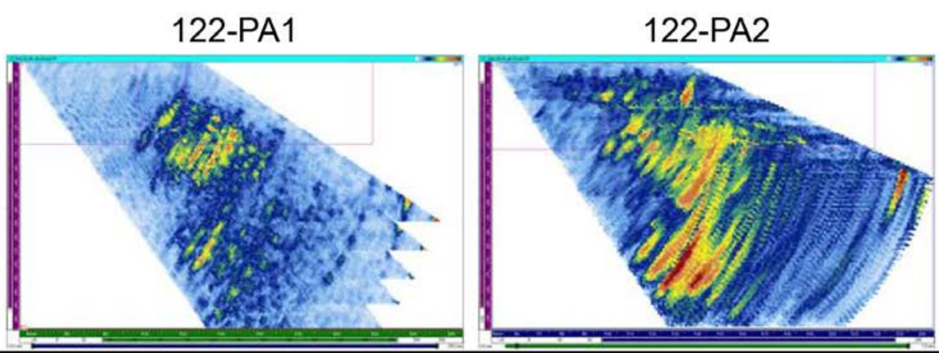

Self-assessment

- Advantages:
  - Techniques are easy to set up for site inspection as well as for laboratory work.
  - The phased array probes are versatile and the search unit (probes+wedge) enables the use of multiple angles and both longitudinal and shear wave modes.
  - The interchangeable wedges enable a large variety of components to be inspected with the same probes.
  - Rather fast data acquisition.
  - Effective data handling because the data can be collected on the same hard disk of the laptop which is used for analysis so no data transfer is required.
  - Data processing prior to data analysis is simple and fast.

Self-assessment

- Disadvantages:
  - Skewing of ultrasonic wave is not possible with the linear probes used for circumferential flaws. Same probe and wedge is used for both shear and longitudinal wave modes so focusing capability is limited.
  - Data analysis requires a lot of effort because of the multiple data merge groups which are analysed separately.
  - Data analysis requires a skilled person.

Overview of the open PARENT RRT in Switzerland

December 2013

PARENT Consortium – Switzerland represented by

K. Germerdonk [1], Hans-Peter Seifert [2], Dominik Nussbaum [3], Hardy Ernst [4], Alex Flisch [5]

[1] Swiss Federal Nuclear Safety Inspectorate – ENSI, Brugg, Switzerland
[2] Paul Scherrer Institute (PSI), Nuclear Energy and Safety Research Department, Laboratory for Nuclear Materials, Villigen, Switzerland
[3] ALSTOM Power Products, NDT METHODOLOGIES, Baden, Switzerland
[4] Swiss Association for Technical Inspections – Nuclear Inspectorate, Wallisellen, Switzerland
[5] EMPA, Swiss Federal Laboratories for Materials Science and Technology, Dübendorf, Switzerland

Open RRT NDE summary presentation

- X-ray computed tomography
- Phased array applications
- Through transmission

2

X-ray computed tomography

CT-Scanner	CITA 101 B+ (Cita Systems)
Beam geometry	Fan beam
X-ray source	X-ray system MG452 (YTU450-D09)
Parameters of X-ray source	450 kV / 3.3 mA / 1.0 mm focal spot
External X-ray filtration	1.5 mm Brass
Detector	Single collimated (W) line detector (CdWO4) with 125 detector channels
Detector aperture [mm]	0.35 x 0.15
Manipulator position	16
Pixel size of CT-slice [mm]	0.12 x 0.12
Slice distance [mm]	0.12
Object diameter [mm]	60
Ray Spacing [mm]	0.18
Integration time [ms]	100
Beam hardening correction	1.5

Photo of test object on CT-scanner:

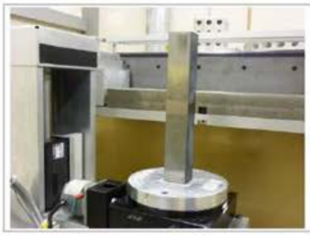

Fig. 1:
Test Block ID: P32 (N 220 AD U TS 5), view from X-ray source towards the line detector. The sample is oriented such that the crack opening is located on the side of the X-ray source.

3

X-ray data

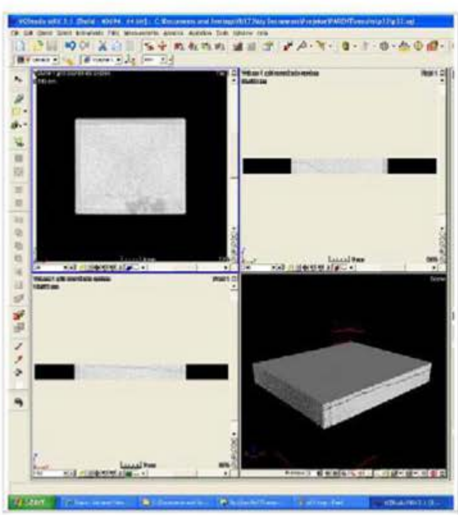

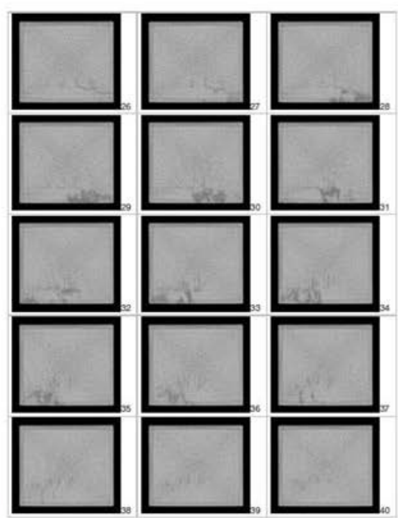

4

X-ray data - depth sizing

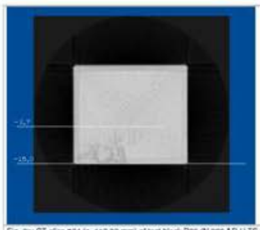

Fig. 2e: CT-slice #34 (z=112.32 mm) of test block P32 (N 220 AD U TS 5), crack depth: 11.3 mm (+/- 2 pixel = 0.24 mm), 37.3% of weld thickness

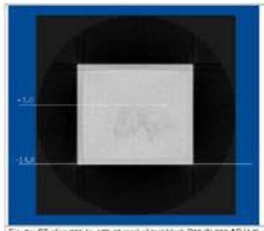

Fig. 2c: CT-slice #06 (z=107.40 mm) of test block P30 (N 220 AD U 7), crack depth: 17.8 mm (+/- 2 pixel = 0.24 mm), 58.7% of weld thickness

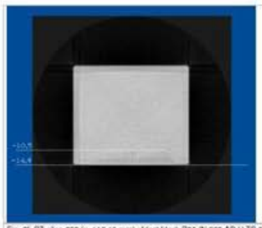

Fig. 2f: CT-slice #29 (z=110.16 mm) of test block P38 (N 220 AD U TS 3), crack depth: 4.4 mm (+/- 2 pixel = 0.24 mm), 14.5% of weld thickness

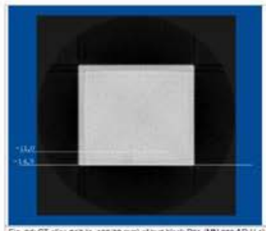

Fig. 2d: CT-slice #17 (z=106.72 mm) of test block P31 (MN 220 AD U 1), crack depth: 3.9 mm (+/- 2 pixel = 0.24 mm), 12.9% of weld thickness

5

Phased array applications using commercial probes

Method	Phased Array Ultrasonic Testing
Array / Technique	Dual / Matrix / Transmit - Receive
Wave Mode	Longitudinal
Angle Range	40° - 70°
Frequency	1.5 MHz
Scan Plan	Manual scanning perpendicular to weld both directions
Scanning Surface	OD

Method	Phased Array Ultrasonic Testing
Array / Technique	Single / Linear / Puls Echo
Wave Mode	Longitudinal
Angle Range	40° - 70°
Frequency	2.33 MHz
Scan Plan	Encoded in +Y and – Y direction
Scanning Surface	W & X

Method	Phased Array Ultrasonic Testing
Array / Technique	Dual / Linear / Transmit - Receive
Wave Mode	Longitudinal
Angle Range	25° - 65°
Frequency	2 MHz
Scan Plan	Manual scanning perpendicular to weld in +Y direction
Scanning Surface	OD

6

Phased array applications for DMW

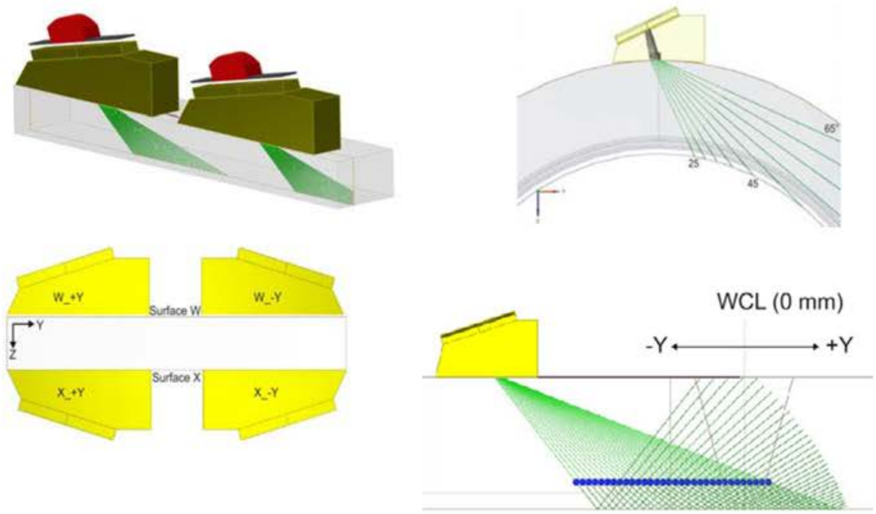

7

Depth sizing - commercial probes

- Absolut Arrival Time Technique (AATT) was used
- Direct signal response from the flaw required
- Flaw depth is calculated by subtracting the remaining ligament from the actual material thickness

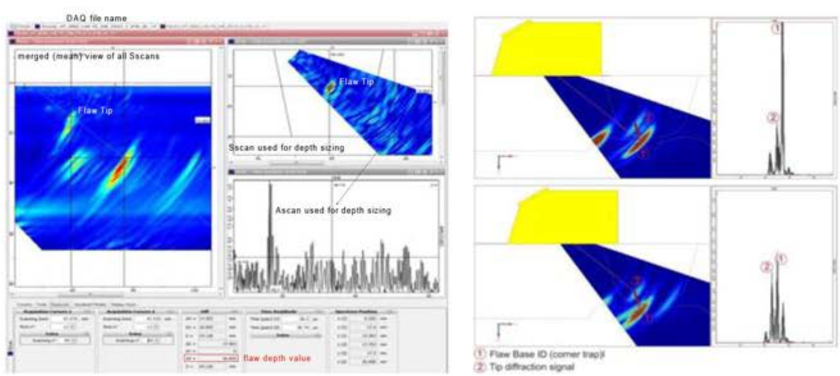

8

Challenges of depth sizing on DMW

Images on specimen P32 (laboratory grown SCC) using same conventional PA-probe

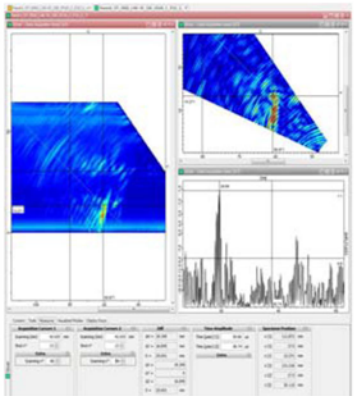

ID – measurement – estimated depth 13.4 mm

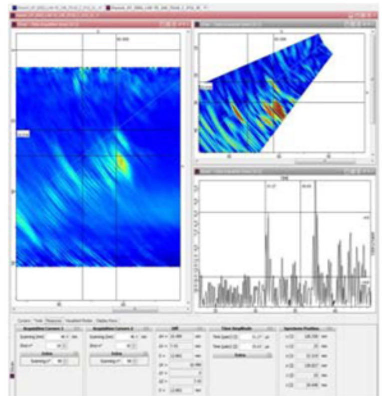

OD – measurement – estimated depth 7.5 mm

Through transmission with reflection on back wall

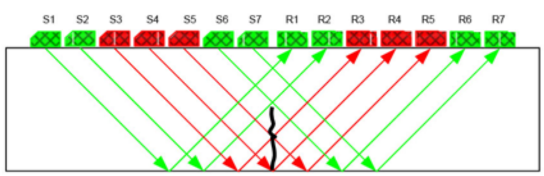

A very simple approach

- Sound is sent from S1 via back wall to R1, from S2 to R2 etc.
- As long as there is no discontinuity of the sound path the receiver will detect high amplitude (green). In case the sound is blocked by discontinuity (red) the receiver will detect much lower amplitude.
- The received amplitude can then be displayed on a C-scan representation

Advantage

- No influence of flaw surface roughness
- Orientation of flaw doesn't influence detectability, but parallel inner surface is necessary
- Very low noise from scattered sound (grain boundaries…) therefore, higher frequencies can be used

Parent consortium - Switzerland, PARENT
Project Update, December 2013

Through transmission data

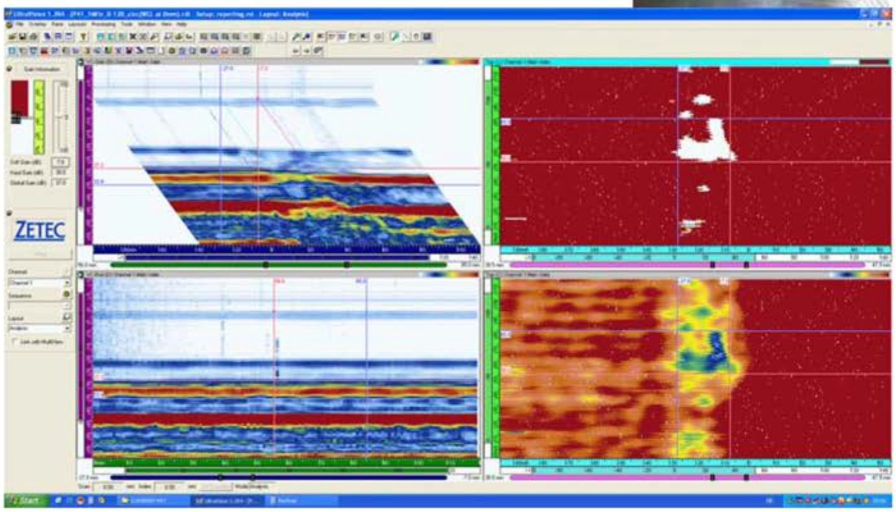

Depth sizing

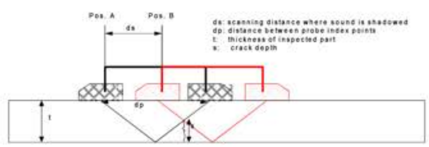

Set-up:
- Two identical probes (aperture, frequency, angle) with an angle of about 40° to 45° (long), fixed in a probe holder.
- Distance between probe index points is optimized to receive the reflected longitudinal wave from the backwall (LL)
- Probe holder is moved over the surface and the distance where sound is shadowed by the crack will be stored (B-scan of the received signal)

Crack depth is given by the following formula:

$a = ds * t / dp$

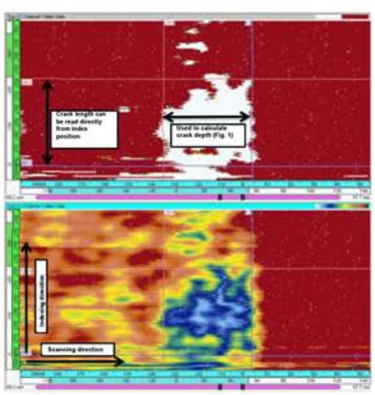

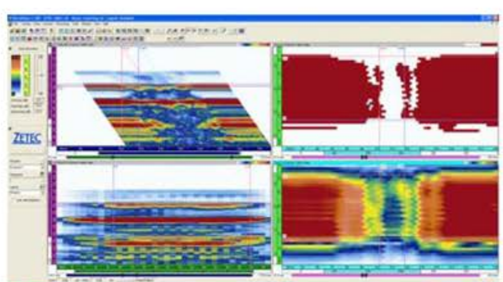

12

A.4 USA Technique 7-ECT1

Technical Description for Technique 7-ECT1

Eddy Current Probe Functionality and Configuration

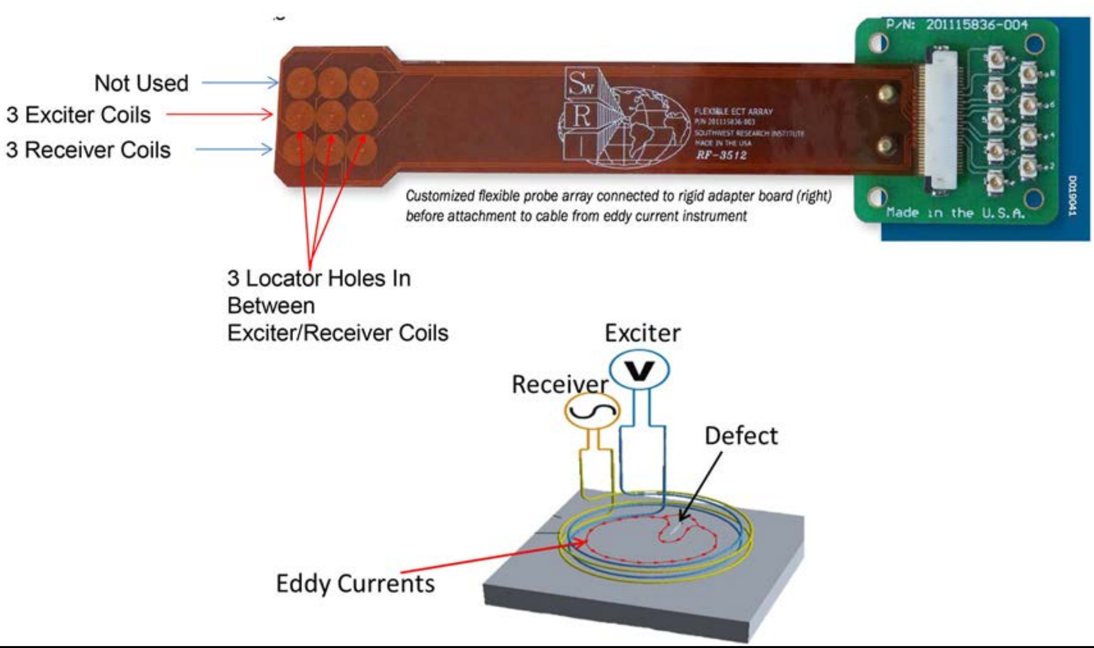

Sample Flaw

Corresponding Screen Shot

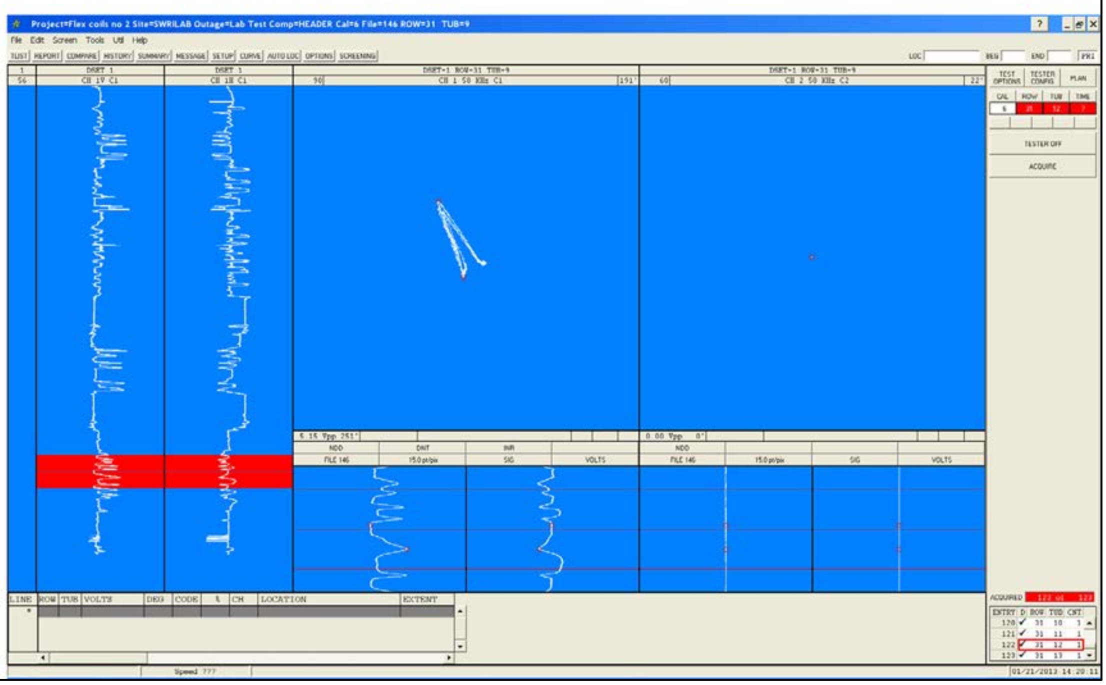

Overview

- Test Blocks Types Examined: BMIs
- NDE Technique: Eddy Current
- Measures: Location/Length of Surface Breaking Flaws
- Data Acquisition: Manual Scans [Measurements & Probe Translation/Rotation]
- Access: J-Groove Weld Surface
- Measurement Instrument: CoreStar Omni 200
- Probe:
  - $\geq$ 50kHz Flexible Array [Southwest Research Institute 201115836-003]
  - 9 coils arranged in a 3x3 square matrix configuration
  - Designed to detect relatively large flaws on rough welded surfaces
- Signal Processing: None
- Signal Analysis/Interpretation: Manual
  - Visually estimate locations of ends of flaws using 6dB drop from maximum amplitude.
  - Manually mark the location on the test block of the 6dB point through the hole in the probe centered between the exciter/receiver coils.
  - Use a Coordinate Measurement Machine (CMM) to determine the X,Y coordinates of the flaw end points with respect to the R,θ,Z zero point as defined in the protocol
  - Translate X,Y coordinates to R,θ.

Test Team's Assessment of the Technique

- Test Blocks Types Examined: BMIs
- NDE Technique: Eddy Current
- Measures: Location/Length of Surface Breaking Flaws
- Data Acquisition: Manual Scans [Measurements & Probe Translation/Rotation]
- Access: J-Groove Weld Surface
- Measurement Instrument: CoreStar Omni 200
- Probe:
  - $\geq$ 50kHz Flexible Array [Southwest Research Institute 201115836-003]
  - 9 coils arranged in a 3x3 square matrix configuration
  - Designed to detect relatively large flaws on rough welded surfaces
- Signal Processing: None
- Signal Analysis/Interpretation: Manual
  - Visually estimate locations of ends of flaws using 6dB drop from maximum amplitude.
  - Manually mark the location on the test block of the 6dB point through the hole in the probe centered between the exciter/receiver coils.
  - Use a Coordinate Measurement Machine (CMM) to determine the X,Y coordinates of the flaw end points with respect to the R,θ,Z zero point as defined in the protocol
  - Translate X,Y coordinates to R,θ.

Test Team's Assessment of the Technique

Advantages:

- Low cost for the part of the probe that will be subject to wear
- Possibility of manufacturing with even greater number of coils to ensure 100% coverage with a single scan
- Fabrication technique ensures accurate manufacturing repeatability
- Probe flexibility greatly simplifies the motions required of a mechanized scanner, especially in the case of penetrations that are not normal to the vessel surface

Disadvantages:

- The use of single layer flexible printed circuit material (used to provide great flexibility) limits the number of turns of the coil; hence the spatial resolution is limited and the operating frequency had to be kept at 50 kHz or greater

A.5 USA Technique 7-PA1

Technical Description for Technique 7-PA1 & 7-PA2

Overview

- Technique 7-PA1: Detection, Characterization, Length Sizing, Positioning
- Technique 7-PA2: Depth Sizing

Common to Both Techniques:

- Test Block Type Examined: DMWs
- NDE Technique: Ultrasonic Phased Array
- Data Acquisition: Automated, Encoded
- Access: Inner Diameter
- Equipment: Zetec Tomoscan-III 32/128 [128 Phased Array Channels]
- Data Analysis Software: Ultravision 1
- Examination Directions: Upstream, Downstream, Clockwise, Counter-clockwise
- Probe Frequency: 1.5MHz

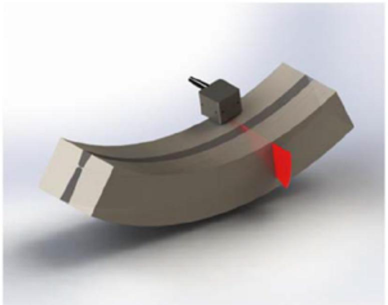

Technique Specifics

Common to Technique 7-PA1:

- Focal Law Gain: 14dB
- Examination Angles:
  - Circumferential & Axial Flaws: 60-88°, 2° Increments
- Maximum Increment Resolution: 0.05" (axial flaws), 0.15" (circumferential flaws)
- Detection: C-scan indications that exhibit echo-dynamics in the B-scan are considered to be flaws
- Characterization: Surface breaking if A-scan shows flaw signal at 0 inches.
- Length Sizing: Determined by measuring the ¼ maximum amplitude in a full-merged C-Scan (top view) for axial and circumferential flaws

Common to Technique 7-PA2:

- Focal Law Gain: 20 dB
- Examination Angles:
  - Circumferential Flaws: 30-70°, 1° Increments
  - Axial Flaws: 60-82° & 40-46°, 2° Increments
  - Maximum Increment Resolution: 0.10" (axial & circumferential flaws)
  - Depth Sizing: Employs a methodology that uses information from merged and unmerged B-scans and D-scans.

Test Team's Assessment of the Procedure/Technique

Advantages:

- The use of multiple inspection angles increases the probability of detection.
- Allows for sectorial scanning and simplification of DMW's with complex geometry.
- A separate detection procedure allows larger indexing for a quicker detection examination.

Disadvantages:

- A more complex examination technique which requires personnel with proper training and /or experience to implement it.
- A separate depth sizing examination at smaller indexing is required after flaw detection is completed.

A.6 ISA Technique 150-PA0

Technical Description for Technique 150-PA0

Phased Array Data Acquisition Equipment

0.2 – 20 MHz

256 channels

Ultravision® software

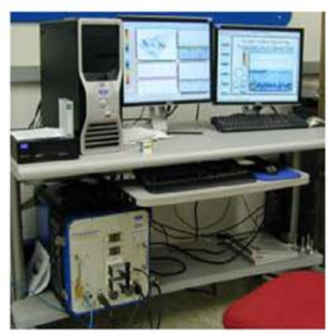

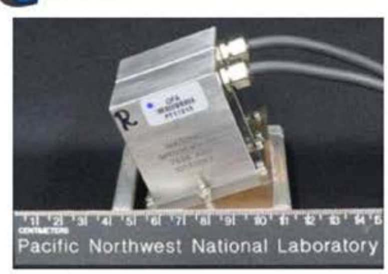

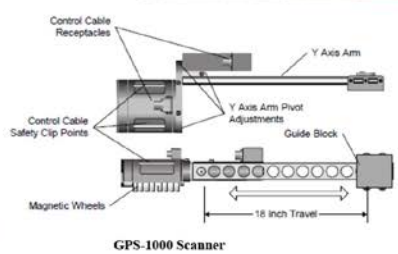

Probe and Scanner Configuration

Pulsing and Scanning Parameters

- 1.0 MHz 2x(10x5) element matrix array [10 Elements in Primary]
  - Transmit-Receive Longitudinal
    - Each element pulsed with 500 ns negative 200V square wave excitation (Dynaray)
  - True Depth and Half Path focusing techniques
  - 20-60 degree azimuthal angle sweep, 3 degree increments
  - 0,±10 degree skew angles
  - OD inspection: Raster scan resolution: 1.0 mm scan, 1.0 mm index
- OD contoured Rexolite wedge
  - 15 degree wedge angle
- 0 pt., coordinates and scan conventions followed from test block information sheet
- Circumferential scans (looking for axial flaws)
  - Collect data in clockwise and counter clockwise directions
- Axial scans (looking for circumferential flaws)
  - Collect data from up stream and down stream locations
- Target Focus: Inner Diameter Regions
  - ID connected flaws (cracks)

Data Imaging and Analysis

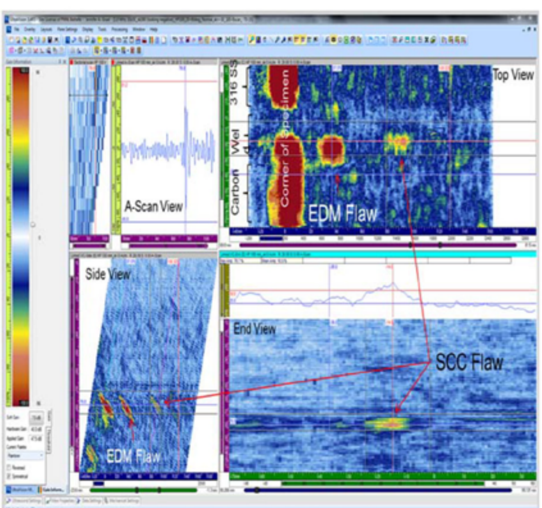

- Phased array image analysis
  - A-Scan (time-amplitude) along selected angles
  - C-Scan (Top View) scan vs. index axes – location and length of flaw
  - B-Scan (Side View) scan vs. ultrasound axes – depth of flaw
  - D-Scan (End View) index vs. ultrasound axes – length and depth of flaw
- Detection
  - Strong response signal(s) present in the ID region of component
    - Signal strength above background noise levels to be considered (greater than 6 dB above background)
- Characterization
  - Detected signals will be length sized using a -6 dB and loss of signal (LOS) method in the D-Scan view
  - Depth sizing will be assessed by measuring maximum flaw extent in the B and/or D Scan view(s)
  - Overall flaw circumferential and axial location assessed with C-Scan view

4

A.7 USA Technique 170-LUV0

Technical Description for Technique 170-LUV0

Laser Ultrasound Visualization (LUV) Technique

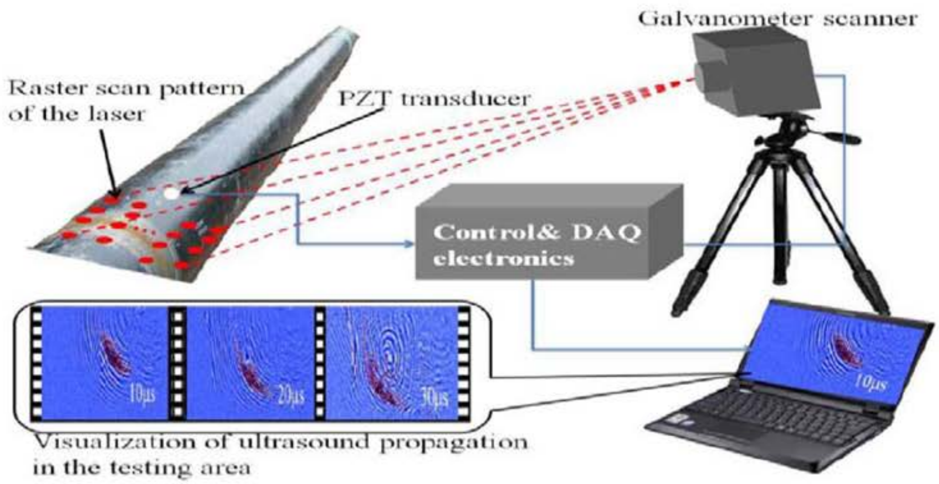

Experimental System

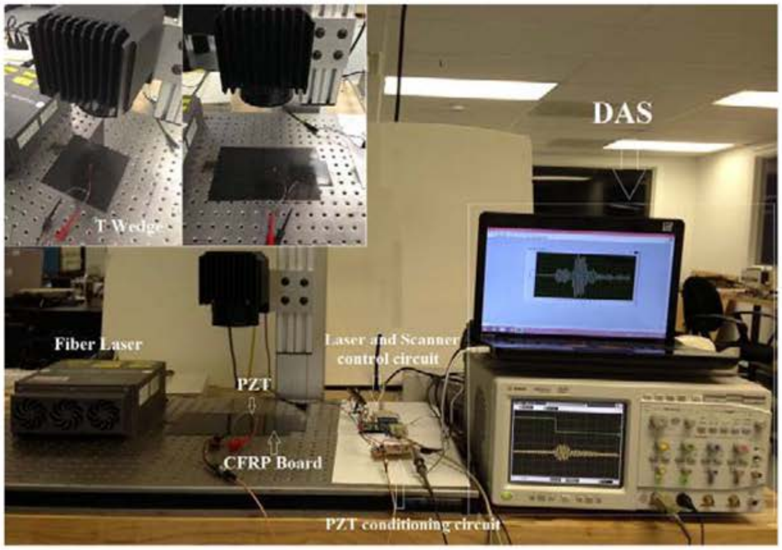

Experimental Samples

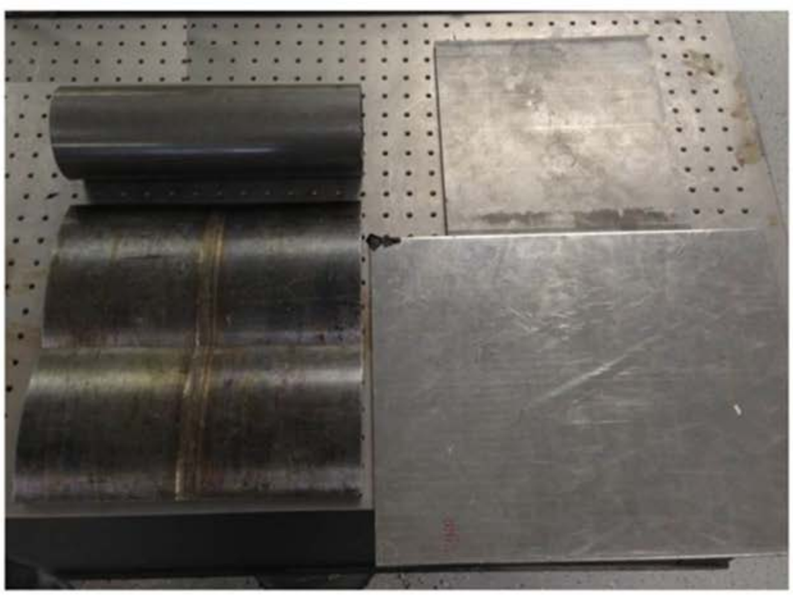

Overview

- Test Blocks Types Examined: BMIs & DMWs
- NDE Technique: Laser Ultrasound Visualization
- Measures:
  - Detects/Locates surface and sub-surface flaws (flaws within the material)
  - Depth/Length sizing capability is to be determined
- Data Acquisition: Automated
  - Spatial Sampling Step Size: ~.1–several mm
  - Sampling Rate: 5-20x10^6 samples/second
- Access: DMW – Outer Diameter, BMI – Surface of the J-Grove Weld
- Measurement Instrument: Commercial Off The Shelf (COTS) Components
  - Laser pulse energy delivery system (thermally induced ultrasound source)
  - Miniature piezoelectric transducer (detector of ultrasound placed on inspection surface)
  - Control and data acquisition electronics system (DAS)
  - Laptop computer
  - Power source - battery
- Signal Processing Approach for Automatic Defect Detection and Location
  - See following slide
- Signal Interpretation: Visual
  - Results are displayed as time based (micro-second scale) movie clips which permit operators to directly see/visualize the propagation of the ultrasound signals in time.
  - Cracks, voids, welding flaws, can easily be visualized by minimally trained personnel.

Algorithm for Automatic Defect Detection & Location

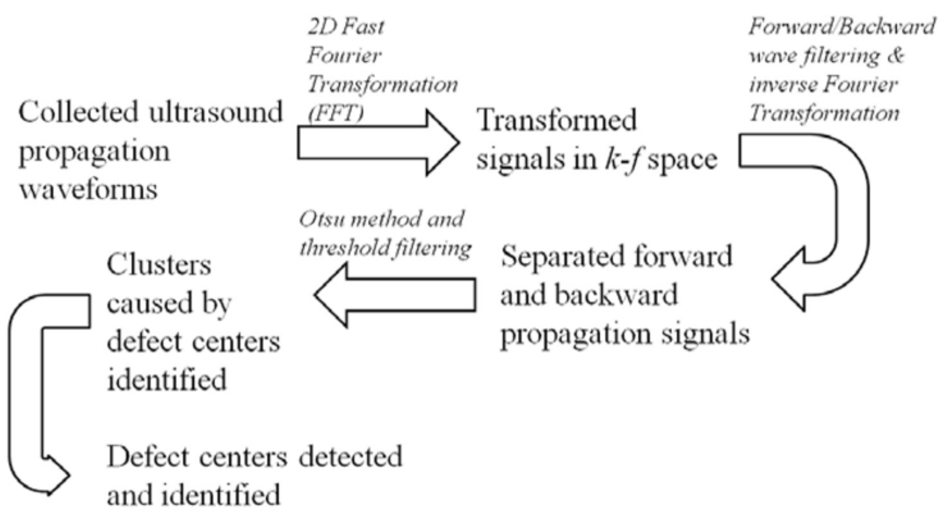

Test Team's Assessment of the Technique

Advantages:

- Makes it possible to detect/identify flaws with a 2-dimensional image versus the 1-dimensional method of traditional ultrasound.
- Detection of flaws with 1-dimensional waveforms is confounded by the propagation modes, boundary reflections, and physical features that heavily convolute the ultrasonic waveforms propagating in real-world weld structures. Complicated modeling is often necessary to overcome these limitations. The LUV technique makes it possible to directly visualize flaws in complicated shapes and configurations.
- Compact, lightweight, portable
- Capable of detecting a wide variety of defects
- Compatible with complex shapes and configurations
- High sensitivity (excellent signal/noise ratio) and good spatial resolution (better than 1mm)
- High measurement throughput – 2m/second X/Y scan speed
- Safe to operators – involves no harmful radiation

Disadvantages:

- Undetermined*

  *The ability of this technique to accurately length size and depth size flaws in BMI/DMW configurations is under investigation, so is unknown at this time.

Appendix B

Europe Detailed Technique Descriptions

Appendix B

Europe Detailed Technique Descriptions

B.1 Through Transmission of Longitudinal Waves, Technique ID 104-UT-P/C0

B.1.1 Overview

Trough transmition of ultrasonic longitudinal waves is amongst others used for detection of delaminations in composites with difficult accoustic properties. Normally the delaminations are expected to be parallel to the inspection surface and sender and receiver probe are on oposite sides of the part to be inspected. In case of a delamiation the sound will be blocked and therefore the receiving probe will detect a reduced amplitude.

For this application there are mainly two things different:

1. The orientation of the crack is more or less perpendicular to the surface.
2. There is only access from one side

To get an interaction between crack and sound beam and to be able to measure the depth extension of the crack, through transmission with angle beam is necessary.

To overcome the problem with the not accessible back wall, the receiving probe will be placed on the same surface as the sending probe and one reflection on the back wall will be used.

With the set-up shown in Figure B.1, it is possible to detect and measure cracks perpendicular to the surface:

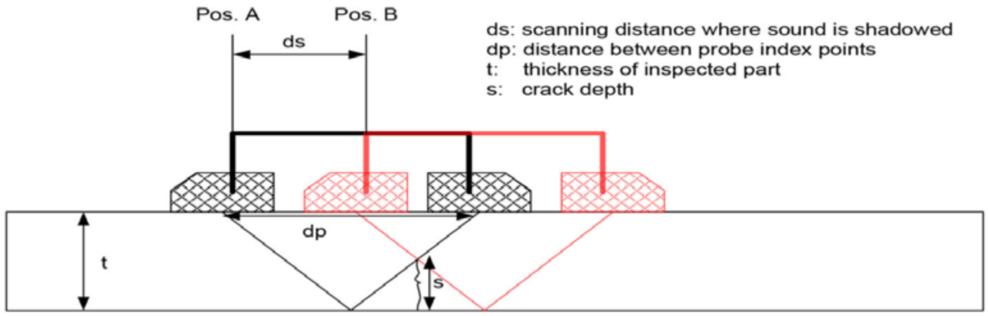

Set-up:
- Two identical probes (aperture, frequency, angle) with an angle of about 40° to 45° (long), fixed in a probe holder.
- Distance between probe index points is optimized to receive the reflected longitudinal wave from the backwall (LL)
- Probe holder is moved over the surface and the distance where sound is shadowed by the crack will be stored (B-scan of the received signal)

Crack depth is given by the following formula:

$s = ds * t / dp$

Figure B.1. Illustration of Inspection Set-up and Calculation of Depth Extension of Crack

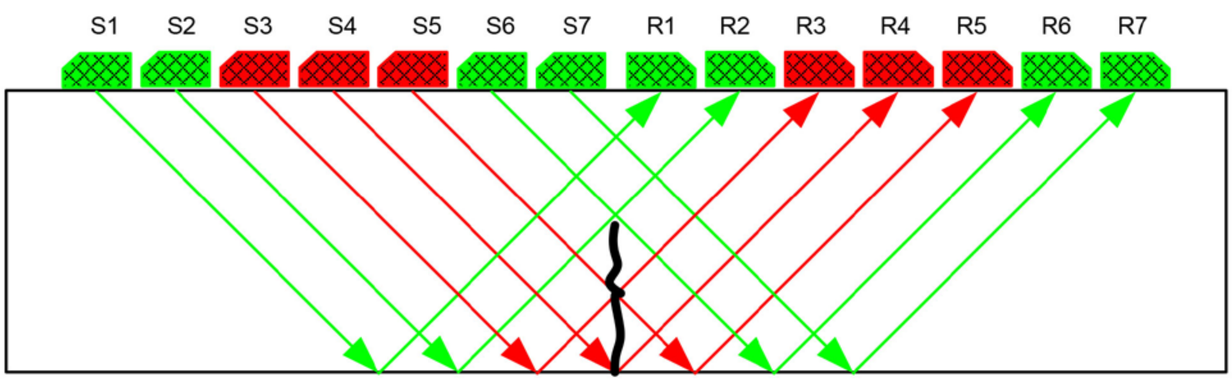

Sound is sent from S1 via back wall to R1, from S2 to R2 etc. As long as there is no discontinuity on the sound path the receiver will detect high amplitude (green). In case sound is blocked by a discontinuity (red) the receiver will detect much lower amplitude. The received amplitude can then be displayed on a C-Scan representation and calculation described in Figure B.1 can be done using this C-Scan. Figure B.4 shows such a C-Scan.

Figure B.2. Inspection Principle

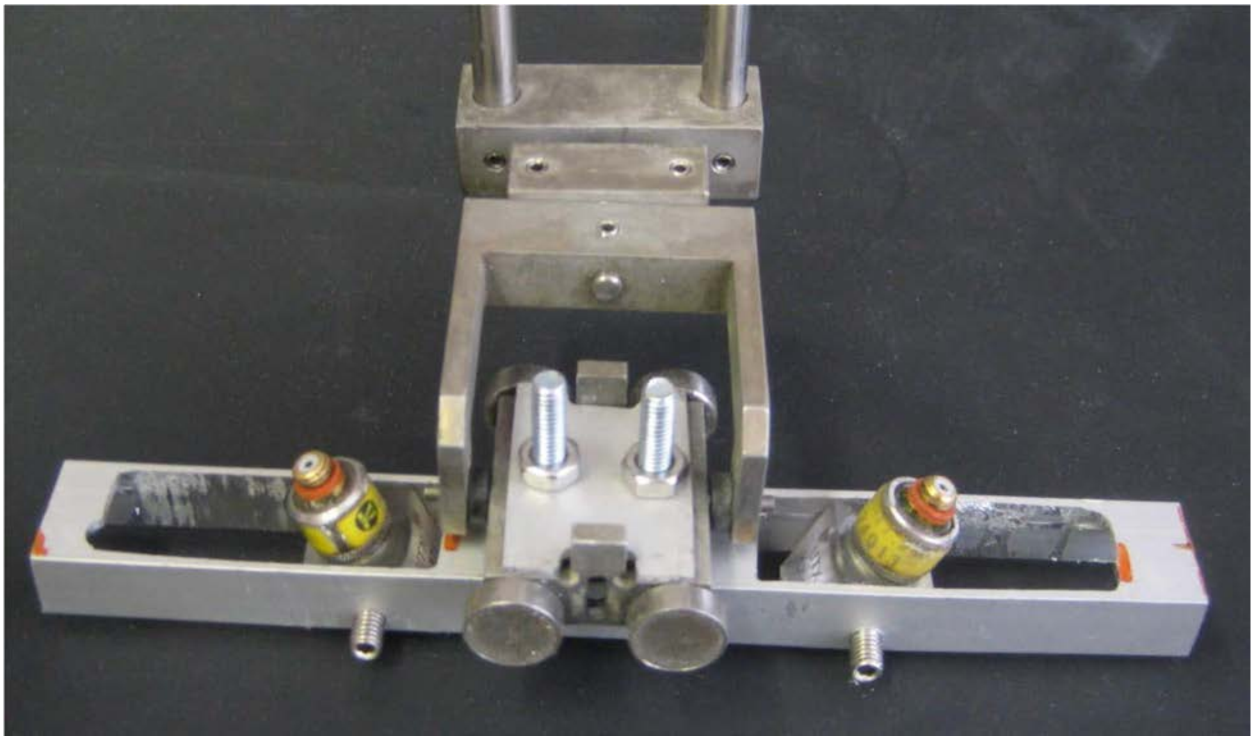

Figure B.3. Probe Holder with Defined Distance between Sender and Receiver

To allow offline evaluation of the data the full A-scan information needs to be stored together with position information (X and Y coordinates).

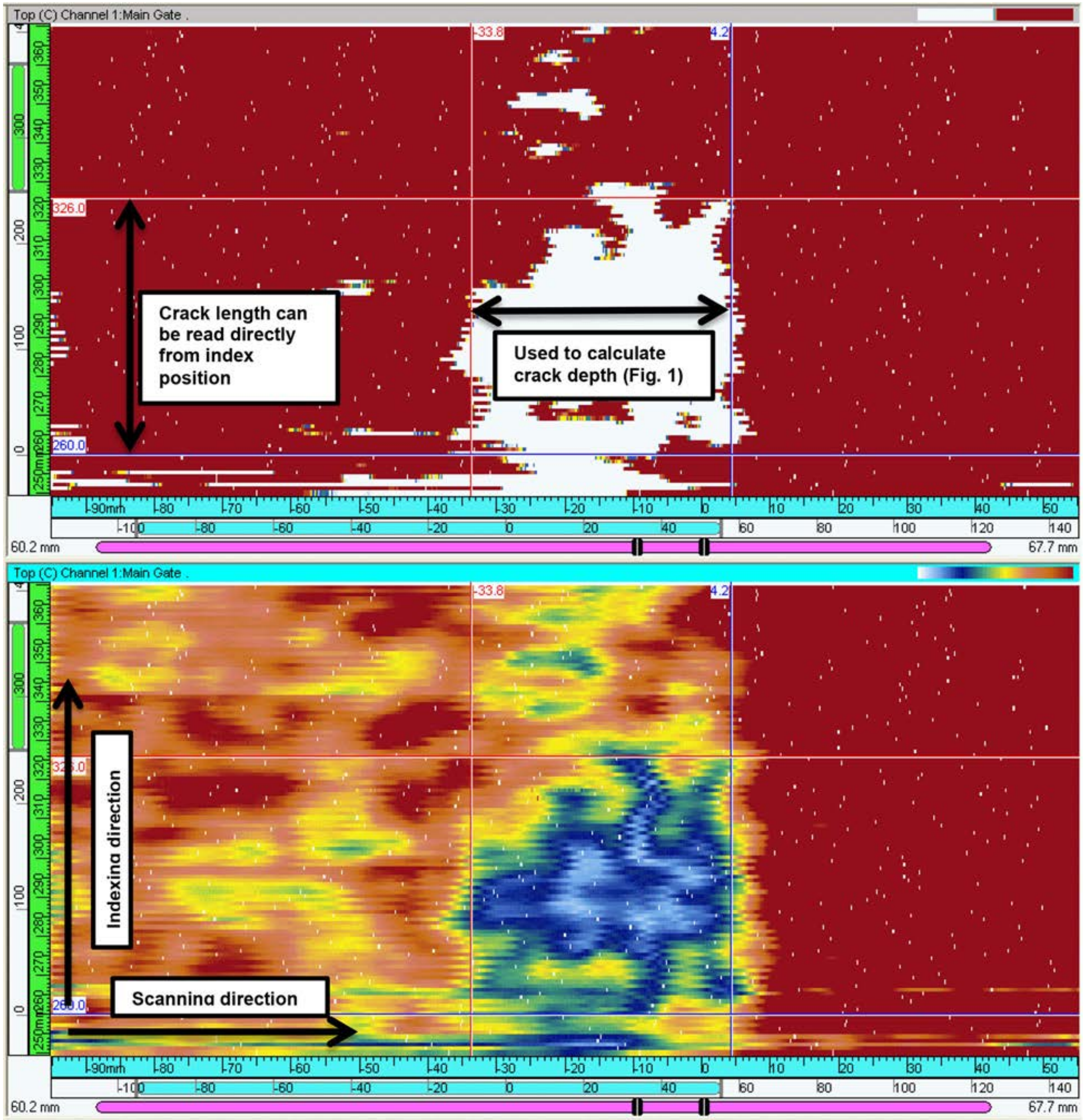

The lower C-Scan shows the received amplitude color coded (0% FSH [white] to 100% FSH [red]). The upper C-Scan shows the C-Scan after using a 6 dB drop filter (0% to 50 % FSH [white] and 50% to 100% FSH [red]). On the left side of the C-Scans the influence of the cladding is visible. The attenuation caused by the cladding is a limiting factor and if it's too high it can make inspection impossible.

Figure B.4. Example of C-Scan Representation Used for Evaluation (circumferential flaw, open to inner surface)

B.1.2 NDE Equipment

A ZScan PA 64 (ZPA5022) from ZETEC together with Ultravision software was used for data aquisition. To facilitate coupling the part to be inspected was immersed in water. An XYZ-scanner was used to move the probe holder over the surface of the part. Encoder information from the scanner was provided to the ZScan to be stored together with A-scan data.

Two Panametrics probes were used:

- C548-SM with a diameter of 10 mm and a frequency of 1.0 MHz (sender)
- A548-SM with a diameter of 10 mm and a frequency of 1.5 MHz (receiver)

Rexolite wedges were used and their angle was machined to get an incident angle of 45° longitudinal wave in the test piece.

Distance between the probe indices is set to two times the wall thickness of the part to be inspected.

B.1.3 Data Acquisition Process (for defects with circumferential orientation)

The probe holder was placed on the outer surface of the part to be inspected in a way that the direction from sender to receiver was parallel to the axial direction of the tube. This set-up is only valid for circumferential crack orientation.

After start of data acquisition in Ultravision the scanner was started as well. Scanning direction was in axial direction and the scanning length was set in a way that both probes were passing weld, buttering and HAZ. After one scan line the probe holder was shifted in circumferential direction (index) and a scan in opposite direction to the first one was performed.

Like this a certain circumferential rage was tested. This range was limited due to the fact that it was not possible to rotate the part while scanning and the probe holder was only able to compensate a limited change of the surface orientation.

B.1.4 Data Analysis

C-scan of 45° LL reflection of back wall was evaluated:

Where no (perpendicular) crack is present the back wall will be detected with high amplitude. At positions where the sound path from sender to receiver is affected by the crack the amplitude will drop. 6 dB drop compared to sound material will be used to define the extensions of the flaw. Additionally pattern recognition will be used.

A crack connected to the inner surface will result in a C-scan where the area with amplitude drop will be continuous whereas an inclusion or lack of fusion will result in two individual (mirrored) areas with amplitude drop).

Length of the crack corresponds to the scanning index distance where the crack will be detected.

Crack depth is calculated from the scanning distance where a drop of amplitude is detected. For calculation of crack depth compare sketch and formula in Figure B.1.

Sizing technique will be used for defect positioning. Centerline (perpendicular to scanning direction) of the area with amplitude drop will be used as defect position whereas the mechanical reference of the C-scan will be the center of the probe assembly.

B.1.5 Self Assessment

Advantages of this UT inspection technique are:

- No influence of flaw surface roughness
- Orientation of flaw doesn't influence detectability
- Very low noise from scattered sound (grain boundaries…), therefore higher frequencies can be used

Disadvantage of this approach are:

- Cladding of the surface influences the amplitude of transmitted sound and therefore alters the inspection results
- A parallel inner surface is necessary. Otherwise Scanning becomes difficult (position dependent distance and/or inspection angle of sender and receiver probe).
- Altered microstructure influences the inspection result. This is mainly the problem when artificial flaws are produced by local heating or welding / brazing of a defective volume into the reference block.

B.2 Phased Ultrasonic Array, Technique ID 131-PA0

B.2.1 Overview

The techniques described in this report were utilized for the examination of the -specimens P28, P29, P30, P31, P32, P42 and P46.

Method	Phased Array Ultrasonic Testing
Array / Technique	Single / Linear / Puls Echo
Wave Mode	Longitudinal
Angle Range	40° – 70°
Frequency	2.33 MHz
UT Instrument	M2M MultiX 64
Scan Plan	Encoded in +Y and – Y direction
Scanning Surface	W & X

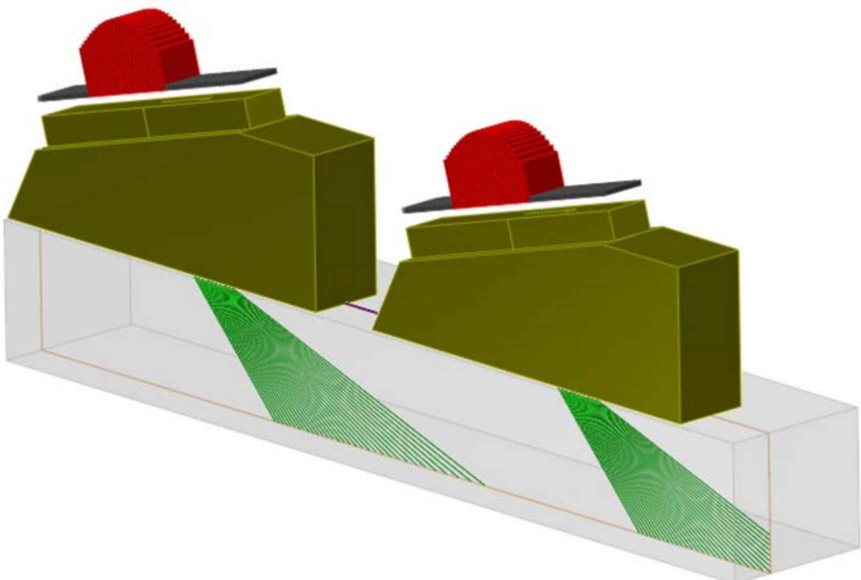

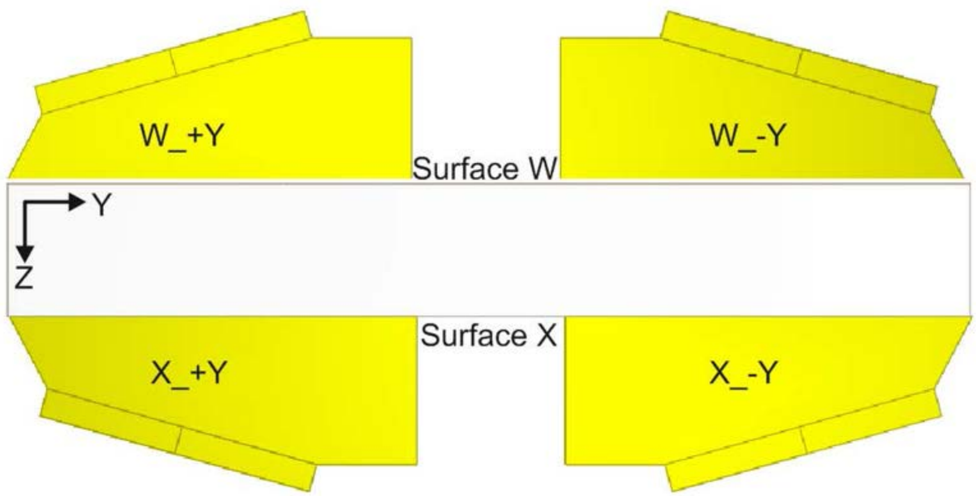

Figure B.5. Technique Overview Illustrations

B.2.2 NDE Equipment / UT Settings

B.2.2.1 Search Unit

For the measurement a sonaxis probe and wedge was used. The essential variables of the search unit are described below.

Crystal Shape

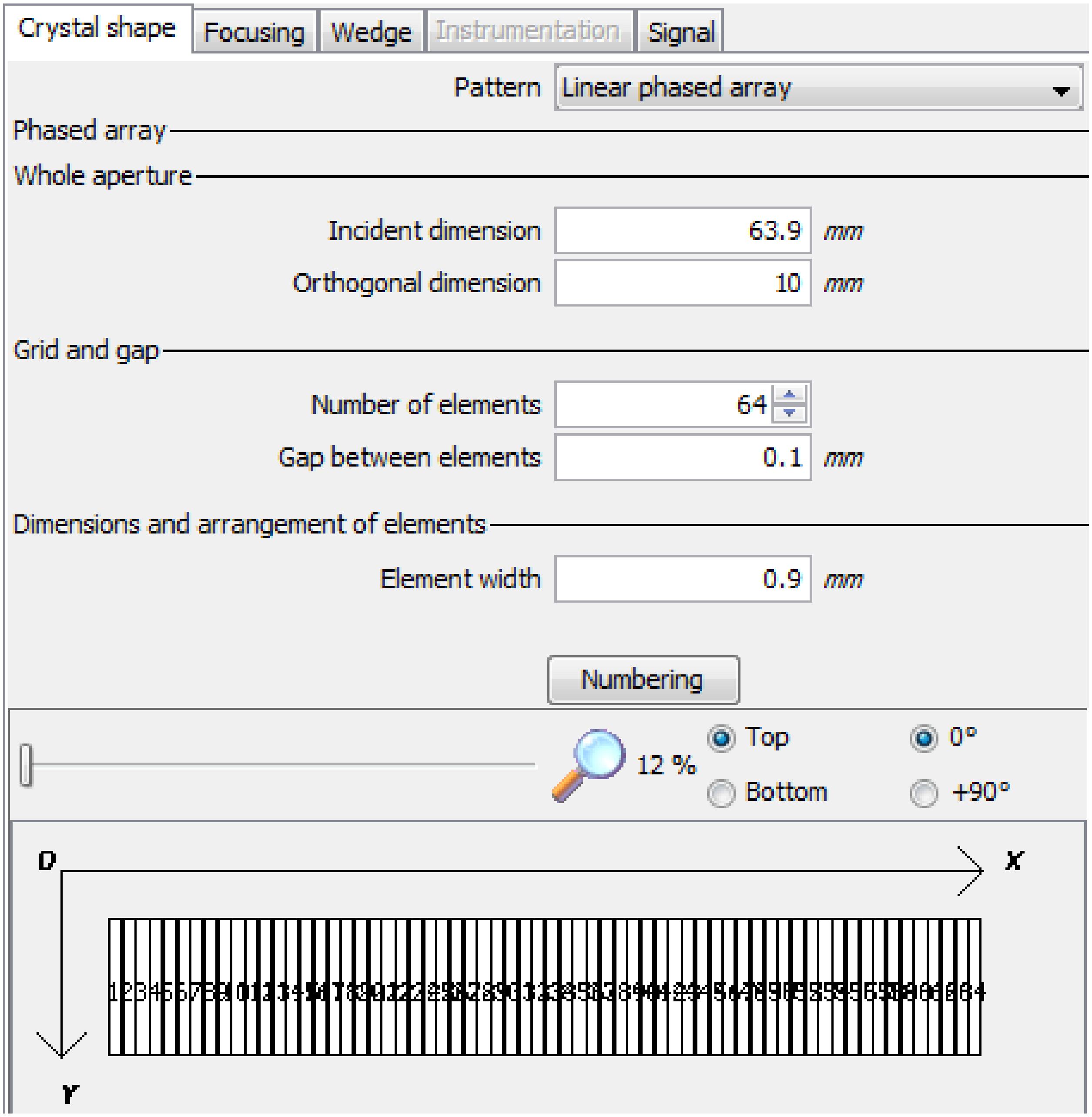

Figure B.6.

Focusing

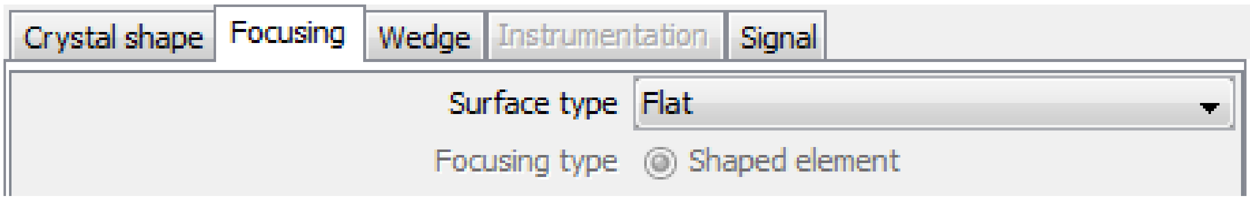

Figure B.7.

Wedge

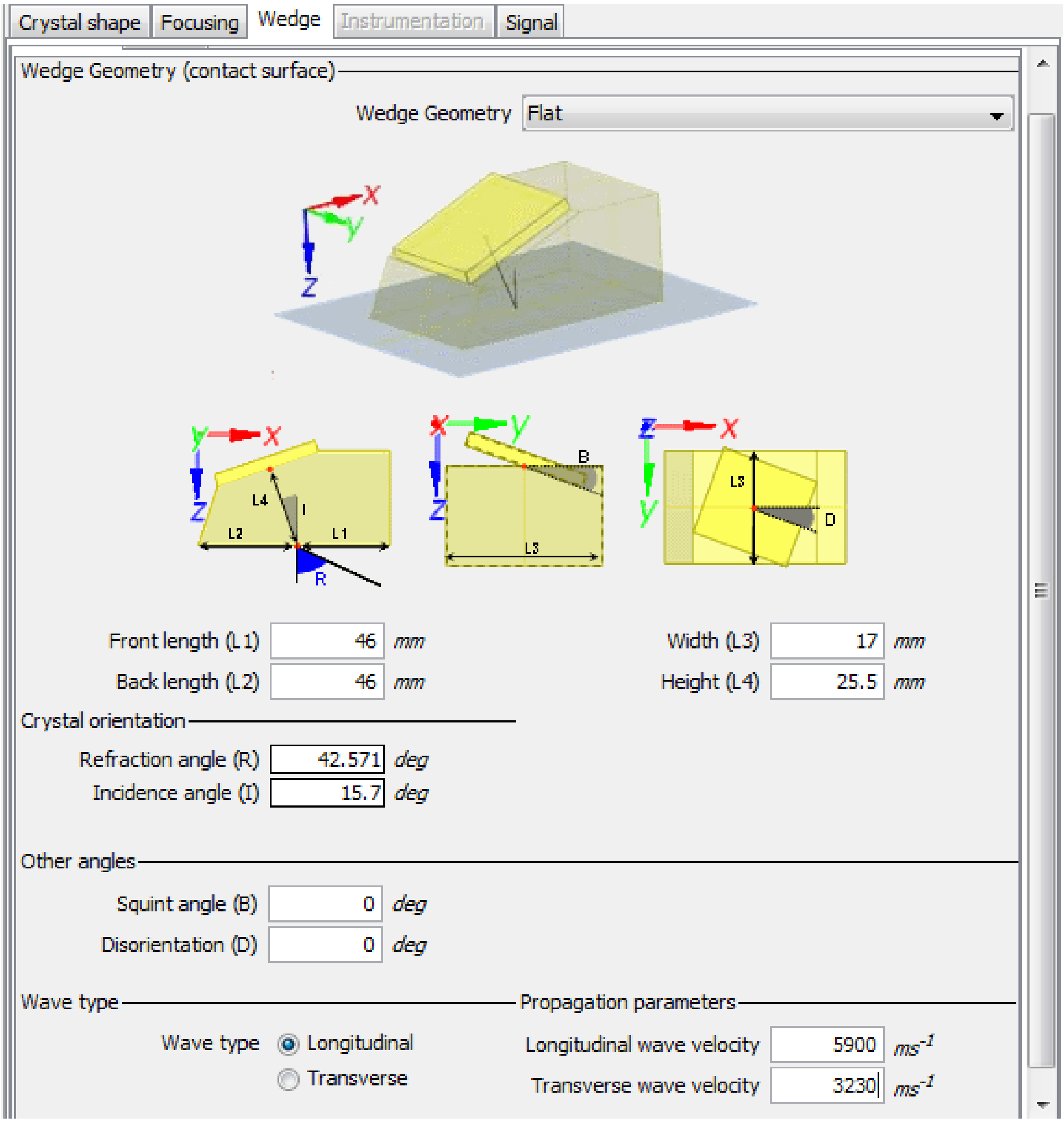

Figure B.8.

Signal

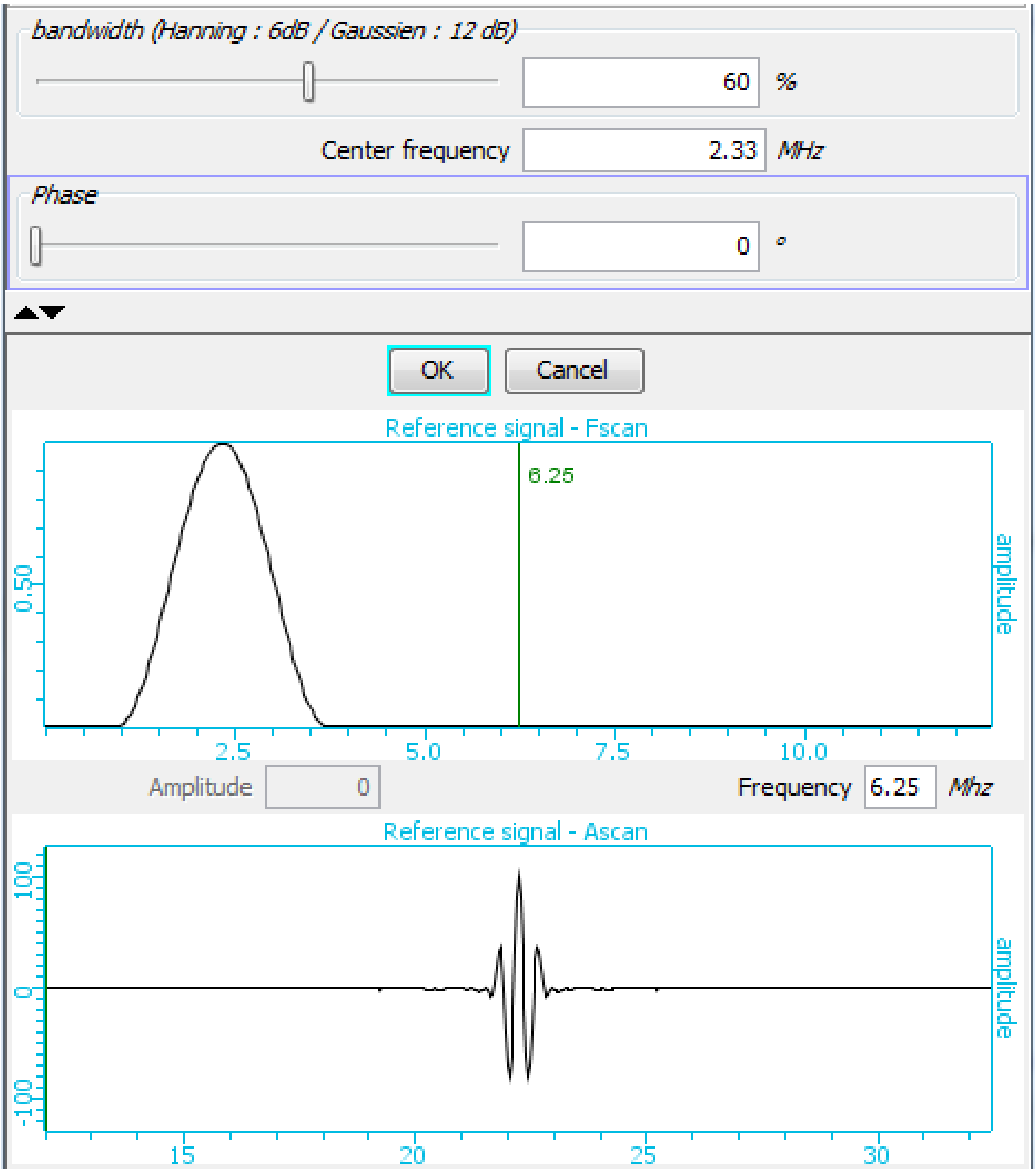

Figure B.9.

B.2.2.2 Phased Array Settings – Focal Law

Initialization

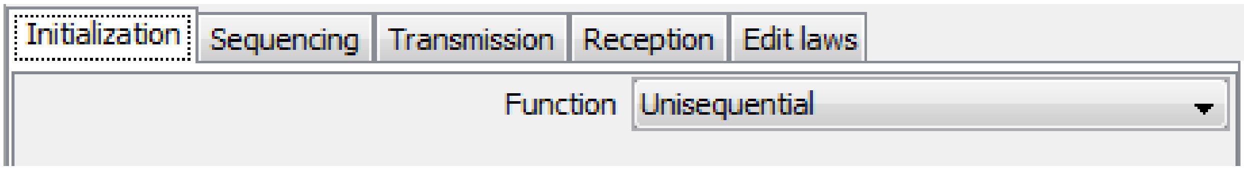

Figure B.10.

Sequencing

The number and position of used elements was chosen to get good beam properties in the range of the expected flaw depth. The values are specified in the Cal and DAC Files of each specimen. The figure below shows an active aperture of 24 Elements (17 to 41).

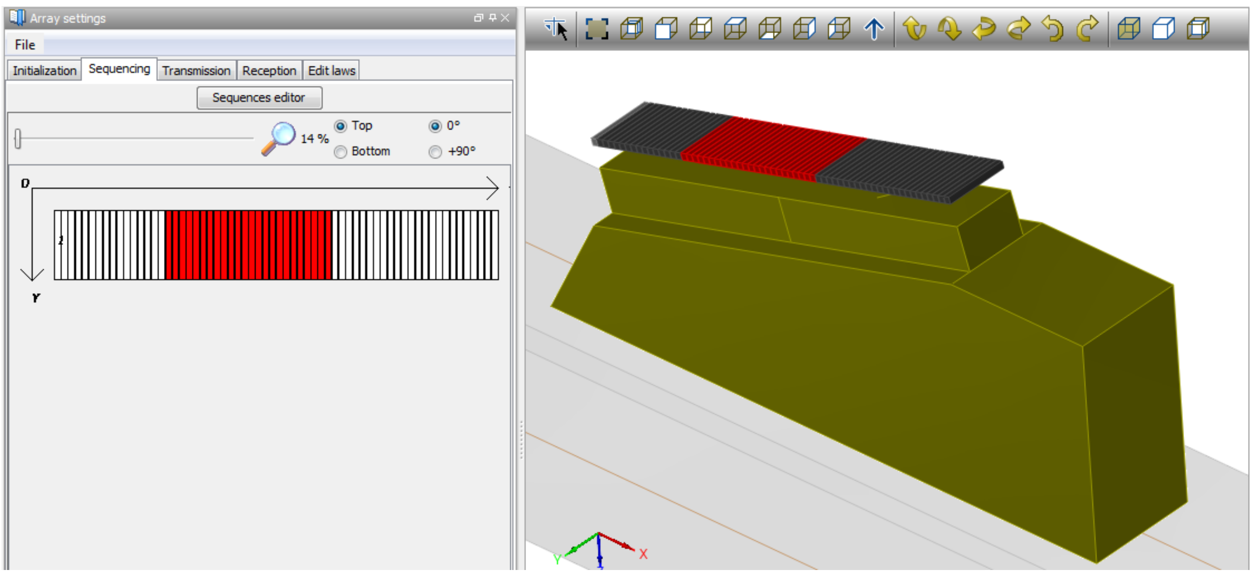

Figure B.11.

Transmission

The sector range goes for all measurements from 40° to 70° (Step 1°) Longwaves. The focal depth was chosen to get good beam properties in the range of the expected flaw depth. The values are specified in the Cal and DAC Files of each specimen. The figure below shows an example of the calculated focal points at 13 mm depth.

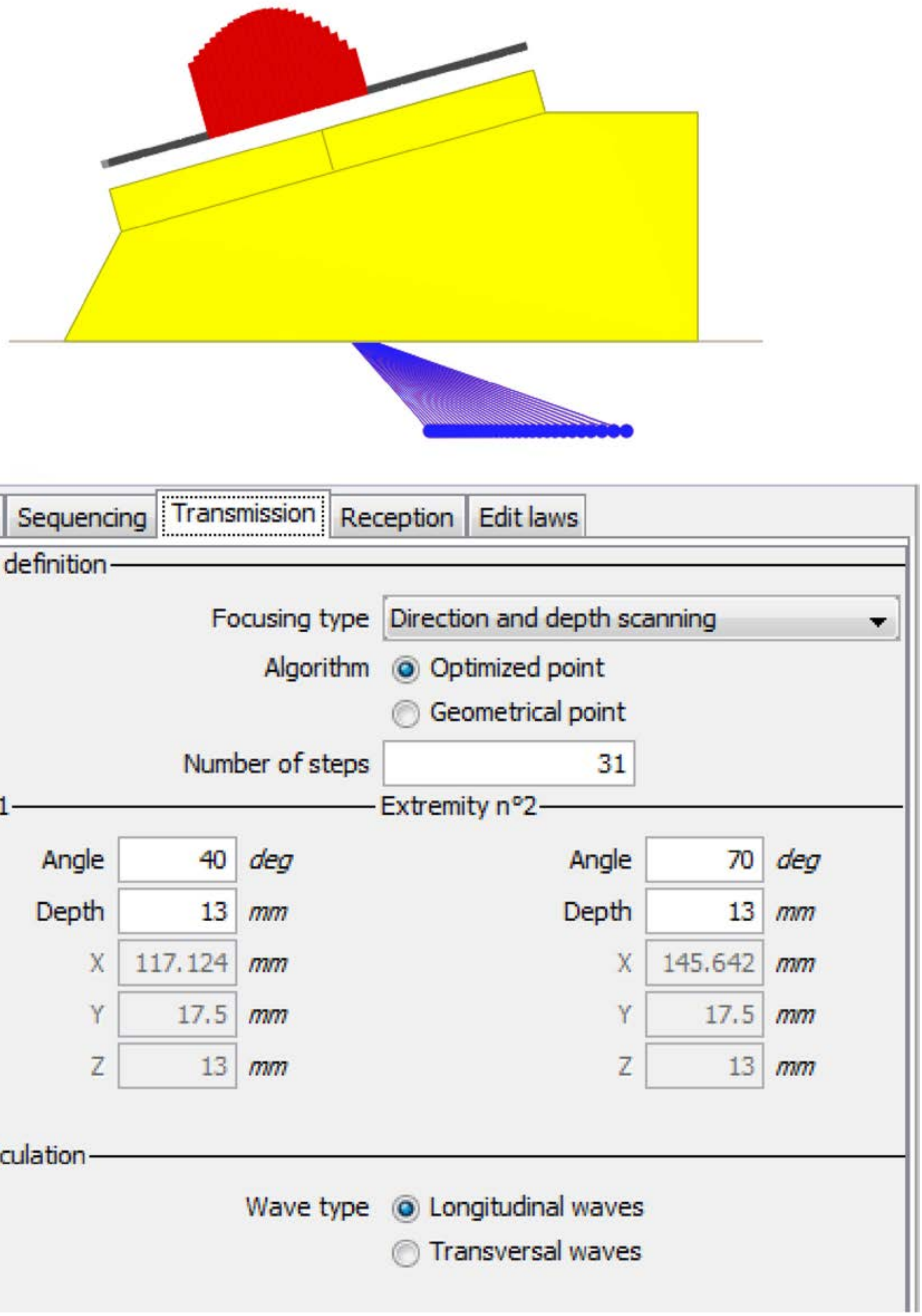
Initialization
Sequencing
Transmission
Reception
Edit laws
Transmission definition
Focusing type
Direction and depth scanning
Algorithm
Optimized point
Geometrical point
Number of steps
31
Extremity n°1
Angle 40 deg
Depth 13 mm
X 117.124 mm
Y 17.5 mm
Z 13 mm
Extremity n°2
Angle 70 deg
Depth 13 mm
X 145.642 mm
Y 17.5 mm
Z 13 mm
Delay law calculation
Wave type
Longitudinal waves
Transversal waves

Figure B.12.

B.2.2.3 UT Equipment Settings - M2M MultiX 64

For the measurements a M2M MultiX UT System was used. MultiX system is a fully parallel architecture with 64 channels. In the following chapters the essential equipment settings are listed.

General Settings

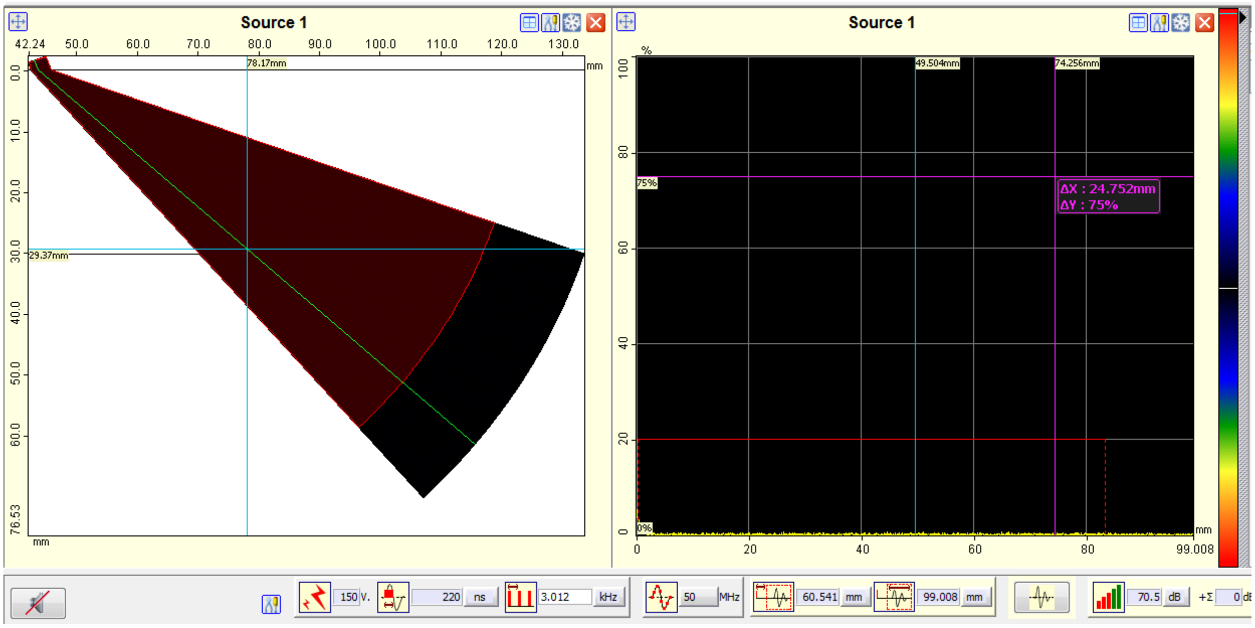

Figure B.13.

Gates

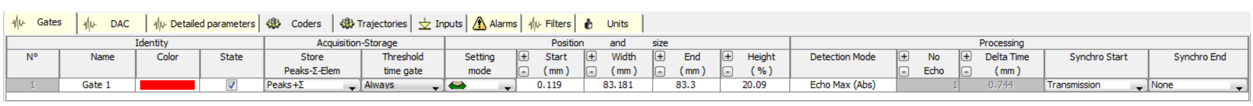

Identity				Acquisition-Storage		Position and size					Processing				
N°	Name	Color	State	Store Peaks-Σ-Elem	Threshold time gate	Setting mode	Start (mm)	Width (mm)	End (mm)	Height (%)	Detection Mode	No Echo	Delta Time (mm)	Synchro Start	Synchro End
1	Gate 1		✓	Peaks+Σ	Always		0.119	83.181	83.3	20.09	Echo Max (Abs)	1	0.744	Transmission	None

Figure B.14.

DAC

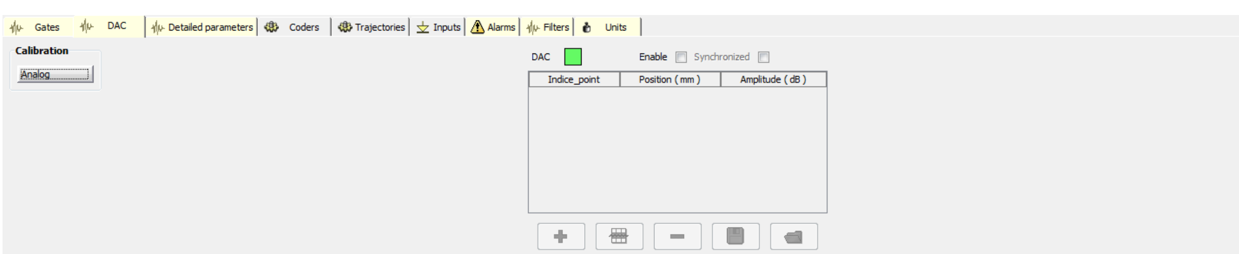

Figure B.15.

Coders

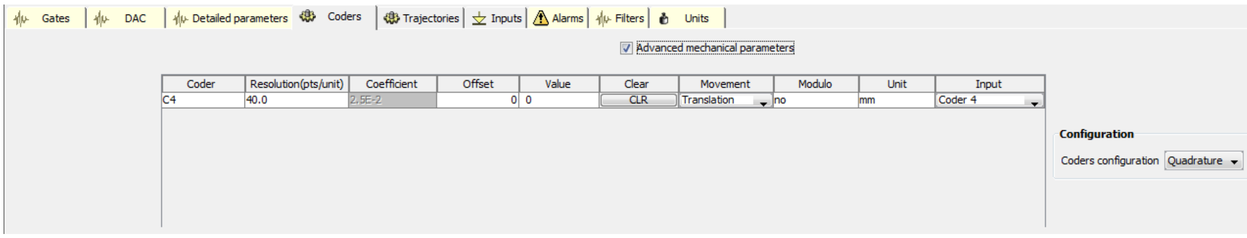

Figure B.16.

Trajectories

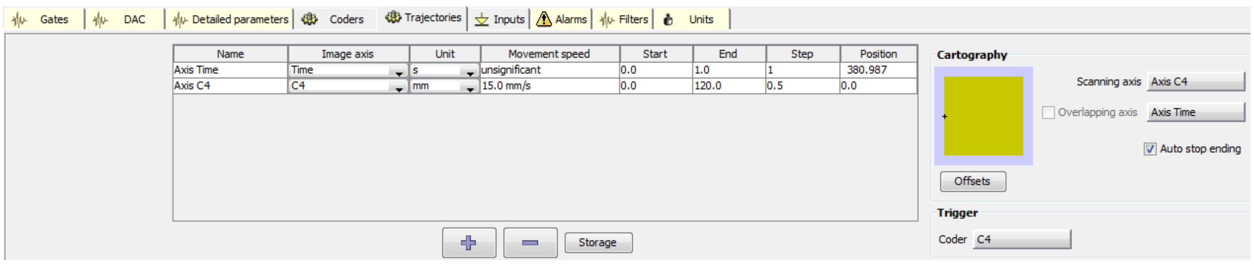

Figure B.17.

Filters

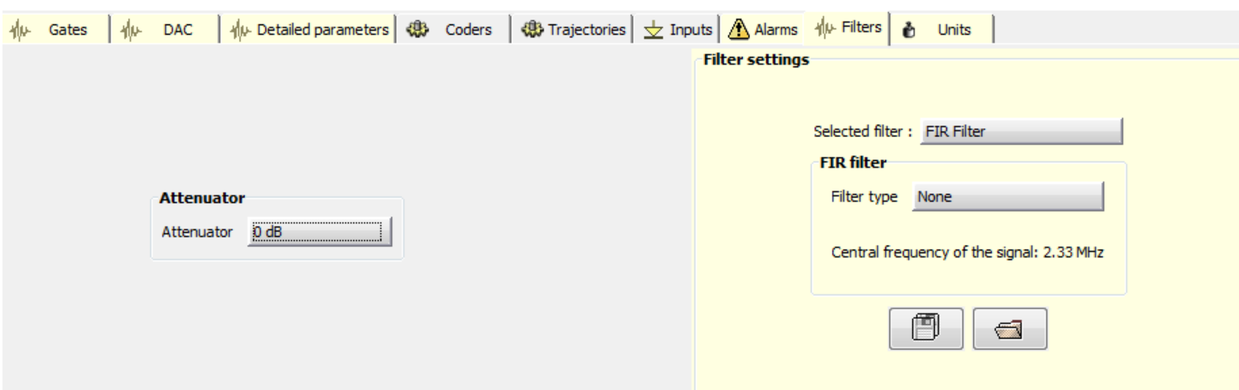

Figure B.18.

Units

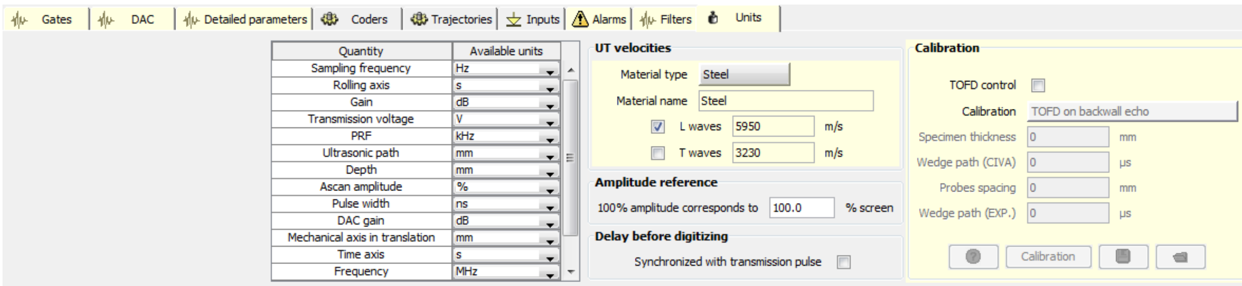

Figure B.19.

B.2.2.4 Calibration

The calibration of the measurement system were conducted direct before data acquisition. In the following sections the calibration process is described.

Probe Element Check (PEC)

- Load File: C:\Users\Multi2000\Desktop\PARENT_L40-70 Contact\02 Default Cal Files\PEC_Sonaxis_64.m2K
- Perform PEC (configuration see figure below)
- Pass criterions: continuous slope - correct wiring, delta dB < 9dB
- Document PEC in Cal Sheet

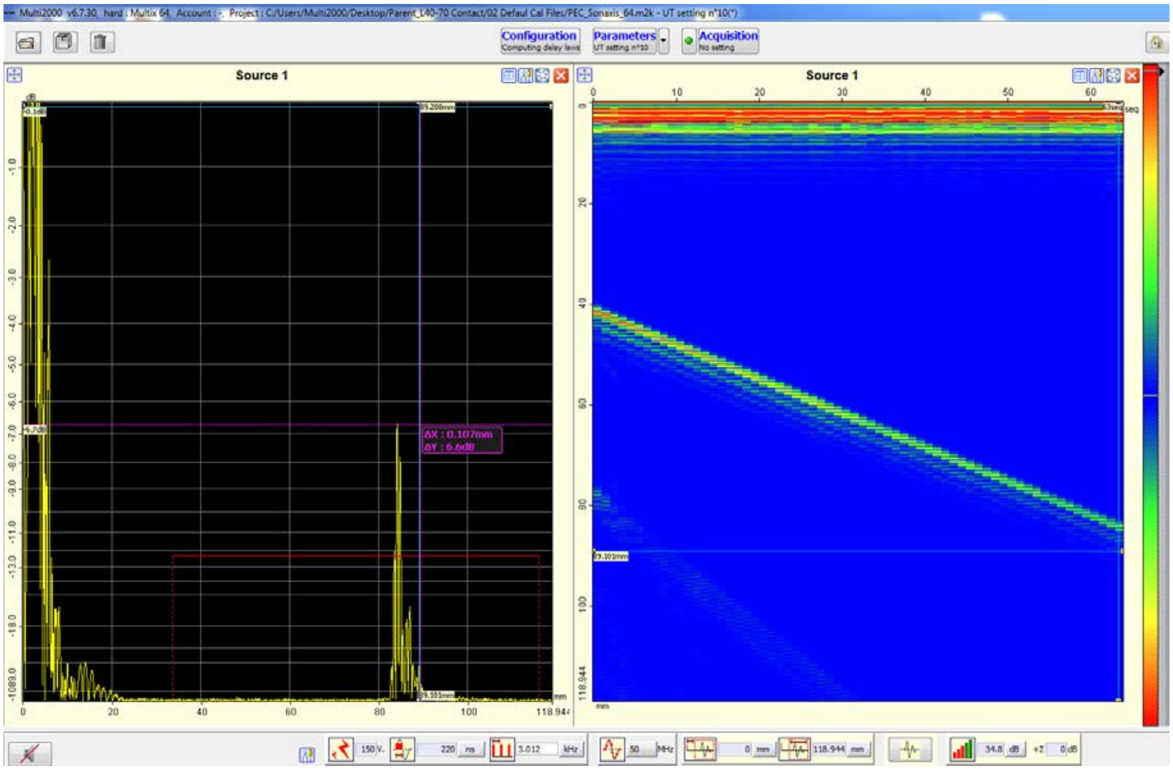

Figure B.20.

Wedge Calibration

- M2M > Parameters > Wedge Calibration
- Drag and Drop Bscan
- Set and adjust the gate on the wedge shoe echo
- Start wedge calibration
- Write values for Computed Angle and Computed Height on Cal Sheet

Define Inspection Configuration

- Load Cal File: Cal*_**Ele_FD**_**_Notch.m2k
- M2M > Configuration > Probe > Wedge > Insert correct values for Computed Angle and Computede Heigth (see Cal Sheet)
- Array settings > Input Patter > Safe
- Array settings > Transmission > Input Focal Depth, and compute Focal Laws
- Change to Parameters by clicking Apply

Probe Exit Point

- Choose shot in Sscan with angle nearest to 50°
- Find Ascan maximum at 100mm radius of ferritic K1, mark the position with green ink on wedge (see picture below), document Reference Sensitivity (FSH) and Probe Index Point on Cal Sheet

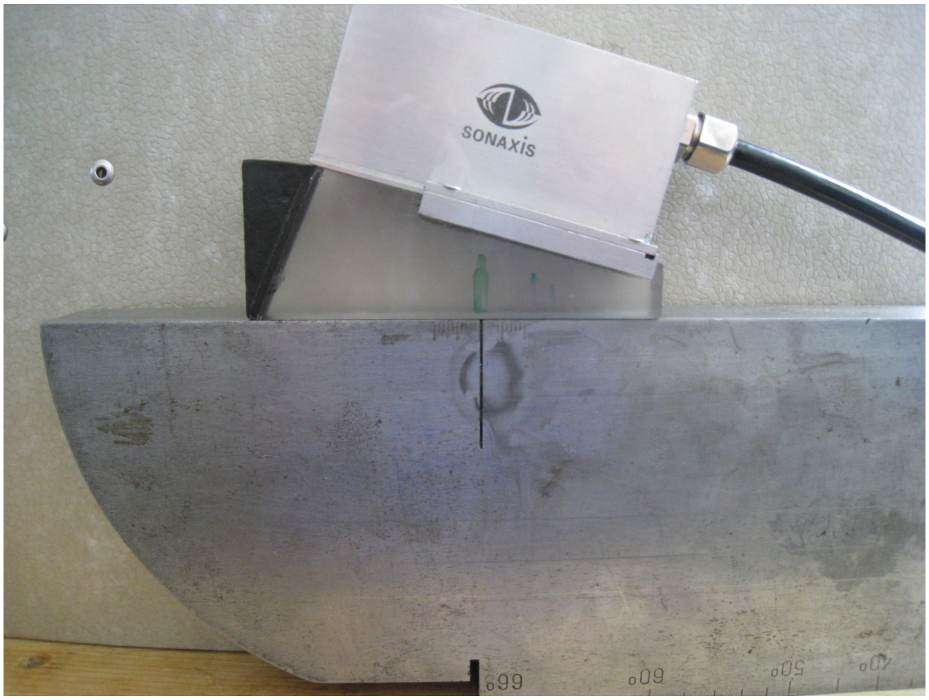

Figure B.21.

Refracted Angle

- Measure Refracted Angle 50° on ferritic K1, document the value in Cal Sheet (see picture below)

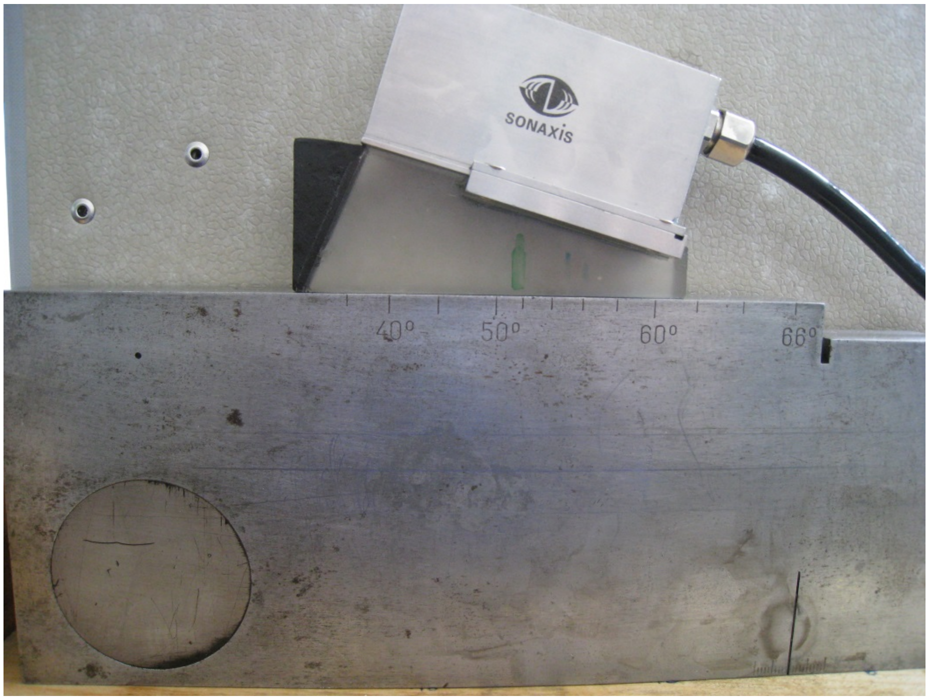

Figure B.22.

Depth Calibration

- Bring Cal Block **KKM_24_18_12_6** (see figure below) *18mm* notch tip to 80% screen height using the 50° angle, document
  - gain/echo height
  - path length (PL) and TWS (Depth)
  - S/N

  in Cal Sheet (in case of OD notch start with 6mm notch)

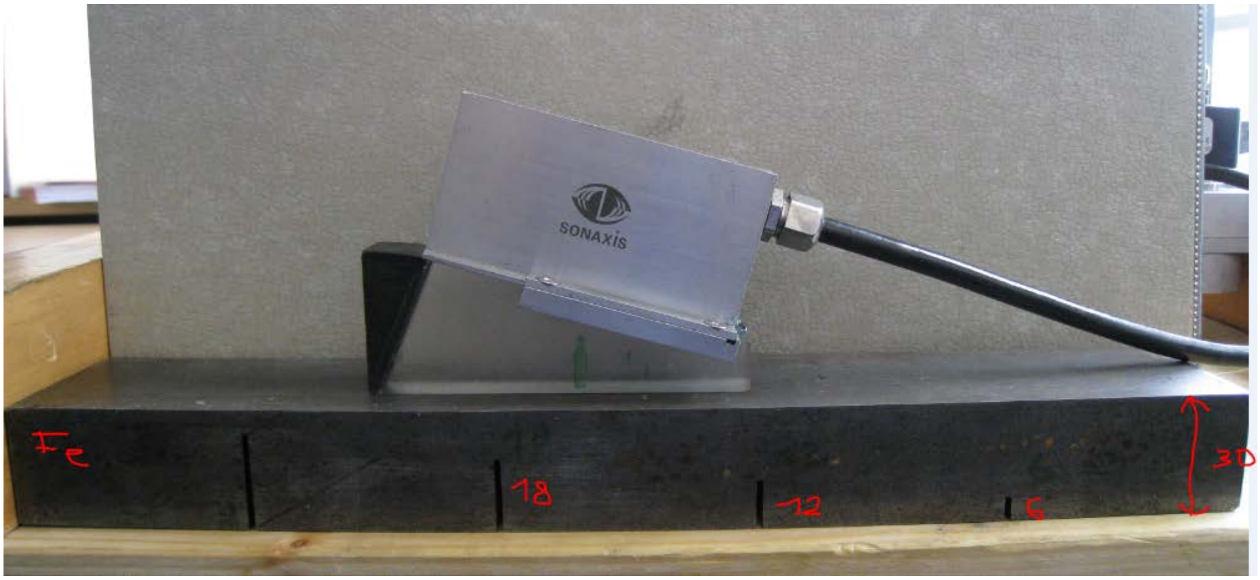

Figure B.23.

- bring Cal Block **KKM_24_18_12_6** 12mm notch tip to maximum using the 50° angle, document echo height, path length/TWS and S/N in Cal Sheet
- bring Cal Block **KKM_24_18_12_6** 12mm notch tip to maximum using the 50° angle, document echo height, path length/TWS and S/N in Cal Sheet
- Save the Cal file
- Save the measurement file

  PARENT_OT_ENSI_L40-70_AAE_FDBB_C_PCC_D_+E.m2k

  AA > Number of Elements
  BB > Focal Depth
  CC > Specimen Number
  D > Scan surface according to figure coordinate system (W or X)
  E > Beam Direction (+Y or -Y)

B.2.3 Data Acquisition

The figure below shows a picture of the measurement setup. A simple string encoder was used for encoded data acquisition.

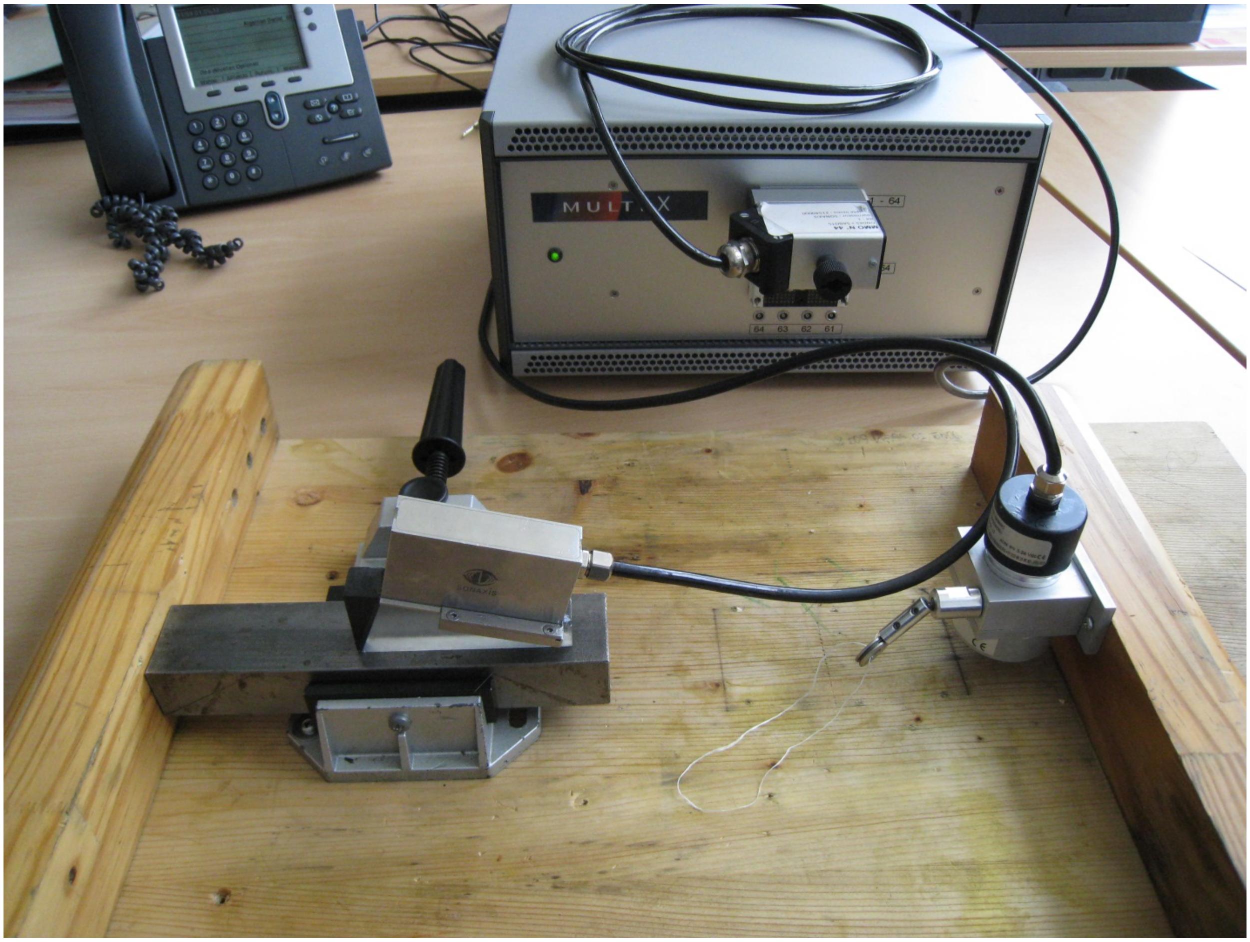

Figure B.24.

The figures below shows the scan plan. Data were just taken along one 120 mm long scan line in the center of the specimen with 0.5mm step width (240 steps).

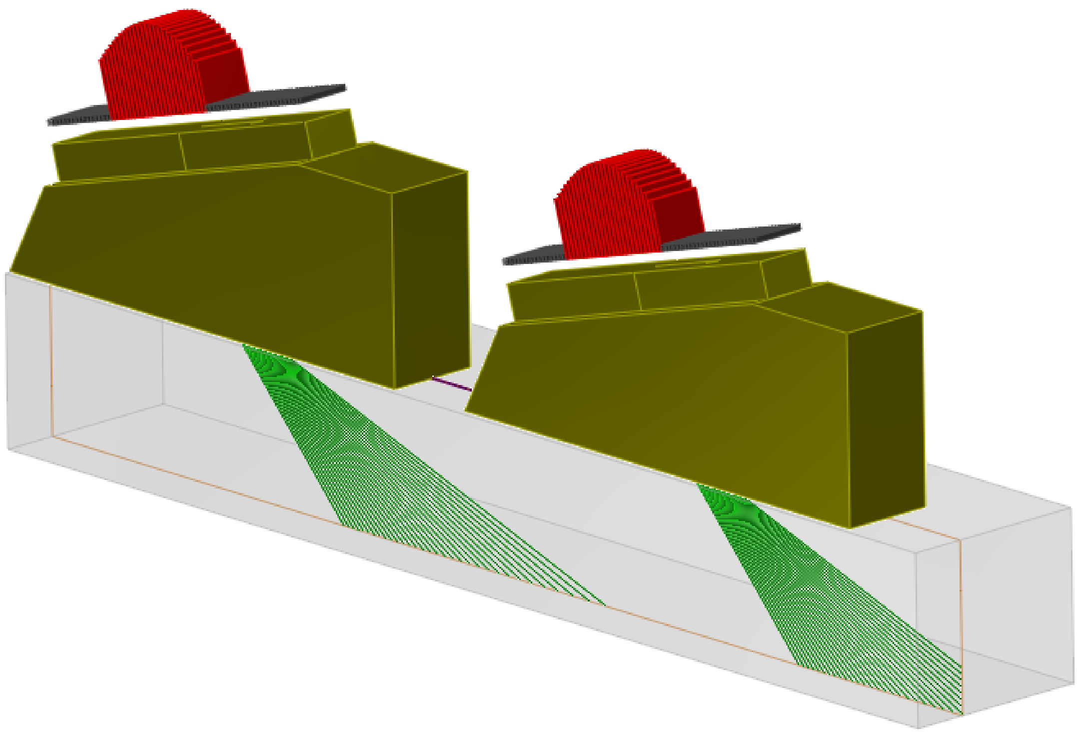

Figure B.25.

The figure below shows the scan coordinate system and a example how it is defined in the data aquisition file name

PARENT_OT_ENSI_L40-70_24E_FD13_C_P28_**W_+Y**

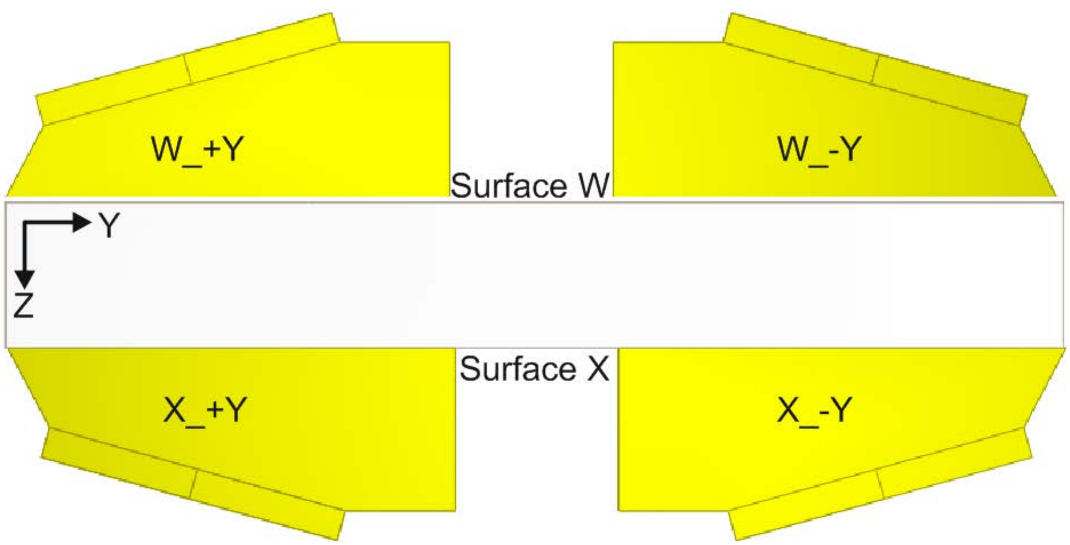

Figure B.26.

B.2.4 Data Analysis

B.2.4.1 Depth Sizing Technique

For flaw depth sizing the Absolut Arrival Time Technique (AATT) is used. The technique relies upon obtaining a direct signal response from the flaw tip using a material depth calibration. From the flaw tip response the amount of unflawed material or remaining ligament can be read directly from the Sscan. Flaw depth is calculated by subtracting the remaining ligament from the actual material thickness.

The figure below illustrates the technique.

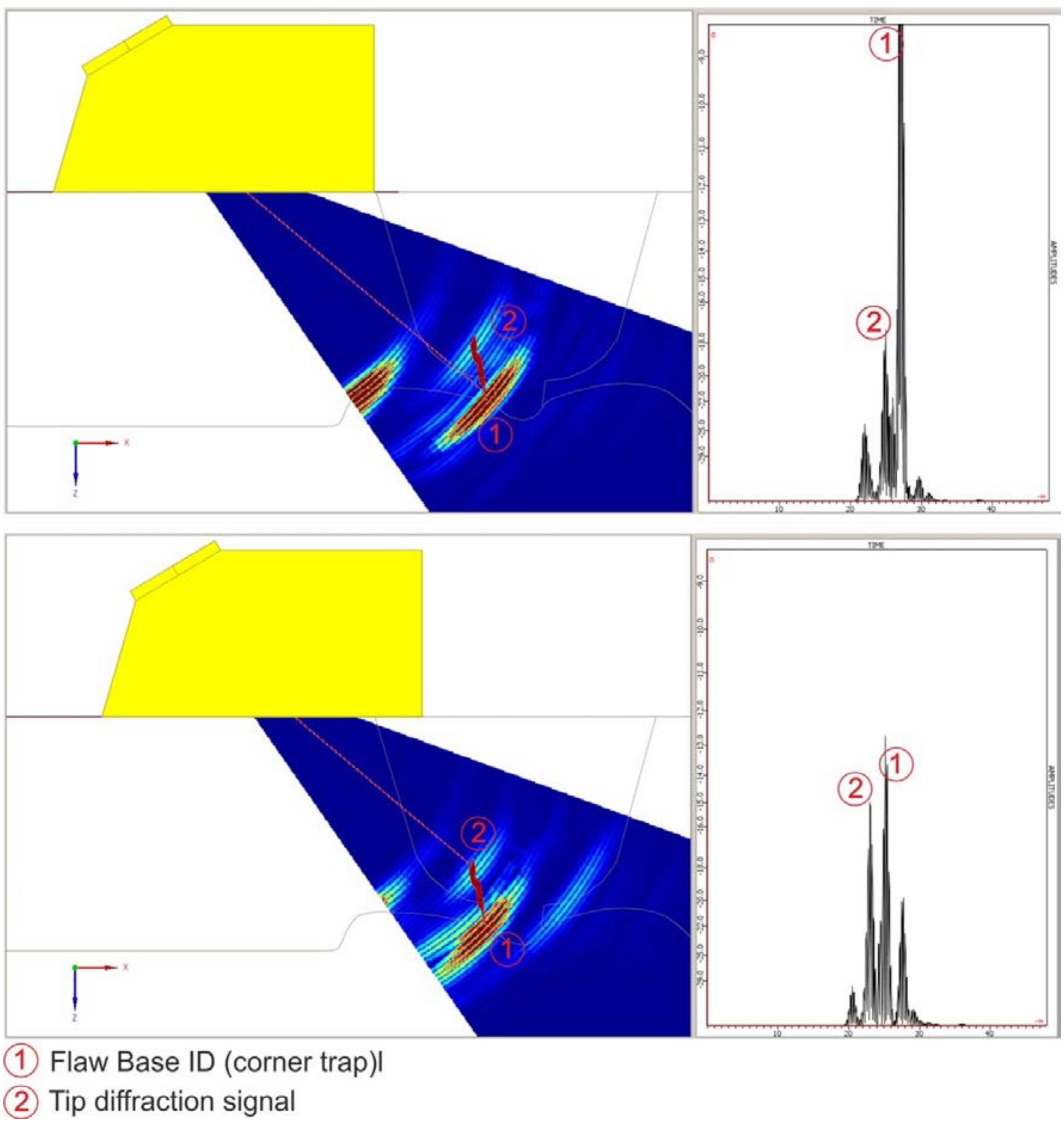

Figure B.27.

B.2.4.2 UT Depth Sizing Images

The figure below shows a typical depth sizing print out used in the measurement report (2012_Par_OT_ENSI Spec_MeasReport_L40-70C_PE). The figure includes remarks for explanation of the UT images.

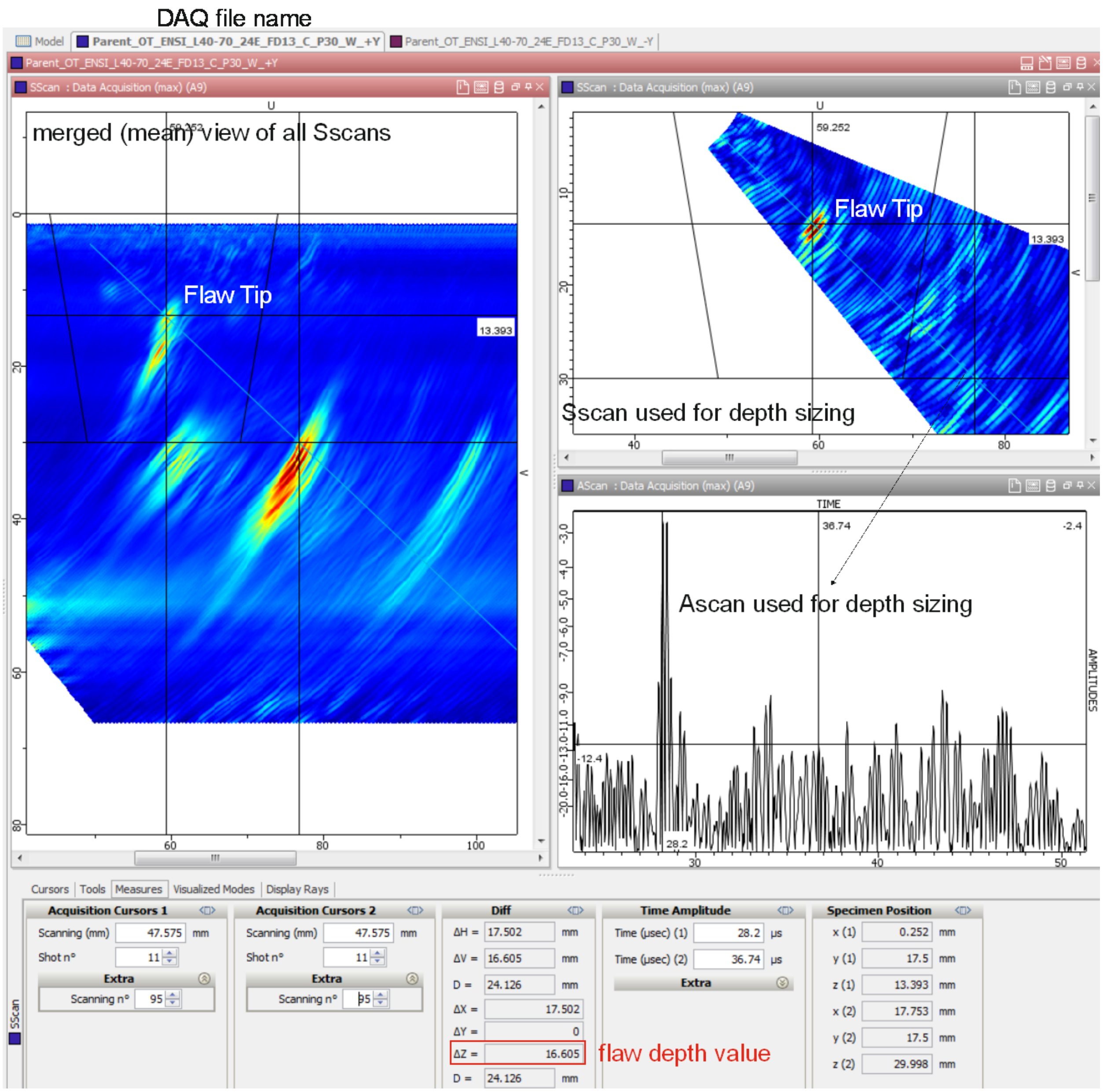

Figure B.28.

B.2.5 RESULTS SPECIMENS P28, P29, P30, P31, P32, P42 AND P46

B.2.5.1 Specimen Information and Coordinate System

PARENT Sp. Designation	P28	P29	P30	P31	P32	P42	P46	P38
PSI Sp. Designation	* 6	* 10	* 7	* 1	* 5	* 12	* 13	* 3
Type of Crack	SCC	SCC	MF	SCC	SCC	EDM		SCC

* MN 220 AD U, MF… Mech. Fatigue, SSC ... Stress Corrosion Crack

Coordinate System P28, P29, P30, P31, P32, P42 and P46

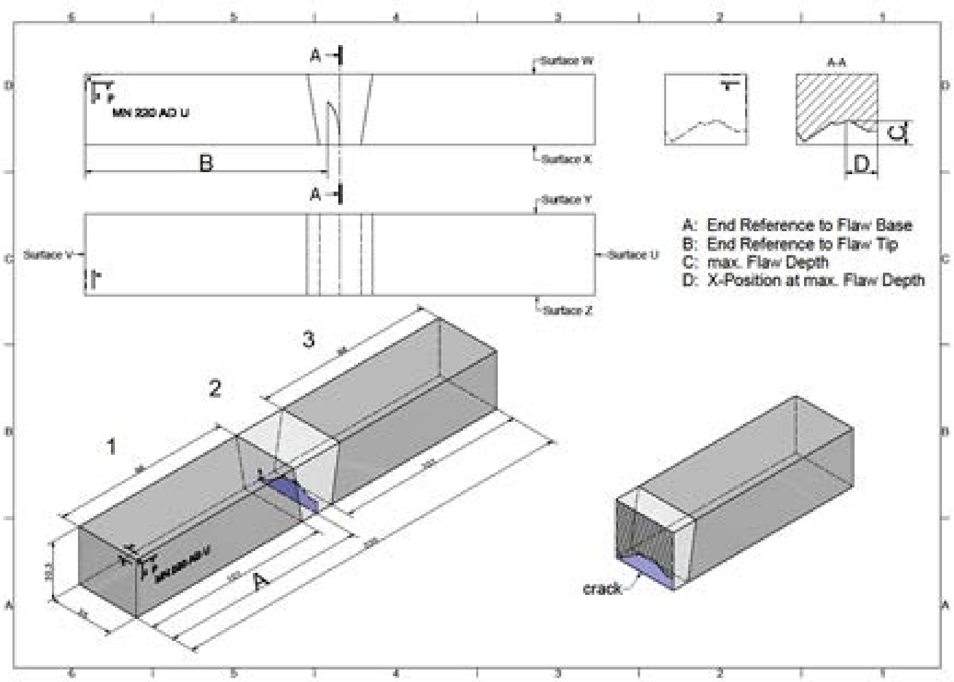

Figure B.29.

Coordinate System P38

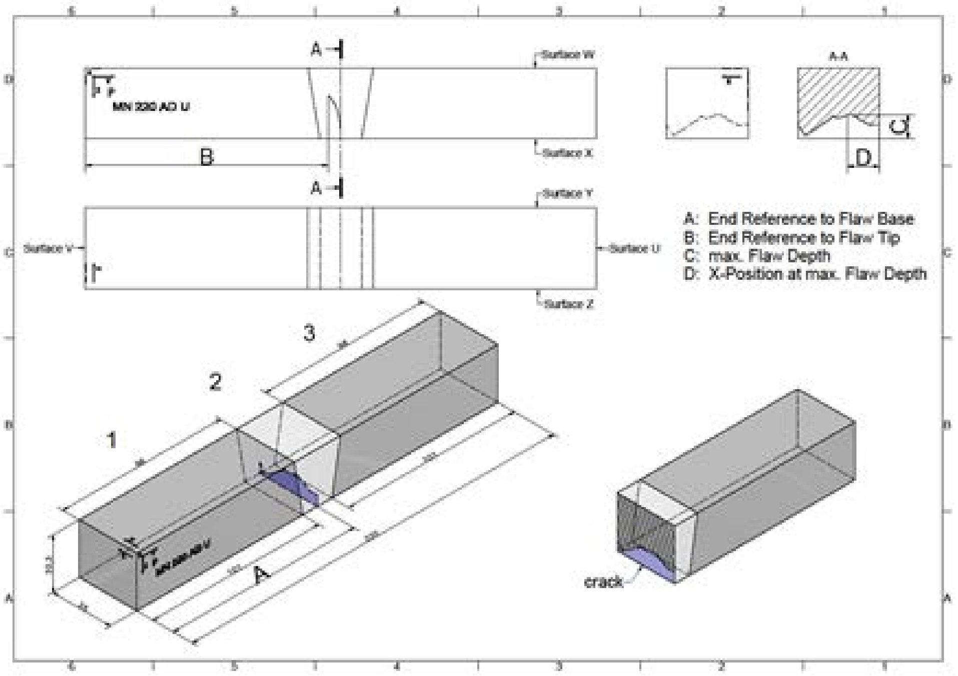

Figure B.30.

B.2.5.2 Flaw Depth Summary Table

Specimen	Scanning Surface	Beam Direction	DAQ File Name	Nb. of Elem.	Focal Depth	Flaw Depth*	UT Analysis / Images Chap.	Cal Sheet No:.
P28	W	+Y	PARENT_OT_ENSI_L40-70_24E_FD13_C_P28_W_+Y	24	13	**13.2**	3.1	1
	W	-Y	PARENT_OT_ENSI_L40-70_24E_FD13_C_P28_W_-Y	24	13	12.7	3.1	1
P29	W	+Y	PARENT_OT_ENSI_L40-70_24E_FD18_C_P29_W_+Y	24	18	**10.7**	3.2	6
	W	-Y	PARENT_OT_ENSI_L40-70_24E_FD18_C_P29_W_-Y	24	18	8.9	3.2	6
P30	W	+Y	PARENT_OT_ENSI_L40-70_24E_FD13_C_P30_W_+Y	24	13	16.6	3.3	1
	W	-Y	PARENT_OT_ENSI_L40-70_24E_FD13_C_P30_W_-Y	24	13	**17.8**	3.3	1
P31	W	+Y	PARENT_OT_ENSI_L40-70_32E_FD25_C_P31_W_+Y	32	25	2.7	3.4	3
	W	-Y	PARENT_OT_ENSI_L40-70_32E_FD25_C_P31_W_-Y	32	25	2.8	3.4	3
	X	+Y	PARENT_OT_ENSI_L40-70_24E_FD13_C_P31_X_+Y	24	13	4.3	3.4	4
	X	+Y	PARENT_OT_ENSI_L40-70_24E_FD13_C_P31_X_-Y	24	13	**4.6**	3.4	4

Specimen	Scanning Surface	Beam Direction	DAQ File Name	Nb. of Elem.	Focal Depth	Flaw Depth*	UT Analysis / Images Chap.	Cal Sheet No:.
P32	W	+Y	PARENT_OT_ENSI_L40-70_24E_FD18_C_P32_W_+Y	24	18	9.5	3.5	6
	W	-Y	PARENT_OT_ENSI_L40-70_24E_FD18_C_P32_W_-Y	24	18	7.5	3.5	6
	X	+Y	PARENT_OT_ENSI_L40-70_32E_FD20_C_P32_X_+Y	32	20	12.4	3.5	5
	X	-Y	PARENT_OT_ENSI_L40-70_32E_FD20_C_P32_X_-Y	32	20	**13.4**	3.5	5
P42	W	+Y	PARENT_OT_ENSI_L40-70_24E_FD13_C_P42_W_+Y	24	13	9.3	3.6	1
	W	-Y	PARENT_OT_ENSI_L40-70_24E_FD13_C_P42_W_-Y	24	13	**9.7**	3.6	1
P38	W	+Y	PARENT_OT_ENSI_L40-70_24E_FD13_C_P38_W_+Y	24	13	6.6	3.7	1
	W	-Y	PARENT_OT_ENSI_L40-70_24E_FD13_C_P38_W_-Y	24	13	6.4	3.7	1
	X	+Y	PARENT_OT_ENSI_L40-70_24E_FD13_C_P38_X_+Y	24	13	5	3.7	4
	X	-Y	PARENT_OT_ENSI_L40-70_24E_FD13_C_P38_X_-Y	24	13	**5.7**	3.7	4

* bolt values are final flaw depth calls

B.2.5.3 UT Analysis Images

Specimen 28

Specimen	Scanning Surface	Beam Direction	DAQ File Name	Nb. of Elem.	Focal Depth	Flaw Depth (mmm)	EVal. Angle (°)	S/N. (dB)
P28	**W**	**+Y**	PARENT_OT_ENSI_L40-70_24E_FD17_C_P28_W_+Y	24	13	13.2	44	7.5

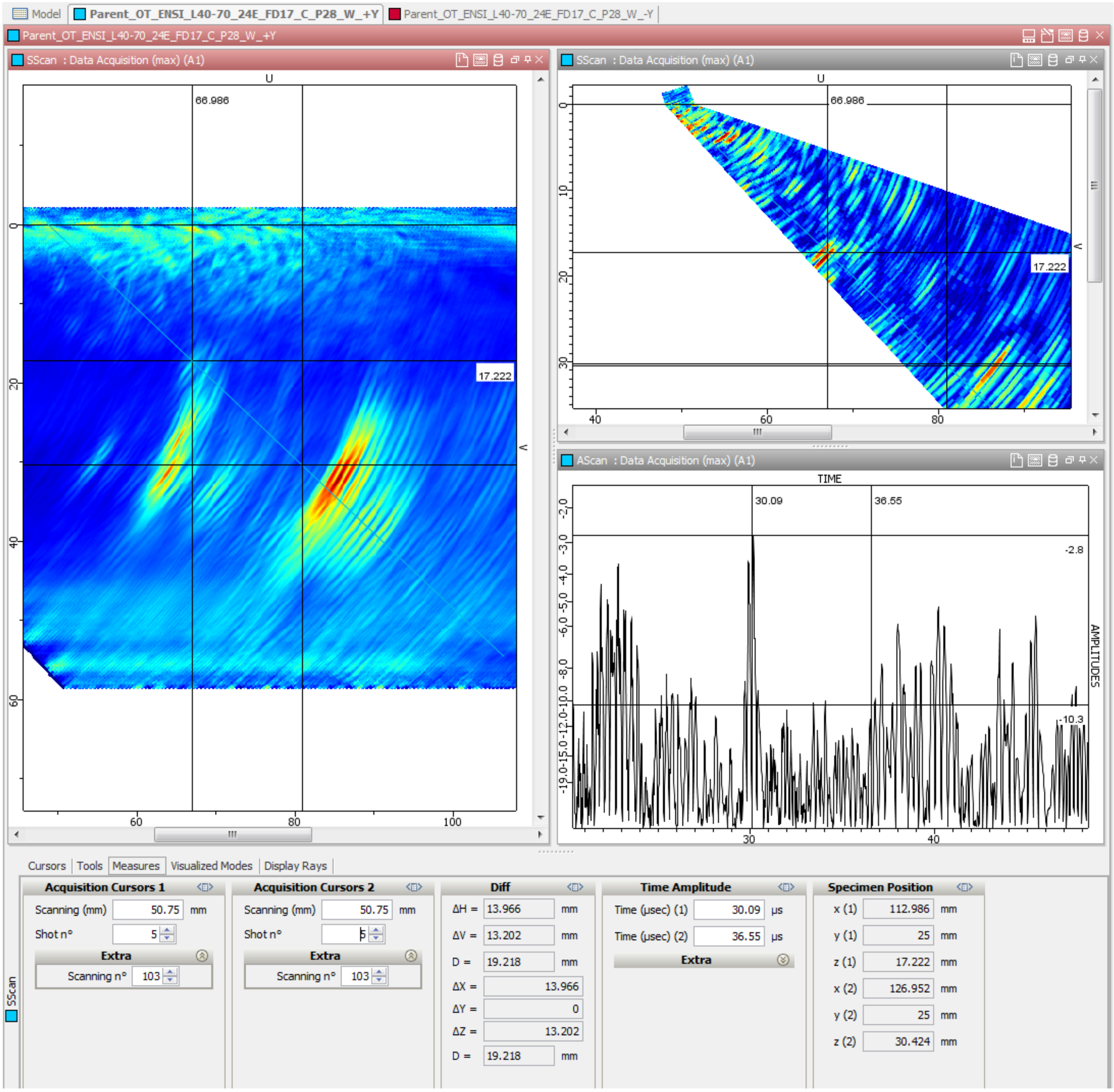

Figure B.31.

D	Scanning Surface	Beam Direction	DAQ File Name	Nb. of Elem.	Focal Depth	Flaw Depth (mmm)	EVal. Angle (°)	S/N. (dB)
P28	W	-Y	PARENT_OT_ENSI_L40-70_24E_FD17_C_P28_W_-Y	24	13	12.7	59	10

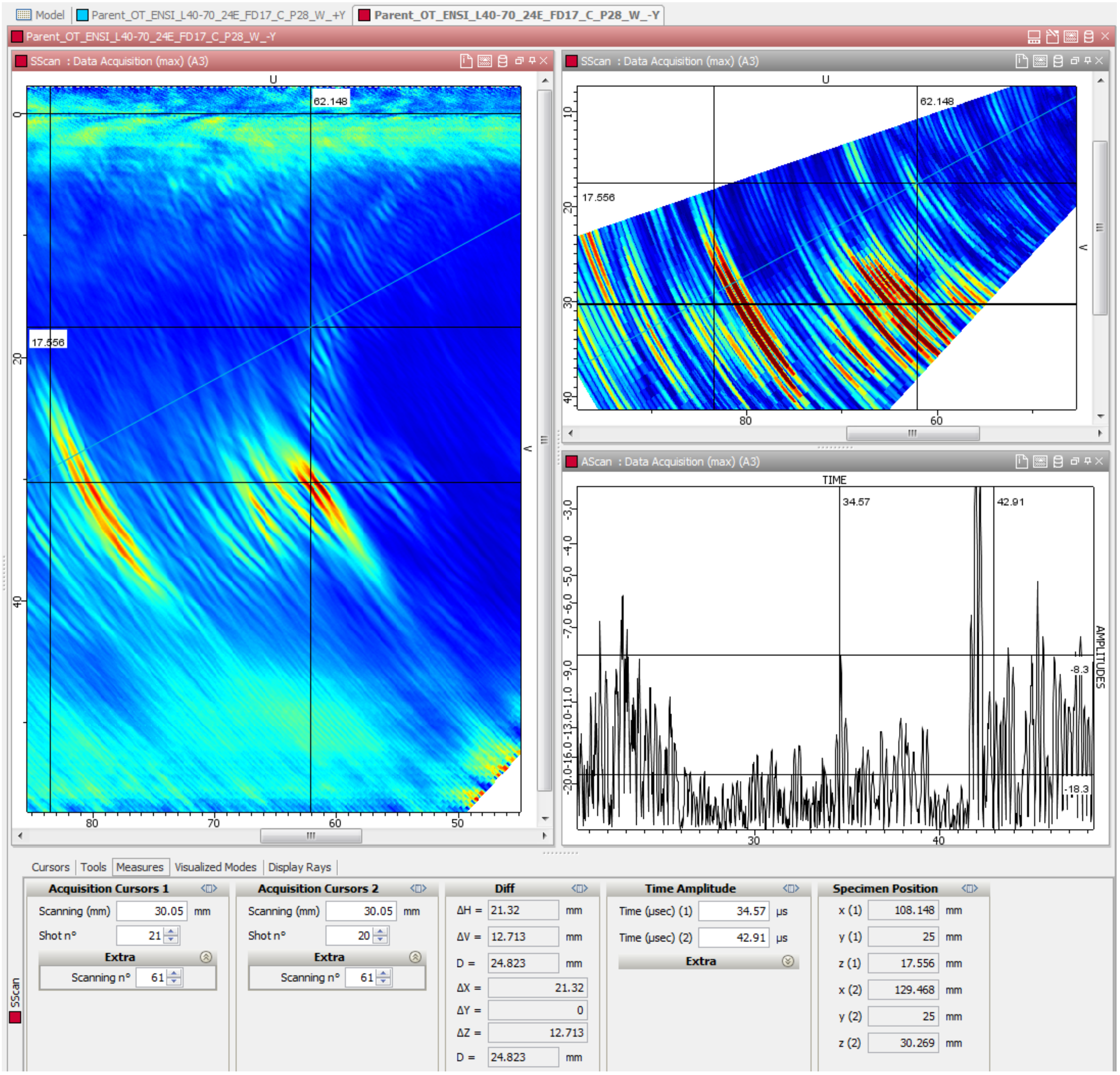

Figure B.32.

Specimen P29

Specimen	Scanning Surface	Beam Direction	DAQ File Name	Nb. of Elem.	Focal Depth	Flaw Depth (mmm)	EVal. Angle (°)	S/N. (dB)
P29	**W**	**+Y**	PARENT_OT_ENSI_L40-70_24E_FD18_C_P29_W_+Y	24	18	10.7	57	9

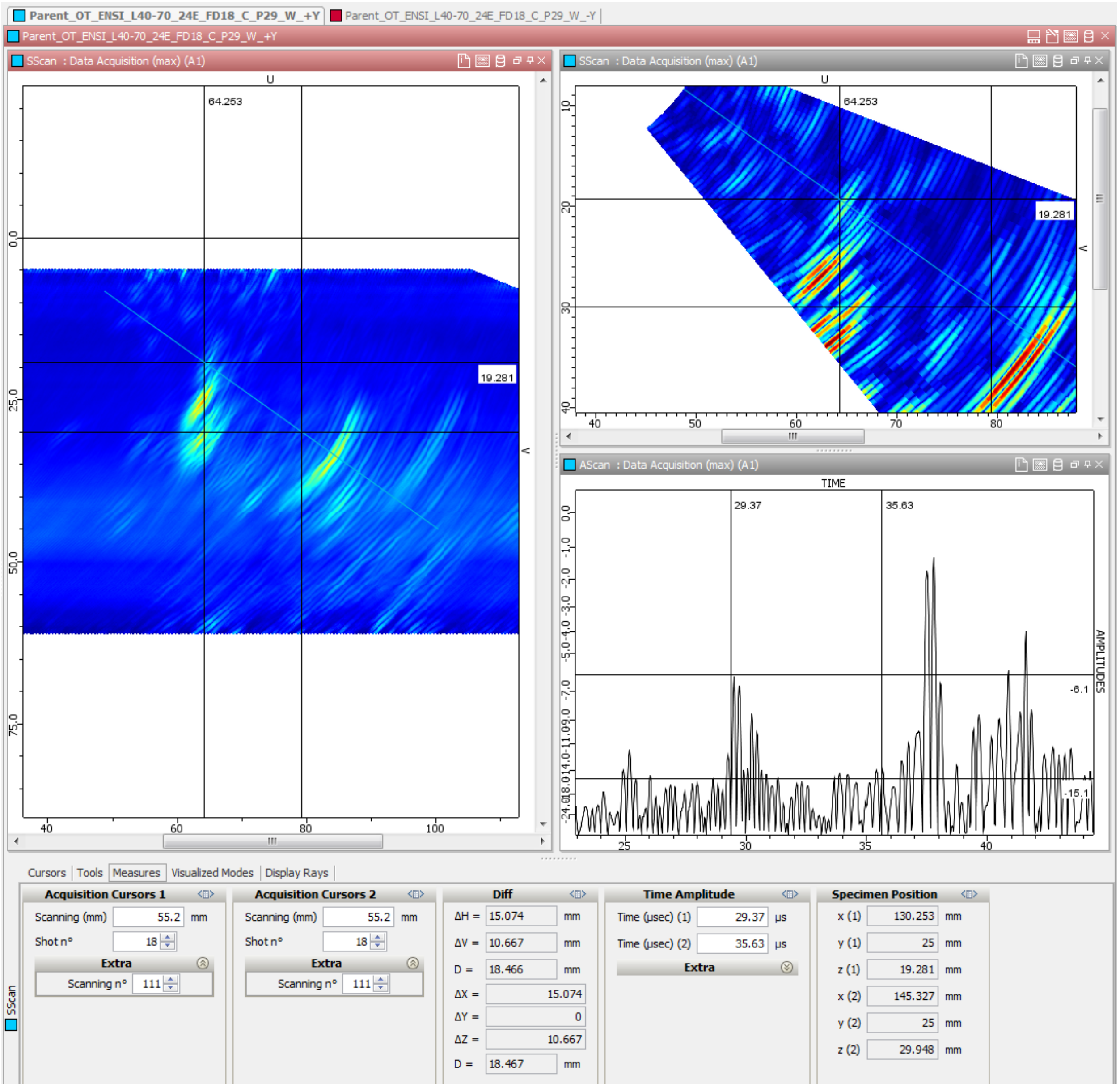

Figure B.33.

Specimen	Scanning Surface	Beam Direction	DAQ File Name	Nb. of Elem.	Focal Depth	Flaw Depth (mmm)	EVal. Angle (°)	S/N. (dB)
P29	**W**	**-Y**	PARENT_OT_ENSI_L40-70_24E_FD18_C_P29_W_+Y	24	18	8.9	61	3

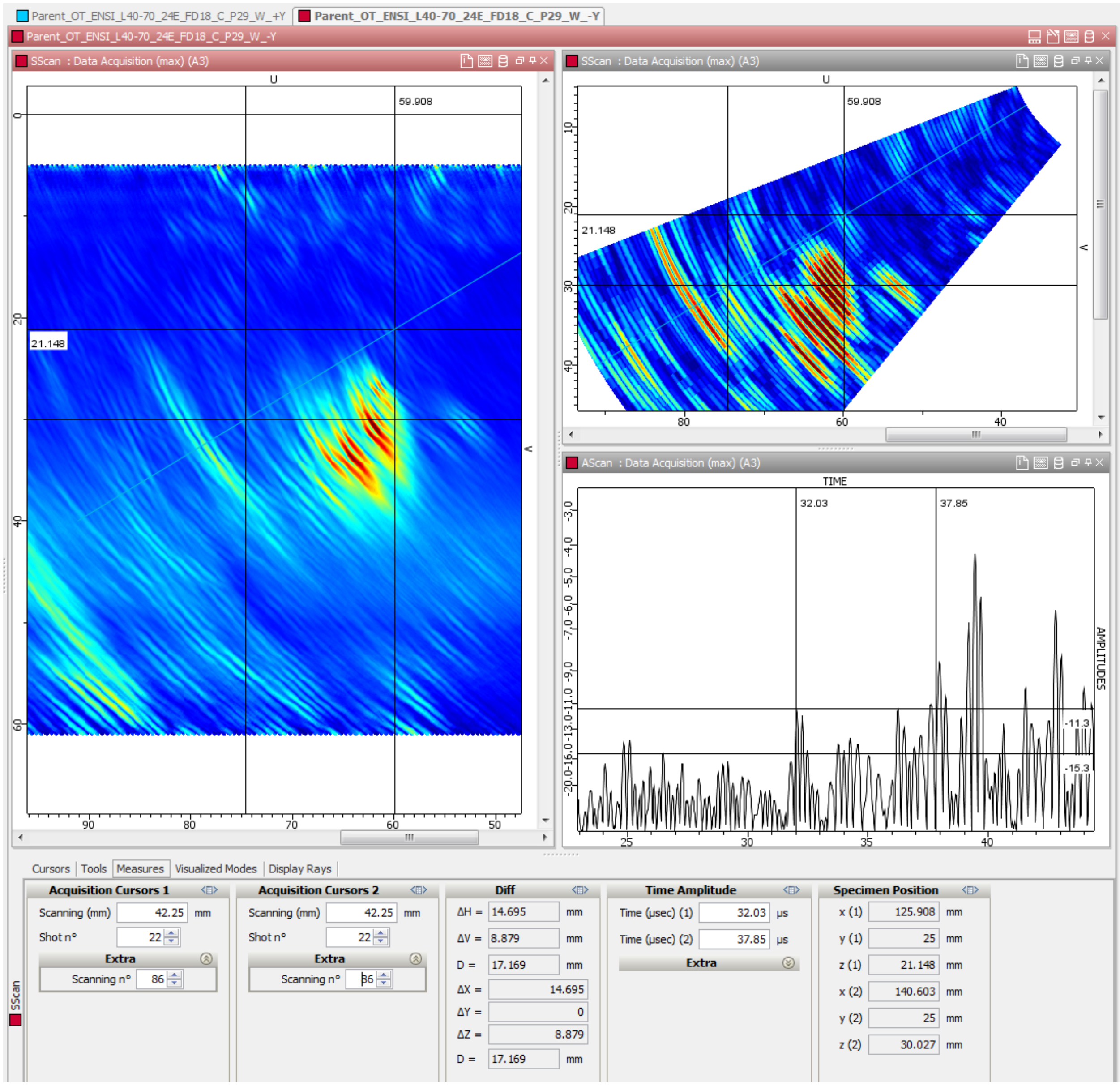

Figure B.34.

Specimen P30

Specimen	Scanning Surface	Beam Direction	DAQ File Name	Nb. of Elem.	Focal Depth	Flaw Depth (mmm)	EVal. Angle (°)	S/N. (dB)
P30	W	+Y	PARENT_OT_ENSI_L40-70_24E_FD13_C_P30_W_+Y	24	13	16.6	50	10

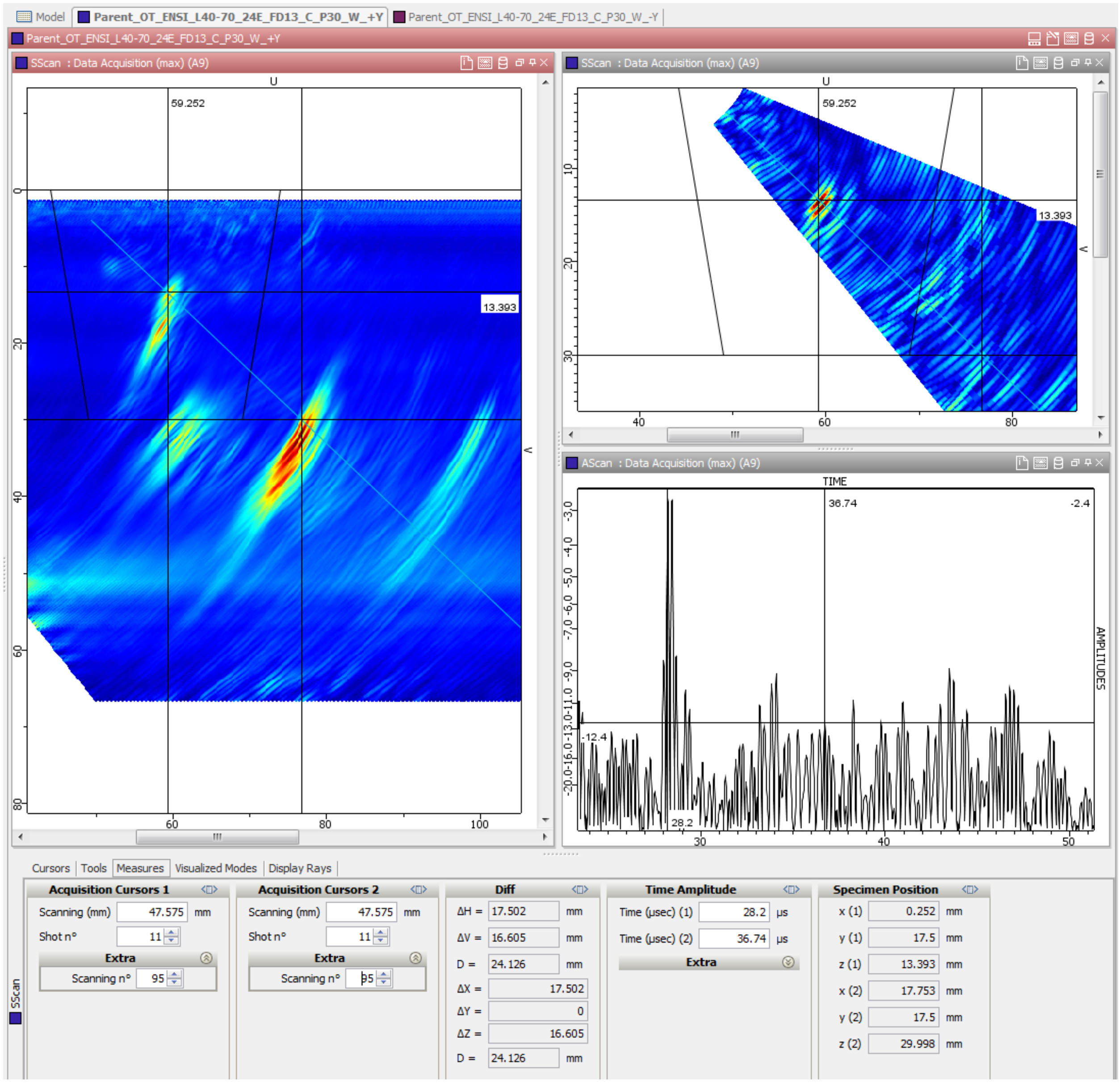

Figure B.35.

Specimen	Scanning Surface	Beam Direction	DAQ File Name	Nb. of Elem.	Focal Depth	Flaw Depth (mmm)	EVal. Angle (°)	S/N. (dB)
P30	**W**	**-Y**	PARENT_OT_ENSI_L40-70_24E_FD13_C_P30_W_-Y	24	13	17.8	59	8

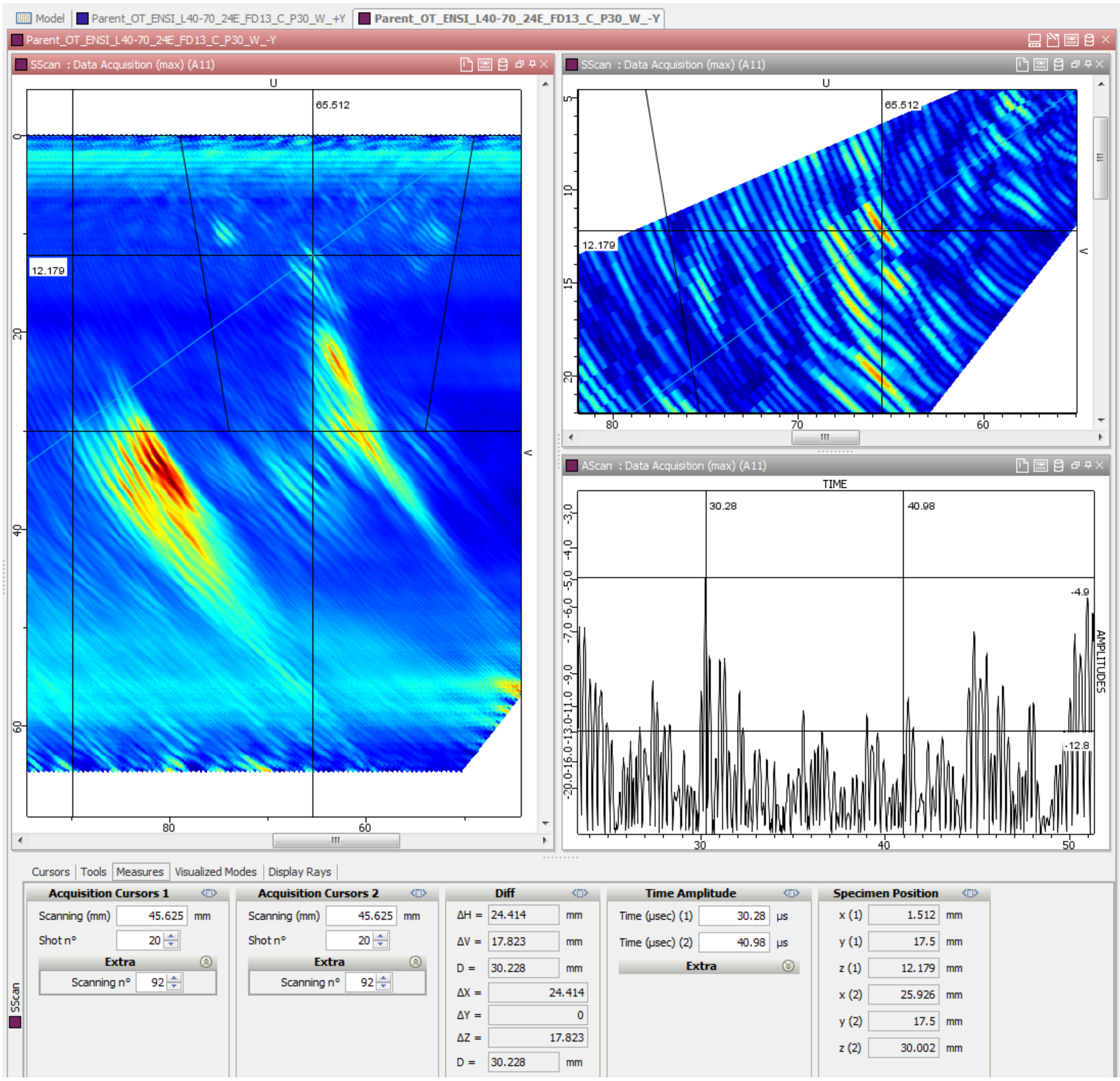

Figure B.36.

Specimen P31

Specimen	Scanning Surface	Beam Direction	DAQ File Name	Nb. of Elem.	Focal Depth	Flaw Depth (mmm)	EVal. Angle (°)	S/N. (dB)
P31	**W**	**+Y**	PARENT_OT_ENSI_L40-70_32E_FD25_C_P31_W_+Y	32	25	2.7*	49	6
* no mode converted TLL - shallow crack, tip weak, bad SN, only RATT								

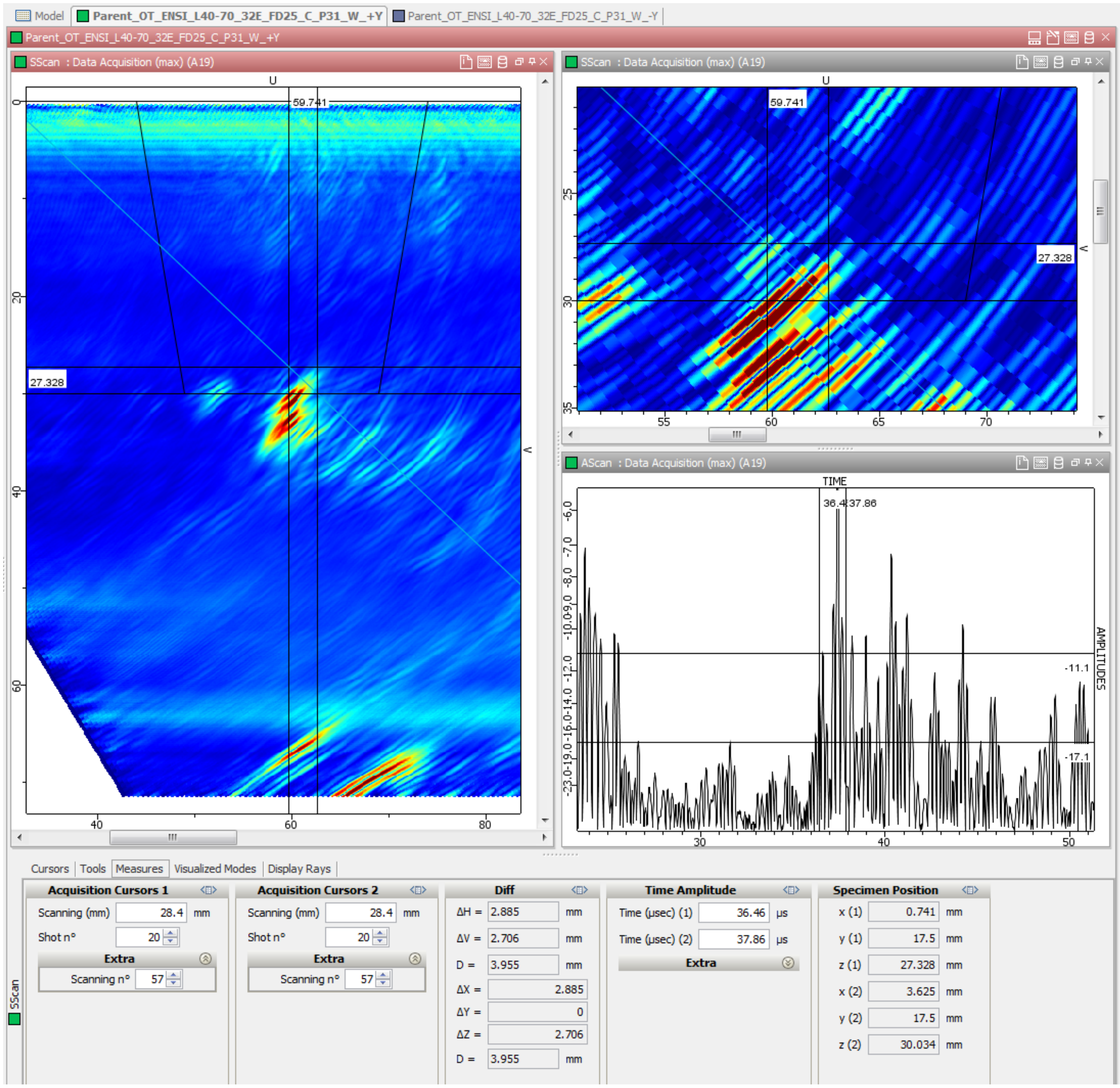

Figure B.37.

Specimen	Scanning Surface	Beam Direction	DAQ File Name	Nb. of Elem.	Focal Depth	Flaw Depth (mmm)	EVal. Angle (°)	S/N. (dB)
P31	**W**	**+Y**	PARENT_OT_ENSI_L40-70_32E_FD25_C_P31_W_-Y	32	25	2.8*	45	3
* no mode converted TLL - shallow crack, tip weak, bad SN, only RATT								

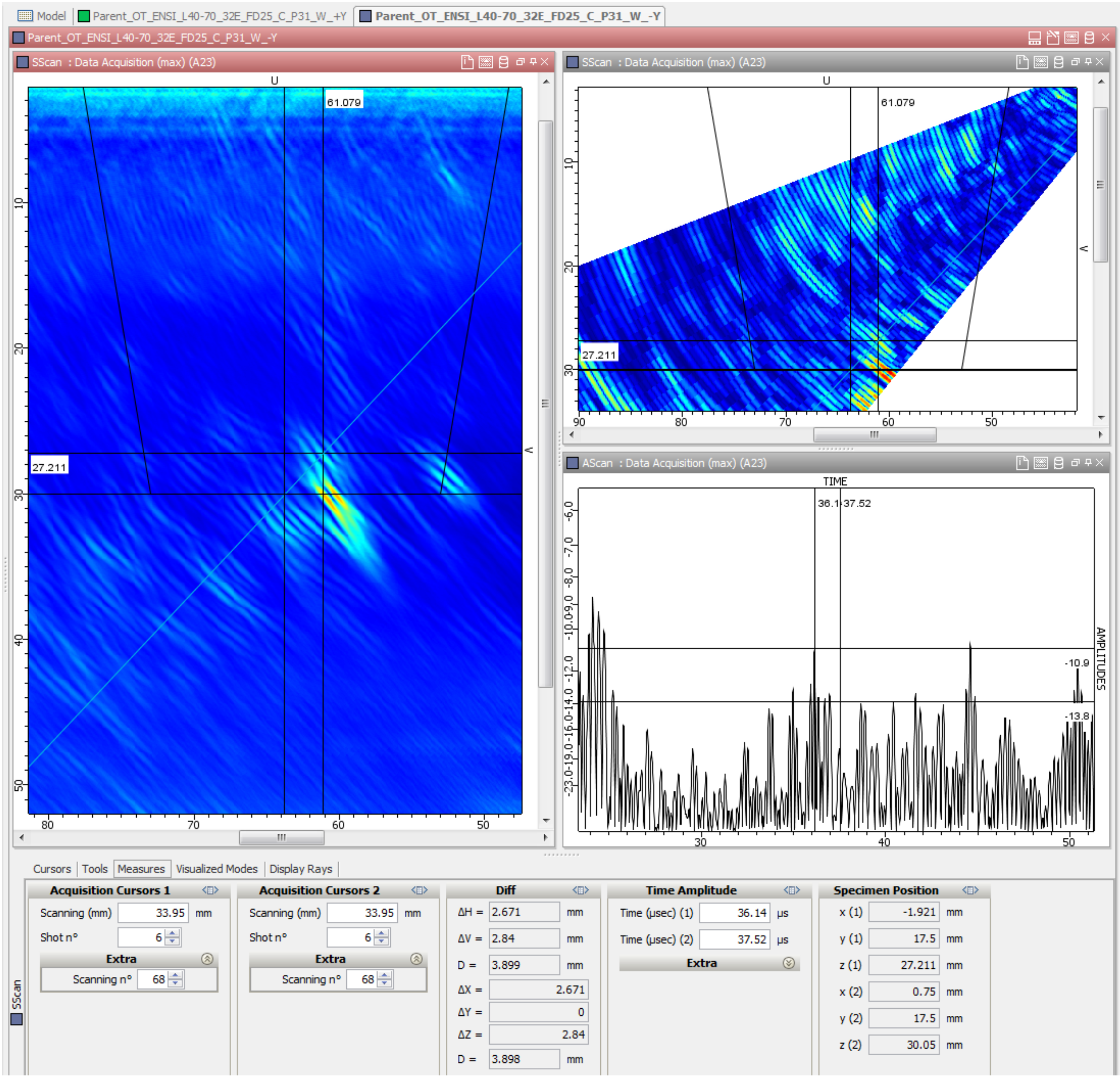

Figure B.38.

Specimen	Scanning Surface	Beam Direction	DAQ File Name	Nb. of Elem.	Focal Depth	Flaw Depth (mmm)	EVal. Angle (°)	S/N. (dB)
P31	**W**	**+Y**	PARENT_OT_ENSI_L40-70_24E_FD13_C_P31_X_+Y	24	13	4.3	63	10
* Remark. Weld drawing not correct.								

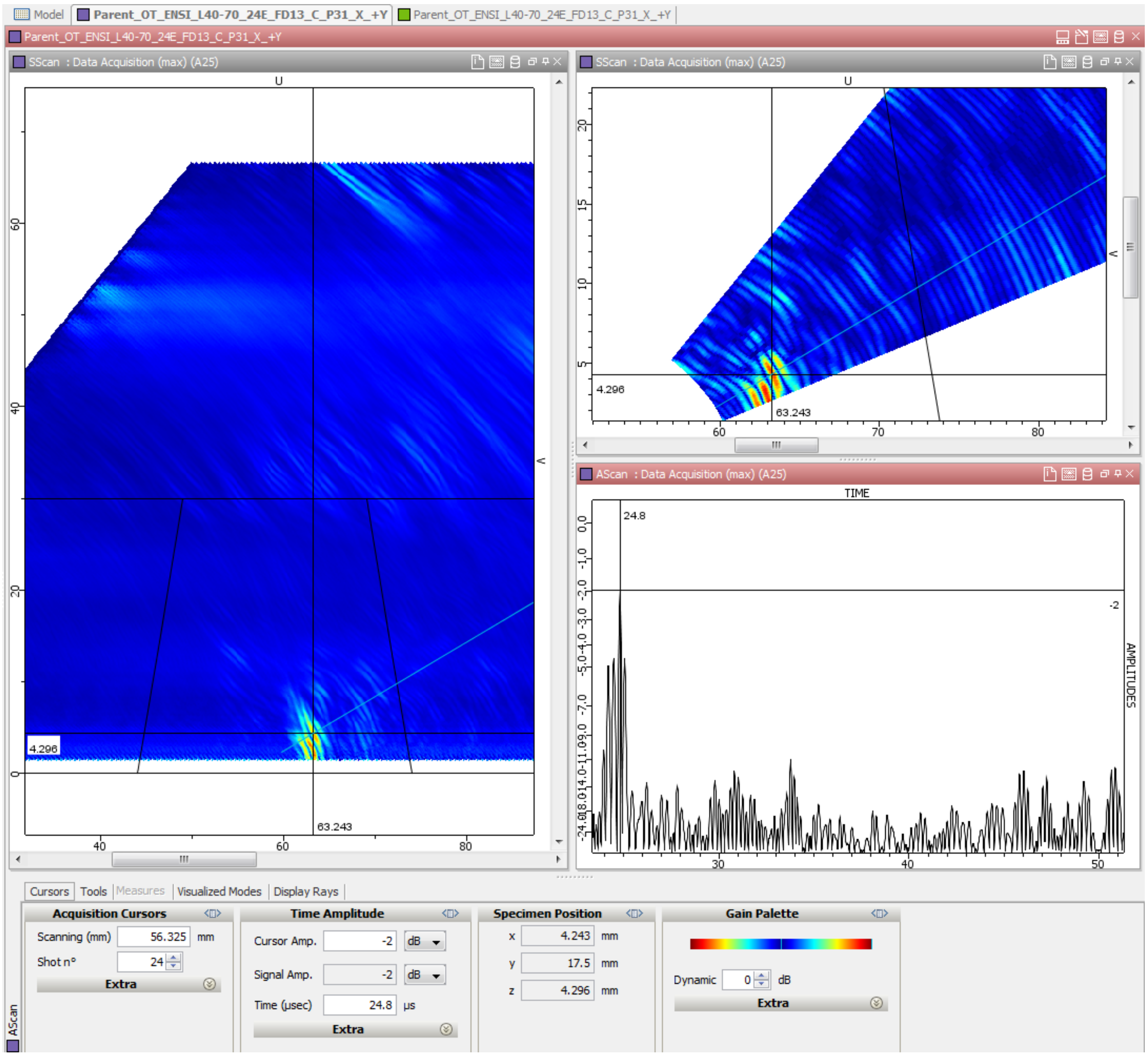

Figure B.39.

Specimen	Scanning Surface	Beam Direction	DAQ File Name	Nb. of Elem.	Focal Depth	Flaw Depth (mmm)	EVal. Angle (°)	S/N. (dB)
P31	**W**	**-Y**	PARENT_OT_ENSI_L40-70_24E_FD13_C_P31_X_-Y	24	13	4.6	50	5
* Remark. Weld drawing not correct.								

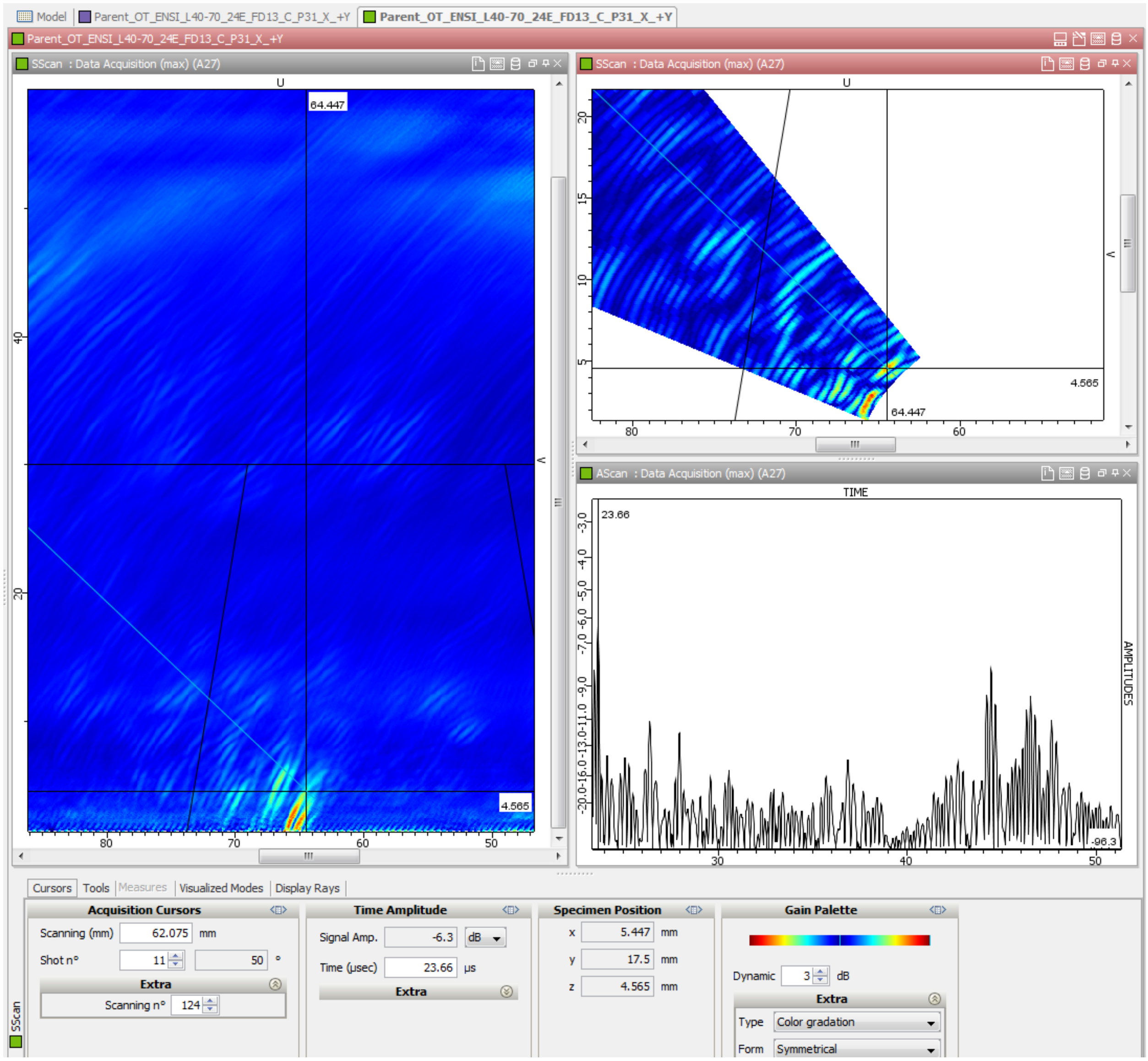

Figure B.40.

Specimen P32

Specimen	Scanning Surface	Beam Direction	DAQ File Name	Nb. of Elem.	Focal Depth	Flaw Depth (mmm)	EVal. Angle (°)	S/N. (dB)
P32	**W**	**+Y**	PARENT_OT_ENSI_L40-70_24E_FD18_C_P32_W_+Y	24	18	9.5	63	6

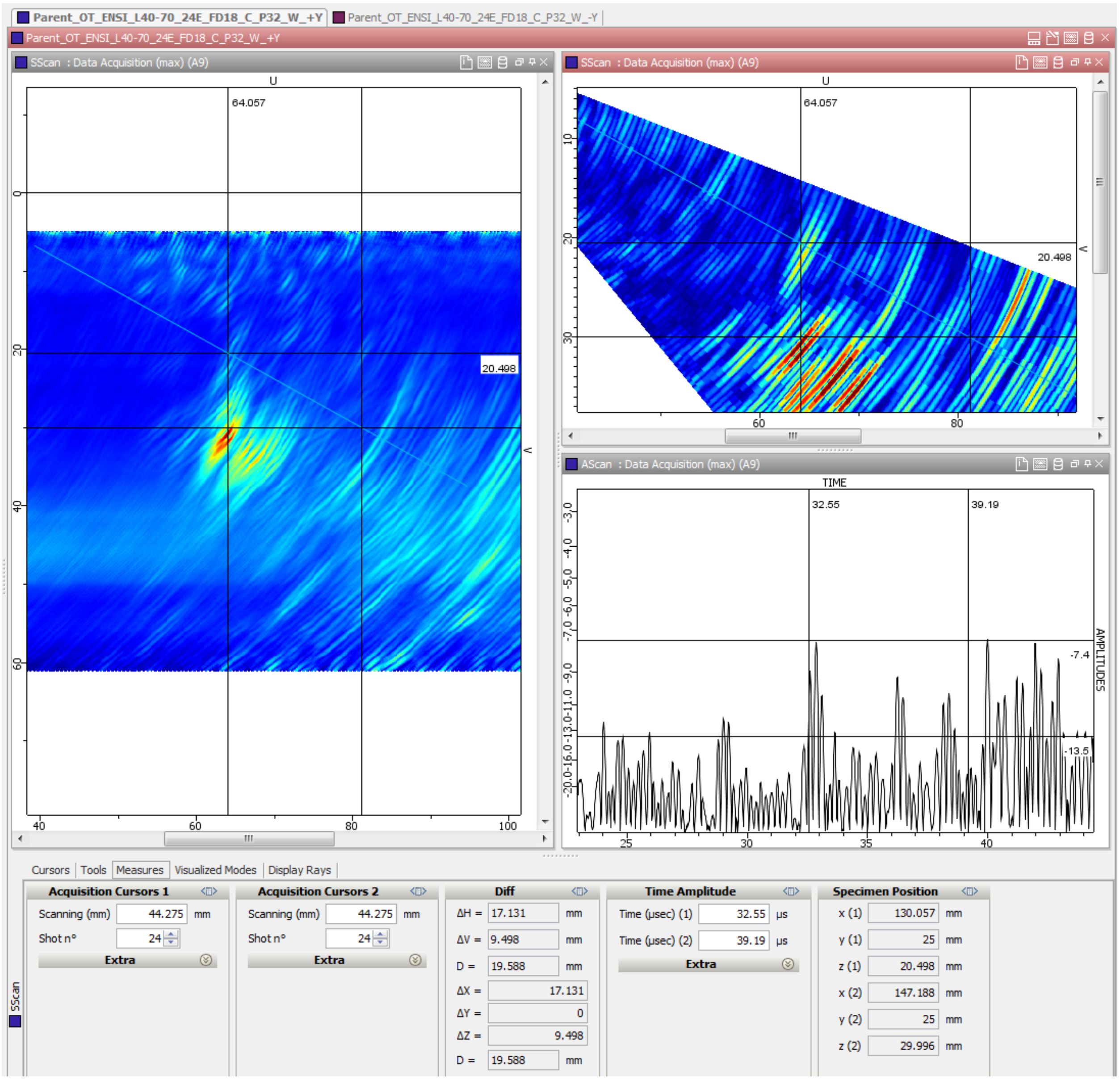

Figure B.41.

Specimen	Scanning Surface	Beam Direction	DAQ File Name	Nb. of Elem.	Focal Depth	Flaw Depth (mmm)	EVal. Angle (°)	S/N. (dB)
P32	**W**	**+Y**	PARENT_OT_ENSI_L40-70_24E_FD13_C_P32_W_-Y	24	13	7.5	57	10

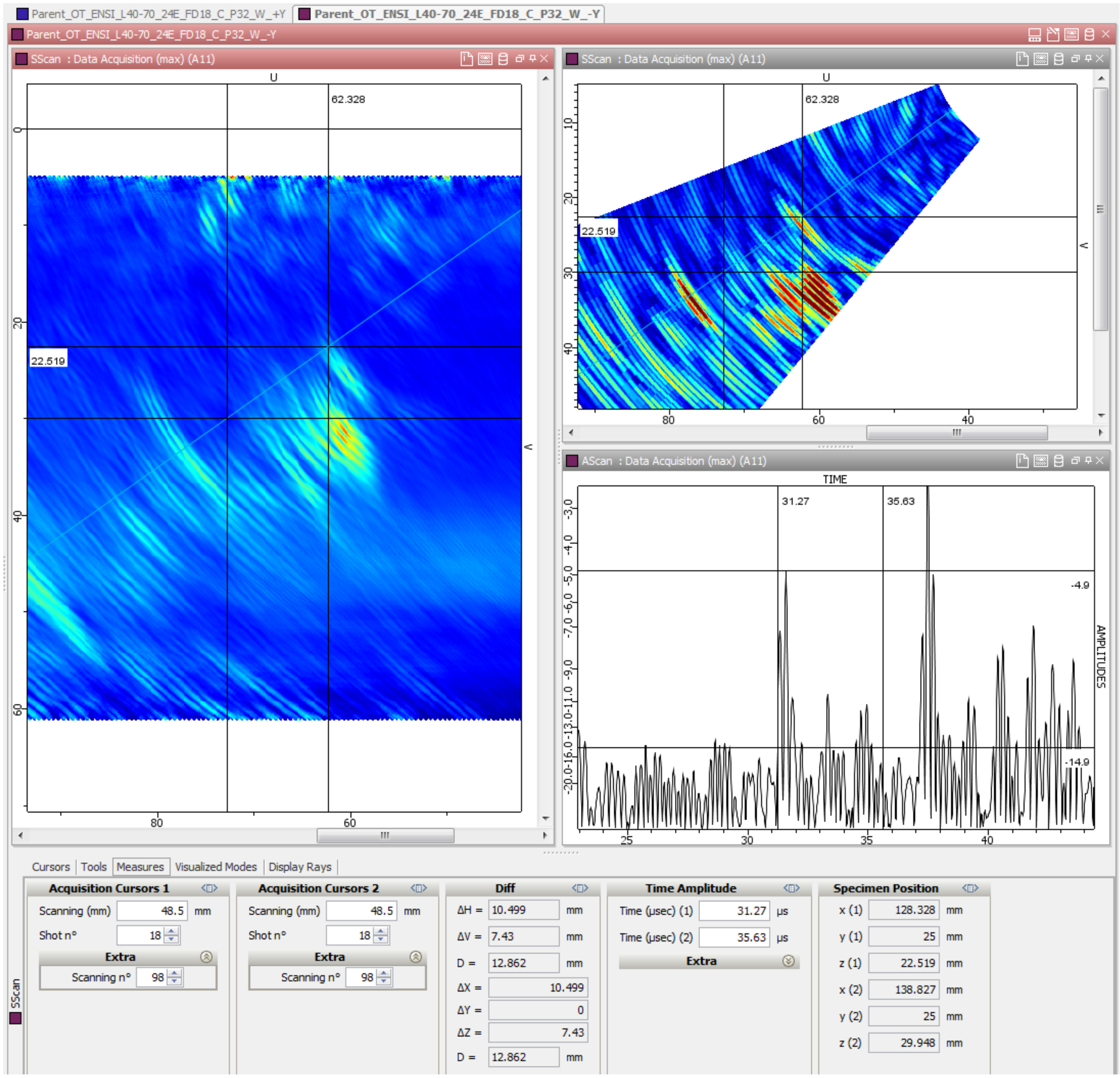

Figure B.42.

Specimen	Scanning Surface	Beam Direction	DAQ File Name	Nb. of Elem.	Focal Depth	Flaw Depth (mmm)	EVal. Angle (°)	S/N. (dB)
P31	**X**	**+Y**	PARENT_OT_ENSI_L40-70_32E_FD20_C_P32_X_+Y	32	20	12.4	61	13

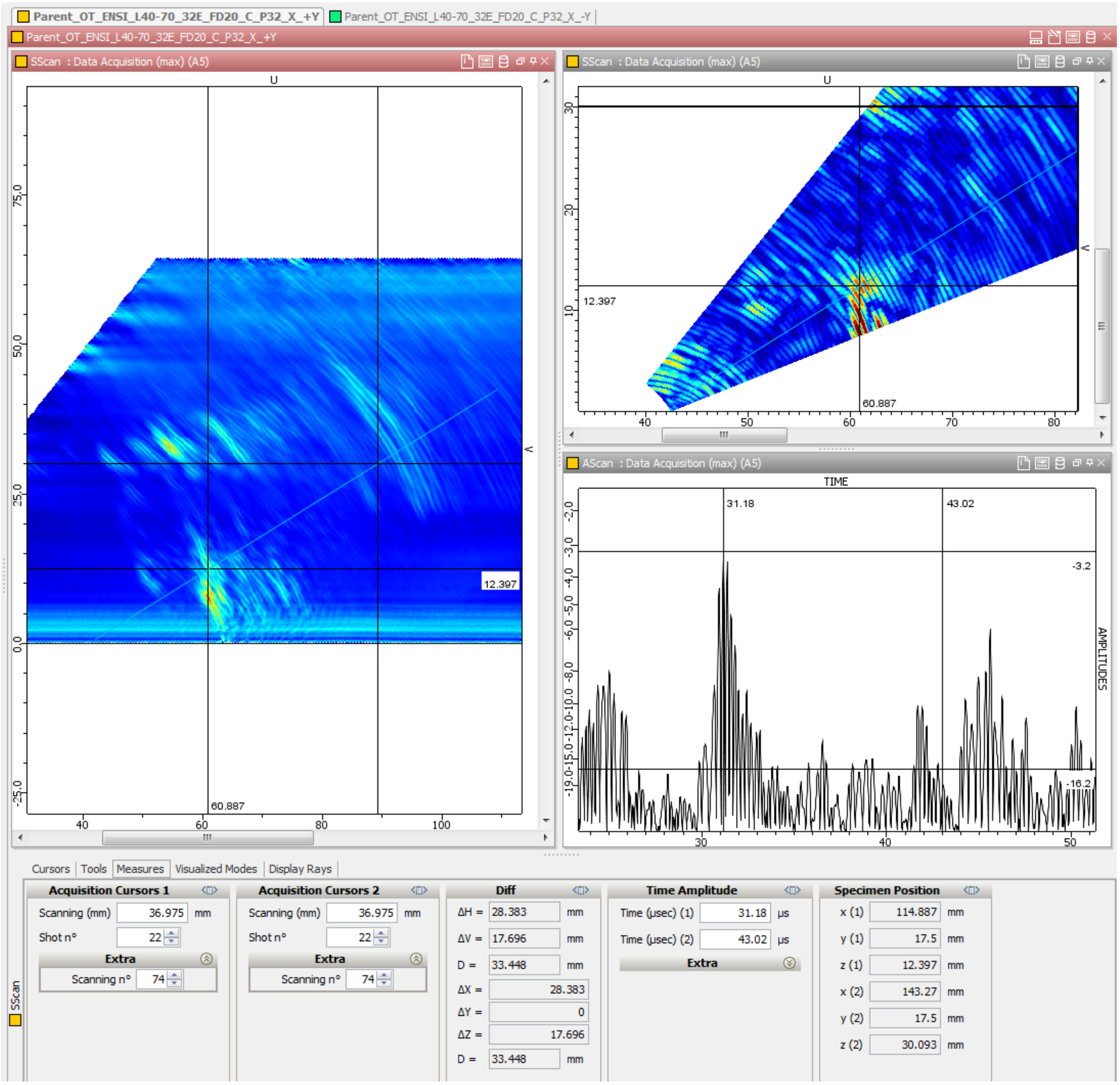

Figure B.43.

Specimen	Scanning Surface	Beam Direction	DAQ File Name	Nb. of Elem.	Focal Depth	Flaw Depth (mmm)	EVal. Angle (°)	S/N. (dB)
P32	**X**	**-Y**	PARENT_OT_ENSI_L40-70_32E_FD20_C_P32_X_-Y	32	20	13.4	52	8

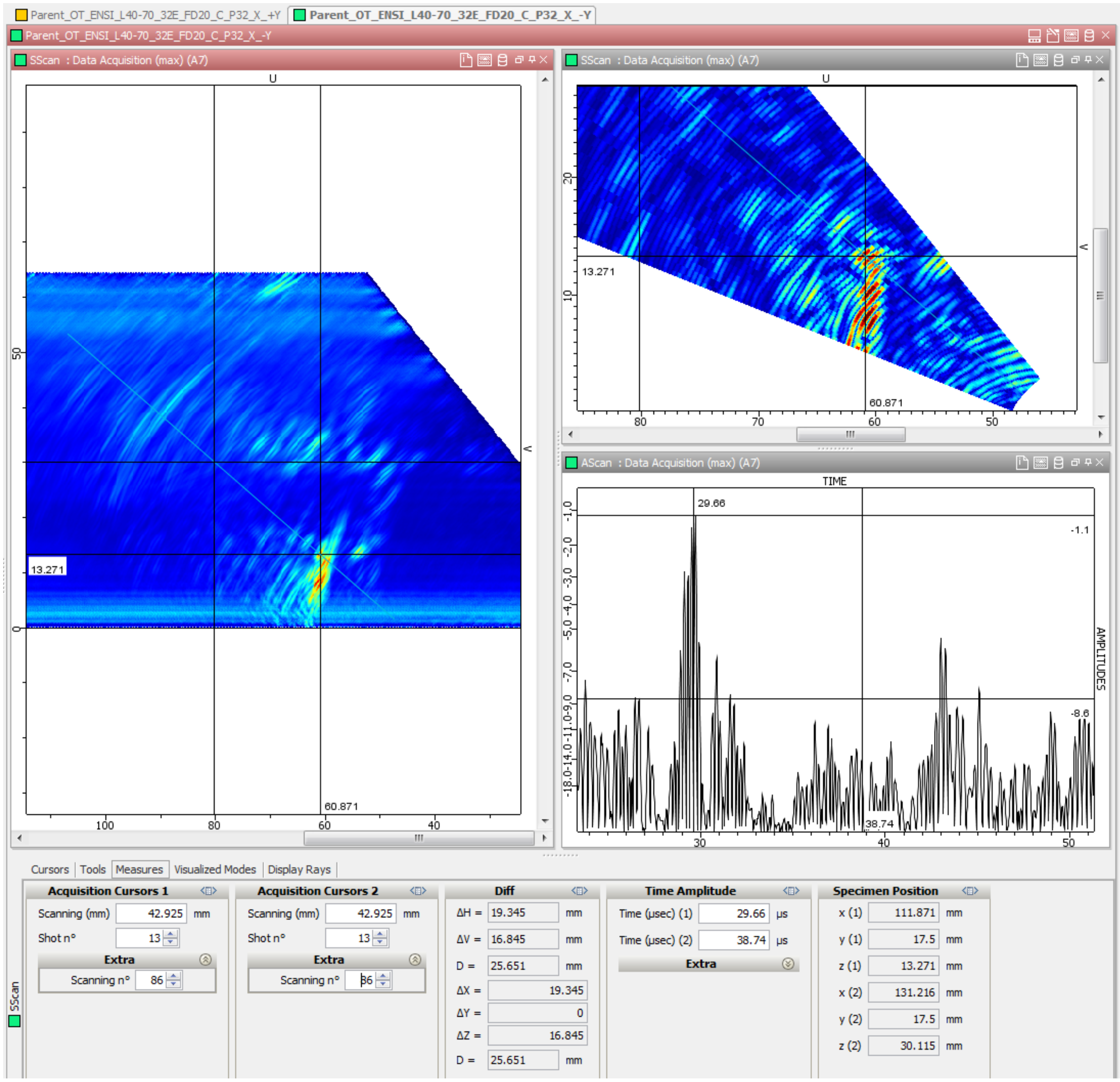

Figure B.44.

Specimen P42

Specimen	Scanning Surface	Beam Direction	DAQ File Name	Nb. of Elem.	Focal Depth	Flaw Depth (mmm)	EVal. Angle (°)	S/N. (dB)
P42	**W**	**+Y**	PARENT_OT_ENSI_L40-70_24E_FD13_C_P42_W_+Y	24	13	9.3	46	11

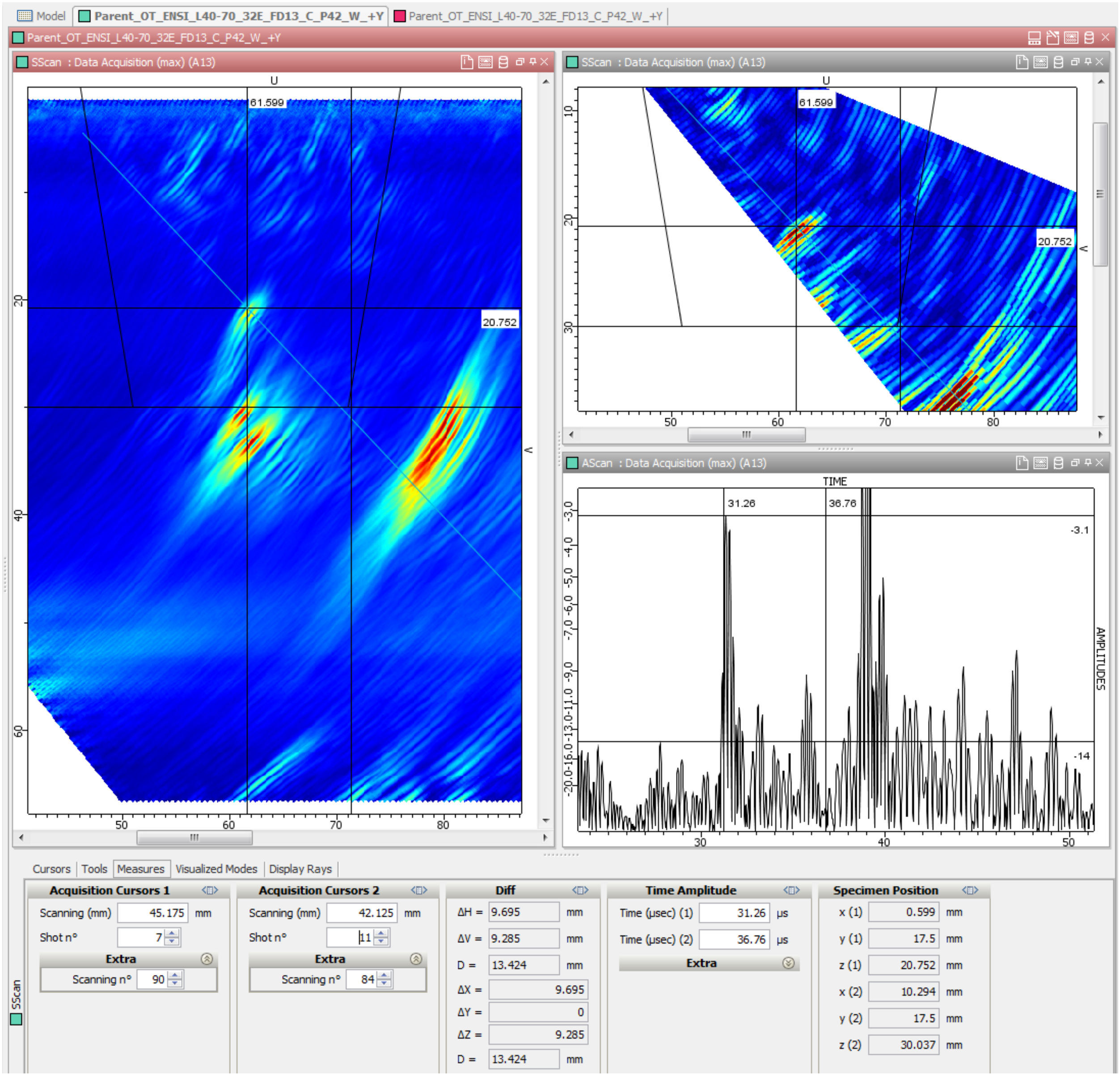

Figure B.45.

Specimen	Scanning Surface	Beam Direction	DAQ File Name	Nb. of Elem.	Focal Depth	Flaw Depth (mmm)	EVal. Angle (°)	S/N. (dB)
P31	**W**	**-Y**	PARENT_OT_ENSI_L40-70_24E_FD13_C_P42_W_-Y	24	13	9.7	48	8

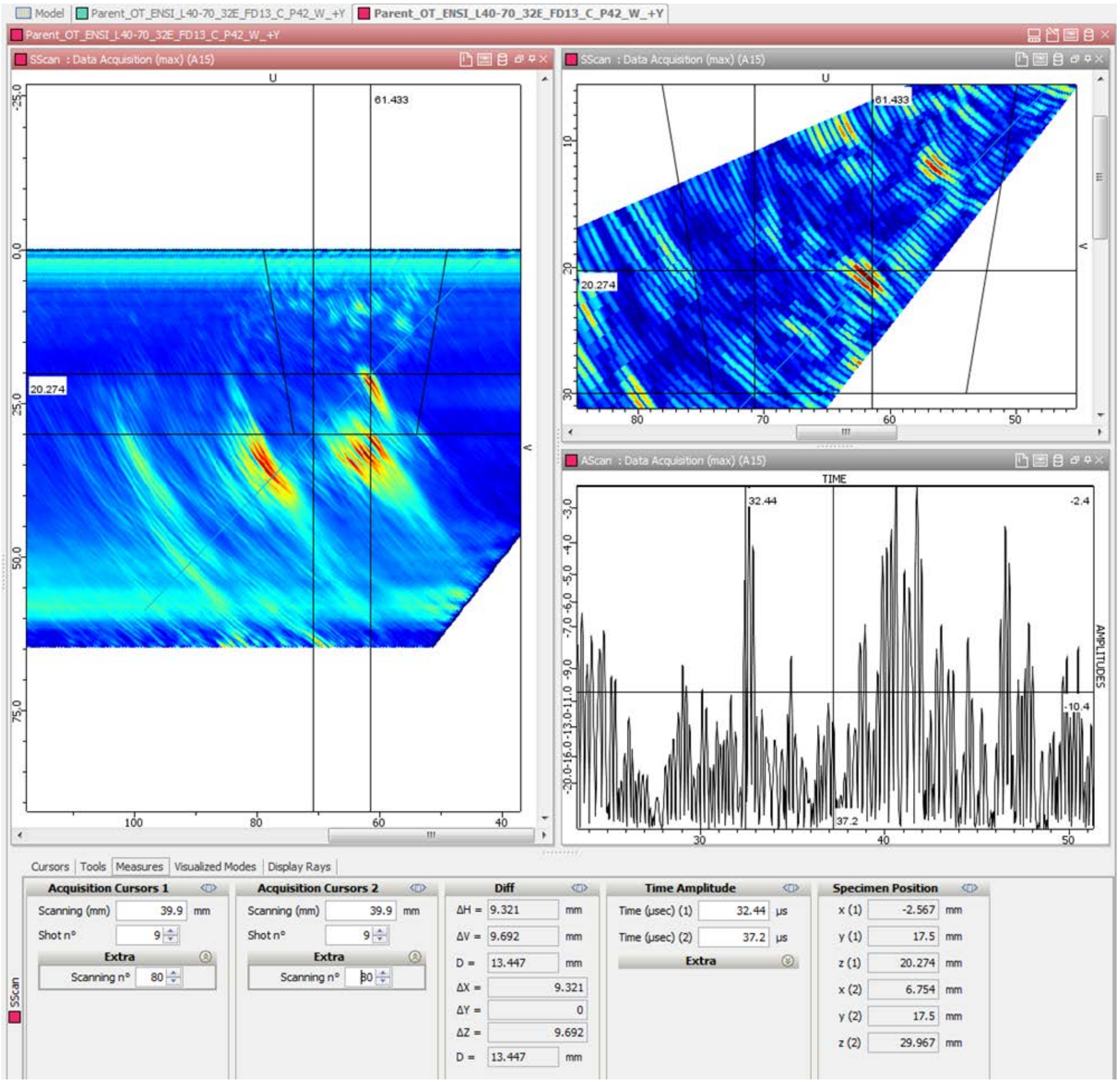

Figure B.46.

Specimen P38

Specimen	Scanning Surface	Beam Direction	DAQ File Name	Nb. of Elem.	Focal Depth	Flaw Depth (mmm)	EVal. Angle (°)	S/N. (dB)
P38	**W**	**+Y**	PARENT_OT_ENSI_L40-70_24E_FD13_C_P38_W_+Y	24	13	6.6	59	4
*weak mode converted TLL - shallow crack, tip very weak, bad SN								

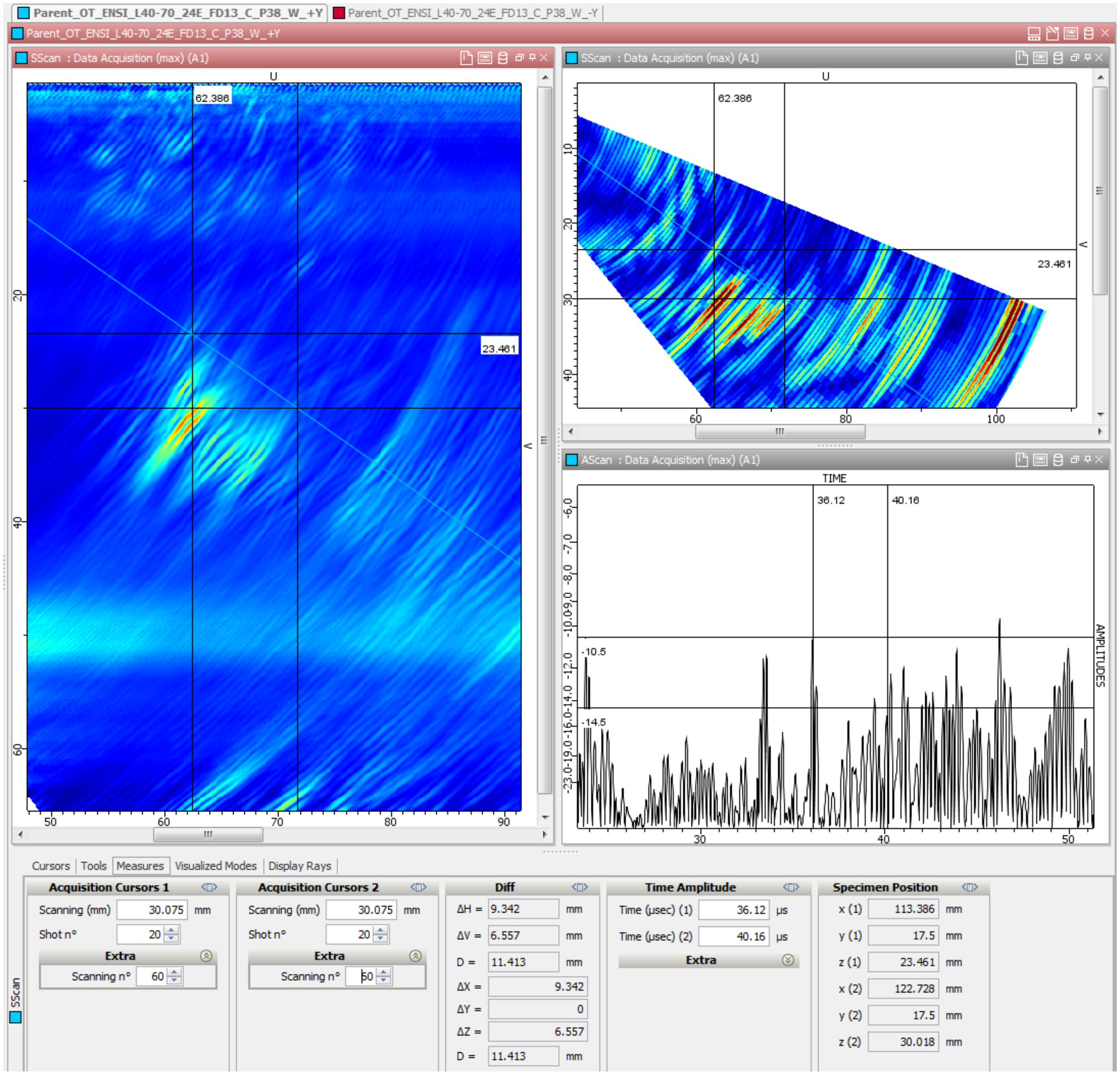

Figure B.47.

Specimen	Scanning Surface	Beam Direction	DAQ File Name	Nb. of Elem.	Focal Depth	Flaw Depth (mmm)	EVal. Angle (°)	S/N. (dB)
P38	**W**	**-Y**	PARENT_OT_ENSI_L40-70_24E_FD13_C_P38_W_-Y	24	13	6.4	59	5.3
*weak mode converted TLL - shallow crack, tip very weak, bad SN								

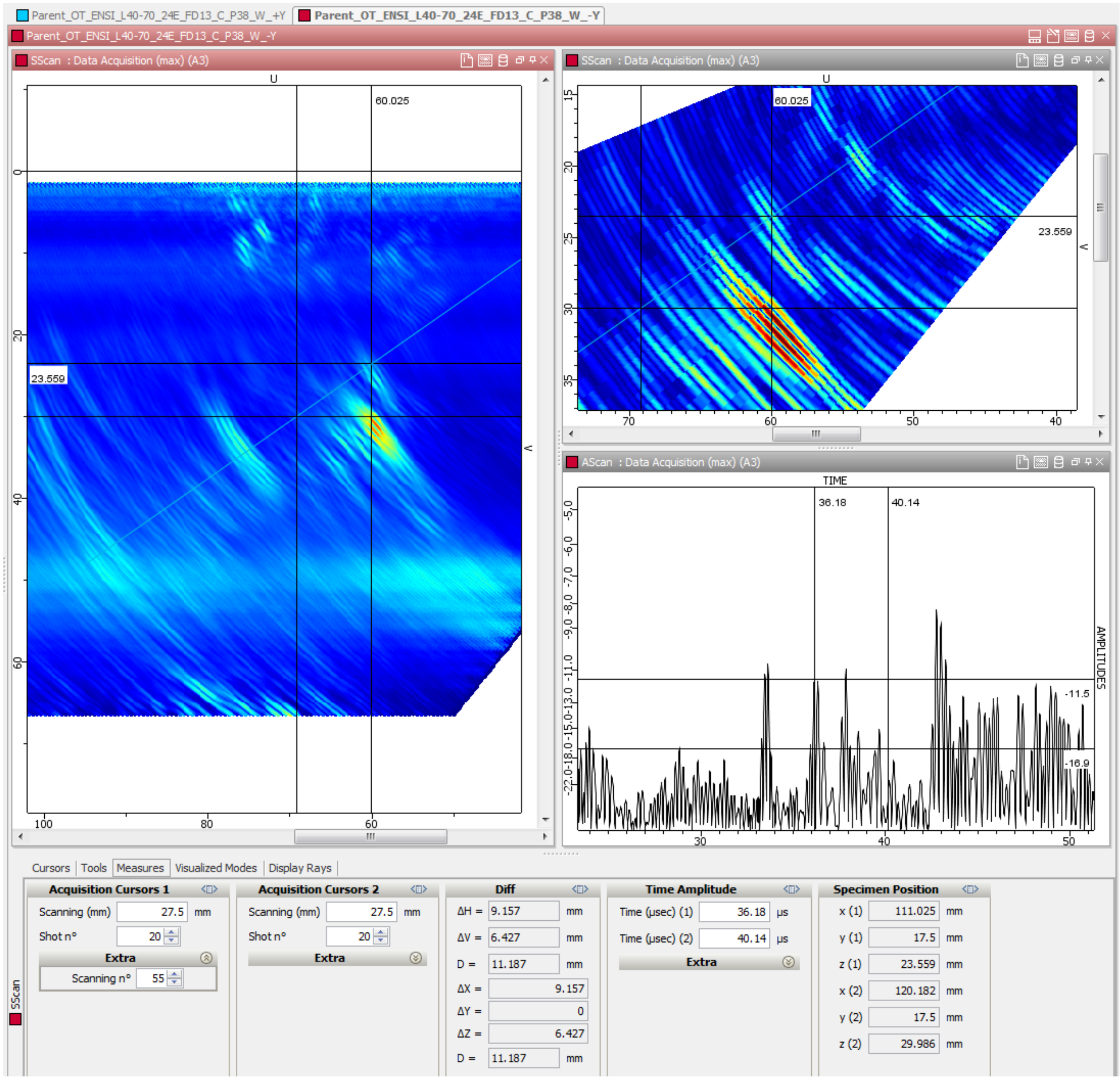

Figure B.48.

Specimen	Scanning Surface	Beam Direction	DAQ File Name	Nb. of Elem.	Focal Depth	Flaw Depth (mmm)	EVal. Angle (°)	S/N. (dB)
P38	**X**	**+Y**	PARENT_OT_ENSI_L40-70_24E_FD13_C_P38_X_+Y	24	13	5	50	11

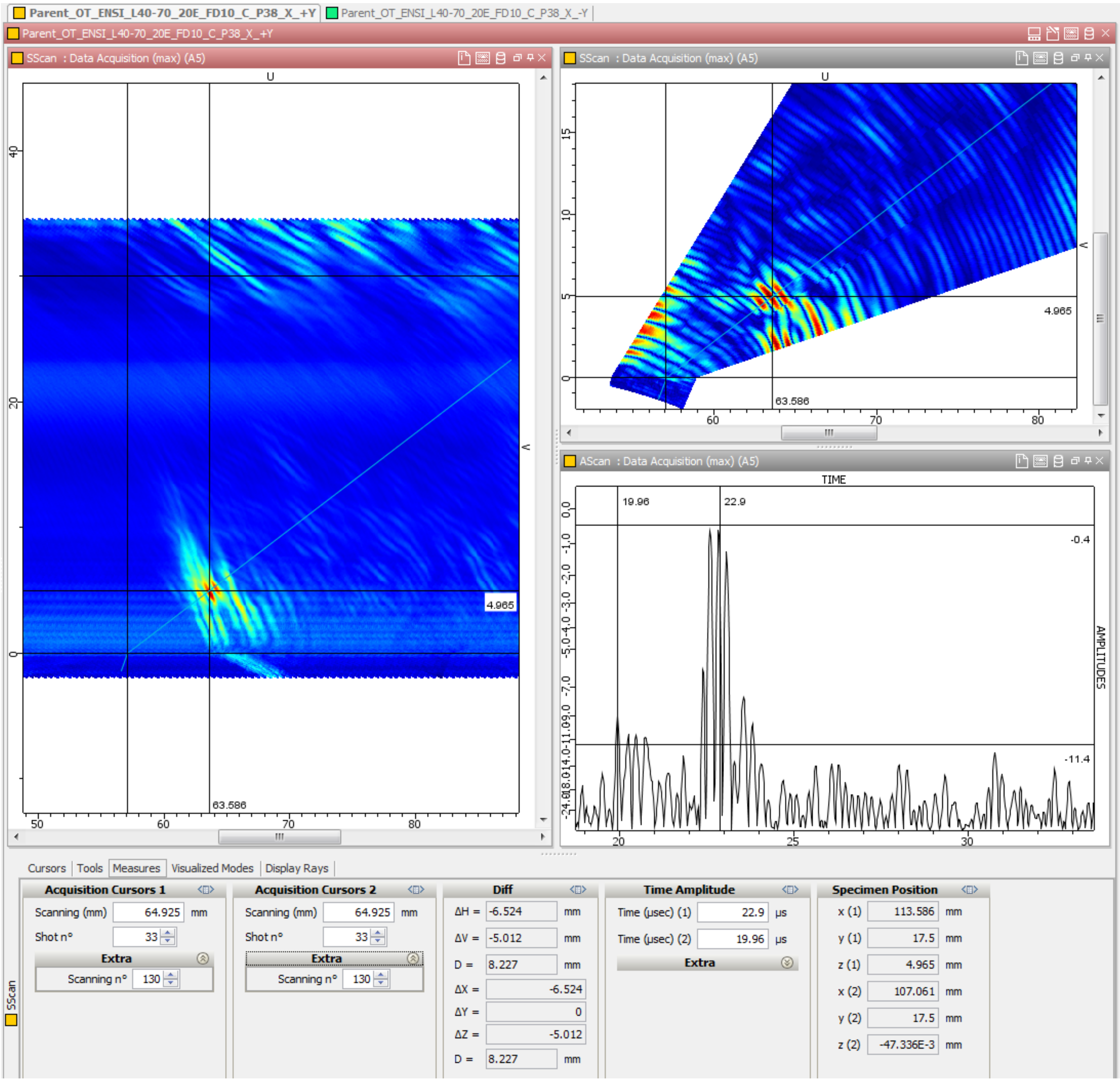

Figure B.49.

Specimen	Scanning Surface	Beam Direction	DAQ File Name	Nb. of Elem.	Focal Depth	Flaw Depth (mmm)	EVal. Angle (°)	S/N. (dB)
P38	**X**	**-Y**	PARENT_OT_ENSI_L40-70_24E_FD13_C_P38_X_-Y	24	13	5.7	51	7

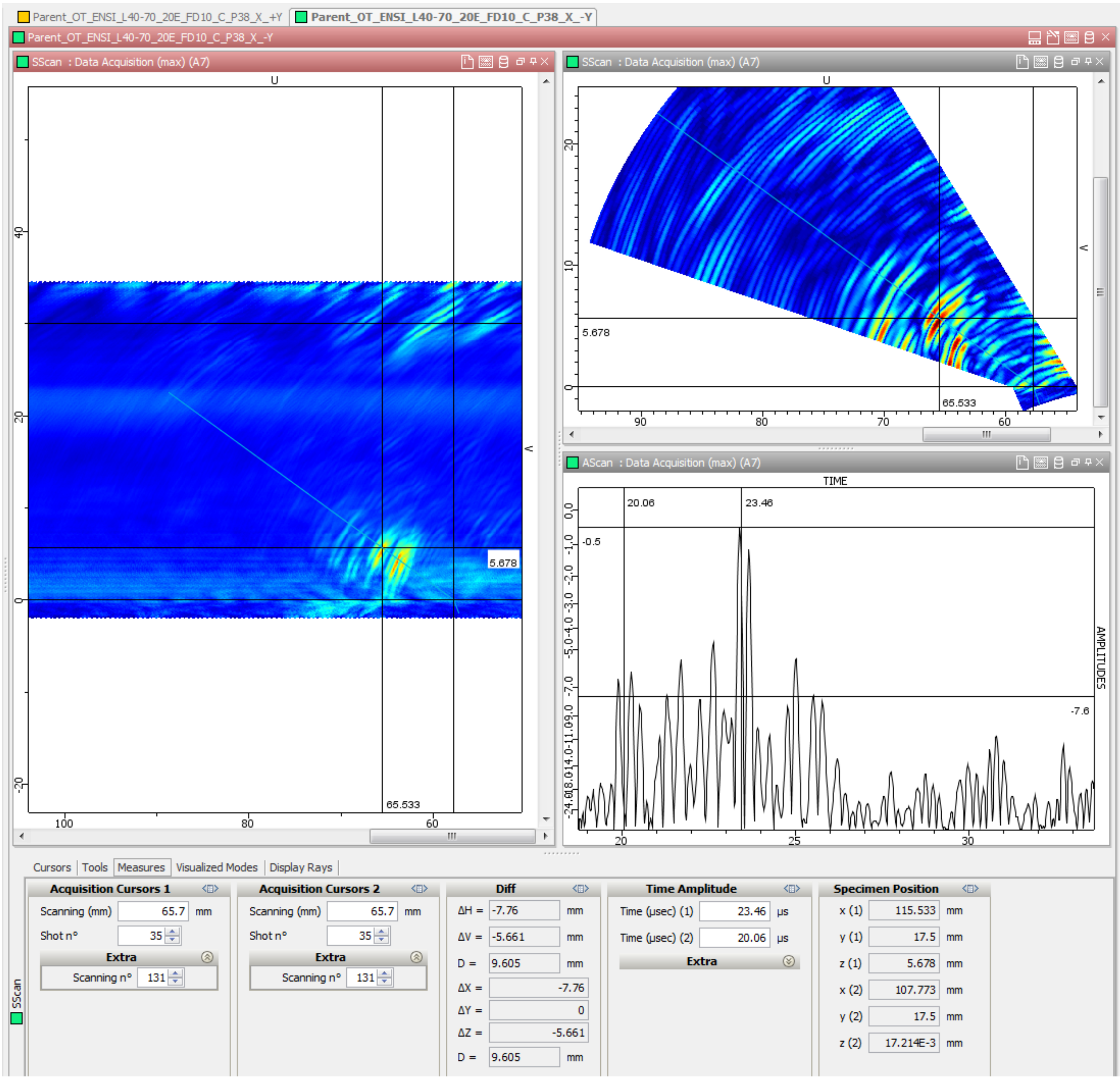

Figure B.50.

B.2.6 Self Assessment

- Good TWS of EDM notch and mechanical fatigue crack, clear tip diffraction echo's from all examination directions visible
- TWS of stress corrosion cracks challenging, tip diffraction echo's not seen from all examination directions (Remark: TWS of specimen SCC under field conditions (surface conditions, access) very hard and sometimes not possible)

B.3 Phased Ultrasonic Array, Technique ID 131-PA1

B.3.1 Overview

The techniques described in this report were utilized for the examination of the PARENT specimens P1 and P41.

Method	Phased Array Ultrasonic Testing
Array / Technique	Dual / Linear / Transmit - Receive
Wave Mode	Longitudinal
Angle Range	25° – 65°
Frequency	2 MHz
UT Instrument	M2M MultiX 64
Scan Plan	Manual scanning parallel and perpendicular to weld from both directions
Scanning Surface	OD

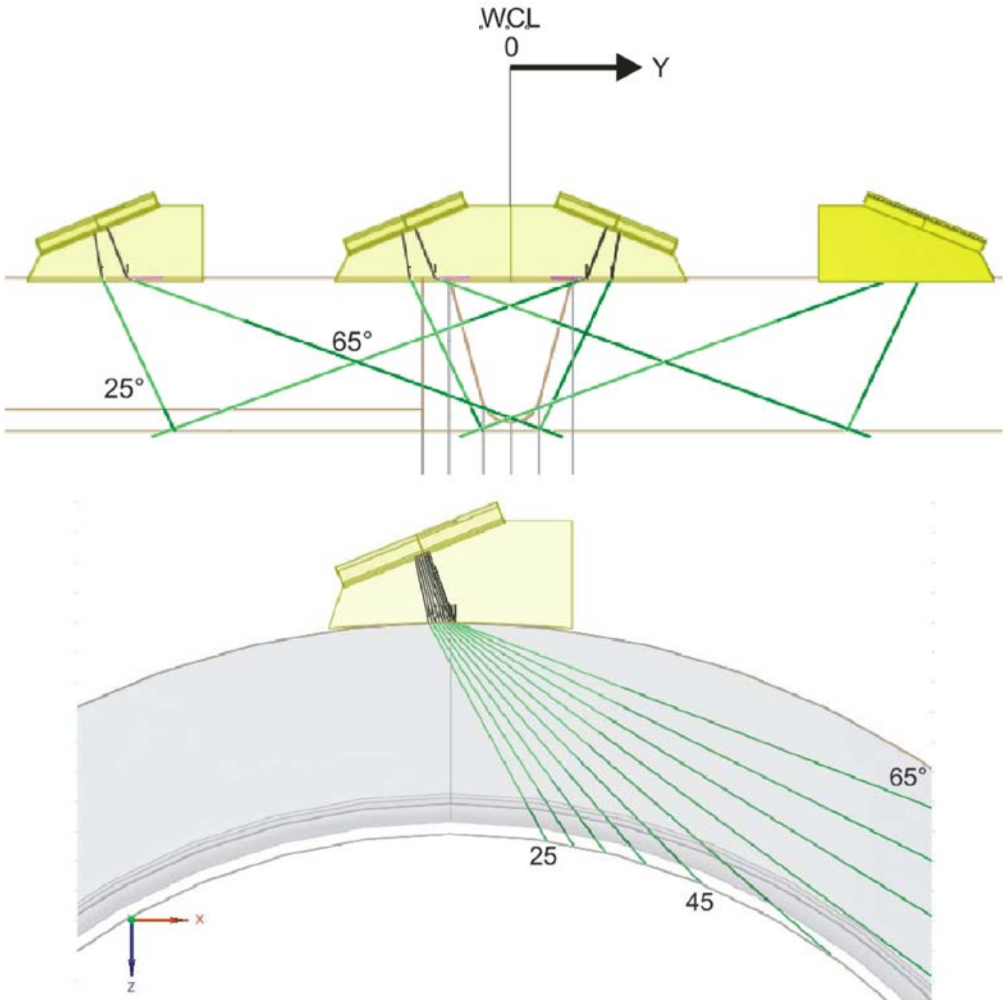

Figure B.51.

B.3.2 NDE Equipment / UT Settings

B.3.2.1 Search Unit

For the measurement a GEIT probe and wedge was used. The essential variable of the search unit are described in the next chapters.

Crystal Shape

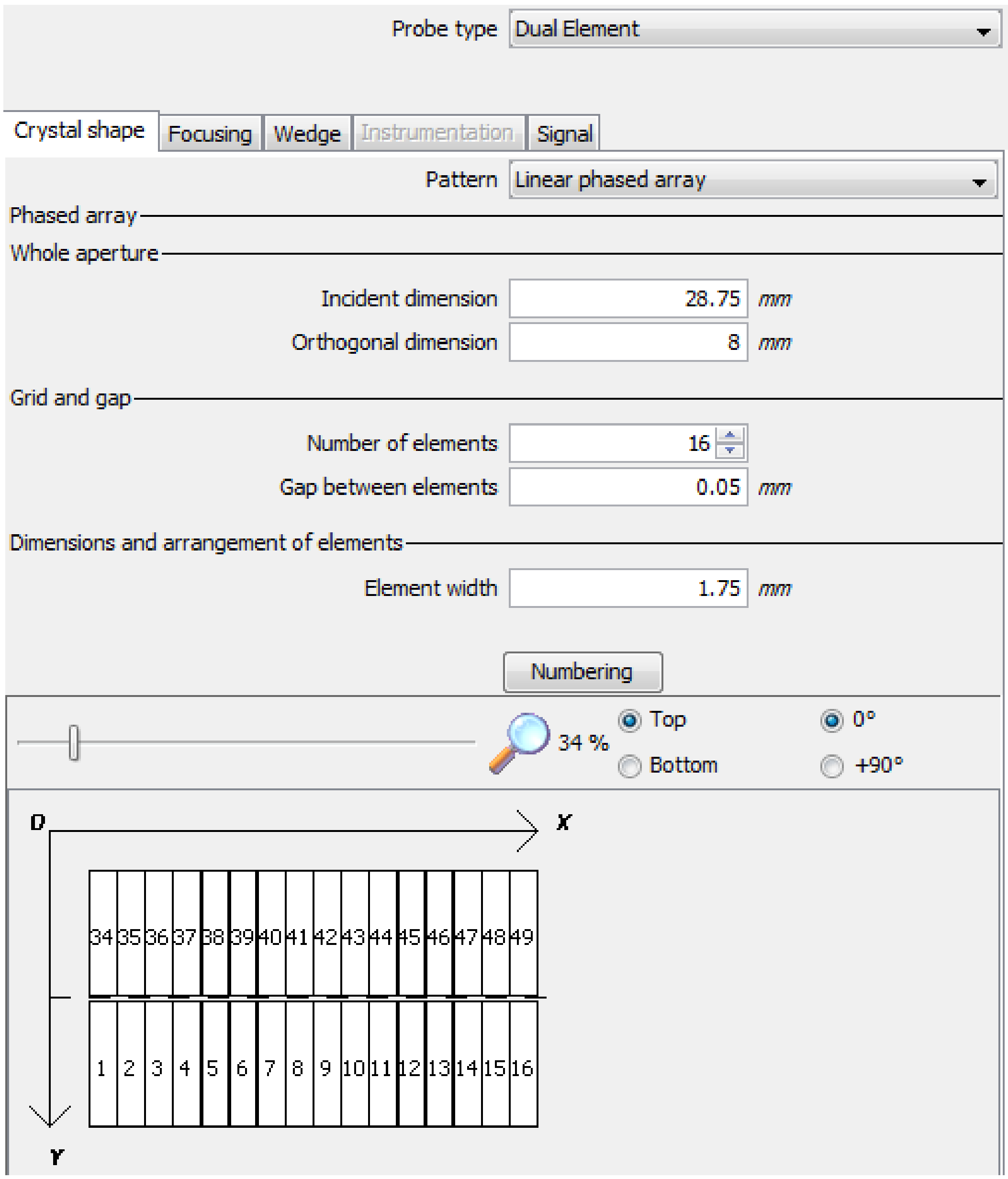

Figure B.52.

Focusing

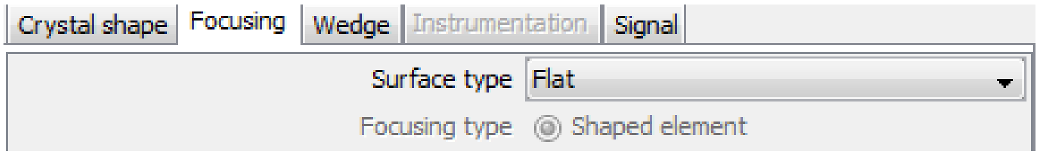

Figure B.53.

Wedge for Axial Scanning (Circ Flaws)

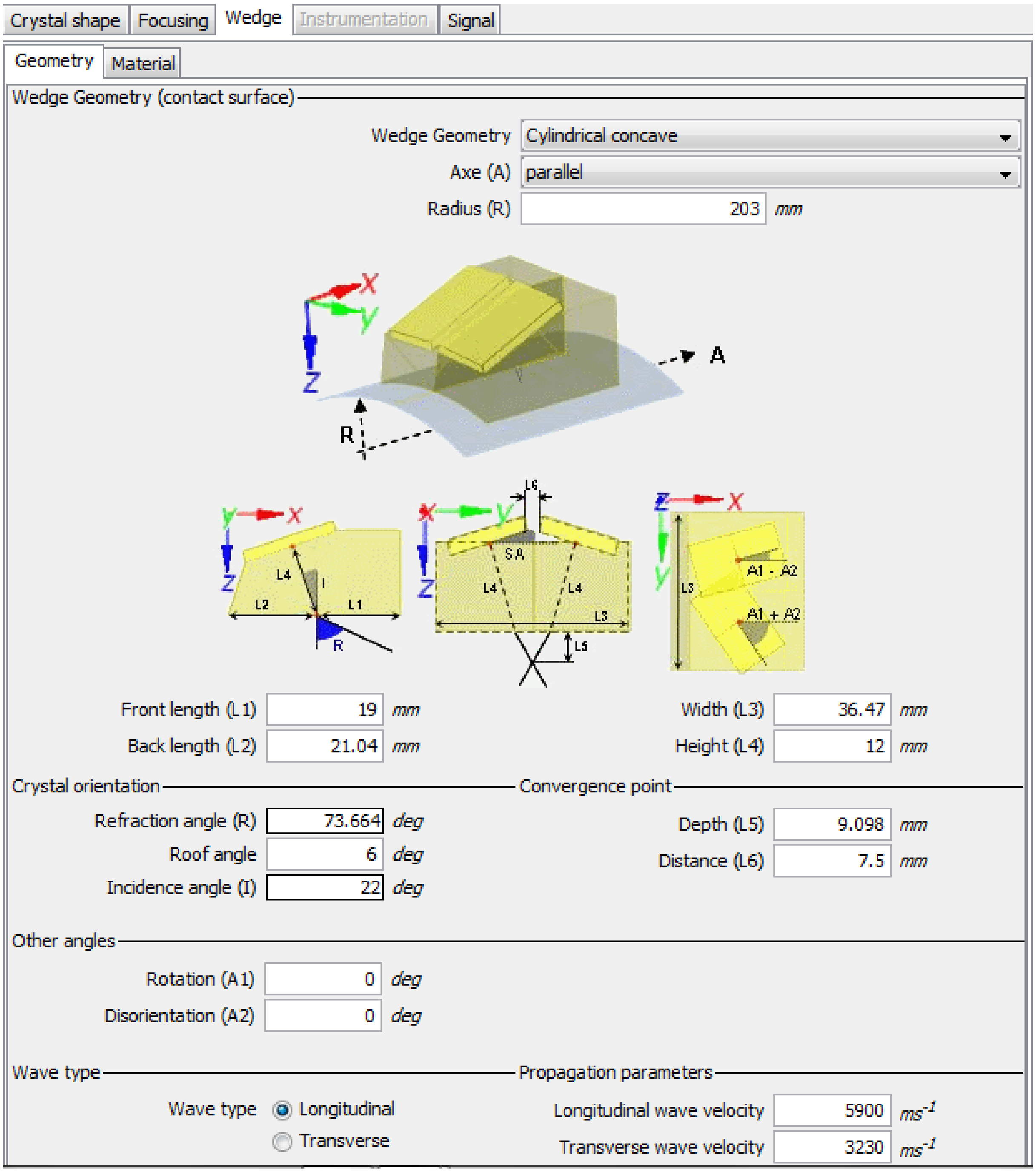

Wedge material: Rexolite cl=2237 m/s

Figure B.54.

Wedge for Circumferential Scanning (Axial Flaws)

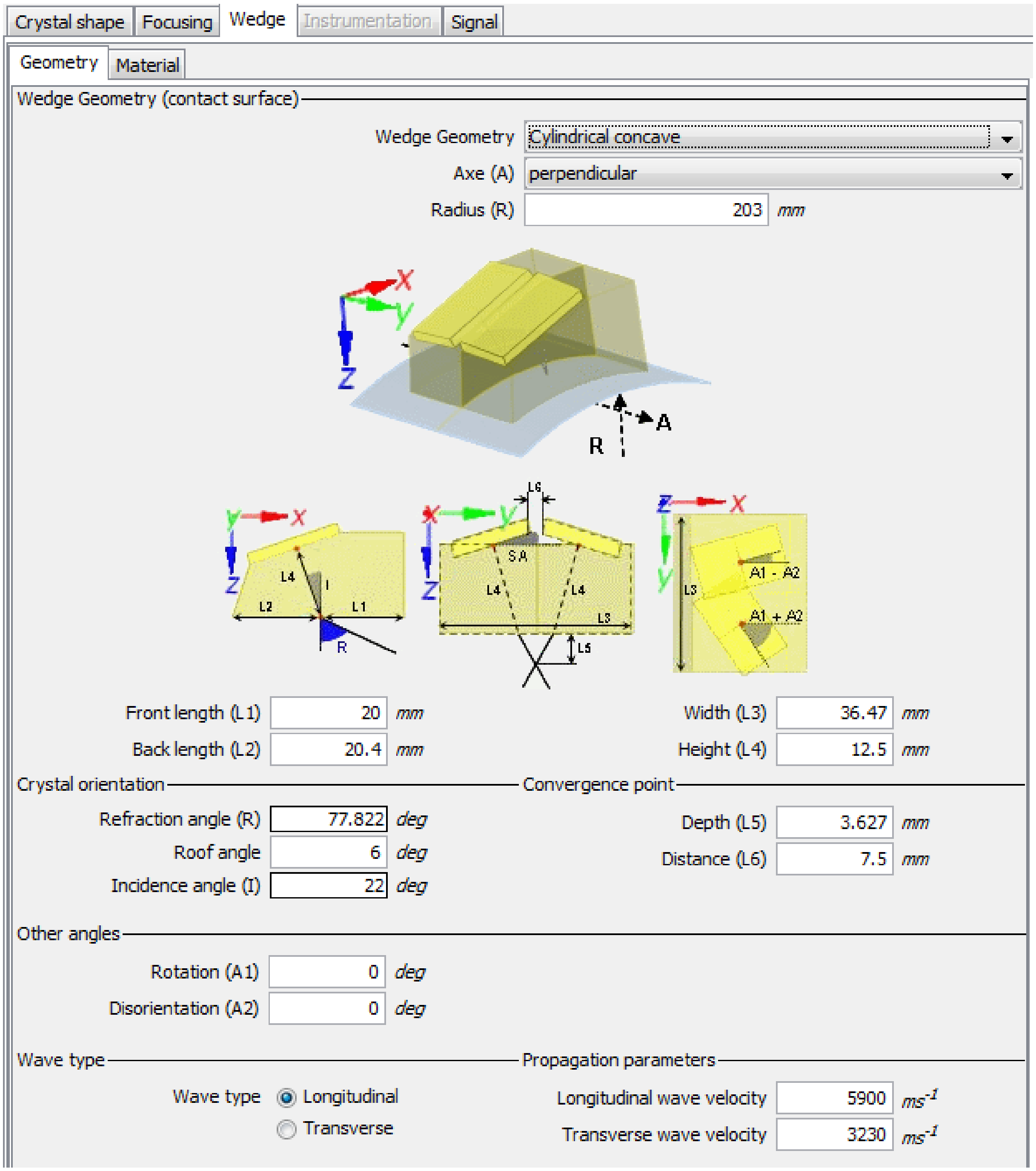

Figure B.55.

Signal

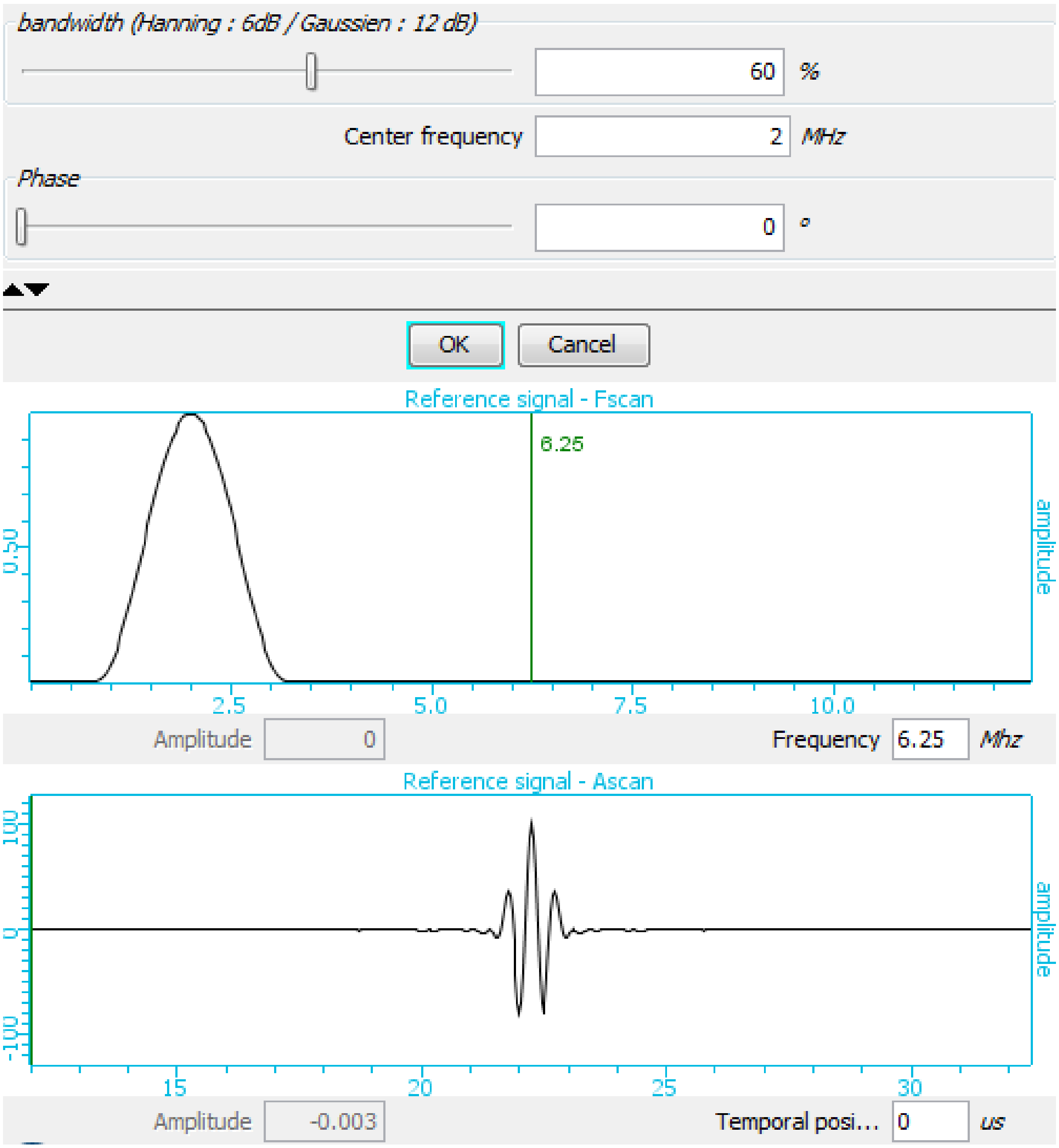

Figure B.56.

B.3.2.2 Phased Array Settings – Focal Laws

Initialization

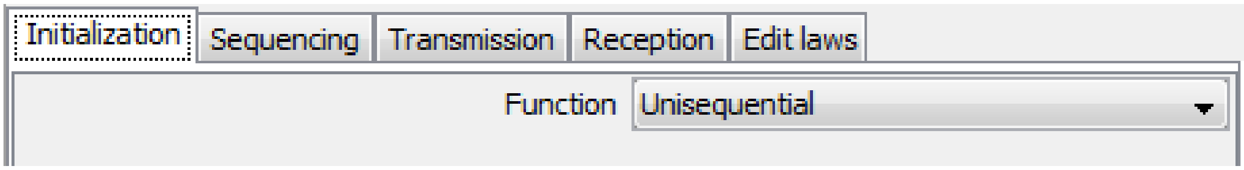

Figure B.57.

Sequencing

Transmission Element 1 (lower wedge end) to Element 14

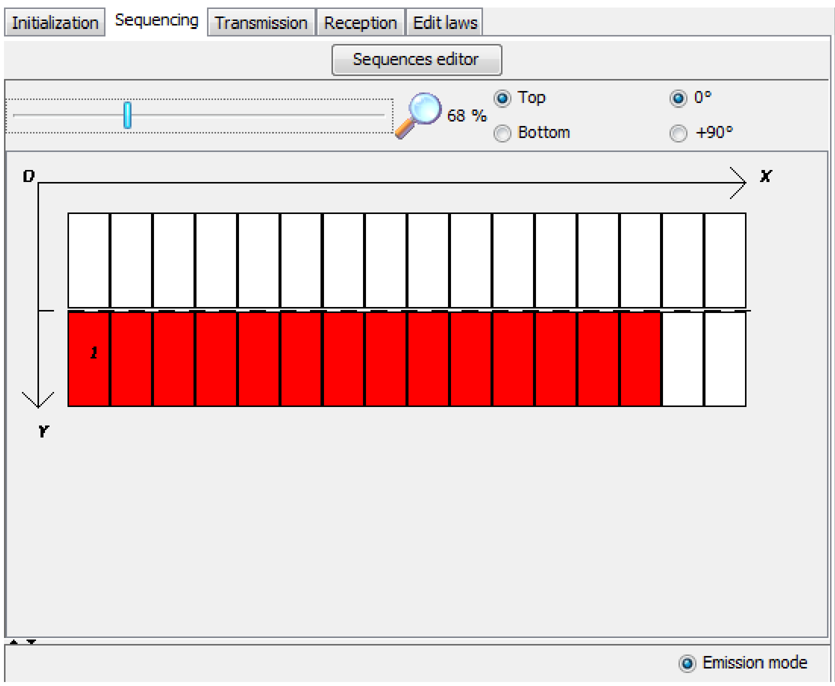

Figure B.58.

Receiving Element 1 (lower wedge end) to Element 14

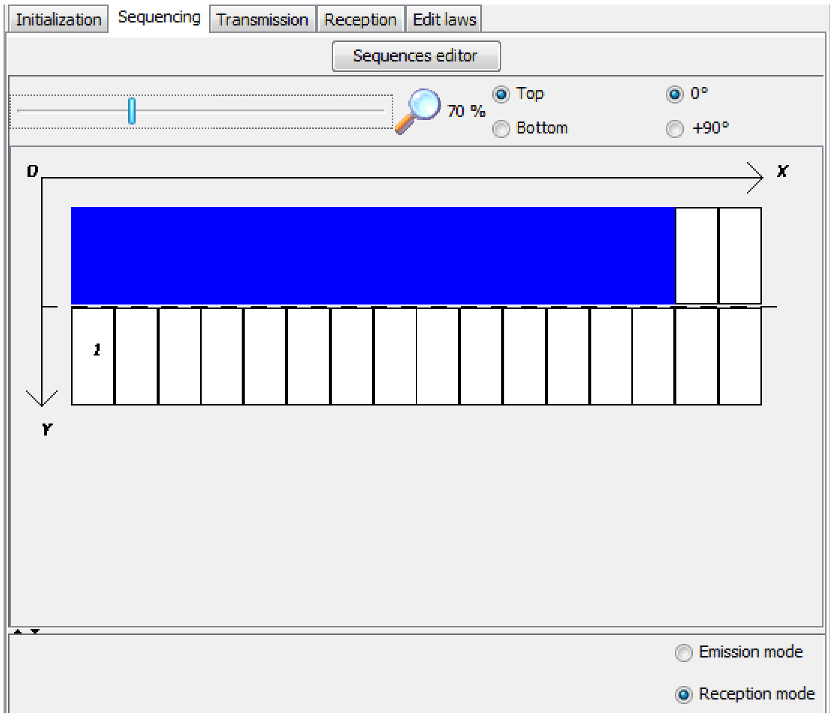

Figure B.59.

Transmission

The focusing type is sectorial scanning. The sector range goes from 25° to 65° (Step 1°) longitudinal waves.

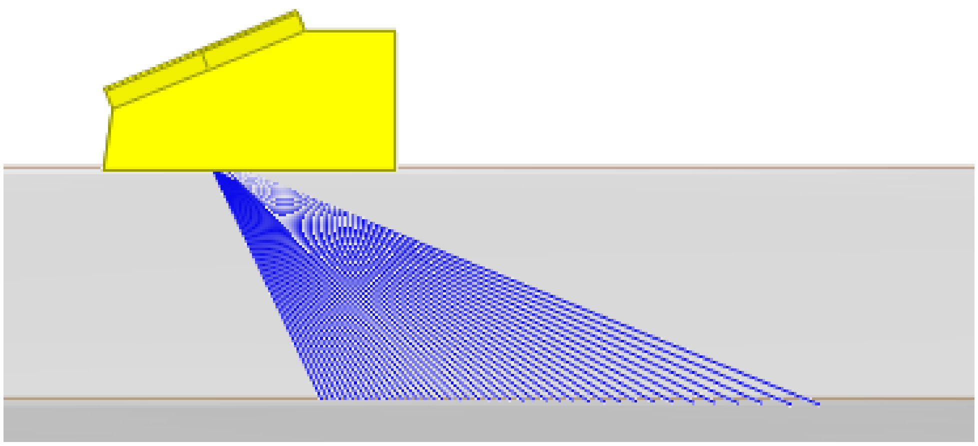

Figure B.60.

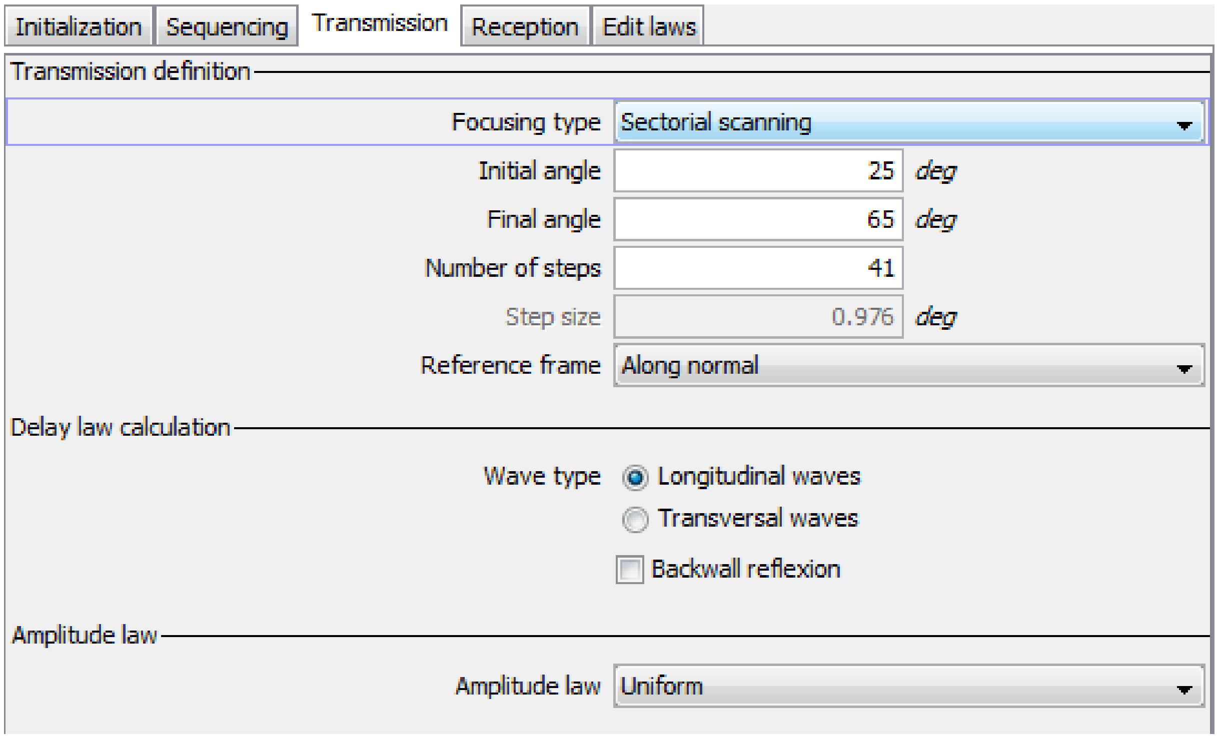

Figure B.61.

B.3.2.3 UT Eqipment Settings - M2M MultiX 64

For the measurements a M2M MultiX UT System was used. MultiX system is a fully parallel architecture with 64 channels. In the following chapters the essential equipment settings are listed.

General Settings

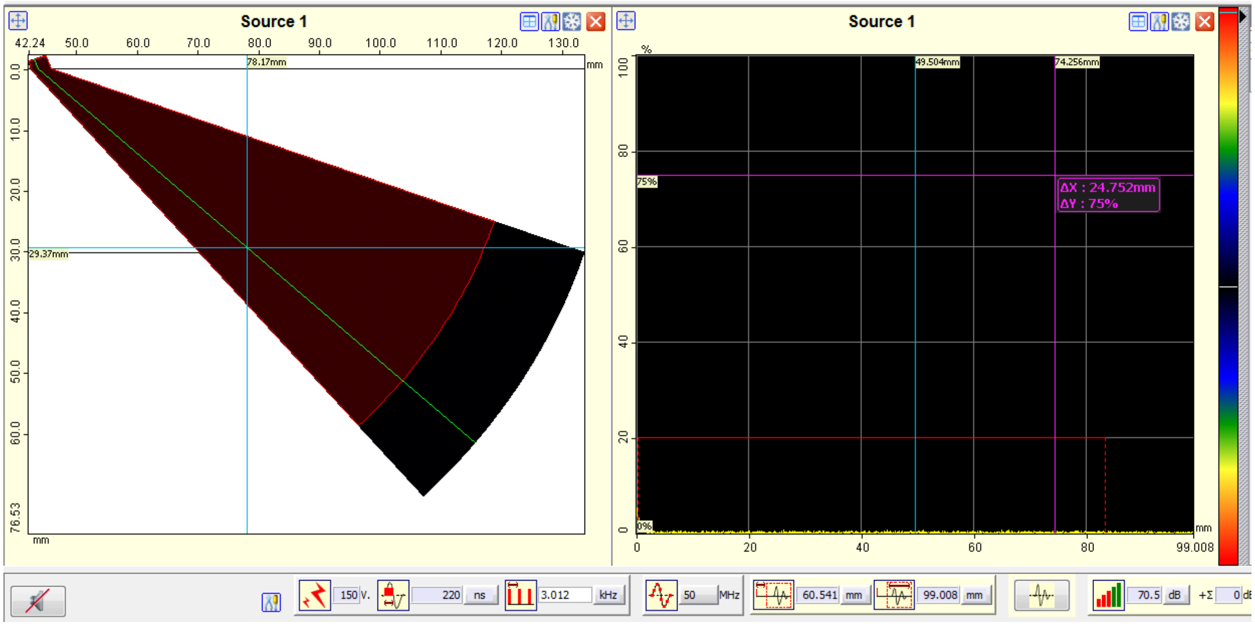

Figure B.62.

Gates

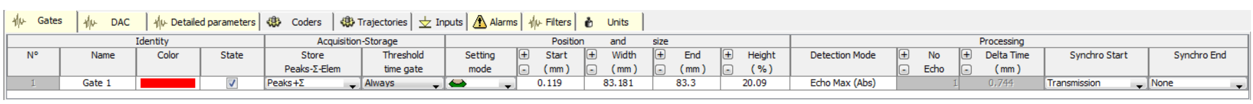

Figure B.63.

DAC

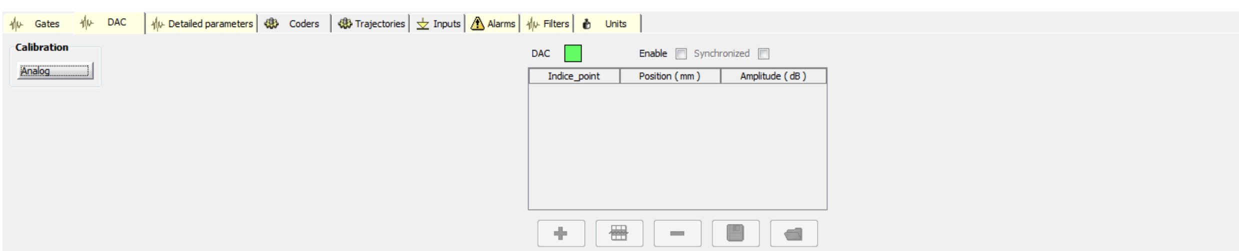

Figure B.64.

Coders

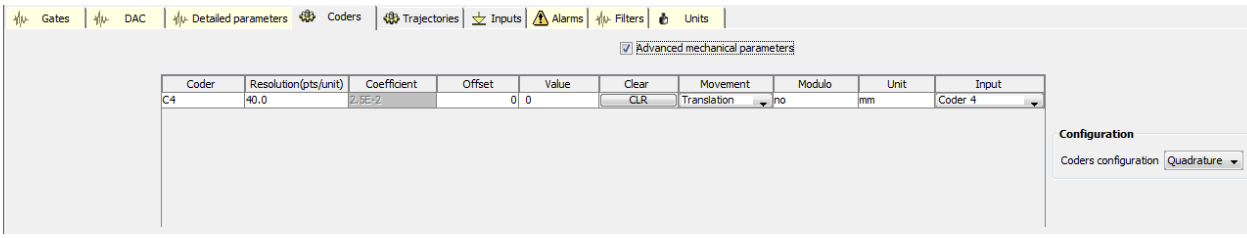

Figure B.65.

Trajectories

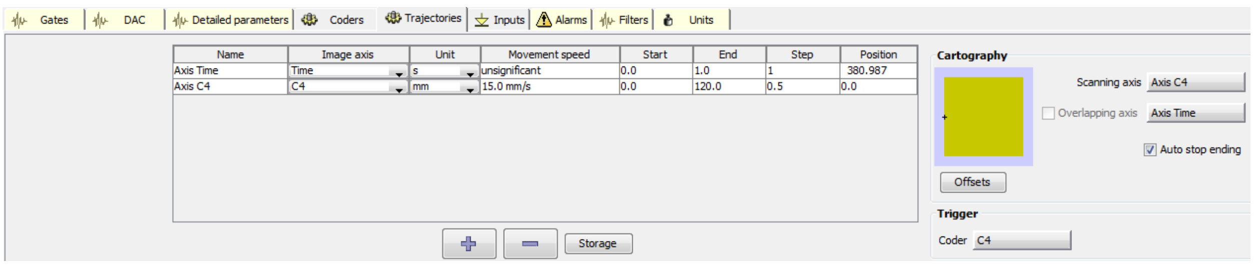

Figure B.66.

Units

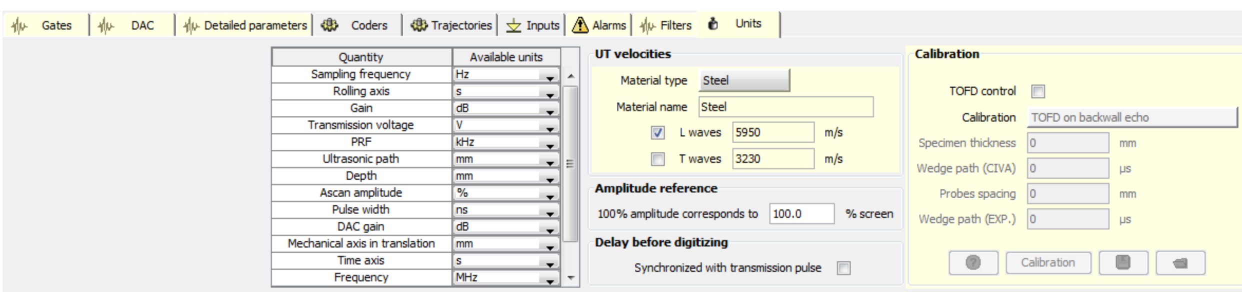

Figure B.67.

B.3.3 Data Acquisition (Scan Plan for Manual Examination)

B.3.3.1 Scanning for Circumferential Flaws

- Beam shall be directed essentially perpendicular to the weld axis from both directions

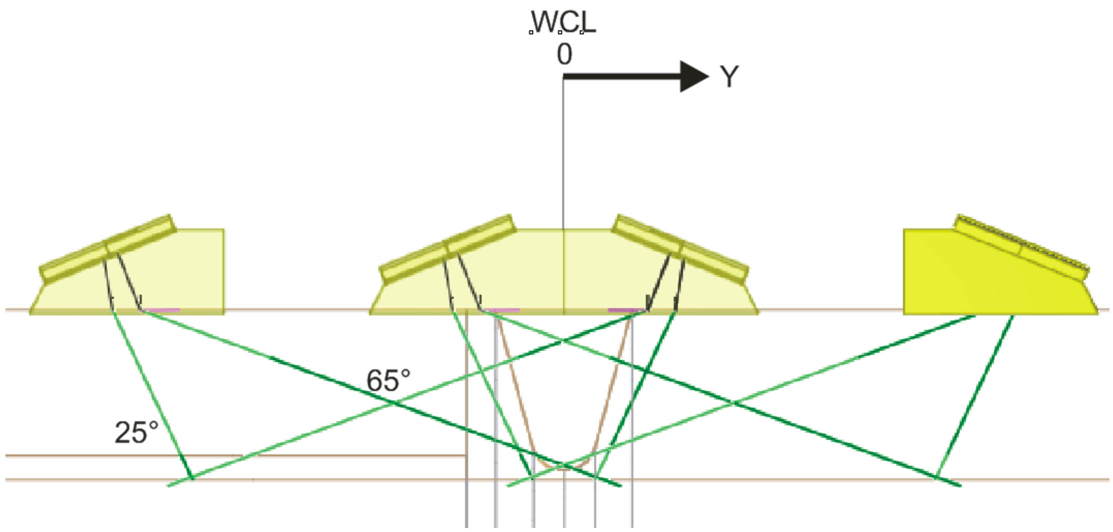

Figure B.68.

B.3.3.2 Scanning for Axial Flaws

- Beam shall be directed essentially parallel to the weld in two opposing directions

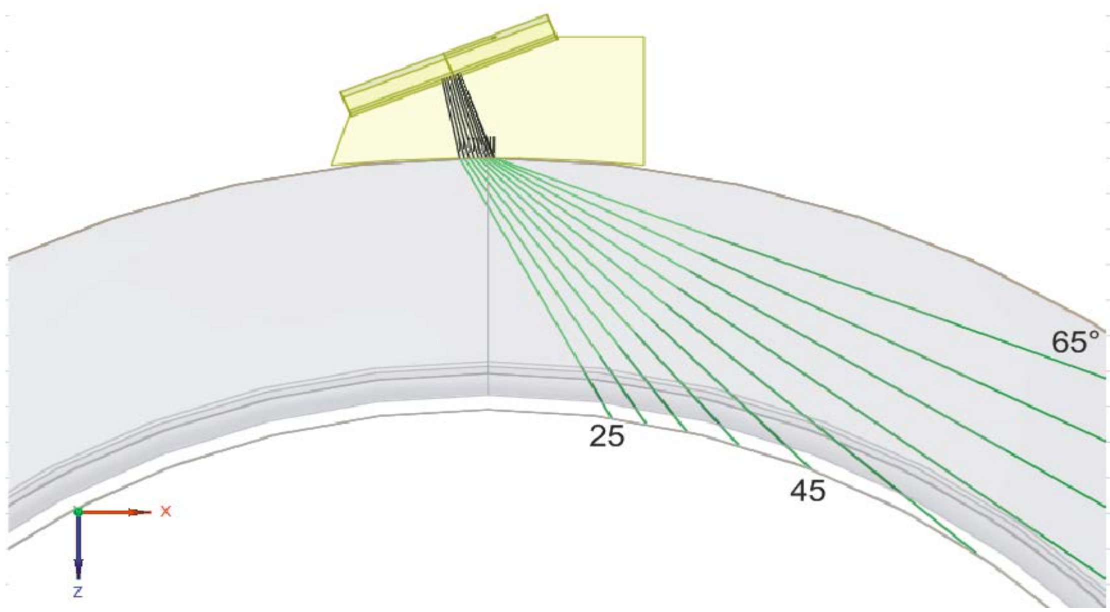

Figure B.69.

B.3.4 Analysis

B.3.4.1 Detection

The detection of surface breaking ID flaws relies upon the corner response being observed.

B.3.4.2 Characterization

The characterization is based on the identification of flaw like indications which cannot be attributed to the component geometry based on the supplied as built drawings, manufacturing defects (reported during previous inspections) or indications due to reflection's or scattering on the anisotropic und heterogeneous weld structure.

Flaw discrimination criterions:

- Good signal to noise ratio (variations along the length)
- Plots to susceptible crack location
- Substantial echo dynamic travel
- Areas of unique amplitude
- Inconsistent time base positions
- Tip signals
- Conformation from the opposite direction
- Seen with many angles
- Mode converted shear signal (only circ flaws with substantial depth)
- Non relevant indications criterions:
- Near WCL or weld geometry
- Seen continuously
- Consistent time & amplitude
- Weak echo dynamic travel

B.3.4.3 Length Sizing

- Length of a flaw is determined by moving the probe along the flaw.
- on the same side of the weld as the indication
- optimize the signal from the flaw indication
- adjust the system gain until the response is ~ 80 % FSH
- scan along the length of the flaw in each direction until the signal response has been reduced to:
  - background noise for far side indication
  - 20% FSH (12 dB drop) for near side indication
- The length on outside diameter is longer than the actual inside diameter length. Calculate correct ID flaw length according to: (ID/OD) x OD flaw length = ID flaw length.

B.3.4.4 Depth Sizing

For flaw depth sizing the Absolut Arrival Time Technique (AATT) is used. The technique relies upon obtaining a direct signal response from the flaw tip using a material depth calibration. From the flaw tip response the amount of unflawed material or remaining ligament can be read directly from the Sscan. Flaw depth is calculated by subtracting the remaining ligament from the actual material thickness.

The figure below illustrates the technique.

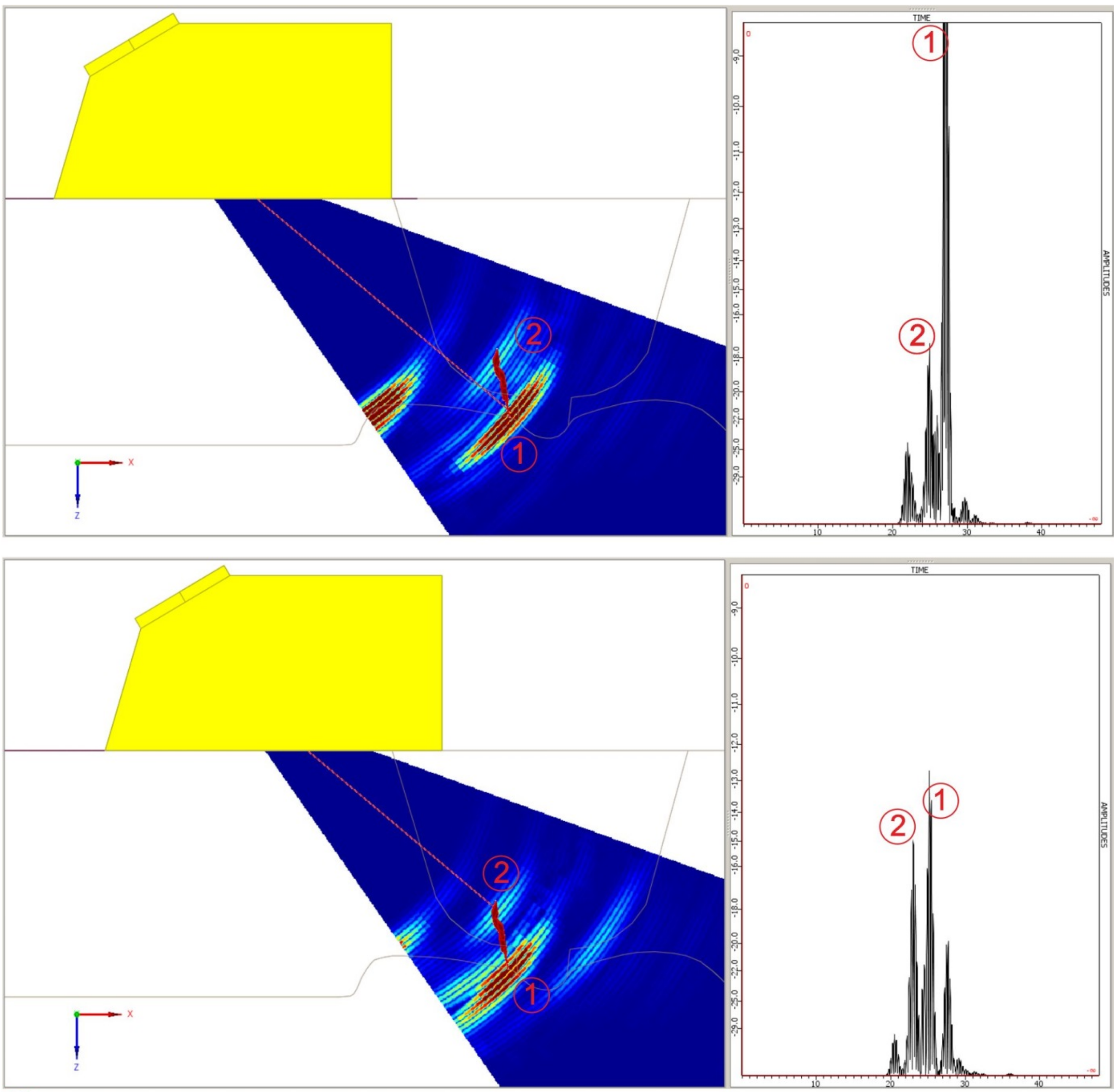

① Flaw Base ID (corner trap)l

② Tip diffraction signal

Figure B.70.

B.3.4.5 Defect Positioning

Due to uncertainties associated with sound propagation in anisotropic, heterogeneous austenitic weld material indication positioning require detailed evaluation. The information provided below may assist indication positioning.

- Perform thickness and surface contour recordings at the indication position.
- Evaluate the flaw signal amplitude responses from each side of the weld. Observe if the signal response appears reduced due to weld volume sound attenuation from one side or another.
- Identify standard benchmark responses (weld root, weld noise, acoustic interfaces) and flaw indication responses.
- Coordinate and plot the information on a cross sectional drawing of the weld.

B.3.5 Self Assessment

The manual Phased Array Technique using a dual linear search unit and longitudinal waves in the range from 25° to 65° demonstrated good detection, length sizing and TWS performance of ID flaws with depth greater than 10% of the wall thickness.

B.4 Phased Ultrasonic Array, Technique ID 131-PA2

B.4.1 Overview

The techniques described in this report were utilized for the examination of the PARENT specimens P4. In case of P4 different techniques were used for examination in +Y and –Y direction.

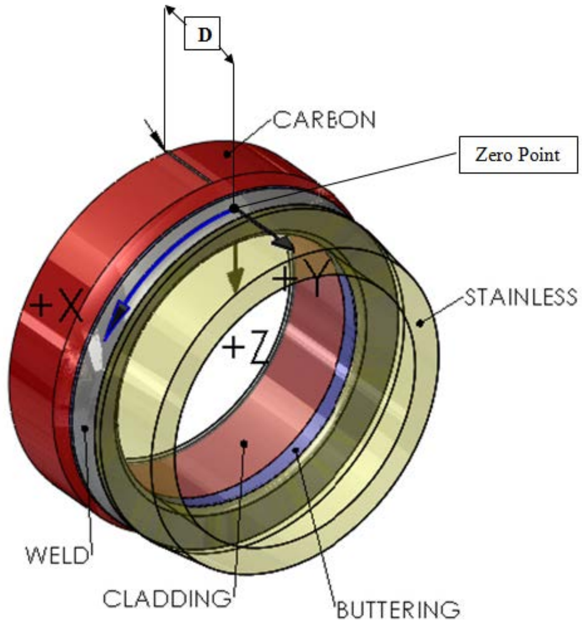

Figure B.71.

B.4.1.1 Scanning for Circumferential Flaws in +Y Direction

Method	Phased Array Ultrasonic Testing
Array / Technique	Dual / Linear / Transmit - Receive
Wave Mode	Longitudinal
Angle Range	25° – 65°
Frequency	2 MHz
UT Instrument	M2M MultiX 64
Scan Plan	Manual scanning perpendicular to weld in +Y direction
Scanning Surface	OD

B.4.1.2 Scanning for Circumferential Flaws in -Y Direction

Method	Phased Array Ultrasonic Testing
Array / Technique	Single / Linear / Puls Echo
Wave Mode	Longitudinal
Angle Range	40° – 75°
Frequency	2.33 MHz
UT Instrument	M2M MultiX 64
Scan Plan	Manual scanning perpendicular to weld in -Y direction
Scanning Surface	OD

B.4.2 NDE Equipment / UT Settings / +Y Technique

B.4.2.1 Search Unit

For the measurement a GEIT probe and wedge was used. The essential variable of the search unit are described in the next chapters.

Crystal Shape

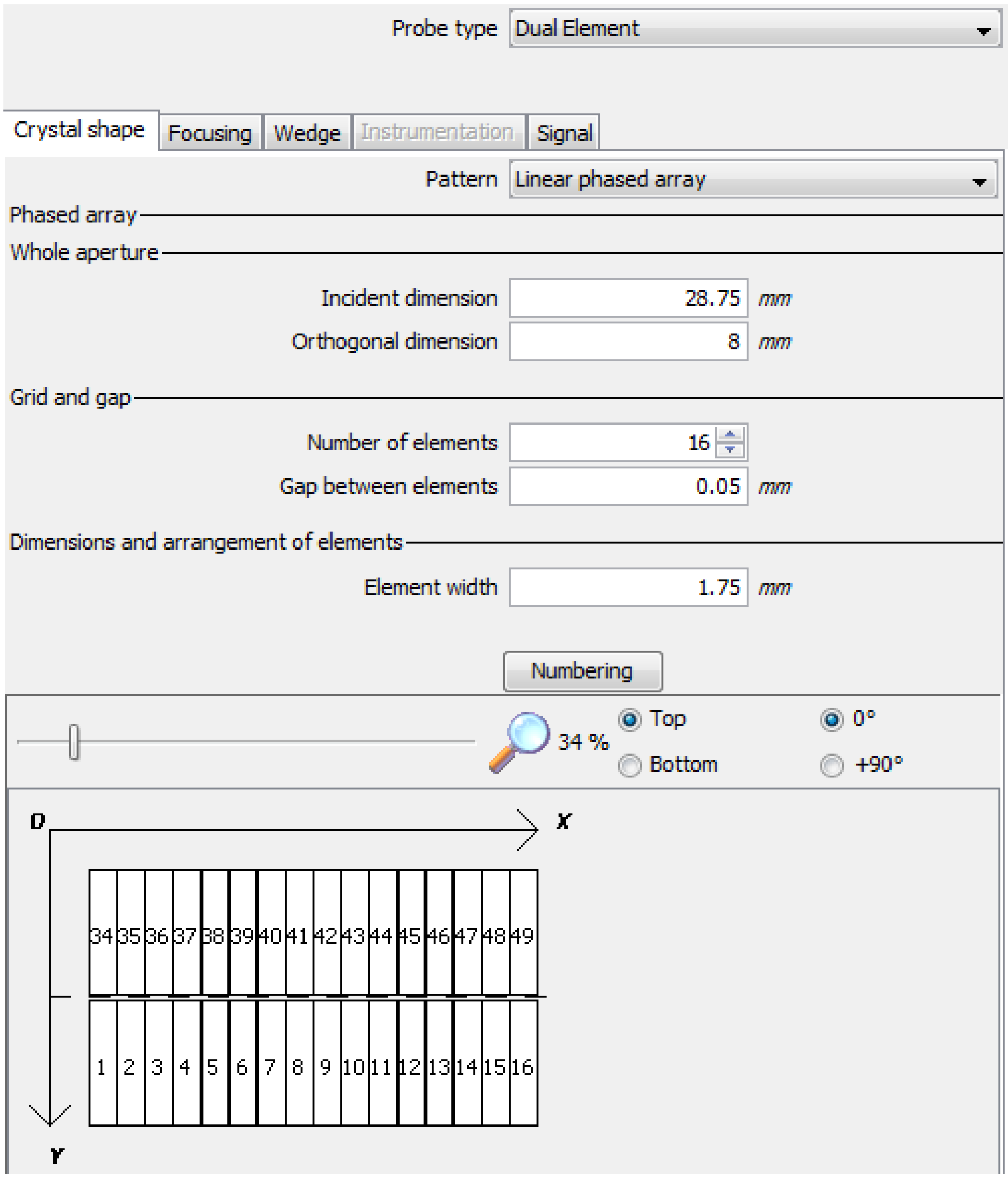

Figure B.72.

Focusing

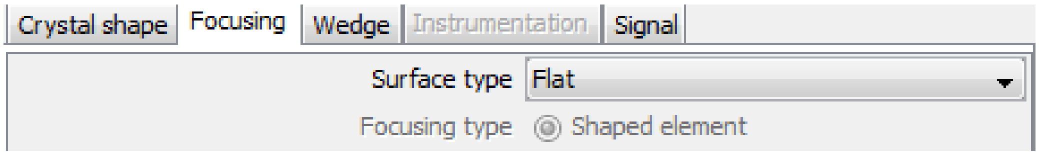

Figure B.73.

Wedge for Axial Scanning (Circ Flaws)

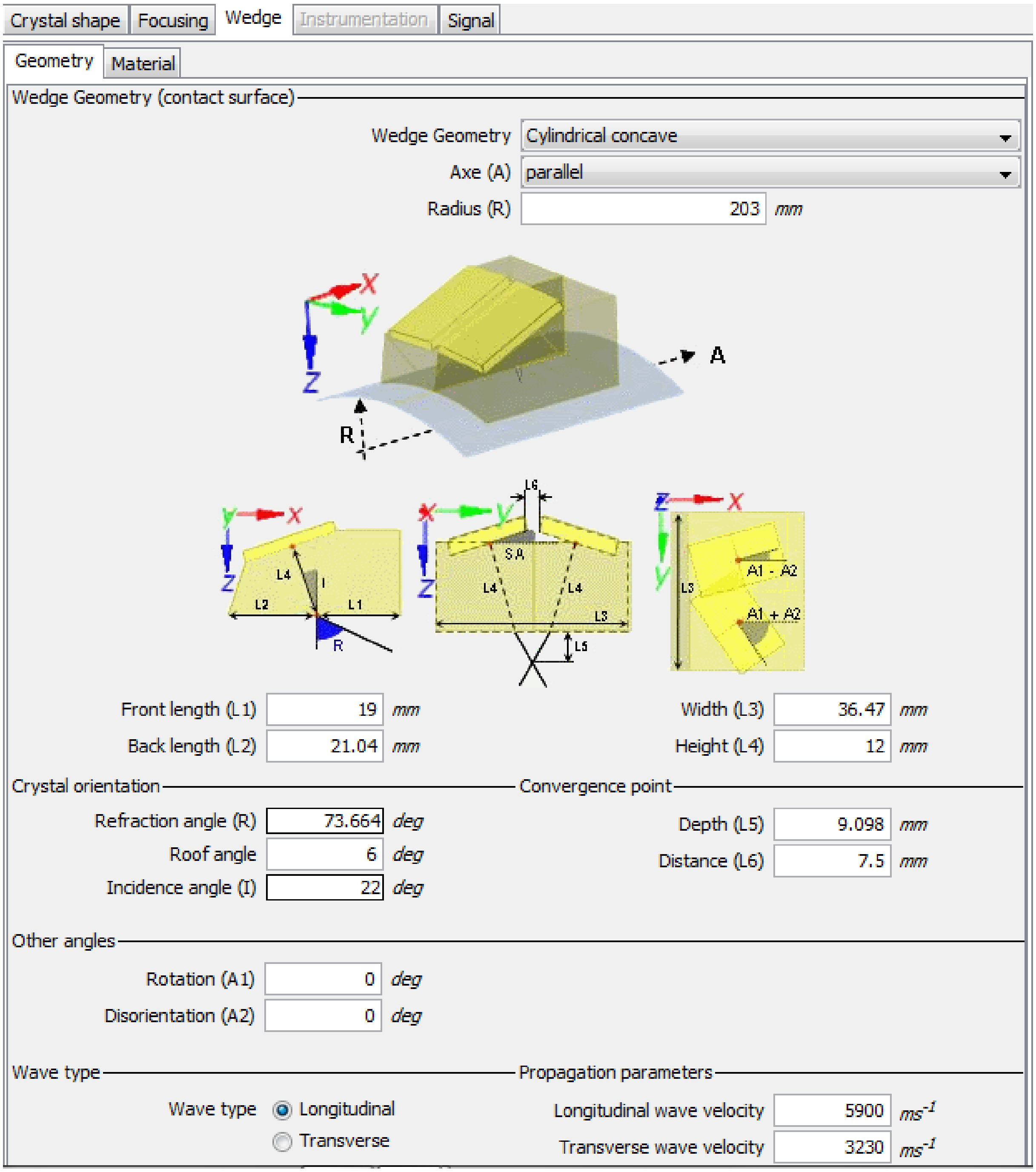

Wedge material: Rexolite cl=2237 m/s

Figure B.74.

Signal

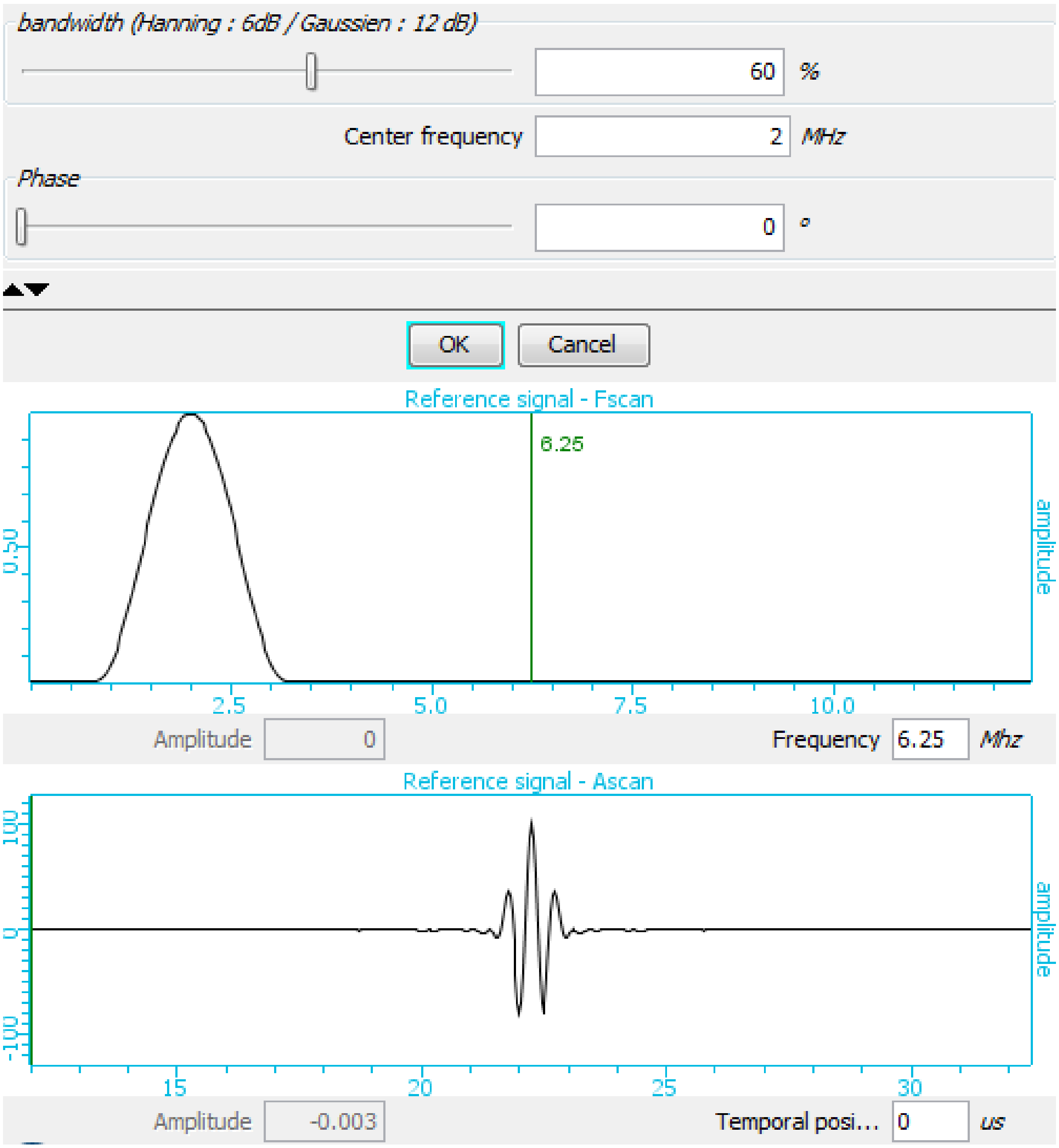

Figure B.75.

B.4.2.2 Phased Array Settings – Focal Laws

Initialization

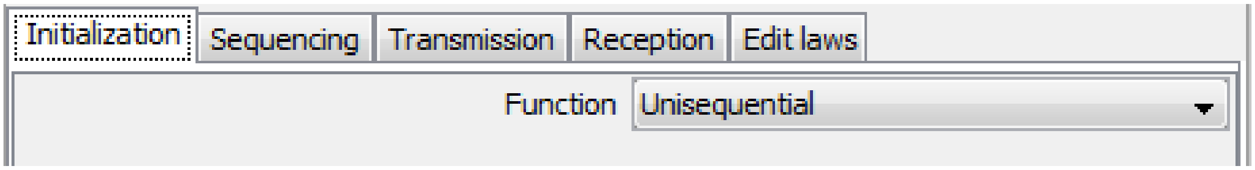

Figure B.76.

Sequencing

Transmission Element 1 (lower wedge end) to Element 14

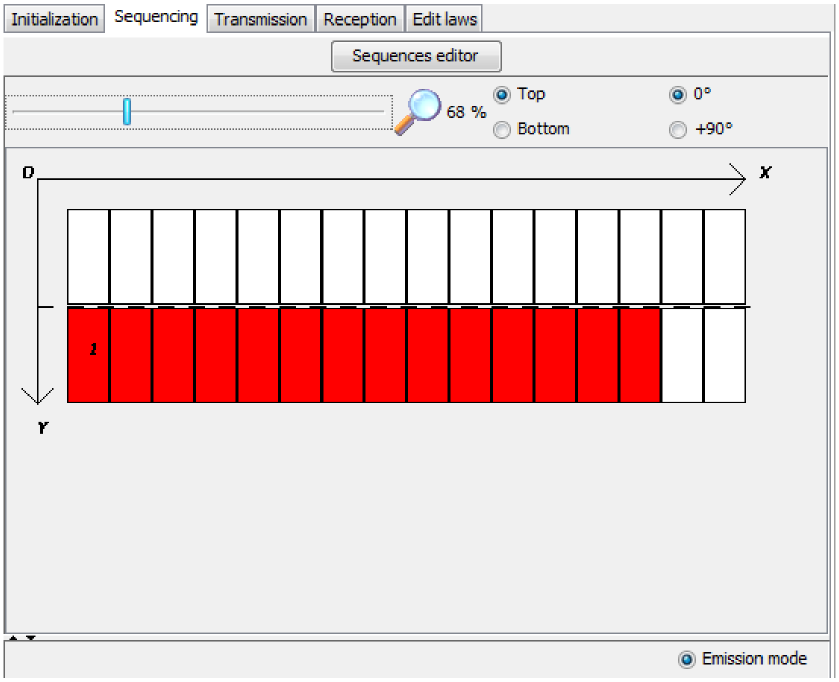

Figure B.77.

Receiving Element 1 (lower wedge end) to Element 14

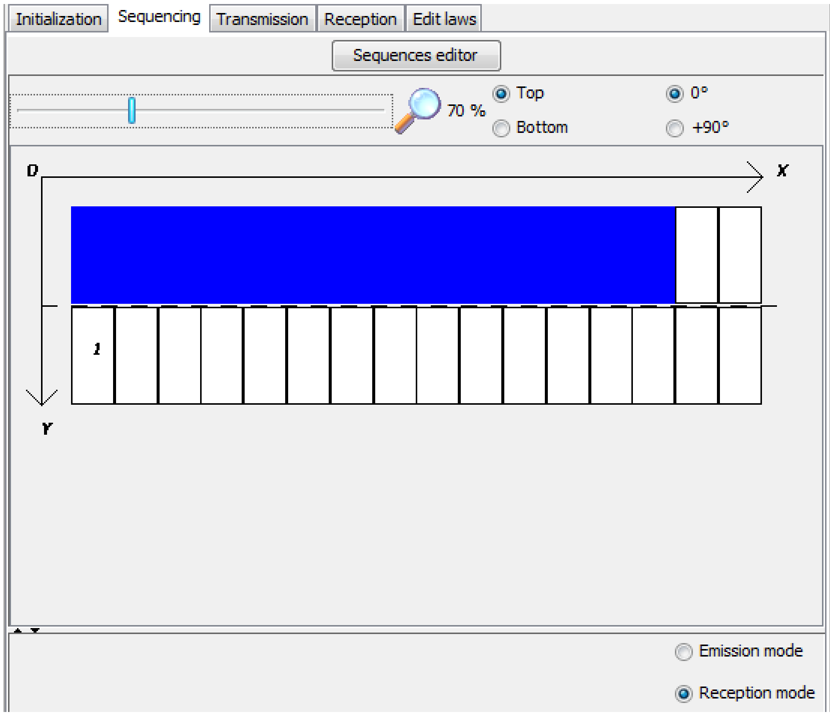

Figure B.78.

Transmission

The focusing type is sectorial scanning. The sector range goes from 25° to 65° (Step 1°) longitudinal waves.

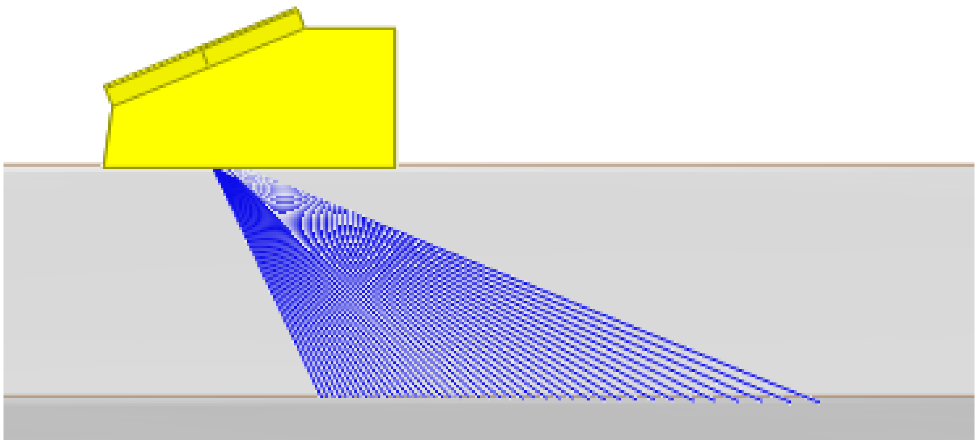

Figure B.79.

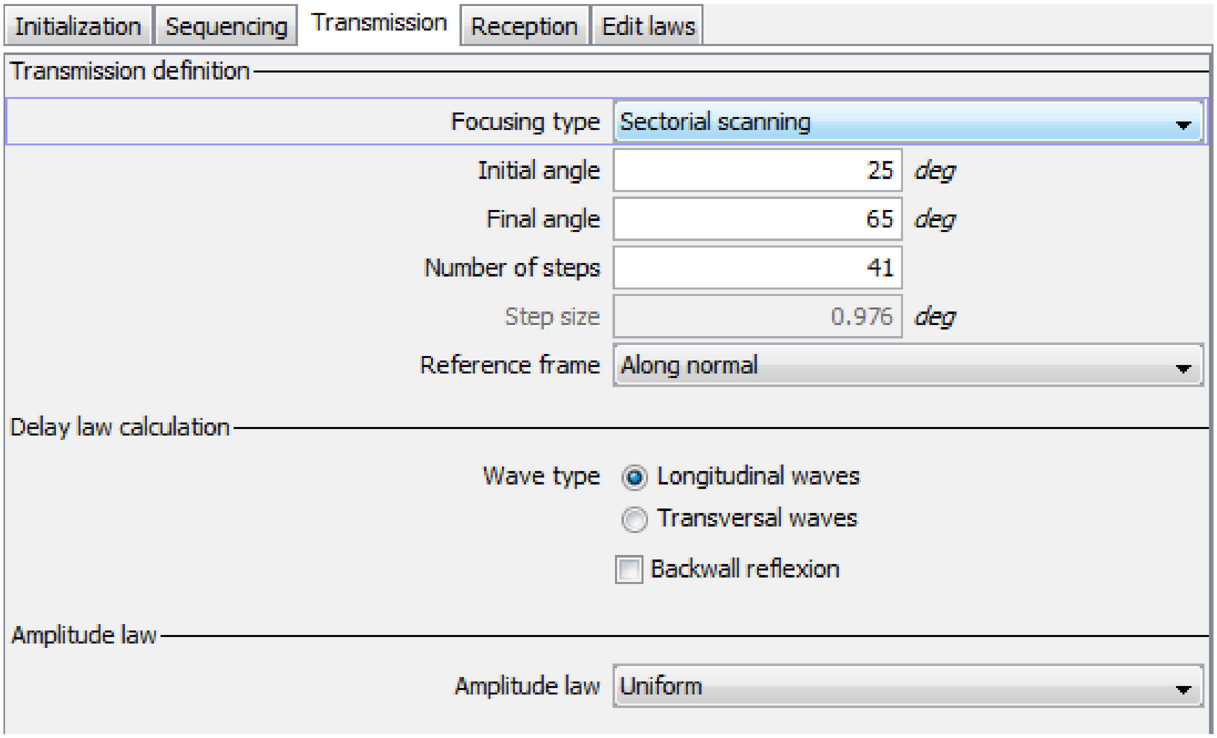

Figure B.80.

B.4.2.3 UT Equipment Settings – M2M MultiX 64

For the measurements a M2M MultiX UT System was used. MultiX system is a fully parallel architecture with 64 channels. In the following chapters the essential equipment settings are listed.

General Settings

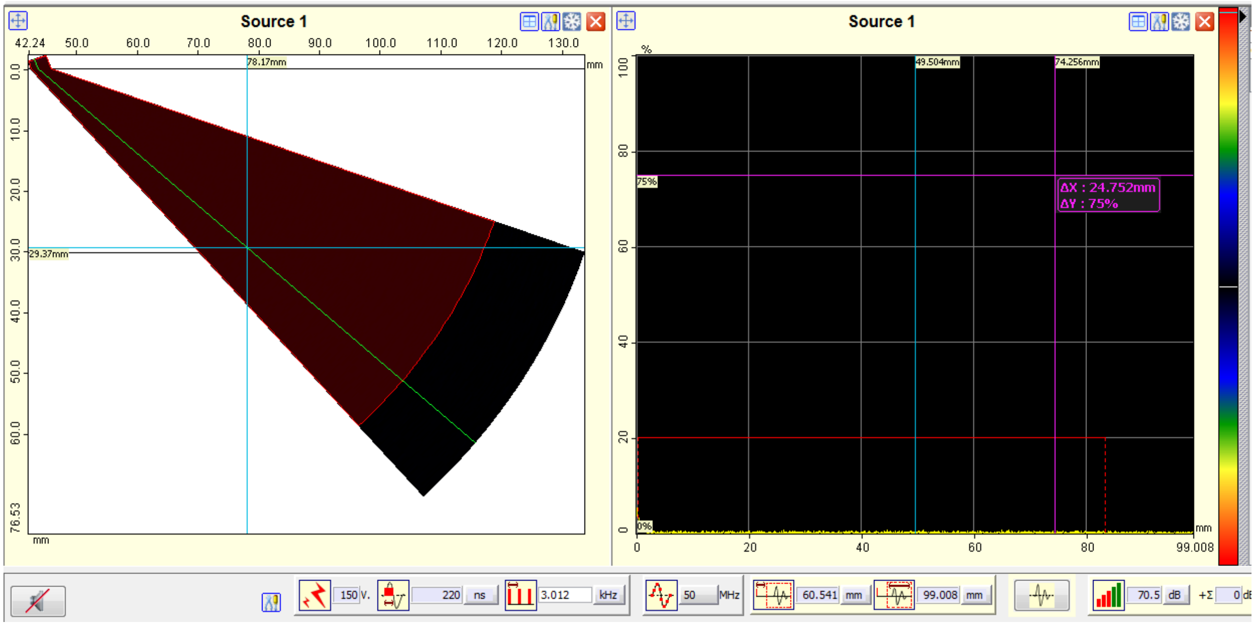

Figure B.81.

Gates

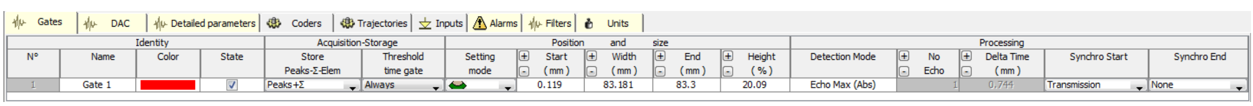

N°	Name	Color	State	Store Peaks-Σ-Elem	Threshold time gate	Setting mode	Start (mm)	Width (mm)	End (mm)	Height (%)	Detection Mode	No Echo	Delta Time (mm)	Synchro Start	Synchro End
1	Gate 1		✓	Peaks+Σ	Always		0.119	83.181	83.3	20.09	Echo Max (Abs)	1	0.744	Transmission	None

Figure B.82.

DAC

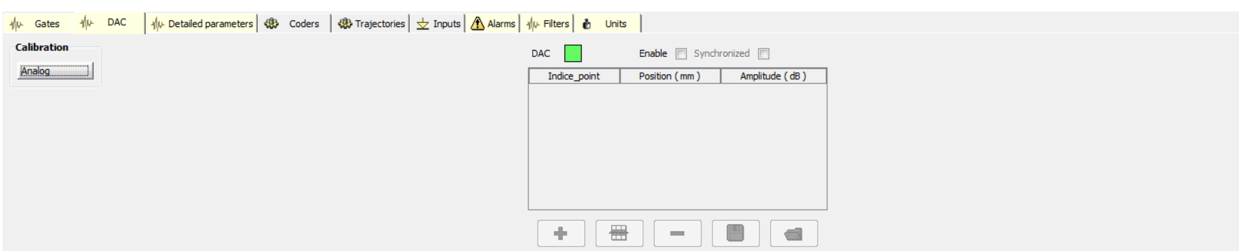

Figure B.83.

Coders

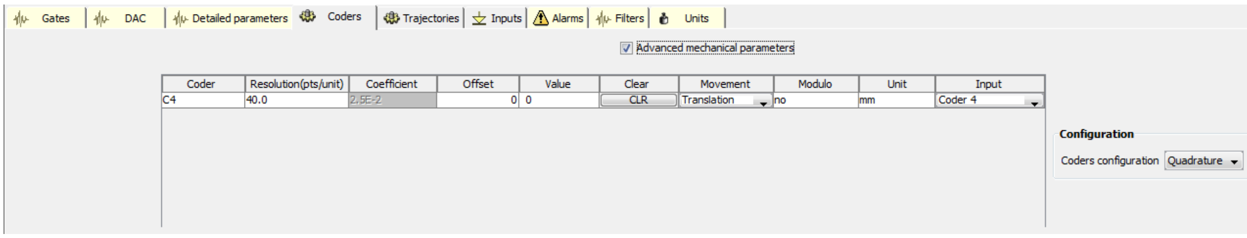

Figure B.84.

Trajectories

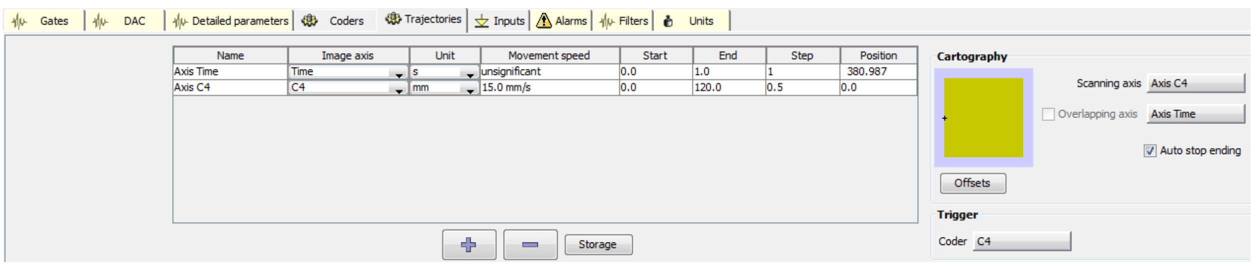

Figure B.85.

Units

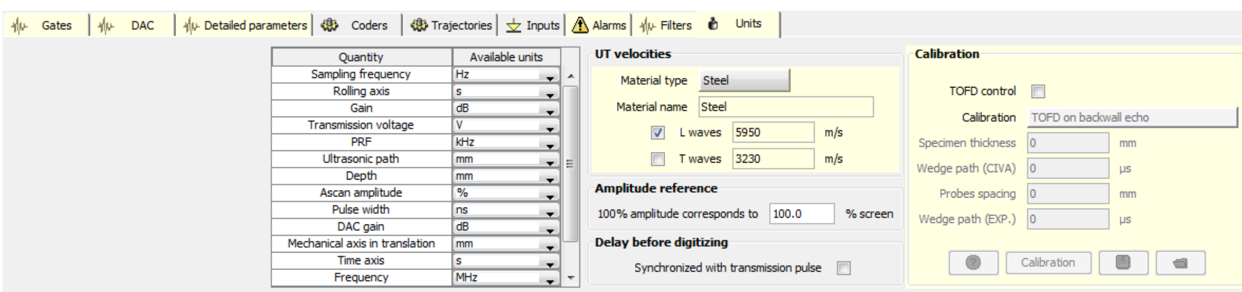

Figure B.86.

B.4.3 NDE Equipment / UT Settings / -Y Technique

B.4.3.1 Search Unit

For the measurement a Sonaxis probe and wedge was used. The essential variable of the search unit are described in the next chapters.

Crystal Shape

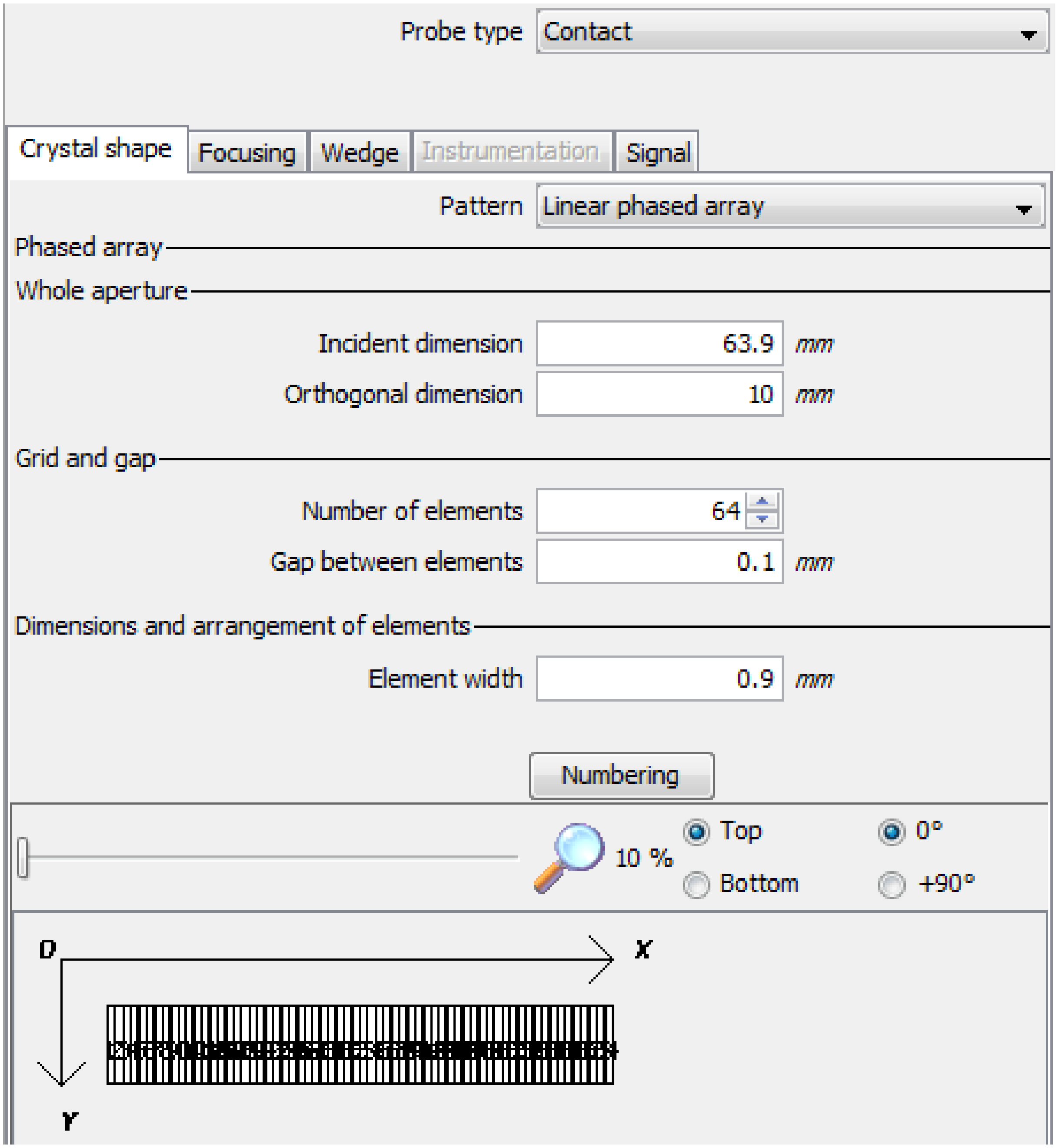

Figure B.87.

Focusing

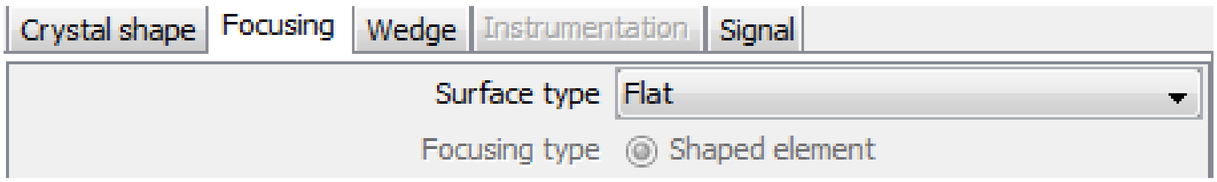

Figure B.88.

Wedge for Axial Scanning (Circ Flaws)

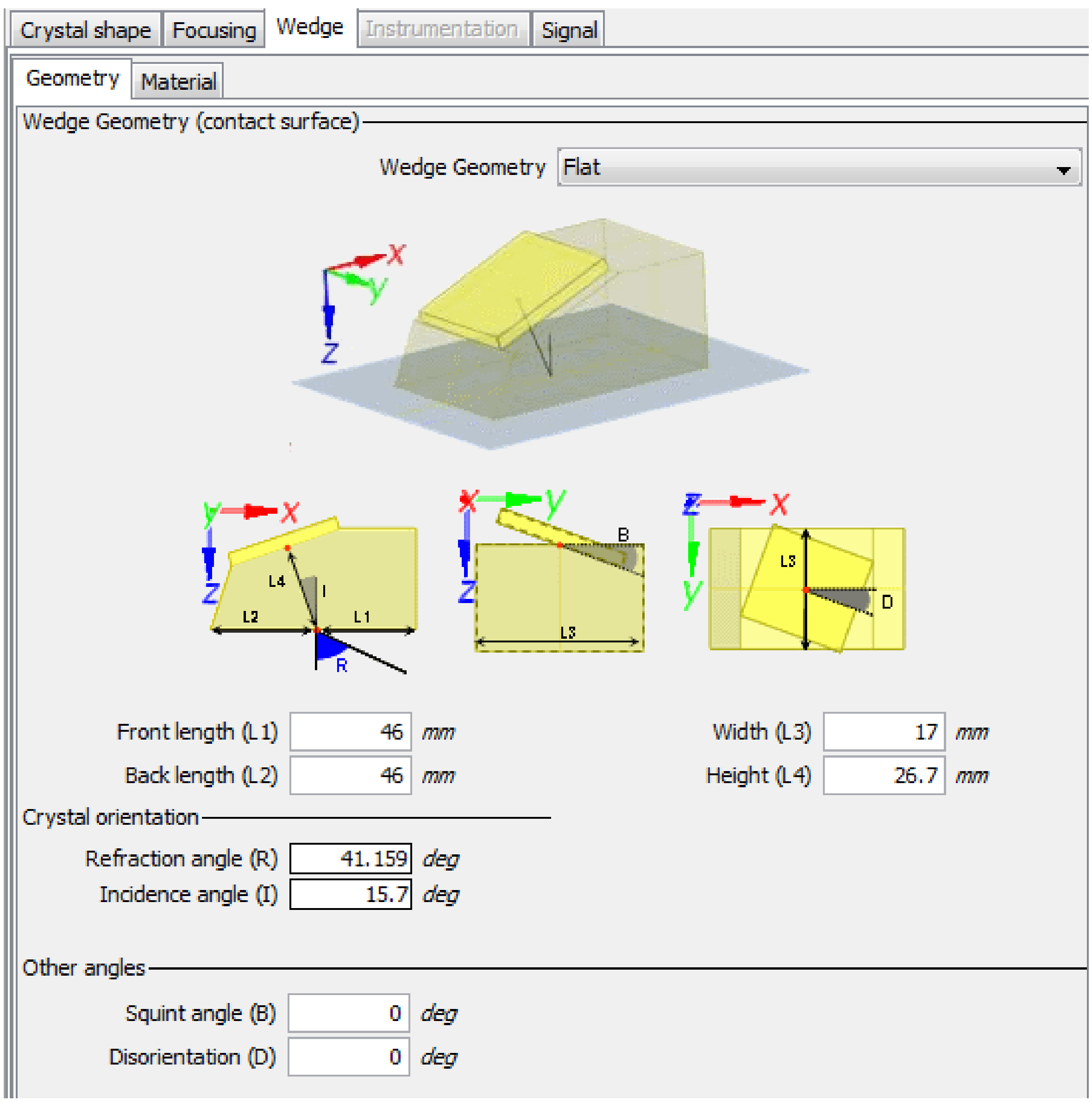

Figure B.89. Wedge Material: Rexolite cl=2237 m/s

Signal

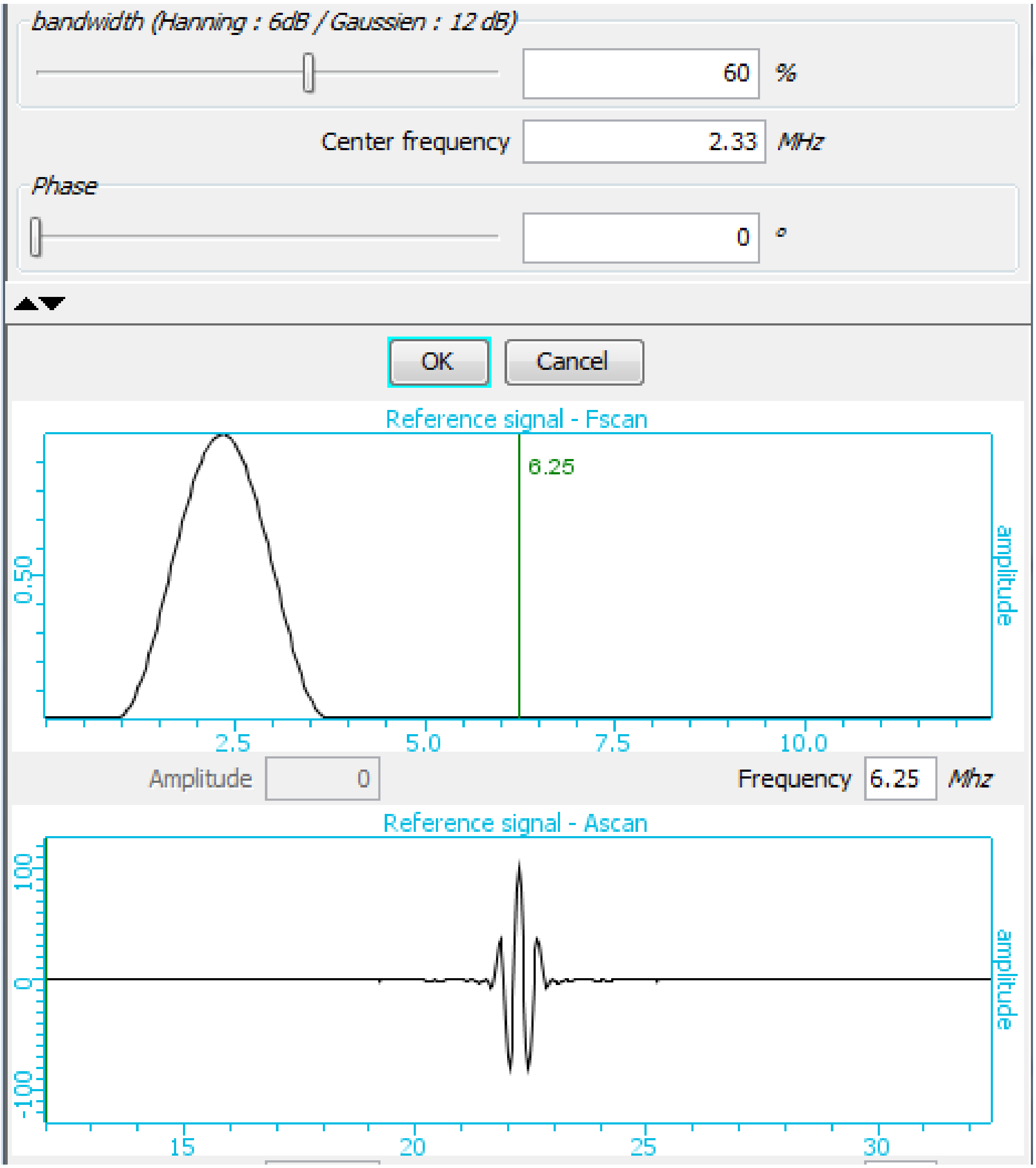

Figure B.90.

B.4.3.2 Phased Array Settings – Focal Laws

Initialization

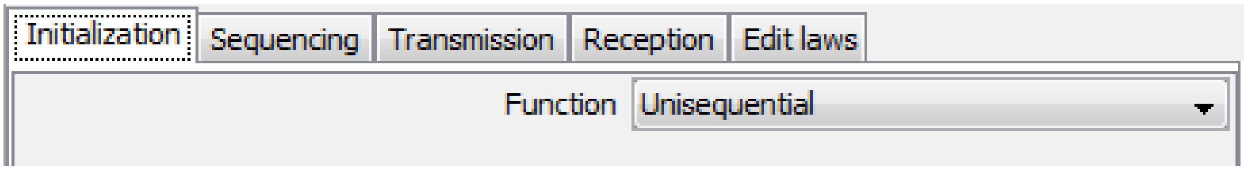

Figure B.91.

Sequencing

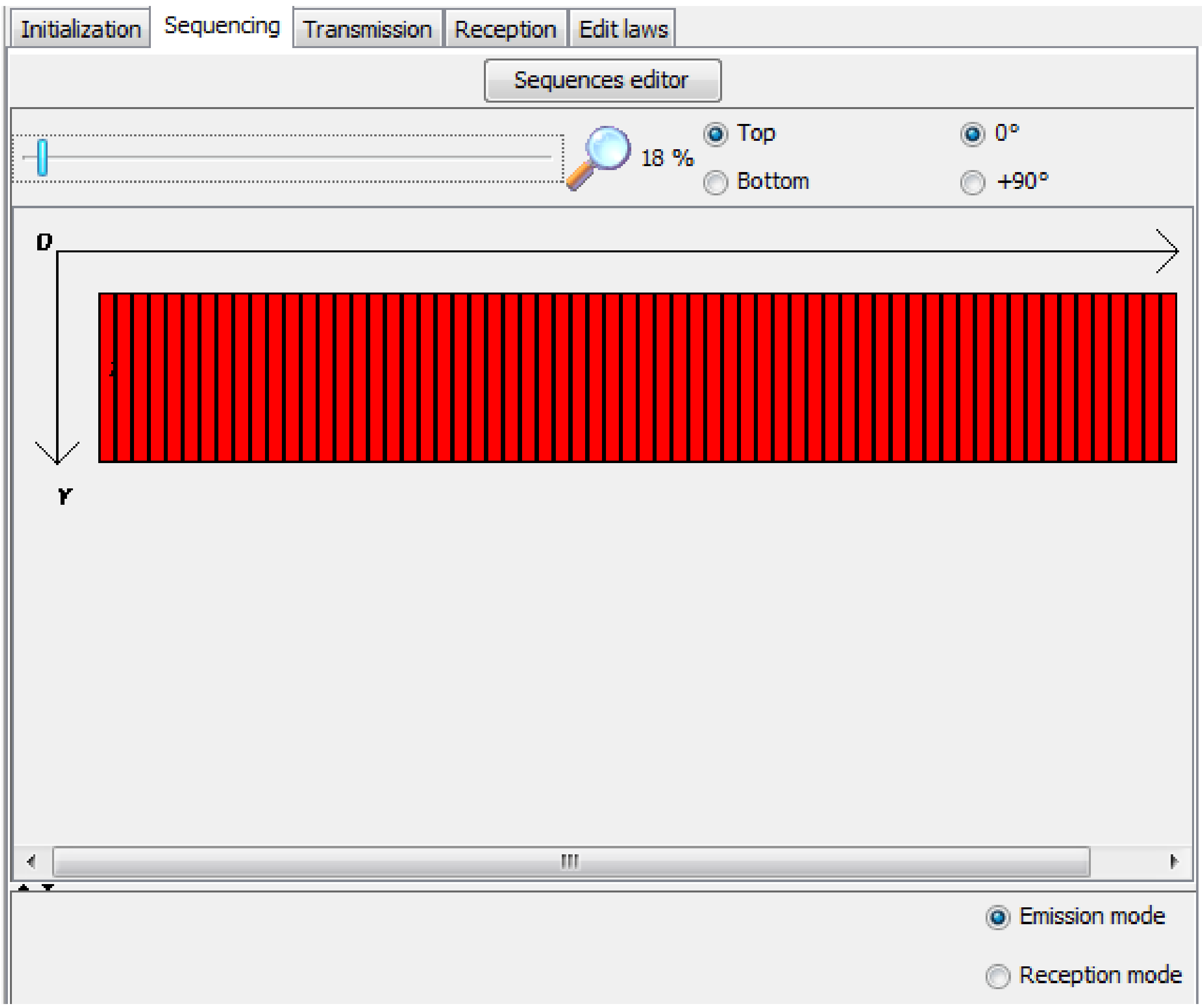

Figure B.92.

Transmission

The focusing type is sectorial scanning with constant focal depth at 35mm. The sector range goes from 45° to 75° (Step 1°) longitudinal waves.

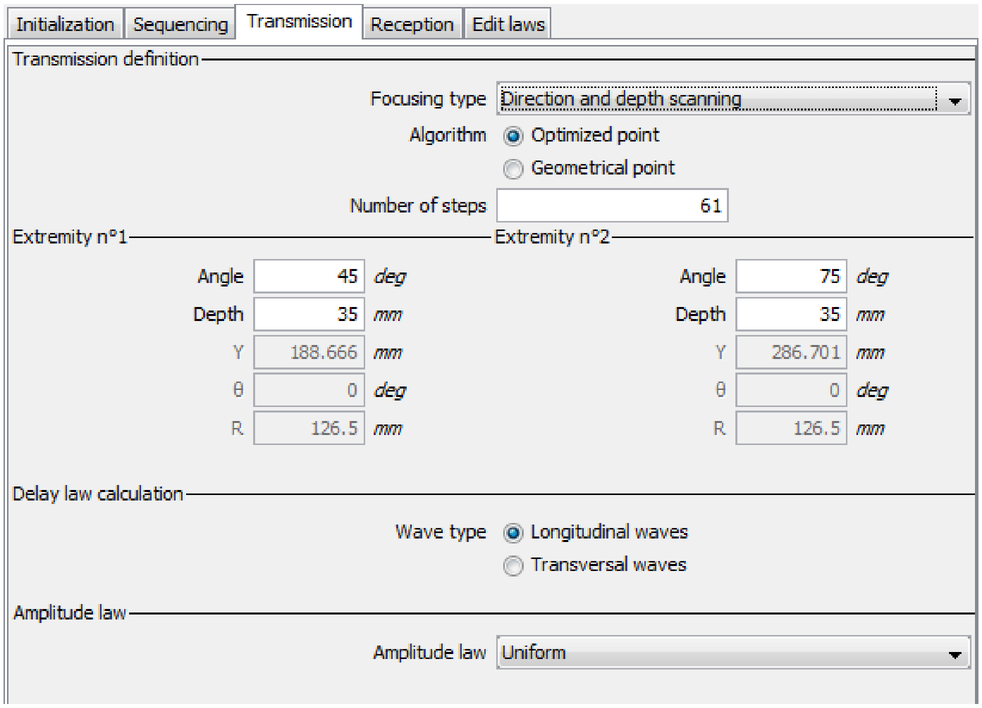

Figure B.93.

Sound Field Simulations for 65° Angle

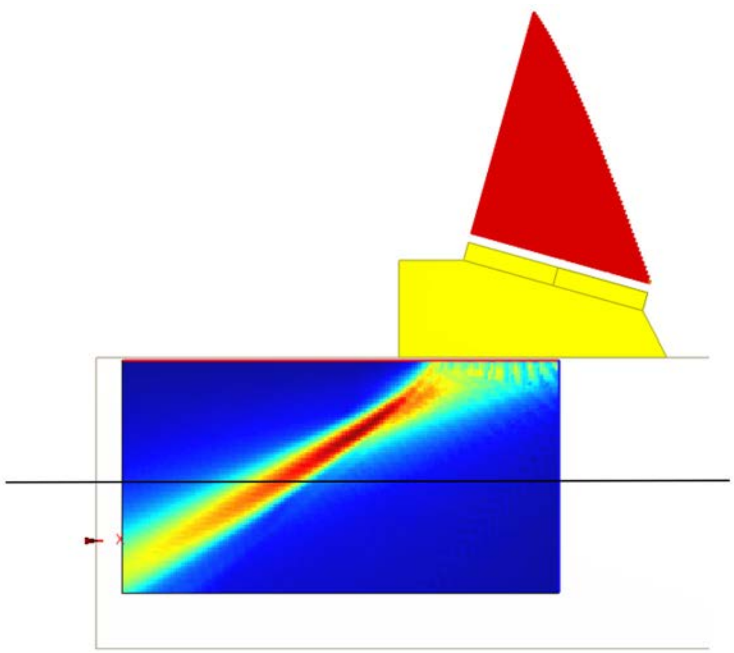

Figure B.94. 65° Beam, Black Line: ID Position ≈ 38 mm

B.4.3.3 UT Equipment Settings - M2M MultiX 64

For the measurements a M2M MultiX UT System was used. MultiX system is a fully parallel architecture with 64 channels. In the following chapters the essential equipment settings are listed.

General Settings

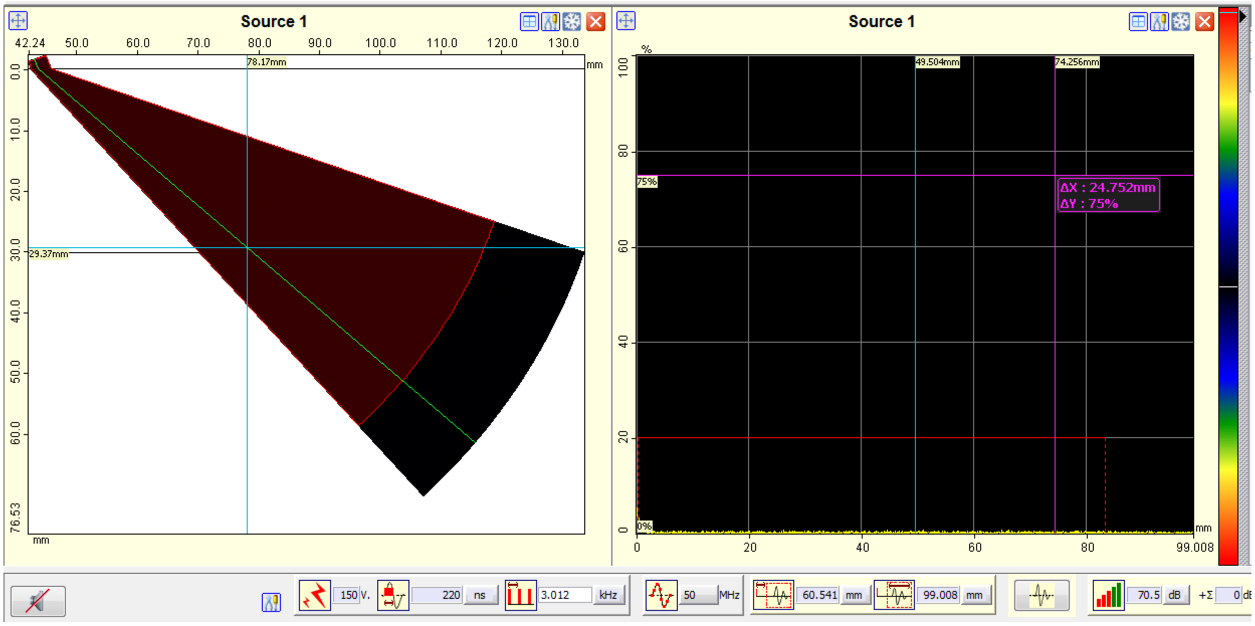

Figure B.95.

Gates

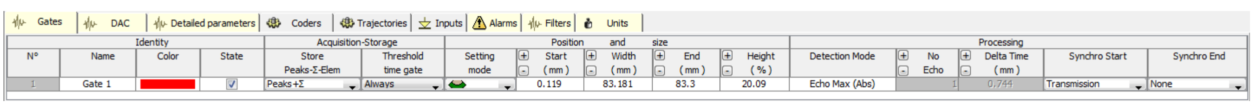

Figure B.96.

DAC

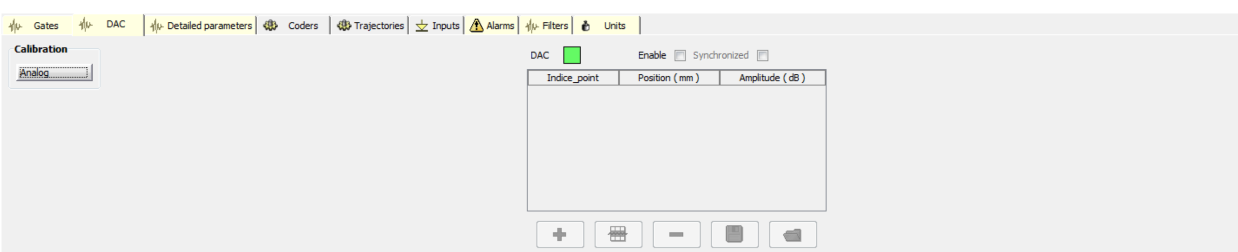

Figure B.97.

Coders

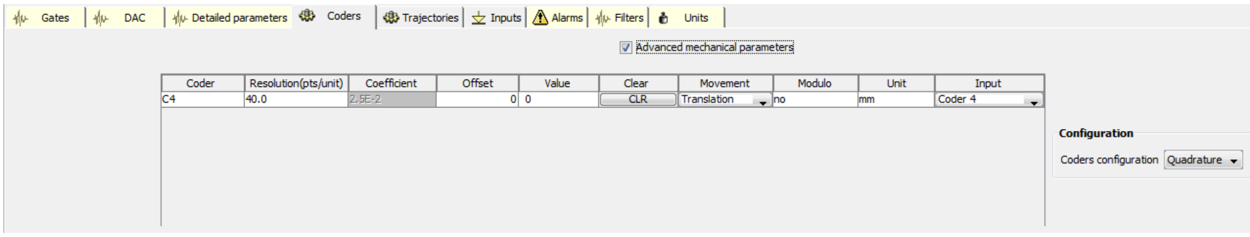

Figure B.98.

Trajectories

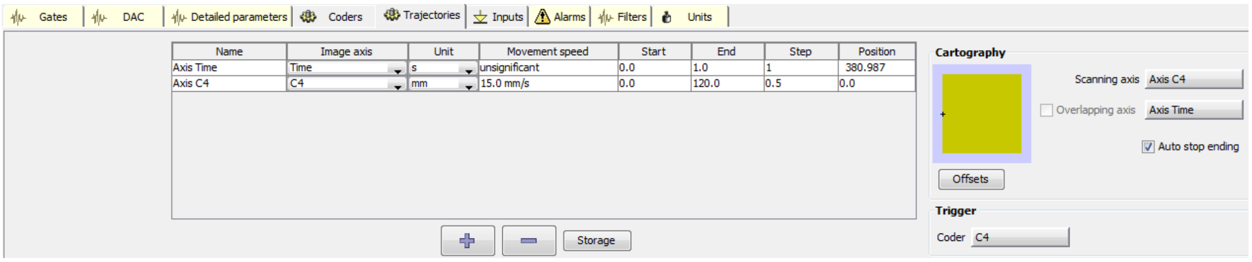

Figure B.99.

Filters

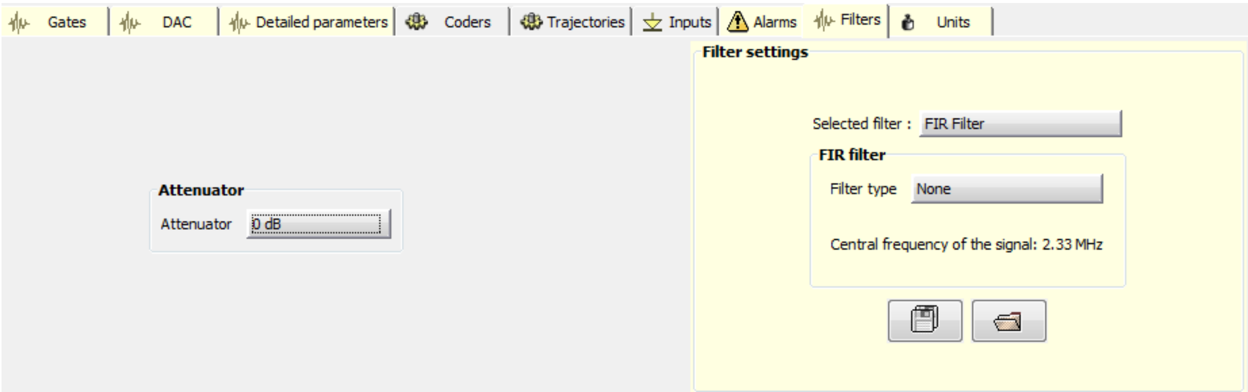

Figure B.100.

Units

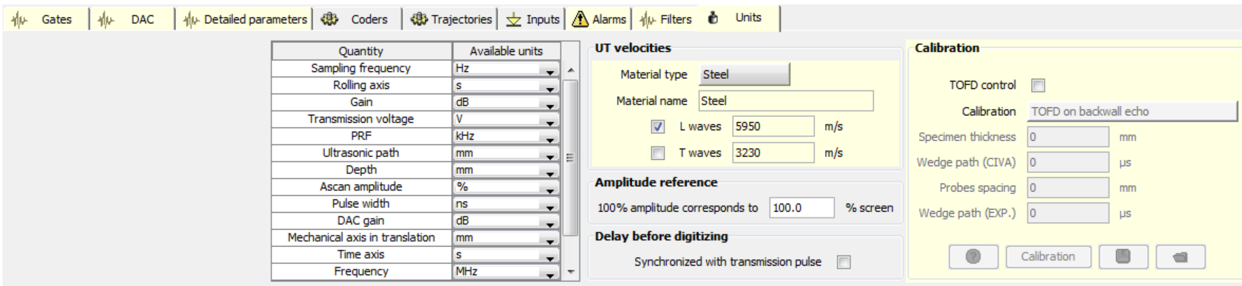

Figure B.101.

B.4.4 Data Acquisition (Scan Plan for Manual Examination)

B.4.4.1 Scanning for Circumferential Flaws

- Beam shall be directed essentially perpendicular to the weld axis from both directions.

B.4.5 Analysis

B.4.5.1 Detection

The detection of surface breaking ID flaws relies upon the corner response being observed.

B.4.5.2 Characterization

The characterization is based on the identification of flaw like indications which cannot be attributed to the component geometry based on the supplied as built drawings, manufacturing defects (reported during previous inspections) or indications due to reflection's or scattering on the anisotropic und heterogeneous weld structure.

Flaw discrimination criterions:

- Good signal to noise ratio (variations along the length)
- Plots to susceptible crack location
- Substantial echo dynamic travel
- Areas of unique amplitude
- Inconsistent time base positions
- Tip signals
- Conformation from the opposite direction
- Seen with many angles
- Mode converted shear signal (only circ flaws with substantial depth)

Non relevant indications criterions:

- Near WCL or weld geometry
- Seen continuously
- Consistent time & amplitude
- Weak echo dynamic travel

B.4.5.3 Length Sizing

- Length of a flaw is determined by moving the probe along the flaw.
- on the same side of the weld as the indication
- optimize the signal from the flaw indication
- adjust the system gain until the response is ~ 80 % FSH
- scan along the length of the flaw in each direction until the signal response has been reduced to:
  - background noise for far side indication
  - 20% FSH (12 dB drop) for near side indication
- The length on outside diameter is longer than the actual inside diameter length. Calculate correct ID flaw length according to: (ID/OD) x OD flaw length = ID flaw length.

B.4.5.4 Depth Sizing

For flaw depth sizing the Absolut Arrival Time Technique (AATT) is used. The technique relies upon obtaining a direct signal response from the flaw tip using a material depth calibration. From the flaw tip response the amount of unflawed material or remaining ligament can be read directly from the Sscan. Flaw depth is calculated by subtracting the remaining ligament from the actual material thickness.

The figure below illustrates the technique.

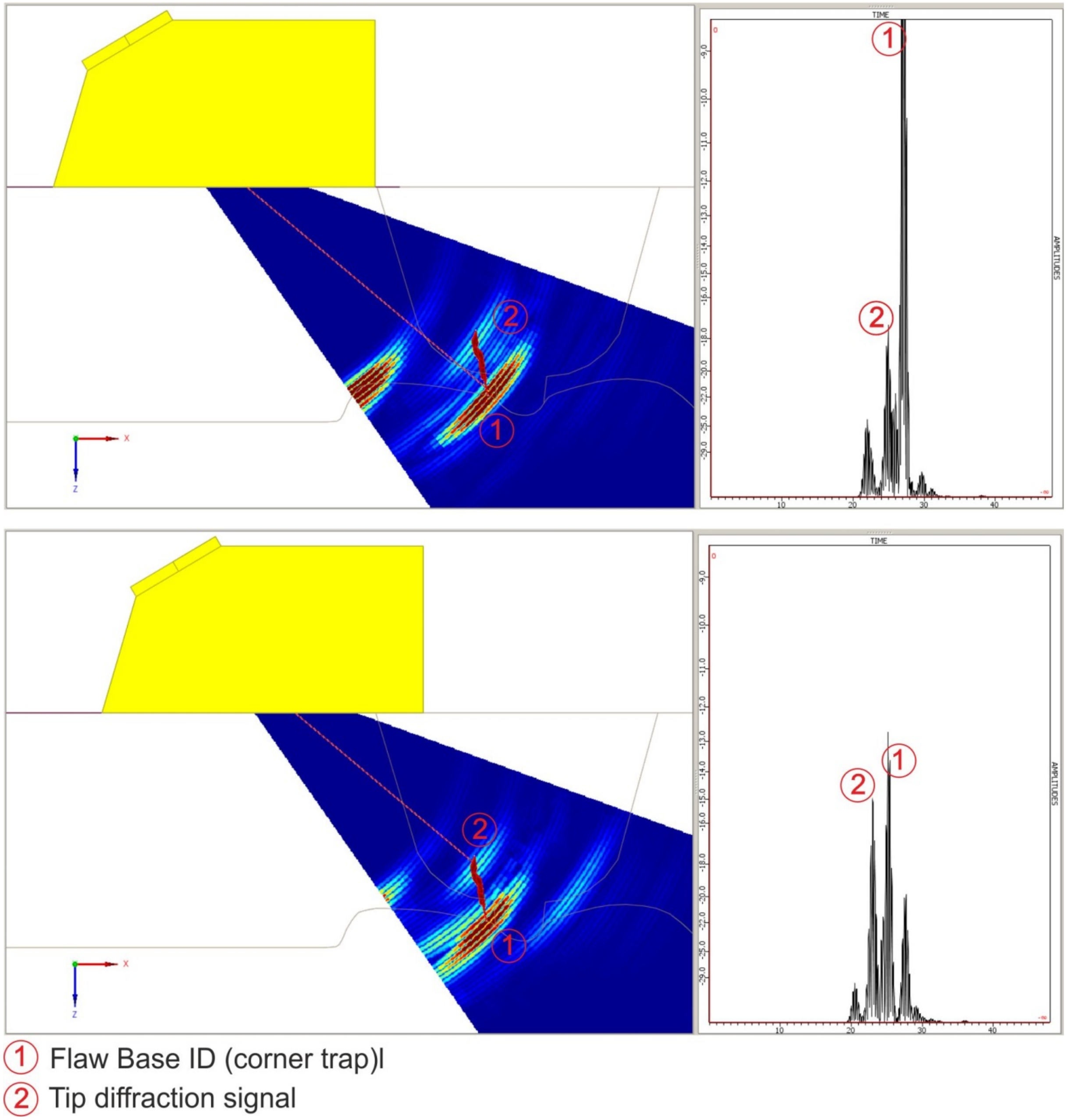

Figure B.102.

B.4.5.5 Defect Positioning

Due to uncertainties associated with sound propagation in anisotropic, heterogeneous austenitic weld material indication positioning require detailed evaluation. The information provided below may assist indication positioning.

- Perform thickness and surface contour recordings at the indication position.
- Evaluate the flaw signal amplitude responses from each side of the weld. Observe if the signal response appears reduced due to weld volume sound attenuation from one side or another.

- Identify standard benchmark responses (weld root, weld noise, acoustic interfaces) and flaw indication responses.
- Coordinate and plot the information on a cross sectional drawing of the weld.

B.4.6 Self Assessment

B.4.6.1 Scanning for Circumferential Flaws in +Y Direction

The manual Phased Array Technique using a dual linear search unit and longitudinal waves in the range from 25° to 65° demonstrated good detection, length sizing and TWS performance of ID flaws with depth greater than 10% of the wall thickness.

B.4.6.2 Scanning for Circumferential Flaws in -Y Direction

Using the +Y direction technique the detection, length sizing and TWS of two flaws in P4 was challenging. Therefore a different search unit was for the –Y direction examinations. The performance of this search unit was better but TWS was still very challenging. It has to be mentioned, that the used linear array probe is due to its size (large footprint) not suitable for field inspections.

B.5 Phased Ultrasonic Array, Technique ID 131-PA3

B.5.1 Overview

The techniques described in this report were utilized for the examination of the PARENT specimen P41.

Method	Phased Array Ultrasonic Testing
Array / Technique	Dual / Matrix / Transmit - Receive
Wave Mode	Longitudinal
Angle Range	40° – 70°
Frequency	1.5 MHz
UT Instrument	Phasor XS
Scan Plan	Manual scanning perpendicular to weld both directions
Scanning Surface	OD

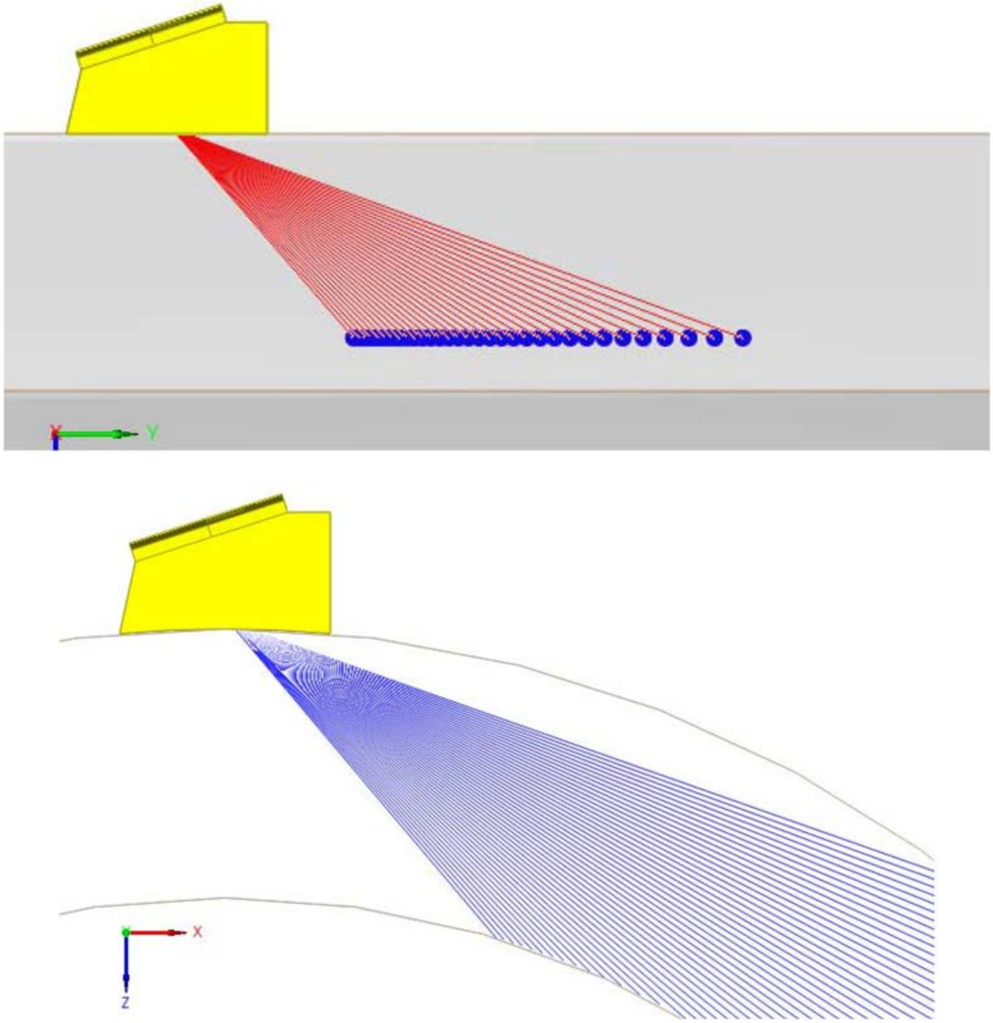

Figure B.103.

B.5.2 NDE Equipment / UT Settings

B.5.2.1 UT Instrument

For the measurements a GEIT Phasor XS was used.

B.5.2.2 Search Unit

For the measurement a GEIT probe and wedge was used. The essential variable of the search unit are described in the next chapters.

Figure B.104.

Crystal Shape

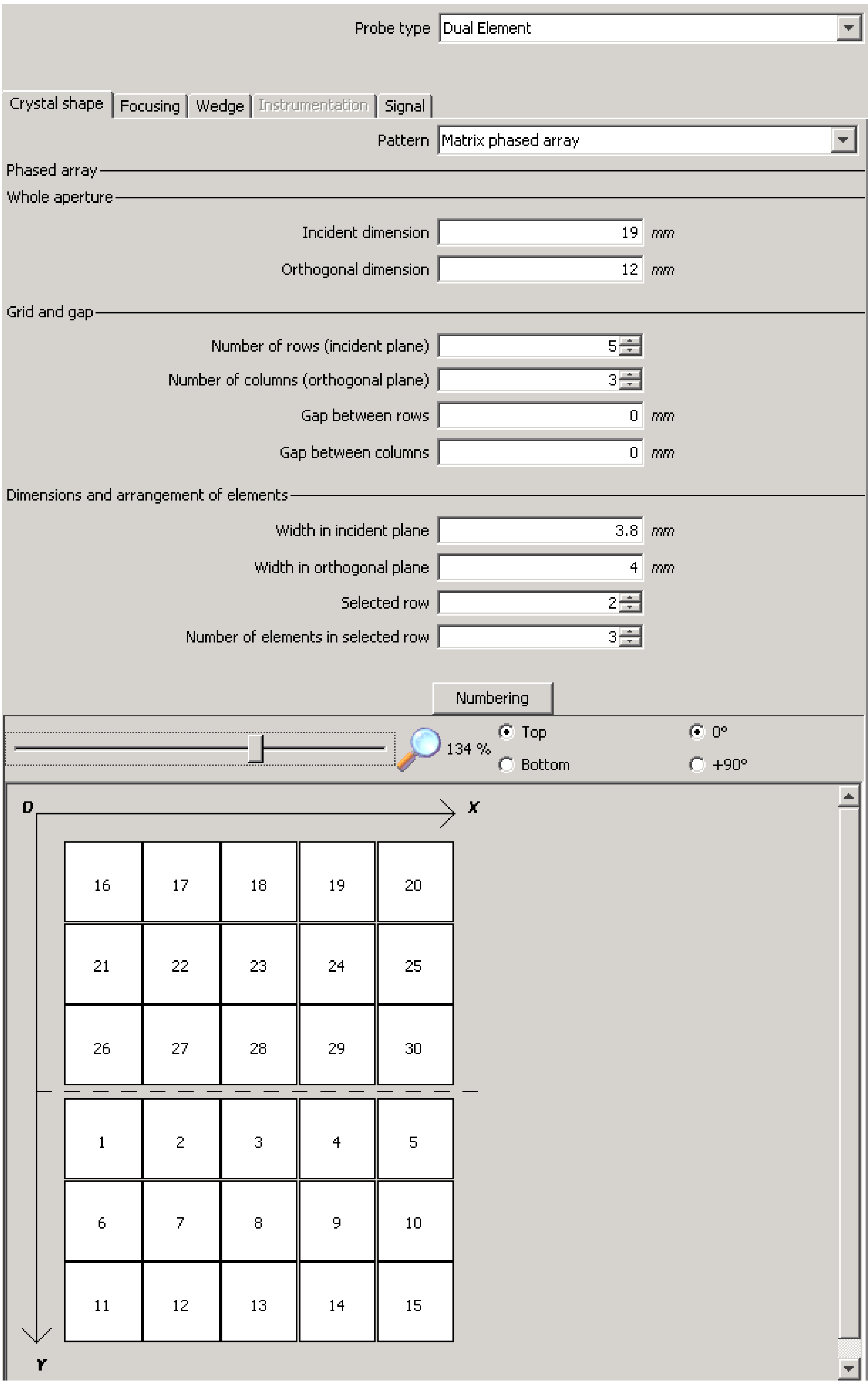

Figure B.105.

Focusing

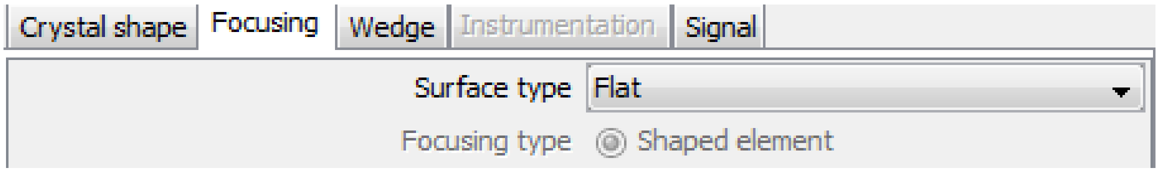

Figure B.106.

Wedge for Axial Scanning (Circ Flaws)

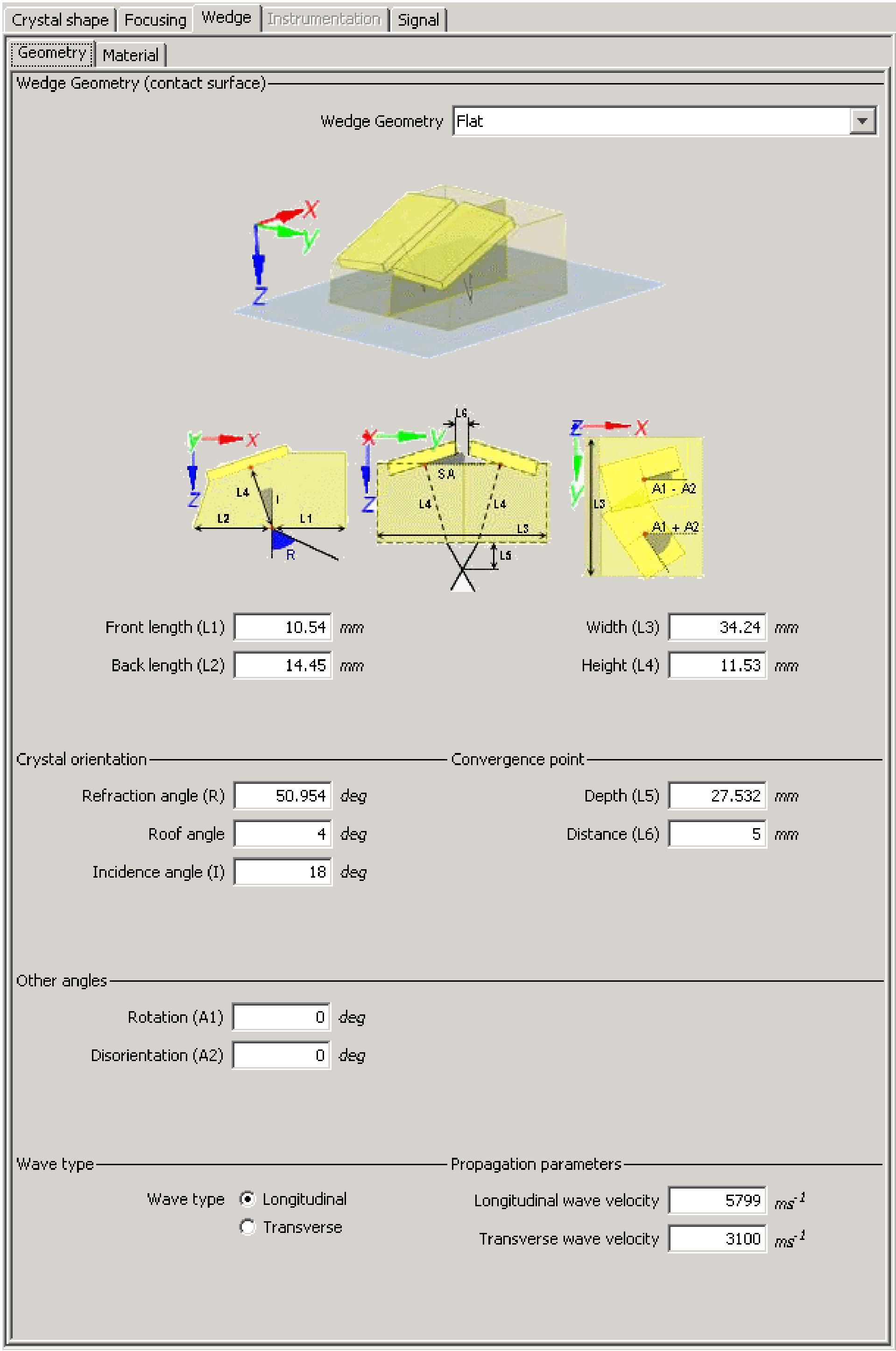

Wedge material: Rexolite cl=2237 m/s

Figure B.107.

Wedge for Circumferential Scanning (Axial Flaws)

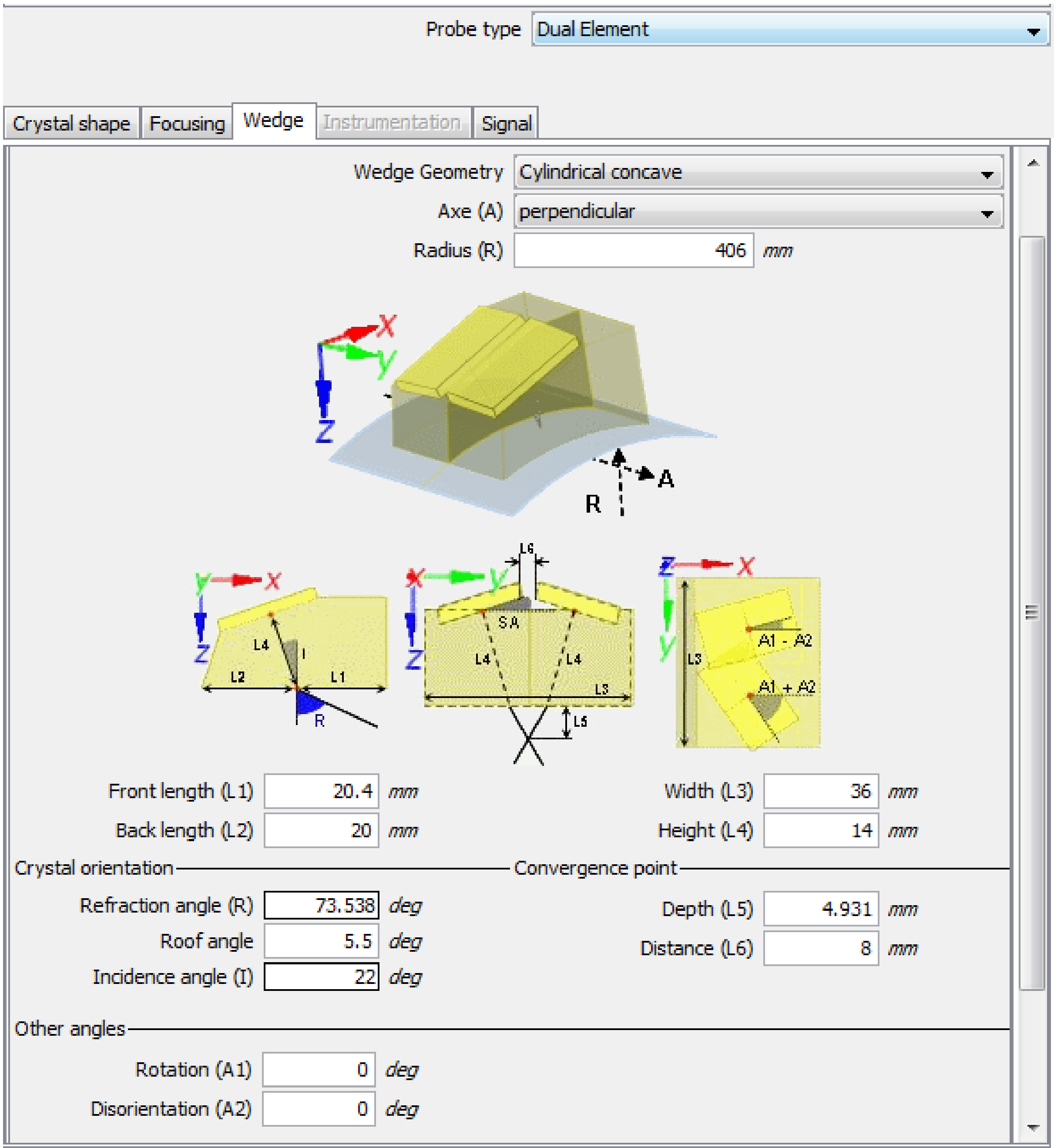

Figure B.108.

Signal

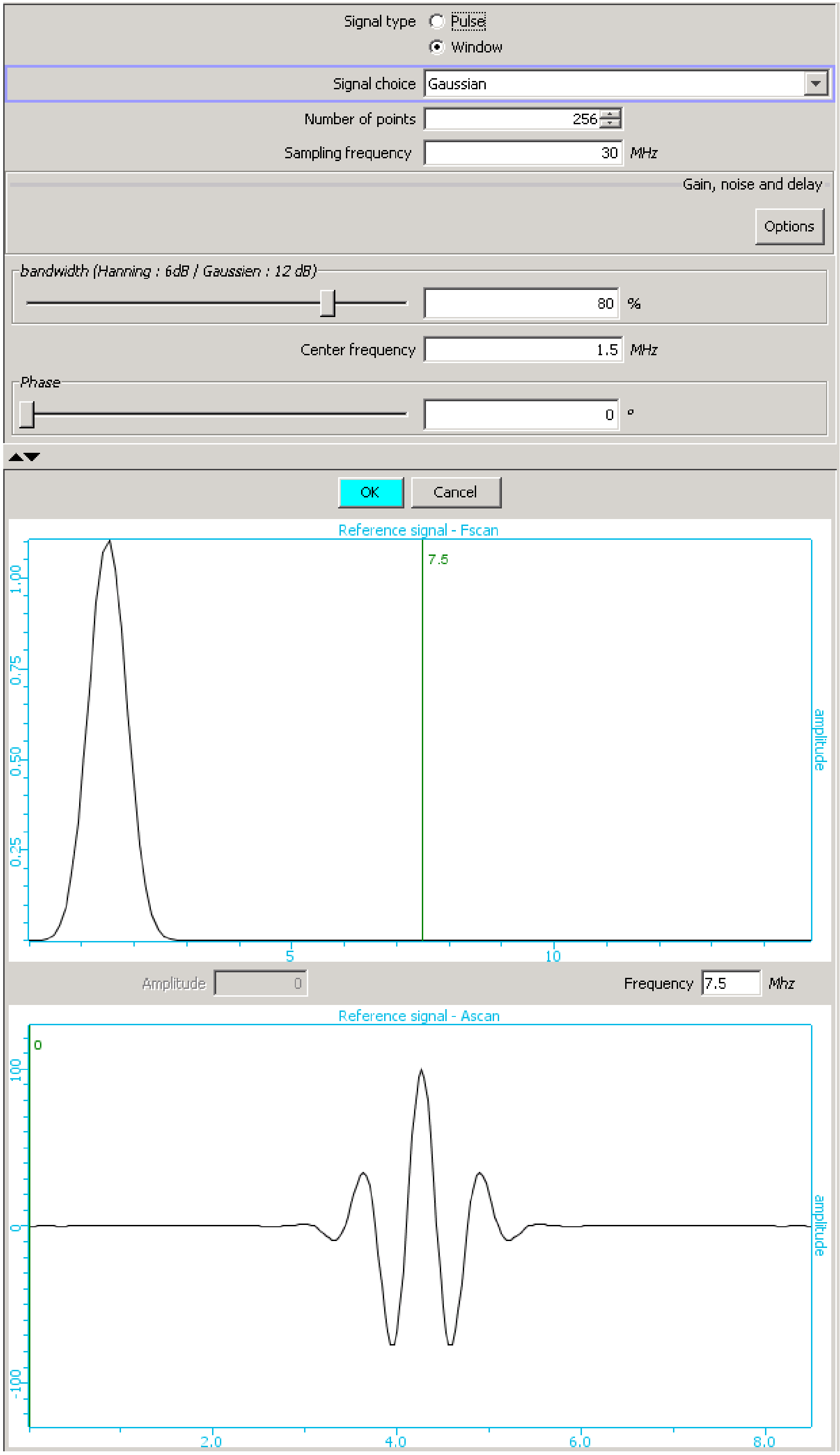

Figure B.109.

B.5.2.3 Phased Array Settings – Focal Laws

Initialization

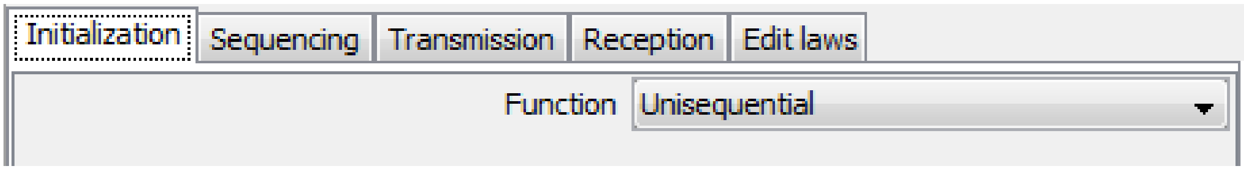

Figure B.110.

Sequencing

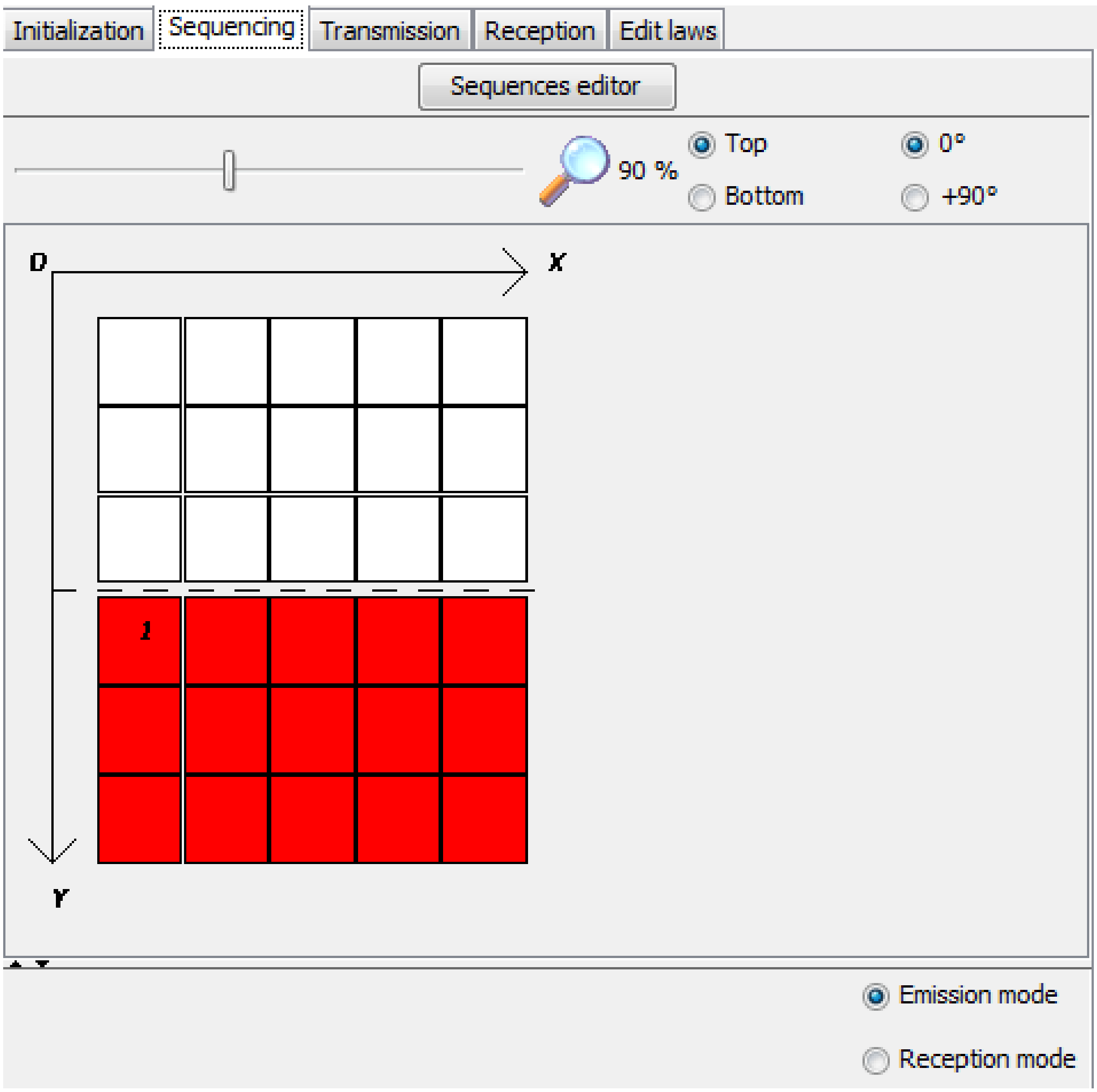

Figure B.111.

Transmission

The focusing type is sectorial scanning at a constant focal depth of 25.4 mm. The sector range goes from 40° to 70° (Step 1°) longitudinal waves.

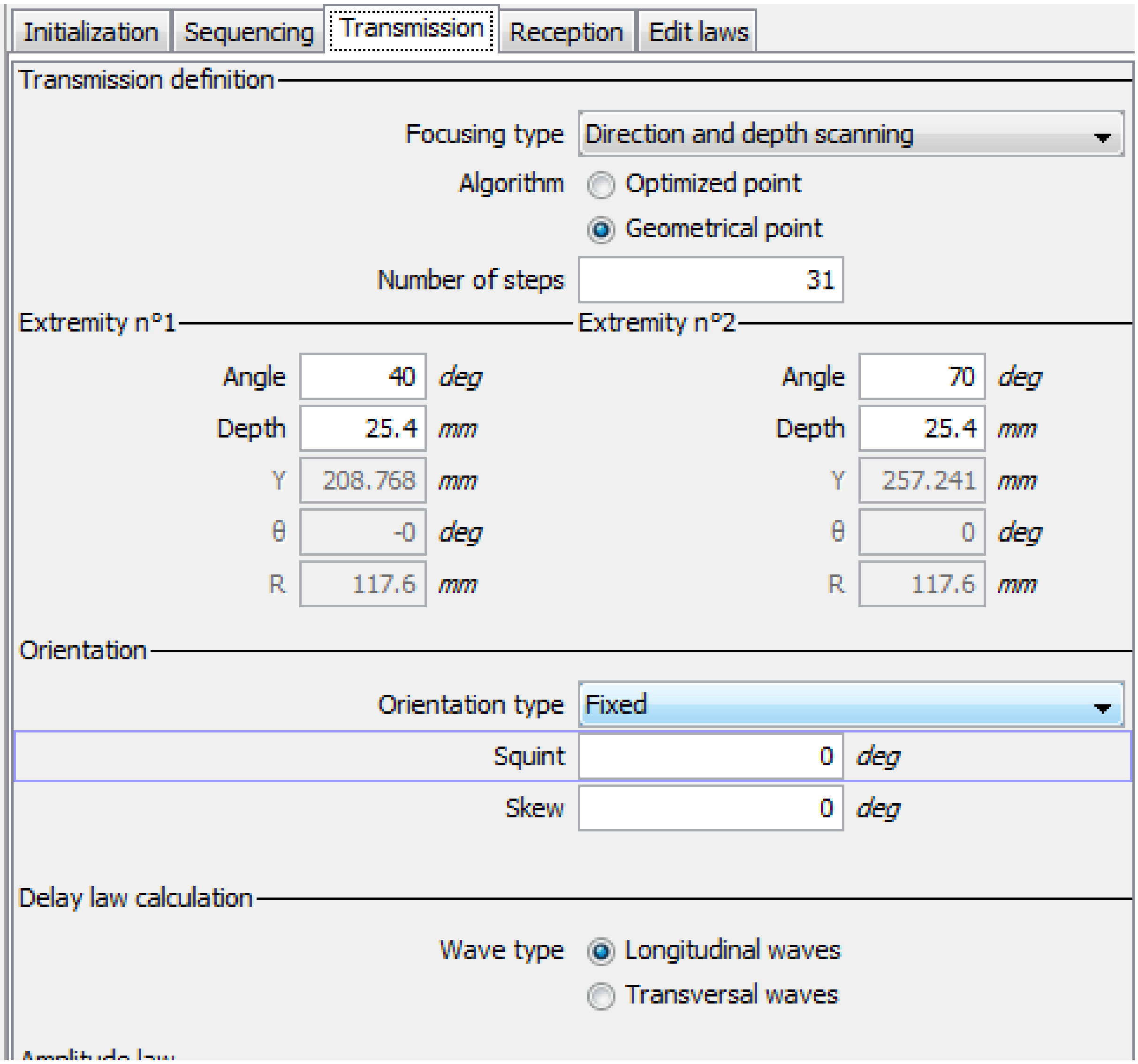

Figure B.112.

B.5.3 Data Acquisition (Scan Plan for Manual Examination)

B.5.3.1 Scanning for Circumferential Flaws

- Beam shall be directed essentially perpendicular to the weld axis from both directions

B.5.3.2 Scanning for Axial Flaws

- Beam shall be directed essentially parallel to the weld in two opposing directions

B.5.4 Analysis

B.5.4.1 Detection

The detection of surface breaking ID flaws relies upon the corner response being observed.

B.5.4.2 Characterization

The characterization is based on the identification of flaw like indications which cannot be attributed to the component geometry based on the supplied as built drawings, manufacturing defects (reported during previous inspections) or indications due to reflection’s or scattering on the anisotropic und heterogeneous weld structure.

Flaw discrimination criterions:

- Good signal to noise ratio (variations along the length)
- Plots to susceptible crack location
- Substantial echo dynamic travel
- Areas of unique amplitude
- Inconsistent time base positions
- Tip signals
- Conformation from the opposite direction
- Seen with many angles
- Mode converted shear signal (only circ flaws with substantial depth)

Non relevant indications criterions:

- Near WCL or weld geometry
- Seen continuously
- Consistent time & amplitude
- Weak echo dynamic travel

B.5.4.3 Length Sizing

- Length of a flaw is determined by moving the probe along the flaw.
- on the same side of the weld as the indication
- optimize the signal from the flaw indication
- adjust the system gain until the response is ~ 80 % FSH
- scan along the length of the flaw in each direction until the signal response has been reduced to:
  - background noise for far side indication

– 20% FSH (12 dB drop) for near side indication

- The length on outside diameter is longer than the actual inside diameter length. Calculate correct ID flaw length according to: (ID/OD) x OD flaw length = ID flaw length

B.5.4.4 Depth Sizing

For flaw depth sizing the Absolut Arrival Time Technique (AATT) is used. The technique relies upon obtaining a direct signal response from the flaw tip using a material depth calibration. From the flaw tip response the amount of unflawed material or remaining ligament can be read directly from the Sscan. Flaw depth is calculated by subtracting the remaining ligament from the actual material thickness.

The figure below illustrates the technique.

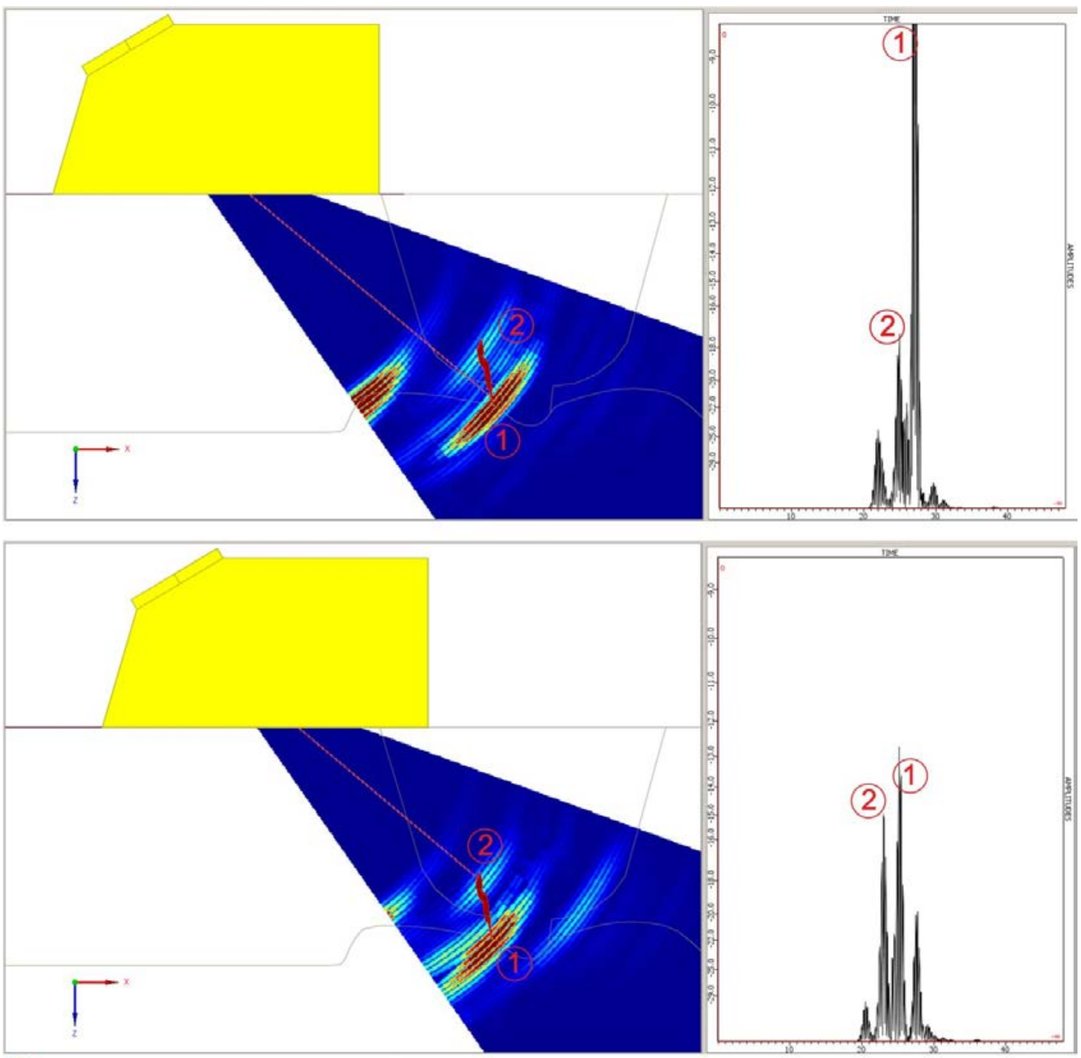

(1) Flaw Base ID (corner trap)l
(2) Tip diffraction signal

Figure B.113.

B.5.4.5 Defect Positioning

Due to uncertainties associated with sound propagation in anisotropic, heterogeneous austenitic weld material indication positioning require detailed evaluation. The information provided below may assist indication positioning.

- Perform thickness and surface contour recordings at the indication position.
- Evaluate the flaw signal amplitude responses from each side of the weld. Observe if the signal response appears reduced due to weld volume sound attenuation from one side or another.
- Identify standard benchmark responses (weld root, weld noise, acoustic interfaces) and flaw indication responses.
- Coordinate and plot the information on a cross sectional drawing of the weld.

B.5.5 Results PARENT Specimen P41

B.5.5.1 Specimen Information and Coordinate System

Geometry

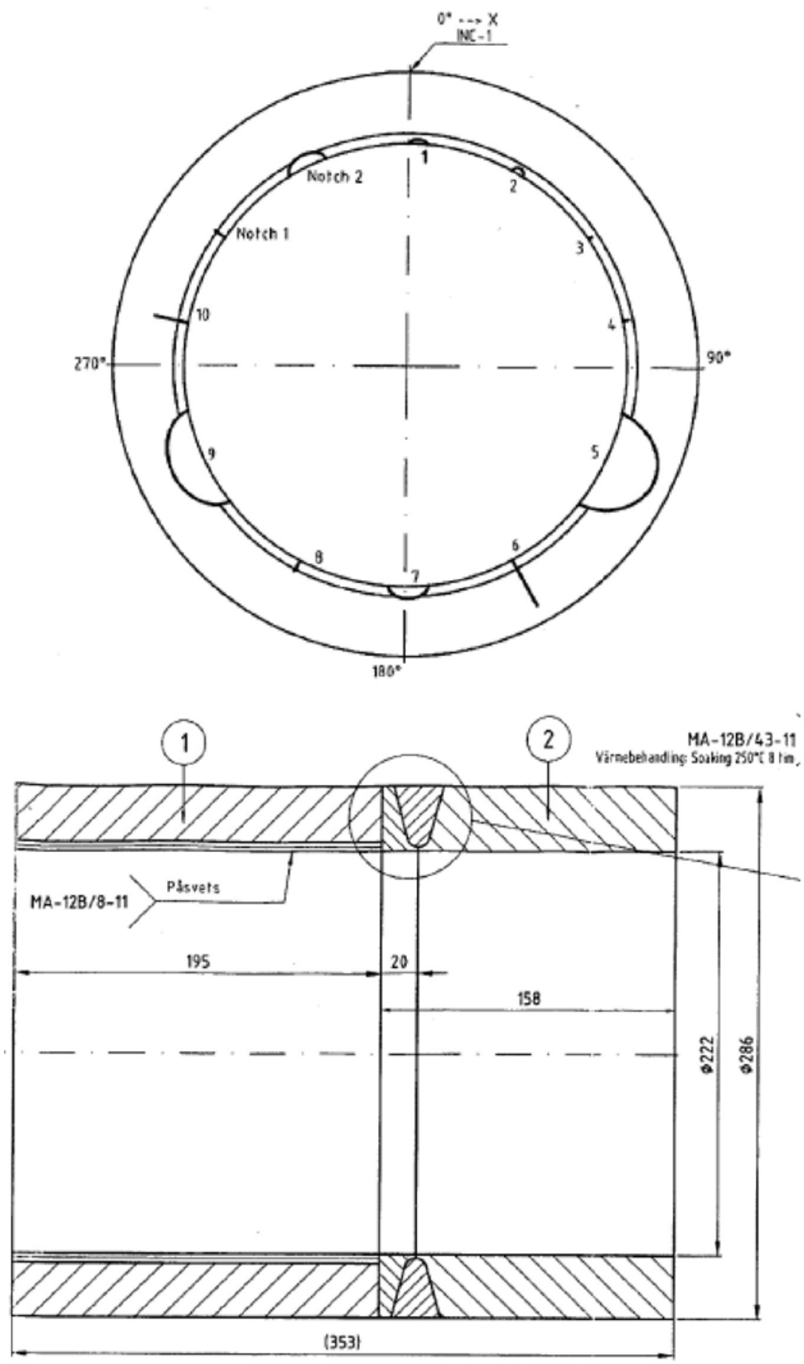

Figure B.114.

Flaw Information

Defekt nr.	1 (Replika)	2 (Replika)	3	4	5	6	7	8 (Replika)	9	10	Notch 1	Notch 2
Skala 1,5:1	CS, Insida, SS								17, 19			
Höjd	2	3	2	3	26	26	6	6	17	17	6	6
Längd	10	6	10	6	50	20	20	20	50	20	20	20
X°/mm, utv.mm	0°/0/0 mm	28°/56/70 mm	54°/105/135mm	77°/150/193mm	101°/195/251mm	150°/290/374mm	173°/335/432mm	206°/400/515mm	230°/445/573mm	279°/540/696mm	302°/585/754mm	325°/630/812mm
Y	13	11	6	5	11	1	10	0	12	0	0	10
Z	Ytbrytande	Ytbrytande	Ytbrytande	Ytbrytande	Ytbrytande Lgn 1)	Ytbrytande Lgn 2)	Ytbrytande Lgn 2)	Ytbrytande Lgn 2)	Ytbrytande Lgn 1)	Ytbrytande Lgn 2)	Ytbrytande	Ytbrytande
Skevning	0°	0°	0°	0°	0°	0°	0°	10°	0°	0°	0°	0°
Lutning	0°	0°	0°	0°	0°	0°	0°	0°	25°	0°	0°	0°
Defekttyp	Stelningsspricka + WTD	Stelningsspricka + WTD	Stelningsspricka + WTD	Stelningsspricka + WTD	Stelningsspricka + WTD	Stelningsspricka + WTD	Stelningsspricka + WTD	Stelningsspricka + WTD	Stelningsspricka + WTD	Stelningsspricka + WTD	EDM notch + WTD	EDM notch + WTD
Orientering	Längs svets	Längs svets	Tvärs svets	Tvärs svets	Längs svets	Tvärs svets	Längs svets	Tvärs svets	Längs svets	Tvärs svets	Tvärs svets	Längs svets
Ligament					10, 4, 14, 7, 15	Se 2) ovan	Se 2) ovan	Se 2) ovan	10, 4, 15, 4, 11, 3, 3	Se 2) ovan		

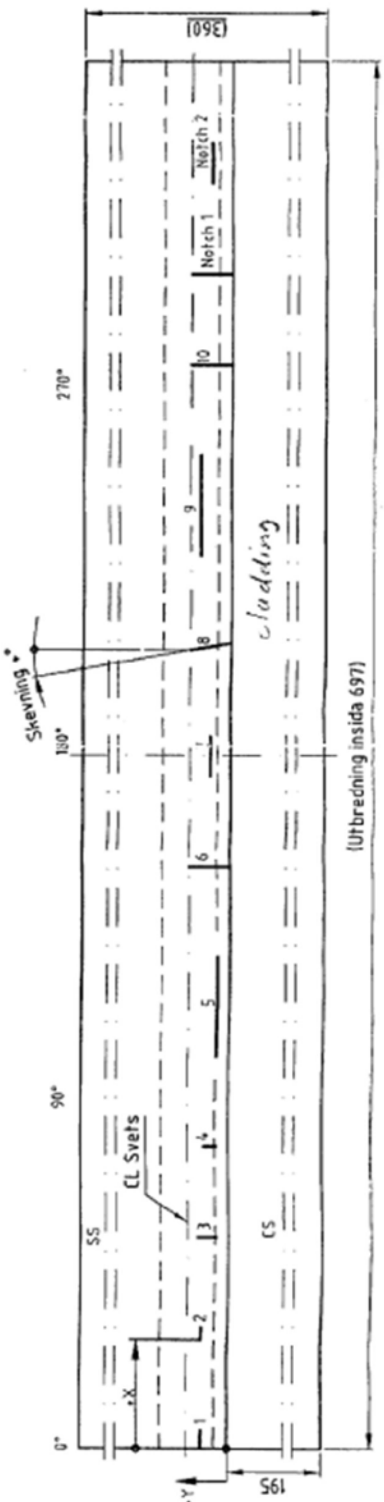

Figure B.115.

Coordinate System

The figure shows the PARENT Coordinate System. The X direction is opposite to the SQC drawing coordinate system. To allow direct comparison of the SQC drawing flaw positions to the measurements in this report the X direction were therefore defined in the opposite direction (see figure).

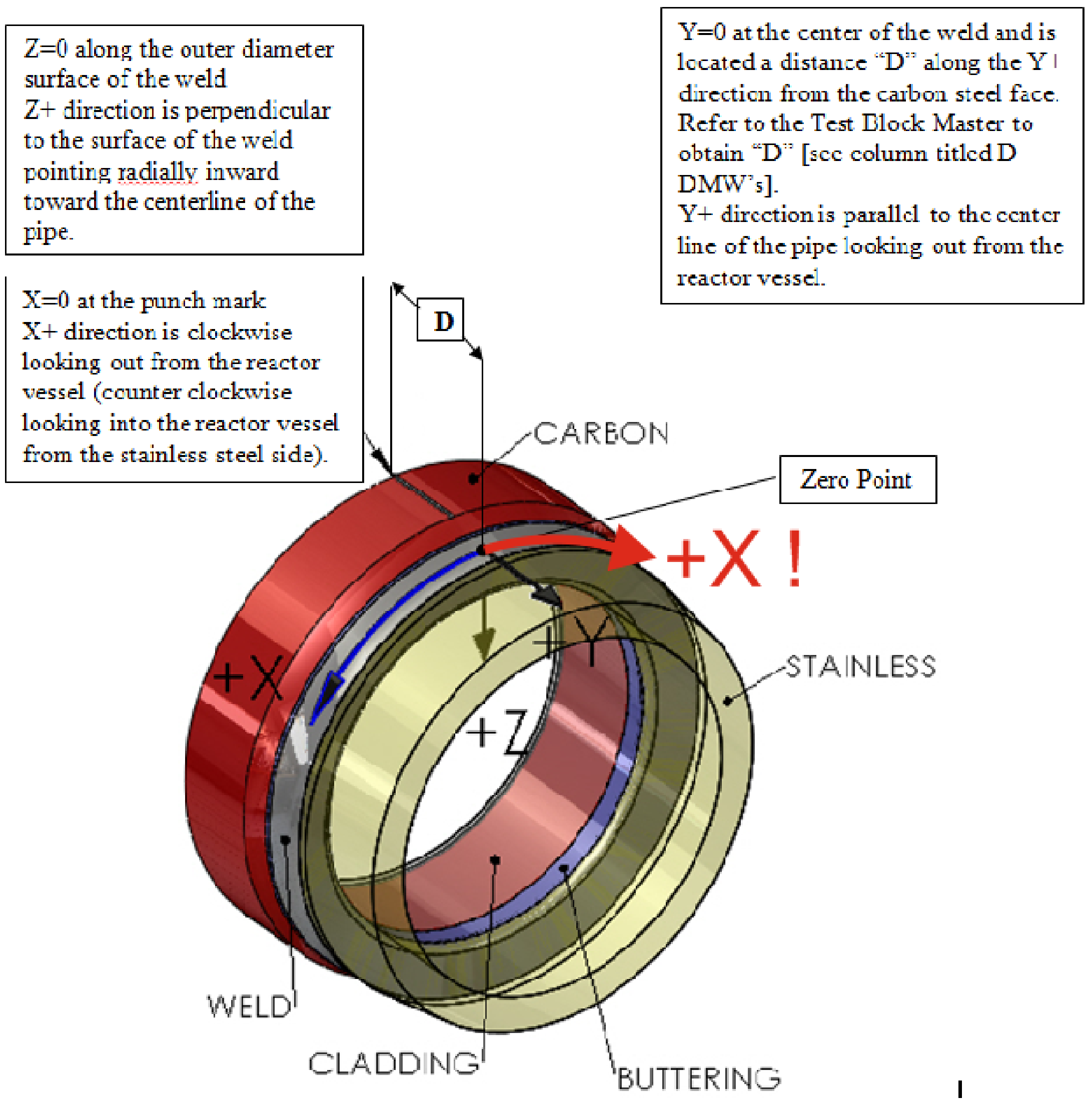

Figure B.116.

Corrected Flaw Positions (PARENT coordinate system)

P41

ORIGINAL DRAWING						PARENT (Inside surface)						PARENT (Outside surface)	
Def. nr	Orient.	X deg	X mm	Y-pos	Length	Def. nr	Orient.	X deg	X mm	Y-pos	Length	X Start	Length
1	Circ	0	0	13	10	12	Circ	354	687	-7	10	885	13
2	Circ	28	54	11	6	11	Circ	328	637	-9	6	821	8
3	Axial	54	105	6/16	10	10	Axial	306	582	-14/-4	10	765	10
4	Axial	77	150	5/11	6	9	Axial	283	541	-15/-9	6	708	6
5	Circ	101	195	11	50	8	Circ	233	452	-9	50	582	64
6	Axial	150	290	1/21	20	7	Axial	210	387	-19/1	20	525	20
7	Circ	173	335	10	20	6	Circ	176	342	-10	20	441	26
8	Axial	206	400	0/20	20	5	Axial	154	277	-20/0	20	385	20
9	Circ	230	445	12	50	4	Circ	104	202	-8	50	260	64
10	Axial	279	540	0/20	20	3	Axial	81	137	-20/0	20	203	20
11	Axial	302	585	0/20	20	2	Axial	58	92	-20/0	20	145	20
12	Circ	325	630	10	20	1	Circ	24	47	-10	20	61	26

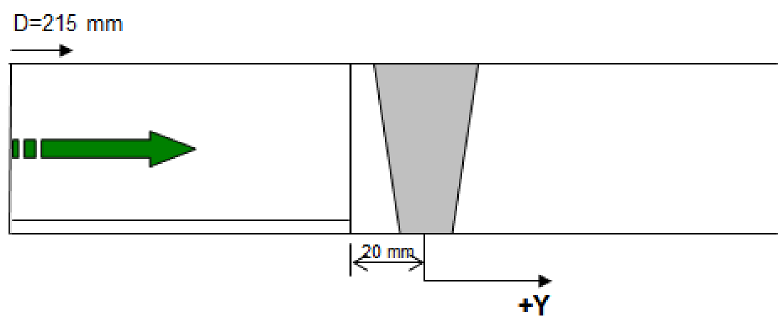

D_i = 222,0 mm, t = 32 mm

Inner circumference = 697,4 mm, which gives 1,94 mm/deg

Outer circumference = 898 mm, which gives 2,50 mm/deg

Figure B.117.

B.5.5.2 Flaw Indication Summary Tables

Circumferential Flaws

<u>Probe Position: Carbon Steel Side / Beam Direction: +Y</u>

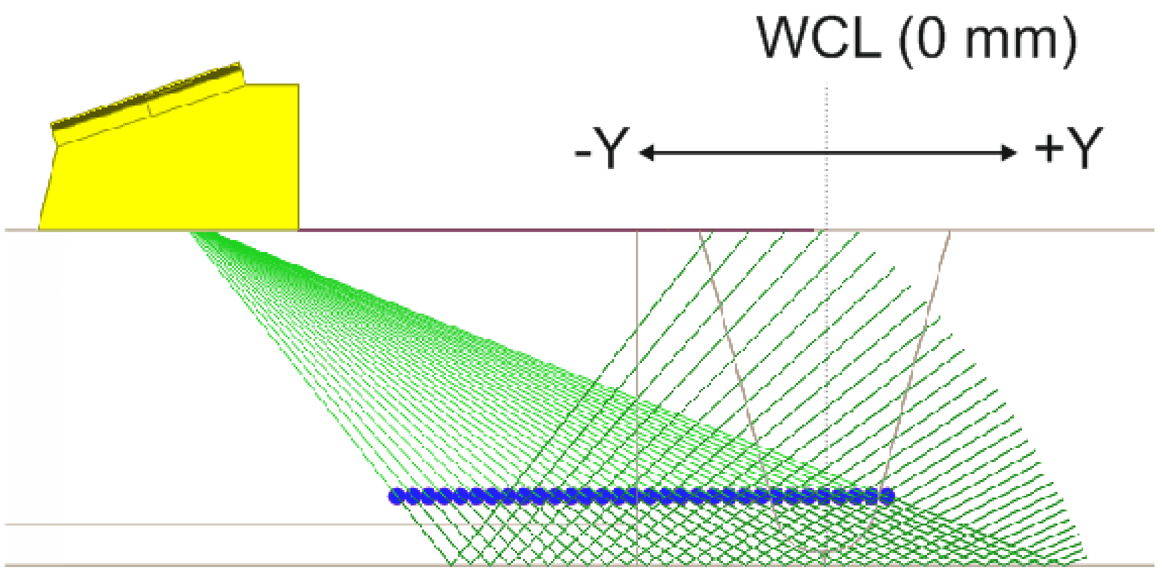

Figure B.118.

Flaw No.:	As Built Information (SQC Drawing)					Measurement Results					Remarks	UT Analysis Section	Cal Sheet No:
	Flaw X Position OD			Flaw Depth	Flaw Y Pos.	Flaw X Position OD			Flaw Depth	Flaw Y Pos.			
	Start	Length	End			Start	Length	End					
	mm	mm	mm	mm		mm	mm	mm	mm				
1	0.0	12.9	12.9	2	CS* B**	895	15	8	3.2	-Y	1)	4.1	1
2	69.9	7.7	77.6	3	CS* B**	72	85	13	3.2	-Y	2)	4.2	1
5	252.1	64.4	316.5	26	CS* B**	250	72	322	26.1	-Y	3)	4.3	2
7	431.8	25.8	457.5	6	CS* B**	432	33	465	5.55	-Y	4)	4.4	3
9	574.0	64.4	638.5	17	CS* B**	578	67	645	14.7	-Y	5)	4.5	4
12	811.1	25.8	836.9	6	CS* B**	813	32	845	5.55	-Y	6)	4.6	3

* Flaw on Carbon Steel (CS) / Buttering (B) Side in respect to weld center line
See next page for Remarks!

Remarks:

1) no separation of tip diffraction from corner trap echo, no TLL echo indicates shallow flaw, flaw depth estimation procedure: if no separation of tip diffraction from corner trap and flaw seems to be shallow the flaw depth is defined per default to 10% pipe thickness at flaw position → 3.2 mm
2) no separation of tip diffraction from corner trap echo, no TLL echo indicates shallow flaw, flaw depth estimation procedure: if no separation of tip diffraction from corner trap and flaw seems to be shallow the flaw depth is defined per default to 10% pipe thickness at flaw position → 3.2 mm
3) for quantitative flaw depth sizing calibration at 24 mm deep notch of calibration block KKM_24_18_12_6 (RL = 6 mm)
4) for quantitative flaw depth sizing calibration at 6 mm deep notch of calibration block KKM_24_18_12_6 (RL = 24 mm)
5) for quantitative flaw depth sizing calibration at 12 mm deep notch of calibration block KKM_24_18_12_6 (RL = 18 mm)
6) for quantitative flaw depth sizing calibration at 6 mm deep notch of calibration block KKM_24_18_12_6 (RL = 24 mm)

Probe Position: Stainless Steel Side / Beam Direction: -Y

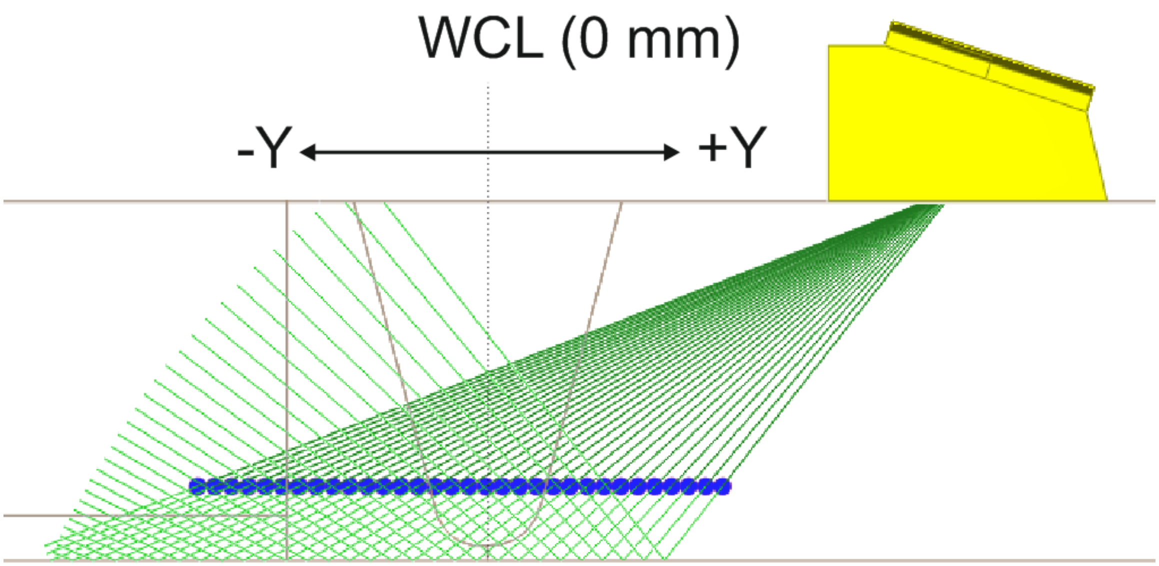

Figure B.119.

Flaw No.:	As Built Information (SQC Drawing)					Measurement Results					Remarks	UT Analysis Section	Cal Sheet No:
	Flaw X Position OD			Flaw Depth	Flaw Y Pos.	Flaw X Position OD			Flaw Depth	Flaw Y Pos.			
	Start	Length	End			Start	Length	End					
	mm	mm	mm	mm		mm	mm	mm	mm				
1	0.0	12.9	12.9	2	CS* B**	no detection from fare side				-Y	-	-	1
2	69.9	7.7	77.6	3	CS* B**	no detection from fare side				-Y	-	-	1
5	252.1	64.4	316.5	26	CS* B**	252	60	312	25.89	-Y	1)	4.7	2
7	431.8	25.8	457.5	6	CS* B**	432	29	461	7.78	-Y	2)	4.8	3
9	574.0	64.4	638.5	17	CS* B**	578	67	645	14.7	-Y	3)	4.9	4
12	811.1	25.8	836.9	6	CS* B**	817	25	842	3.2	-Y	4)	4.10	1

* Flaw on Carbon Steel (CS) / Buttering (B) Side in respect to weld center line
See below for remarks!

1) For quantitative flaw depth sizing calibration at 24 mm deep notch of calibration block KKM_24_18_12_6 (RL = 6 mm)
2) Very hard to find the tip for depth sizing, only possible if inspector knows in witch depth region he has to look for tips; flaw depth estimation procedure: if flaw is seen with high angles of the Sscan and there is a quiet strong TLL reflection it indicates that flaw has at least some true wall extension (20-40%); delta to as built depth may result from beam redirection in heterogeneous anisotropic weld material
3) For quantitative flaw depth sizing calibration at 12 mm deep notch of calibration block KKM_24_18_12_6 (RL = 18 mm), delta to as built depth may result from beam redirection in heterogeneous anisotropic weld material
4) No separation of tip diffraction from corner trap echo, no TLL echo indicates shallow flaw, flaw depth estimation procedure: if no separation of tip diffraction from corner trap and flaw seems to be shallow the flaw depth is defined per default to 10% pipe thickness at flaw position → 3.2 mm

Axial Flaws

Scan Direction: + X

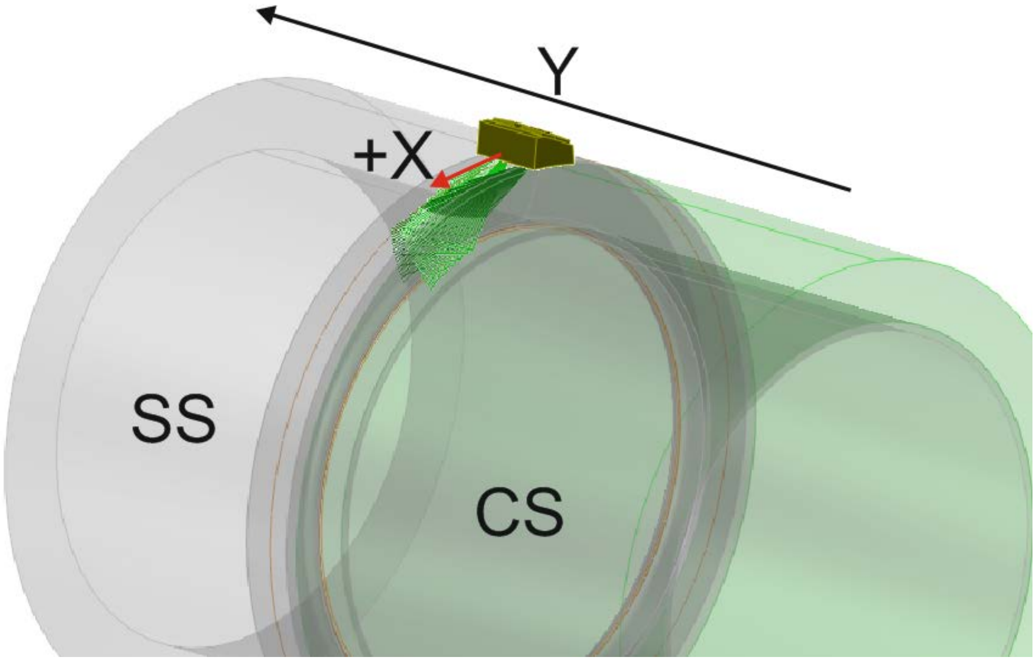

Figure B.120.

Flaw No.:	As Built Information (SQC Drawing)				Measurement Results				Remarks	UT Analysis Section	Cal Sheet No:
	Flaw X Position OD	Length	Flaw Depth	Flaw Y Pos.	Flaw X Position OD	Length	Flaw Depth	Flaw Y Pos.			
	mm	mm	mm		mm	mm	mm				
3	135	10	2	CS* B**	135	≈ 10	3.2	-Y	1)	4.11	6
4	193	6	3	CS* B**	195	≈ 6	3.2	-Y	2)	4.12	6
6	374	20	26	CS* B**	370	≈ 30	26	-Y	3)	4.13	7
8	515	20	6	CS* B**	515	≈ 25	6.07	-Y	4)	4.14	8
10	696	20	17	CS* B**	698	20	16.74	-Y	5)	4.15	9
11	754	20	6	CS* B**	750	20	6.67	-Y	6)	4.16	8

*   Flaw on Carbon Steel (CS) / Buttering (B) Side in respect to weld center line
See next page for remarks!

Remarks

1) Very hard to detect with manual inspection; length sizing hard lots of noise from buttering; no separation of tip diffraction from corner trap echo, no TLL echo indicates shallow flaw, flaw depth estimation procedure: if no separation of tip diffraction from corner trap and flaw seems to be shallow the flaw depth is defined per default to 10% pipe thickness at flaw position → 3.2 mm
2) Hard to detect with manual inspection; length sizing hard lots of noise from buttering; no separation of tip diffraction from corner trap echo, no TLL echo indicates shallow flaw, flaw depth estimation procedure: if no separation of tip diffraction from corner trap and flaw seems to be shallow the flaw depth is defined per default to 10% pipe thickness at flaw position → 3.2 mm
3) Length sizing hard lots of noise from buttering; for quantitative flaw depth sizing calibration with 9 mm deep SDH (Ø 1,5 mm) of calibration block "SVTI AS_D270_T30"
4) Length sizing hard lots of noise from buttering; depth sizing only possible when probe is skewed (flaw skew angle 10°); for quantitative flaw depth sizing calibration with 26 mm deep SDH (Ø 1,5 mm) of calibration block "SVTI AS_D270_T30"
5) Quantitative flaw depth sizing calibration with 15 mm deep SDH (Ø 1,5 mm) of calibration block "SVTI AS_D270_T30"
6) Flaw depth sizing hard, very week tip signal; quantitative flaw depth sizing calibration with 26 mm deep SDH (Ø 1,5 mm) of calibration block "SVTI AS_D270_T30"

Scan Direction: - X

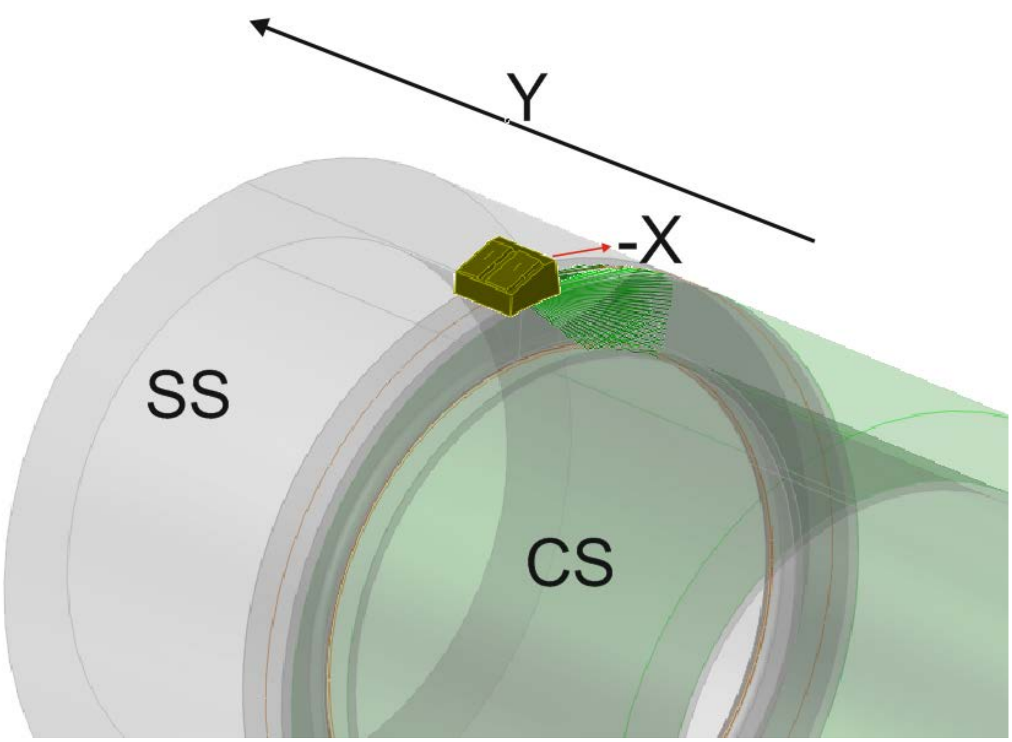

Figure B.121.

Flaw No.:	As Built Information (SQC Drawing)				Measurement Results				Remarks	UT Analysis Section	Cal Sheet No:
	Flaw X Position OD	Length	Flaw Depth	Flaw Y Pos.	Flaw X Position OD	Length	Flaw Depth	Flaw Y Pos.			
	mm	mm	mm		mm	mm	mm				
3	135	10	2	CS* B**	135	≈ 10	3.2	-Y	1)	4.17	6
4	193	6	3	CS* B**	195	≈ 6	3.2	-Y	2)	4.18	6
6	374	20	26	CS* B**	370	≈ 20	26.48	-Y	3)	4.19	7
8	515	20	6	CS* B**	515	≈ 25	6.81	-Y	4)	4.20	8
10	696	20	17	CS* B**	698	≈ 25	16.74	-Y	5)	4.21	9
11	754	20	6	CS* B**	750	20	6.37	-Y	6)	4.22	8

* Flaw on Carbon Steel (CS) / Buttering (B) Side in respect to weld center line
See below for remarks!

1) Very hard to detect with manual inspection; length sizing hard lots of noise from buttering; no separation of tip diffraction from corner trap echo, no TLL echo indicates shallow flaw, flaw depth estimation procedure: if no separation of tip diffraction from corner trap and flaw seems to be shallow the flaw depth is defined per default to 10% pipe thickness at flaw position → 3.2 mm
2) Hard to detect with manual inspection; length sizing hard lots of noise from buttering; no separation of tip diffraction from corner trap echo, no TLL echo indicates shallow flaw, flaw depth estimation procedure: if no separation of tip diffraction from corner trap and flaw seems to be shallow the flaw depth is defined per default to 10% pipe thickness at flaw position → 3.2 mm
3) Length sizing hard lots of noise from buttering; for quantitative flaw depth sizing calibration with 9 mm deep SDH (Ø 1,5 mm) of calibration block "SVTI AS_D270_T30"
4) Length sizing hard lots of noise from buttering; depth sizing hard only possible when probe is skewed (flaw skew angle 10°); for quantitative flaw depth sizing calibration with 26 mm deep SDH (Ø 1,5 mm) of calibration block "SVTI AS_D270_T30"
5) Quantitative flaw depth sizing calibration with 15 mm deep SDH (Ø 1,5 mm) of calibration block "SVTI AS_D270_T30"
6) Flaw depth sizing good, good tip signal; quantitative flaw depth sizing calibration with 26 mm deep SDH (Ø 1,5 mm) of calibration block "SVTI AS_D270_T30"

B.5.5.3 UT Analysis Images

Flaw 1 / Probe Position: Carbon Steel Side / Beam Direction: -Y

Flaw No.:	As Built Information (SQC Drawing)					Measurement Results					Remarks	UT Analysis Section	Cal Sheet No:
	Flaw X Position OD			Flaw Depth	Flaw Y Pos.	Flaw X Position OD			Flaw Depth	Flaw Y Pos.			
	Start	Length	End			Start	Length	End					
	mm	mm	mm	mm		mm	mm	mm	mm				
1	0.0	12.9	12.9	2	CS* B**	895	15	8	3.2	-Y	1)	3.1	1

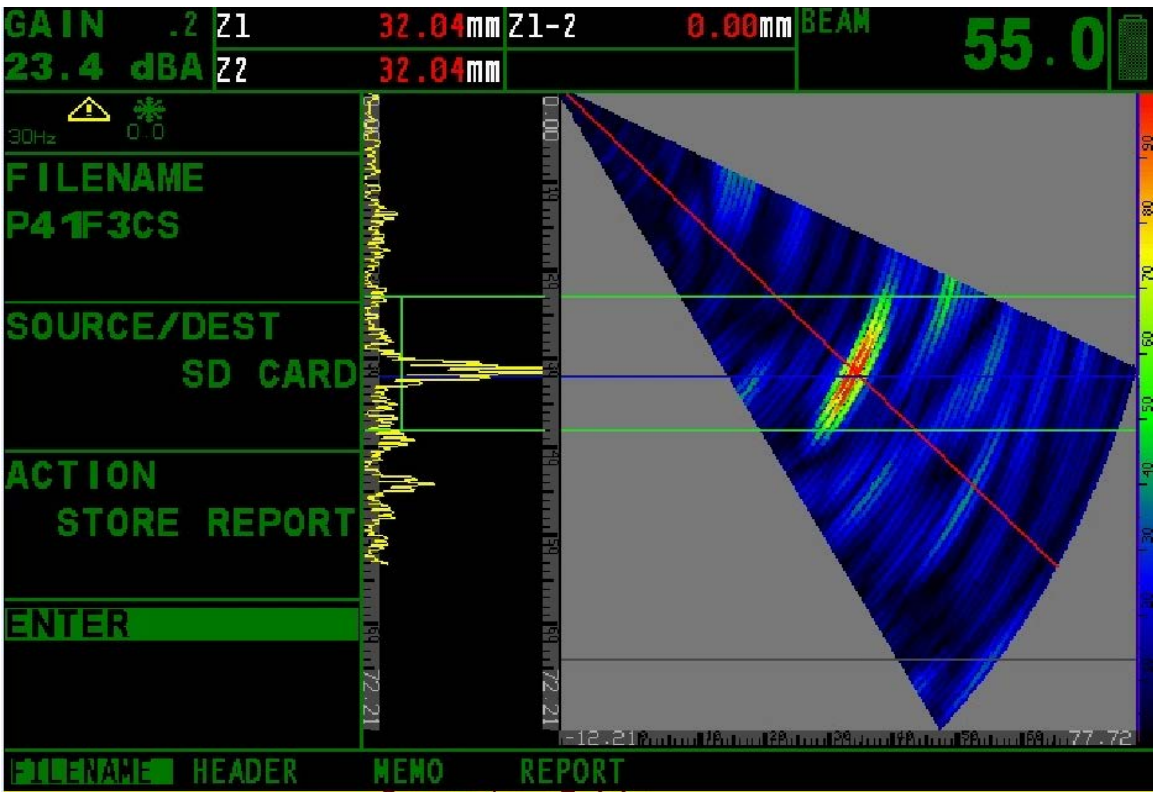

No separation of tip diffraction from corner trap echo, no TLL echo indicates shallow flaw, flaw depth estimation procedure: if no separation of tip diffraction from corner trap and flaw seems to be shallow the flaw depth is defined per default to 10% pipe thickness at flaw position → 3.2 mm

Remarks: File name in picture not correct (coordinate system problem), file name has been renamed correctly during analysis

Figure B.122.

Flaw 2 / Probe Position: Carbon Steel Side / Beam Direction: -Y

Flaw No.:	As Built Information (SQC Drawing)					Measurement Results					Remarks	UT Analysis Section	Cal Sheet No:
	Flaw X Position OD			Flaw Depth	Flaw Y Pos.	Flaw X Position OD			Flaw Depth	Flaw Y Pos.			
	Start	Length	End			Start	Length	End					
	mm	mm	mm	mm		mm	mm	mm	mm				
2	69.9	7.7	77.6	3	CS* B**	72	85	13	3.2	-Y	2)		1

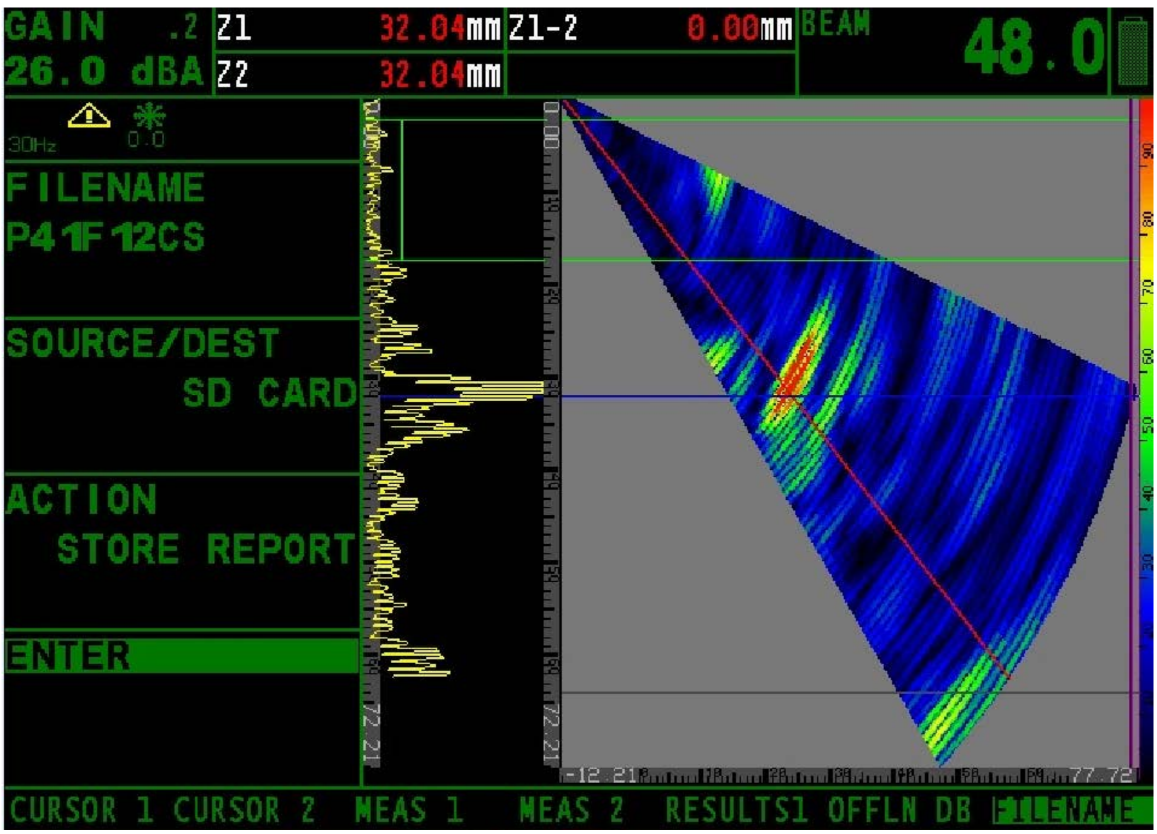

Hard to detect; no separation of tip diffraction from corner trap echo; no TLL echo indicates shallow flaw; flaw depth estimation procedure: if no separation of tip diffraction from corner trap and flaw seems to be shallow the flaw depth is defined per default to 10% pipe thickness at flaw position → 3.2 mm

Remarks: File name in picture not correct (coordinate system problem), file name has been renamed correctly during analysis

Figure B.123.

Flaw 5 / Probe Position: Carbon Steel Side / Beam Direction: -Y

Flaw No.:	As Built Information (SQC Drawing)					Measurement Results					Remarks	UT Analysis Section	Cal Sheet No:
	Flaw X Position OD			Flaw Depth	Flaw Y Pos.	Flaw X Position OD			Flaw Depth	Flaw Y Pos.			
	Start	Length	End			Start	Length	End					
	mm	mm	mm	mm		mm	mm	mm	mm				
5	252.1	64.4	316.5	26	CS* B**	250	72	322	26.11	-Y	3)		2

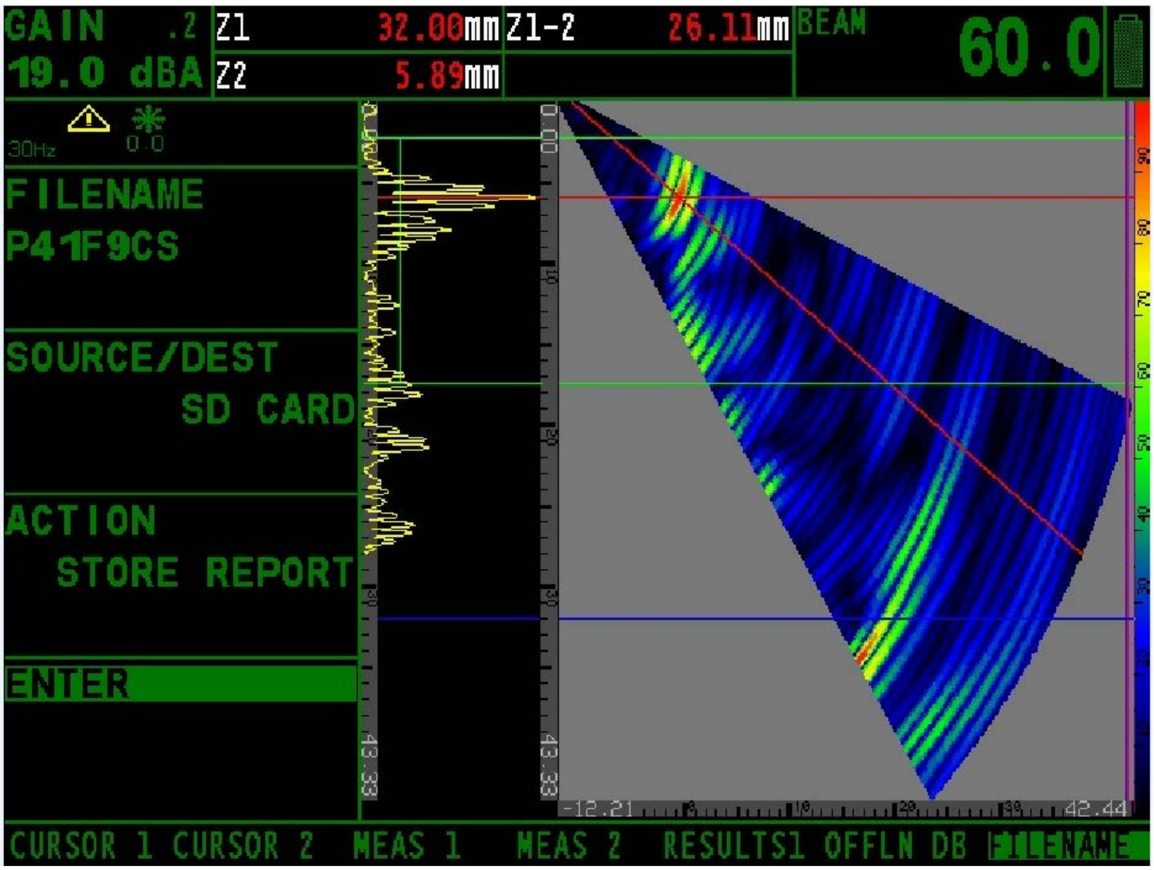

For quantitative flaw depth sizing calibration at 24 mm deep notch of calibration block KKM_24_18_12_6 (RL = 6 mm)

Remarks: File name in picture not correct (coordinate system problem), file name has been renamed correctly during analysis

Figure B.124.

Flaw 7 / Probe Position: Carbon Steel Side / Beam Direction: -Y

Flaw No.:	As Built Information (SQC Drawing)					Measurement Results					Remarks	UT Analysis Section	Cal Sheet No:
	Flaw X Position OD			Flaw Depth	Flaw Y Pos.	Flaw X Position OD			Flaw Depth	Flaw Y Pos.			
	Start	Length	End			Start	Length	End					
	mm	mm	mm	mm		mm	mm	mm	mm				
7	431.8	25.8	457.5	6	CS* B**	432	33	465	5.55	-Y	4)		3

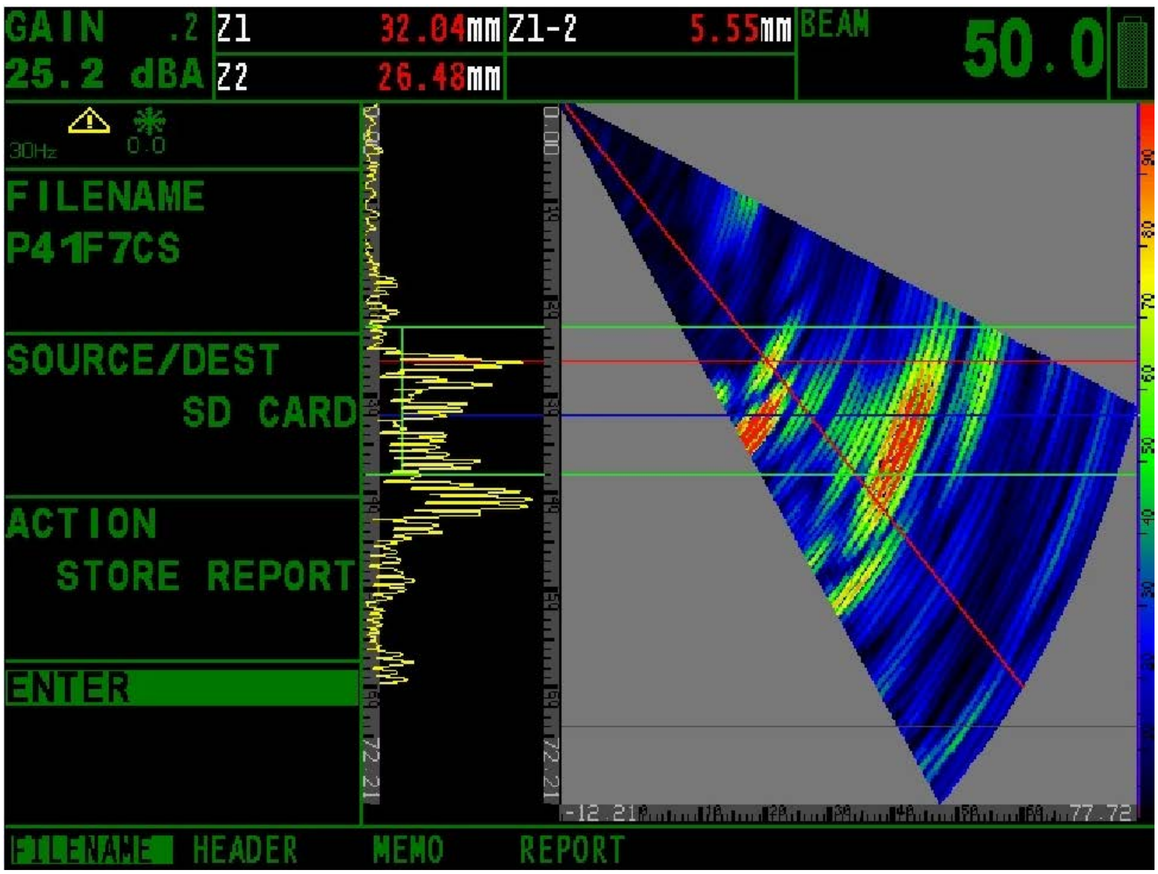

For quantitative flaw depth sizing calibration at 6 mm deep notch of calibration block KKM_24_18_12_6 (RL = 24 mm)

Figure B.125.

Flaw 9 / Probe Position: Carbon Steel Side / Beam Direction: -Y

Flaw No.:	As Built Information (SQC Drawing)					Measurement Results					Remarks	UT Analysis Section	Cal Sheet No:
	Flaw X Position OD			Flaw Depth	Flaw Y Pos.	Flaw X Position OD			Flaw Depth	Flaw Y Pos.			
	Start	Length	End			Start	Length	End					
	mm	mm	mm	mm		mm	mm	mm	mm				
9	574.0	64.4	638.5	17	CS* B**	578	67	645	14.7	-Y	5)		4

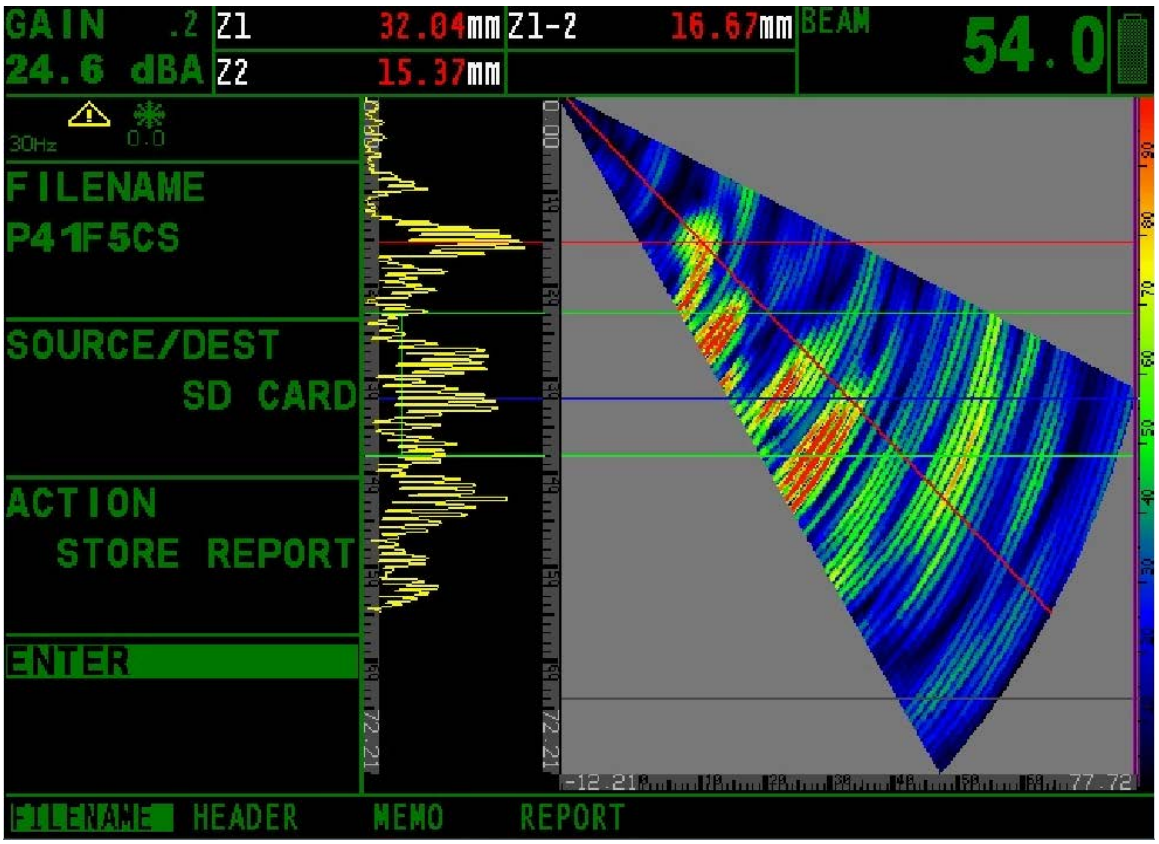

For quantitative flaw depth sizing calibration at 12 mm deep notch of calibration block KKM_24_18_12_6 (RL = 18 mm)

Remarks: File name in picture not correct (coordinate system problem), file name has been renamed correctly during analysis

Figure B.126.

Flaw 12 / Probe Position: Carbon Steel Side / Beam Direction: -Y

Flaw No.:	As Built Information (SQC Drawing)					Measurement Results					Remarks	UT Analysis Section	Cal Sheet No:
	Flaw X Position OD			Flaw Depth	Flaw Y Pos.	Flaw X Position OD			Flaw Depth	Flaw Y Pos.			
	Start	Length	End			Start	Length	End					
	mm	mm	mm	mm		mm	mm	mm	mm				
12	811.1	25.8	836.9	6	CS* B**	813	32	845	5.55	-Y	6)		3

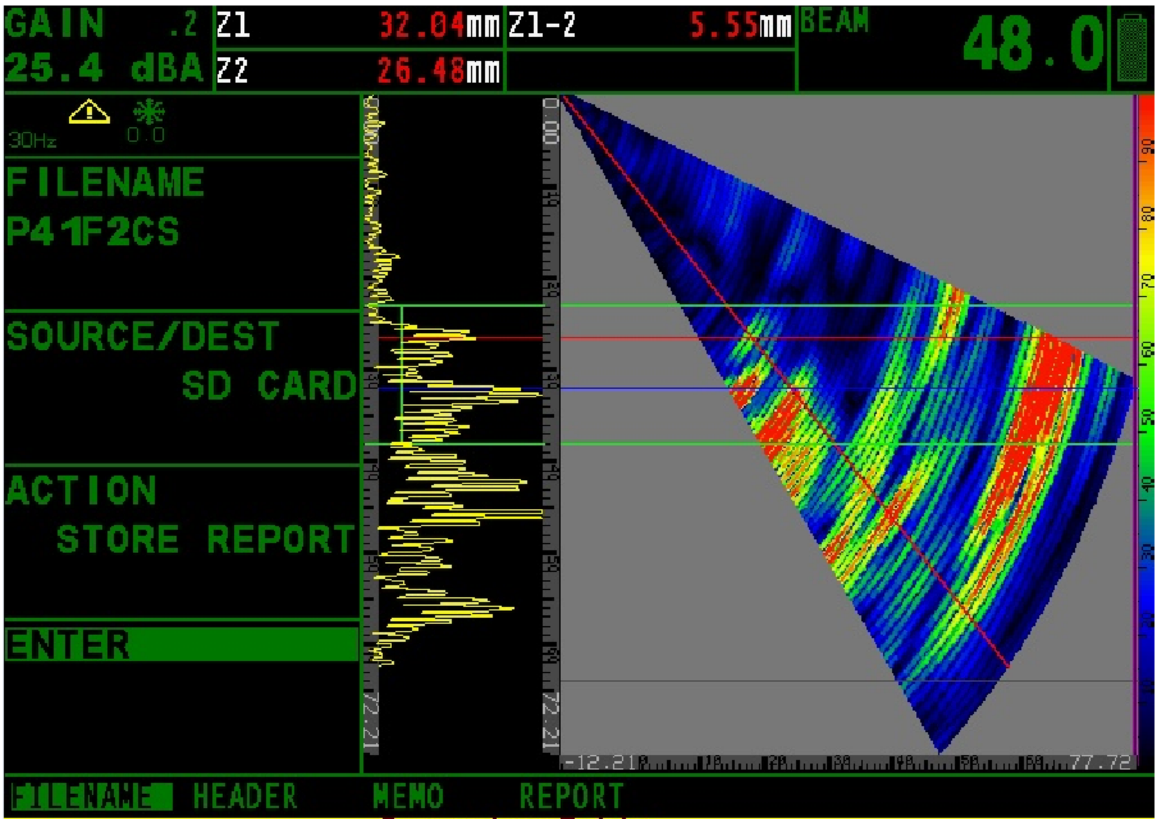

For quantitative flaw depth sizing calibration at 6 mm deep notch of calibration block KKM_24_18_12_6 (RL = 24 mm)

Remarks: File name in picture not correct (coordinate system problem), file name has been renamed correctly during analysis

Figure B.127.

Flaw 5 / Probe Position: Stainless Side / Beam Direction: +Y

Flaw No.:	As Built Information (SQC Drawing)					Measurement Results					Remarks	UT Analysis Section	Cal Sheet No:
	Flaw X Position OD			Flaw Depth	Flaw Y Pos.	Flaw X Position OD			Flaw Depth	Flaw Y Pos.			
	Start	Length	End			Start	Length	End					
	mm	mm	mm	mm		mm	mm	mm	mm				
5	252.1	64.4	316.5	26	CS* B**	252	60	312	25.89	-Y	1)	4.7	2

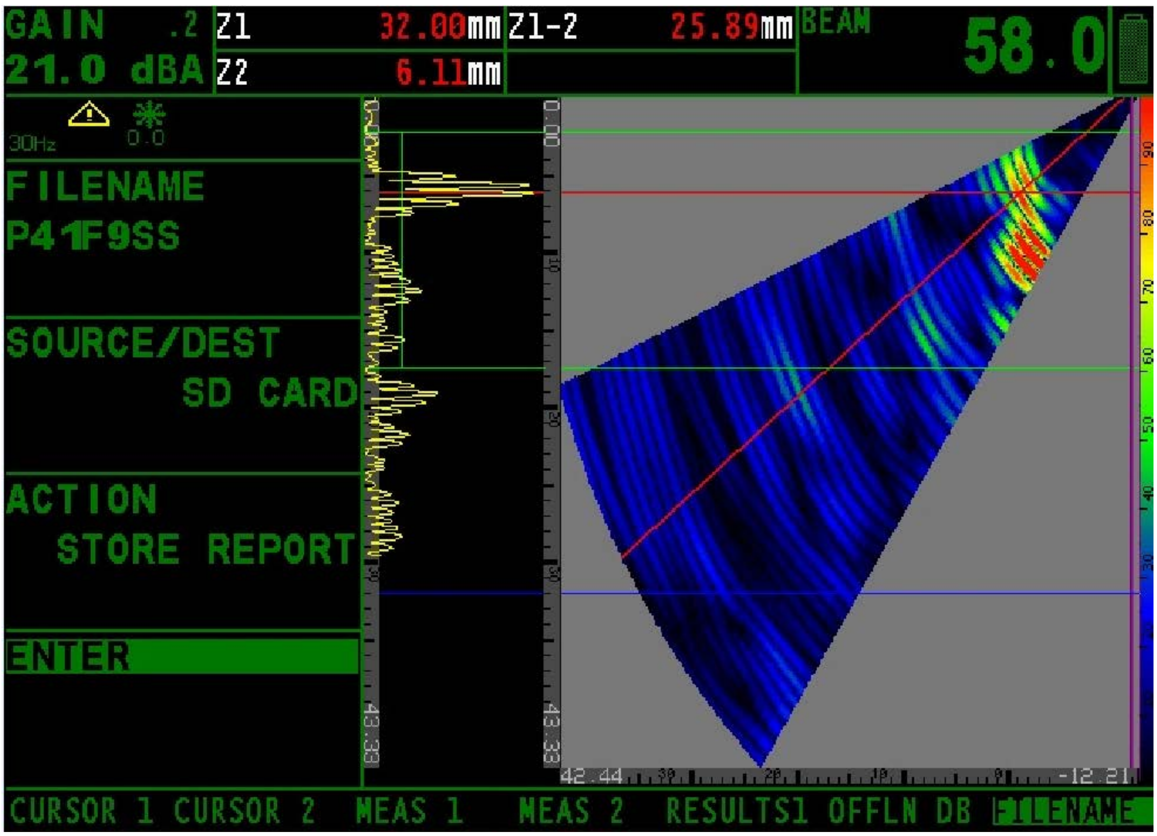

For quantitative flaw depth sizing calibration at 24 mm deep notch of calibration block KKM_24_18_12_6 (RL = 6 mm)

Remarks: File name in picture not correct (coordinate system problem), file name has been renamed correctly during analysis

Figure B.128.

Flaw 7 / Probe Position: Stainless Side / Beam Direction: +Y

Flaw No.:	As Built Information (SQC Drawing)					Measurement Results					Remarks	UT Analysis Section	Cal Sheet No:
	Flaw X Position OD			Flaw Depth	Flaw Y Pos.	Flaw X Position OD			Flaw Depth	Flaw Y Pos.			
	Start	Length	End			Start	Length	End					
	mm	mm	mm	mm		mm	mm	mm	mm				
7	431.8	25.8	457.5	6	CS* B**	432	29	461	7.78	-Y	2)	4.8	3

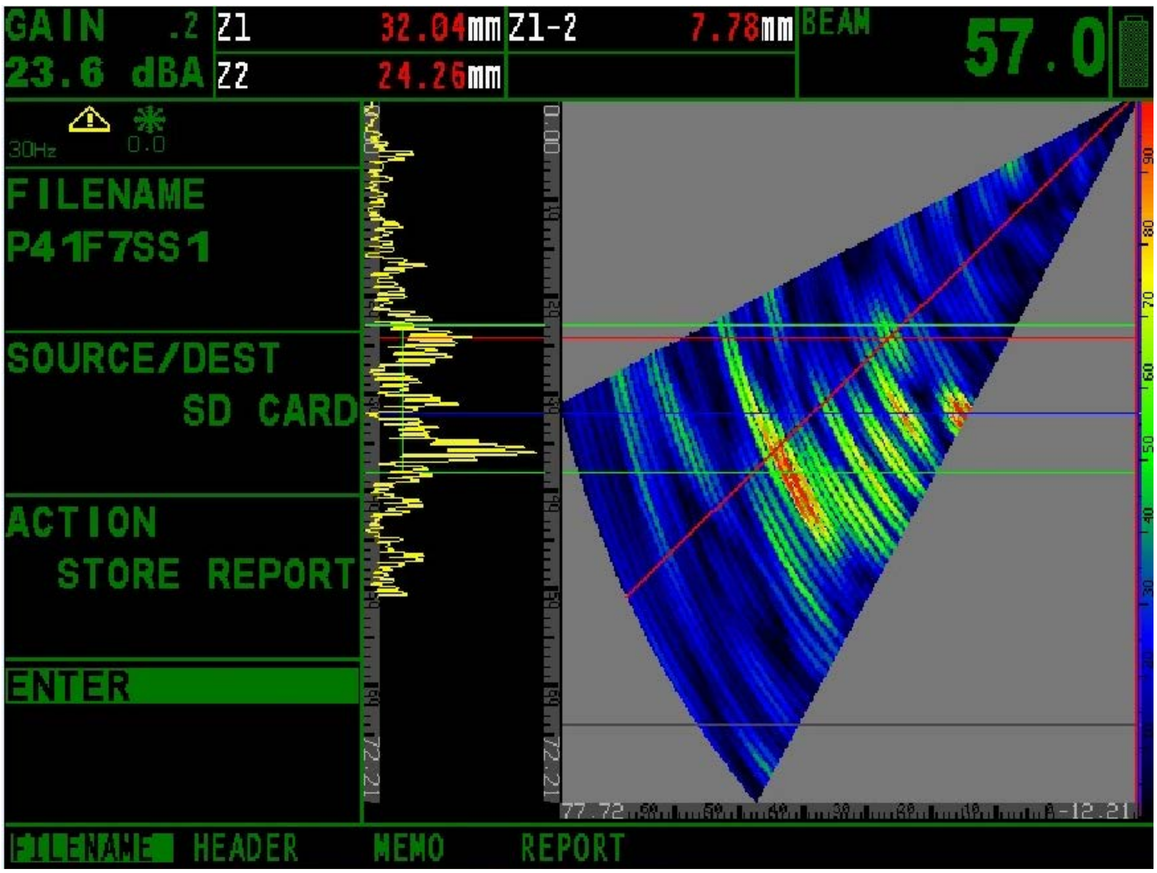

Very hard to find the tip for depth sizing, only possible if inspector knows in witch depth region he has to look for tips; flaw depth estimation procedure: if flaw is seen with high angles in the Sscan and there is a quiet strong TLL reflection it indicates that flaw has at least some true wall extension (20-40%); delta to as built depth may result from beam redirection in heterogeneous anisotropic weld material.

Figure B.129.

Flaw 9 / Probe Position: Stainless Side / Beam Direction: +Y

Flaw No.:	As Built Information (SQC Drawing)					Measurement Results					Remarks	UT Analysis Section	Cal Sheet No:
	Flaw X Position OD			Flaw Depth	Flaw Y Pos.	Flaw X Position OD			Flaw Depth	Flaw Y Pos.			
	Start	Length	End			Start	Length	End					
	mm	mm	mm	mm		mm	mm	mm	mm				
9	574.0	64.4	638.5	17	CS* B**	578	67	645	14.7	-Y	3)	4.9	4

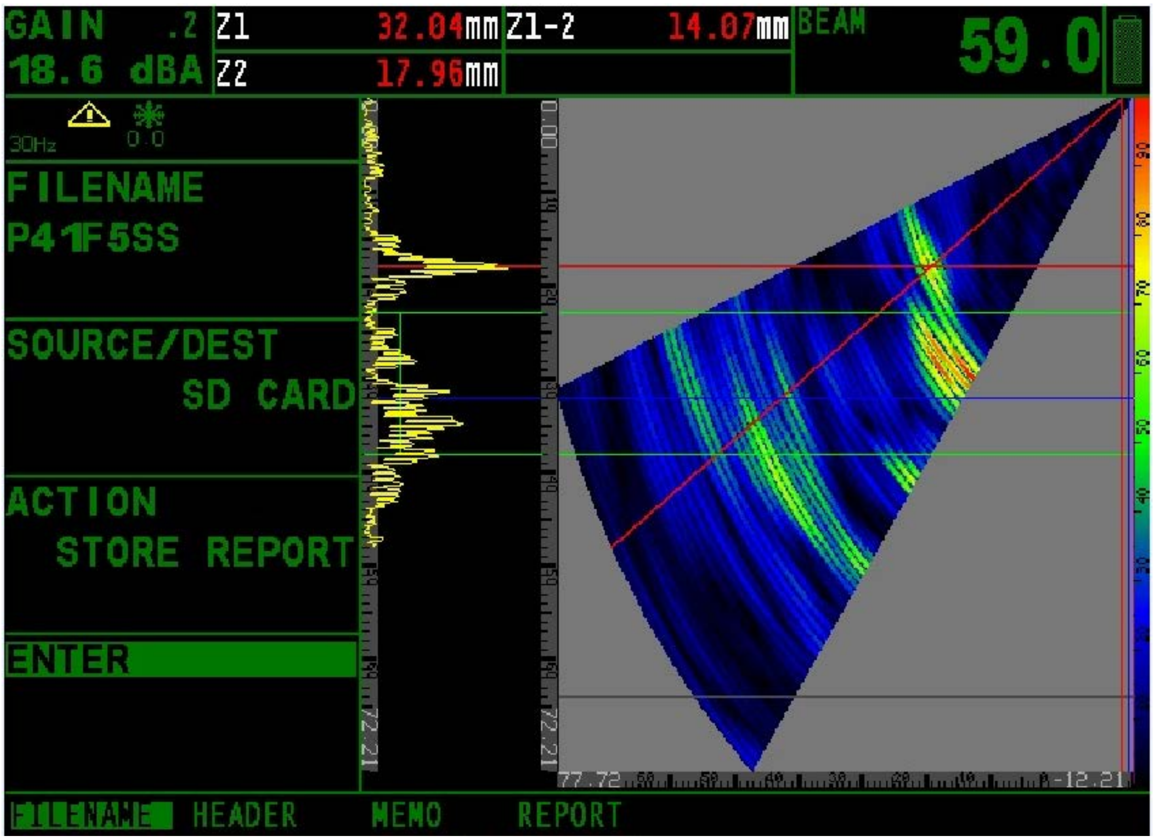

For quantitative flaw depth sizing calibration at 12 mm deep notch of calibration block KKM_24_18_12_6 (RL = 18 mm), delta to as built depth may result from beam redirection in heterogeneous anisotropic weld material

Remarks: File name in picture not correct (coordinate system problem), file name has been renamed correctly during analysis

Figure B.130.

Flaw 12 / Probe Position: Stainless Side / Beam Direction: +Y

Flaw No.:	As Built Information (SQC Drawing)					Measurement Results					Remarks	UT Analysis Section	Cal Sheet No:
	Flaw X Position OD			Flaw Depth	Flaw Y Pos.	Flaw X Position OD			Flaw Depth	Flaw Y Pos.			
	Start	Length	End			Start	Length	End					
	mm	mm	mm	mm		mm	mm	mm	mm				
12	811.1	25.8	836.9	6	CS* B**	817	25	842	3.2	-Y	4)	4.10	3

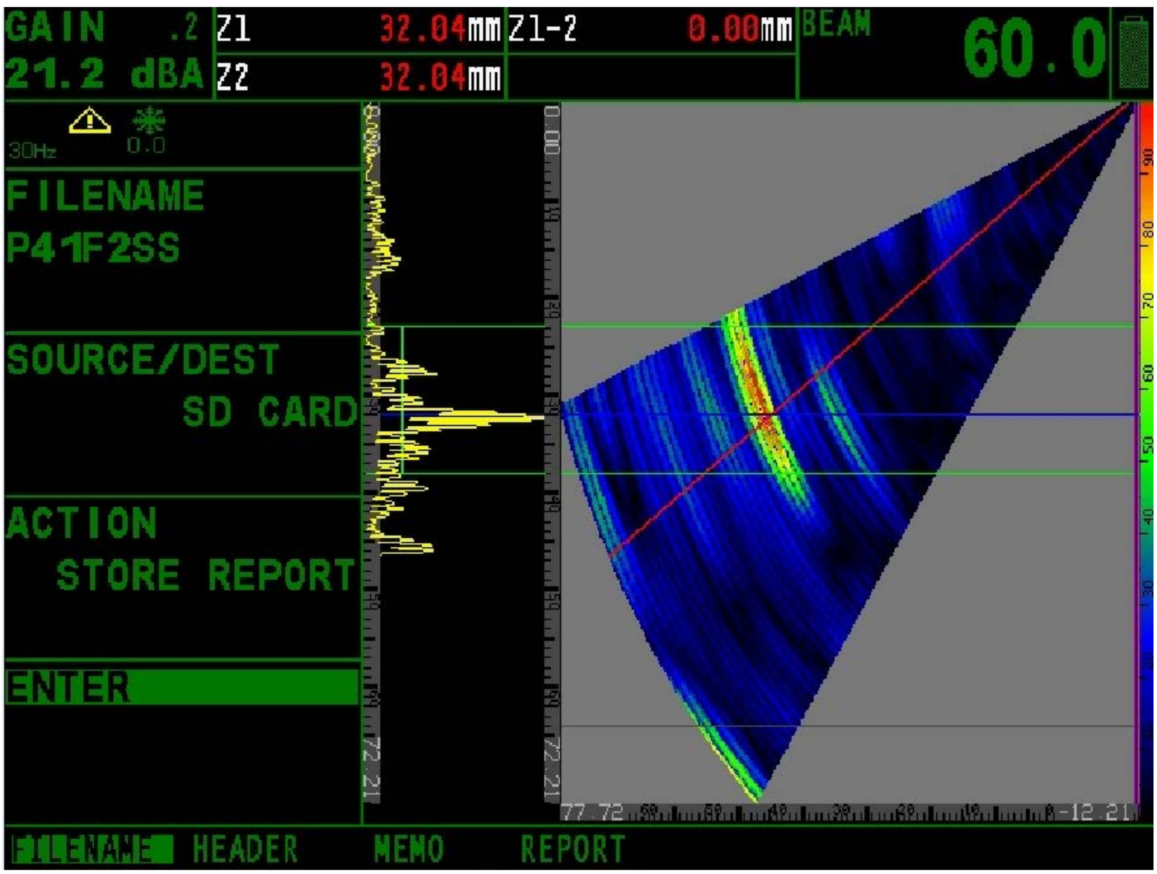

No separation of tip diffraction from corner trap echo, no TLL echo indicates shallow flaw, flaw depth estimation procedure: if no separation of tip diffraction from corner trap and flaw seems to be shallow the flaw depth is defined per default to 10% pipe thickness at flaw position → 3.2 mm

Remarks: File name in picture not correct (coordinate system problem), file name has been renamed correctly during analysis

Figure B.131.

Flaw 3 / Scan Direction: + X

Flaw No.:	As Built Information (SQC Drawing)				Measurement Results				Remarks	UT Analysis Section	Cal Sheet No:
	Flaw X Position OD	Length	Flaw Depth	Flaw Y Pos.	Flaw X Position OD	Length	Flaw Depth	Flaw Y Pos.			
	mm	mm	mm		mm	mm	mm				
3	135	10	2	CS* B**	135	≈ 10	3.2	-Y	1)	4.9	

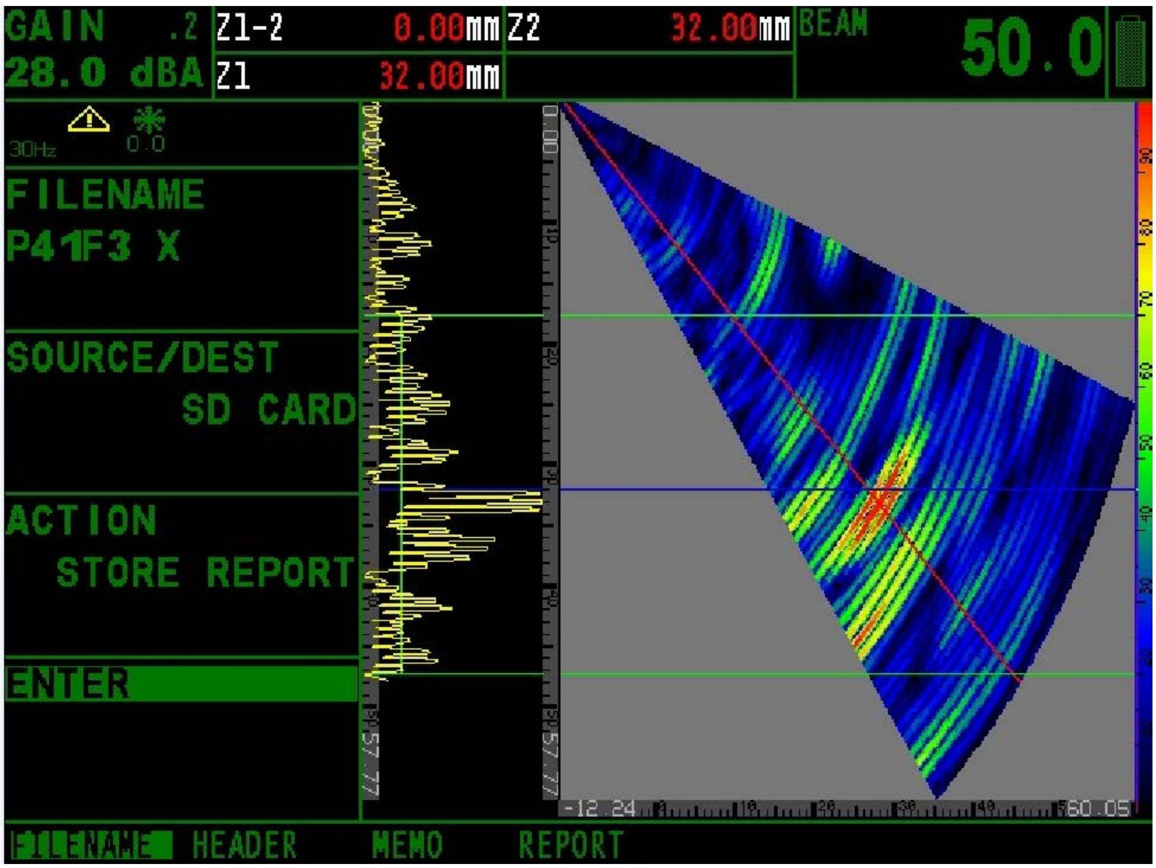

Very hard to detect with manual inspection; length sizing hard lots of noise from buttering; no separation of tip diffraction from corner trap echo, no TLL echo indicates shallow flaw, flaw depth estimation procedure: if no separation of tip diffraction from corner trap and flaw seems to be shallow the flaw depth is defined per default to 10% pipe thickness at flaw position → 3.2 mm.

Figure B.132.

Flaw 4 / Scan Direction: + X

Flaw No.:	As Built Information (SQC Drawing)				Measurement Results				Remarks	UT Analysis Section	Cal Sheet No:
	Flaw X Position OD	Length	Flaw Depth	Flaw Y Pos.	Flaw X Position OD	Length	Flaw Depth	Flaw Y Pos.			
	mm	mm	mm		mm	mm	mm				
4	193	6	3	CS* B**	195	≈ 6		-Y	2)		

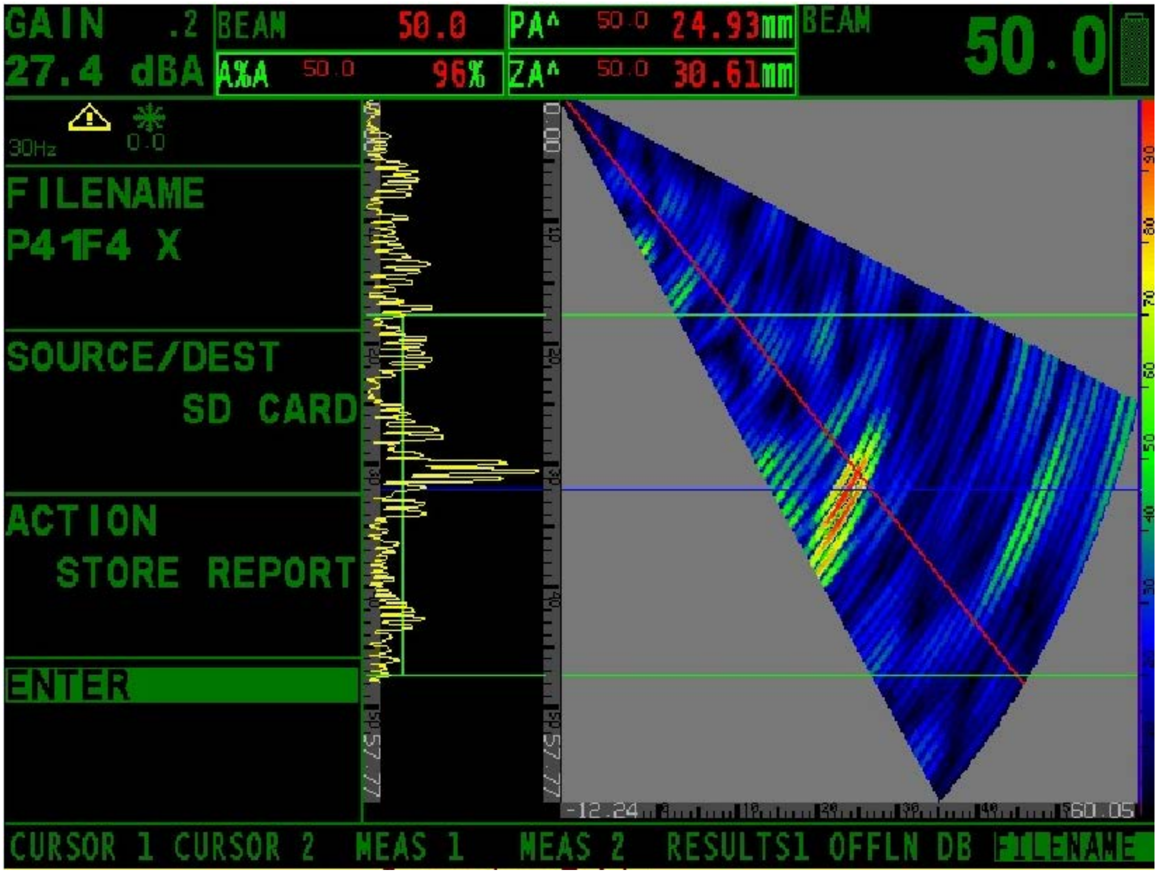

Hard to detect with manual inspection; length sizing hard lots of noise from buttering; no separation of tip diffraction from corner trap echo, no TLL echo indicates shallow flaw, flaw depth estimation procedure: if no separation of tip diffraction from corner trap and flaw seems to be shallow the flaw depth is defined per default to 10% pipe thickness at flaw position → 3.2 mm.

Figure B.133.

Flaw 6 / Scan Direction: + X

Flaw No.:	As Built Information (SQC Drawing)				Measurement Results				Remarks	UT Analysis Section	Cal Sheet No:
	Flaw X Position OD	Length	Flaw Depth	Flaw Y Pos.	Flaw X Position OD	Length	Flaw Depth	Flaw Y Pos.			
	mm	mm	mm		mm	mm	mm				
6	374	20	26	CS* B**	370	≈ 30	26.02	-Y	3)	4.13	4

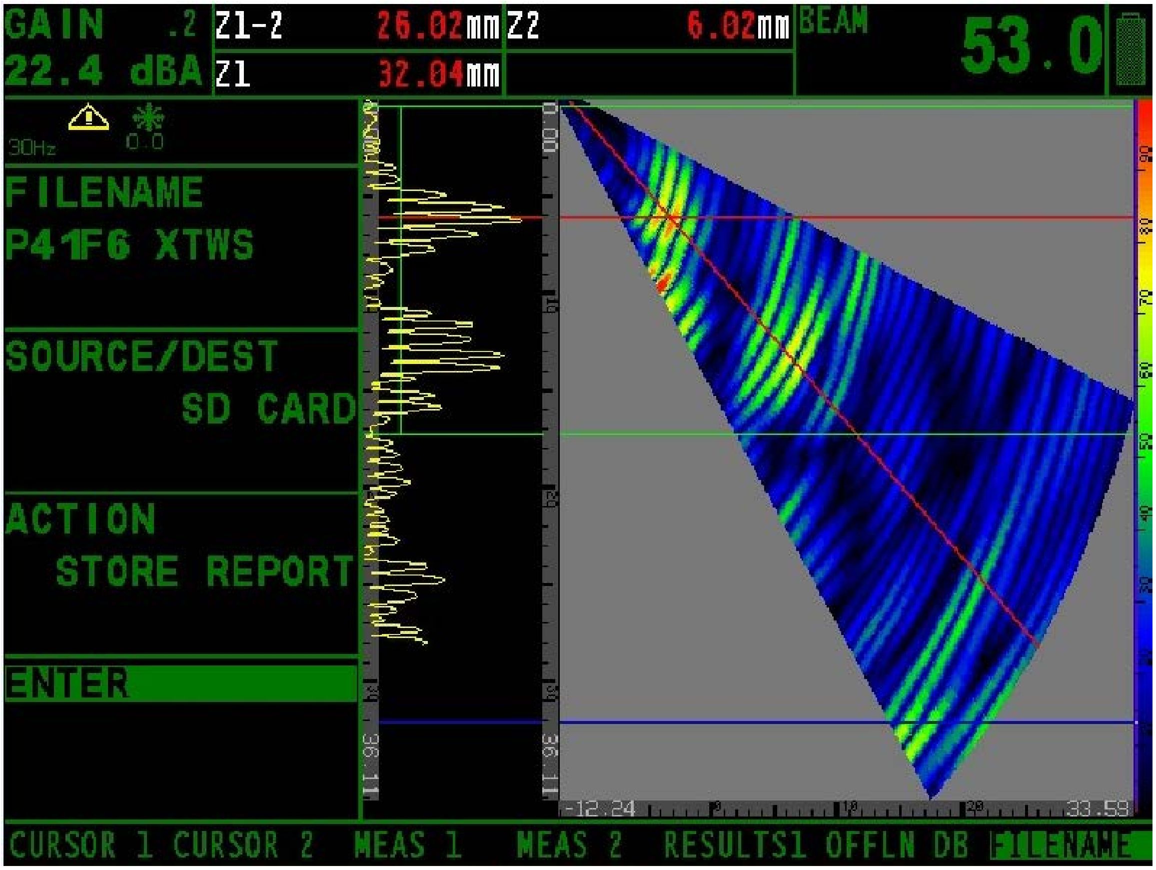

Length sizing hard lots of noise from buttering; for quantitative flaw depth sizing calibration with 9 mm deep SDH (Ø 1,5 mm) of calibration block “SVTI AS_D270_T30”

Figure B.134.

Flaw 8 / Scan Direction: + X

Flaw No.:	As Built Information (SQC Drawing)				Measurement Results				Remarks	UT Analysis Section	Cal Sheet No:
	Flaw X Position OD	Length	Flaw Depth	Flaw Y Pos.	Flaw X Position OD	Length	Flaw Depth	Flaw Y Pos.			
	mm	mm	mm		mm	mm	mm				
8	515	20	6	CS* B**	515	≈ 25	6.07	-Y	4)	4.14	5

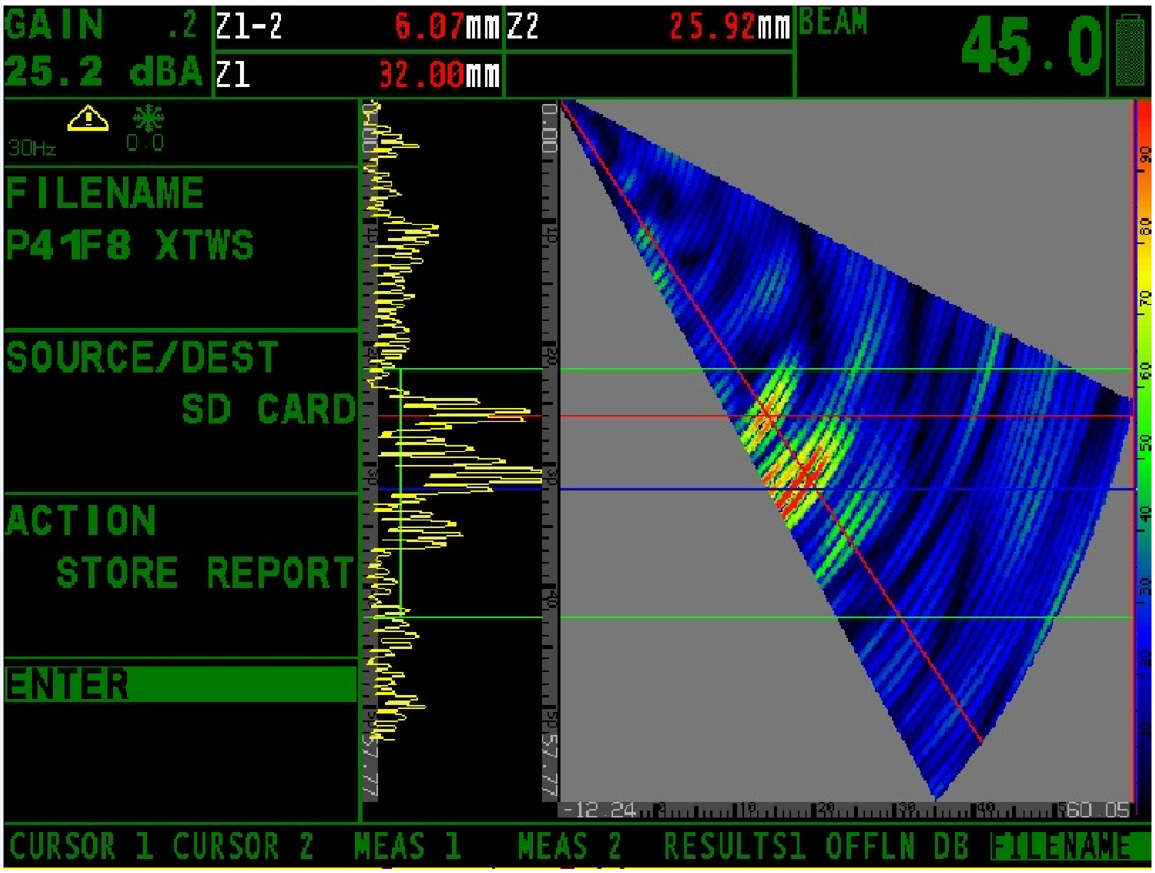

Length sizing hard lots of noise from buttering; depth sizing only possible when probe is skewed (flaw skew angle 10°); for quantitative flaw depth sizing calibration with 26 mm deep SDH (Ø 1,5 mm) of calibration block “SVTI AS_D270_T30”

Figure B.135.

Flaw 10 / Scan Direction: + X

Flaw No.:	As Built Information (SQC Drawing)				Measurement Results				Remarks	UT Analysis Section	Cal Sheet No:
	Flaw X Position OD	Length	Flaw Depth	Flaw Y Pos.	Flaw X Position OD	Length	Flaw Depth	Flaw Y Pos.			
	mm	mm	mm		mm	mm	mm				
10	696	20	17	CS* B**	698	20	16.74	-Y	5)	4.15	6

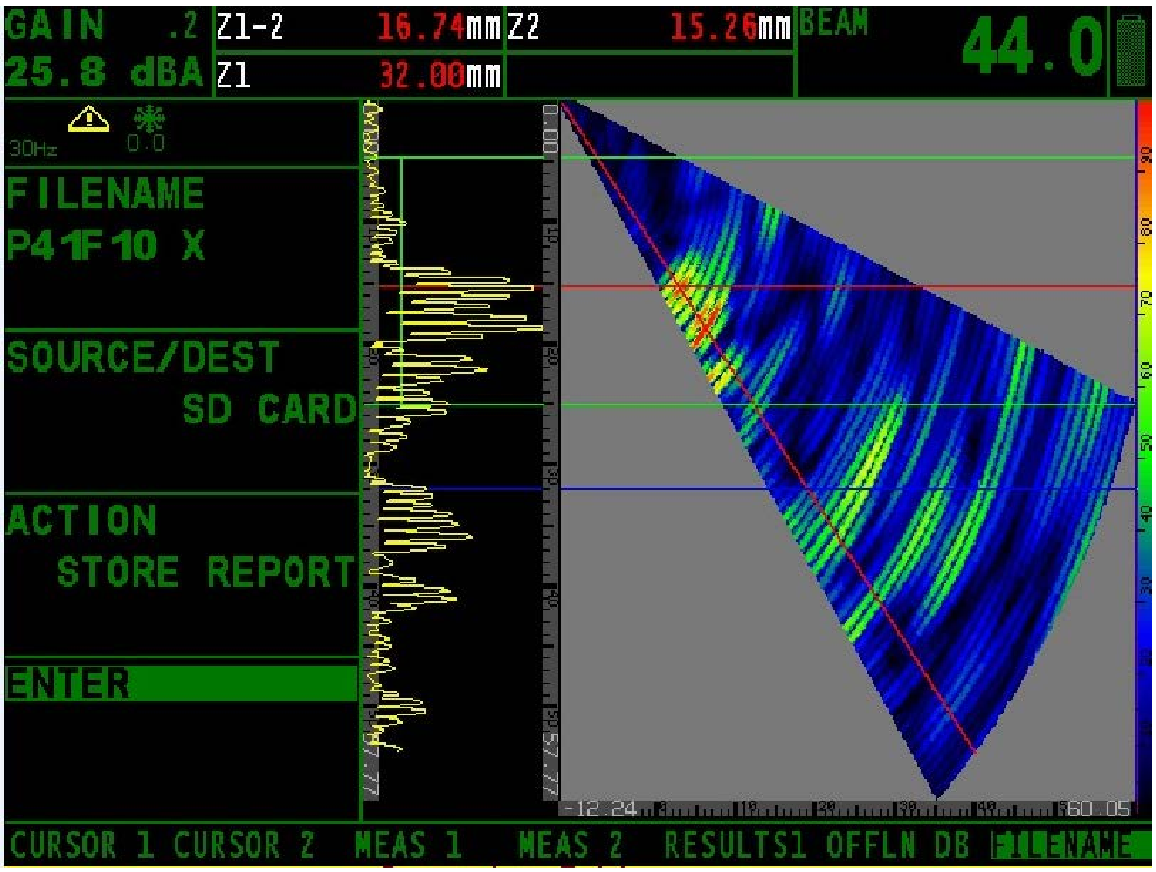

Quantitative flaw depth sizing calibration with 15 mm deep SDH (Ø 1,5 mm) of calibration block “SVTI AS_D270_T30”

Figure B.136.

Flaw 11 / Scan Direction: + X

Flaw No.:	As Built Information (SQC Drawing)				Measurement Results				Remarks	UT Analysis Section	Cal Sheet No:
	Flaw X Position OD	Length	Flaw Depth	Flaw Y Pos.	Flaw X Position OD	Length	Flaw Depth	Flaw Y Pos.			
	mm	mm	mm		mm	mm	mm				
11	754	20	6	CS* B**	750	20	6.67	-Y	6)	4.16	5

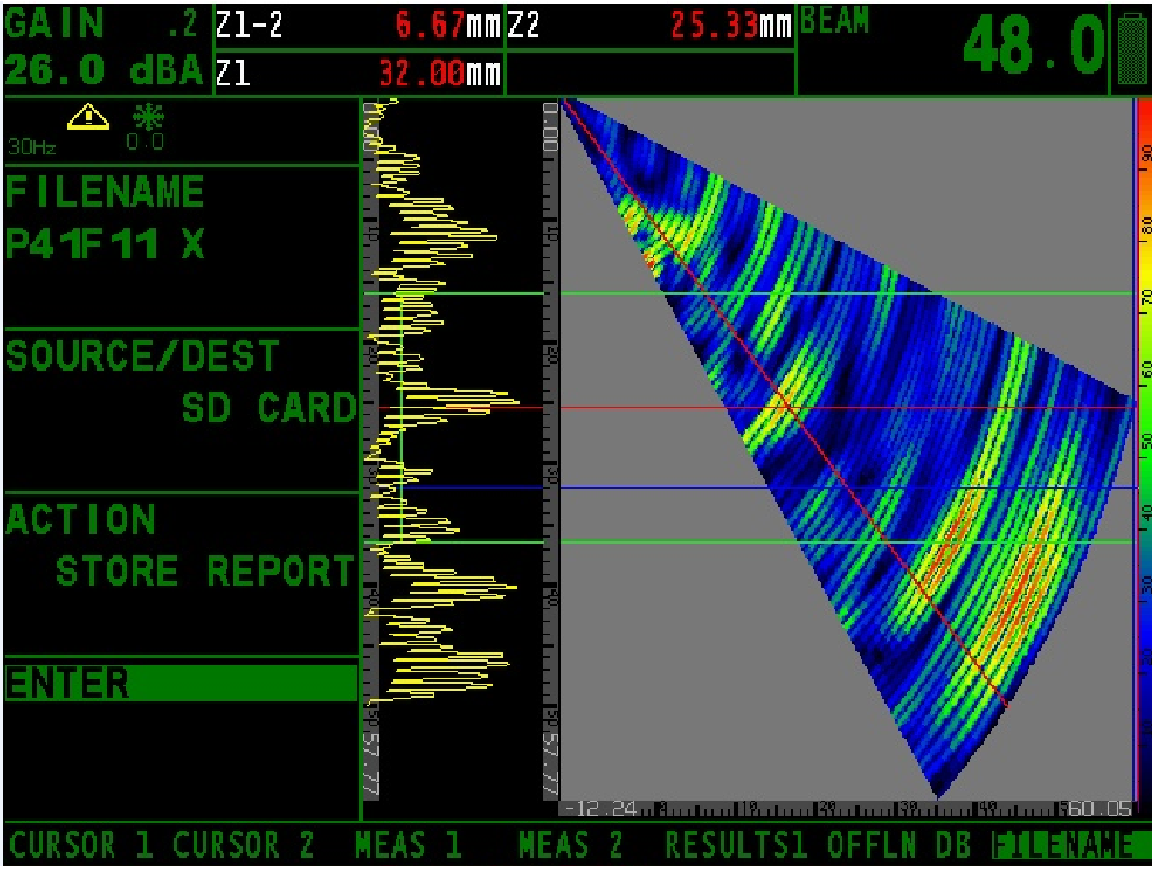

Flaw depth sizing hard, very week tip signal; quantitative flaw depth sizing calibration with 26 mm deep SDH (Ø 1,5 mm) of calibration block “SVTI AS_D270_T30”

Figure B.137.

Flaw 3 / Scan Direction: - X

Flaw No.:	As Built Information (SQC Drawing)				Measurement Results				Remarks	UT Analysis Section	Cal Sheet No:
	Flaw X Position OD	Length	Flaw Depth	Flaw Y Pos.	Flaw X Position OD	Length	Flaw Depth	Flaw Y Pos.			
	mm	mm	mm		mm	mm	mm				
3	135	10	2	CS* B**	135	≈ 10	3.2	-Y	1)		

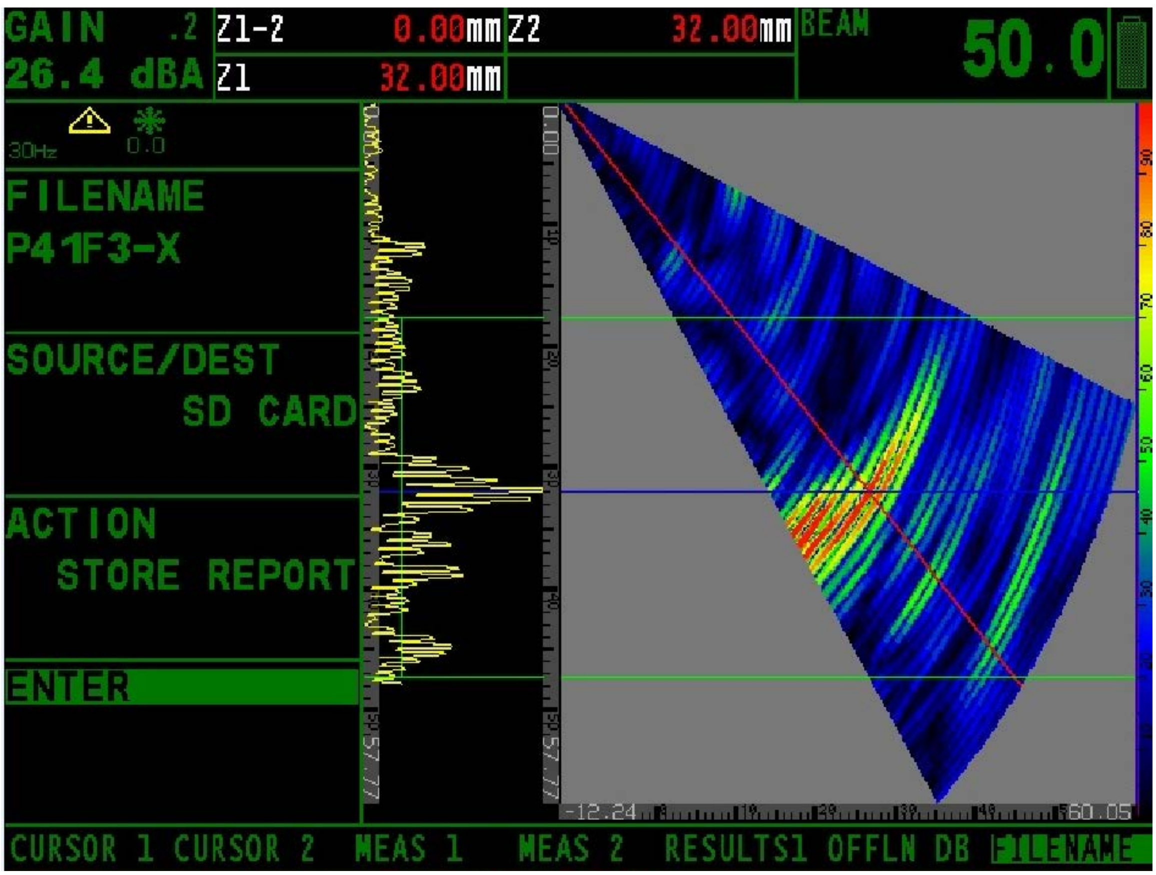

Very hard to detect with manual inspection; length sizing hard lots of noise from buttering; no separation of tip diffraction from corner trap echo, no TLL echo indicates shallow flaw, flaw depth estimation procedure: if no separation of tip diffraction from corner trap and flaw seems to be shallow the flaw depth is defined per default to 10% pipe thickness at flaw position → 3.2 mm

Figure B.138.

Flaw 4 / Scan Direction: - X

Flaw No.:	As Built Information (SQC Drawing)				Measurement Results				Remarks	UT Analysis Section	Cal Sheet No:
	Flaw X Position OD	Length	Flaw Depth	Flaw Y Pos.	Flaw X Position OD	Length	Flaw Depth	Flaw Y Pos.			
	mm	mm	mm		mm	mm	mm				
4	193	6	3	CS* B**	195	≈ 6		-Y	2)		

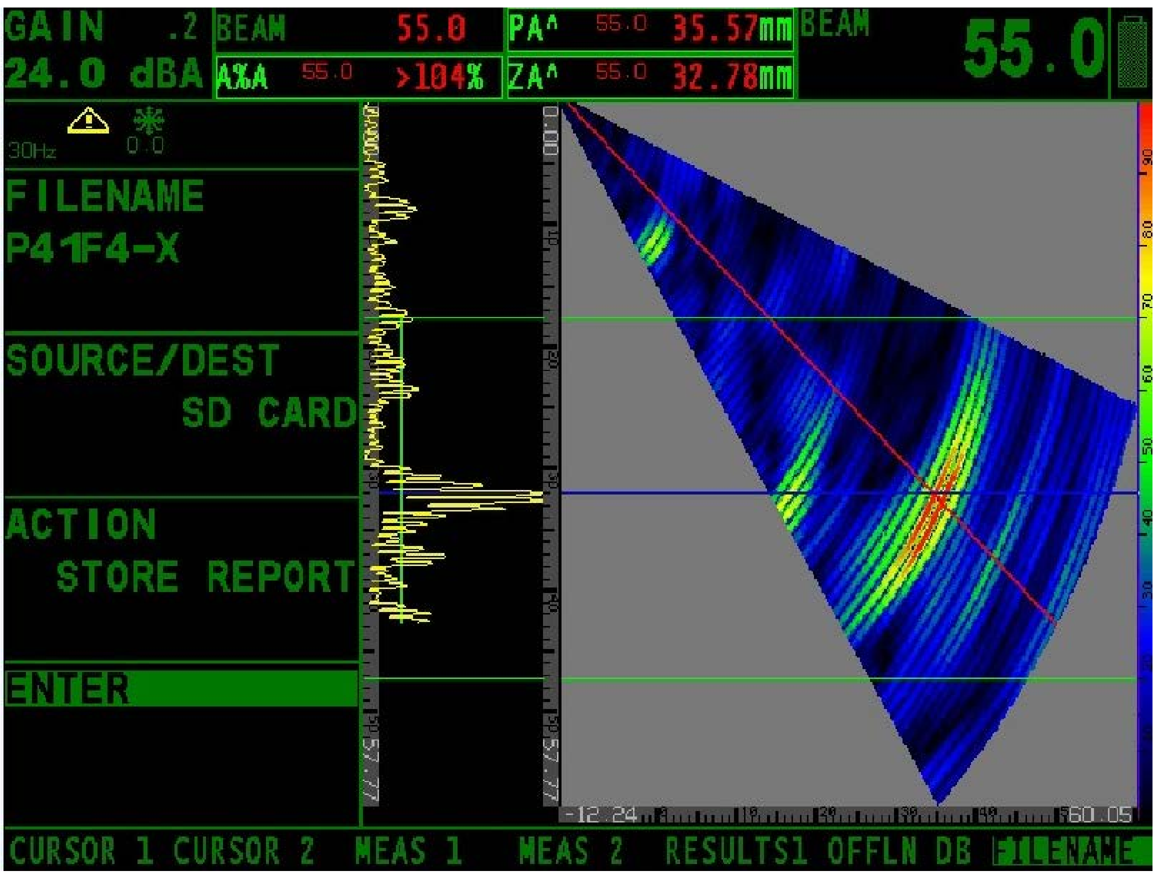

Hard to detect with manual inspection; length sizing hard lots of noise from buttering; no separation of tip diffraction from corner trap echo, no TLL echo indicates shallow flaw, flaw depth estimation procedure: if no separation of tip diffraction from corner trap and flaw seems to be shallow the flaw depth is defined per default to 10% pipe thickness at flaw position → 3.2 mm

Figure B.139.

Flaw 6 / Scan Direction: - X

Flaw No.:	As Built Information (SQC Drawing)				Measurement Results				Remarks	UT Analysis Section	Cal Sheet No:
	Flaw X Position OD	Length	Flaw Depth	Flaw Y Pos.	Flaw X Position OD	Length	Flaw Depth	Flaw Y Pos.			
	mm	mm	mm		mm	mm	mm				
6	374	20	26	CS* B**	370	≈ 20	26.48	-Y	3)		4

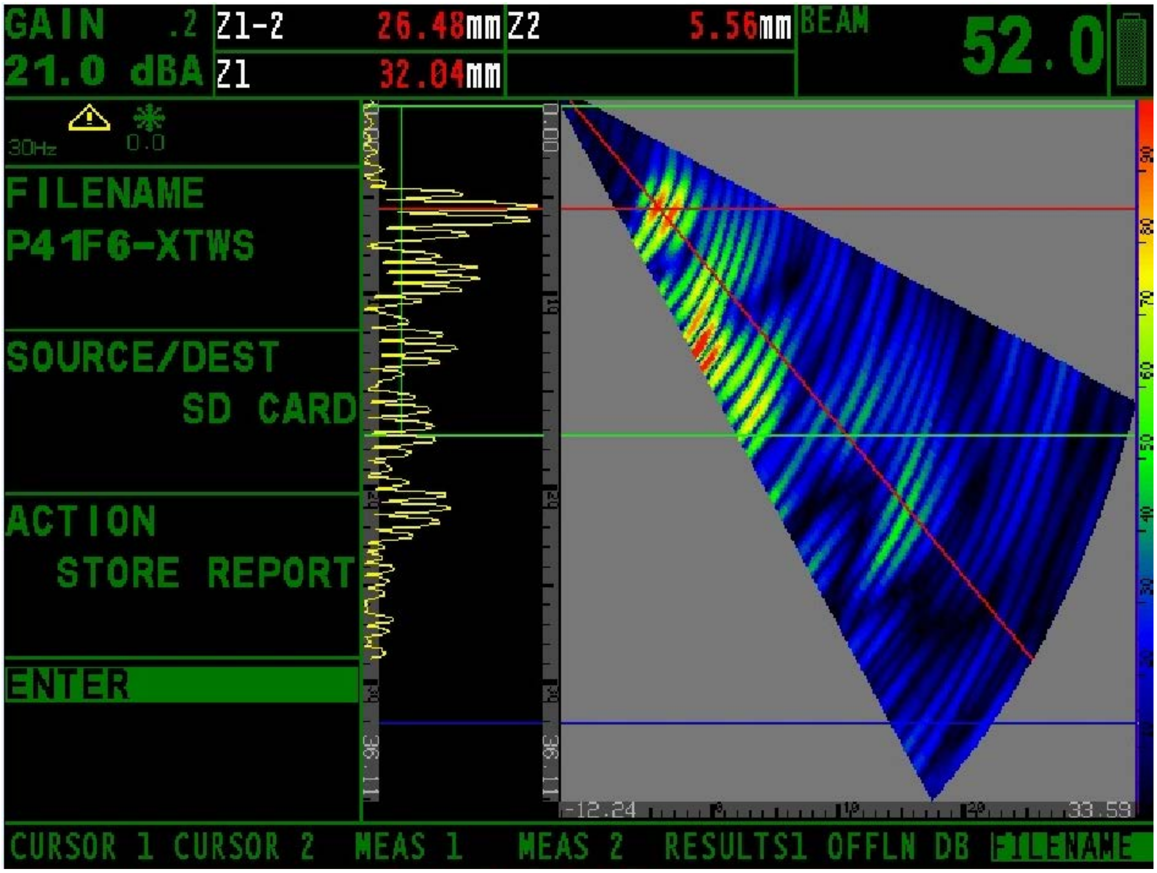

Length sizing hard lots of noise from buttering; for quantitative flaw depth sizing calibration with 9 mm deep SDH (Ø 1,5 mm) of calibration block “SVTI AS_D270_T30”

Figure B.140.

Flaw 8 / Scan Direction: - X

Flaw No.:	As Built Information (SQC Drawing)				Measurement Results				Remarks	UT Analysis Section	Cal Sheet No:
	Flaw X Position OD	Length	Flaw Depth	Flaw Y Pos.	Flaw X Position OD	Length	Flaw Depth	Flaw Y Pos.			
	mm	mm	mm		mm	mm	mm				
8	515	20	6	CS* B**	515	≈ 25	6.81	-Y	4)		5

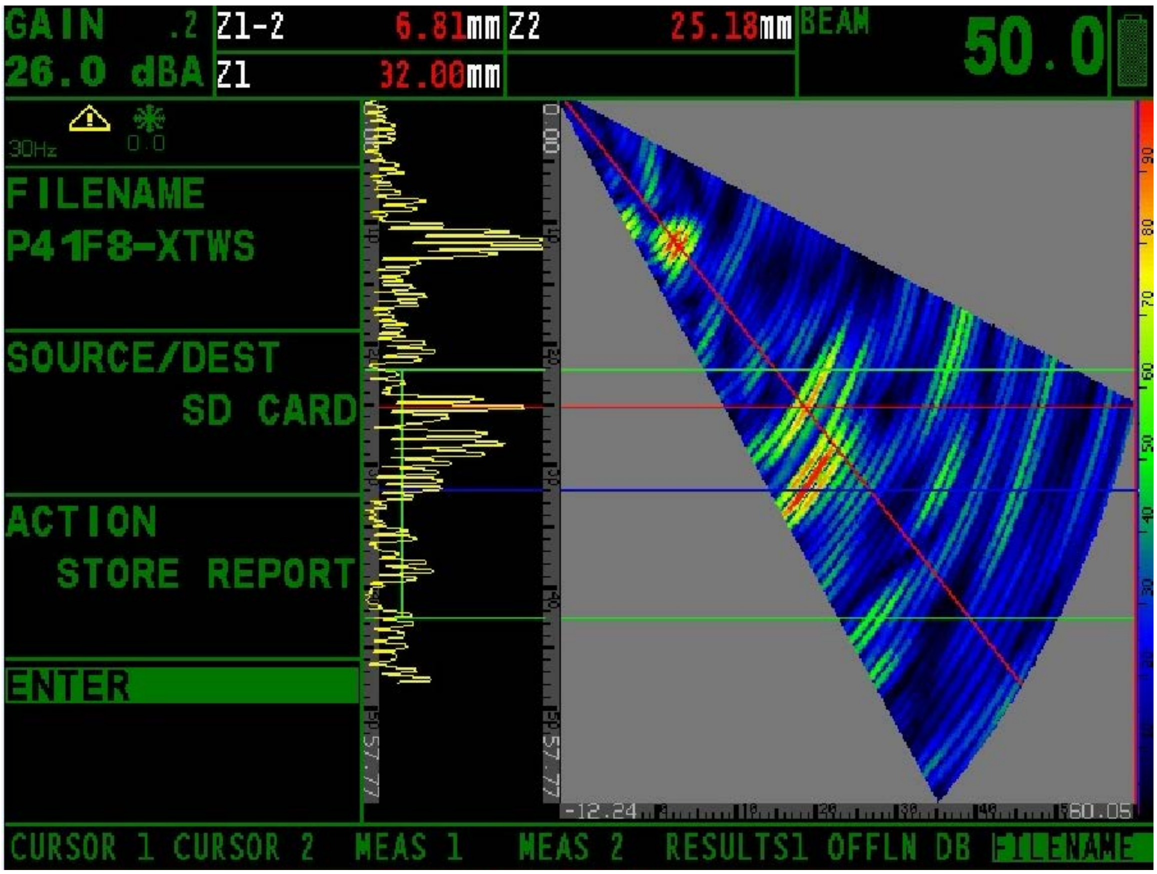

Length sizing hard lots of noise from buttering; depth sizing hard only possible when probe is skewed (flaw skew angle 10°); for quantitative flaw depth sizing calibration with 26 mm deep SDH (Ø 1,5 mm) of calibration block “SVTI AS_D270_T30”

Figure B.141.

Flaw 10 / Scan Direction: - X

Flaw No.:	As Built Information (SQC Drawing)				Measurement Results				Remarks	UT Analysis Section	Cal Sheet No:
	Flaw X Position OD	Length	Flaw Depth	Flaw Y Pos.	Flaw X Position OD	Length	Flaw Depth	Flaw Y Pos.			
	mm	mm	mm		mm	mm	mm				
10	696	20	17	CS* B**	698	≈ 25	16.74	-Y	5)		

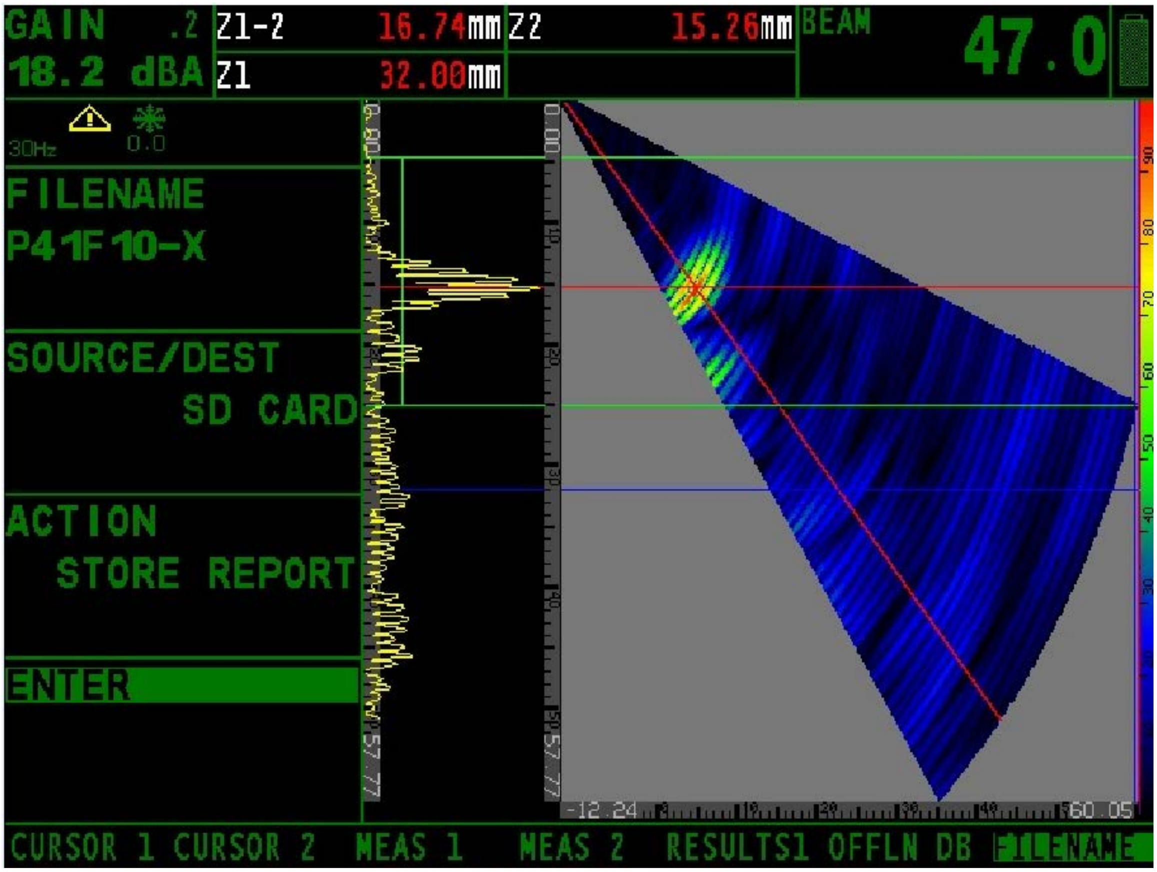

Quantitative flaw depth sizing calibration with 15 mm deep SDH (Ø 1,5 mm) of calibration block "SVTI AS_D270_T30"

Figure B.142.

Flaw 11 / Scan Direction: - X

Flaw No.:	As Built Information (SQC Drawing)				Measurement Results				Remarks	UT Analysis Section	Cal Sheet No:
	Flaw X Position OD	Length	Flaw Depth	Flaw Y Pos.	Flaw X Position OD	Length	Flaw Depth	Flaw Y Pos.			
	mm	mm	mm		mm	mm	mm				
11	754	20	6	CS* B**	750	20	6.37	-Y	6)		

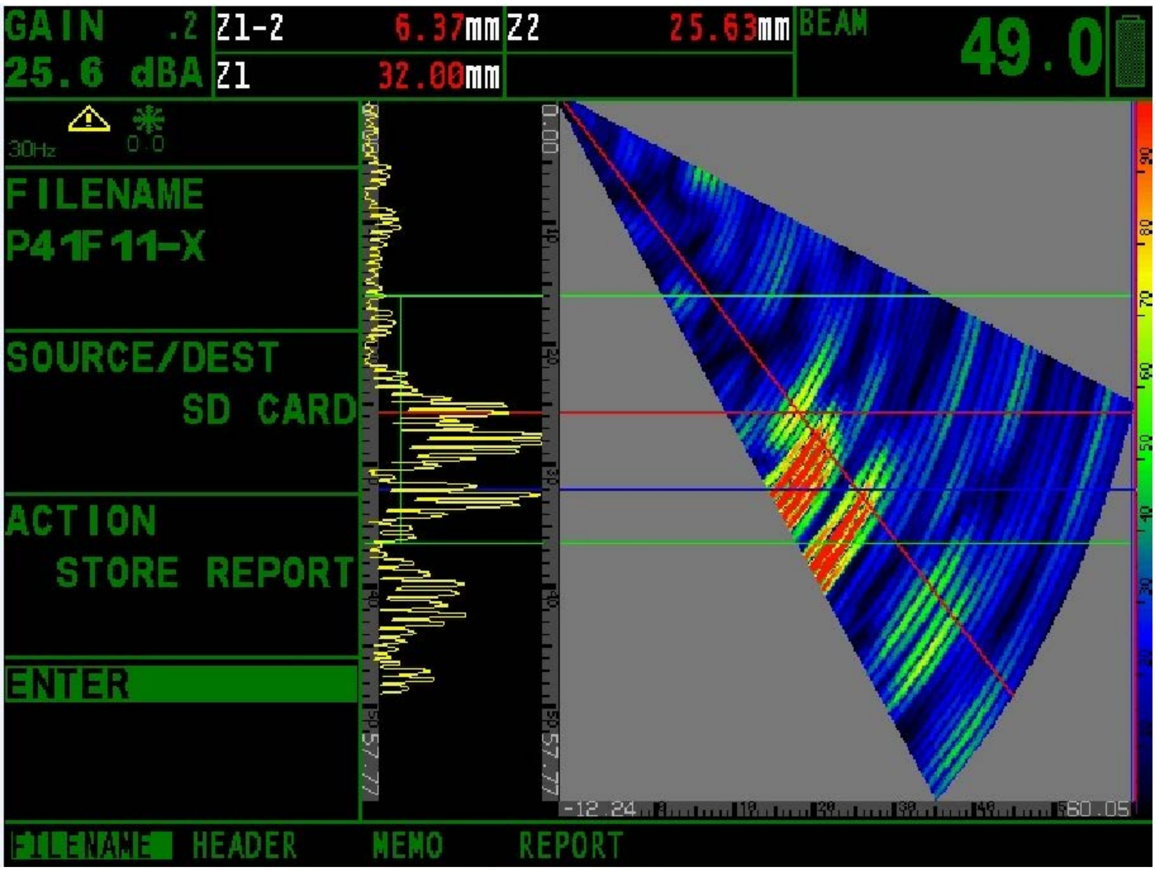

Flaw depth sizing good, good tip signal; quantitative flaw depth sizing calibration with 26 mm deep SDH (Ø 1,5 mm) of calibration block “SVTI AS_D270_T30”

Figure B.143.

B.5.6 Self Assessment

The manual Phased Array Technique using a dual matrix search unit and longitudinal waves in the range from 40° to 70° demonstrated good detection, length sizing and TWS performance of ID flaws with depth greater than 10% of the wall thickness.

B.6 Computer Tomography, Technique ID 109-CT0

B.6.1 Assignment of Task

Analysis of crack depth in weld of PARENT Test Blocks by means of X-ray computed tomography according procedure elaborated for Sample P32.

B.6.2 Test Objects

Test object	PARENT Test Block
Material	Base metal: 22 NiMoCr 3 7 (SA 508 Class 2) Weld: Alloy 182
Dimensions [mm]	ca. 35 x 30.3 x 220
Weight [kg]	1.84 kg
Fixation on CT-scanner	double sided adhesive tape

Photo of test object on CT-scanner:

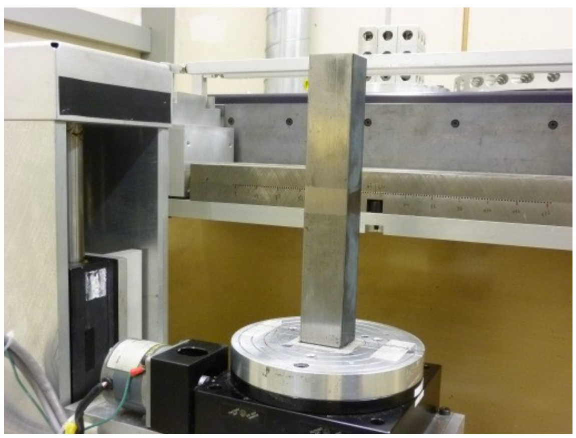

Figure B.144. Test Block ID: P32 (N 220 AD U TS 5), view from X-ray source towards the line detector. The sample is oriented such that the crack opening is located on the side of the X-ray source.

B.6.3 Parameters for Data Acquisition

CT-Scanner	CITA 101 B+ (Cita Systems)
Beam geometry	Fan beam
X-ray source	X-ray system MG452 (YTU450-D09)
Parameters of X-ray source	450 kV / 3.3 mA / 1.0 mm focal spot
External X-ray filtration	1.5 mm Brass
Detector	Single collimated (W) line detector (CdWO4) with 125 detector channels
Detector aperture [mm]	0.35 x 0.15
Manipulator position	16
Pixel size of CT-slice [mm]	0.12 x 0.12
Slice distance [mm]	0.12
Object diameter [mm]	60
Ray Spacing [mm]	0.18
Integration time [ms]	100
Beam hardening correction	1.5

B.6.3.1 Specific Parameters

Test Block ID	**P28**	**P29**	**P30**	**P31**	**P32**	**P38**
Number of slices	39	32	25	30	41	40
Z position of 1st slice [mm]	109.68	110.64	106.80	106.80	108.36	106.80
Vertical scanning range [mm]	4.56	3.72	2.88	3.48	4.80	4.68

B.6.4 Analysis of Crack Depth

Test Block ID	**P28**	**P29**	**P30**	**P31**	**P32**	**P38**
Slice # of max. crack depth	31	26	06	17	34	29
Z position of max. crack depth [mm]	113.28	113.64	107.40	108.72	112.32	110.16
Crack depth [mm]	14.0	13.0	17.8	3.9	11.3	4.4
Weld thickness [mm]	30.3	30.3	30.3	30.3	30.3	30.3
Crack depth in % of weld thickness	46.2	42.9	58.7	12.9	37.3	14.5

B.6.5 CT Images

Figure B.145 shows the CT-slices of the six test blocks in which the maximum crack depth is assumed. The crack depth is measured from the sample surface and is indicated in the CT-images. Figure B.146 shows a stack of 15 CT-slices per test block. Figure B.147 shows the 3D-CT visualisation of the six test blocks with VGStudioMax.

All CT-slices are available on the FTP server of EMPA as individual TIFF or 16 bit raw image files and as 3D-CT volumes in VGStudioMax format.

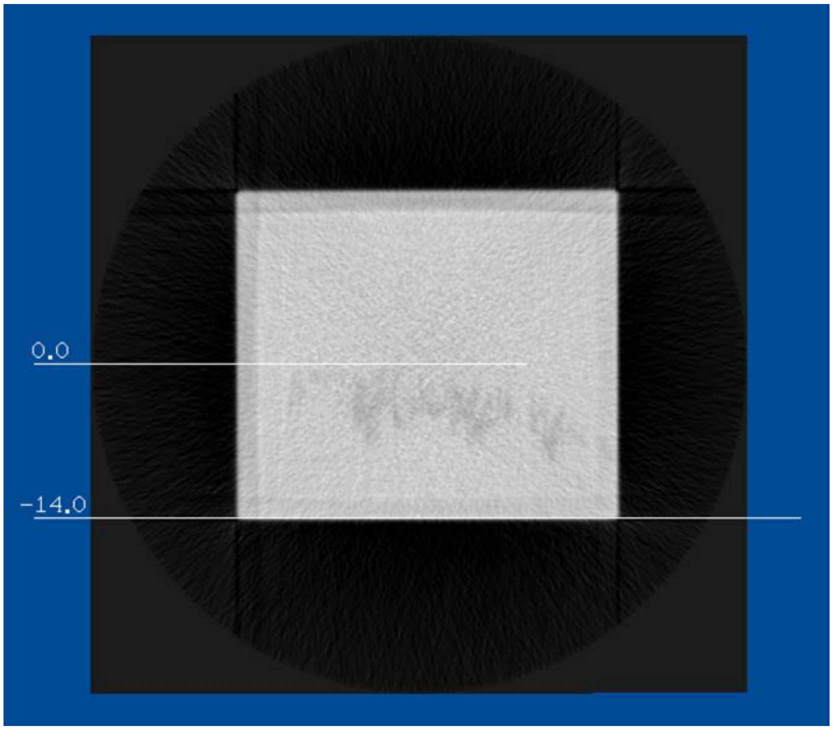

Figure B.145a. CT-slice #31 (z=113.28 mm) of test block P28 (N 220 AD U 6), crack depth: 14.0 mm (+/- 2 pixel = 0.24 mm), 46.2% of weld thickness

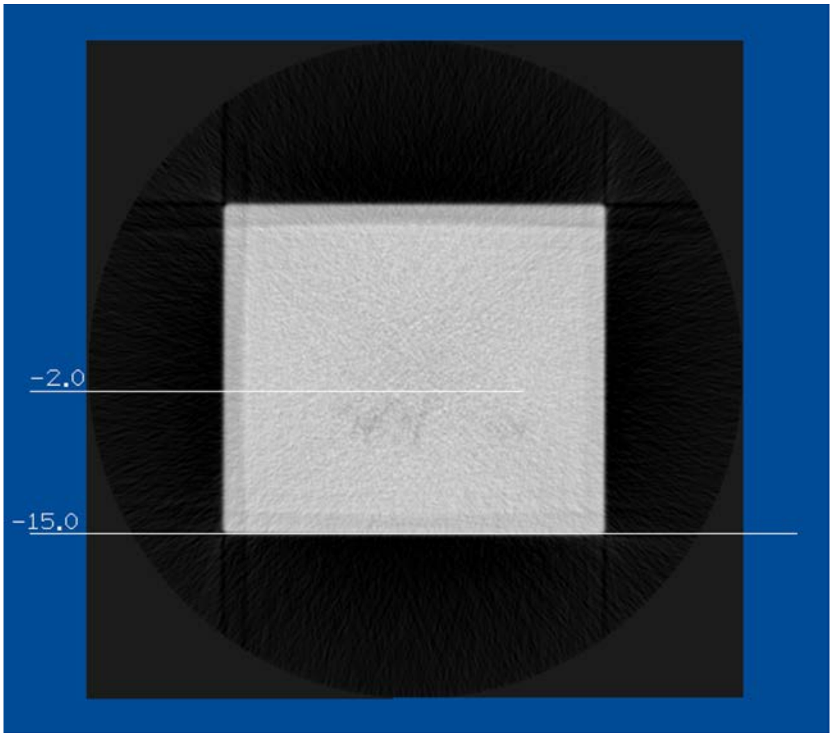

Figure B.145b. CT-slice #26 (z=113.64 mm) of test block P29 (N 220 AD U 10), crack depth: 13.0 mm (+/- 2 pixel = 0.24 mm), 42.9% of weld thickness

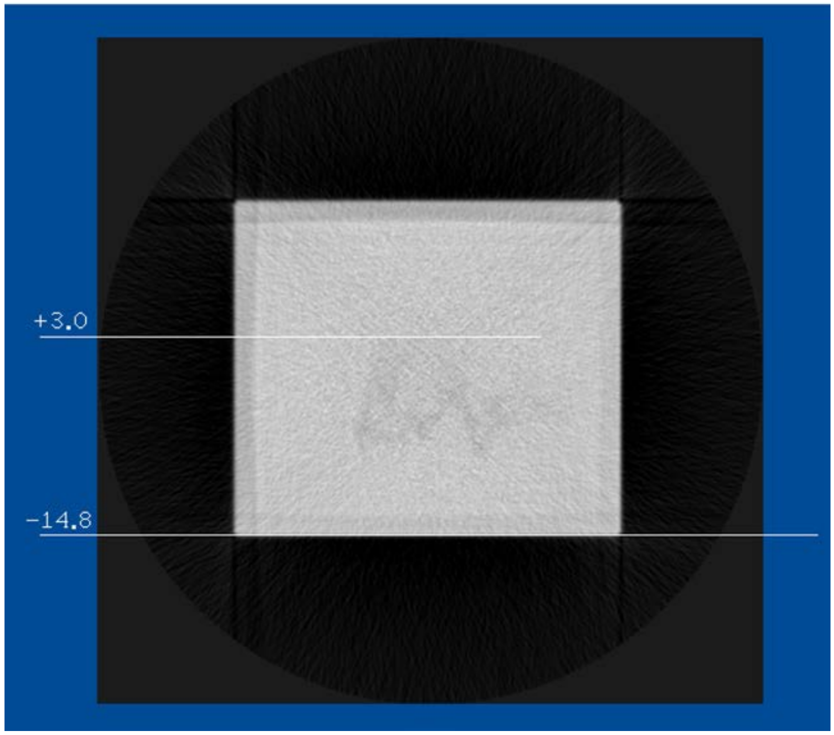

Figure B.145c. CT-slice #06 (z=107.40 mm) of test block P30 (N 220 AD U 7), crack depth: 17.8 mm (+/- 2 pixel = 0.24 mm), 58.7% of weld thickness

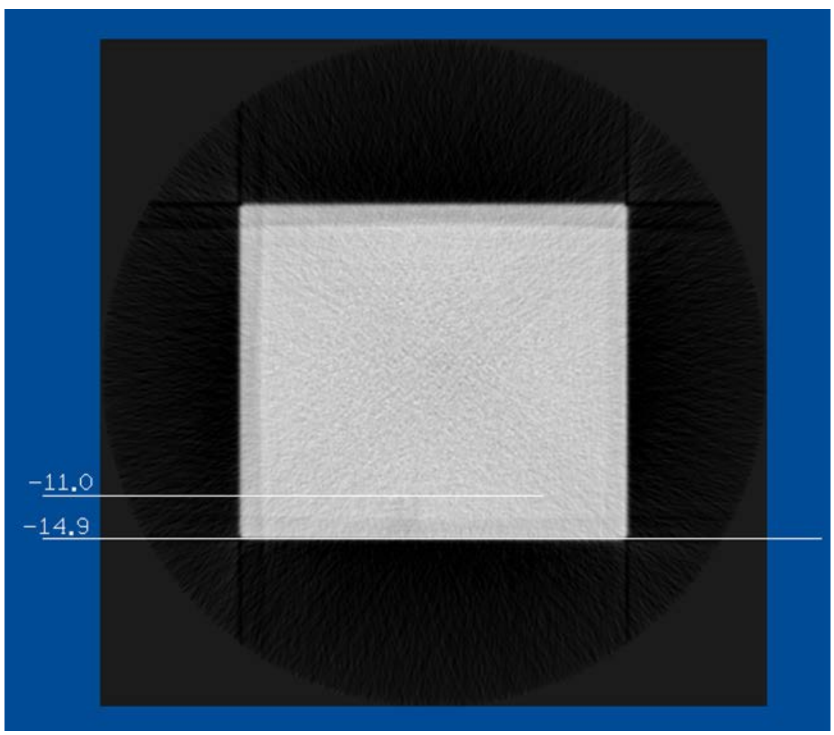

Figure B.145d. CT-slice #17 (z=108.72 mm) of test block P31 (MN 220 AD U 1), crack depth: 3.9 mm (+/- 2 pixel = 0.24 mm), 12.9% of weld thickness

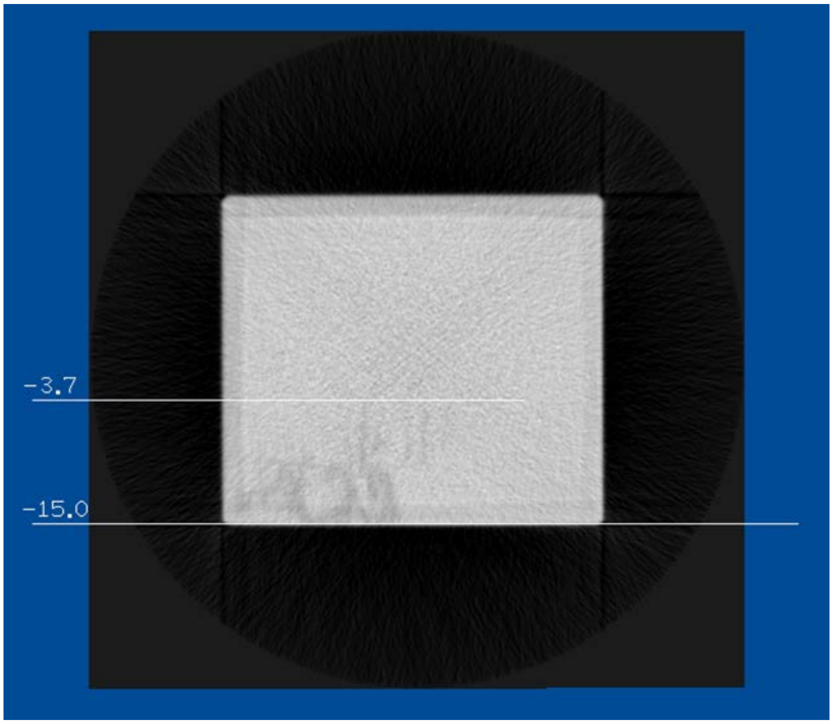

Figure B.145e. CT-slice #34 (z=112.32 mm) of test block P32 (N 220 AD U TS 5), crack depth: 11.3 mm (+/- 2 pixel = 0.24 mm), 37.3% of weld thickness

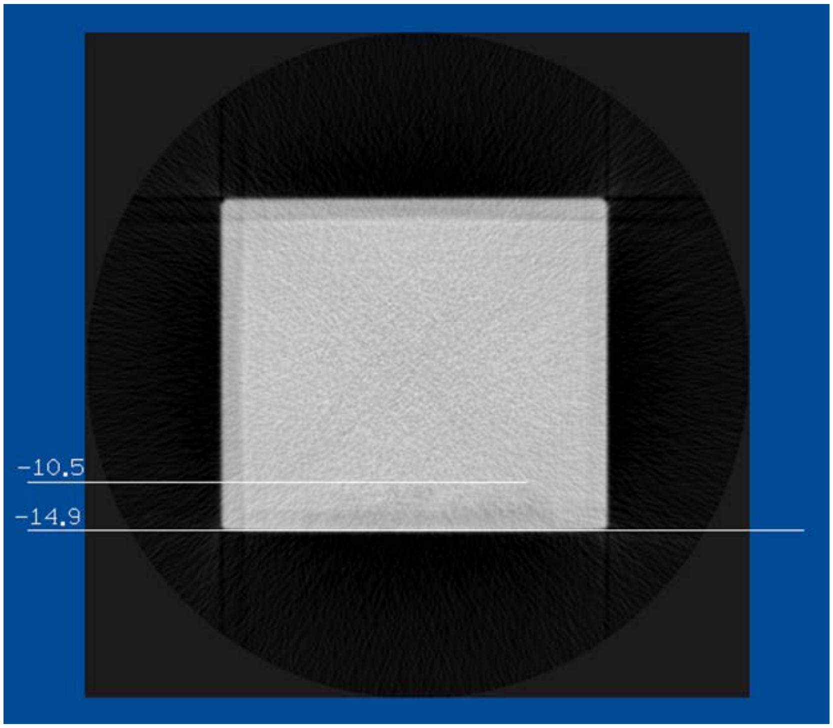

Figure B.145f. CT-slice #29 (z=110.16 mm) of test block P38 (N 220 AD U TS 3), crack depth: 4.4 mm (+/- 2 pixel = 0.24 mm), 14.5% of weld thickness

B.6.5.1 Test Block P28 (N 220 AD U 6)

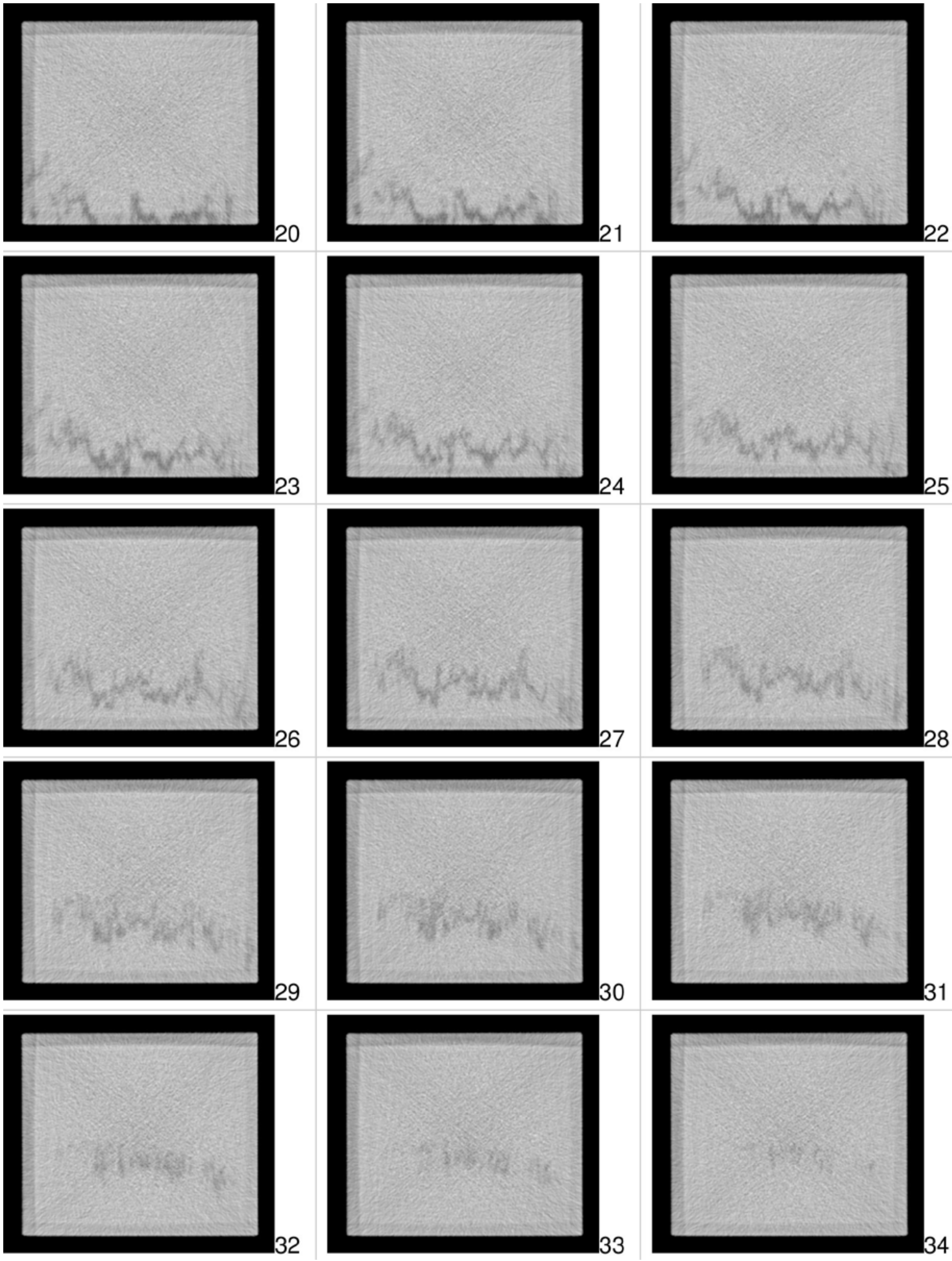

Figure B.146a. 15 CT-slices in stack of 39, starting with slice #20 and ending with #34

B.6.5.2 Test Block ID P29 (N 220 AD U 10)

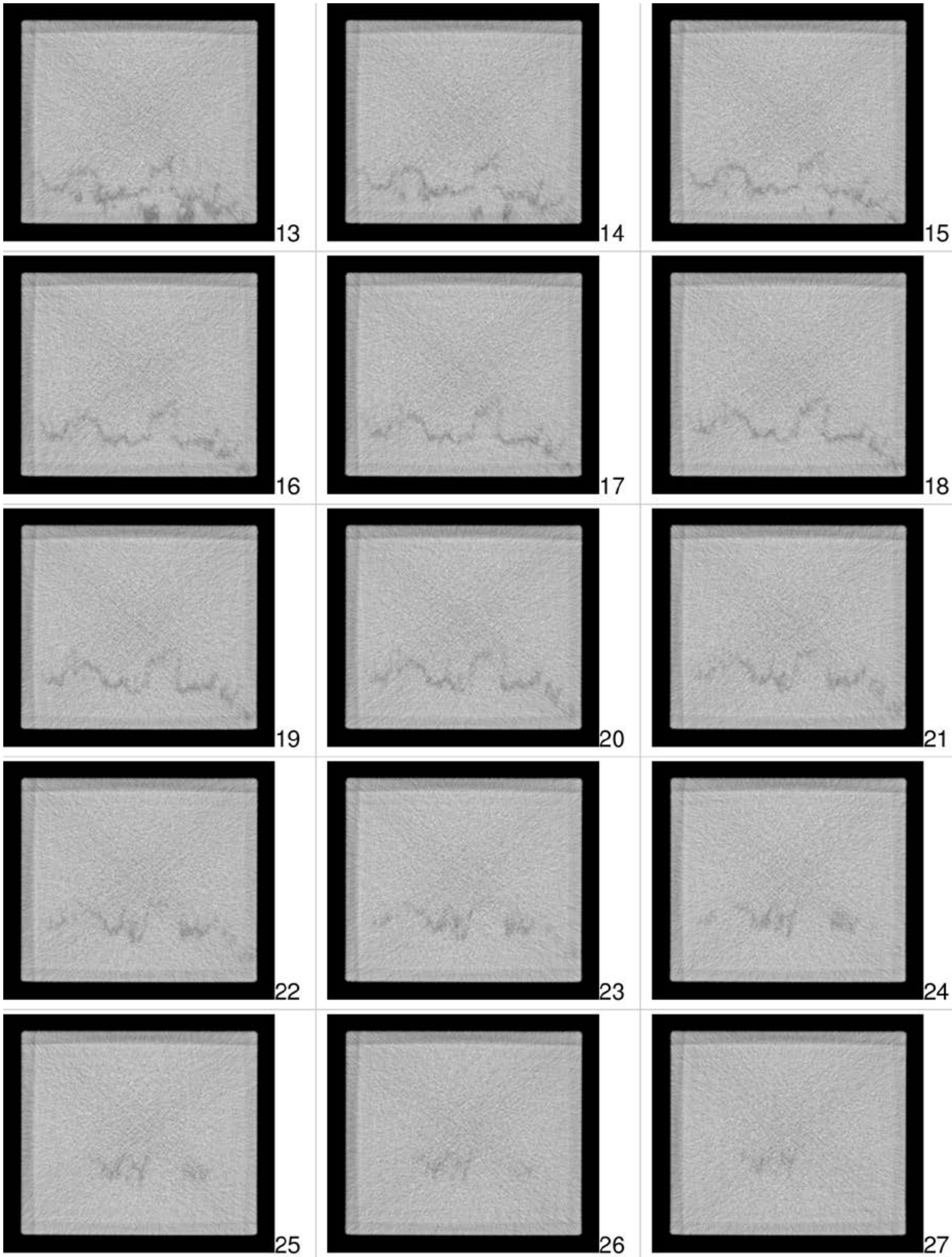

Figure B.146b. 15 CT-slices in stack of 32, starting with slice #13 and ending with #27

B.6.5.3 Test Block ID P30 (N 220 AD U 7)

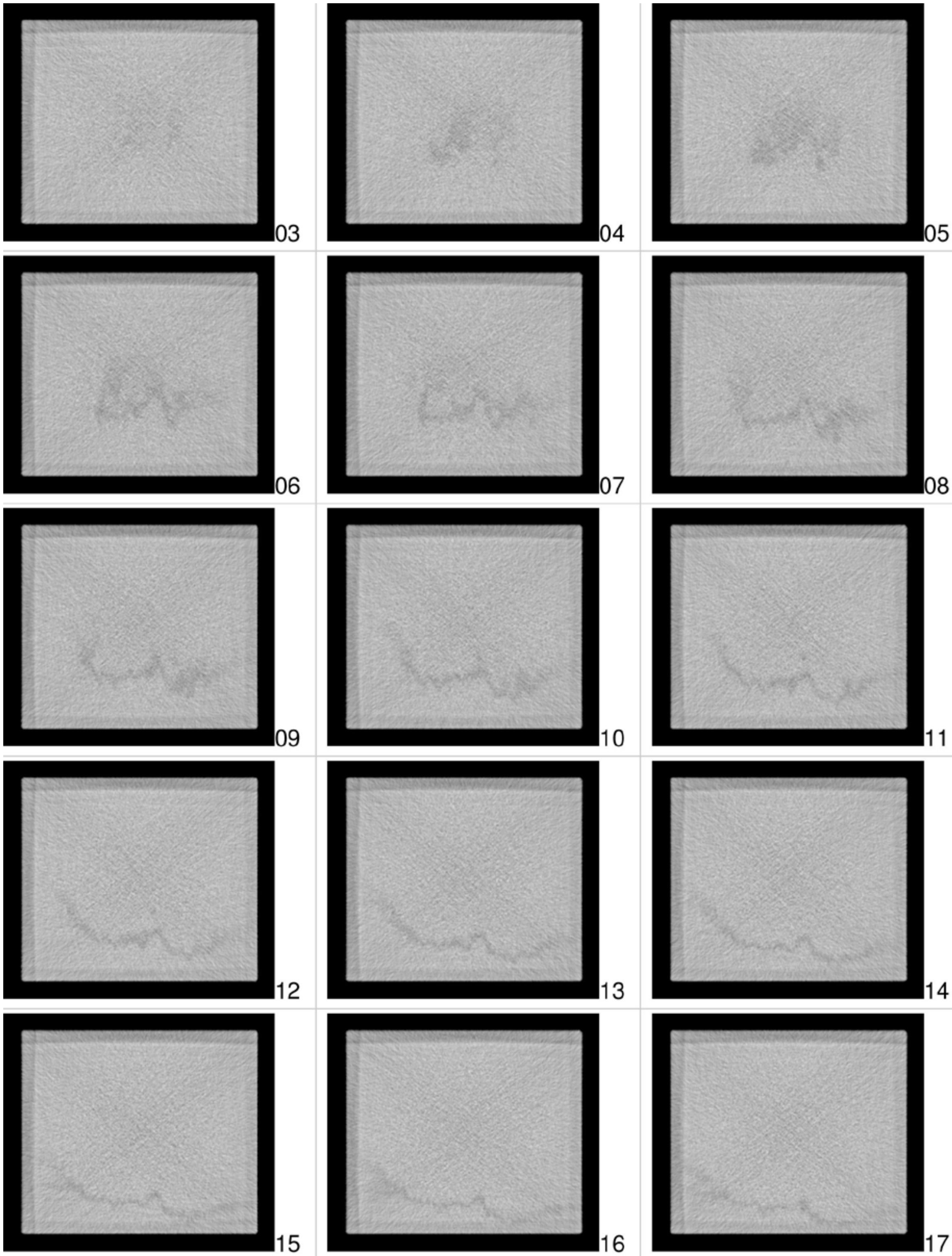

Figure B.146c. 15 CT-slices in stack of 25, starting with slice #3 and ending with #17

B.6.5.4 Test Block ID P31 (MN 220 AD U 1)

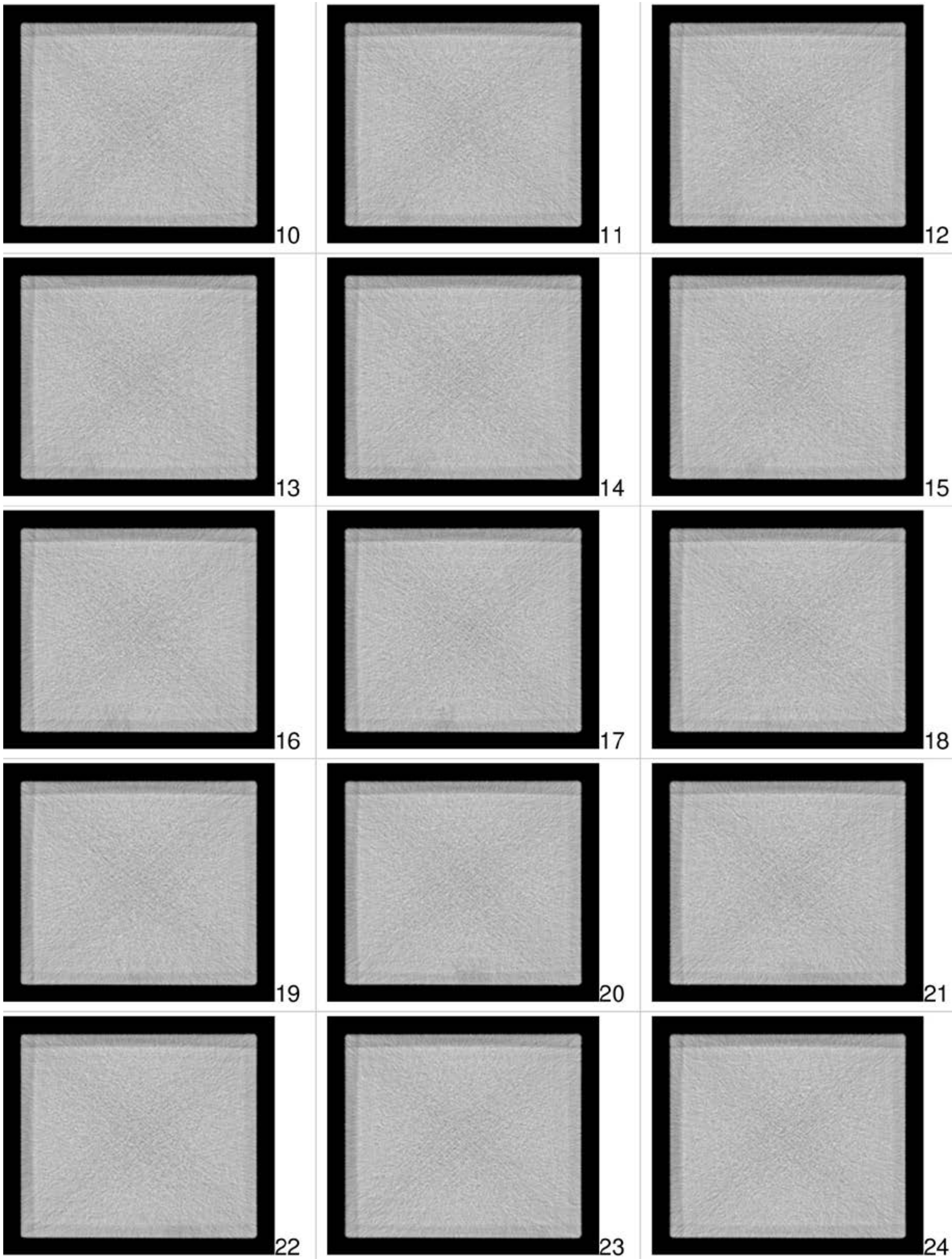

Figure B.146d. 15 CT-slices in stack of 30, starting with slice #10 and ending with #24

B.6.5.5 Test Block ID P32 (N 220 AD U TS 5)

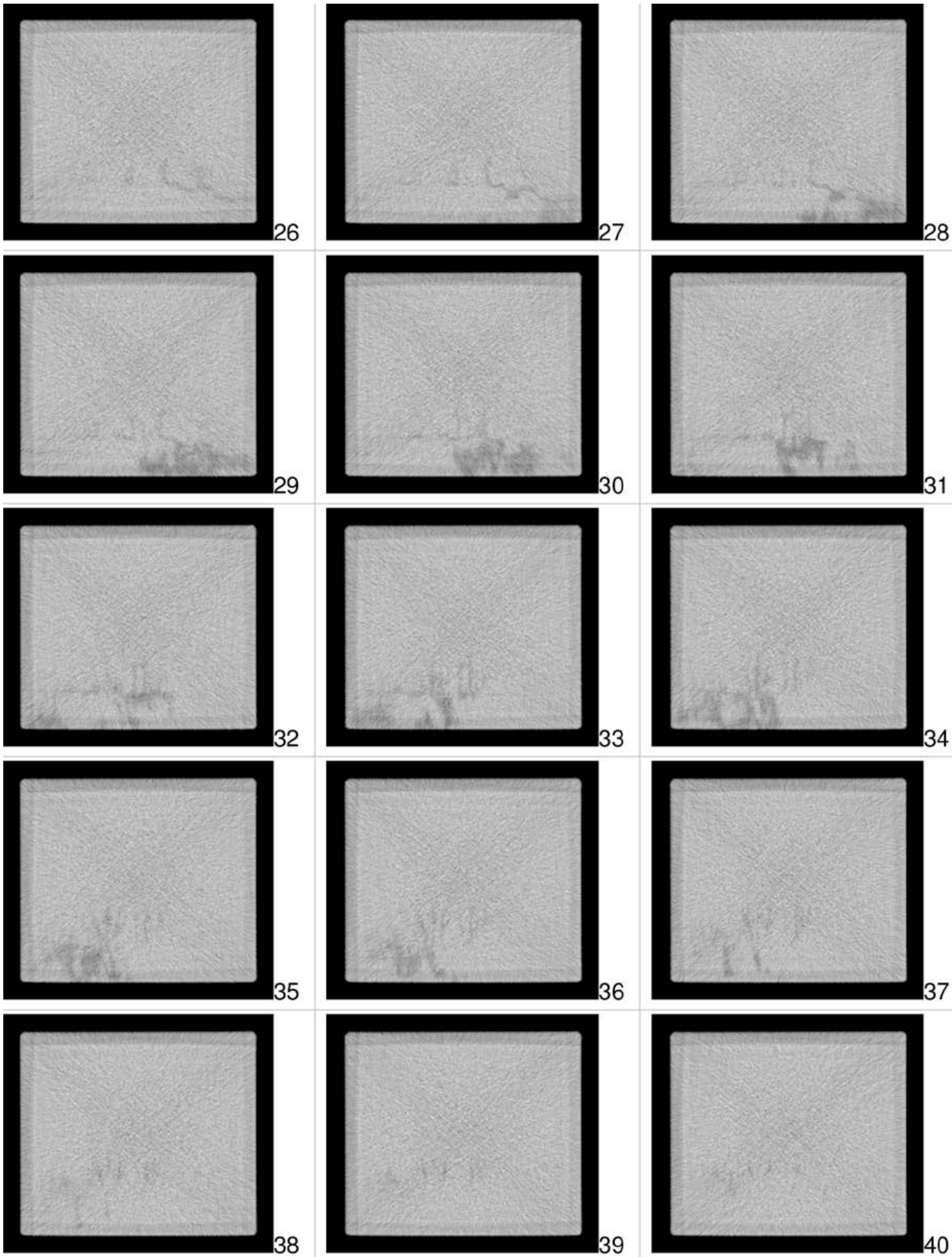

Figure B.146e. 15 CT-slices in stack of 41, starting with slice #26 and ending with #40

B.6.5.6 Test Block ID P38 (N 220 AD U TS 3)

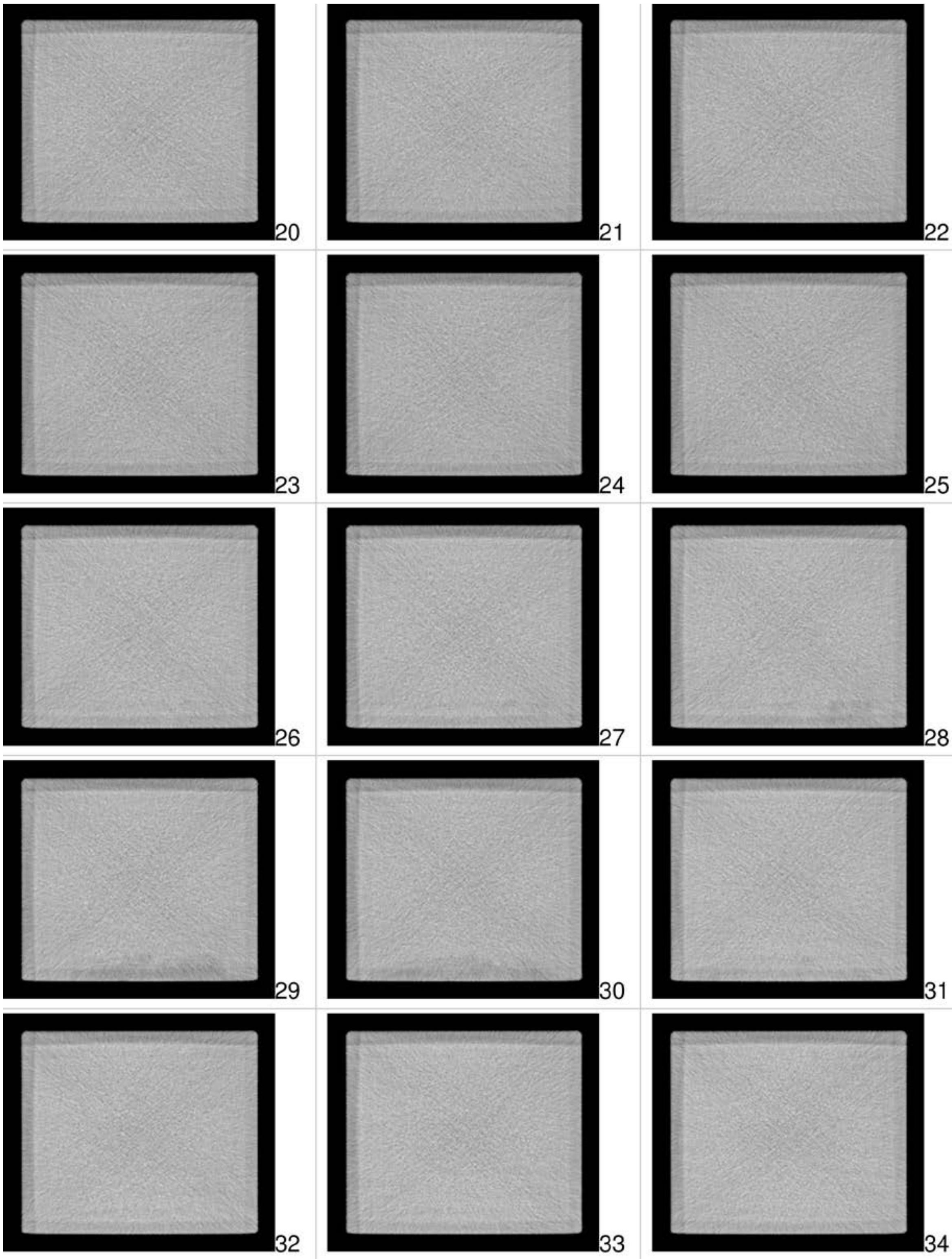

Figure B.146f. 15 CT-slices in stack of 40, starting with slice #20 and ending with #34

B.6.5.7 Test Block ID P28 (N 220 AD U 6)

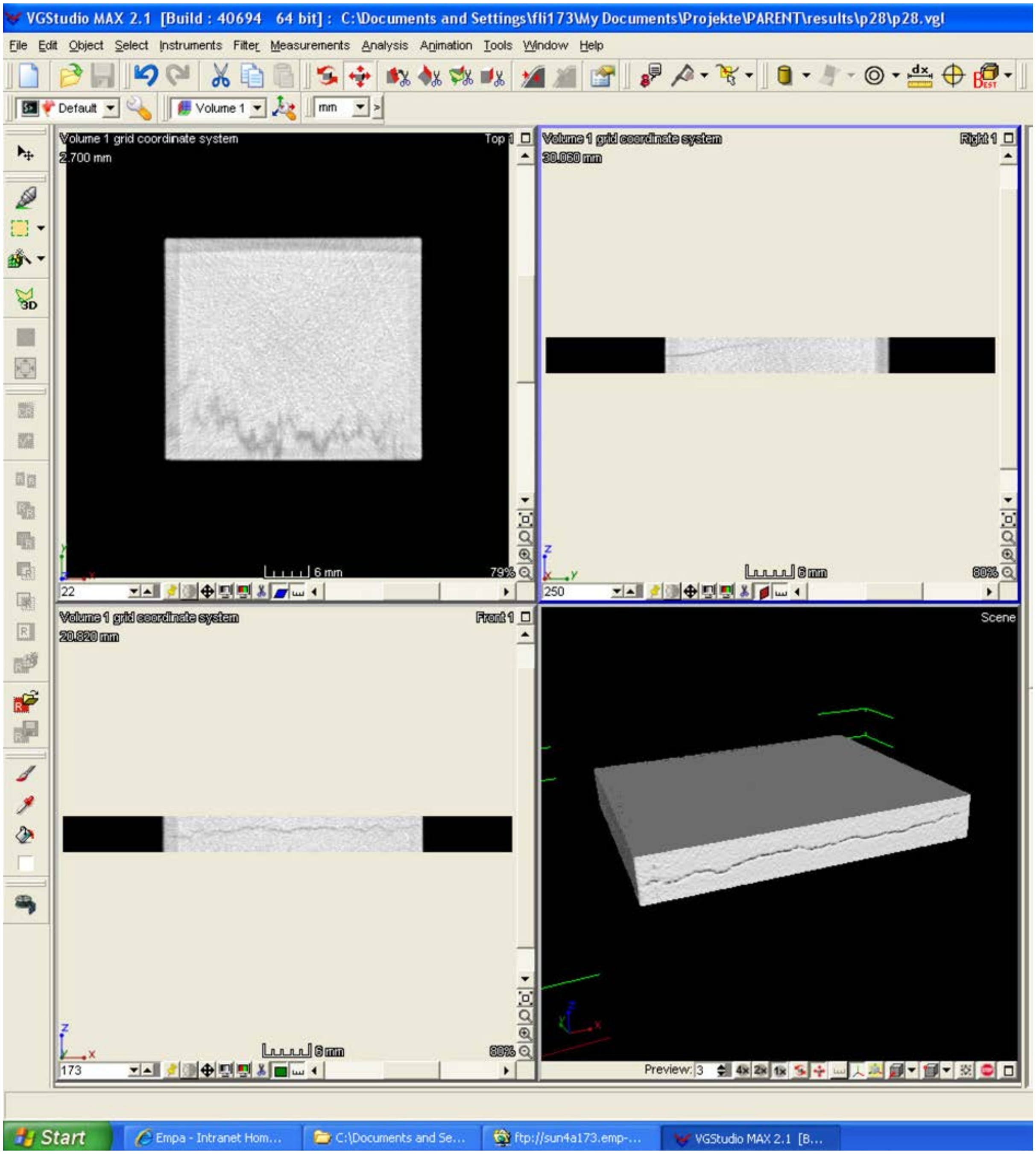

Figure B.147a. Visualisation of 3D-CT volume of test block P28 with VGStudioMax

B.6.5.8 Test Block ID P29 (N 220 AD U 10)

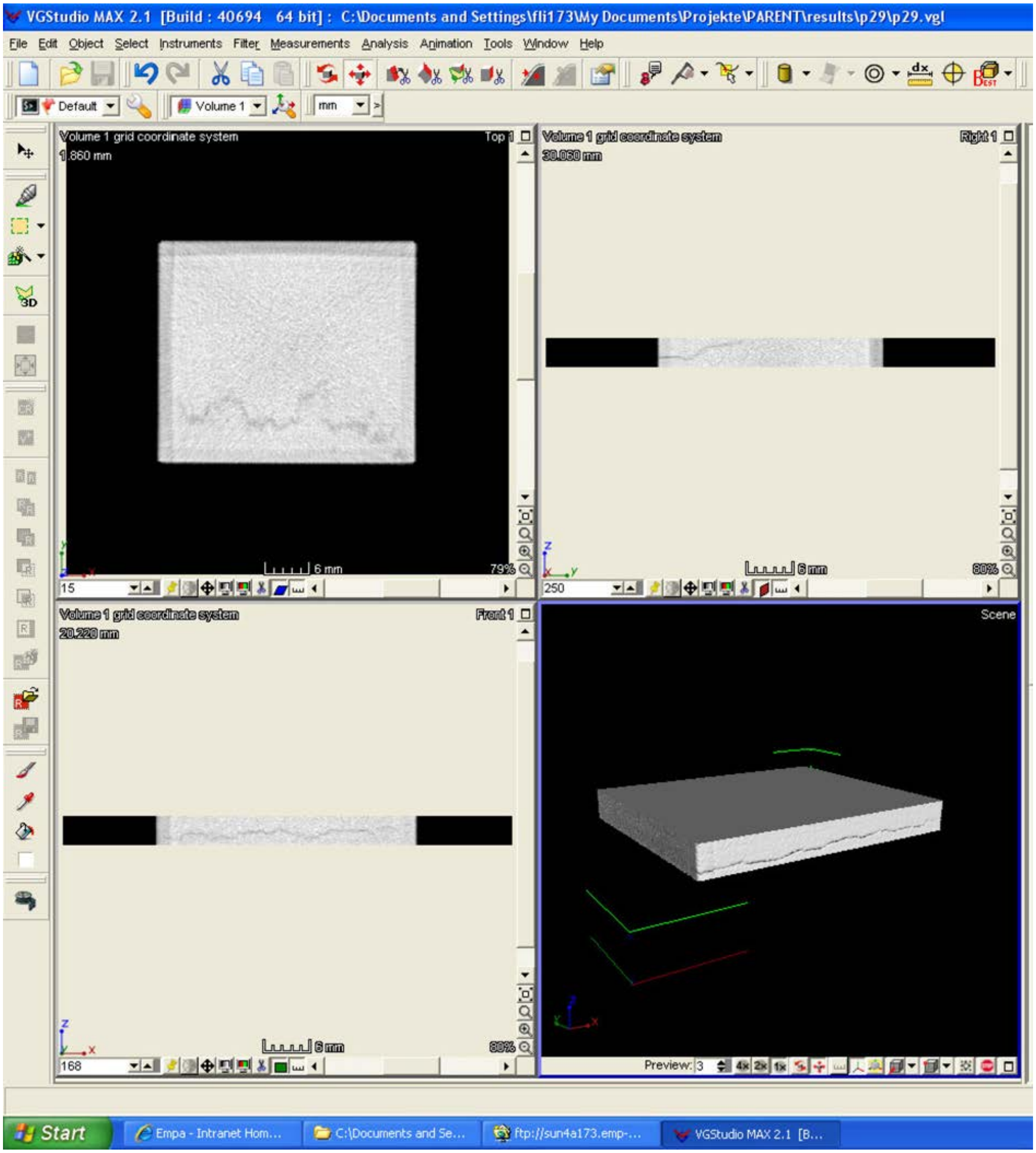

Figure B.147b. Visualisation of 3D-CT volume of test block P29 with VGStudioMax

B.6.5.9 Test Block ID P30 (N 220 AD U 7)

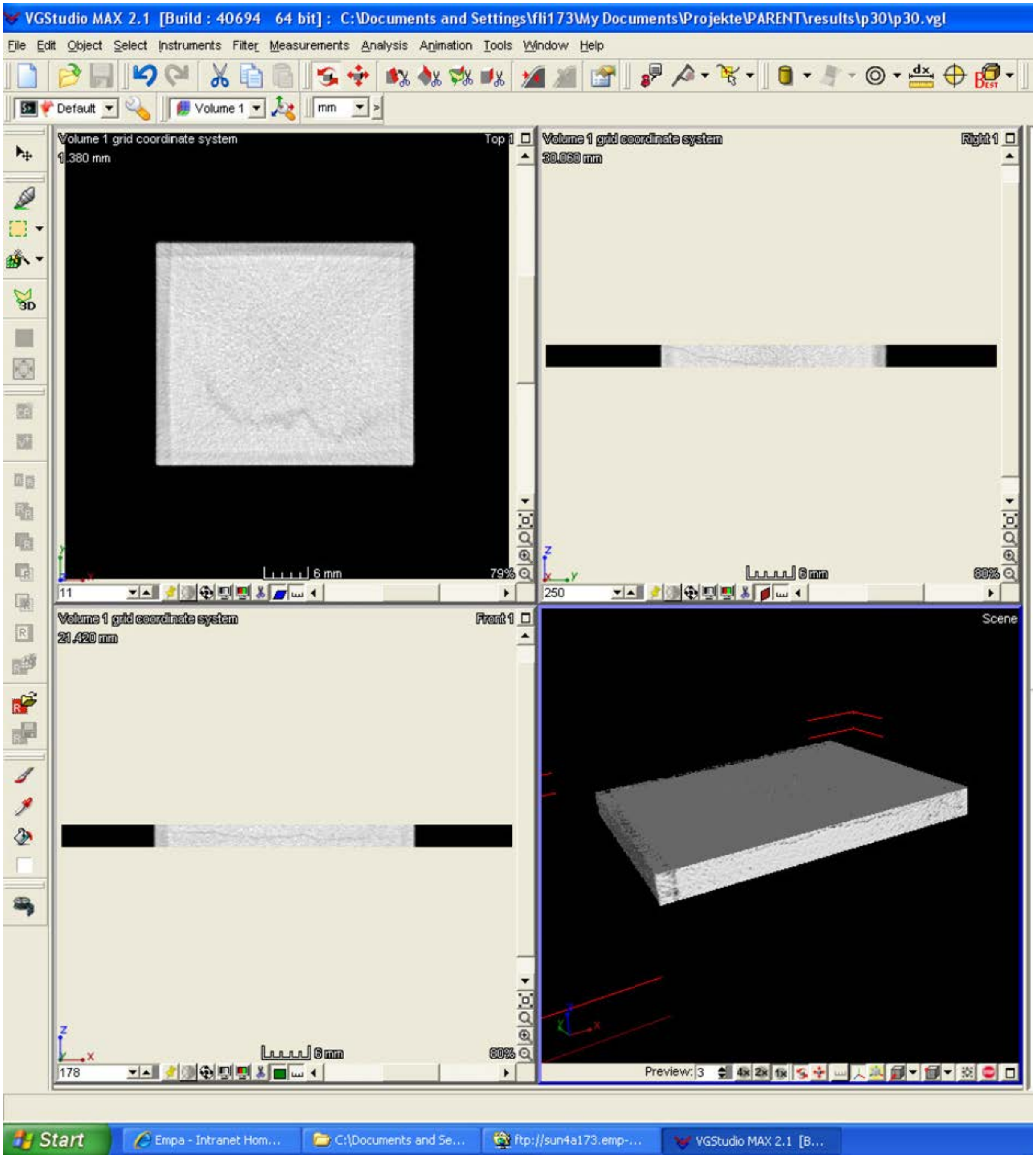

Figure B.147c. Visualisation of 3D-CT volume of test block P30 with VGStudioMax

B.6.5.10 Test Block ID P31 (MN 220 AD U 1)

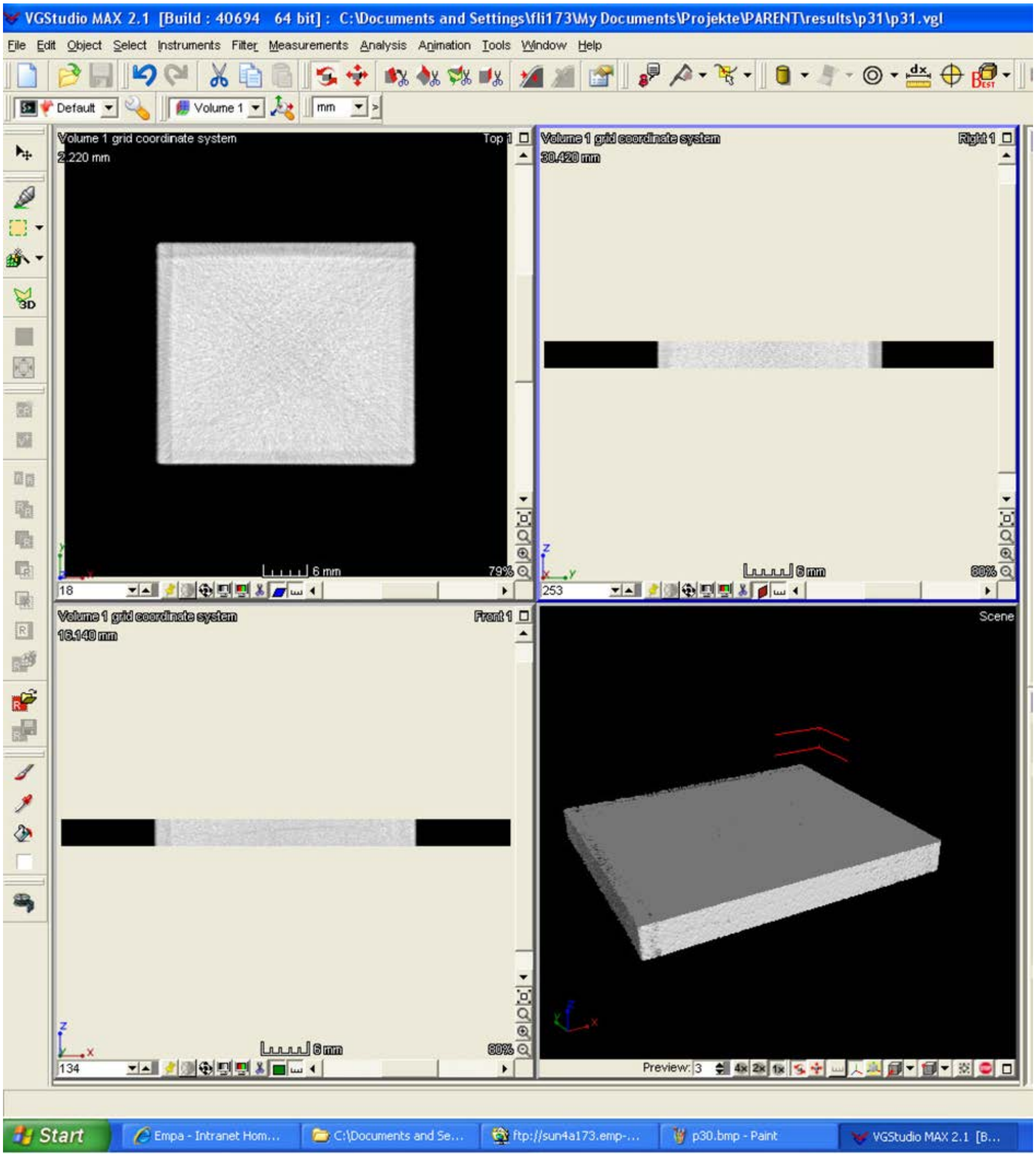

Figure B.147d. Visualisation of 3D-CT volume of test block P31 with VGStudioMax

B.6.5.11 Test Block ID P32 (N 220 AD U TS 5)

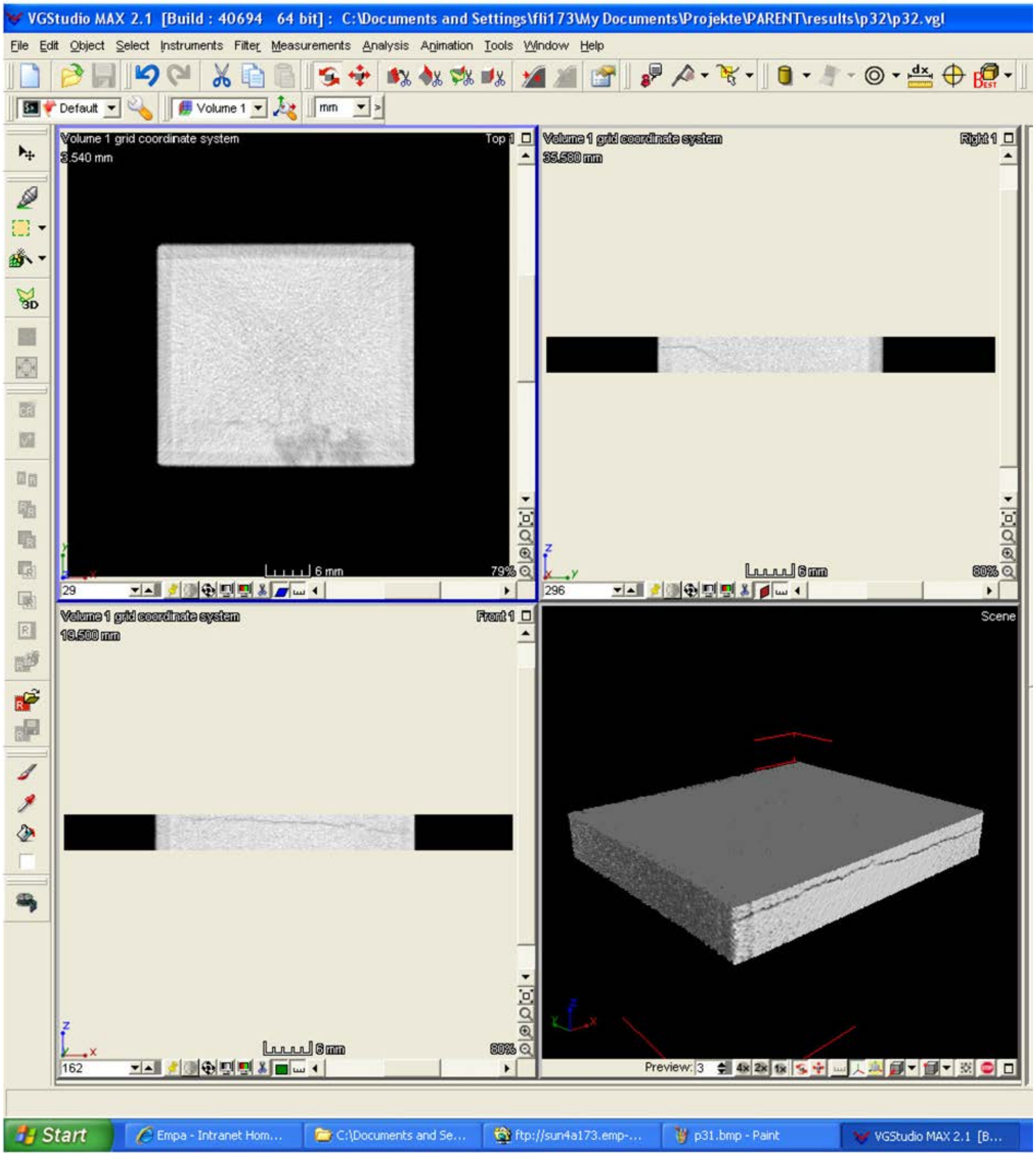

Figure B.147e. Visualisation of 3D-CT volume of test block P32 with VGStudioMax

B.6.5.12 Test Block ID P38 (N 220 AD U TS 3)

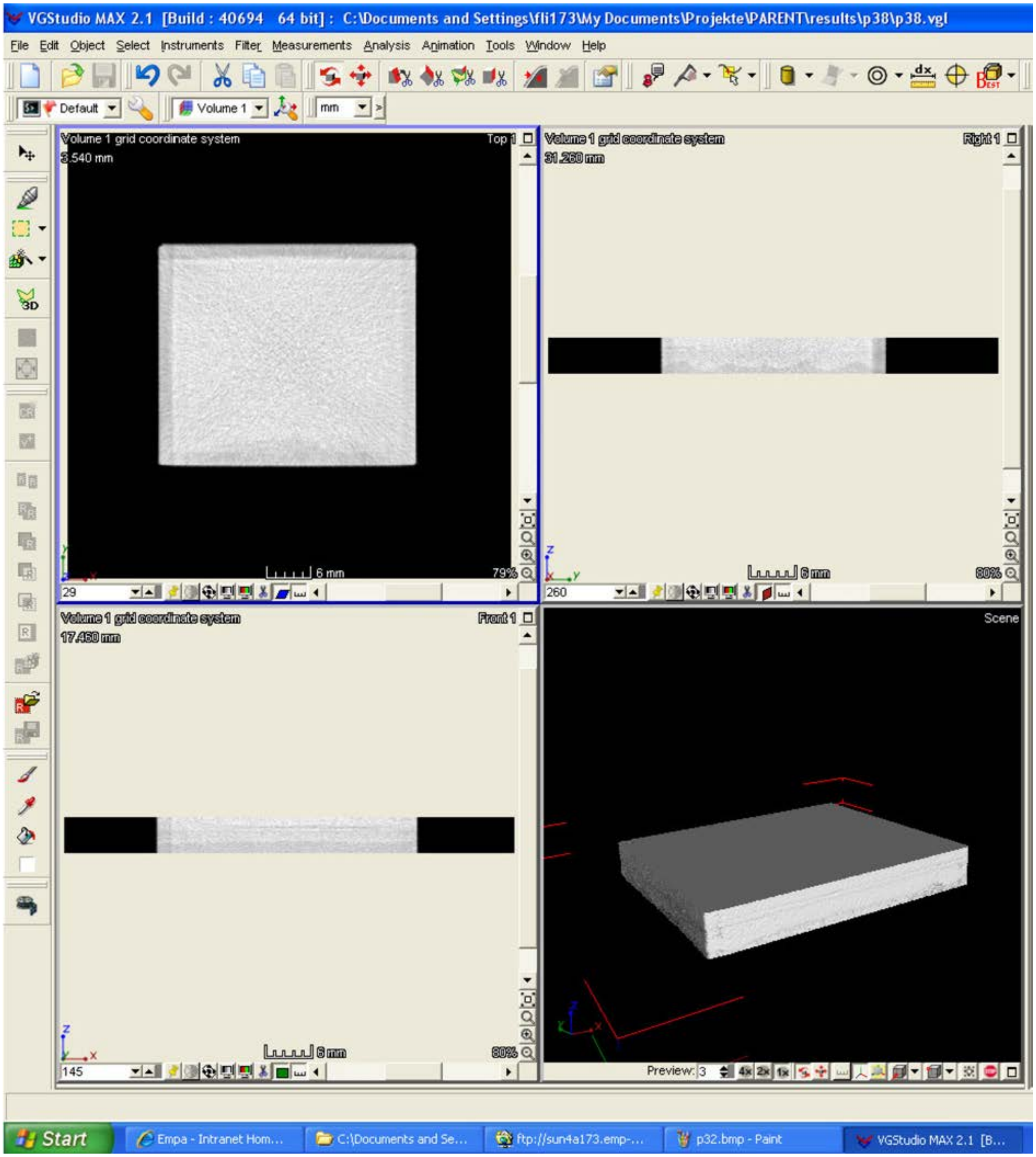

Figure B.147f. Visualisation of 3D-CT volume of test block P38 with VGStudioMax

B.7 High Resolution X-ray, Technique ID 112-HRT0

B.7.1 Introduction

This report describes an x-ray technique that has been developed for detection and characterization of service induced defects, e.g., intergranular stress corrosion cracking (IGSCC). The x-ray source is a 450 kV x-ray machine and the detector is CCD-based with fiber optic lens and glass fiber optic scintillation screen. The objects are positioned and rotated by a rotation unit which is stepper motor driven.

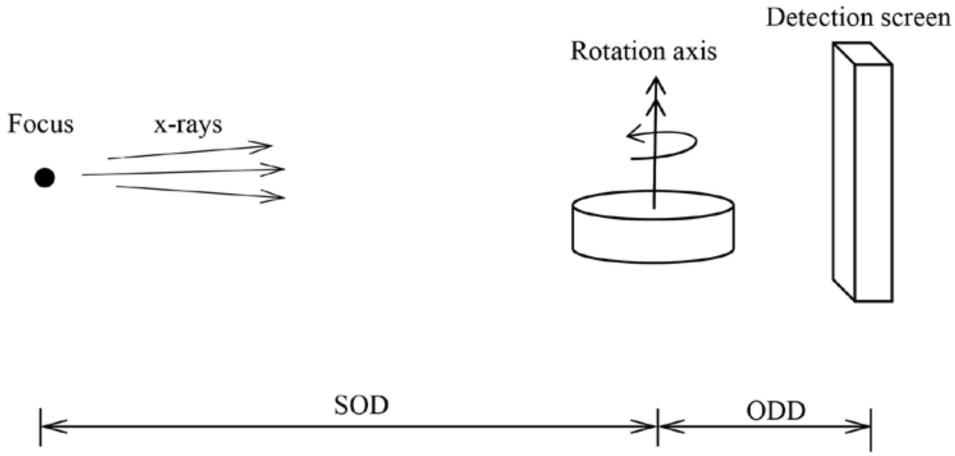

Figure B.148. Set Up

B.7.2 X-ray Machine

The X-ray machine is a GE Titan 450 kV constant potential with ISOVOLT 450 M2/0.4-1.0HP tube. This is a high power tube with a small focus, f, of only 0,4 mm (25 % modulation).

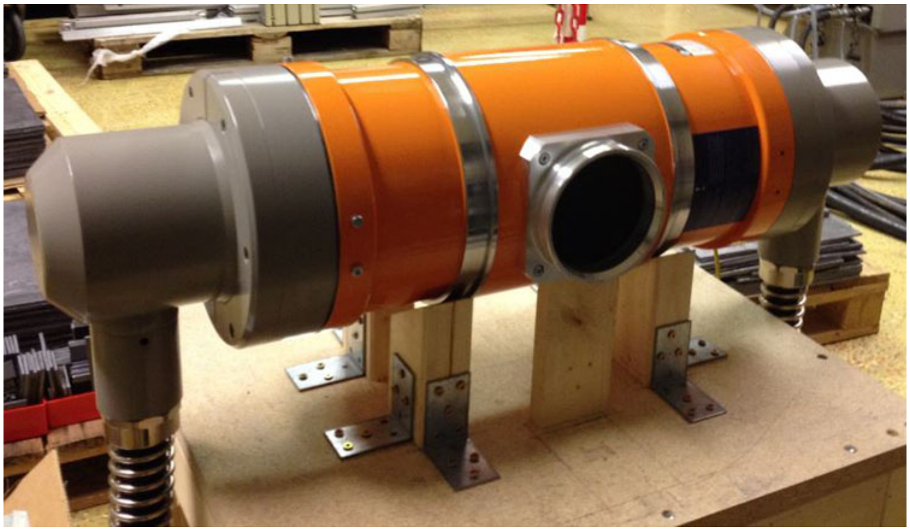

Figure B.149. X-ray Tube

The source to object distance (SOD) has been 650 mm and object to detector distance (ODD) was 50 mm. In this case the crack opening is defined as the object. The geometrical unsharpness is less than 0,04 mm.

$$U_g = \frac{f \cdot ODD}{SOD} \quad [mm] \tag{B.1}$$

B.7.3 Digital Detector

The x-ray camera is an imaging detector with a scintillating screen of glass fiber optics. It is a new design of a proven concept where the design issue was to minimize the amount radiation induced noise. This was done by bending the fiber optic lens (image conduit) which moved CCD-chip out of the primary beam. The spatial resolution is increased by using a new type of scintillating face plate. The new scintillating faceplate has unique properties which have eliminated the internal light spread and increased the spatial resolution.

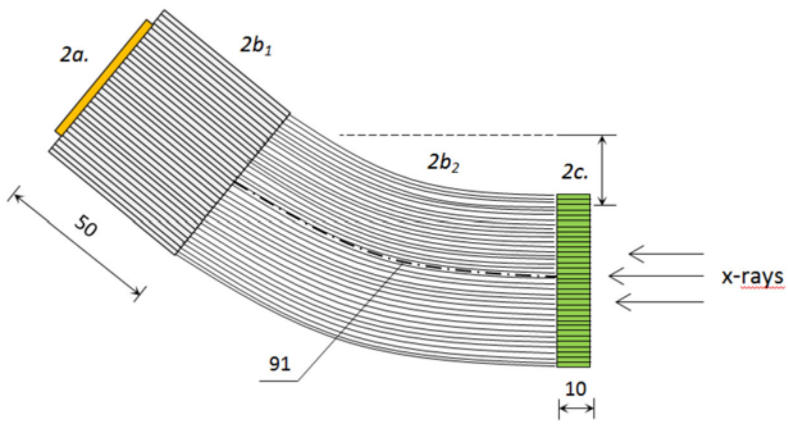

Figure B.150. Fiber Optic Lenses and Scintillating Faceplate

The new detector is based on a front illuminated full frame CCD camera (EEV CCD42-40) (2K x 2K) with pixel size of 13,5x13,5 µm. It is Peltier cold down to -30°C and is equipped with fiber optic input window. The input window is a fiber optic lens with fiber diameter of 4,5 µm with a length of 50 mm (see Figure B.150). In the front of the camera, the bended fiber optic lens with the scintillating screen is mounted.

The imaging area is only 27 x 27 mm (see Figure B.151) but the spatial resolution is very high. The detector unsharpness is measured to be less than 0,08 mm. Better than 50% modulation of the 13:th wire pair with the EN462-5 double wire IQI.

Figure B.151. The X-ray Detector with a Cu-filter in Front

B.7.4 Exposure Data

For the test blocks P28-P30 the following data was applied:

- U= 300 kV; I= 2,25 mA; 30 mm Iconel
- Exposure time: 8 x 60 s (18 mAmin)
- For the test block P41 is following data used:
- U= 450 kV; I= 1,5 mA, 64 mm Inconel
- Exposure time: 8 x 120 s (24 mAmin)

The reason to use such a long exposure time is that it corresponds to an optical density between 3,0-3,5 with Agfa D5 industrial x-ray film. We are using the cooled CCD to be able to integrate for long exposure times. In other word we have similar exposure time as film but much better image quality.

B.7.5 Test Procedure

The object coordinate system is placed so the crack opening is coincident to the axis of rotation in the object manipulator. The defects in test block P41 are orientated in two directions, axial and circumferential and P41 test block is thus in two different positions.

- The test block P28-P30 (square bars) is placed in such a way that its X-axis is parallel to the axis of rotation of the object manipulator in the coordinates Y=0 and Z=30,3 [mm] (see Figure B.152).
- In the position for testing axial defects in test block P41, the Y-axis of the test object coincident to the axis of rotation of the object manipulator in coordinate Z=0 [mm] and the polar coordinate X [degrees]of the defect (see Figure B.153).
- In the position for testing circumferential defects the tangent of the defects polar X-coordinate coincident with the axis of rotation of the object manipulator. The Y-coordinate is the value for the actual defect and Z=0 [mm].

X-ray radiography is a volumetric method and to be able to detect cracks or parts of cracks the orientation has to be reasonably parallel with the x-ray beams. Therefor each defect is radiographed in series of projections. The projection angle is from -10° to +10°, with increments of 2°.

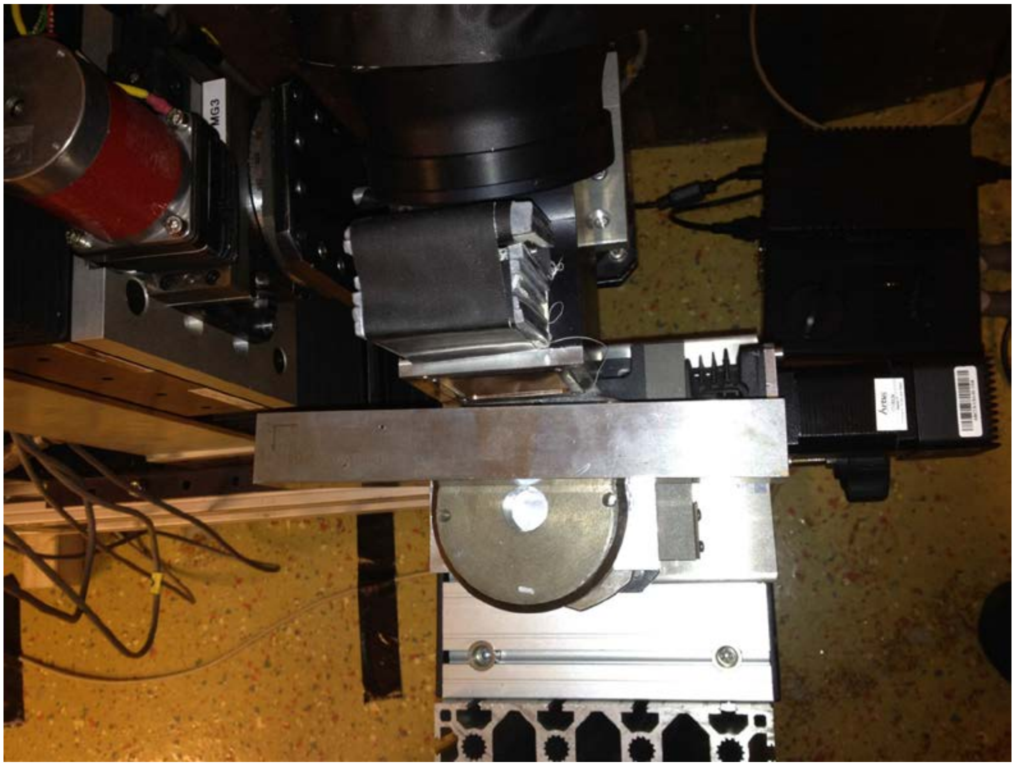

Figure B.152. Test Block P28–P30

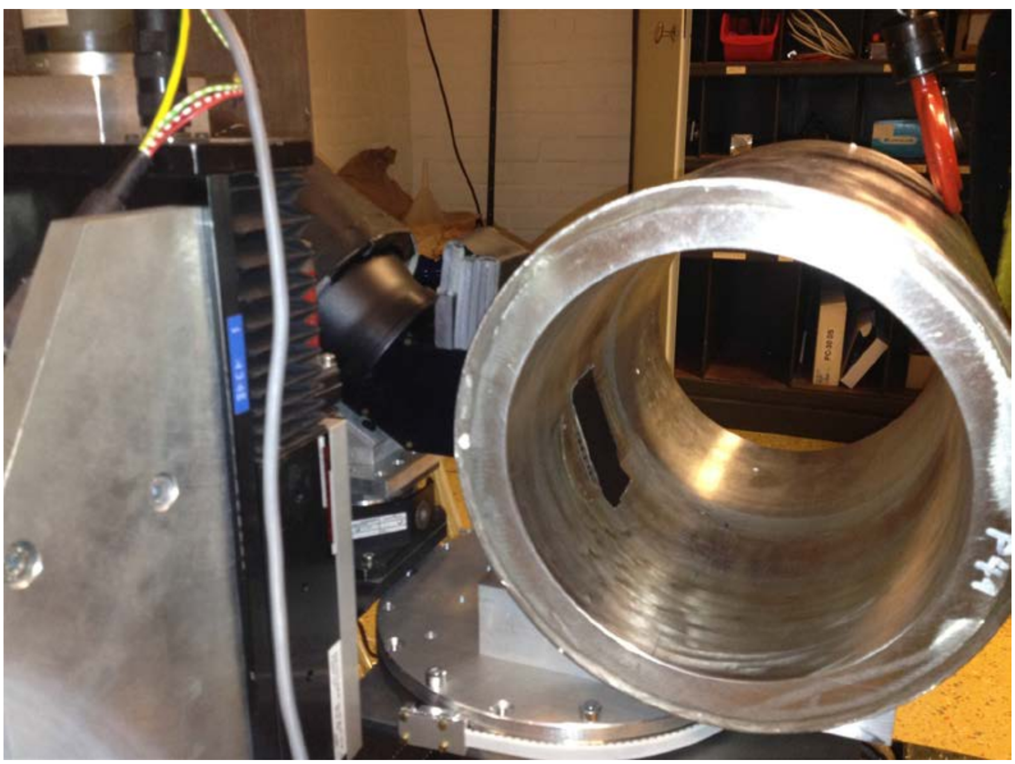

Figure B.153. Test Block P41. Position for axial defects.

B.7.6 Image Processing

Each x-ray image is divided in eight exposures. They are then integrated to improve the signal-to-noise (SNR) ratio. As each image also can contain radiation induced noise they are compared statistically and the noise (white dots) are removed. Conventional background and flat field correction to remove the structural noise is done in the next step. Finally a “lifting”-operation is done by multiplying the corrected raw image with an interpolated surface based on curve fitting in the perpendicular direction of the cracks. The Fourier-series of third grade is used as function for curve fitting as it can adapt nearly any shape in a “smooth” way.

The images are presented in an animation (link below each image). By using animations the crack can be seen clearly and it is easy to characterize them.

B.7.7 Size

To determine the size or the depth (z-coordinate) an expression (see Figure B.154) is developed which describes the depth, d, as function of the movement of the observed crack tip between the end positions in the series of exposures.

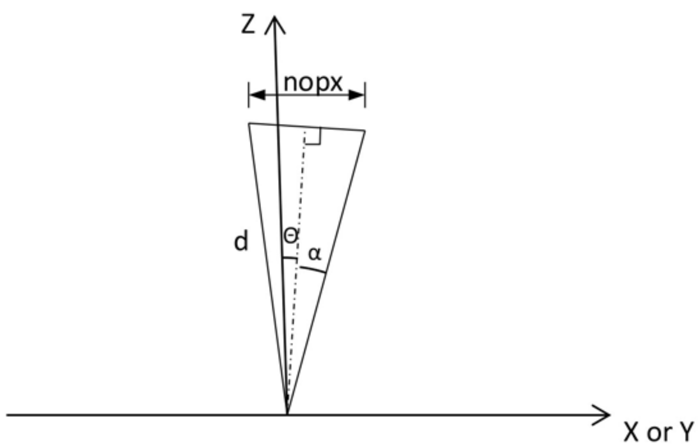

Figure B.154. Crack Depth Calculation

Where, Θ, is the projection angle of the crack tip in the center position of the projection series. The angle, α, is half the angle between the end positions. The distance, nopx, is measured between the end positions of the crack tip. The pixel size is pxsize=0,0135 [mm]. The geometrical enlargements is M=1,045. And finally, d, is the depth of the defect (Z_{max}-coordinate).

$$d = \frac{nopx \cdot pxsize}{2 \cdot M \cdot \cos\theta \cdot \tan\alpha} \quad [mm] \tag{B.2}$$

The measured width (nopx) can be seen in Figure B.155.

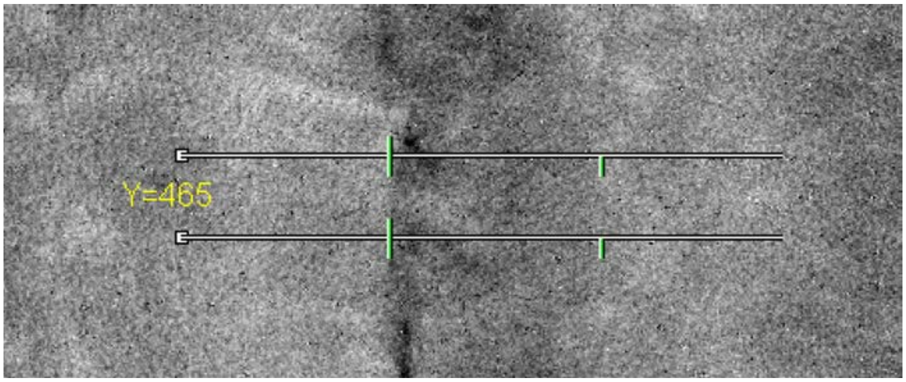

Figure B.155. Measurement of the Distance, nopx

Sizing of each defect is presented in a table with:

- X X-coordinate of the defect [mm or degrees].
- X_1 , X_2 Coordinates of the line profile.
- nopx No. of pixels (projected width).
- Z_{max}[(a)] Maximum Z-coordinate (=d, maximum depth of the defect).
- Length Real length in the image plane.

All images are of same size, 26,45 x 26,45 mm^2, which is the real size in the image plane. The size in the detector plane is compensated by the geometrical enlargement, M.

(a) The Z_{max} is systematically under estimated in the case of "real" defects such as SCC and fatigue in P28-P30. This is because the volume in the crack close to the crack tip goes to zero. Experience from earlier work with SCC gave an under estimation of about 1–2 mm.

In the test block P41 where the defects are artificially produced the Z_{max} estimation is more correct.

B.7.7.1 U6 (SCC)

α=10°and Θ=8°; From -10° to +10°; 2°/pos; 11 positions

X [mm]	X_1	X_2	nopx	Z_{max} [mm]
27,8	85	341	256	9,5
22,7	71	323	252	9,3
17,5	93	329	236	8,7
12,3	93	381	288	10,6
7,2	97	358	261	9,7

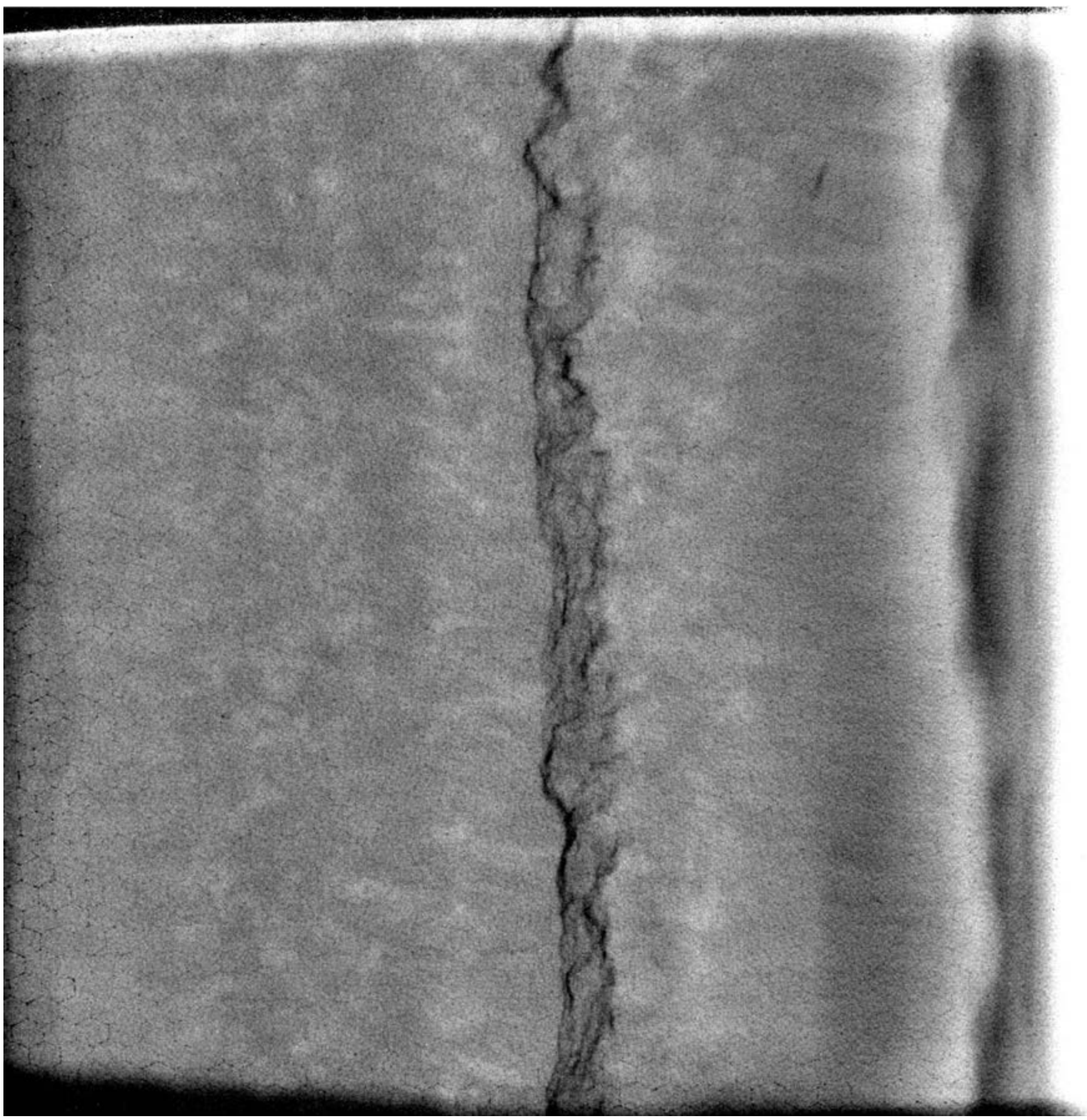

Figure B.156. U6, 6:th position (Image size 26,45 x26,45 mm^2)

P28 MN 220 AD U6 spline 8 bit 512 inv.avi

B.7.7.2 U7 (Fatigue)

α=6° and Θ=5°; From +1° to -11°; 1°/pos; 13 positions				
X [mm]	**X_1**	**X_2**	**nopx**	**Z_{max} [mm]**
27,8	82	289	207	12,8
22,7	94	366	272	16,8
17,5	60	295	235	14,5
12,3	94	311	217	13,4
7,2	96	271	175	10,8

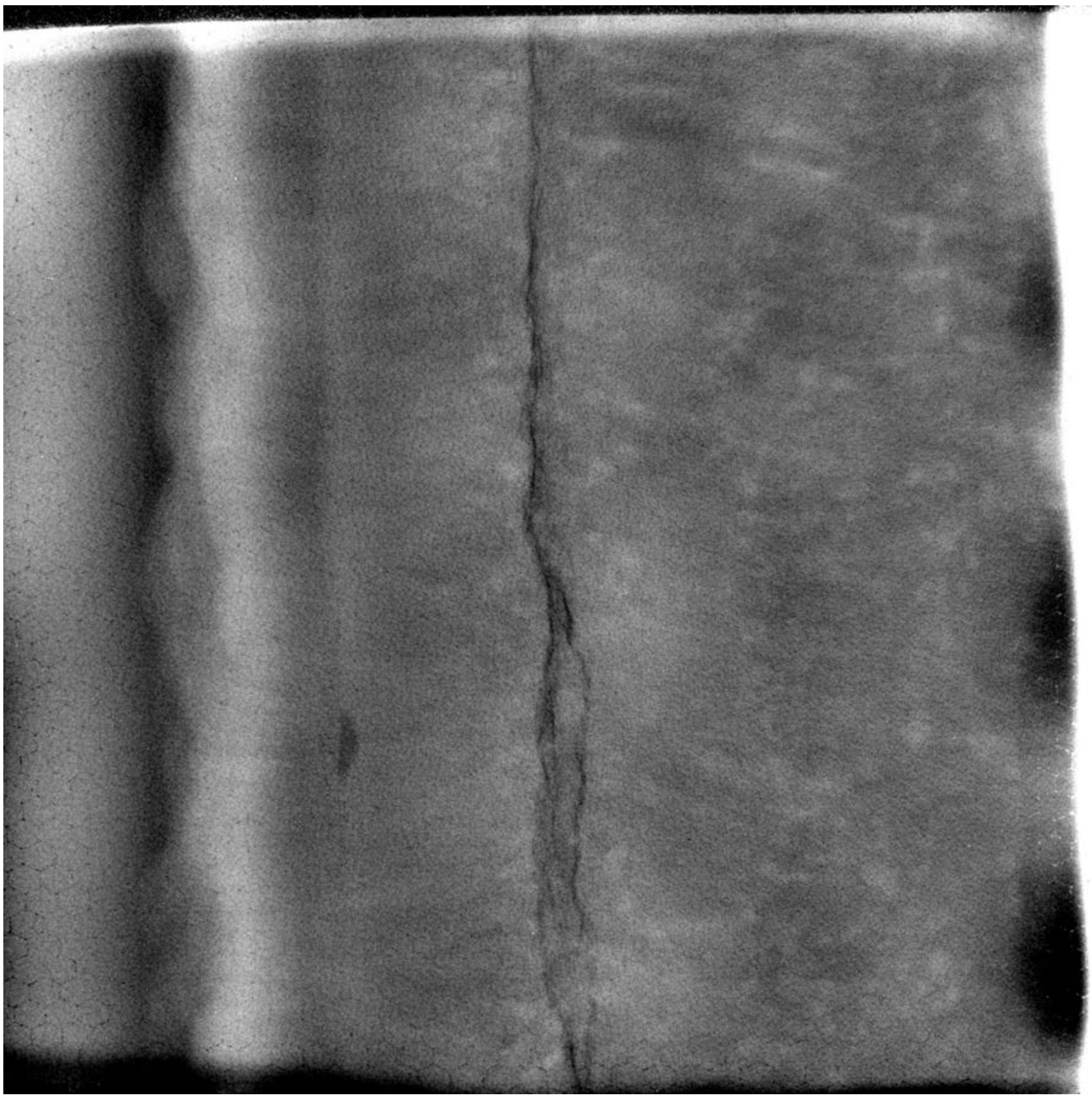

Figure B.157. U7, 7:th position (Image size 26,45 x26,45 mm^2)

P30 MN 220 AD U7 spline 8 bit 512 inv.avi

B.7.7.3 U10 (SCC)

α=10°and Θ=6°; From -10° to +10°; 2°/pos; 11 positions				
X [mm]	**X_1**	**X_2**	**nopx**	**Z_{max} [mm]**
27,8	90	260	170	6,2
22,7	81	309	228	8,4
17,5	186	462	276	10,1
12,3	136	386	250	9,2
7,2	149	411	262	9,6

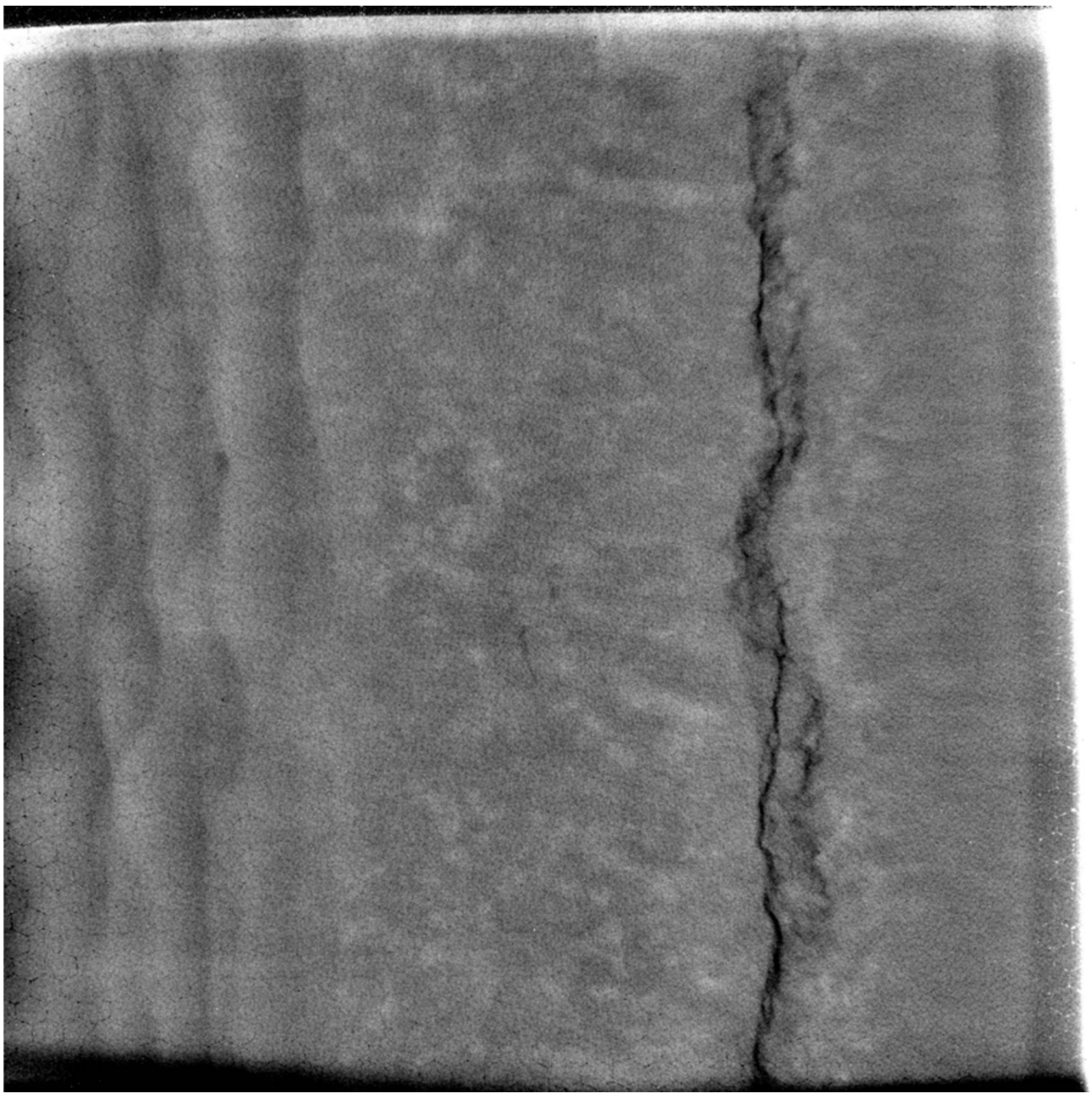

Figure B.158. U10, 6:th position (Image size 26,45 x26,45 mm²)

P29 MN 220 AD U10 spline 8bit 512 inv.avi

B.7.7.4 Defect nr1 (P41)

α=8°and Θ=8°; From -8° to +8°; 2°/pos; 9 positions

X [mm]	X_1	X_2	nopx	Z_{max} [mm]	Length [mm]
0	86	118	32	1,5	10,7

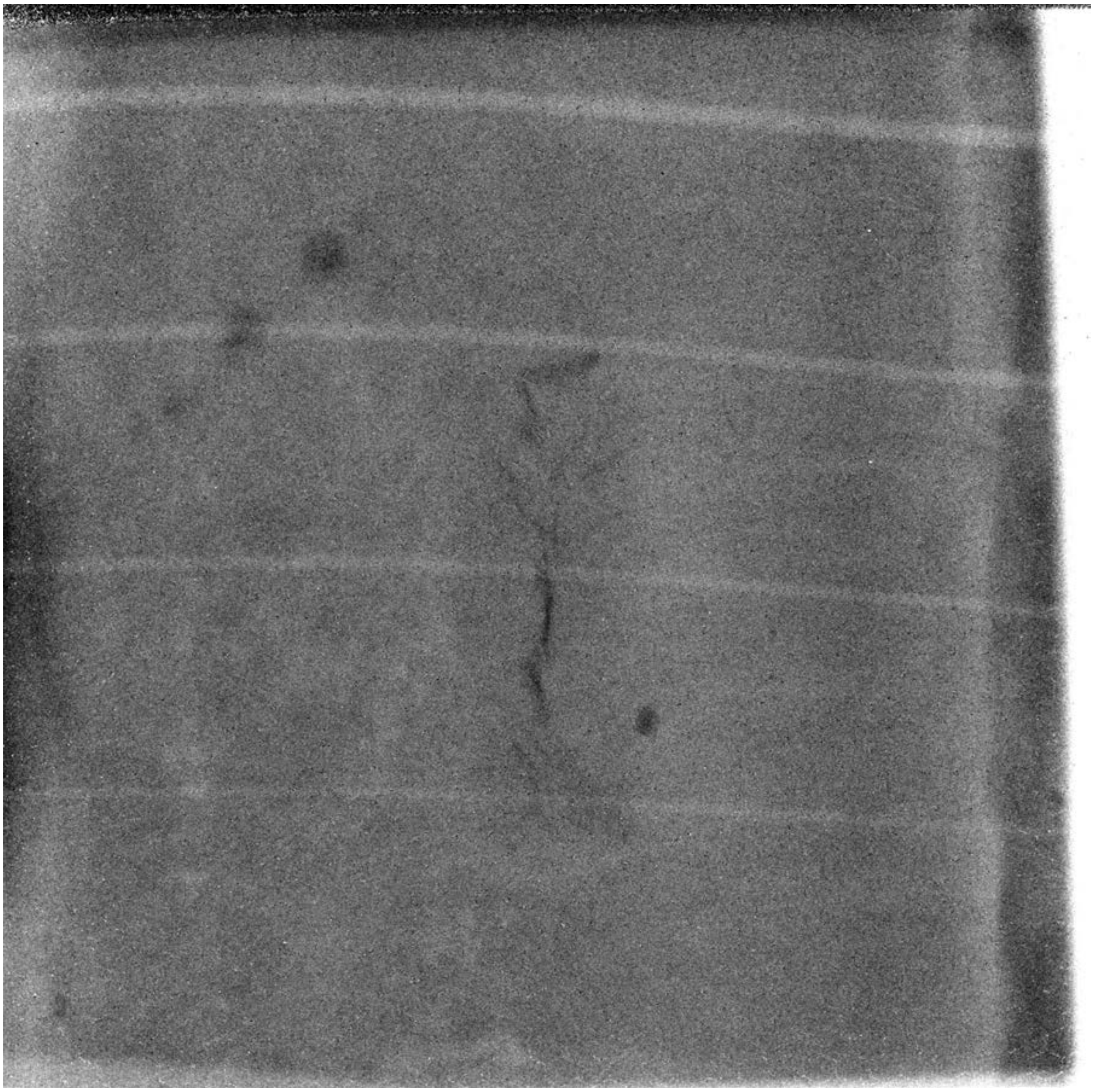

Figure B.159. Defect nr1, (P41) 3:rd position (Image size 26,45 x26,45 mm^2)

P41 nr1 0 deg spline 8 bit 512 inv.avi

B.7.7.5 Defect nr2 (P41)

α=8°and Θ=4°; From -8° to +8°; 2°/pos; 9 positions

X [mm]	X_1	X_2	nopx	Z_{max} [mm]	Length [mm]
0	69	112	43	2,0	7,4

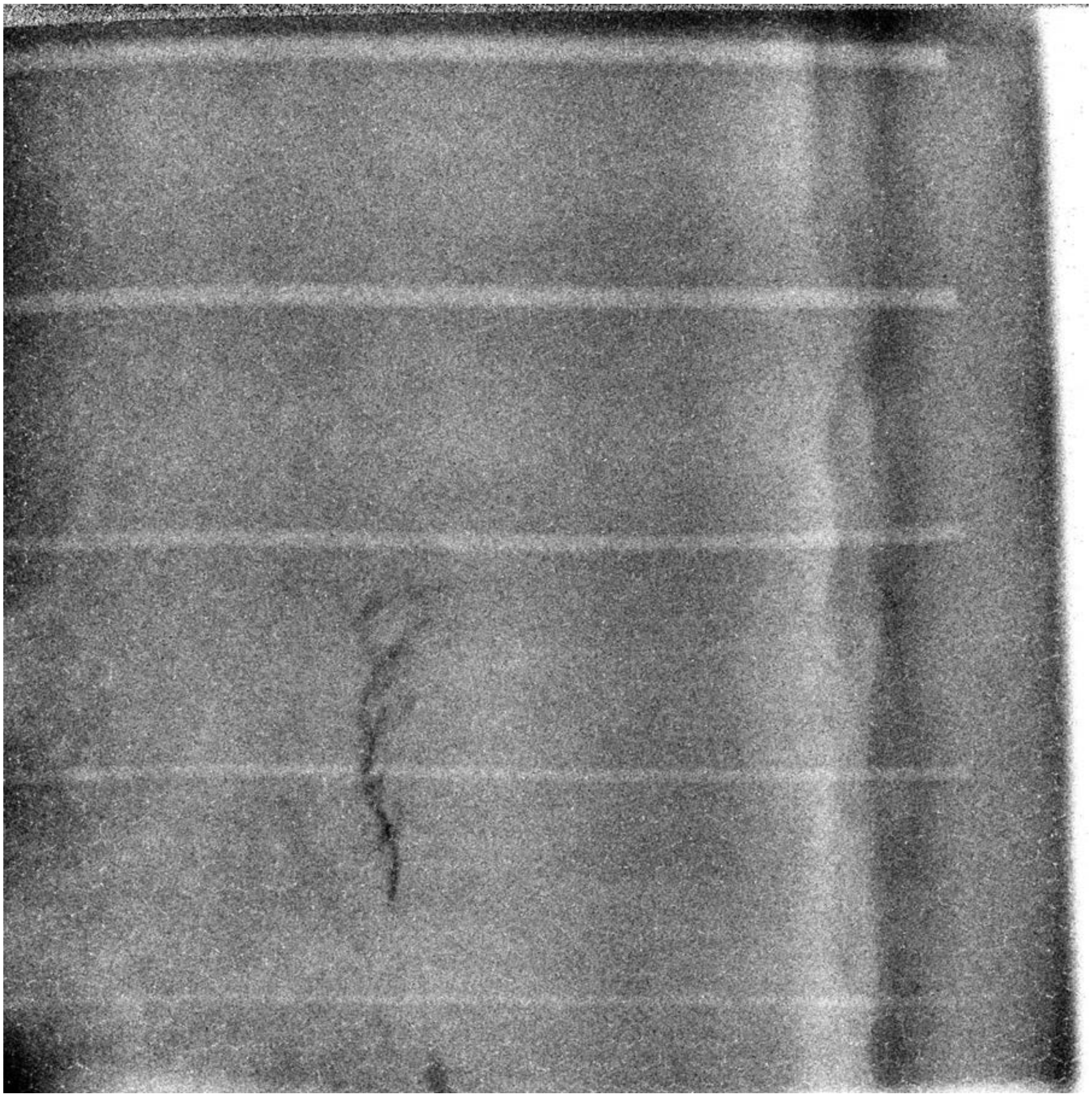

Figure B.160. Defect nr2, (P41) 2:nd position (Image size 26,45 x26,45 mm^2)

P41 nr2 28 deg spline 8 bit 512 inv.avi

B.7.7.6 Defect nr3 (P41)

α=8°and Θ=4°; From -8° to +8°; 2°/pos; 9 positions

X [mm]	X_1	X_2	nopx	Z_{max} [mm]	Length [mm]
0	73	116	43	2,0	11,4

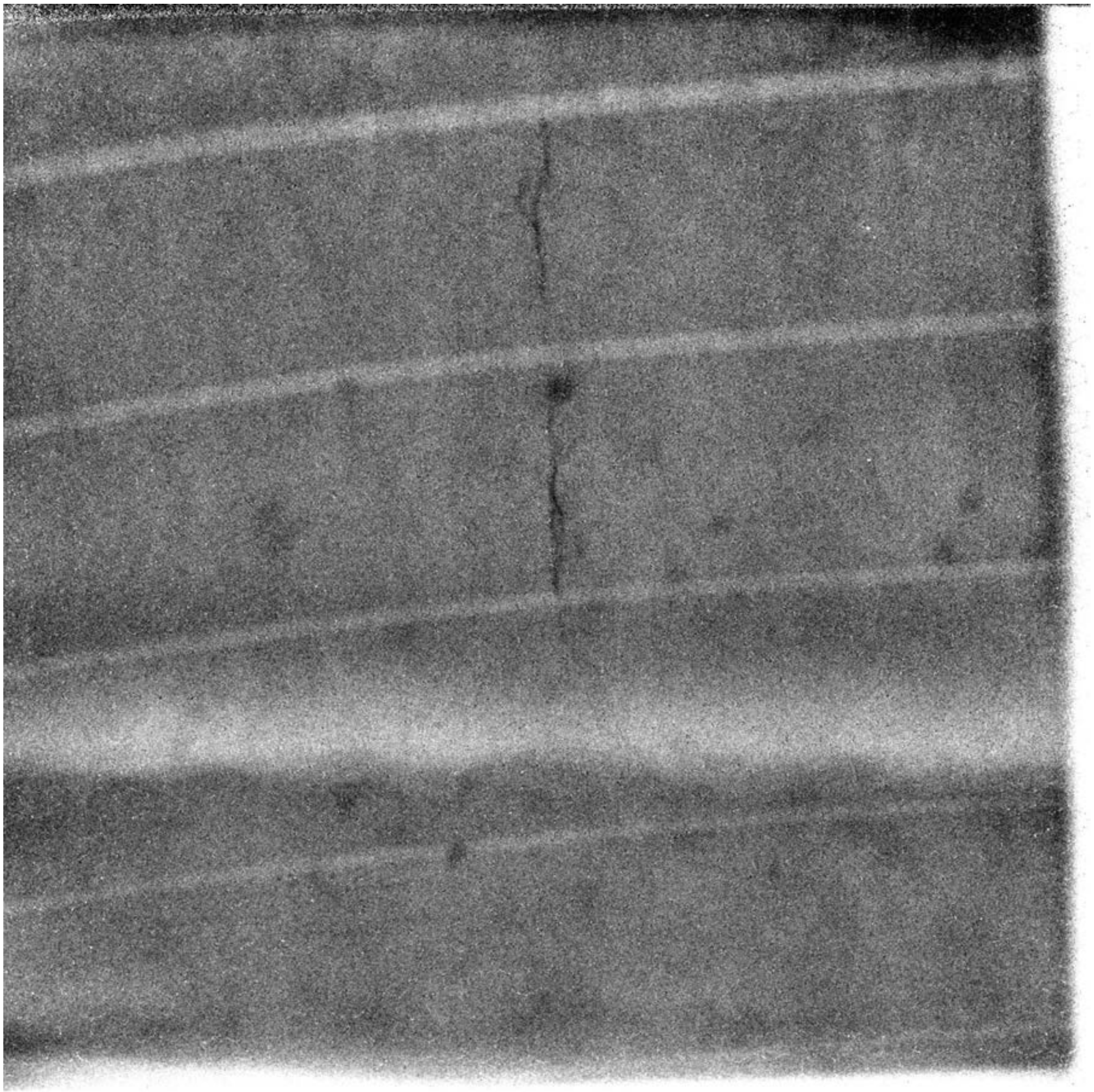

Figure B.161. Defect nr3, (P41) 6:th position (Image size 26,45 x26,45 mm^2)

P41 nr3 54 deg spline 8 bit 512 inv.avi

B.7.7.7 Defect nr4 (P41)

α=8°and Θ=4°; From -8° to +8°; 2°/pos; 9 positions

X [mm]	X_1	X_2	nopx	Z_{max} [mm]	Length [mm]
0	97	124	27	1,5*	7,2

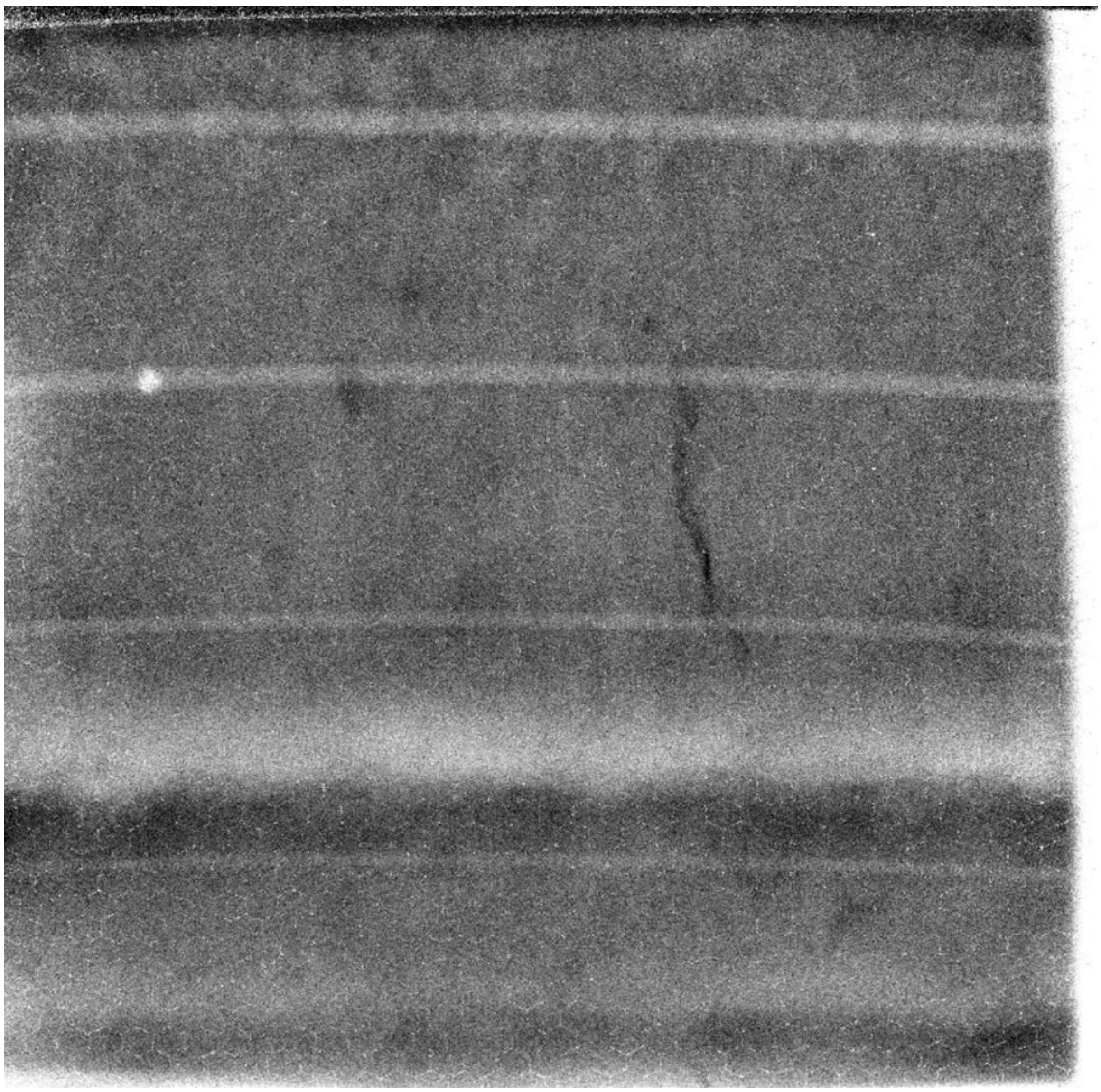

Figure B.162. Defect nr4, (P41) 2:nd position (Image size 26,45 x26,45 mm^2)

P41 nr4 77 deg spline 8 bit 512 inv.avi

B.7.7.8 Defect nr7 (P41)

α=8°and Θ=8°; From -8° to +8°; 2°/pos; 9 positions

X [mm]	X_1	X_2	nopx	Z_{max} [mm]	Length [mm]
0	34	237	237	11,0	22,6

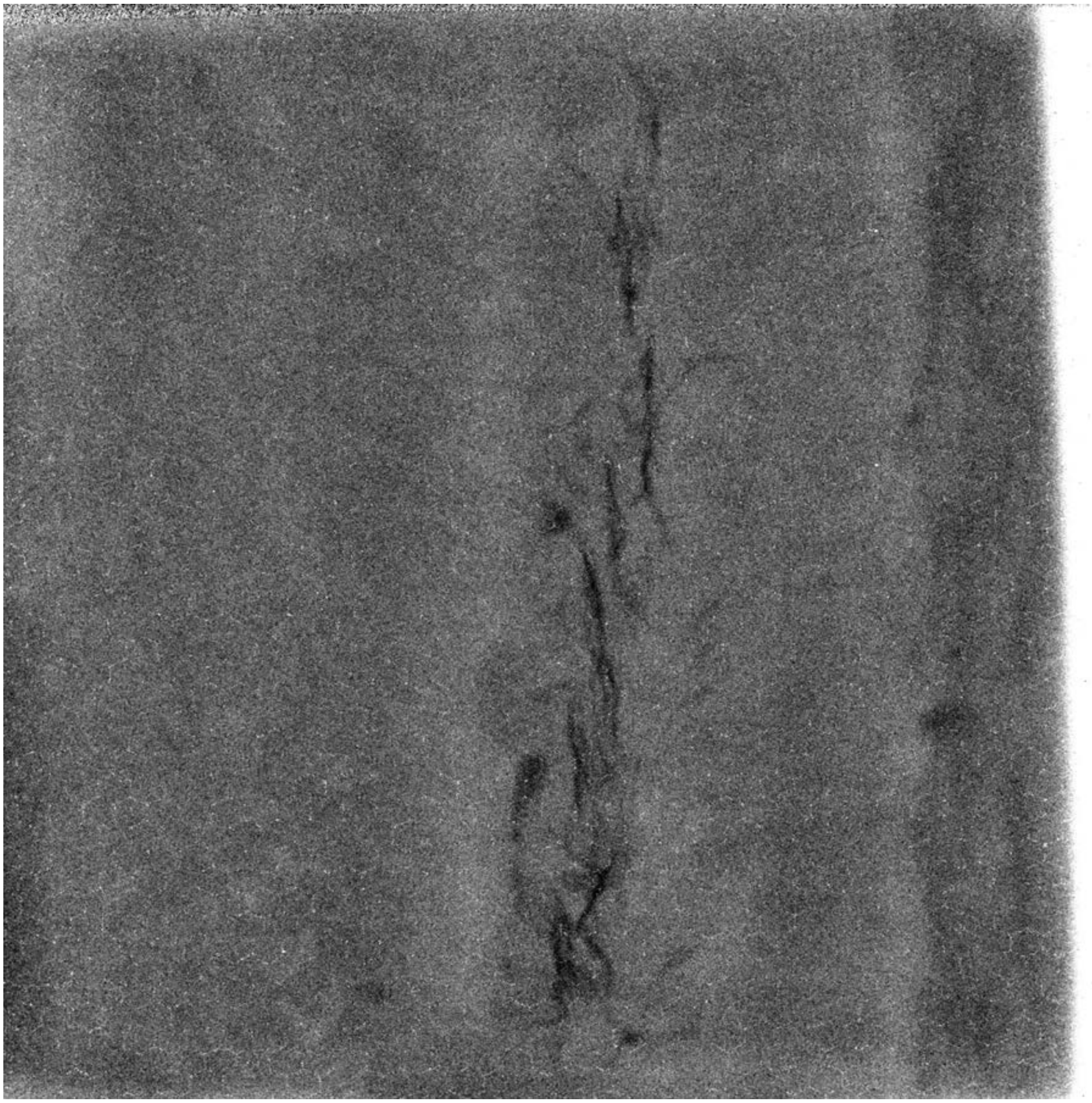

Figure B.163. Defect nr7, (P41) 8:th position (Image size 26,45 x26,45 mm^2)

P41 nr7 173 deg spline 8 bit 512 inv.avi

B.7.7.9 Defect nr8 (P41)

α=8°and Θ=2°; From -8° to +8°; 2°/pos; 9 positions

X [mm]	X_1	X_2	nopx	Z_{max} [mm]	Length [mm]
0	116	236	120	5,5	22,7

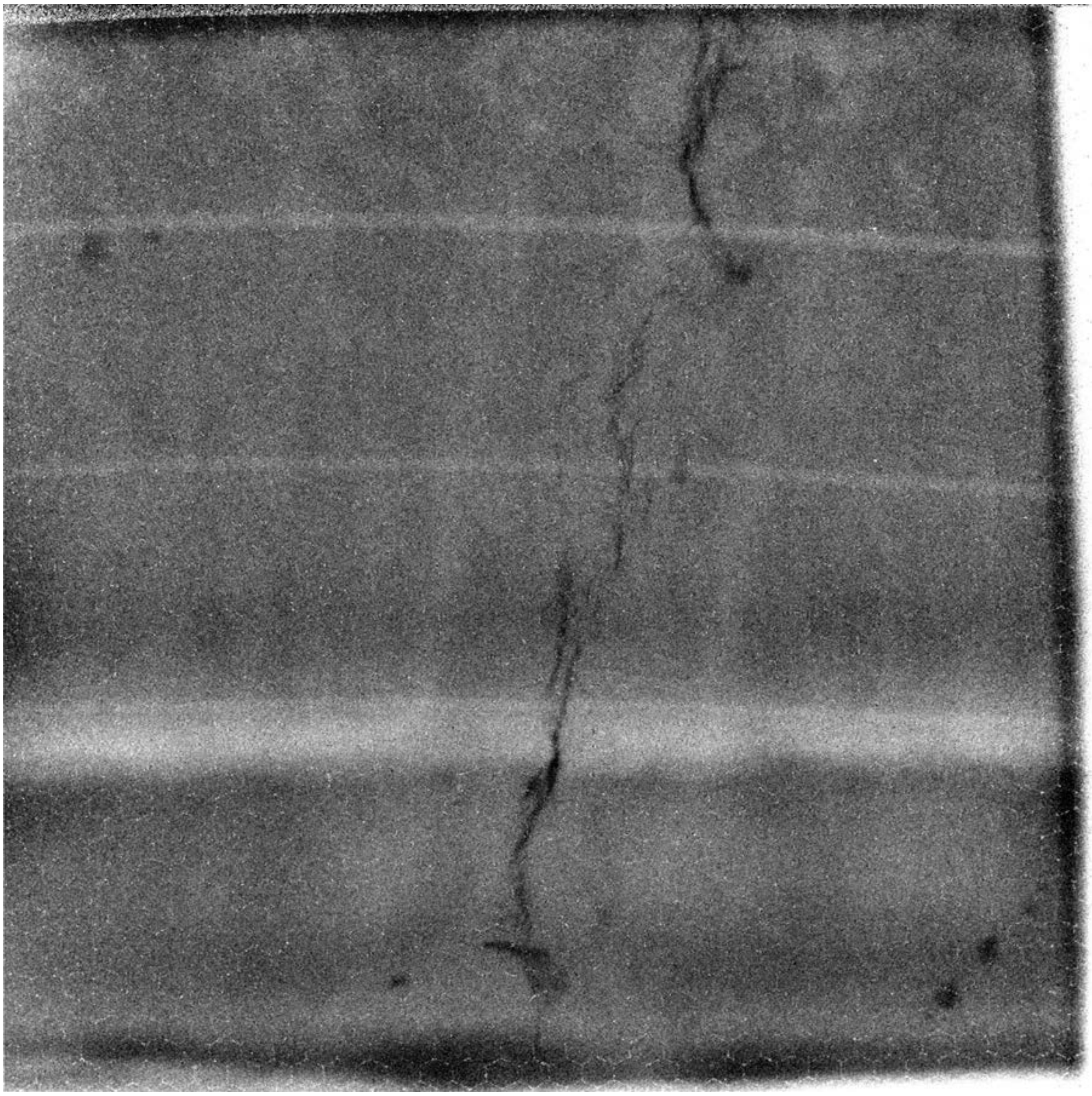

Figure B.164. Defect nr8, (P41) 6:th position (Image size 26,45 x26,45 mm^2)

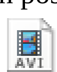

P41 nr8 206 deg spline 8 bit 512 inv.avi

Appendix C

Korea Detailed Technique Descriptions

Appendix C

Korea Detailed Technique Descriptions

C.1 Nonlinear Resonant Ultrasound Spectroscopy, Technique ID 11-NRUT0

C.1.1 Overview

C.1.1.1 Principles of Nonlinear Resonant Ultrasound Spectroscopy

The studies on nonlinear acoustic effects have focused on identifying structural material characteristics and damage features. Different nonlinear effects include second harmonic generation, modulation of sound by low-frequency vibrations, amplitude-dependent internal friction, and amplitude-dependent resonance frequency shifts. The first applications of the nonlinear acoustic technique for material characterization used measurements of the second harmonic generated by the nonlinear distortion of a primarily sinusoidal acoustic wave propagating in a medium with defects. Later it was realized that harmonic generation analysis is not the only, and not always the best way to implement the effective nonlinear acoustic NDE. Other nonlinear techniques include the cross-modulation (frequency mixing) of low and high-frequency sound and studies of the amplitude dependence of the mode resonance peak in a specimen conducted at Los Alamos National Laboratory. All these techniques are based on nonlinear wave interactions and nonlinear resonances. Due to the use of resonant modes, these methods need much less acoustic power than the travelling-wave methods used before. In particular, acoustic effects due to material hysteresis what is often associated with the crack presence have been observed in these experiments. It was also found that the nonlinear methods turn out to be more sensitive to damage-related structural alterations than any known method based on the measurements of linear parameters such as wave speed and attenuation. It was also confirmed that the macroscopic nonlinear response of a material is largely determined by its microstructure, which is understood as structural inhomogeneities with the scales small as compared to the sample sizes and the acoustic wavelength.

C.1.1.2 Nonlinear Resonance Frequency Shift

Resonance frequency shift, together with wave damping in resonance, is analysed as a function of the peak acceleration amplitude. A detailed discussion of the corresponding experimental apparatus can be found in papers published by the Nonlinear Elasticity group of Los Alamos National Laboratory in collaboration with several European laboratories and universities. One example is an experiment with a thin, rectangular beam (400mm × 26mm × 4mm) made of fibre-cemented artificial slate used in roofing constructions. The synthetic fibres (4 mm thick) used in the production process have a principal orientation perpendicular to the length-wise direction of the beam. The beam is excited at its lowest-order flexural (bending) resonance mode by a low-distortion speaker, positioned at 2 cm from the beam middle, parallel to its surface. The sample is suspended with nylon wires at the nodal points of the considered mode. The coupling medium between the specimen and the speaker is air (non-contact excitation). The speaker is driven in discrete frequency steps by a function generator through a high-power amplifier. In order to take the amplitude-frequency response near resonance, 4 to 10 sweeps over the same frequency interval, encompassing the first flexural mode resonance, were made at successively increasing voltages.

C.1.1.3 1.3 Materials Characterization Using Nonlinear Acoustic Parameters

To characterize the properties of the media, the conventional acoustic NDT technique utilizes linear acoustic parameters, such as sound speed and attenuation coefficient. Similarly, the non-linear technique employs the non-linear parameter (parameters) for the material characterization. The classical approach to describe the nonlinearity of a homogeneous elastic media is based on Taylor expansion of the dependence between the stress and strain tensors in the material and considers the coefficients of this expansion as the parameters of nonlinearity. In a simple example of one-dimensional longitudinal deformations in an isotropic solid, this expansion can be taken in a scalar form:

$$\sigma = \rho_o c_1^2 \left(\varepsilon + \beta\varepsilon^2 + \gamma\varepsilon^3 + \ldots \right), \tag{C.1}$$

where ρ_0 and c_1 are the density and the longitudinal sound speed in the medium, respectively, σ is the stress, ε is the strain, β, γ, … are the non-linear parameters, which characterize, respectively, the quadratic and cubic non-linearity of the medium.

Typical values of the non-linear parameter β do not exceed 10 for homogeneous media without defects (where nonlinearity is due to the inter-atomic forces acting in the crystal lattice), so that the contribution of the non-linear quadratic term into the relationship (1) is very small for practically all non-destructive strains, and the medium exhibits a linear behavior. The same is even more applicable for the cubic term with the coefficient γ. However, the presence of structural inhomogeneities such as grains, pores, cracks, and other defects is able to increase the nonlinear response of a material by orders of magnitude. This is true for a large variety of natural and constructive material such as rock and many metals.

The practical importance of using the parameters of acoustic nonlinearity as a possible tool for non-destructive testing, including that of the material defects caused by fatigue of external damage has been fully recognized during the last decade. Still, the crucial steps to transition the use of nonlinear acoustic techniques from the laboratory to practical applications is yet to be accomplished. Indeed, the nonlinear properties of many materials are more complicated than described by simple models. An important aspect of "structural nonlinearity" is that stress-strain dependence is hysteretic. In other words, the material behaves differently at the compression and dilatation phases of the loading cycle. This feature, known before in strong static loading, is now known to be present in very low dynamic strains, in the order of 10^{-7}–10^{-8}. The corresponding stress-strain dependence has a singularity and in a simplest case, it reads

$$\sigma = \rho_o\, c_1^2 \left[\varepsilon \pm \eta\left(\varepsilon^2 - \varepsilon^2 0 \right) \right], \tag{C.2}$$

where η is the coefficient of hysteretic nonlinearity and the "+" and "–" signs are taken for stress increase and decrease phases, respectively. As a result, the observed nonlinear behavior is quite specific; for instance, the resonance frequency shift is proportional to the amplitude of the basic signal rather than to the square of it as could be expected from the "normal" behavior corresponding to the expansion (C.1).

To obtain quantitative relationships between the state of the measured characteristics and the state of the material, a reliable theoretical basis must be created.

Recent research has demonstrated that nonlinear acoustic parameters of the material are closely related to the crack size distribution and elastic properties of the defects and, therefore, high acoustical nonlinearity due to cracks can be used for the damage assessment.

In summary;

- As the driving voltage increases, a shifting of resonance frequency is observed.
    - ✓ This resonance peak shifting indicates a nonlinearity of the specimen.
    - ✓ Resonance peak shift and peak width is related to Moduli E and Q-value of the materials.
- Normalized resonance pattern also reflects the nonlinearity.
    - ✓ If the resonance pattern is identical as the driving voltage increases, the specimen shows no nonlinearity (linear elastic response)
    - ✓ Otherwise (if the peak amplitude decreases as the driving voltage increases), the specimen reveals a nonlinear elasticity.

C.1.2 Equipment Apparatus and Setup the Transducer to the Specimen

All active acoustic methods of NDE are based on radiation of the required acoustic signals, reception and signal processing. The different regimes of operations require different kinds of radiation signals and different types of processing. The NRUS is a fully digital system that radiates and processes any acoustic signal.

The Nonlinear Resonant Ultrasound Spectroscopy (NRUS) methods are based on excitation of sweep frequency signals in the tested material and measurements of the dependence of the recorded signal amplitude on frequency. In this regime the sweep frequency signal is formed within the PC and is transformed to the transmitter channel of the NRUS system. The developed NRUS software provides radiation of sweep frequency signal in defined frequency band and sweep time. The Amplitude Frequency Responses (AFR) between transmitting and receiving are recorded for various output voltages. The results are presented in the normalized form where the received signal is divided to the system output. In the linear case the measured Normalized Amplitude Frequency Response (NAFR) does not depend on the applied signal amplitude and difference in the Normalized Amplitude Frequency Responses shows the presence of the tested part nonlinearity (Resonance frequency shift and amplitude dependable losses).

Figure C.1 shows a photo for the measurement system of nonlinear resonant ultrasound spectroscopy (NRUS). An arbitrary waveform generator and high power amplifier supply a sinusoidal wave with swept frequency. The piezoelectric elements are bonded on a side of the specimen for generation of the ultrasonic waves and reception of the waves (Figure C.2). In addition, a laser doppler vibrometer (Polytec LDV) was used for an acquisition of the ultrasonic waves (Figure C.3). A PC program controls all the equipment in the system and data acquisition.

In order to get an accurate ultrasonic resonance signals, following equipment are assembled as;

- An arbitrary waveform generator to generate the sinusoidal signals with specific frequency

- An high frequency amplifier to amplify the sinusoidal signal to 1~100 Vpp. The frequency response of the amplifier ranges up to 300 kHz. The output or the amplifier applied to a wide-band piezoelectric transducer to vibrate the specimen with frequency sweep.
- A digital oscilloscope for monitoring the waveform in time domain.
- A PC with software program to sweep the desired frequency range and store and display the spectrum in frequency domain.
- A laser Doppler vibrometer to measure the high frequency vibration or displacement the specimen.

An actual NRUS system is assembled for the Open RRT, shown in Figure C.4.

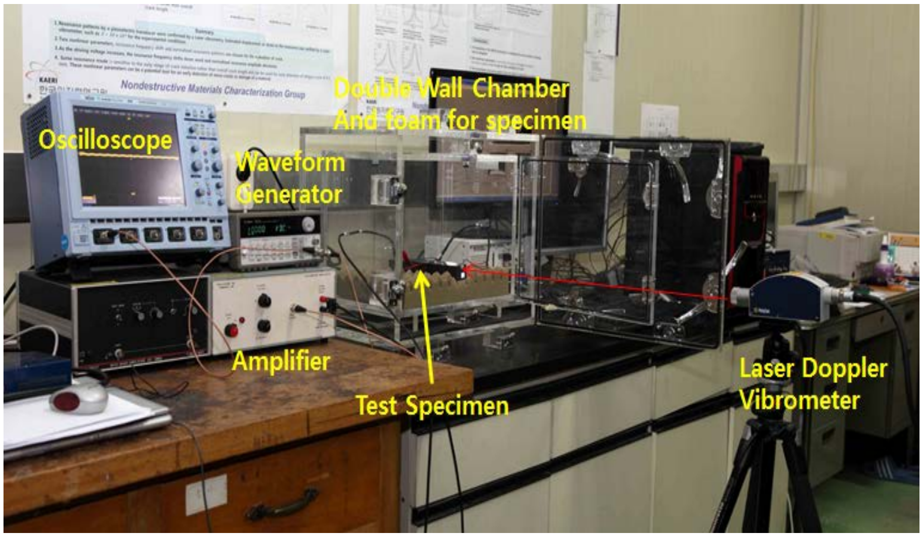

Figure C.1. Photo of Nonlinear Resonant Ultrasound Spectroscopy (NRUS) with a Laser Doppler Vibrometer

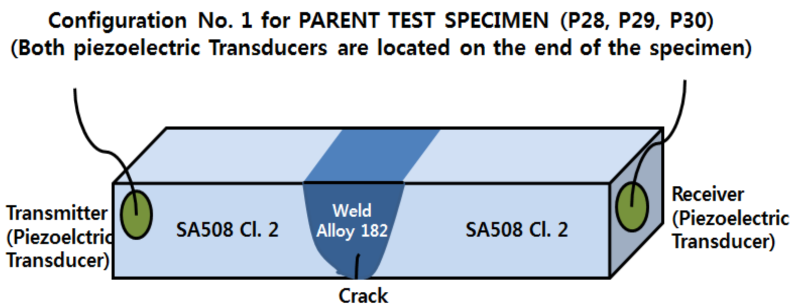

Figure C.2. Schematic Drawing of the Configuration No. 1 of the Piezoelctric Transducer and the PARENT Specimen for Nonlinear Resonant Ultrasound Spectrocopy

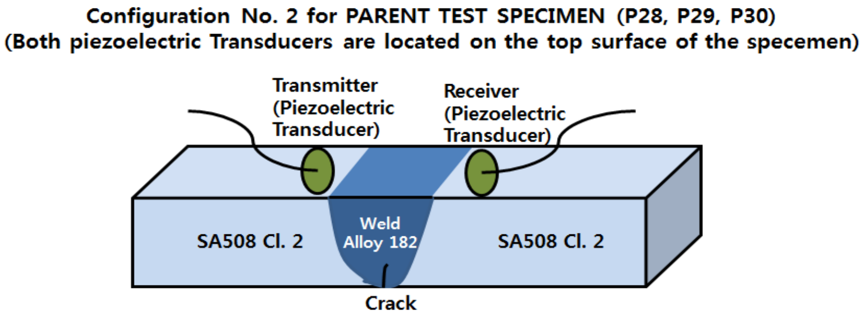

Figure C.3. Schematic Drawing of the Configuration No. 2 of the Piezoelctric Transducer and the PARENT Specimen for Nonlinear Resonant Ultrasound Spectrocopy

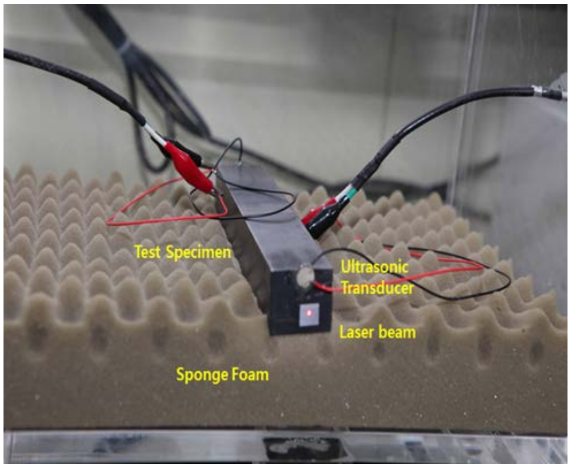

Figure C.4. Photo Shows a PARENT Specimen (P28) at the NRUS Experiment. The resonance spectrum was acquired by both a piezoelctric transducer and a laser Doppler vibrometer.

C.1.3 Preliminary Estimation of Resonance Frequencies of the Specimens (P28, P29, and P30)

Resonance frequencies and vibration modes are estimated by the LANL RPR code[1] (rectangular parallelepiped model). The specimen (SA 508 cl. 2) was assumed as a low carbon steel with an elastically isotropic material. The input parameters for the estimation are the dimension of the specimen (d_1 = 22 cm, d_2 = 3.03 cm, d_3 = 3.5 cm), density = 7.8 gm/cc and initial guess of ε_{11} = 277.0 GPa, ε_{44} = 79.14 GPa (Cheong et al. 2000).

Table C.1 shows the estimated resonance frequencies and vibration modes for the specimen. Table C.1 lists the first 50 resonance frequencies with the vibration modes and orders. The abbreviations of the vibration modes, "k" are summarized as,

[1] RUSpec software by Magnaflux Quasar Inc.

k=1 uniform translation along x-direction
k=2 rotation about y-axis
k=3 rotation about z-axis
k=4 rotation about x-axis
k=5 volume oscillation
k=6 uniform translation along z-direction
k=7 uniform translation along y-direction
k=8 complex motion.

The number of vibration orders are also listed in the column 'i'.

Table C.1. Estimated Resonance Frequencies and Vibration Modes for the Specimen P28, P29, and P30

n	fex	fr	fr [kHz]	%err	wt	k	i
1	0.030078	0.003078	3.08	-89.77	0	7	2
2	0.003489	0.003489	3.49	0.01	0	6	2
3	0.006526	0.006526	6.53	0	0	4	1
4	0.007716	0.007716	7.72	-0.01	0	3	2
5	0.008548	0.008548	8.55	0	0	2	2
6	0.011546	0.011546	11.55	0	0	5	1
7	0.01305	0.01305	13.05	0	0	8	2
8	0.013578	0.013578	13.58	0	0	7	3
9	0.014746	0.014746	14.75	0	0	6	3
10	0.01957	0.01957	19.57	0	0	4	2
11	0.020068	0.020068	20.07	0	0	3	3
12	0.02143	0.02143	21.43	0	0	2	3
13	0.022972	0.022972	22.97	0	0	1	2
14	0.026099	0.026099	26.10	0	0	8	3
15	0.026897	0.026867	26.87	-0.11	0	7	4
16	0.02829	0.02829	28.29	0	0	6	4
17	0.03264	0.03264	32.64	0	0	4	3
18	0.034122	0.034122	34.12	0	0	5	2
19	0.03456	0.03456	34.56	0	0	3	4
20	0.03578	0.03579	35.79	0.03	0	2	4
21	0.04038	0.040384	40.38	0.01	0	8	4
22	0.041924	0.041924	41.92	0	0	7	5
23	0.042493	0.042493	42.49	0	0	6	5
24	0.044754	0.044754	44.75	0	0	1	3
25	0.046332	0.046332	46.33	0	0	2	5
26	0.047535	0.047535	47.54	0	0	4	4
27	0.050986	0.050986	50.99	0	0	6	6
28	0.052126	0.052126	52.13	0	0	3	5
29	0.052191	0.052191	52.19	0	0	2	6
30	0.05225	0.052251	52.25	0	0	8	5
31	0.05272	0.052723	52.72	0.01	0	4	5
32	0.05444	0.054439	54.44	0	0	5	3
33	0.05507	0.055073	55.07	0.01	0	3	6
34	0.05564	0.05564	55.64	0	0	7	6
35	0.05874	0.058742	58.74	0	0	7	7
36	0.05917	0.05917	59.17	0	0	6	7
37	0.05982	0.059824	59.82	0.01	0	8	6
38	0.06006	0.060069	60.07	0.01	0	3	7
39	0.06015	0.060157	60.16	0.01	0	4	6
40	0.06052	0.060518	60.52	0	0	7	8
41	0.06074	0.060745	60.75	0.01	0	4	7
42	0.0609	0.0609	60.90	0	0	8	7
43	0.06132	0.06132	61.32	0	0	1	4
44	0.06134	0.061338	61.34	0	0	5	4
45	0.06137	0.061373	61.37	0	0	3	8
46	0.06187	0.061869	61.87	0	0	2	7
47	0.06228	0.062282	62.28	0	0	1	5
48	0.06266	0.062656	62.66	-0.01	0	8	8
49	0.06282	0.062815	62.82	-0.01	0	7	9
50	0.06492	0.06492	64.92	0	0	8	9

C.1.4 Data Analysis of NRUS Data

C.1.4.1 Examples of NRUS Applications

It is seen that variations of NRUS spectrum for the cracked ring are much higher than for the intact ring. We used steel bearing ring (#1, left specimen of Figure C.5) and two bearing rings made from sintered metal (middle and right specimens of Figure C.5). It was not completely sintered ("green" part) and specimen #2 (middle specimen of Figure C.5) has several cracks that provided high acoustic nonlinearity. Nonlinear amplitude frequency response of intact specimen (#1) is shown Figure C.6 and cracked specimen (#2) shown in Figure C.7.

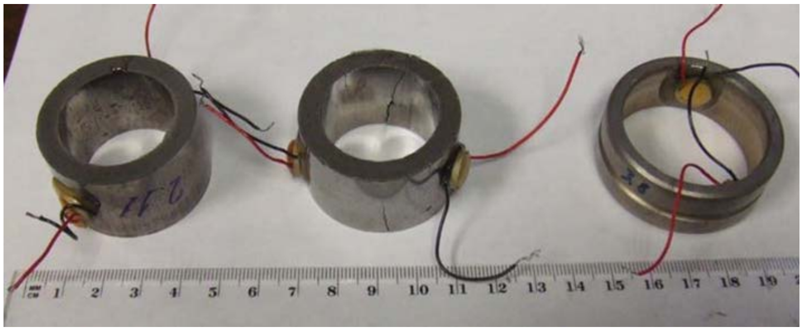

Figure C.5. Reference Tested Specimens

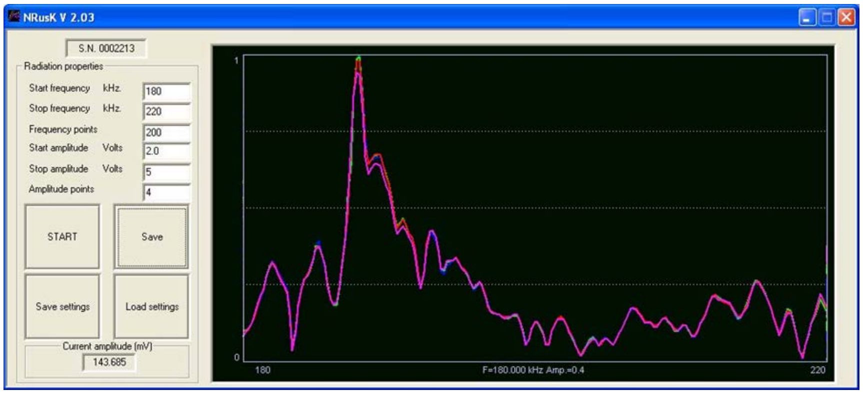

Figure C.6. Measured Nonlinear Amplitude Frequency Response (NAFR) for Intact "Green" Ring (Sample #1) in the Frequency Band 180–220 kHz

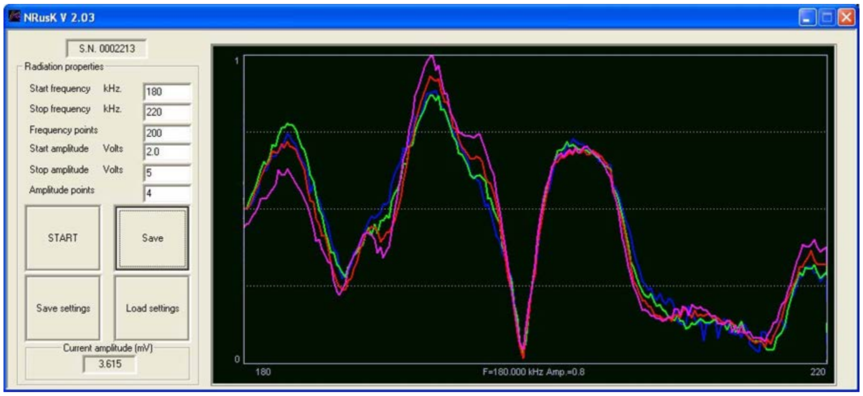

Figure C.7. Measured Nonlinear Amplitude Frequency Response (NAFR) for Cracked "Green" Ring (Sample #2) in the Frequency Band 180–220 kHz

Another example of resonance frequency shift in a CT (Compact Tension) specimen with a stage of crack initiation and a specimen with a long crack, such as crack length of 7 mm are shown in Figure C.8. Resonance pattern from an intact CT specimen shows a little shift of resonance frequency even the driving amplitude varies. It means a little nonlinearity and almost no non-uniformity in the specimen. However, significant amount of the resonance frequency shifts downward is observed in the cracked specimen, as the driving voltage increases. As the crack length is in the range of mm, resonance frequency shifts downward and the normalized amplitude decreases as the driving voltage increases.

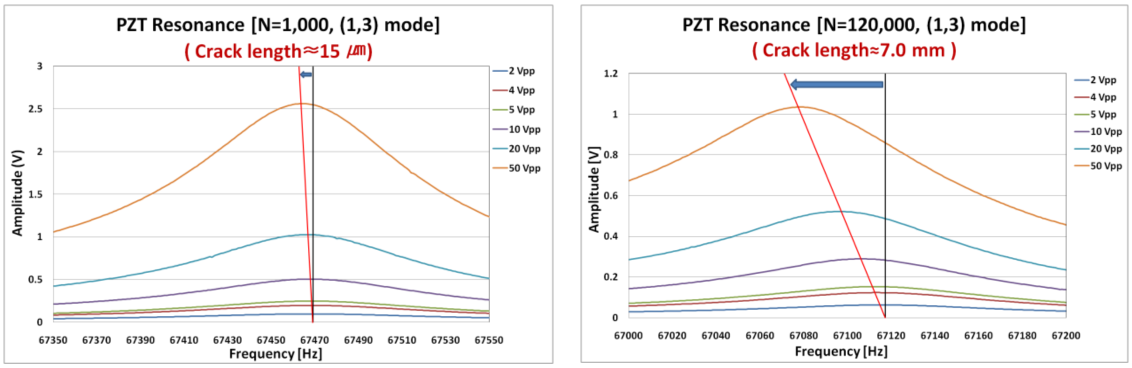

Figure C.8. Resonance Frequency Frequency Shift in (a) CT Specimen in the Early Stage of Crack Initiation (left) and (b) CT Specimen with Crack Length of 7.0 mm (right)

C.2 Pulsed Eddy Current, Technique ID 11-PECT0

PEC testing has been demonstrated to be one of the most effective methods, and is capable of tackling different inspection tasks, such as sub-surface defect detection in complex structures. Among the available conventional NDT methods, eddy current testing (ECT) is the most promising technique to detect flaws in conductive materials. The conventional ECT uses single-frequency sinusoidal excitation for the detection of defects or flaws as a function of changes in voltage, impedance, or phase, because of limited depths of penetration and complexity in a signal analysis ECT was confined to limited applications. Unlike a conventional ECT, PEC uses multiple frequency sinusoidal excitation pulse of the electric current through the excitation coil. PEC is more economical than other NDT methods. Because of many advantages of PEC over a conventional eddy current method, such as low power consumption owing to a short pulse excitation and the broad band nature of a pulse, PEC has the capability to penetrate different depths in a conductive material and provides the depth information of the defects. Even though the use of PEC has long been considered for the testing of materials, in recent decades, PEC testing has become the subject of wide spread interests in NDT because of its advancement in technologies such as computer data acquisition and digital signal processing. Furthermore, PEC has the capability to measure the thickness, conductivity, and in particular, sub-surface crack measurements, crack reconstruction, and depth estimation.

C.2.1 Overview

The PEC testing is the new promising technological approach to NDT, and it has been principally developed for surface, subsurface flaws measurements and corrosion in the multilayered structures. Among the available conventional NDT methods, one of the most used is eddy current testing (ECT) to detect the flaws in conductive materials. Unlike conventional ECT the PEC uses pulse of electric current through the excitation coil. In contrast to the conventional ECT (operates with single sinusoidal frequency), the pulse ECT employ repetitive pulses having short duration in time (having broad band), which yields a signal having frequency contents from DC to several KHz or higher. Skin depth is a function of the resistivity and permeability of the test material, and test frequency. Because the eddy current diffusion depth depends on the excitation frequency the PEC technique has the potential for bringing up deeper information about the tested sample. In order to detect deep crack from the surface, the magnetic field has to penetrate the sample and arrive up to the crack. Therefore, high current and reasonable frequency range are essential for the detection of defects using PEC. In PEC, a response pulse always comes after an excitation pulse is over, so this method is less susceptible to interference, moreover the pulse excitation can minimize the power consumption, which is more capable in the development of portable instruments. Because of the potential advantages of the PEC, prevalent investigations on this technique have been made, such as for detection of subsurface crack and corrosion in aircraft multi-layer structure.

C.2.2 PEC Equipment

The block diagram of the PEC system design is shown in Figure C.9. The system consists of a rectangular waveform generator, a probe integrated with an excitation coil and a Hall-sensor, an amplifier to amplify the signal from Hall-sensor, a data acquisition card and a PC with signal processing software. The system works as follows; the waveform generator produces a rectangular waveform with variable frequency and duty cycle. The waveform is fed to a coil driver circuit, which excites the induction coil in the probe with pulsed current. When the probe is mounted on the metal structure, the pick-up sensor will measure the vertical resultant magnetic field, which is the vector sum of the one generated by the excitation coil and the opposing one generated by the induced eddy current in the sample (Primary flux $\Phi 1$ created by driving coil induces EC in the conducting medium, induced EC produces counter flux $\Phi 2$. Now pick-up sensor measures total flux $\Phi = \Phi 1 + \Phi 2$.). A voltage amplifier with variable gain amplifies the signal from the pick-up sensor. The A/D card will convert the input signal into digital data ready to be processed by written software in the PC. The software performs communication with the data acquisition card. Signal pre-processing, feature extraction, defect categorization, and the presentation of the results are on the PC monitor.

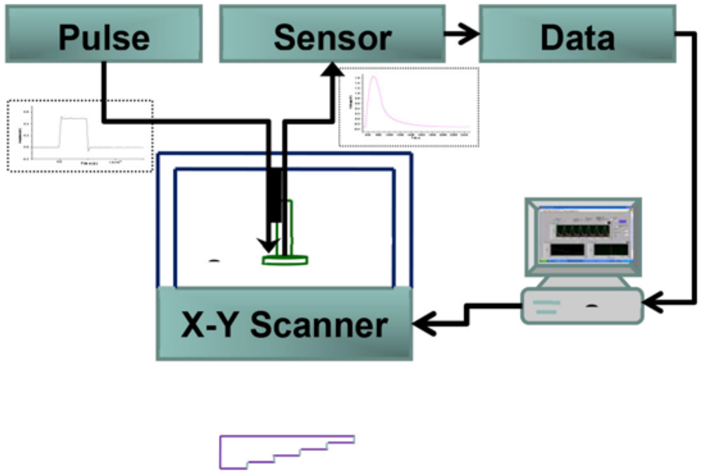

Figure C.9. Block Diagram of the PEC System

The amplifier supplies the high current uni-polar (+Ve) pulse to the Driving Coil or exciting coil which is in the PEC probe. With this amplifier we can control the pulse width considering the skin depth of sample (from 1 ms–10 ms) in case of nonmagnetic materials, pulse frequency (500 MHz–50 Hz), and pulse amplitude (max- 100 A). The excitation coil is a copper wire which has square cross section with 1×3 mm having total resistance 0.92 Ω, wound 132 turns on the cylindrical ferrite core. The probe has a 60mm height and 9mm inner diameter, and the Hall-sensor was positioned in the center of probe to detect the induced signal from defects. The cylindrical type ferrite core not only reduces the magnetic leakage but also improves the detection sensitivity by sustaining adequate excitation intensity. The Hall-sensor gives the frequency independent sensitivity from DC to 100 kHz, high spatial resolution having less power consumption with increased sensitivity and simple readout circuitry. When we bring the probe proximity to conducting plate, the steep exciting pulse induces eddy currents and its associated magnetic field dissipates exponentially to approach its steady state. The induced eddy currents flow in the opposite direction to the currents which are flowing in the exciting coil, hence when the probe is placed on the conducting plate, the detected field rises slowly to the maximum peak value.

C.2.3 Tested Sample and Detection of Crack

The three kinds of test blocks with ID 28, 29, and 30 provided by ALSTOM, and the flaw types of these test blocks are BWR/NWC SCC Crack, Fatigue Crack, and PWR SCC crack, respectively. The sample was composed by the welding of two base metals, and the composition of base metal is 22NiMoCr37, and the welding metal is alloy 182. A 10 mSec pulse width and 15A excitation current is applied to exciting coil of the probe to test the sample. The PEC probe is fixed to the X-Y scanner to perform the manual scanning on the defect free side of the tested sample. A LabVIEW-based data acquisition program was developed to continuously monitor the variation in the thickness of the sample and is observed on the computer screen. The time domain feature which is the peak value of detected pulse is used for the scanning test to detect the sub-surface cracks in the tested sample.

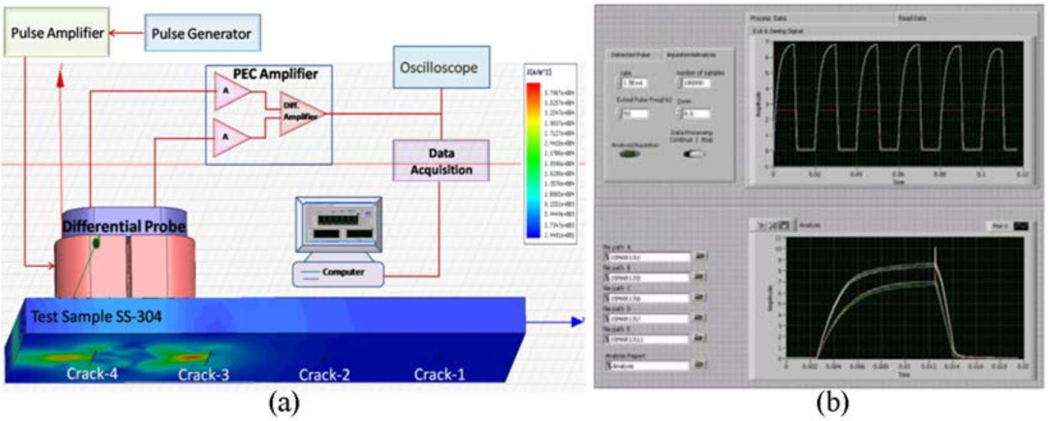

Figure C.10. (a) Configuration of PEC System; (b) LabVIEW Data Acquisition Front Panel

The pulse width (from 1 ms–10 ms)
Pulse frequency (500 Hz–50 Hz),
Pulse amplitude (max- 100 A).

The excitation coil total resistance 0.92 Ω,
132 turns on the cylindrical ferrite core.
The probe: 60 mm height; 9 mm ID

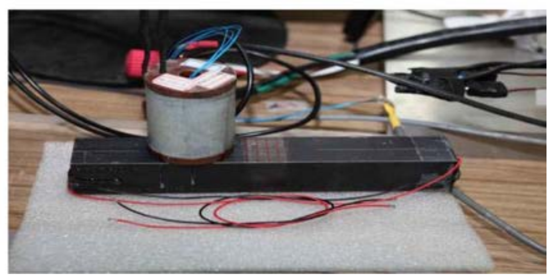

Figure C.11. Pulsed Eddy Current System and Experimental Setup (Probe on Sample)

C.2.4 Configuration of PARENT Test Specimen (P28, P29, P30)

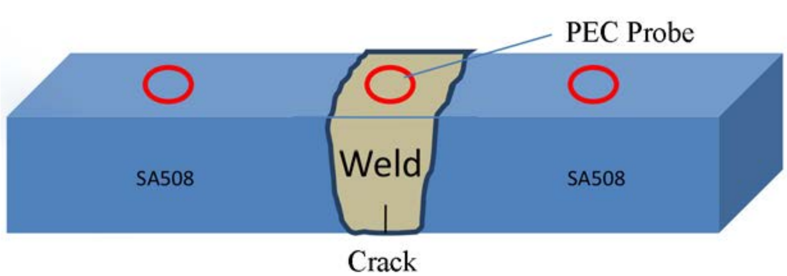

Figure C.12. Schematic of PARENT Test Specimen. PECT probe is located on the opposite side of crack surface.

C.2.5 Experimental Results and Feature Extraction

If the probe placed on the test sample in such a position, then the typical response signal shown in Figure C.13, is the induced signal detected by the Hall-sensor from test block.

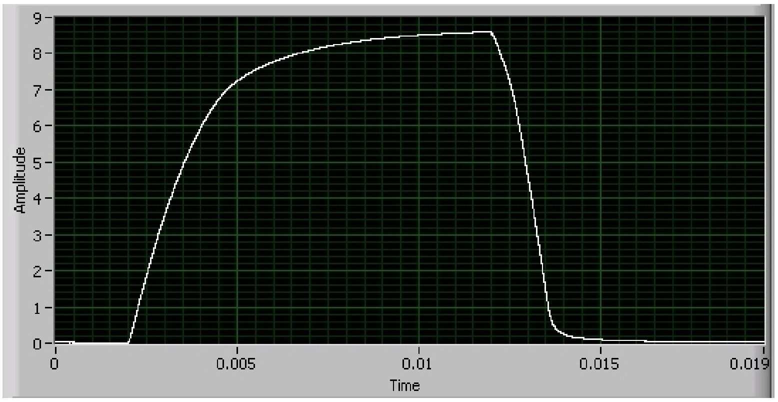

Figure C.13. Typical PEC Signal Induced in the Hall-sensor from the Test Block

Calibration of PEC signal with standard specimen is essential to obtain a reliable experimental result. Because of no calibration sample is prepared, the validity of experiment was verified using the difference of the PEC peak amplitude obtained in the crack and opposite side (Figure C.14). The base metal of sample block 22NiMoCr37 is ferromagnetic and welding material alloy 182 is nonmagnetic material. Therefore, the PEC amplitude measured in the ferromagnetic part is higher than that of the nonmagnetic part. The y coordinate 10 and 12 cm neighborhood is the interface region between ferromagnetic and nonmagnetic material. The crack is positioned in the neighborhood of y coordinate 11 cm, which shows the minimum PEC signal amplitude.

The important characteristic of detected signal to interpret the results is the peak value of the pulse. The measuring points were selected as a x-y coordinate, the x points were fixed at the center of transverse direction and y points were selected along the longitudinal direction. Figure C.15 show the change of PEC peak amplitude along the coordinate.

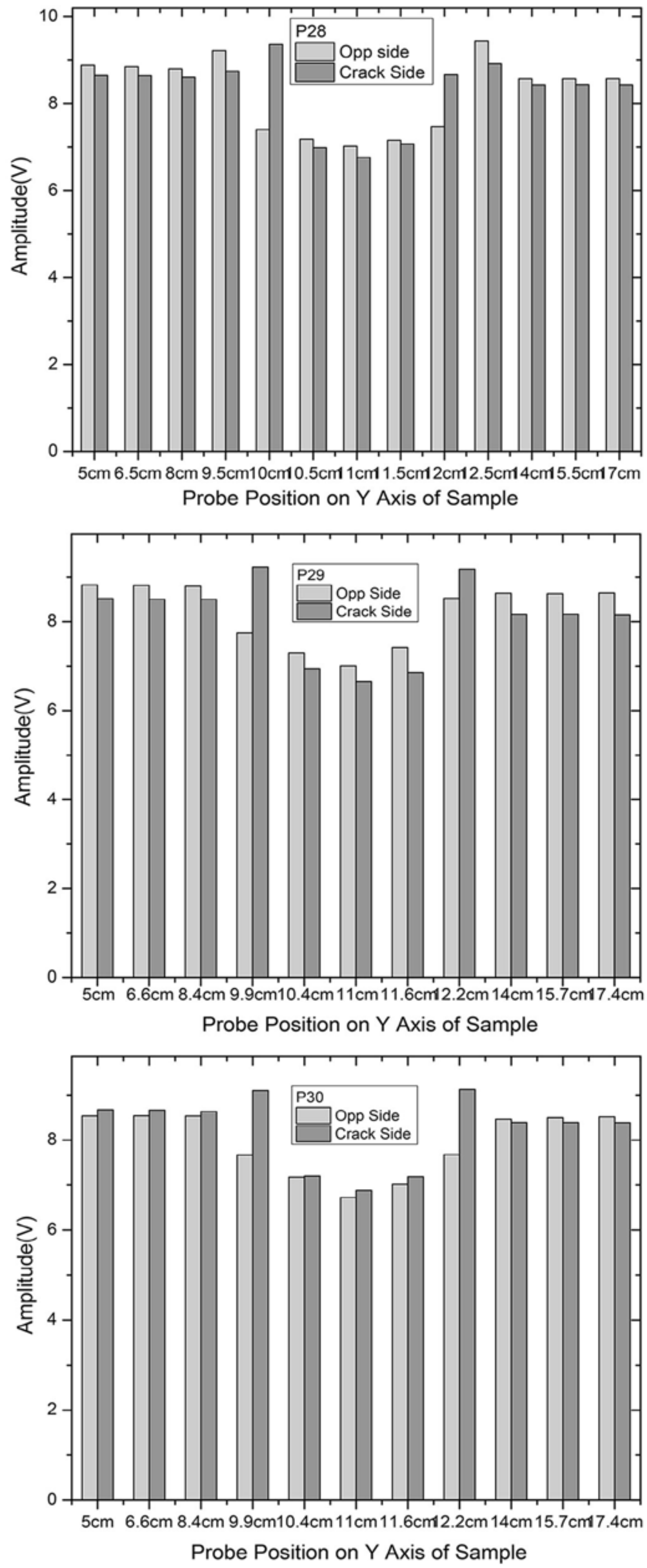

Figure C.14. The Difference of the PEC Peak Amplitude Obtained in the Crack and Opposite Side for P28, P29 and P30

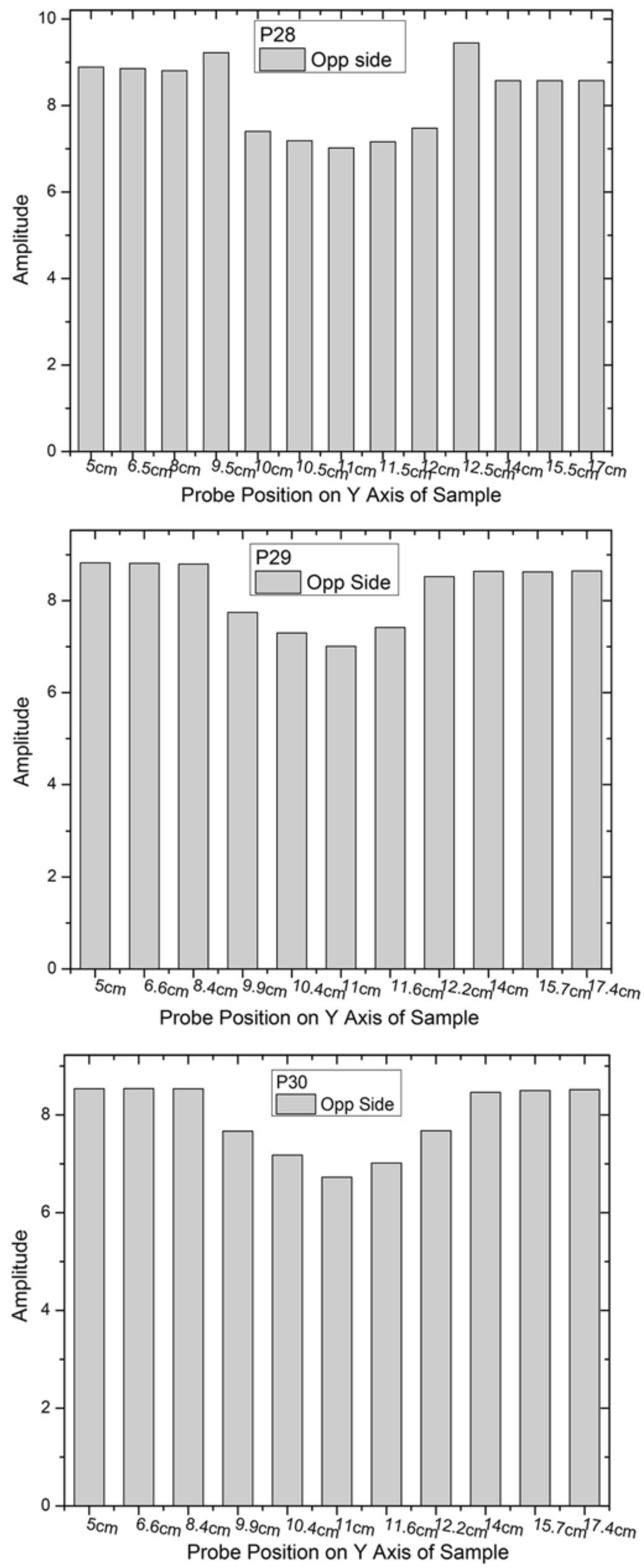

Figure C.15. The Difference of the PEC Peak Amplitude Obtained in the Crack and Opposite Side for P28, P29 and P30

C.2.6 Summary

The nondestructive evaluation (NDE) using PEC to detect the sub surface crack under the thick plate has been performed on the PARENT round robin sample. The PEC amplitude measured in the ferromagnetic part is higher than that of the nonmagnetic part; therefore, it is not certain that the decrements of amplitude are attributed to the defects or nonmagnetic part. The y coordinate 10 and 12 cm neighborhood is the interface region between ferromagnetic and nonmagnetic material. The crack is positioned in the neighborhood of y coordinate 11 cm, which shows the minimum PEC signal amplitude.

C.3 Phased Ultrasonic Array, Technique ID 20-PA1, 20-PA2

C.3.1 Scope

- This procedure is applicable to ultrasonic examination of dissimilar metal weds and adjacent material utilizing phased array technique (PAUT).
- The objective of examination performed in accordance with this procedure is to accurately detect, length sizing and depth sizing within the specified examination volume.

C.3.2 Personnel Requirement

- Personnel performing exams has an experience for equipment setup, calibration, examination and data evaluation.

C.3.3 Equipment

- Olympus-Omniscan MXU (16:128) instrument with 8 channels
- Software (TomoView-2.R3) capable of collecting and storing full waveform signals

C.3.4 Transducer and Wedge

- Total element: 32 or 64
- Focal range: 40–60 mm
- Frequency: 2.25 or 5 MHz
- Wedge: Angle/Length/Width
- Element size: Length/Width/Pitch

C.3.5 Calibration

- Velocity calibration for angle beam probe using IIW radius block
- Instrument linearity check (Screen height/Amplitude control/Transducer values)
- Examination range and signal amplitude calibration
- Sensitivity calibration using calibration block

– A detailed drawings for calibration block with dimension shall be provided

C.3.6 Inspection Technique

- Examination volume

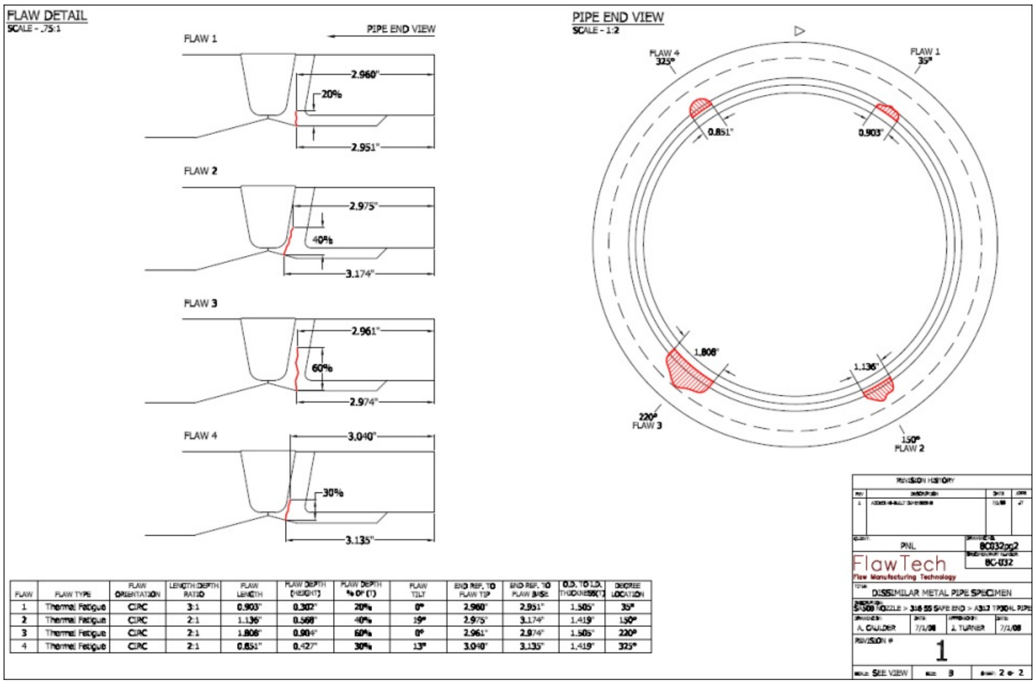

Figure C.16. P1 Specimen

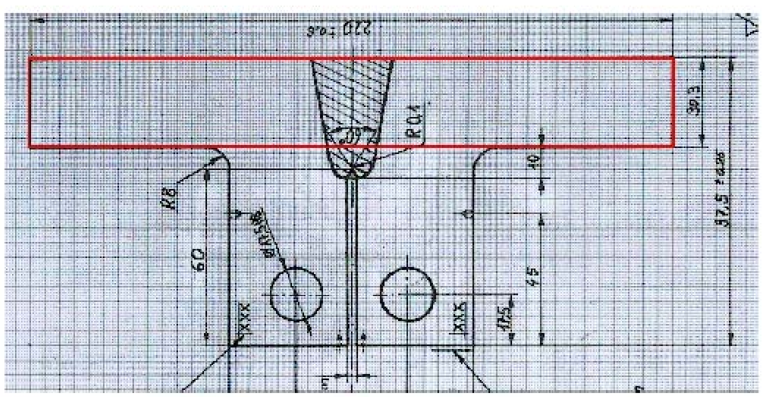

Figure C.17. P28, P29, P30, P31, P32

- Axial examination
  - For examination reflectors oriented parallel with the weld, scanning shall be directed essentially perpendicular to the weld axis from two directions (Up/Down)

- Circumferential examination
  - For examination of reflectors oriented perpendicular with weld, scanning shall be performed along the weld axis in both clockwise and counter-clockwise directions (CW/CCW)
- Scan speed
  - Scan speed shall be not excited 2.0 inches per second for examination
- Overlap
  - Scan pattern shall provide min of 50 % overlap the transmitting element in the indexing direction
- Examination sensitivity
  - Scan image shall be established on the component to be examined and adjust the gain level until the signal response from the inside diameter (ID roll) is between 5 % and 20 % FSH
- All suspected flaw indications, regardless of amplitude, shall be investigated to the extent necessary to provide accurate characterization, identify, and location

C.3.7 Inspection Classification

- Flaw indications
  - All images produced by reflectors within the volume to be examined, regardless of amplitude that cannot be clearly attributed to the geometrical or metallurgical properties of the well configuration shall be considered as flaw indications.
- Non-relevant indication (Geometric/Metallurgical)
  - All image produced by reflectors within the volume to be examined that can be attributed to the geometry of the weld configuration shall be considered as non-relevant indicators.

C.3.8 Indication Discrimination

- Indication has a good image along the length of the component
- Indication provides substantial and unique flaw image

C.3.9 Indication Sizing

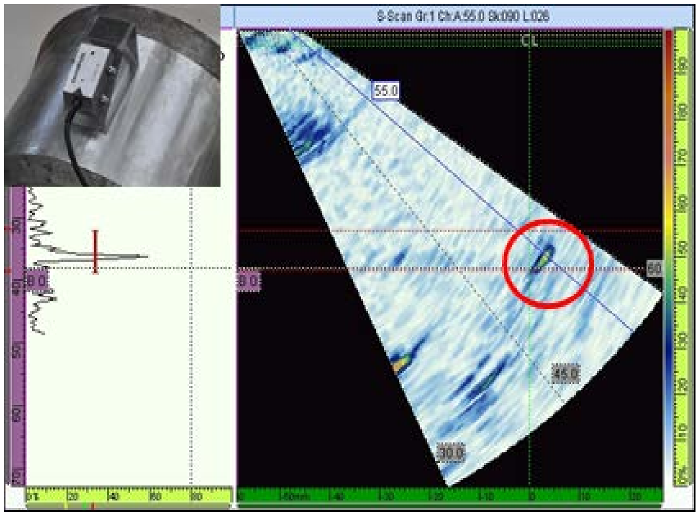

Figure C.18. PAUT Image from Flaw

C.3.10 Recording of Reflectors

- The datum “0” reference points used for recording indications shall be in accordance with the system shown in following figure.

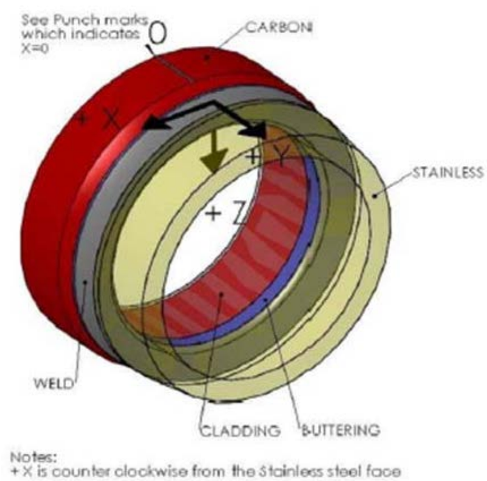

- Flaw indications
  - For flaw indications (images) the following information shall be recorded regardless of amplitude
  - Record the flaw location (Y1 and Y2) from weld center line zone
  - The length dimension (X1 and X2) from “0” reference points
  - The dimension Z1 (upper) and Z2 (lower) through wall

C.3.11 Examination Reporting

- Examination data shall be recorded on a data sheet
  - calibration data sheet
  - examination personnel and examination data
  - examination procedure number/revision number
  - equipment serial number, manufacturer, model=
  - search unit angle, manufacturer, serial number, model=
  - search unit frequency, size, mode, shape, beam focus, wedge
  - cable type, length, couplant type
  - signal response amplitude and sweep position obtained from reflectors
  - examination sensitivity and location of reflectors

C.3.12 Calibration Data Sheet for Phased Array Ultrasonic Examination

Calibration Data Sheet for Phased Array Ultrasonic Examination

Data sheet No.

Object of Inspection	Name:	No.:	Inspection Method:	Dtate:	
Inspection Method	Fabricator:	Model:	Serial No.:	Inspected by:	Level:
Reference Block	No.:	Nominal Size:	Material:	Confirmed by:	Level:

Probe	Refraction Angle		Freq.	Fabricator	Model	Serial No.	Probe Index Point (mm)	Specified Sensitivity(dB)	Echo Height (CRT%) / Beam Path Length (mm)			
	Nominal	Measured							1/8 S	2/8 S	3/8 S	
1												
2												
3												
4												

Probe: 1 Probe: 2 Probe: 3

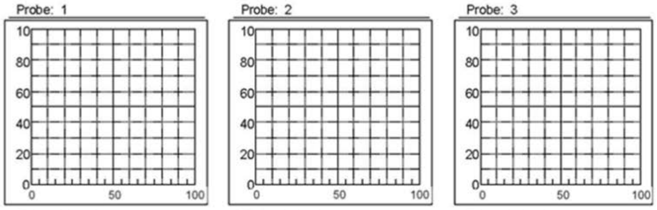

Full scale(mm): Full scale(mm): Full scale(mm):

Couplant: Cable Length:

Remarks:

Signature

C.3.13 PARENT RRT Data Sheet

ATTACHMENTS 2.

PARENT RRT – DATA SHEET

Inspection Results, One Technique
Data Sheet No:

For Piping Test Blocks
☐ Inspection from Outer Diameter
☐ Inspection from Inner Diameter
D = _______ (mm) See Appendix 2

Test piece: Date: Team code: Weld volume inspected:

X1 (*) = X2 (*) =
Y1 (mm) = Y2 (mm) =
Z1 (mm) = Z2 (mm) =

Results based on One technique:
Detection:
Characterization:
Length sizing:
Depth sizing:

* X Units are millimeters for piping test blocks and degrees for BMI test blocks. Y and Z units are always inmm.

Defect No:	X1(*)	X2(*)	Y1 (mm)	Y2 (mm)	Z1 (mm)	Z2 (mm)	Y_{max} (mm)	Ampl 100% ± dB	Surface breaking Yes	No	Comments

TEAM SIGN: **INVIGILATOR SIGN:**

C.3.14 DAG Technique Summary

- Inspection company: KRISS
- Team code : KRISS TEAM 20
- Inspection Procedure: KRISS-PAUT-01
- Specimen: P1, P7, P28, P29, P30, P31, P32
- Inspection type: Manual Phased Array Ultrasonic Examination from OD
- Scan type: Scanning for circumferential flaw (oriented parallel to the weld) and scanning for axial flaw (oriented transverse to the weld)
- Detection

Technique detection	Evaluation methodology detection
PAUT with curved wedge based on reflection from flaw - Pulse echo PAUT probe with 32 elements, 2.25 MHz, reflection (Longitudinal-wave)	Based on PAUT image from echo dynamic pattern and/or signal amplitude - Evaluation of images by PAUT Tx-Rx dynamic focusing algorithm

- Characterization

Technique characterization	Evaluation methodology characterization
PAUT with curved wedge contact technique based on reflection of flaw. - Image by PAUT pulse echo method 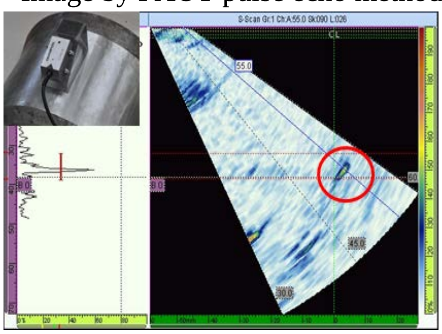	Difference between flaw image and non-relevant indication (geometric/metallurgical) - Whether the images can be clearly attributed to the geometric/metallurgical properties of weld configuration or not - Characterized as embedded flaws if the image doesn't show evidence of flaw from the inside back wall

- Length and width sizing and flaw positioning

Length sizing and positioning	Evaluation methodology sizing and positioning
PAUT with curved wedge contact technique based on reflection of flaw. - Image by PAUT pulse echo method	PAUT equipment provides the size of flaw and position from the sector scan image

C.4 Ultrasound Infrared Thermography, Technique ID 20-UIR0

C.4.1 Outline

- Inspection procedures include record of mandatory variable used to determine the defect detection, characterization and defect size
- Procedures written in English (MS Word) (Design/Review/Approved, Procedures/Revision number, Date)
- Before the start of the RRT, documents submit to the supervisor/ supervisor Review
- DAG (Data Analysis Group) Technique Summary writing / submit to the supervisor
  - Brief summary of technique for defect detection, characterization and defect size to ease data evaluation /review

C.4.2 Mandatory Variable to be Included in Inspection Procedures (IP)

- Weld shape
- Inspection technique
- Used equipment
- Surface emissivity
- Horn type, Frequency, Output
- Thermal imaging equipment calibration
- Defect sizing
- Data acquisition

C.4.2.1 UIR Techniques Essential Variable

- Equipment
  - Horn type
- Horn displacement
- Ultrasound output
- The contact direction and location of horn
  - Defect sizing method
- Lock-in thermography
- Horn contact force
- Ultrasound duration

C.4.3 TD Document that must be Included in the Essential Variables

C.4.3.1 Scope

- This procedure is applied to non-destructive examination of dissimilar metal welds and adjacent materials utilizing ultrasound infrared thermography or vibration infrared thermography.
- The objective of examination performed in accordance with this procedure is to accurately detect length sizing and width sizing of defect within the specified examination volume

C.4.3.2 Personnel Requirement

- Personnel performing exams has an experience for equipment setup, calibration, examination and data evaluation.

C.4.3.3 Equipment (ultrasound generator, infrared thermography)

- Ultrasound generator by UlTec–SEE2 Sonic
- Infrared thermography by Flir Cedip siver480

C.4.3.4 Transducer and Horn

- Frequency (20 kHz)
- Output (420 W)
- Horn type (Point)
- Contact area (mm^2)
- Horn material (STS304)

C.4.3.5 Calibration

- Frequency and displacement check using ultrasound generator and horn
- Performance test of Infrared thermography camera using blackbody
- Maintenance more than 0.95 of surface emissivity for inspection body using flat black paint

C.4.3.6 Inspection Technique

- Examination volume

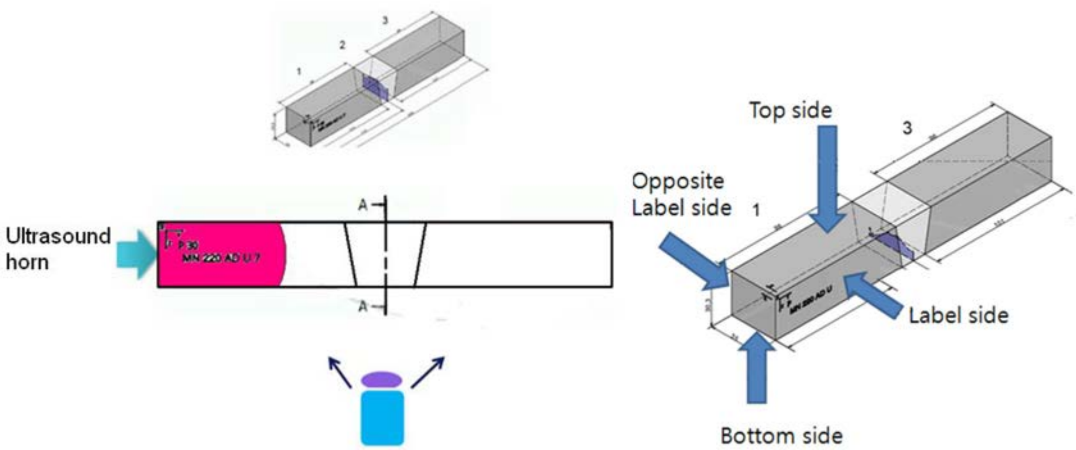

Figure C.19. P28, P29, P30, P31, P32, P38 Specimen

- Examination – After occurring ultrasound in a base metal outside of welds and heat-affected zone, examination shall be performed by detecting heat of welds using infrared thermography
- Inspection speed – Inspection speed shall be not exceed 20 minutes after occurring ultrasound
- Examination Sensitivity – After setting the components that can be examined, the contact force shall be adjusted so that displacement containing welds can be in the range of 100 µm.
- All suspected defect indications, shall be investigated to the extent necessary to provide accurate characterization, identify, and location

C.4.3.7 Inspection Classification

- Defect indications – All indications produced by infrared thermal image and lock-in phase image with temperature difference within the volume to be examined shall be considered as defect indications, after exciting the basic material near the welds by ultrasonic waves after for a certain amount of time
- Non – relevant indication – All indications produced by infrared thermal image and lock-in phase image without temperature difference within the volume to be examined shall be considered as non-relevant indication, after exciting the basic material near the welds by ultrasonic waves after for a certain amount of time

C.4.3.8 Indication Discrimination

- Indication has a healthy image to show temperature difference (< 0.15°C) along the position of component
- Indication provides substantial and unique temperature and lock in phase travel

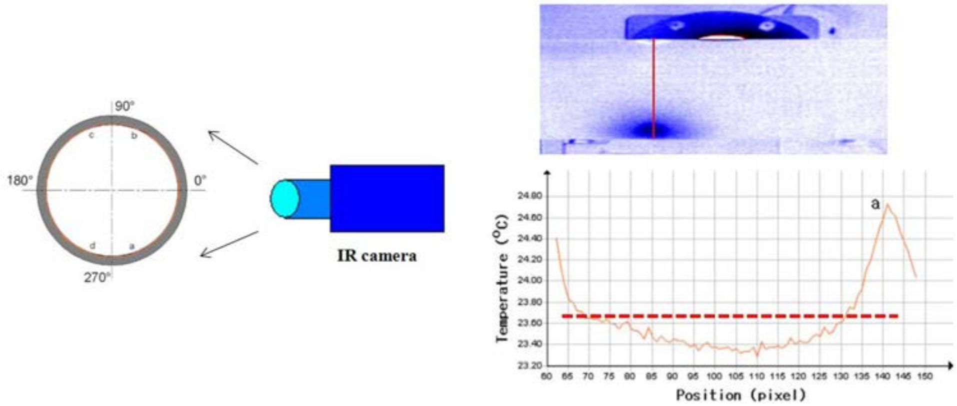

Figure C.20

C.4.3.9 Indication Sizing

- Lock-in phase thermography technique
  - Defect size is computed to pixel and measuring image

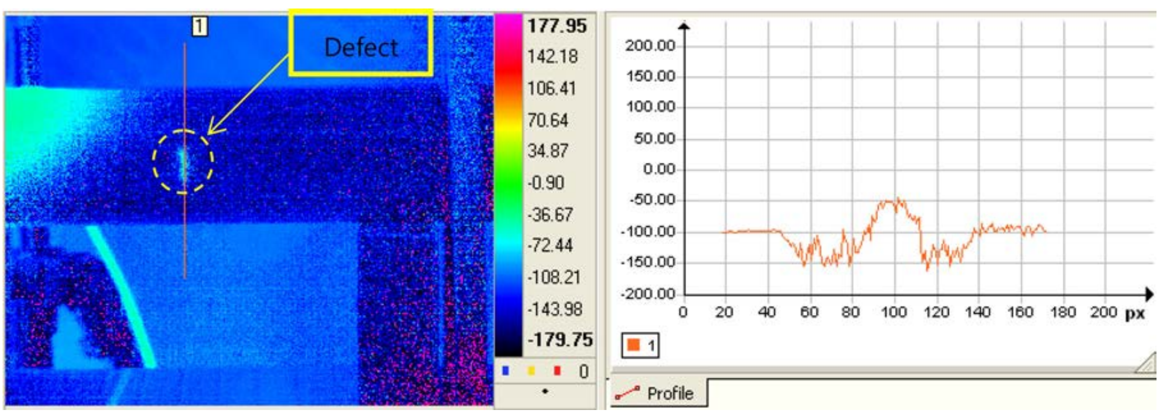

Figure C.21

C.4.3.10 Recording of Thermography

- As shown in Figure C.22, the specimen is rotated to 4 directions with 90° interval during the test.
- The "0" reference points used for recording indications shall be in accordance with the system shown in Figure C.22

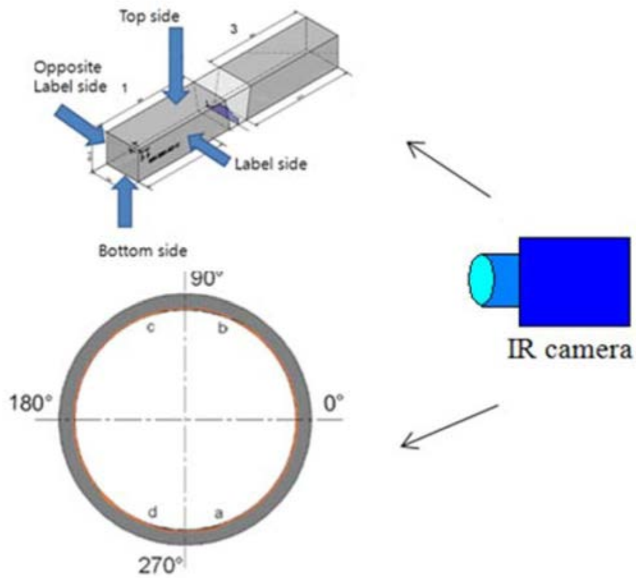

Figure C.22

- Defect indications
- For defect indications the following information shall be recorded shown in Figure C.23
  - Record the defect location (Y1 and Y2) from weld center line zone
  - The length dimension (X1 and X2) from "0" reference points
  - The dimension Z1 (Upper) and Z2 (Lower) through wall

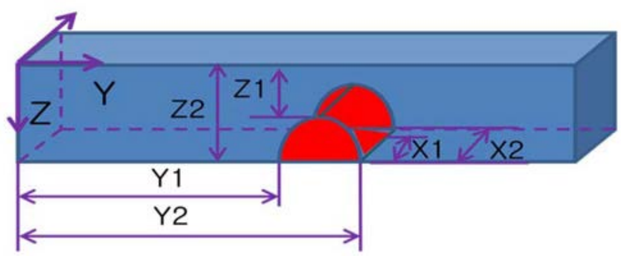

Figure C.23

C.4.3.11 Examination Reporting

- Examination data shall be recorded on a data sheet
  - Examination personnel and examination data
  - Examination procedure number/revision number
  - Equipment serial number, manufacturer, model
  - Search unit angle, manufacturer, serial number, model

– Search unit frequency, size, mode, shape, displacement, horn

– Calibration data sheet

C.4.3.12 Calibration Data Sheet for Ultrasound Infrared Thermography

Calibration Data Sheet for Ultrasound Infrared Thermography

Object of Inspection	Name:Parent RRT	No:P28	Inspection Method:UIR	IR Camera Temperature calibration	Date: 2013. 03. 5	
Inspection Method	Fabricator:Ul-Tech	Model:SEE-SONIC II	Serial No:1372	Black body Tem(℃) : 35.00	Inspected by:	Level:
Reference Block	No: P28	Nominal Size:	Material: SA508+Alloy18+SA508	Camera Tem(℃) : 35.00	Confirmed by:	Level:

Transducer Horn	Frequency (kHz)	Fabricator	Model	Serial No	Horn index point (mm²)	Displacement Sensitivity (㎛)	distance from horn to welded zone (mm)	Displacem 100 ㎛
1	19.6	Ul-Tech	cone- horn	Cone-1	7 mm²	0.1	110	100/406
2								
3								
4								

Remarks:

Signature:

C.4.3.13 PARENT RRT Data Sheet

PARENT RRT – DMW TECHNIQUE DATA SHEET

Procedure ID: 20.2	Tech ID: UIR
Inspection ID:20.P28.1	Access: OUT
Test Block ID: P28	Date: 2013/03/05
Team ID:20	

Weld Volume Inspected

Detection: yes	X1: 0.00 mm	X2: 35.00 mm
Length sizing: yes	Y1: 0.00 mm	Y2: 160.70 mm
Depth sizing: yes	Z1:0.00 mm	Z2:30.30 mm

Defect No:	X1 (mm)	X2 (mm)	Y1 (mm)	Y2 (mm)	Z1 (mm)	Z2 (mm)	Defect max Tem(℃)	Defect min Tem(℃)	Surface breaking	Comments
1			103.84	119.76	18.76	30.30	22.48	21.32	y	Label side view
-BLANK-										

TEAM SIGN :

INVIGILATOR SIGN:

C.4.3.14 DAG Technique Summary

- Inspection company: KRISS
- Team code: 20.2 (KRISS TEAM 1)

- Inspection Procedure: 20.2.1 (KRISS-UIR-01)
- Specimen:P28, P29, P30, P31, P32, P38
- Inspection type: Manual Ultrasound Thermography from specimen
- Scan type: The Specimen has been rotated to 4 directions with 90° interval during the test.
- Detection

Technique detection	Evaluation methodology detection
Thermal energy is based on a ultrasound forces • Sine wave : 20 kHz • Displacement : 100 µm • Frequency : 30 MHz UIR technique is based on image of infrared thermography	-Based on temperature, Lock-in phase or amplitude image • Evaluation of lock in phase images with temperature distribution through the temperature and position • Temperature difference to evaluate defect is more than 0.15°C -Hot spot defect images will have measured during the ultrasound excite.

- Characterization

Technique characterization	Evaluation methodology characterization
UIR technique is based on ultrasound forces and infrared thermography • Characterization is determination between health area and defect area	-Temperature difference(T) between defect indication and health indication • If T>0.15°C, the area is classified as a defect, if not the area is classified as a health °C -All indications produced by infrared thermal image and lock-in phase image with temperature difference within the volume to be examined shall be considered as defect indications

C.4.3.15 DAG Technique Summary

- Inspection company: KRISS
- Team code: 20.2. (KRISS TEAM 1)
- Inspection Procedure: 20.2.2 (KRISS-UIR-01)
- Specimen: P28 , P29, P30, P31, P32, P38
- Inspection type: Manual Ultrasound Thermography from specimen
- Scan type: The Specimen has been rotated to 4 directions with 90° interval during the test.

- Length & width sizing

Technique length sizing	Evaluation methodology length sizing
UIR technique is based on ultrasound forces and infrared thermography	-If T>0.15°C, the area is classified as a defect, if not the area is classified as a health °C • Evaluation of defect size using spatial resolution of pixel image • Evaluation of lock in phase images with temperature distribution through the temperature difference. -Hot spot image indications produced by infrared thermal image and lock-in phase image with temperature difference within the volume to be examined shall be measurement as defect size

- Defect positioning

Technique defect Positioning	Evaluation methodology Technique defect positioning
Based on technique for detection, length and width sizing	Based on previous described methodology for detection, length and width sizing • X position, along defect, is taken from length sizing • Y position, across defect, is taken from width sizing • Z position, across defect, is taken from width sizing

C.5 Guided Ultrasonic Wave, Technique ID 21-GW1, 21-GW2

C.5.1 Overview

C.5.1.1 Introduction of Guided Wave

Guided wave (GW) technique was employed for PARENT Open Test specimen (P4 and P5) to investigate defects size.

Traditional Bulk wave ultrasonic inspection method can do thickness measurements, defect detection and material property characterization in a local area. This technique has disadvantage on large area inspection. Transducer should move point by point to cover a large region to scan whole area. Also, it is difficult to inspect inaccessible structure and area by traditional bulk wave inspection method.

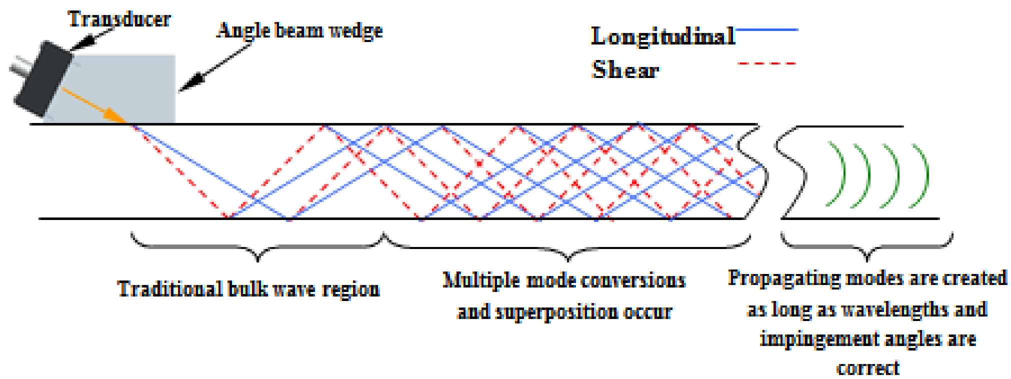

Figure C.24. Guided Wave Generation and Propagation

A guided wave inspection technique which is presented on this technical description has different feature compared to conventional bulk wave ultrasonic test. Guided waves are generated with special frequency and excited angle on certain specimen geometry and boundary condition. Once ultrasonic wave is generated as Figure C.24 bulk wave (longitudinal and transverse wave) will propagate on the specimen. Those waves will reflect on the boundary and wave mode conversion will occur to produce guided wave mode with special condition. A guided wave travels along with inspecting material. Guided waves have great advantage on large area inspection due to the propagation on long distance without losing wave energy. However, guided waves include infinite wave mode with different distribution in the structure. This feature makes people hard to analysis and gives more or less sensitivity on different types of defects and loading condition. Guided wave mode and loading condition can be chosen by structure condition and defect size and location, such as on the surface or sub surface.

It is physically and scientifically based approach to generate certain guided wave mode. Guided wave mode is very much dependent on frequency and geometry of specimen. The main characteristic of guided wave is dispersion. Figure C.25 shows guided wave dispersion curve on cylindrical coordinate.

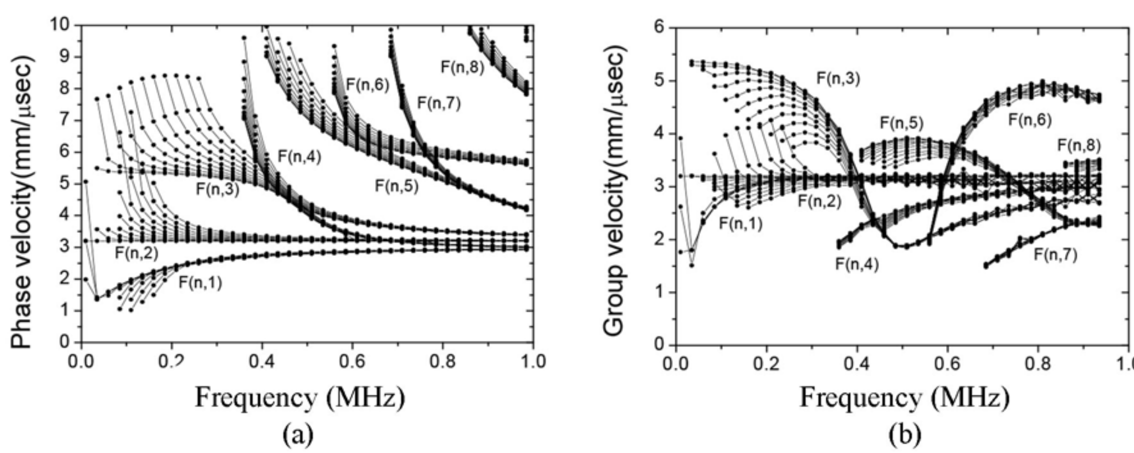

Figure C.25. Guided Wave Dispersion Curves on Cylindrical Coordinate. (a) Phase velocity dispersion curve, (b) Group velocity dispersion curve

Every possible propagation mode can be show on dispersion curve. Through the contribution of advanced computational power and analysis, nowadays, it is possible to deal with advanced understanding and utilization. Wave structure profiles can be obtained for a given structure due to the generation of a dispersion curve. Wave structure profiles can be obtained according to the dispersion curve. How many types of energy are distributed along the thickness of the structure is shown, looking into the profiles of the wave structure. Guided waves ease Structural health monitoring by taking these concepts. Moreover, it is possible to monitor very large areas with great accuracy by using tomographic algorithms with Guided waves. In addition, multiple phased array exciters can be used to focus guided wave energy within structures.

- Pulse echo (PE)

This technique shown as Figure C.26 is pulse echo method in guided wave inspection technique. Guided waves propagate from the fixed position with single transducer. Transducer receives reflected signal from discontinuities. Once we tuned guided wave mode, then defect distance from transducer position based on wave mode velocity.

Figure C.26. Pulse Echo Technique

- Pitch Catch (Pc)

This technique shown as Figure C.27 is pitch catch method in guided wave inspection technique. Guided waves are generated from one transducer and propagate through the specimen. The other receiving transducer detects wave signal at the distance from excitation transducer. If there are any discontinuities on the specimen, received signal amplitude will be decreased or wave mode will be changed with respect to specimen thickness.

Figure C.27. Pitch Catch Technique

C.5.1.2 Personnel Requirement for Guided Wave Inspection

- Personnel performing exams has an experience for equipment setup, calibration, examination and data evaluation.
- Guided wave mode analysis and dispersion curve analysis knowledge.

C.5.1.3 Inspection Equipment

- Tone-bust pulser
  - Ritec – Ritec RPR 4000 instrument with high power voltage
- Oscilloscope
  - LeCroy Wave Surfer 42Xs, Sampling rate is 2.5GS/s
- Transducer and Wedge
  - Frequency (500 kHz, 1 MHz, 1.5 MHz, 2.25 MHz)
  - Inspection range (Length with respect to Frequency)
  - Wedge (20° ~ 70°)
- Calibration
  - Wave mode selection
  - Group velocity calibration
  - Measure weld and edge signal

C.5.2 Inspection Technique

C.5.2.1 Examination Volume

- P4 specimen

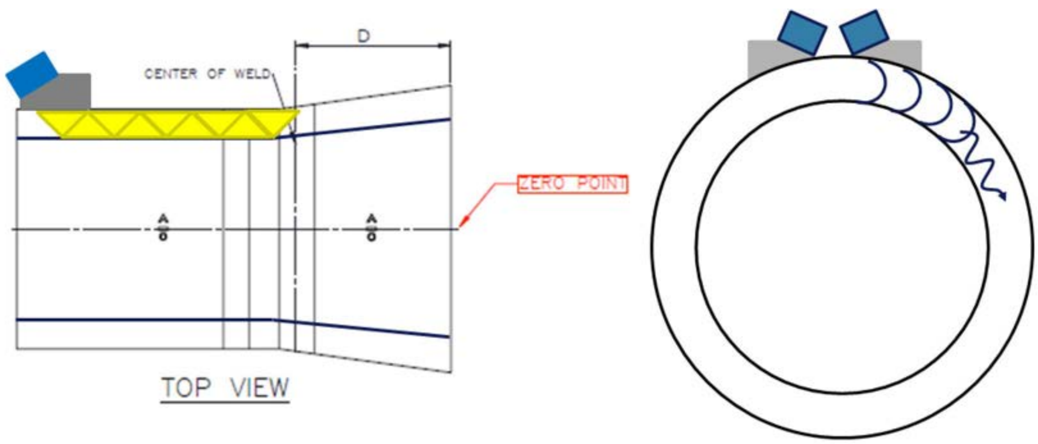

Figure C.28

Guided wave propagates into the specimen. This inspection method can be applied two different ways. First, guided wave is generated from axial direction to the specimen, so reflect signal from defect and weld can be detected by transducer. The other way is generate guided wave along the circumferential direction. Guided wave propagates through the specimen and travel whole specimen volume and receive signal from the other transducer.

- P5 specimen

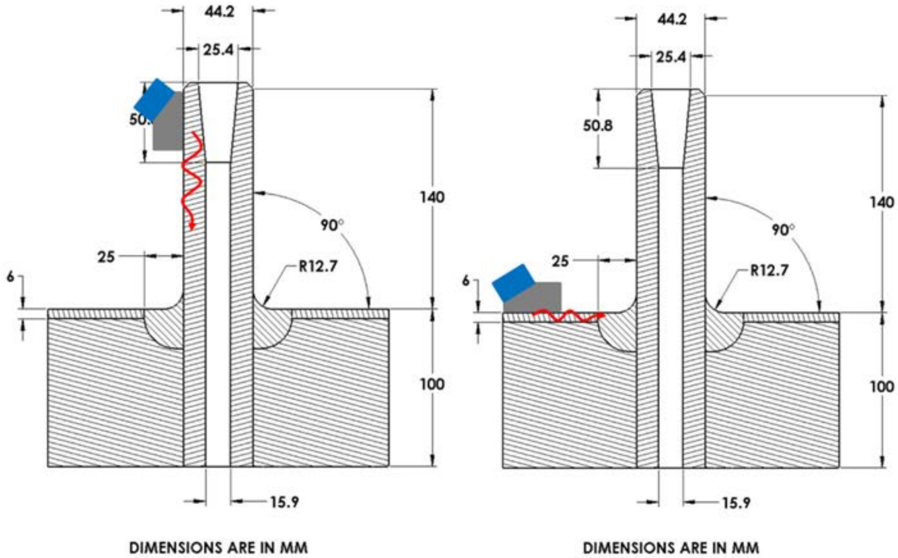

Figure C.29

There are two different way to inspect on P5 specimen. One is generating guided wave on the bottom block. The other way is that generate guided wave from nozzle to weld part. It can detect weld delamination and defect between nozzle and weld.

C.5.3 Data Analysis of Guided Wave Signal

Guided wave can propagate long distance on the inspection specimen. With long propagation distance, there are several features on wave RF signal. Over the distance, it is shown on Figure C.30, over the long distance on the pipe, some key feature information can be found on the signal.

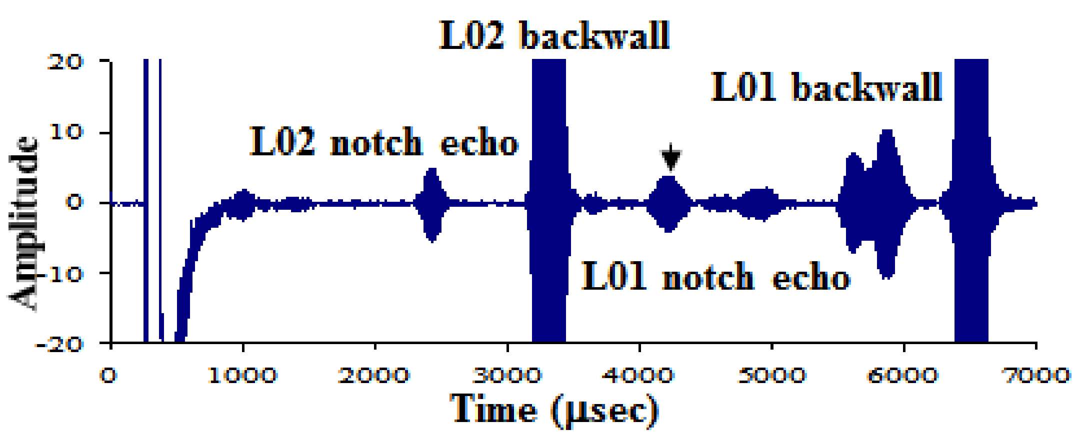

Figure C.30. Guided Wave Inspection Signal on the Long Distance Pipe

C.6 Phased Ultrasonic Array, Technique ID 22-PA-SAFT1, 22-PA-SAFT2, 22-PA-TRT1, 22-PA-TRT2

C.6.1 Introduction

C.6.1.1 Scope

- This technical description is applicable to ultrasonic examination for dissimilar metal welds and adjacent material utilizing phased array ultrasonic techniques and applicable to the open RRT specimens.
- The objective of examination performed in accordance with this procedure is to accurately detect, length size and depth size for EDM notches, thermal fatigue cracks, fatigue cracks in the specified examination volume.

C.6.1.2 Personnel Requirement

- Personnel performing exams have experience for equipment setup, calibration, examination, time delay setup, signal interpretation, and data evaluation.

C.6.2 Specimens

- P29 specimen has one fatigue crack.

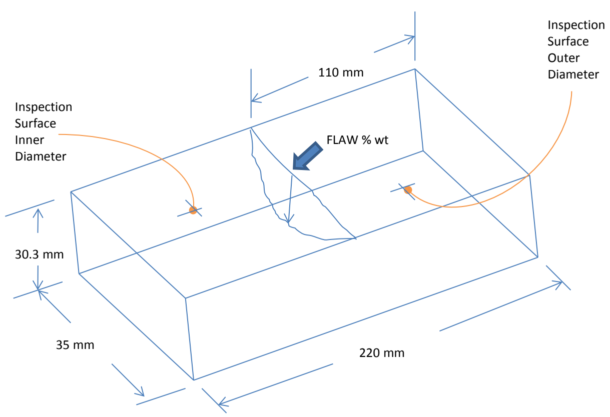

Figure C.31. Schematic Diagram of P29 Specimen

C.6.3 Overview of Inspection System

C.6.3.1 System

- Phased Array Ultrasonic Testing System: Olympus Omniscan
- Scanner: Manual Scanner
- Software: Tomoview (collection and storing full waveforms)

– MATLAB Program is used for determination of time delay using time reversal method.

C.6.3.2 Transducer and Wedge

- Total Number of Element: 16 and 32 Olympus Phased Array Ultrasonic Probes
- Frequency: 2.25 MHz
- Elements Size (Length/Width/Pitch): 44.8 mm/26 mm/2 mm (for 16 elements)

  : 24 mm/24 mm/0.75 mm (for 32 elements)

C.6.3.3 Calibration of System

- Instrument linearity check
- Sensitivity of each element using calibration block:
  - Scanning on the calibration block with scanning phased array ultrasonic probes
  - Checking the received scattering signals from the SDH in the calibration block
  - Adjust amplitude of the received signals to uniform by controlling gain value

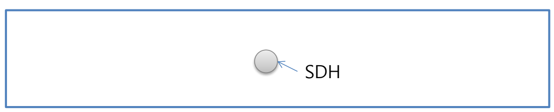

Figure C.32. Calibration Block

C.6.4 Inspection Technique

C.6.4.1 Description of Inspection Technique

- To enhance flaw detectability, focusing of ultrasonic waves on a target in an inhomogeneous medium is a key issue.
- Time Reversal Technique provides a very robust technique to focus ultrasonic waves through inhomogeneous media as compared to conventional focusing techniques.

If we consider the wave equation in a lossless fluid medium without body force, we have the wave equation of pressure, $p(\mathbf{x},t)$, as:

$$\nabla^2 p(\mathbf{x},t) - \frac{1}{c^2}\frac{\partial p(\mathbf{x},t)}{\partial t^2} = 0 \tag{C.3}$$

In Eq. (C.3), the wave equation contains a second-order time-derivative operator. Thus, if $p(\mathbf{x},t)$ is solution of Eq. (C.3), then $p(\mathbf{x},-t)$ also is another solution. Time reversal techniques rely on this property. So, if we have a received signal scattered from a flaw located in complex material, we have another wave theoretically that is time reversed one. Thus, using this property, we could precisely focus on a flaw.

The D.O.R.T. method is a detection technique that is derived from the theoretical analysis of TRM. As shown in Figure C.33, the signal received by the l^{th} element of the array transducer, which has N elements, is defined as

$$r_l(t) = \sum_{m=1}^{N} k_{lm}(t) \otimes e_m(t) \tag{C.4}$$

where $e_m(t)$ is the input signal applied to the m^{th} element, $k_{lm}(t)$ is the impulse response from the l^{th} element to the m^{th} element and $\otimes$ is the convolution in the time domain.

If we take the Fourier transform of Eq. (C.3) and use matrix notation, we have

$$\mathbf{R}(\omega) = \mathbf{K}(\omega)\mathbf{E}(\omega) \tag{C.5}$$

where $\mathbf{K}(\omega)$, the transfer matrix, is an $N \times N$ matrix (Prada et al. 1996). Since we consider the linear-time-invariant system, the new input signal at the i^{th} iteration, $\mathbf{E}^i(\omega)$, can be defined by

$$\mathbf{E}^i(\omega) = \mathbf{K}^*(\omega)\mathbf{E}^{i-1*}(\omega) \tag{C.6}$$

where * denotes complex conjugation corresponding to a time reversal. Thus, the received signal at the i^{th} iteration, $\mathbf{R}^i(\omega)$, can be written as

$$\mathbf{R}^i(\omega) = \left[\left\lfloor \mathbf{K}(\omega)^* \mathbf{K}(\omega) \right\rfloor \mathbf{E}^{i-1}(\omega)\right] \tag{C.7}$$

where $\mathbf{K}(\omega)^* \mathbf{K}(\omega)$ is called the time reversal operator (Prada et al. 1996).

Based on the assumptions, a linear time-invariant system and lossless medium, the transfer matrix is symmetrical. Thus, the time reversal operator is Hermitian positive. Also, the number of significant eigenvalues of the time reversal operator is equal to the number of well resolved scatterers (Prada et al. 1996). From the eigenvector corresponding to significant eigenvalues, we can obtain the time delays required to focus on the scatterer using Eq. (C.8).

$$\Delta t_i = \frac{\Delta \phi_i}{\omega} \tag{C.8}$$

where ϕ_i is the phase of the eigenvector.

- Procedure of pre-focused time reversal techniques as follow:

(1) Exciting ultrasonic waves with pre-calculated time delay using conventional method

(2) Received signals are measured by each element of the phased array probe

(3) Calculating eigenvalues and eigenvectors using the receive signals

(4) Determined number of flaws in the specimen using number of signification eigenvalues

(5) Calculating time delay using the eigenvalues for focusing ultrasonic waves on the flaws

(6) Re-firing ultrasonic waves using the calculated time delay

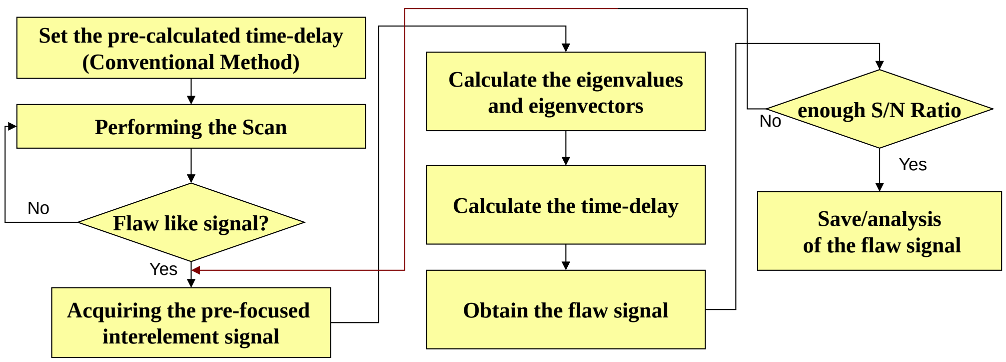

Figure C.33. Procedure of Pre-focused TR Technique

C.6.4.2 Inspection Classification

- Flaw Indications:
  - All indications produced by reflectors, except signals that can be clearly attributed to the geometrical or metallurgical properties of the weld configuration, shall be considered as flaw indication.
  - Amplitude of signals and/or image is more than two time bigger than noise could be considered as indications.
- Flaw Location:
  - Location of flaw determines based on time of flight of the flaw indications and sound velocity of the specimen
- Flaw Sizing:
  - Size of the flaw calculate from amplitude of reflected signals from cracks including EDM notches
  - Also, tip echo method (one of Tip Diffraction Methods) will be apply to calculate size of the flaws

C.6.4.3 Examination Reporting

- Examination reporting is following PARENT RRT guideline:

(1) Parent RRT-Procedure Summary Data Sheet

(2) Parent RRT-DMW Technique Data Sheet

(3) Parent RRT-DMW Inspection Summary Data Sheet

(4) Calibration Data Sheet

- Also, provide A-Scan signals and Scan images of detected flaws in the specimens

C.6.5 Appendix

C.6.5.1 Calibration Data Sheet

Calibration Data Sheet for Ultrasonic Examination (Phased Array Examinaion)

Data sheet No.

Object of Inspection	Name: Parent RRT	No.: P29	Inspection Method: Phased Array UT	Dtate: 2013.03.05~06
Inspection Equipment	Fabricator: R/D TECH	Model: TomoScan FOCUS LT	Serial No.: FLJ-1026	Inspected by: Hak-Joon Kim / Level:
Reference Block	No.: :ASTM E164 FTW TYPI	Nominal Size:	Material:	Confirmed by: / Level:

Array Probe	Element Size(mm):	10 × 38.4	Element Pitch(mm):	0.6	Number of Element:	64

Condition	Evaluation Angle		Freq.	Fabricator	Model	Serial No.	Probe Index Point(mm)	Reference Sensitivity(dB)	EL:Echo Height (CRT%) / PL: Beam Path Length (mm)			
	Nominal	Measured										
1	45	45	5									
2												
3												

Couplant: Ultra Gel

Cable Length: 2m

Remarks:

Signature

PAGE: 12 of 12

C.6.5.2 PARENT RRT-Procedure Summary Data Sheet

Round Robin Test Forms for Protocol Revision 17 PNNL

PARENT RRT – PROCEDURE SUMMARY Data Sheet

Procedure ID:22.1
Procedure Type: PAUT
Scan Direction: *Axial*
Length Sizing: *yes*
Scan Type: *Man*

Team ID:22
Scan Access: *OD*
Detection: *yes*
Depth Sizing: *yes*

Description for Combining Techniques:

Detection

Tech-ID	Description	Evaluation Method
1	PAUT(P-WAVE)	Synthetic Aperture Focusing Technique
2	PAUT(S-WAVE)	Synthetic Aperture Focusing Technique
3	PAUT(P-WAVE)	Time Reversal Technique
4	PAUT(S-WAVE)	Time Reversal Technique

Characterization

Tech-ID	Description	Evaluation Method
1	PAUT(P-WAVE)	Echo Dynamic Pattern
2	PAUT(S-WAVE)	Echo Dynamic Pattern
3	PAUT(P-WAVE)	Echo Dynamic Pattern
4	PAUT(S-WAVE)	Echo Dynamic Pattern

Length Sizing

Tech-ID	Description	Evaluation Method
1	Amplitude Analysis(P-WAVE)	6DB Method
2	Amplitude Analysis(S-WAVE)	6DB Method
3	Amplitude Analysis(P-WAVE)	6DB Method
4	Amplitude Analysis(S-WAVE)	6DB Method

Depth Sizing

Tech-ID	Description	Evaluation Method
1	Amplitude and time Analysis(P-WAVE)	Tip Echo Method
2	Amplitude and time Analysis(S-WAVE)	Tip Echo Method
3	Amplitude and time Analysis(P-WAVE)	Tip Echo Method
4	Amplitude and time Analysis(S-WAVE)	Tip Echo Method

Defect Positioning

Tech-ID	Description	Evaluation Method
1	Amplitude and time Analysis(P-WAVE)	Echo Dynamic Pattern, Signal Amplitude, Time Delay
2	Amplitude and time Analysis(S-WAVE)	Echo Dynamic Pattern, Signal Amplitude, Time Delay
3	Amplitude and time Analysis(P-WAVE)	Echo Dynamic Pattern, Signal Amplitude, Time Delay
4	Amplitude and time Analysis(S-WAVE)	Echo Dynamic Pattern, Signal Amplitude, Time Delay

C.6.5.3 PARENT RRT-DMW Techniques Data Sheet

Round Robin Test Forms for Protocol Revision 17 PNNL

PARENT RRT – DMW TECHNIQUE Data Sheet

Procedure ID:22.1
team-id seq-no
Inspection ID:22.P29.1
team-id block-id seq-no
Test Block ID: P29
Team ID:22

Tech ID:1

Access: *OD*

Date: *2012/03/05~06*

Weld Volume Inspected:

Detection: *yes*
Length Sizing: yes
Depth Sizing: *no*

X1(mm):0 X2(mm):35
Y1(mm):130 Y2(mm):150
Z1(mm):0 Z2(mm):0

Defect No	X1 mm	X2 mm	Y1 mm	Y2 mm	Z1 mm	Z2 mm	Y_{max} mm	Amp dB	Surface Breaking	Comments
1	0	35	110	110	N/A	N/A	17.5	45	YES	Using Longitudinal Wave, Synthetic Aperture Focusing

TEAM SIGN: **INVIGILATOR SIGN:**

Round Robin Test Forms for Protocol Revision 17 PNNL

PARENT RRT – DMW TECHNIQUE Data Sheet

Procedure ID:22.1
team-id seq-no
Inspection ID:22.P29.1
team-id block-id seq-no
Test Block ID: P29
Team ID:22

Tech ID:2

Access: *OD*

Date: *2012/03/05~06*

Weld Volume Inspected:

Detection: *yes*
Length Sizing: yes
Depth Sizing: *no*

X1(mm):0 X2(mm):35
Y1(mm):130 Y2(mm):150
Z1(mm):0 Z2(mm):0

Defect No	X1 mm	X2 mm	Y1 mm	Y2 mm	Z1 mm	Z2 mm	Y_{max} mm	Amp dB	Surface Breaking	Comments
1	0	35	110	110	N/A	N/A	17.5	45	YES	Using Shear Wave, Synthetic Aperture Focusing

TEAM SIGN: **INVIGILATOR SIGN:**

PARENT RRT – DMW TECHNIQUE Data Sheet

Procedure ID:22.1
team-id seq-no
Inspection ID:22.P29.1
team-id block-id seq-no
Test Block ID: P29
Team ID:22

Tech ID:3
Access: *OD*
Date: *2012/03/05~06*

Weld Volume Inspected:

Detection: *yes*
Length Sizing: yes
Depth Sizing: *yes*

X1(mm):0 X2(mm):35
Y1(mm):130 Y2(mm):150
Z1(mm):0 Z2(mm):0

Defect No	X1 mm	X2 mm	Y1 mm	Y2 mm	Z1 mm	Z2 mm	Y_{max} mm	Amp dB	Surface Breaking	Comments
1	0	35	110	110	21.9	30.3	17.5	45	YES	Using Longitudinal Wave, Time Reversal Technique

TEAM SIGN: **INVIGILATOR SIGN:**

PARENT RRT – DMW TECHNIQUE Data Sheet

Procedure ID:22.1
team-id seq-no
Inspection ID:22.P29.1
team-id block-id seq-no
Test Block ID: P29
Team ID:22

Tech ID:4
Access: *OD*
Date: *2012/03/05~06*

Weld Volume Inspected:

Detection: *yes*
Length Sizing: yes
Depth Sizing: *yes*

X1(mm):0 X2(mm):35
Y1(mm):130 Y2(mm):150
Z1(mm):0 Z2(mm):0

Defect No	X1 mm	X2 mm	Y1 mm	Y2 mm	Z1 mm	Z2 mm	Y_{max} mm	Amp dB	Surface Breaking	Comments
1	0	35	110	110	20.3	30.3	17.5	45	YES	Using Shear Wave, Time Reversal Technique

TEAM SIGN: **INVIGILATOR SIGN:**

C.6.5.4 PARENT RRT-DMW Inspection Summary Data Sheet

Round Robin Test Forms for Protocol Revision 17 PNNL

PARENT RRT – DMW INSPECTION SUMMARY Data Sheet

Inspection ID: 22.P29.1
team-id block-id seq-no
Test Block ID:P29
Team ID:22

Procedure ID: 22.1
team-id seq-no
Date: *2012/03/05~06*

Weld Volume Inspected:

X1(mm):0 X2(mm):35
Y1(mm):130 Y2(mm):150
Z1(mm):0 Z2(mm):0

Defect No	X1 mm	X2 mm	Y1 mm	Y2 mm	Z1 mm	Z2 mm	Y_{max} mm	Amp dB	Surface Breaking	Comments
1	0	35	110	110	20.3	30.3	17.5	45	YES	Using Shear Wave(Tech No. 4)

TEAM SIGN: **INVIGILATOR SIGN:**

C.7 Higher Harmonic Ultrasound Technique, Technique ID 30-HHUT0, 30-HHUT1

C.7.1 Overview

C.7.1.1 Introduction of Nonlinear Ultrasonic Technique

We applied the nonlinear ultrasonic technique (NUT), higher harmonic ultrasonic technique (HHUT) for PARENT Open Test specimens (ID 28, 29 and 30) having the crack in DWM to detect the existence of the close crack and measure its depth.

In PARENT Open RRT, we investigated the higher-harmonic generation effect at the crack. Its basic principle is the contact acoustic nonlinearity (CAN) that generates the harmonic frequency components owing to the crack temporarily closed and opened or the nonlinear pressure-displacement relation at the contact interface when ultrasonic waves encounter the imperfect interfaces shown as Figure C.34. As the result, the acoustic wave waveform becomes distorted and the higher harmonic frequency components are generated in the transmitted wave or in the reflected wave from the crack. The magnitude of the harmonic frequency component depends on the crack opening distance (COD) or the contact stiffness of crack interfaces (Buck et al. 1978; Jhang 2000; Abeele and Windels 2006; Biwa et al. 2006; Kim et al. 2006; Solodov et al. 2006; Ulrich et al. 2008).

Thus, it would be possible to detect closed cracks by monitoring the magnitude of the higher harmonic frequency component generated in the transmitted or the reflected wave. Usually, considering up to the second order nonlinearity, the relative nonlinear parameter (β') defined by the ratio of the second order harmonic frequency magnitude to the power of the fundamental frequency magnitude is used as the monitoring parameter, which is convenient for the relative evaluation (Jhang 2000). We were expecting that this parameter would much more sensitive to closed-cracks than the conventional linear characteristics of ultrasonic waves. Many studies have been done for modeling and verifying this phenomenon (Buck et al. 1978; Solodov 1998; Ohara et al. 2003; Biwa et al. 2006; Hirsekorn et al. 2006; Kim et al. 2006).

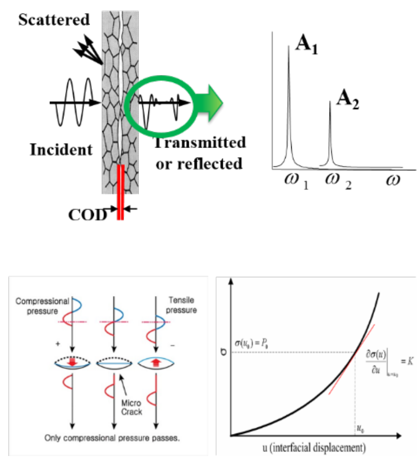

Figure C.34. The Basic Principle of the Contact Acoustic Nonlinearity

For the test, we designed the measurement system with PZT transducers and the pneumatic clamping equipment. By doing so, the experimental conditions could be consistent, which assured the reliable measurement of the β'. In our experiments, two kinds of inspection methods were carried out as follows.

- **Pulse echo (PE)**

This technique shown as Figure C.35 is one of common techniques in ultrasonic testing where a pulsed wave is transmitted into the sample and then the reflected signal from discontinuities is received. When we know the wave velocity in the material, we can locate the defect. As the application of this technique for HHUT, we will use the broadband transducer of 5 MHz main-resonance frequency. We generated the longitudinal waves of 3 MHz high power tone burst.

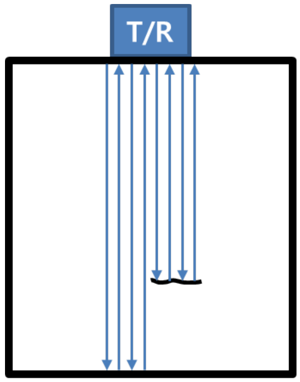

Figure C.35. Pulse Echo Technique

- **V-scan (VS)**

In this technique, the ultrasonic beam path follows V-line shown as Figure C.36. The beam path looks V-line when two transducers for transmitting and receiving the ultrasonic are put oppositely within one skip distance space. If a crack exists on the beam path, the amplitude of the received signal will decrease. By doing so, we can identify the existence of a crack. As the application of this technique for HHUT, we used two 45° angle beam transducers. The transducer of 2 MHz main-resonance frequency was used as a transmitter and one of 4 MHz was used as a receiver to measure the harmonic frequency component sensitively.

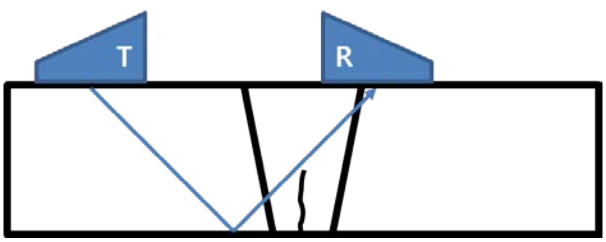

Figure C.36. V-scan Technique

C.7.1.2 Sensitivity and Resolution of HHUT

There is no report on the sensitivity and the resolution of HHUT since it is strongly dependent on the equipment and the measurement skill at the present stage. Instead, we have tried to show the excellence of HHUT in sizing performance by comparing the lengths of defects artificially fabricated in the acrylic and the aluminum specimens by using conventional linear ultrasonic technique (UT) and HHUT. UT measures only the amplitude of the reflection or the transmission signal, whereas HHUT measures nonlinear parameter by measuring the ratio of the fundamental and the second harmonic frequency magnitudes in the transmission or the reflection signal. The measured result showed HHUT was more accurate than UT. Details are shown in below.

- **Acrylic Specimen**

An acrylic specimen was made of two blocks by being contacted together. One of the blocks has flat surface and the other has unevenness on the contacting surfaces. Thus only the outside of uneven area will be contacted. Unevenness was fabricated by polishing with #220 sand papers. The picture of the specimens is shown as Figure C.37. There are two kinds of specimens with different uneven areas. The change of the contact area according to the contacting pressure is shown as Figure C.38 , which was taken by ink print. The initial noncontact area in No. 1 specimen is bigger than that in No. 2 specimen, and the initial axial length of noncontact areas were measured as approximately 40 mm and 30 mm, respectively. According to the increase of pressure, the noncontact area became decreased: The decreasing rate in No. 1 was faster than in No. 2, which means that the unevenness of No. 1 specimen is smaller than No. 2 specimen.

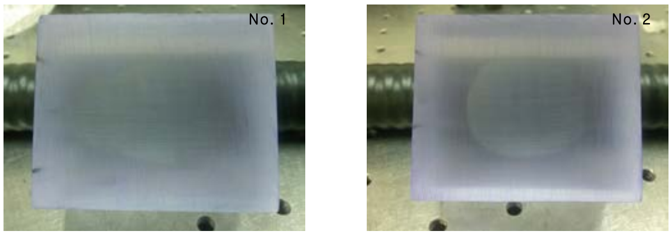

Figure C.37. Shape of Defects in Acrylic Specimens

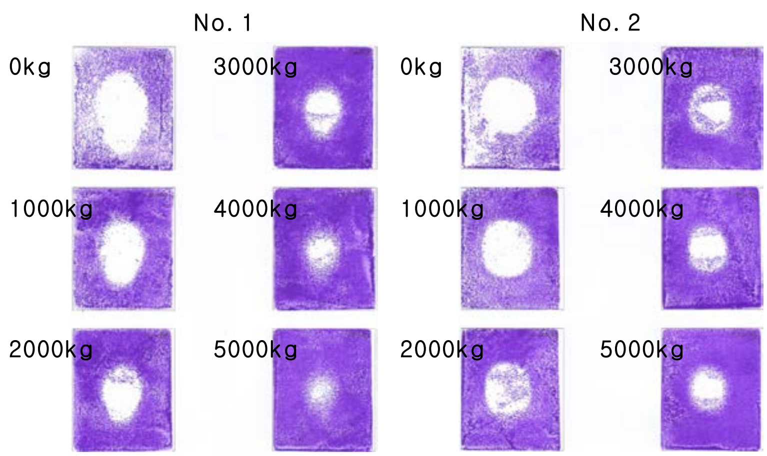

Figure C.38. The Change of the Contact Area According to the Increase of Contacting Pressure

When changing the contacting pressure, the result of ultrasonic test is shown as Figure C.39. The left side of the figure shows the result of the linear method, and right side shows the nonlinear parameter using the pulse echo method. The result of the linear method shows the large amplitude at the noncontact area while the nonlinear parameter showed the large amplitude at the boundaries of contact and noncontact interfaces. This means that the boundaries act as partially closed interfaces so that the contact acoustic nonlinearity is activated in maximum there.

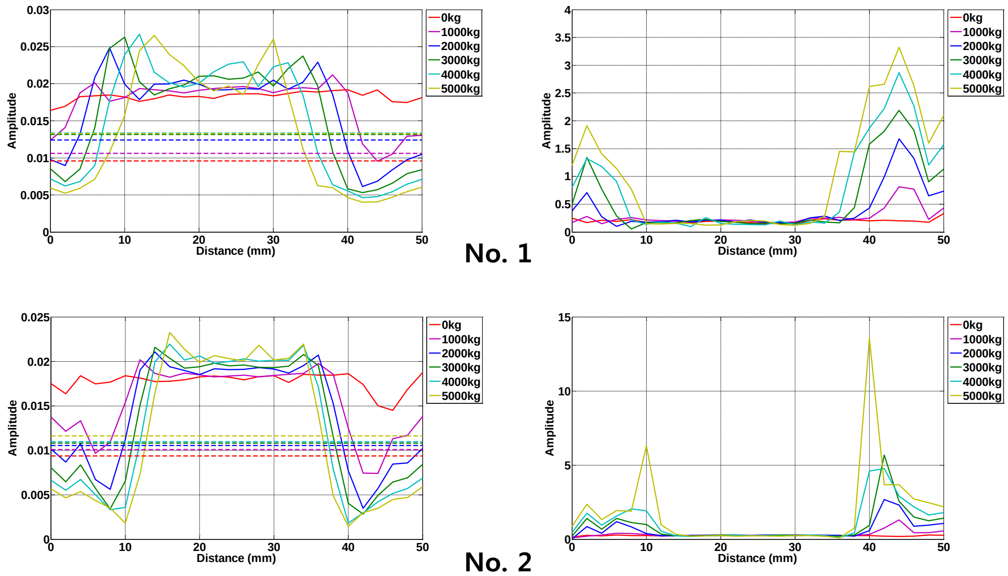

Figure C.39. Amplitude of (left) −6 dB Method and (right) Relative Nonlinear Parameter

Table C.2 shows the results of measuring the axial length of the noncontact area by using the 6 dB drop method in UT and by measuring the distance between left and right side peaks of nonlinear parameter in HHUT. UT evaluated the size smaller than the real size. Moreover, the measured size is decreasing by the increase of the contact pressure. On the other hand, HHUT evaluated the size in similar to real size regardless of the contact pressure. These results support the usefulness of HHUT for the detection of closed interfaces and for the improvement of the sizing accuracy.

Table C.2. Result of Unevenness Size Measurement at Different Loading (dimension in mm)

Load	No. 1		No. 2	
	6 dB drop method	Consider β’	6 dB drop method	Consider β’
0 kg	-	-	-	-
1000 kg	43	43	34.2	38
2000 kg	35	42	29.6	32
3000 kg	30.8	42	27.2	30
4000 kg	28.2	42	25.3	30
5000 kg	24.5	42	23.7	30

- **CT Specimen**

The dimension of the specimen used in our investigation is shown as Figure C.40, which is a compact tension (CT) specimen of Al6061 material. This specimen was degraded by the fatigue test to initiate a micro-crack from the notch. There are opened cracks around V-notch and closed cracks around crack tip. The measurement size from notch to crack tip is roughly 10 mm.

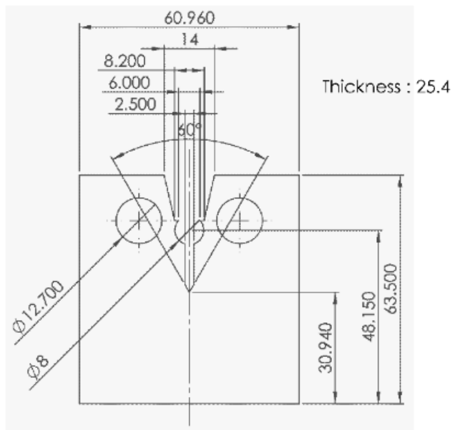

Figure C.40. Geometry of Specimen (dimension in mm)

The magnitudes of the fundamental frequency and the second harmonic frequency at different measuring positions along the crack direction from notch are shown as Figure C.41. For this, the pulse echo technique was used. The maximum magnitude of the fundamental frequency appears at 4 mm, and the crack length was measured by 6.5 mm by using 6 dB drop method. On the other hand, the second harmonic magnitude shows the maximum value at 5 mm as well as has large value until 9 mm, which is close to the real size of the crack.

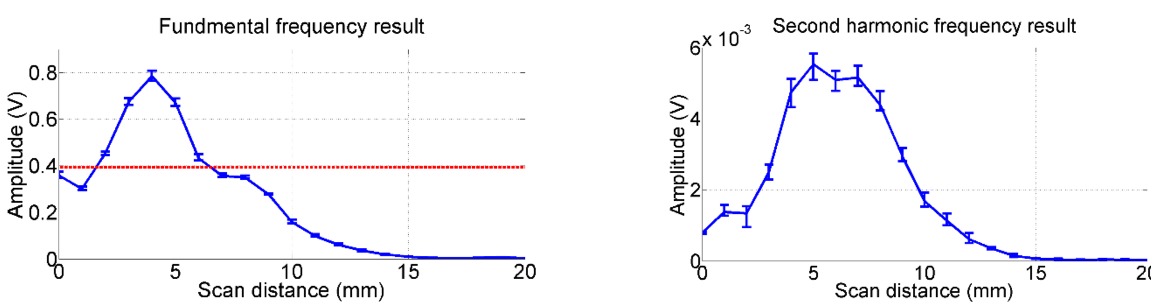

(a) Magnitude of the fundamental component (b) Magnitude of the second harmonic component

Figure C.41. Result of Crack Length Using Pulse Reflection Method and Nonlinear Ultrasound

From this result, we will be able to solve the problem of the conventional ultrasonic technique that is to underestimate the size of the crack. The conventional ultrasonic techniques was sensitive to only the open crack. However, nonlinear ultrasonic technique was sensitive to the closed crack. Therefore, the evaluation method of the length of the crack using the nonlinear ultrasonic, it may become an important technique to verify the integrity of the structure.

C.7.2 Introduction of the Experimental Equipment and Setup

C.7.2.1 Experimental Equipment

The broadband transducer (Olympus) of 5 MHz main-resonance frequency is shown as Figure C.42(a). The diameter of the transducer is 10 mm. The angle beam transducer (Krautkramer) is shown as Figure C.42(b). The yellow one and the blue one have 2 MHz and 4 MHz main-resonance frequencies, respectively. The size of the transducer is 8 X 9 mm.

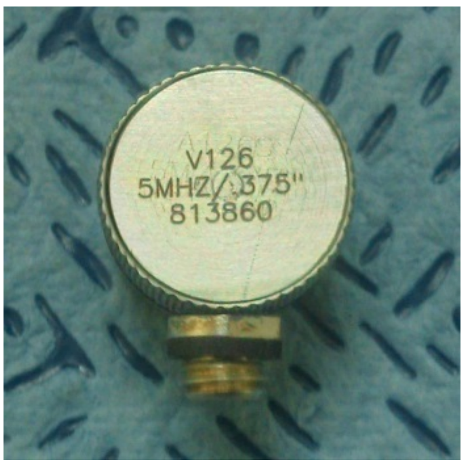

(a)

(b)

Figure C.42. Transducers Used in (a) Pulse Echo Method and (b) V-scan Method

To generate a high power tone-burst signal, a high-power gated amplifier (RAN-5000 SNAP) was used.

Figure C.43. High Power Pulser-Receiver (RAM-5000 SNAP)

In the experiment, the received signal was A/D converted by using NI PCI-5122 board (National Instruments). The board has 100 M/s real time sampling and its resolution is 14 bits.

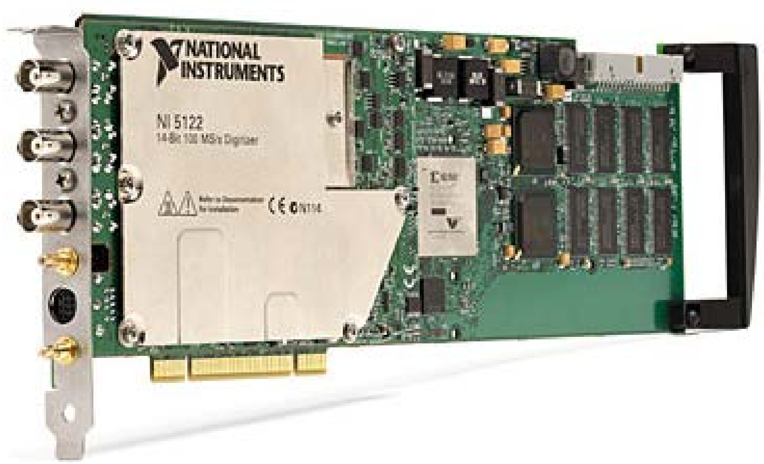

Figure C.44. A/D Board (NI PCI-5122)

When the received signal level is too low, it should be amplified. For that, the pulser-receiver 5077PR (Olympus) was used.

Figure C.45. Pulser-Receiver (5077PR)

Universal motion controller / driver ESP300 (Newport) was used to move the transducer in the interval of 1 mm. This controller / driver is used with the motorized linear stage M-433 (Newport).

Figure C.46. Universal Motion Controller / Driver (ESP300)

Figure C.47. The Motorized Linear Stage (M-433)

And pneumatic system (self-production) was employed to keep constant pressure between transducers and specimens. The loaded pressure was 0.7 MPa.

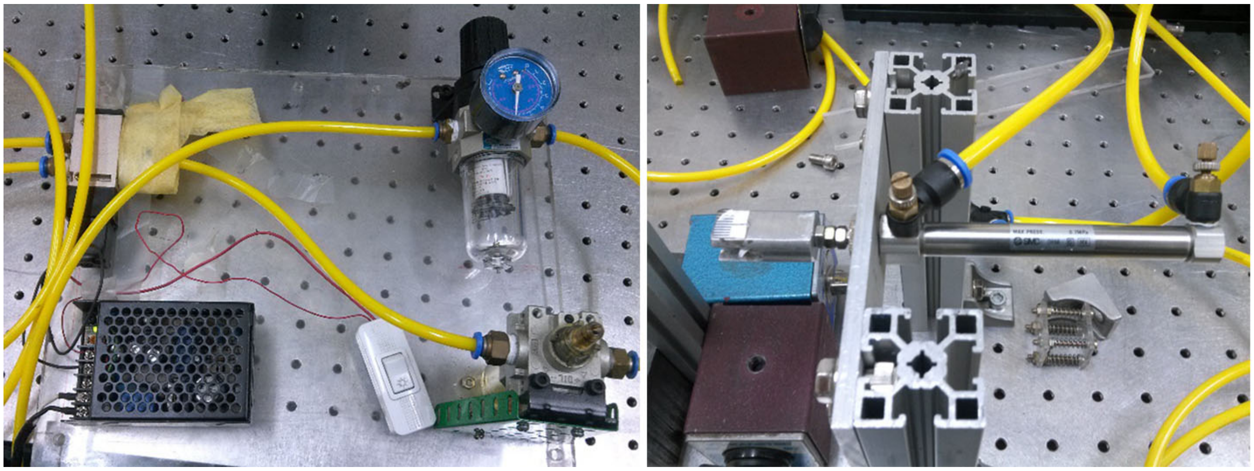

Figure C.48. Pneumatic System

C.7.2.2 Experimental Setup (Pulse Echo)

To apply the pulse-echo method, the experimental system was set shown as Figure C.49. The experimental conditions and parameters were controlled as Table C.3.

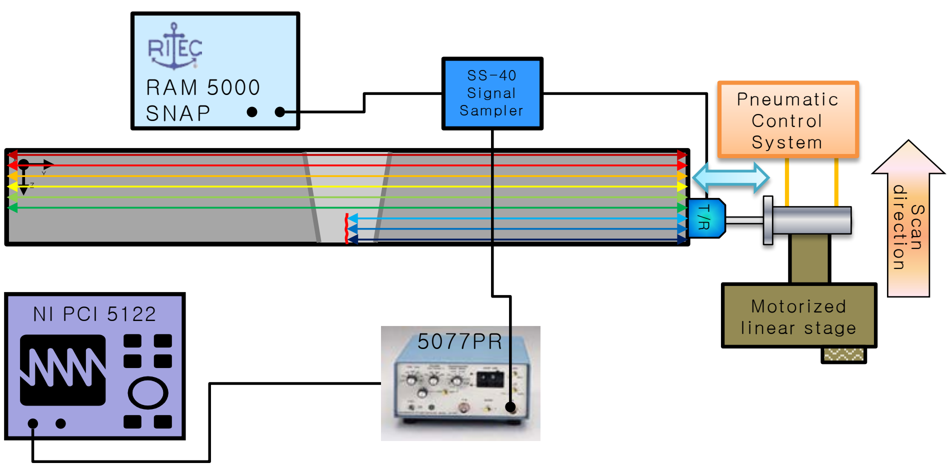

Figure C.49. Experimental Setup

Table C.3. RAM-5000 & 5077PR Setting Condition

RAM-5000 & 5077PR Setting	
Frequency	3
No. of Cycle	11
GA Output	50
Gain	+ 30 dB
HPF	1 MHz
LPF	FULL BW

In the pulse-echo method, the specimen was scanned from 23 mm to 7 mm on Z-axis at interval of 1 mm. This Z-axis measurement was conducted repeatedly from 7.5 mm to 22.5 on X-axis at interval of 5 mm.

C.7.2.3 Experimental Setup (V scan)

To apply the V-scan method, the experimental system was set shown as Figure C.50. The experimental conditions and parameters were controlled as Table C.4.

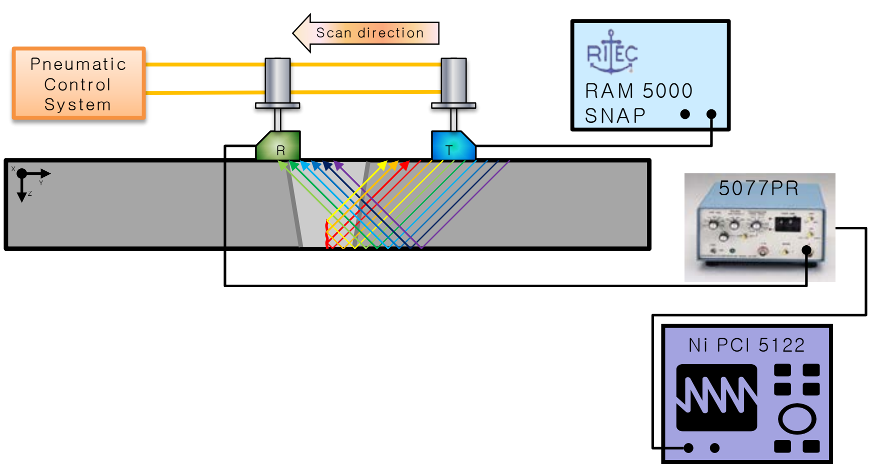

Figure C.50. Experimental Setup

Table C.4. RAM-5000 & 5077PR Setting Condition

RAM-5000 & 5077PR Setting	
Frequency	2
No. of Cycle	11
GA Output	60
Gain	+ 10 dB
HPF	OUT
LPF	FULL BW

In the V-scan technique, the specimen was scanned on Y-axis at interval of 1 mm. Likewise, with the pulse-echo method, the specimen was scanned on X-axis at interval of 5 mm.

C.7.3 The Data Acquisition Process/Parameters

For acquiring the data by using HHUT method in PARENT specimen, A-scan signal was measured in the way of the pulse-echo method shown as Figure C.51. Select a signal from the full time echo signal by using a fixed time gate, of which time range covers the echo from the welded area only.

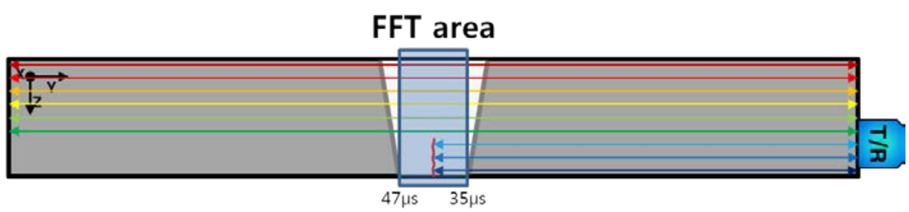

Figure C.51. The Region of Data Acquire (PE)

On Z-axis, the scan was carried out from the bottom to the top (23 ~ 7 mm) at interval of 1 mm by using motorized linear stage. On X-axis, the data was manually acquired from 7.5 mm to 22.5 mm at interval of 5 mm. Transducer was placed on the right side of the specimen in order to transmit the ultrasonic wave towards the direction perpendicular to the crack propagation direction. The other information such as the transmit frequency, the number of cycle and the gain of the receiver is tabulated in Table C.3.

In the V-scan method, A-scan signal was acquired shown as in Figure C.52. Select a signal from the full time echo signal by using a fixed time gate, of which time range covers the echo from the welded area only.

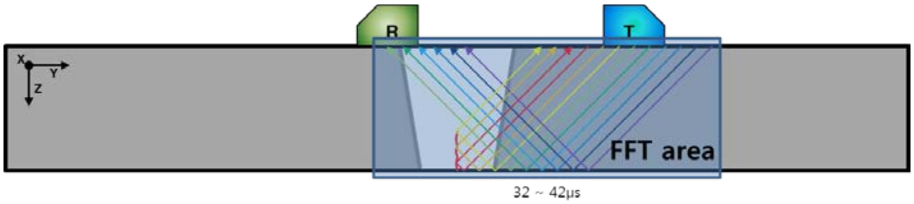

Figure C.52. The Region of Data Acquire (VS)

On Z-axis, the receiver was manually moved from 76 mm to 114 mm and the transmitter was manually moved from 136 mm to 174 mm at interval of 1 mm by using motorized linear stage. On X-axis, the data was manually acquired from 7.5 mm to 22.5 mm at interval of 5 mm same as PE. Transducer was placed on the top side of the specimen. The other information such as the transmit frequency, the number of cycle and the gain of the receiver is tabulated in Table C.4.

By converting the scan data from the relevant area same as Figure C.53, the crack size can be measured. Here, Z0 is the first scan point and Z30 is the last scan point.

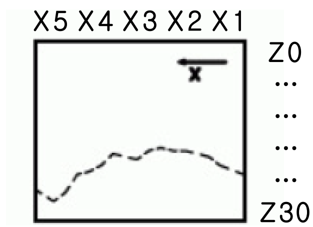

Figure C.53. The Converted Axis (VS)

C.7.4 Signal Processing Performed on the Acquired Data

From the acquired data with each method, the magnitudes of the fundamental frequency (A_1) and the second harmonic frequency (A_2) were obtained by using fast-Fourier transform in the time interval (PE: 35 ~ 47 μs, VS: 32 ~ 42 μs) presumed to be the crack signal. The relative nonlinear parameter (β') was calculated from Eq. (C.9).

$$\beta' = \frac{A_2}{A_1^2} \tag{C.9}$$

Fast-Fourier transform was processed in MATLAB. Here, zero-padding was 200 times to length of the data and any window function was not applied.

C.7.5 Acquired Data Analysis for the Technique

Through the signal processing, the depth of the crack was estimated from the magnitudes of fundamental and the second harmonic frequency components, the relative nonlinear parameter. The estimation algorithm was shown as Figure C.54.

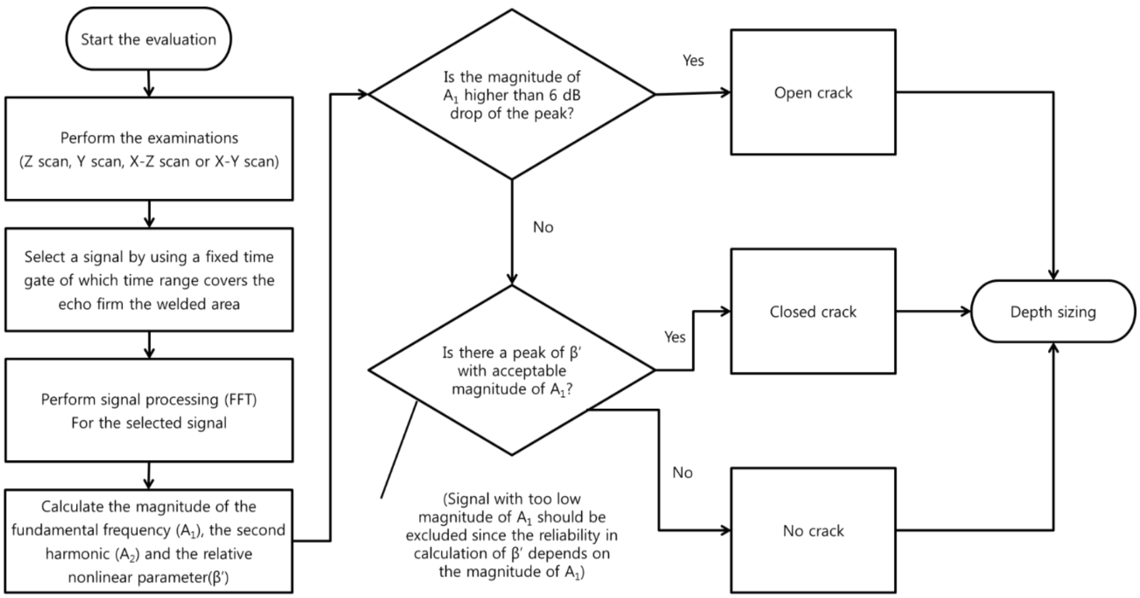

Figure C.54. Flow Chart for Detection and Depth Sizing of Crack

C.8 References

Abeele K and F Windels. 2006. "Characterization and Imaging of Microdamage Using Nonlinear Resonance Ultrasound Spectroscopy (NRUS): An Analytical Model." In *Universality of Nonclassical Nonlinearity*, pp. 369-388, Ch. 23. ed: P Delsanto. Springer, New York.

Biwa S, S Hiraiwa and E Matsumoto. 2006. "Experimental and Theoretical Study of Harmonic Generation at Contacting Interface." *Ultrasonics* 44, Supplement:e1319-e1322.

Buck O, WL Morris and JM Richardson. 1978. "Acoustic Harmonic Generation at Unbonded Interfaces and Fatigue Cracks." *Applied Physics Letters* 33(5):371-373.

Cheong YM, JH Kim, JW Hong and HK Jung. 2000. "Measurement of Dynamic Elastic Constants of RPV Steel Weld due to Localized Microstructural Variation." *Journal of Korean Society of Nondestructive Testing* 20(5):390-396. In Korean.

Hirsekorn S, M Hirsekorn and PP Delsanto. 2006. "Nonlinear Ultrasonic Transmission Through Thin Bonded Interfaces: Theoretical Background and Numerical Simulations." In *Universality of Nonclassical Nonlinearity*, pp. 231-250, Ch. 15. ed: P Delsanto. Springer, New York.

Jhang K-Y. 2000. "Applications of Nonlinear Ultrasonics to the NDE of Material Degradation." *IEEE Transactions on Ultrasonics, Ferroelectrics and Frequency Control* 47(3):540-548.

Kim J-Y, A Baltazar, JW Hu and SI Rokhlin. 2006. "Hysteretic Linear and Nonlinear Acoustic Responses from Pressed Interfaces." *International Journal of Solids and Structures* 43(21):6436-6452.

Ohara Y, K Kawashima, M Murase and N Hirose. 2003. "Identification of Sintered Irons with Ultrasonic Nonlinearity." In *Review of Progress in Quantitative Nondestructive Evaluation, Vol. 22,* pp. 1257-1264. July 14-19, 2002, Bellingham, Washington. American Institute of Physics, Melville, New York.

Prada C, S Manneville, D Spoliansky and M Fink. 1996. "Decomposition of the Time Reversal Operator: Detection and Selective Focusing on Two Scatterers." *The Journal of the Acoustical Society of America* 99(4):2067-2076.

Solodov I, K Pfleiderer and G Busse. 2006. "Nonlinear Acoustic NDE: Inherent Potential of Complete Nonclassical Spectra." In *Universality of Nonclassical Nonlinearity*, pp. 467-486, Ch. 29. ed: P Delsanto. Springer, New York.

Solodov IY. 1998. "Ultrasonics of Non-linear Contacts: Propagation, Reflection and NDE-applications." *Ultrasonics* 36(1–5):383-390.

Ulrich TJ, AM Sutin, RA Guyer and PA Johnson. 2008. "Time Reversal and Non-linear Elastic Wave Spectroscopy (TR NEWS) Techniques." *International Journal of Non-Linear Mechanics* 43(2):209-216.

Appendix D

USA Detailed Technique Descriptions

Appendix D

USA Detailed Technique Descriptions

D.1 Eddy Current Technique, Technique ID 7-ECT1

D.1.1 Overview

The data were taken using an eddy current insptection technique. This is a well-established technique for finding surface defects in conducting materials. In it, a coil is excited with an AC current at one or more frequencies. The magnetic field from the coil induces eddy currents in the test specimen. These eddy currents diffuse through the specimen. Defects in the specimen cause changes in the amplitude and direction of these eddy currents. These changes can be measured as changes in either the impedance of the exciting coil, or as changes in the amplitude and phase of the voltage induced in a second receiving coil. In the technique used here, we employed the receiving coil. This approach is illustrated in the Figure D.1.

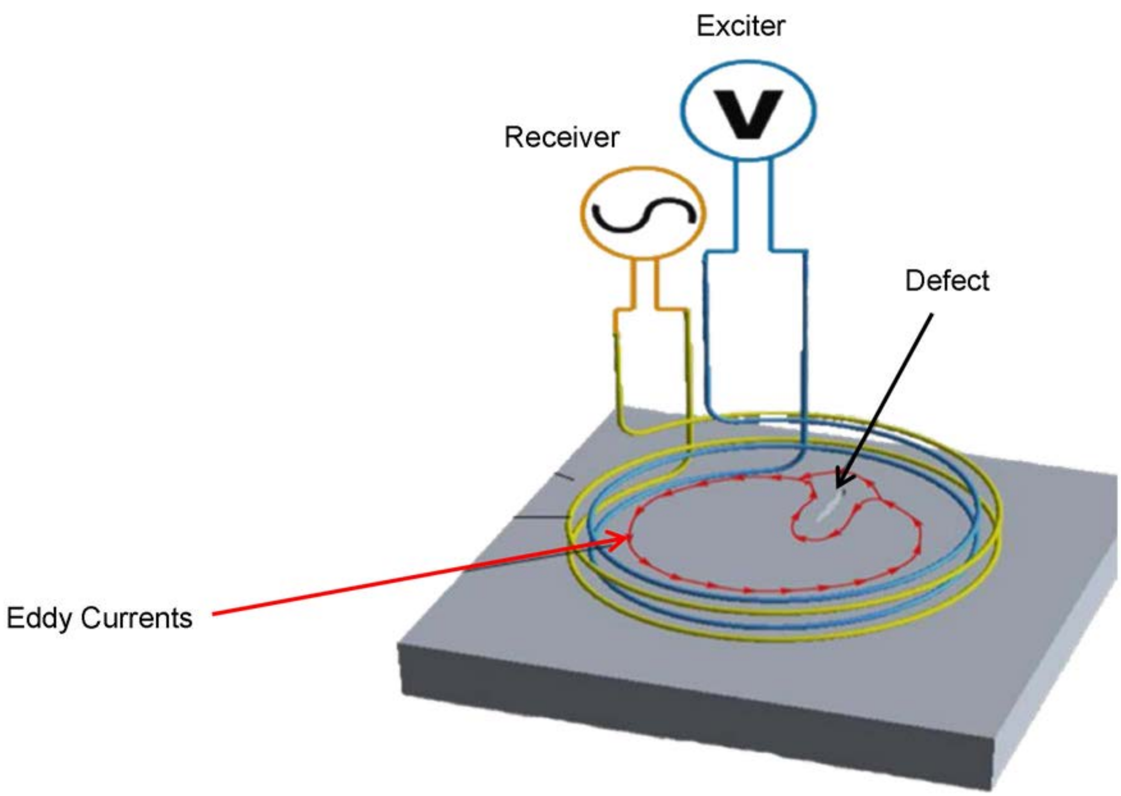

Figure D.1. Illustration of Eddy Current Testing Flaw Detection Using Separate Exciter and Receiver Coils

In the approach used for these tests, a flexible probe consisting of an array of exciter and receiver coils shown in Figure D.2 was used. The exciter and receiver coils are physically displaced in the test surface plane, as can be seen in the figure; the displacement was chosen to reduce signal variations caused by probe liftoff variations. The largest flaw signal is obtained when the flaw lies along the axis formed by the centers of the two displaced coils. In operation, the probe is scanned over the surface of the specimen. For these tests, the scanning was performed manually.

Figure D.2. Flexible Eddy Current Probe and Rigid Adapter Board

D.1.2 NDE Equipment

A CoreStar Omni 200 ET instrument and a Southwest Research Institute (SwRI) flexible eddy current probe, shown in the Figure D.2, were used. The probe was SwRI Part Number 201115836-003. A rigid adapter board (also shown in Figure D.2), Part Number 201115836-004, was used to connect the flexible array to the eddy current instrument cables. The probe includes 9 coils arranged in 3 rows of 3 coils each. The 3 coils in the center are operated as exciters; each additional row of 3 coils on either side of the exciter row are used as sensors, with the probe operated in driver-pickup mode; that is, one coil is used as an exciter and the other as a receiver, for each channel used. The spacing between the exciters and receivers had been chosen to minimize the effect of liftoff variations based on tests on different (carbon steel) specimens. The probe was operated at a test frequency of 50 kHz. Only a single exciter/receiver coil set on the probe was used for these tests. The probe phase was adjusted so that liftoff variations on the specimens were primarily in the horizontal direction on the instrument. The probe was designed for detection of relatively large flaws on rough welded surfaces, and for operation at frequencies greater than 50 kHz; it was therefore not surprising that there was no siginficant phase difference information that could be used to estimate flaw depth.

D.1.3 Data Acquisition Process

For the test performed, the instrument was first set up on a calibration plate. The plate is A36 steel; it contains 3 EDM notches. The probe was scanned around the plate; the phase of the display was rotated to make liftoff variations be primarily in the horizontal direction.

For data acquisition, the probe was scanned manually around the penetration, held against the surface by manual pressure. The orientation of the probe was also varied manually; the probe was rotated to maximize the response to any observed defect.

D.1.4 Data Analysis

No additional signal processing was performed on the data. The technique was developed to detect and locate surface-breaking defects. Therefore, analysis consisted primarily of estimating the location of the ends of the flaws.

Flaw position was estimated using a visual technique in order to eliminate the need for a mechanized scanner. Holes were punched in gaps between coils of the probe. Flaw edges were estimated by manually scanning the probe and observing the amplitude of coil pairs that had the largest signal indication. Locations where the amplitude dropped by 6 dB were designated as ends of flaws, and a marker was used to mark the mockup surface through the holes in the probe. Generally, 4 marks were made for each observed flaw. The marks can be seen in the photographs shown with each flaw. The eddy current instrument impedance plane display was recorded at the location of maximum flaw amplitude response.

The position of the marks, and therefore the estimated position of the flaws, was first measured using a coordinate measuring machine (CMM) at SwRI. This machine is maintained in calibration, with an accuracy much better than 0.1 mm. The machine was set up so that it reported X-Y coordinates, with the origin at the plane of the surface of the block and at the center of the penetration. The CMM machine was used to generate position values for the marks that had been placed on the specimens. Flaw ends were estimated by averaging the 2 pairs of locations marked for each flaw. Then the X-Y coordinates were converted into R-theta values for reporting.

After following this procedure, it was noted that the angular positions were generally accurate, but the values of R1 and R2 were too large, especially on blocks P21 and P22. The errors were typically 5 to 9 mm. Visual examination of the photographs showing the flaws and the marks on these blocks clearly showed that the flaw ends were marked much more accurately than reported. Therefore, a different method was used for measuring the locations for blocks P21 and P22. For block P21, which consists of radially oriented EDM notches, the theta values as determined by the CMM were retained. The values of R1 and R2 were determined by measuring the error in pixels in the photographs, and determining a scale factor of pixels per mm using the known flaw length. For block P22, the location of the flaw ends and the marks were measured in pixels. The 2 marks near each flaw end were averaged to provide a positon of each flaw end. Then the error in pixels between each actual flaw end and the estimated flaw end was calculated. The error in pixels was converted to mm using the reported flaw length. The same scale factor of pixels to mm was used for both X and Y axes. Then the estimated flaw end locations were converted to mm, and these X-Y coordinates were converted to R-theta coodinates.

D.1.5 Self Assessment

The advantages of this type of ET probe are

- Low cost for the part of the probe that will be subject to wear.
- Possibility of manufacturing with even greater number of coils to ensure 100% coverage with a single scan.
- Fabrication technique ensures accurate manufacturing repeatability.

- Probe flexibility greatly simplifies the motions required of a mechanized scanner, especially in the case of penetrations that are not normal to the vessel surface.

The disadvantage of this approach was

- The use of single layer flexible printed circuit material (used to provide great flexibility) limits the number of turns of the coil; hence, the spatial resolution is limited and the operating frequency had to be kept at 50 kHz or greater.

PARENT RRT – BMI TECHNIQUE Data Sheet

Procedure ID:	7.1	Tech ID:	7-ECT1
Inspection ID:	7.P21.1	Access:	*OD*
Test Block ID:	P21	Date:	*2012/11/28*
Team ID:	7		

Weld Volume Inspected:

Detection:	*Yes*	$\theta 1$:	0	$\theta 2$:	360
Length Sizing:	*Yes*	R1:	10	R2:	90
Depth Sizing:	*No*	Z1:	0	Z2:	0

Defect No	$\theta 1$ Deg.	$\theta 2$ Deg.	R1 mm	R2 mm	Z1 mm	Z2 mm	R_{max} mm	Amp dB	Surface Breaking	Comments
BTE-1	358.5	358.6	27.6	32.1	n/a	n/a	n/a	n/a	yes	See below
BTE-2	269.7	268.8	27.0	33.7	n/a	n/a	n/a	n/a	yes	See below
BTE-3	178.5	177.5	26.3	33.3	n/a	n/a	n/a	n/a	yes	See below
BTE-4	88.9	89.6	22.2	38.2	n/a	n/a	n/a	n/a	yes	See below

Note: Flaw location end points were determined by using an amplitude drop technique and physically marking the probe location at the flaw edges (reference the attached test specimen photos showing the marks made on the block to show flaw location). Each mark was then measured using the BMI coordinate system.

PARENT RRT – BMI INSPECTION SUMMARY Data Sheet

Inspection ID:	7.P21.1	Procedure ID:	7.1
Test Block ID:	P21	Date:	*2012/11/28*
Team ID:	7	Access:	OD

Weld Volume Inspected:

Detection:	yes	$\theta 1$:	0	$\theta 2$:	360
Length Sizing:	yes	R1:	10	R2:	90
Depth Sizing:	no	Z1:	0	Z2:	0

Defect No	$\theta 1$ Deg.	$\theta 2$ Deg.	R1 mm	R2 mm	Z1 mm	Z2 mm	R_{max} mm	Amp dB	Surface Breaking	Comments
BTE-1	358.5	358.6	27.6	32.1	n/a	n/a	n/a	n/a	yes	
BTE-2	269.7	268.8	27.0	33.7	n/a	n/a	n/a	n/a	yes	
BTE-3	178.5	177.5	26.3	33.3	n/a	n/a	n/a	n/a	yes	
BTE-4	88.9	89.6	22.2	38.2	n/a	n/a	n/a	n/a	yes	

PARENT RRT – BMI TECHNIQUE Data Sheet

Procedure ID:	7.1	Tech ID:	7-ECT1
Inspection ID:	7.P22.1	Access:	*OD*
Test Block ID:	P22	Date:	*2012/11/28*
Team ID:	7		

Weld Volume Inspected:

Detection:	*Yes*	$\theta 1$:	0	$\theta 2$:	360
Length Sizing:	*Yes*	R1:	20	R2:	90
Depth Sizing:	*No*	Z1:	0	Z2:	0

Defect No	$\theta 1$ Deg.	$\theta 2$ Deg.	R1 mm	R2 mm	Z1 mm	Z2 mm	R_{max} mm	Amp dB	Surface Breaking	Comments
BHE-1	355.7	4.3	29.6	30.0	n/a	n/a	n/a	n/a	yes	See below
BHE-2	262.0	276.8	27.9	29.5	n/a	n/a	n/a	n/a	yes	See below
BHE-3	166.8	173.0	27.6	32.0	n/a	n/a	n/a	n/a	yes	See below
BHE-4	69.1	110.4	25.0	31.1	n/a	n/a	n/a	n/a	yes	See below

Note: Flaw location end points were determined by using an amplitude drop technique and physically marking the probe location at the flaw edges (reference the attached test specimen photos showing the marks made on the block to show flaw location). Each mark was then measured using the BMI coordinate system.

PARENT RRT – BMI INSPECTION SUMMARY Data Sheet

Inspection ID:	7.P22.1	Procedure ID:	7.1
Test Block ID:	P22	Date:	*2012/11/28*
Team ID:	7	Access:	OD

Weld Volume Inspected:

Detection:	yes	$\theta 1$:	0	$\theta 2$:	360
Length Sizing:	yes	R1:	20	R2:	90
Depth Sizing:	no	Z1:	0	Z2:	0

Defect No	$\theta 1$ Deg.	$\theta 2$ Deg.	R1 mm	R2 mm	Z1 mm	Z2 mm	R_{max} mm	Amp dB	Surface Breaking	Comments
BHE-1	355.7	4.3	29.6	30.0	n/a	n/a	n/a	n/a	yes	
BHE-2	262.0	276.8	27.9	29.5	n/a	n/a	n/a	n/a	yes	
BHE-3	166.8	173.0	27.6	32.0	n/a	n/a	n/a	n/a	yes	
BHE-4	69.1	110.4	25.0	31.1	n/a	n/a	n/a	n/a	yes	

PARENT RRT – BMI TECHNIQUE Data Sheet

Procedure ID:	7.1	Tech ID:	7-ECT1
Inspection ID:	7.P5.1	Access:	*OD*
Test Block ID:	P5	Date:	*2012/11/28*
Team ID:	7		

Weld Volume Inspected:

Detection:	*Yes*	$\theta 1$:	0	$\theta 2$:	360
Length Sizing:	*Yes*	R1:	23	R2:	100
Depth Sizing:	*No*	Z1:	0	Z2:	0

Defect No	$\theta 1$ Deg.	$\theta 2$ Deg.	R1 mm	R2 mm	Z1 mm	Z2 mm	R_{max} mm	Amp dB	Surface Breaking	Comments
1	11.2	31.5	30.8	31.2	n/a	n/a	n/a	n/a	yes	See below
2	154.0	166.7	42.6	40.6	n/a	n/a	n/a	n/a	yes	See below
3	284.9	286.1	25.7	39.3	n/a	n/a	n/a	n/a	yes	See below

Note: Flaw location end points were determined by using an amplitude drop technique and physically marking the probe location at the flaw edges (reference the attached test specimen photos showing the marks made on the block to show flaw location). Each mark was then measured using the BMI coordinate system.

PARENT RRT – BMI INSPECTION SUMMARY Data Sheet

Inspection ID:	7.P5.1	Procedure ID:	7.1
Test Block ID:	P5	Date:	*2012/11/28*
Team ID:	7	Access:	OD

Weld Volume Inspected:

Detection:	yes	$\theta 1$:	0	$\theta 2$:	360
Length Sizing:	yes	R1:	23	R2:	100
Depth Sizing:	no	Z1:	0	Z2:	0

Defect No	$\theta 1$ Deg.	$\theta 2$ Deg.	R1 mm	R2 mm	Z1 mm	Z2 mm	R_{max} mm	Amp dB	Surface Breaking	Comments
1	11.2	31.5	30.8	31.2	n/a	n/a	n/a	n/a	yes	
2	154.0	166.7	42.6	40.6	n/a	n/a	n/a	n/a	yes	
3	284.9	286.1	25.7	39.3	n/a	n/a	n/a	n/a	yes	

PARENT RRT – BMI TECHNIQUE Data Sheet

Procedure ID:	7.1	Tech ID:	7-ECT1
Inspection ID:	7.P7.1	Access:	*OD*
Test Block ID:	P7	Date:	*2012/11/28*
Team ID:	7		

Weld Volume Inspected:

Detection:	*Yes*	$\theta 1$:	0	$\theta 2$:	360
Length Sizing:	*Yes*	R1:	23	R2:	100
Depth Sizing:	*No*	Z1:	0	Z2:	0

Defect No	$\theta 1$ Deg.	$\theta 2$ Deg.	R1 mm	R2 mm	Z1 mm	Z2 mm	R_{max} mm	Amp dB	Surface Breaking	Comments
1	57.7	57.3	55.3	45.6	n/a	n/a	n/a	n/a	yes	See below
2	109.0	111.5	47.8	55.9	n/a	n/a	n/a	n/a	yes	See below
3	162.5	165.0	27.7	36.4	n/a	n/a	n/a	n/a	yes	See below
4	293.3	298.8	36.7	54.0	n/a	n/a	n/a	n/a	yes	See below

Note: Flaw location end points were determined by using an amplitude drop technique and physically marking the probe location at the flaw edges (reference the attached test specimen photos showing the marks made on the block to show flaw location). Each mark was then measured using the BMI coordinate system.

PARENT RRT – BMI INSPECTION SUMMARY Data Sheet

Inspection ID:	7.P7.1	Procedure ID:	7.1
Test Block ID:	P7	Date:	*2012/11/28*
Team ID:	7	Access:	OD

Weld Volume Inspected:

Detection:	yes	$\theta 1$:	0	$\theta 2$:	360
Length Sizing:	yes	R1:	23	R2:	100
Depth Sizing:	no	Z1:	0	Z2:	0

Defect No	$\theta 1$ Deg.	$\theta 2$ Deg.	R1 mm	R2 mm	Z1 mm	Z2 mm	R_{max} mm	Amp dB	Surface Breaking	Comments
1	57.7	57.3	55.3	45.6	n/a	n/a	n/a	n/a	yes	
2	109.0	111.5	47.8	55.9	n/a	n/a	n/a	n/a	yes	
3	162.5	165.0	27.7	36.4	n/a	n/a	n/a	n/a	yes	
4	293.3	298.8	36.7	54.0	n/a	n/a	n/a	n/a	yes	

D.2 Phased Ultrasonic Array, Technique ID 7-PA1, 7-PA2

D.2.1 Overview

The data was taken using an automated ultrasonic phased array contact examination technique that was conducted from the inside surface of each test specimen. The phased array technique allows the use of multiple examination angles generated by a single search unit to improve both detection capability and examination efficiency. The examinations were performed with the UT search unit looking in four directions (toward, away, clockwise, counter clockwise) for detection and sizing of flaws both parallel and transverse to the weld. Flaws are detected and chacterized by evaluating fully merged data from all four directions. Detection is based on multi-directional confirmation, signal and spatial characteristics of the flaw. All suspect indications, regardless of amplitude, are investigated to the extent necessary to determine accurate characterization of the nature of the indication. A separate depth sizing examination was conducted after the detection examination to attain the through-wall dimension of each flaw.

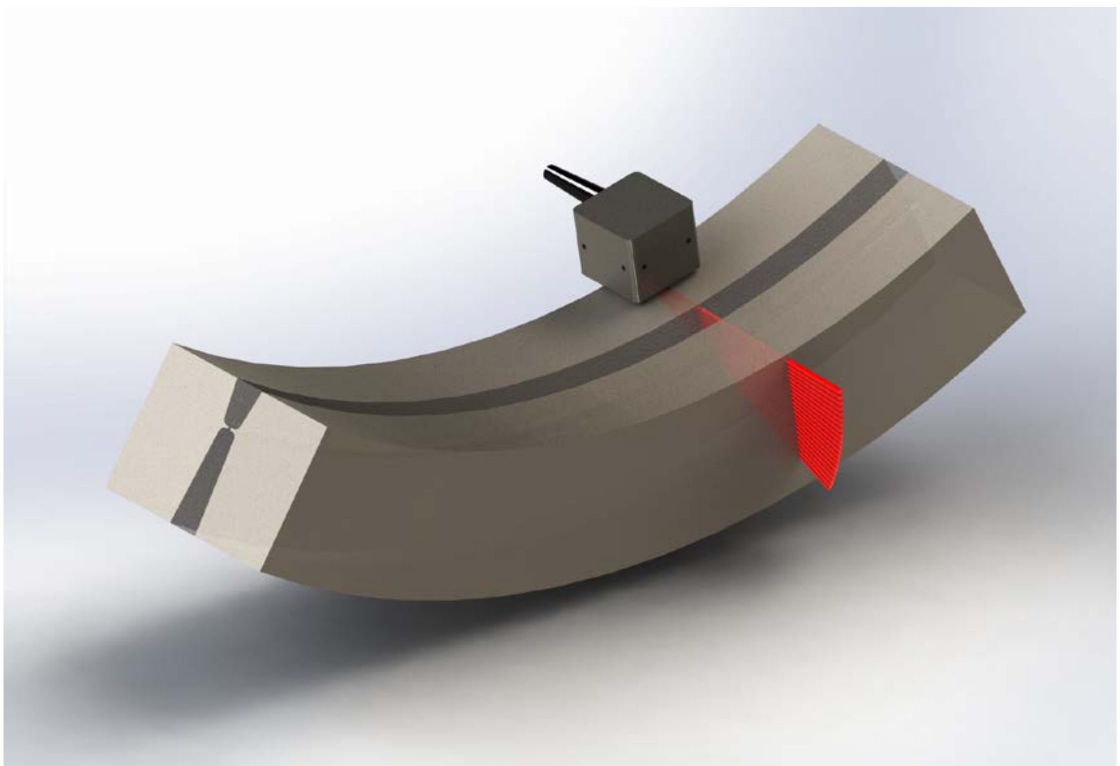

Figure D.3. Graphical Illustration of Phased Array Examination on Test Block

D.2.2 NDE Equipment

A Zetec Tomoscan-III PA 32/128 UT instrument was used for data acquisition. This system is capable of handling up to 128 phased array channels. The system utilizes Ultravision acquisition and analysis software, which is Windows-based and uses standard PC hardware for acquisition and analysis.

Once the system is set up and calibrated, all of the UT parameter and scan parameter settings can be saved and then recalled for future use. A-scan, B-scan, end-, side-, and C-scan views are available as well as composite views and other options that allow the analyst a broad selection of software analysis tools.

The UT phased array search units for detection and sizing were designed to produce the desired beam angles and waveforms in the DM weld materials, yet be small enough to maintain satisfactory contact when wavy or rough surfaces are encountered on the inside surface of the weld. The 1.5 MHz search unit contains two linear arrays in a pitch-ctach configuration mounted on an integral wedge, which incorporates a roof angle to provide geometric focusing of the two arrays in the near 1/3 of the weld thickness for the examination of the standard ASME Section XI examination volume. The search unit design allows electronic sweeping of the examination angle from 60° to 88° at 2° increments. Calibration of the search units and instrument is attained by using a standard IIW reference block of the same or similar material containing a 1-inch and 4-inch radius that are used for measuring angles, exit points, establishing system delay and reference sensitivity. The 4-inch radius was used to establish system delay and reference sensitivity.

An encoded scanner capable of providing accurate position information was utlized. The scanner was capable of performing scan and indexing movements as required and provided adequate force to keep the search unit coupled to the component surface.

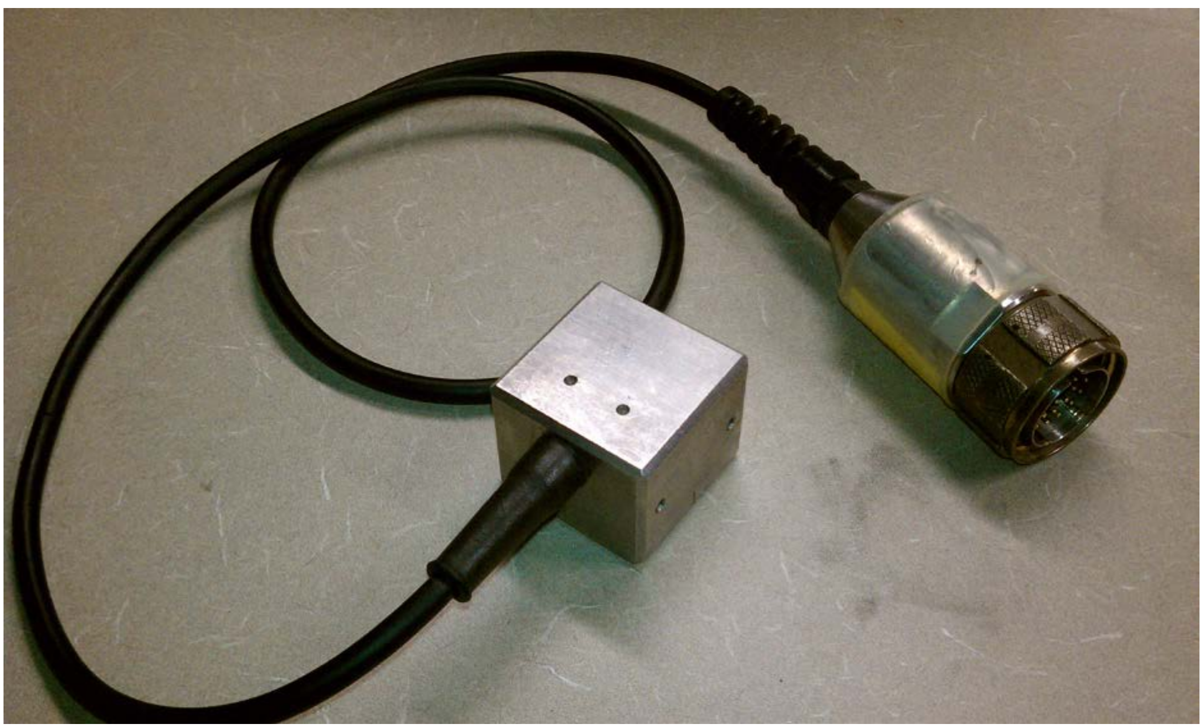

Figure D.4. 22-Element Phased Array Search Unit

Data Acquisition Process: The data acquisition was performed in instrument Log mode with a focal law gain of 14 dB for the detection and length sizing examination and 20 dB for the depth sizing examinations. The Log mode allows the T-III acquisition system to utilize the dynamic gain range of the amplifier. Data acquisition was performed with the scanner moving circumferentially and indexing axaially for both axial and circumferential flaws. Beam direction was parallel to the weld for axial flaws and perpendicular to the weld for circumferential flaws. The search unit movement rate did not exceed 2-inches per second for circumferential flaw detection and depth sizing, 1.5-inches per second for transverse flaw detection, and 0.75-inches per second for transverse flaw depth sizing. The maximum increment resolution for detection of circumferential flaws was 0.15-inches while the maximum increment for detection of axial flaws was 0.05-inches. The maximum increment resolution for depth sizing was 0.10-inches.

D.2.3 Data Analysis

D.2.3.1 Detection

Prior to analyzing data, the Data Analyst ensures the quality of the data by verifying a number of items (20-point checklist is used to verify data quality) and areas not meeting the quality acceptance criteria are re-exmained. After the data quality is verified, the appropriate data file is loaded, ensuring that each data file has been fully merged. In all of the volume corrected displays, the cursors are adjusted to envelop the entire scan area. The color palette range is adjusted to provide resolution of the various reflectors throughout the scan and to provide optimum image contrast and to ensure that indications are not masked with the background noise. The volumetric images for each channel are analyzed to identify areas that exhibit deviation from the component geometrical or metallurgical interface responses. Patterns from the VC Top (C) pane that exhibit echo-dynamics in the VC (B) pane are considered flaws. All suspect indications, regardless of amplitude, are investigated to the extent necessary to determine accurate characterization of the nature of the indication. Profilimetry data, thickness measurements, contours, and previous data are also utilized in analyzing the detection data. Flaw descrimination is procedurialized and conditions are provided and used by the analyst to determine if a flaw is present and to determine the flaw location including the determination if a flaw is surface breaking. Surface breaking characterization is based on signal and spatial characteristics. The flaw signal will drive to 0 inches on the a-scan when the flaw is surface breaking.

D.2.3.2 Depth Sizing

A data quality assessment is made similar to the detection analysis as previously stated prior to determining the flaw depth. After data quality is determined to be acceptable, the depth sizing evaluation is made as described below for axial and circumferential flaws:

Circumferential Flaws: Circumferential depth sizing data is taken using two dual 1.5 MHz 1D linear array probes phasing at a 30°–70° azimuthal scans with 1-degree resolution. Data from two beam directions (Twd & Awy) is considered and an evaluation of the unmerged data is made for several discrete beam angles to establish the flaw depth range and to identify the channel providing the greatest flaw depth. Depth sizing data is then evaluated using full and discrete merges and Z1 and Z2 are identified. Correction values are considered and applied as well as an evaluation of search unit contact that may be affected due to complex inside surface geometry. Search units can tilt when indexing over changing elevations so profilometry data is considered when evaluating sizing data.

Axial Flaws: Axial depth sizing data is taken using dual 1.5 MHz 1D linear arrays phasing at a 60°–82° and 40°–46° azimuthal scans with 2-degree resolution. Data from two beam directions (Cw & CCw) is considered. Depth sizing unmerged data from two opposing channels is evaluated to identify Z1 and Z2. Depth measurements are read directly and corrected for cylinder geometry using the software tooling.

D.2.4 Self Assessment

The advantages of this type of technique include:

- Allows the use of multiple elements within a single search unit for multiple inspection angles that can be steered and focused to the examination area of interest.
- The use of multiple inspection angles increases the probability of detection.
- Allows for sectorial scanning and simplification of DMW's with complex geometry.
- A separate detection procedure allows larger indexing for a quicker detection examination.

The disadvantages of this type of technique include:

- A more complex examination technique which requires personnel with proper training and /or experience to implement it.
- A separate depth sizing examination at smaller indexing is required after flaw detection is completed.

D.3 Phased Ultrasonic Array, Technique ID 150-PA0

D.3.1 Overview

The mockup components (P12 & P37) were evaluated using an encoded outside diameter (OD) transmit-receive longitudinal (TRL) ultrasonic phased array technique with continuous flow water coupling. Given that the specimen is composed of carbon and stainless steels (dissimilar metal weld) and is considered large-bore (thickness between 77–79 mm), a phased array probe was chosen with a center frequency of 1.0 MHz for inspection. A frequency of 1.0 MHz will provide excellent penetration into the inner diameter (ID) regions of these components while maintaining good overall flaw characterization resolution as the nominal wavelength in stainless steel is approximately 5 mm. The phased array technique was applied as it is a very versatile and adaptable inspection technique. It can be applied to a multitude of different components due to the ability to apply a variety of focal styles, a range of focal depths and refracted and skewed angles in order to insonify the region or regions of interest with a well-focused beam. This volumetric assessment technique can be used to characterize the length, depth, and location of flaws present in the inspected volume.

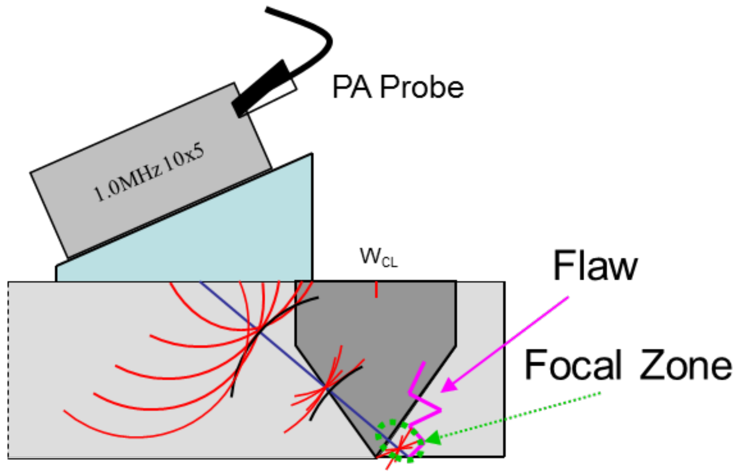

Figure D.5. Graphic Showing Electronic Focusing Used in Phased Array Technique

D.3.2 Phased Array Equipment

D.3.2.1 Phased array data acquisition hardware

Data acquisition was accomplished using the DYNARAY® system for all PA probes evaluated in this study. This commercially available system is equipped to accommodate a maximum of 256 channels from PA probes and requires the use of Ultravision® 3 software. Its frequency pulsing electronics will drive probes in the 0.2–20 MHz range. The laboratory workstation and DYNARAY® data acquisition system are shown in Figure D.6.

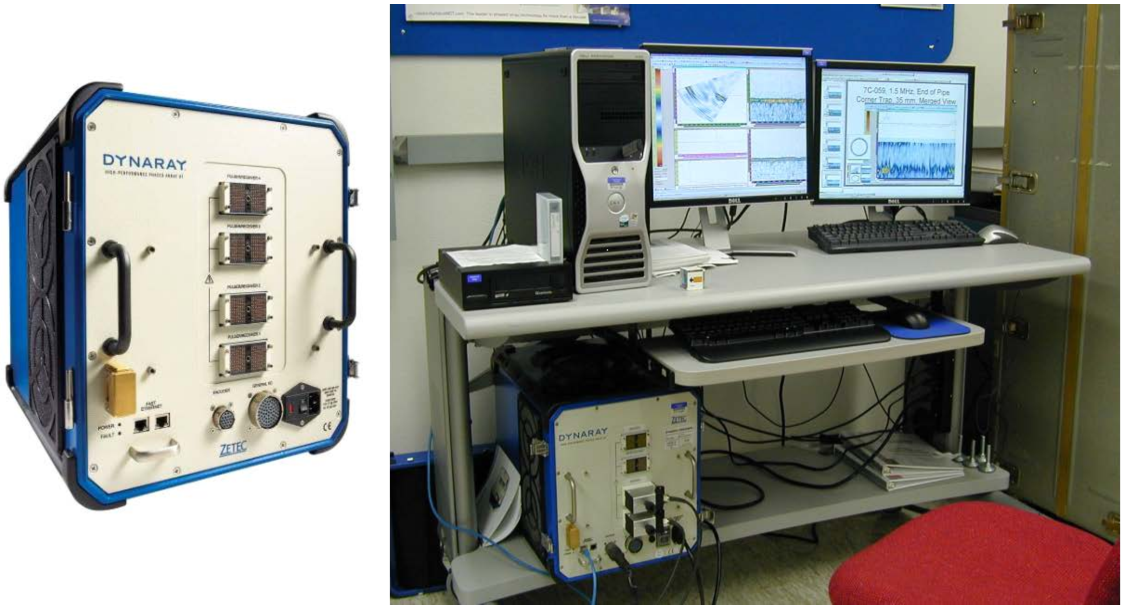

Figure D.6. Data Acquisition System and Laboratory Workstation. Left: DYNARAY® phased array data acquisition system (courtesy of ZETEC®). Right: Laboratory workstation for both data acquisition and data analysis, with the DYNARAY® system on the lower shelf.

D.3.3 Necessary Equipment and *Function* (Figure D.7)

- Dynaray Acquisition System (Zetec Inc.)
  - Dynaray Lite will also work – Need minimum of 50 P/R channels
    - *Pulse/Receive phased array probe and collect Phased array data*
- Ultravision 3 software (Zetec Inc.)
  - *Setup focal laws and execute scanning*
- Ultrasonic phased array probe (Imasonic Inc.)
  - *Inspection array*
- Desktop or Laptop computer with Ethernet connection
  - *Run the software for data collection and analysis*
- Motion control drive unit (MCDU) (Zetec Inc.)
  - *Provide power and control for scanner. Relay positional information*
- GPS 1000 Scanner unit (ATCO Inc.)
  - *Provide scan and index motion and special encoding information*

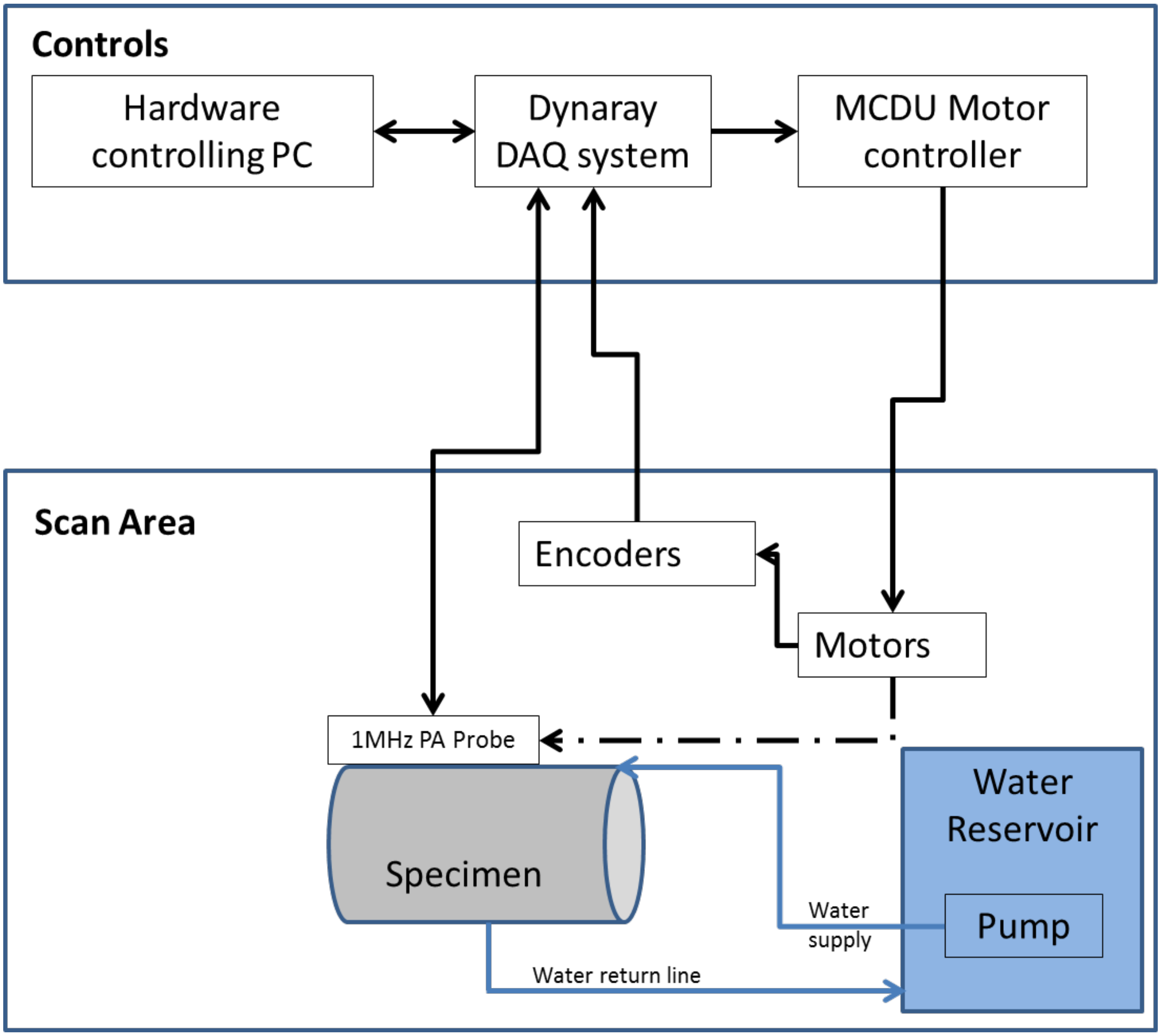

Figure D.7. Phased Array Data Acquisition Connection Schematic

D.3.3.1 Phased Array Probe

The 1.0 MHz Imasonic TRL array (Figure D.8) was originally designed for evaluating inspection effectiveness of PA methods on components with inlays, onlays, and overlays. It consists of two 10-element by 5-element matrix arrays. Each element of the array is 3.5 mm × 3.5 mm with separation of 0.5 mm on each side, thus primary and secondary axis pitch is 4.0 mm. One array is used for transmitting, the other for receiving ultrasonic signals. This probe has a 58% bandwidth (BW) at −6 dB and an approximately 50-mm^2 (1.97-in.^{2}) footprint with a customized wedge for data collection in tight geometrical configurations. The 1.0 MHz probe was used with a removable outside diameter (OD) contoured Rexolite wedge assembly with a wedge angle of 15 degrees. The probe's nominal wavelength in stainless steel is 5.31 mm (0.21 in.) at its average center frequency of 1.1 MHz. Skew angles of ±20 degrees were possible with this array.

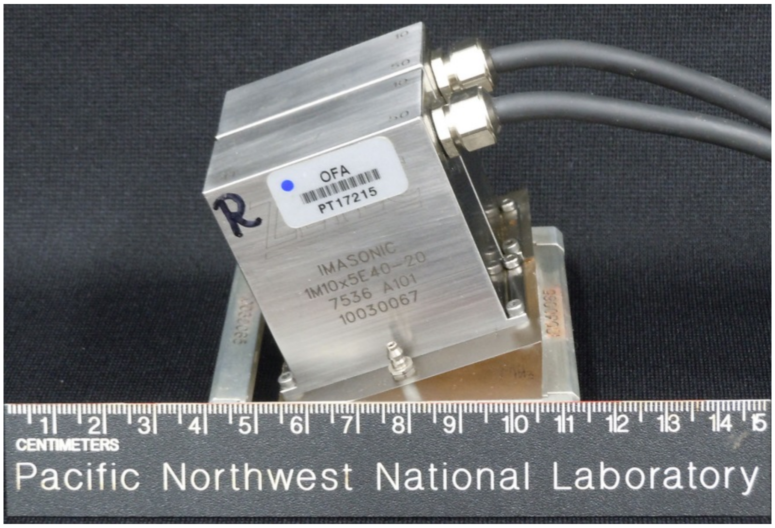

Figure D.8. 1.0 MHz Transmit-Receive Phased Array Probe

D.3.4 Data Acquisition Process and Parameters

D.3.4.1 Focal Law Development

Before a phased-array probe can be used to perform an examination, a set of focal laws must be produced to control the firing of individual elements. The focal laws are inputs to the Ultravision® control software, which determines specific elements to excite at specific times to allow for proper beam-forming in the material to be examined. The focal laws also contain details about the angles being generated, the focal point of the sound field, the delays associated with the wedge and electronics, and the orientation of the probe. The inspection team uses a software package contained in the Ultravision® 3 software program for producing focal laws known as the "ZETEC® Advanced Focal Law Calculator." The software package performs two functions: 1) focal law generation and 2) simulation of the ultrasonic field produced by the probe when using the generated laws. The user enters the physical information about the PA probe, such as the number of elements and the sizes of the elements, and the wedge information, such as the wedge angle and the wedge size, into the program. The desired angles and focal distances are then entered, and the software generates the needed delays for each element to produce the desired beam steering and focusing in the material. The software beam simulation produces a simple image of the probe on the wedge, ray-tracing to show the focal depth and steering desired, and density mapping to enable the viewer to see how well the sound field responds for a particular angle and whether grating lobes exist that may be detrimental to the examination. Figure D.9 shows an example of the ray tracing for a probe on the left with the sound field density mapping on the right. It should be noted that this simulation is performed in isotropic material; that is, the velocity of sound is maintained throughout any angle for a particular wave mode, which is not really the true state for CASS, but enables the user to estimate sound field parameters and transducer performance for optimal array design and focal law development.

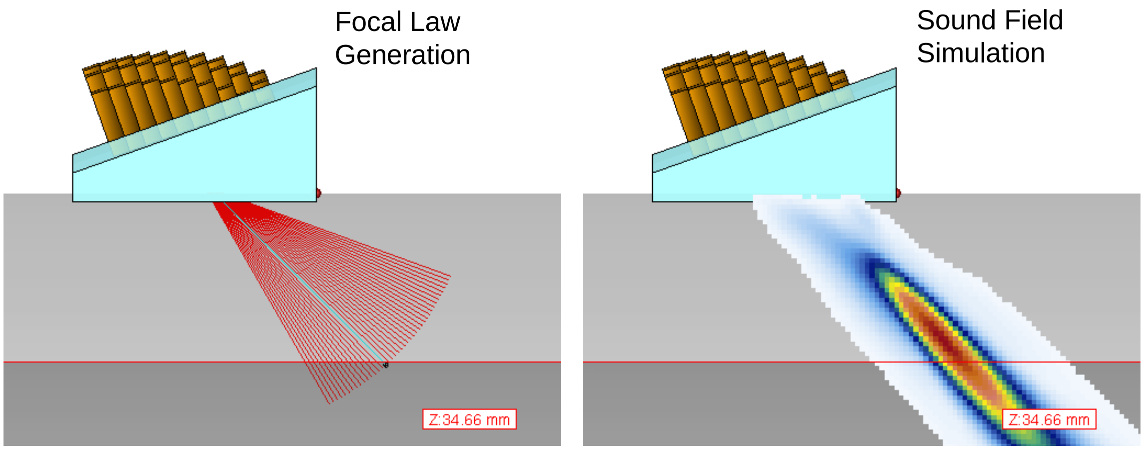

Figure D.9. The ZETEC® Advanced Phased Array Calculator is Useful for Generating Focal Laws (left) and Simulating the Sound Field for the Focal Law (right) to Determine Beam Characteristics

D.3.4.2 Data Acquisition Parameters

- 1.0 MHz 2×(10×5) element matrix array
  - Transmit-Receive Longitudinal
  - Each element pulsed with 500 ns negative 200V square wave excitation (Dynaray)
  - True Depth and Half Path focusing techniques (Figure D.10)
  - 20–60 degree azimuthal angle sweep, 3 degree increment
  - 0,±10 degree skew angles
- Outside Diameter (OD) inspection
  - Raster scan resolution: 1.0 mm scan, 1.0 mm index
  - Automated and encoded
- OD contoured Rexolite wedge
  - 15 degree wedge angle
- 0 pt., coordinates and scan conventions followed from test block information sheet
- Continuous water loop used for ultrasonic coupling between the wedge and the component
- Circumferential scans (looking for axially oriented flaws)
  - Collect data in clockwise and counter clockwise directions
- Axial scans (looking for circumferentially oriented flaws)
  - Collect data from up-stream and down-stream locations
- Target Focus: Inner Diameter Regions
  - ID connected flaws (cracks)

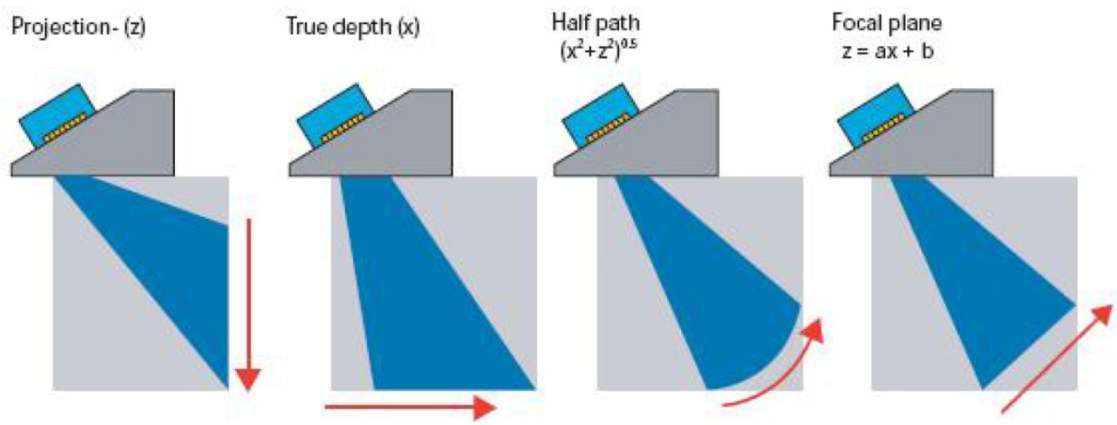

1. Projection – focusing in a specific vertical plane. Parameters: distance from probe reference point, sweep angles (start, stop, interval), skew angle(s).

2. True depth – focusing at specific constant depth with all angles focused at this depth. Parameters: focusing depth, sweep angles (start, stop, interval), skew angle(s).

3. Half-path – sound path held constant as beam is swept. Parameters: sound path length, sweep angles (start, stop, interval), skew angle(s).

4. Focal plane – arbitrary user-defined plane of focus. Low angle path length, high angle path length, sweep angles (start, stop, interval), skew angle(s).

Figure D.10. Beam Focusing Options for Phased Array Probes

D.3.5 Signal Processing of the Phased Array Data

- Ultravision 3 software was used to reconstruct the phased array data into images. No additional filtering or manipulations of the data were conducted.

D.3.6 Analysis of the Phased Array Data

- Phased array image analysis was conducted using Ultravision 3 software to display a variety of images including: (Figure D.11)
  – A-Scan (time-amplitude) along selected angles
  – C-Scan (Top View) scan vs. index axes – location and length of flaw
  – B-Scan (Side View) scan vs. ultrasound axes – depth of flaw
  – D-Scan (End View) index vs. ultrasound axes – length and depth of flaw
- Detection
  – Strong response signal(s) present in the ID region of component
    ○ Signal strength above background noise levels to be considered (greater than 6 dB above background)

- Characterization
  - Detected signals will be length sized using a −6 dB and loss of signal (LOS) method in the D-Scan view
  - Depth sizing will be assessed by measuring maximum flaw extent in the B- and/or D-Scan view(s)
  - Overall flaw circumferential and axial location assessed with C-Scan view

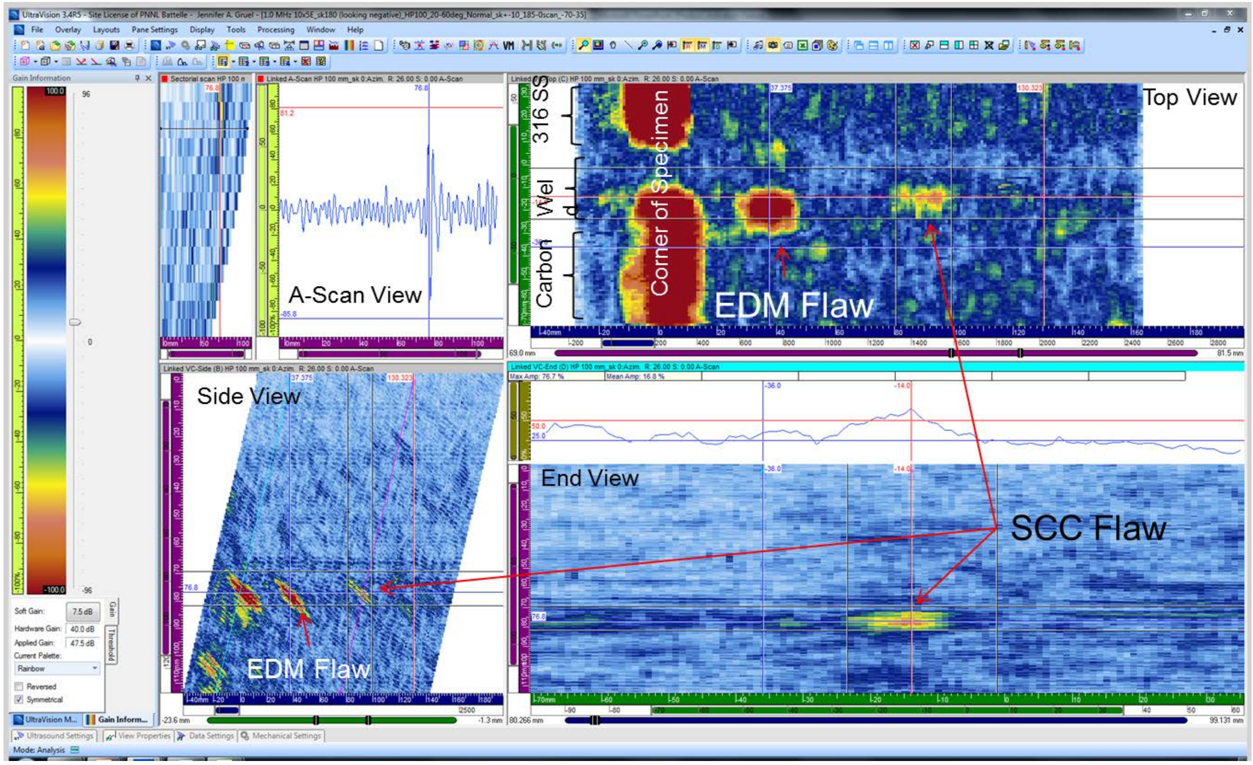

Figure D.11. Example of Phased Array Image Data

D.4 Laser Ultrasound Visualization Method, Technique ID LUV0, LUV-ASW0, LUV-BSW0

Figure D.12 illustrates the laser ultrasound visualization system for material nondestructive evaluation/testing. The proposed laser ultrasound visualization system is a fully standalone, self-contained and battery-powered sensor unit. It consists of four major components: laser pulse energy delivery system, a miniature piezoelectric transducer (PZT), control and data acquisition electronics, and a laptop computer for signal processing and visualization. The processes for defect/flaw inspections are as follows: The sensor unit will be placed at a standoff distance from the object under testing with the galvanometer scanner facing the surface of the testing areas. The end user will push a button, which will generate a trigger signal to start the inspection process. Control signals will be generated by the sensor electronics and sent to the pulsed laser and the galvanometer scanner. Consequently, the laser pulses are precisely delivered onto different locations of the testing object, and swept in a raster scan pattern. As the laser pulses are delivered onto each spot, they generate local heating, which induces minute surface motions. Such a surface motion propagates through other area of the object, thus leading to the generation of ultrasound pulses. It should be emphasized that the laser pulse energy used for the ultrasound generation is several orders of magnitude lower than the laser material damage threshold, thus causing no damages to testing object. A PZT transducer will be placed at a convenient location by the end user on the outer surface of the testing object to detect the ultrasound pulses. The PZT sensor signals will be recorded and stored in a laptop computer. After a complete scan in the testing area, the stored ultrasound propagation data will be processed and displayed. The ultrasound signal propagation characteristics in the testing area can be mapped with laser ultrasound generations at different spots. Those signals will be in the form of a movie clip for the end users to visualize the ultrasound signal propagation characteristics. Consequently, defects including mechanical cracks, stress corrosion cracks, voids, welding flaws etc., can all be easily visualized without any complicated pattern recognition algorithm, ultrasound modeling tools or a well-trained technician. Any maintenance personnel should be able to operate the proposed sensor without any difficulty because the detections of those defects are straightforward. For example, small mechanical cracks inside the testing structure will act as ultrasound wave scatterers, which lead to the formation of ring patterns around those cracks in the ultrasound propagation images.

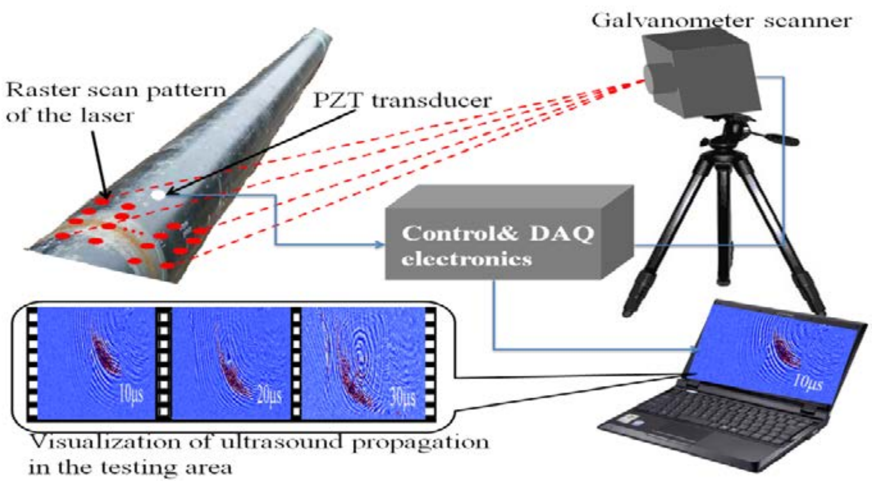

Figure D.12. A Schematic of the Envisioned Laser Ultrasound Visualization System Used for Inline Pipeline Integrity Assessment

It should be noted that the underlying principle of proposed laser ultrasound visualization technique is similar to the traditional ultrasound testing in that the ultrasound propagation characteristics in the specimens are monitored, based on which various defects and the state of the specimen can be detected and identified. One distinct difference between the proposed laser ultrasound and the traditional ultrasound testing is that the proposed method allows the defect detection and identification based on two dimensional images instead of only an one-dimensional waveform. This is because the ultrasound wave propagations in real-world structures are very complicated, as a lot of propagation modes and features could arise due to multiple wave bouncing from various boundaries, weld seams, walls and interfaces. Consequently, those one-dimensional waveforms are heavily convoluted, and the detections of specific features are very challenging. Often, very complicated modeling works are required, making it difficult to interpret the ultrasound data. The proposed laser ultrasound technique, however, can form the two dimensional images to reveal the ultrasound wave propagations in structures. The defects present in structures with complicated shapes and configurations can be directly visualized.

The merits of the proposed laser ultrasound visualization sensor system and its advantages over other techniques are listed below:

1. **Compact, lightweight, and portable**: Using a compact, lightweight and low power consumption fiber laser, the whole laser ultrasound sensor system will have a size ~12"×12"×8", weigh around 20 lbs, and can be powered by a 24V battery. The compactness, lightweight and portability of the proposed laser ultrasound visualization system makes it practical to be used in the field.
2. **Capable of detecting a wide variety of defects**: Defects including cracks (partial or full cracks), delamination/debonding, voids, porosity, foreign particle inclusions, moisture ingression, and material fatigue and work hardening can all be detected using the proposed sensor.
3. **Compatible with complex shapes and configurations**: With the proposed laser ultrasound system, there is no need to control the laser incidence angle and laser focus, thus making it possible to inspect objects with any arbitrary shapes and configurations.
4. **High sensitivity and good spatial resolution**: The combination of using short ns- laser pulse for ultrasound generation and miniature PZT transducers for ultrasound detection enables very high signal to noise ratio, thus leading to very high sensitivity in defect detection. Additionally, the laser ultrasound system should allow very good spatial resolution (i.e., hundreds of micrometer to ~1 mm) in detecting defected area.
5. **High measurement throughput**: The high measurement throughput is a direct result of the high speed enabled by the laser galvanometer scanner, which can scan in both x and y direction with a maximum speed of 2 m/s.
6. **Easy and safe to the operators**: In the traditional ultrasound technique, the defect detection is based on one-dimensional waveforms. The data interpretations are not straightforward and typically involve complicated modeling. The proposed laser ultrasound system, however, allows defect detection and identification based on visual images of the ultrasound propagation characteristics in the testing object. Additionally, compared to the X-ray tomography technique, the laser ultrasound visualization system is much safer to the operators, as it does not involve any harmful radiations.

Appendix E

Japanese Detailed Technique Descriptions

Appendix E

Japanese Detailed Technique Descriptions

E.1 Phased Array Asymmetrical Beam TOFD and Phased Array Twin Probe, Technique ID 29-PA-ATOFD0, 29-PA-ATOFD1, 29-PA-ATOFD2, 29-PA-TP0

The TOFD method can precisely measure crack depth, but is not suitable for materials with high ultrasonic attenuation, such as stainless steel cast piping, austenitic stainless steel piping welds and dissimilar welds in vessel nozzles in nuclear power plant equipment.

INSS has developed two kinds of scanning methods with phased array system and an analysis method of these scanning data in cooperation with Non-Destructive Inspection Co., Ltd. (Ishida and Kitasaka 2013).

One of these scanning methods is a TOFD method with asymmetrical ultrasonic beams of a transmitter and a receiver (hereafter PA-ATOFD method; phased array asymmetrical beam TOFD method").

The other is a phased array twin probe method with a transmitter and a receiver (hereafter PA-TP method).

An analysis method synthesizes plural scanning data with different refraction angles and path lengths (hereafter "MA method; multi-angle synthesis method") acquired by the PA-ATOFD or the PA-TP method.

E.1.1 Principle of Scanning and Synthesis Methods

E.1.1.1 Phased Array Asymmetrical Beam TOFD Method (PA-ATOFD Method)

Figure E.1 illustrates a schematic diagram of the conventional TOFD method. Two probes with a single element are used for the transmitter and receiver. To change the refraction angle with a reflection source it is necessary to change the probes with another incident angle or the distance between the transmitter and receiver.

Figure E.2 illustrates a schematic diagram of the phased array TOFD method. We can set the focus and convergence point of the ultrasonic beams of the transmitter and receiver at arbitrary different positions in a material. However, to change the refraction angle with a reflection source it is necessary to change the distance between the transmitter and receiver.

Figure E.3 illustrates a schematic diagram of the phased array asymmetrical beam TOFD method. Ultrasonic beams with different refraction angles and path lengths of the transmitter and receiver are set at an arbitrary focal and convergence point in the material in order to acquire the tip echo of the SCC with different refraction angles. Furthermore, the scanning data are synthesized with different refraction angles and different depths of focus point. This synthesis is expected to enable us to distinguish easily the echo from reflected sources and noise.

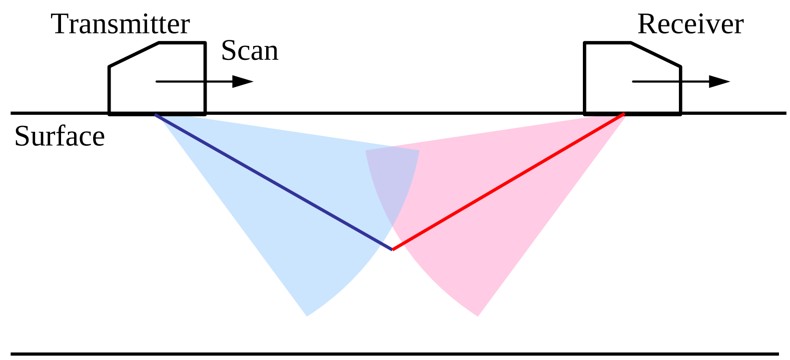

Figure E.1. Conventional TOFD Method

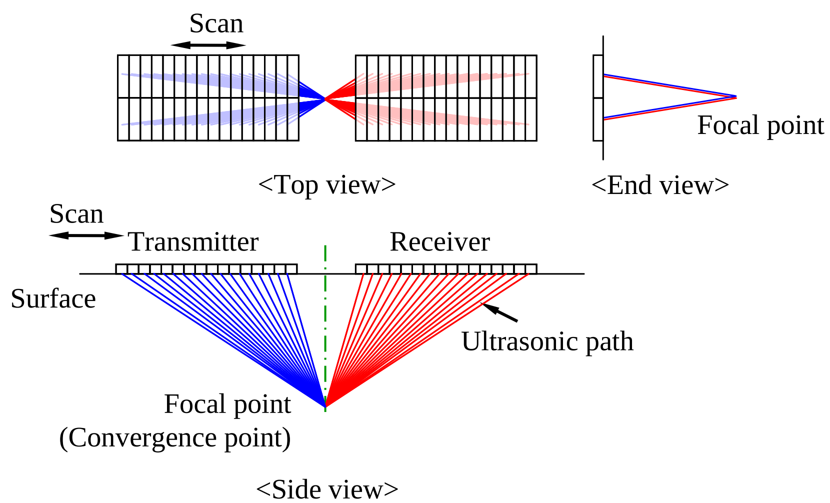

Figure E.2. Phased Array TOFD Method

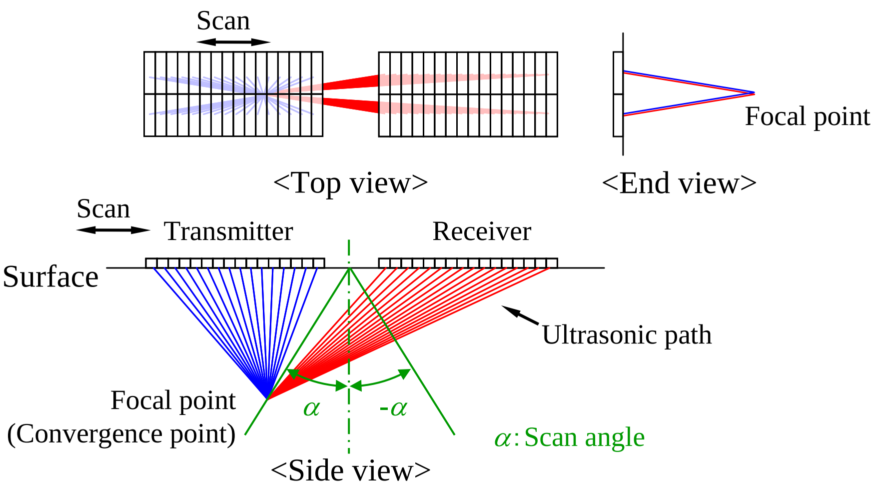

Figure E.3. Phased Array Asymmetrical Beam TOFD Method (PA-ATOFD Method)

E.1.1.2 Phased Array Twin Probe Method (PA-TP Method)

Figure E.4 shows a schematic drawing of a phased array twin probe method. In the longitudinal (back/forth) direction to the incidence of ultrasound waves, the element arrangement in this direction can focus the ultrasonic beam on different refracting angles and different focus point depths. The elements were arranged in right/left directions to focus the ultrasonic beam at different depths in this direction as well.

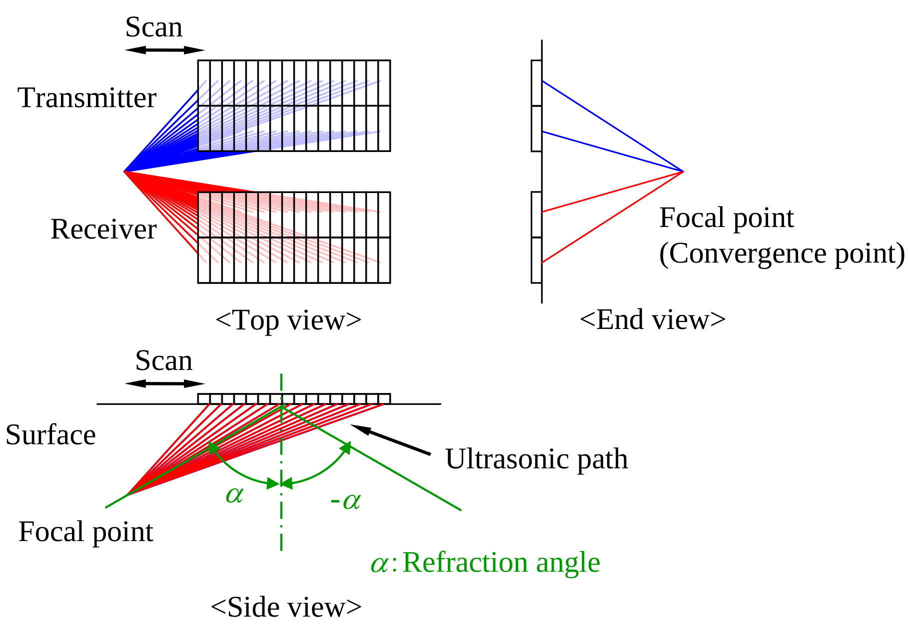

Figure E.4. Phased Array Twin Probe Method

E.1.1.3 Multi-angle Synthesis Method (MA Method)

Figure E.5 illustrates the multi-angle synthesis method. The scanning data are synthesized with different scan or refraction angles and different depths of focal point. This synthesis is expected to enable us to distinguish easily the echo from reflected sources and noise.

The scanning data are synthesized by an original calculation program on a PC.

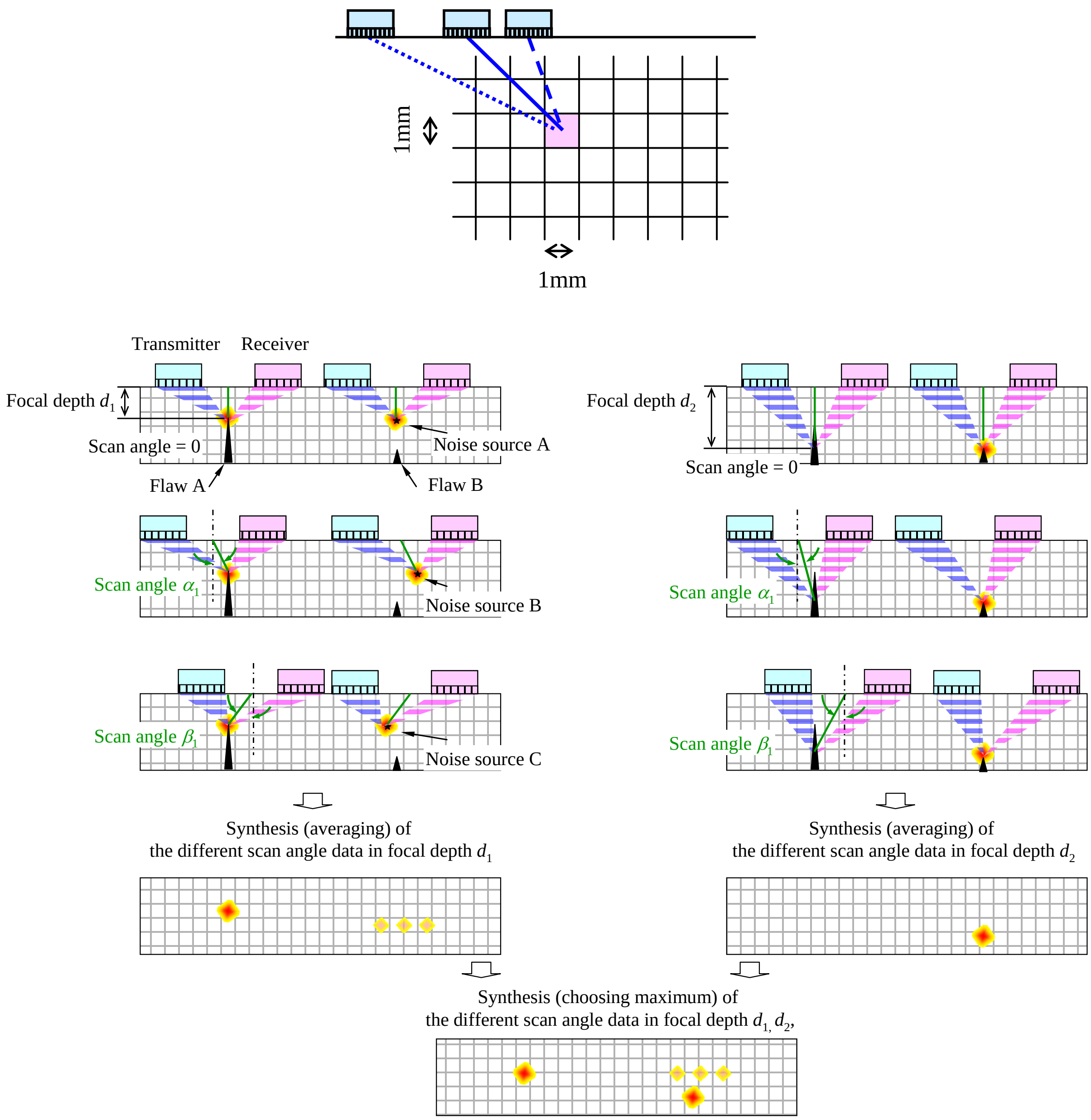

(1) Synthesis of PA-ATOFD method data

Figure E.5. Multi-angle Synthesis Method (MA Method) (1/2)

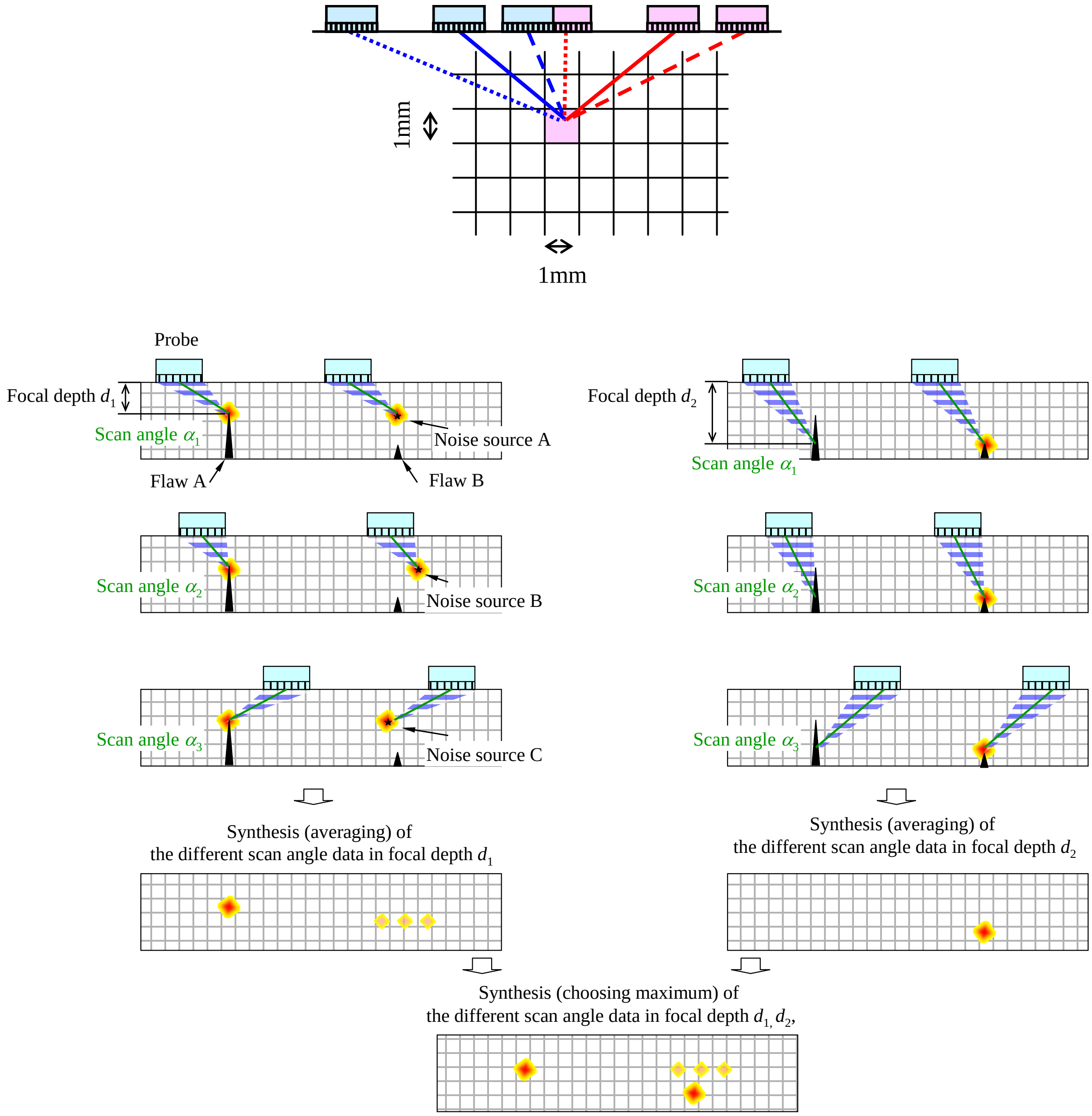

(2) Synthesis of PA-TP method data

Figure E.5. Multi-angle Synthesis Method (MA Method) (2/2)

E.1.2 Inspection Procedure

E.1.2.1 PA-ATOFD Method

(A) Procedure

1. Scan and acquire data by PA-ATOFD method
2. Determine an analysis section for B-scan analysis by MA method analysis

3. Analyze and draw a B-scope image by MA method analysis

(B) Equipment

- Transducer (Figure E.6, Table E.1)
  - 2×16 matrix array (Inner surface (near crack side))
  - 4×8 matrix array (Inner surface (near crack side))
  - 10×25 matrix array (Outer surface (far crack side)
  - Transducers are fit with a wedge on the surface of the specimen.
- Pulser/Receiver (Figure E.7)
  - Zetec Dynaray (256ch P/R)
- Delay setting / Imaging software (Figure E.7)
  - Zetec Ultravision[(a)]
- Scanner (Figure E.7)
  - X-Y

(C) Calibration

- Use reference block with side drilled hole to calibrate echo height and path length
  - (ϕ3mm, 4, 8, 12 ~ 36, 40 mm depth)

(D) Scan

• Scan direction	Perpendicular to the crack surface
• Scan pitch	1 mm
• Index pitch	2 mm
• Scan angle	+40 ~ −40 deg. (maximum)
• Images	B, C, D-scope (Ultravision) B-scope (MA method)

(E) MA Method Analysis

- PC
- Synthesis calculation program on the MATLAB

• Imaging	B-scope
• Synthesis pitch	1 mm

(a) Ultravision has no function of TOFD using phased array transducers. So INSS set the delay time of array probe originally.

E.1.2.2 PA-TP Method

(A) Procedure

1. Scan and acquire data by PA-TP method
2. Determine an analysis section for B-scan analysis by MA method analysis
3. Analyze and draw a B-scan image by MA method analysis

(B) Equipment

- Transducer (Figure E.6, Table E.1)
  - 10×25 matrix array (Outer surface (far crack side))
  - Transducers are fit with a wedge on the surface of the specimen.
- Pulser/Receiver (Figure E.7)
  - Zetec Dynaray (256ch P/R)
- Delay setting / Imaging software (Figure E.7)
  - Zetec Ultravision
- Scanner (Figure E.7)
  - X-Y

(C) Scan

- Scan direction Perpendicular to the crack surface
- Scan pitch 1 mm
- Index pitch 2 mm
- Scan angle +45 ~ −45 deg. (maximum)
- Images B, C, D-scope (Ultravision)
  B-scope (MA method)

(D) MA Method Analysis

- PC
- Synthesis calculation program on the MATLAB
- Imaging B-scope
- Synthesis pitch 1 mm

Table E.1. Array Transducers

Type	2×16 Matrix Array	4×8 Matrix Array	10×25 Matrix Array
Frequency (MHz)	2.25	2.25	2
Elements	32	32	250
Array of elements (width × length)	2×16	4×8	10×25
Size (mm) (width × length)			
Element	7.4×1.8	3.8×1.8	3.8×3.0
Aperture	14.9× 31.8	15.8×15.8	39.8×79.8

(1) 2×16 matrix array

(2) 4×8 matrix array

(3) 10×25 matrix array

(4) Example of probe with the wedge

Figure E.6. Transducer

Figure E.7. Measurement Set-up (Example for the Specimen P37)

E.1.3 Team's Assessment of the Technique Based on the Round-Robin Test Results

E.1.3.1 Met Our Expectation

- Better result by PA-TP method with MA method for the outer surface scan.
  - PA-TP method gives us a defect position by the corner echo. But PA-ATOFD method gives us a tip echo only. It is difficult to discriminate a tip eco directly by PA-ATOFD.
  - But for the inner surface scan, PA-ATOFD method gives us a defect position by lack of the signal.

E.1.3.2 To be Improved

- Develop a coupling supply system for the large aperture transducer.
  - We frequently met lack of coupling (glycerin paste) on the scanning surface.

- Determine the best transducer specification of the PA-ATOFD method for the inner surface.
  - We could not detect the tip echo of the deep defect (20mm~) on the inner surface by our PA-ATOFD probe. This result tells us necessity of the larger aperture probe.

Further detailed assessment should be evaluated with defect destructive information.

E.2 Three-Dimensional Synthetic Aperture Focusing, Technique ID 17-SAFT1

E.2.1 Principle

Synthetic Aperture Focusing Technique (SAFT) is used to construct an ultrasonic image from ultrasonic signals obtained with several transmitter-receiver combinations. When an array transducer is used for the acquisition of these ultrasonic signals, ultrasonic waves transmitted by one selected transducer element are received by all the transducer elements. By shifting the element used for the transmitter, the ultrasonic signals for every transmitter-receiver combination are collected.

Let $\boldsymbol{x}_i$ be the position of the transmitter, $\boldsymbol{x}_j$ be the position of the receiver and $\boldsymbol{x}$ be the position of a defect. Here we suppose that an ultrasonic wave transmitted from $\boldsymbol{x}_i$ is reflected at $\boldsymbol{x}$ and received at $\boldsymbol{x}_j$ (Figure E.8). The distance between $\boldsymbol{x}_i$ and $\boldsymbol{x}$ is denoted by $r_i = |\boldsymbol{x}_i - \boldsymbol{x}|$, and the distance between $\boldsymbol{x}_j$ and $\boldsymbol{x}$ is denoted by $r_j = |\boldsymbol{x}_j - \boldsymbol{x}|$. If the wave velocity is given by v, the propagation time from $\boldsymbol{x}_i$ to $\boldsymbol{x}_j$ via $\boldsymbol{x}$ is calculated by $t_{ij} = (r_i + r_j)/v$.

Conversely, the sum of the distances $r_i + r_j$ can be calculated with the wave velocity v and the propagation time t_{ij}, which can be derived from the ultrasonic signals obtained with the receiver. If the total travel distance $r_i + r_j$ is known, the defect position $\boldsymbol{x}$ can be narrowed down. The defect position $\boldsymbol{x}$ should be on the circumference of the ellipse determined by the conditions that its focal points are $\boldsymbol{x}_i$ and $\boldsymbol{x}_j$ and the sum of the distances from any point on this ellipse to these focal points is $r_i + r_j$. A different transmitter-receiver combination provides a different ellipse on the circumference of which the defect position $\boldsymbol{x}$ is located. Then, multiple transmitter-receiver combinations specify the defect position $\boldsymbol{x}$.

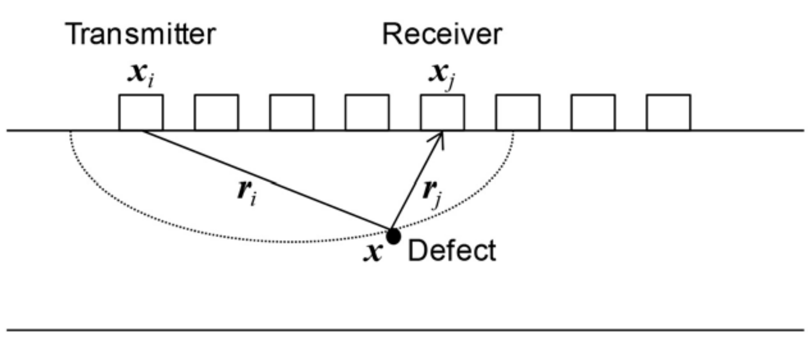

Figure E.8. One Combination of Transmitter and Receiver

Let us denote the ultrasonic signals obtained with the combination of the transmitter at $\boldsymbol{x}_i$ and the receiver at $\boldsymbol{x}_j$ by $u_{ij}(t)$, which is a function of time. Because the signal amplitude becomes large at the time when the ultrasonic wave reflected by the defect arrives at the receiver, $u_{ij}(t_{ij})$ is expected to have a large amplitude. By using the definitions shown above, $u_{ij}(t_{ij})$ can be expressed as

$$u_{ij}(t_{ij}) = u_{ij}\left(\frac{r_i + r_j}{v}\right) = u_{ij}\left(\frac{|\mathbf{x}_i - \mathbf{x}| + |\mathbf{x}_j - \mathbf{x}|}{v}\right).$$

This expression implies that, for an arbitrary position $\boldsymbol{x}$, $u_{ij}(t_{ij})$ has a large amplitude when a defect exists at $\boldsymbol{x}$. To construct an ultrasonic image by SAFT, a data array is prepared to store the accumulation of $u_{ij}(t_{ij})$ for each discrete point $\boldsymbol{x}$ in the target area of a test object. After the ultrasonic signals $u_{ij}(t)$ are acquired by measurement for each i and j, the accumulation $S(\boldsymbol{x})$ is calculated by

$$S(\boldsymbol{x}) = \sum_{i=1}^{N}\sum_{j=1}^{N}\left|u_{ij}\left(\frac{|\boldsymbol{x}_i - \boldsymbol{x}| + |\boldsymbol{x}_j - \boldsymbol{x}|}{v}\right)\right| \quad \text{for each } \boldsymbol{x}\,,$$

where N is the number of the elements of the array transducer. Then, $S(\boldsymbol{x})$ itself provides an ultrasonic image that shows high intensity at the place where a defect may exist.

In the above example, the transducer elements are linearly aligned, but the idea of SAFT can be expanded for an array transducer that has a two-dimensional array of transducer elements to deal with three-dimensional ultrasonic images. That is called three-dimensional SAFT (3D SAFT).

The feature and advantages of 3D SAFT UT technique is shown in Figure E.9 as compared with the principle of usually used UT technique such as conventional angle beam technique and phased array technique (Komura and Furukawa 2010).

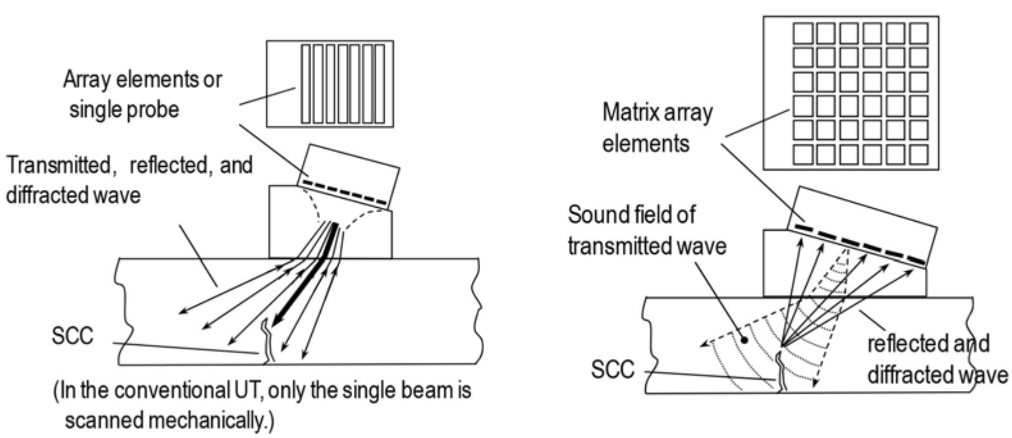

(a) Phased array technique (b) 3D SAFT UT technique

Figure E.9. The Difference of Principle between Phased Array Technique and 3D SAFT UT Technique

In the case of conventional angle beam technique and phased array technique shown in Figure E.9(a), the ultrasonic beam is transmitted to the particular direction, and returned beam from the same direction as to the transmitted direction caused by the reflection and/or diffraction of defects, geometrical and metallurgical discontinuities. The imaging results of inspection show the image which is observed from particular direction of beam transmitted. Then the noise echoes, such as geometrical and metallurgical echo, are displayed in the same way as the defect indication. Therefore it is difficult to discriminate the defect indications from noise echoes. Furthermore it required the probe scanning in order to transmit the UT beam to the exact position of SCC opening and SCC tip, and to acquire the inspection data under the suitable conditions.

In the case of 3D-SAFT UT, on the other hand, UT beam is transmitted by one element of matrix array probe, and reflected or diffracted UT wave from the opening of SCC, face of SCC, and tip of SCC is detected by transmitted element and other all elements of matrix array probe. This action is repeated for transmitting by all matrix array elements. Then the data of (the number of line elements × the number of column elements) are stored in the memory of equipment. These all data are used to the calculation of SAFT processing as shown in Figure E.8, and 3D image within the inspected volume are displayed. By this 3D image data, three 2D images, C-scan/B-scan/D-scan image, are drawn.

In this 3D-SAFT technique, the waveform data which have different beam path by the combination of transmitted element and received element are used for the image calculation. Therefore obtained defect image is the image which is constructed by the data of different view directions. Then, random signals such as metallurgical noises are eliminated each other and SN ratio of true defect is increased. Furthermore this performance of 3D-SAFT is achieved by the inspection without probe scanning. It means the possibility of monitoring the SCC growth at the fixed position.

E.2.2 Equipment

Figure E.10 shows the inspection system used for this measurement. The inspection instrument is Matrixeye™ 256ch manufactured by Toshiba corporation (Karasawa et al. 2009). The ultrasonic transducer consists of 16×16 transducer elements and its nominal frequency is 2 MHz. The wedge combined with the transducer is an angle beam wedge made of polystyrene, and its nominal refraction angle is 45° for longitudinal waves in stainless steel. Table E.2 provides more detailed information.

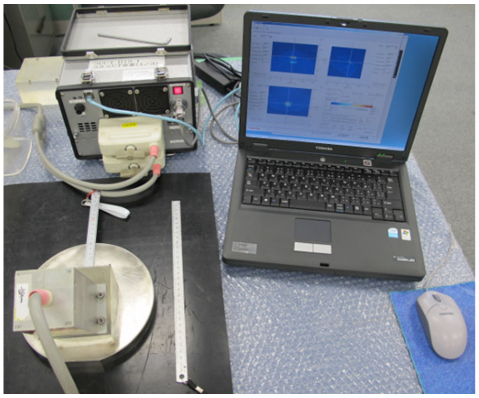

(a) Matrixeye™ 256ch

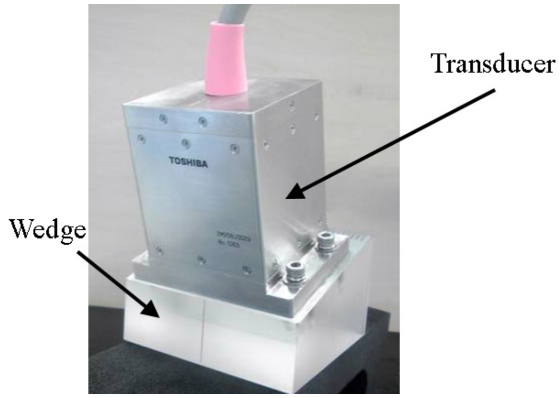

(b) Ultrasonic transducer

Figure E.10. Inspection System

Table E.2. Detailed Information about Inspection System

Item	Description
Testing method	Direct coupling
Couplant	Sonicoat
Frequency	2 MHz
Transducer elements	16×16 (3 mm-pitch)
A/D sampling	30 MHz
Wedge	Polystyrene (2,360 m/s)
Sound velocity of test object	5,750 m/s
Refraction angle (calculated)	45.1°
Gain	30 dB
Averaging	8
T/R pattern	Ttidori-Rall

E.2.3 Data Acquisition

Defects are open on the inner surface of the pipe specimens. The inspections are carried out from the outer surface of the specimens. The transducer is placed in such a way that the incident direction is perpendicular to the longer direction of the defect. The inspection is performed toward both sides of the defect (Figure E.11). Figure E.12 shows how the transducer is actually placed. The contact surface of the wedge is flat for the ENSI blocks, and it is respectively contoured for the pipe specimens to be matched to the specimen surface where the transducer is placed for each case that the incident direction is the axial or circumferential direction.

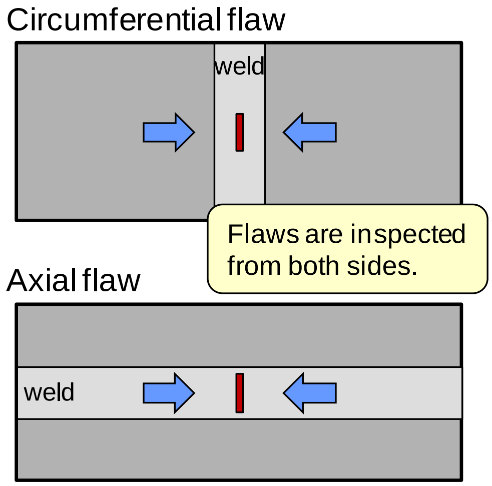

Figure E.11. Inspection Direction

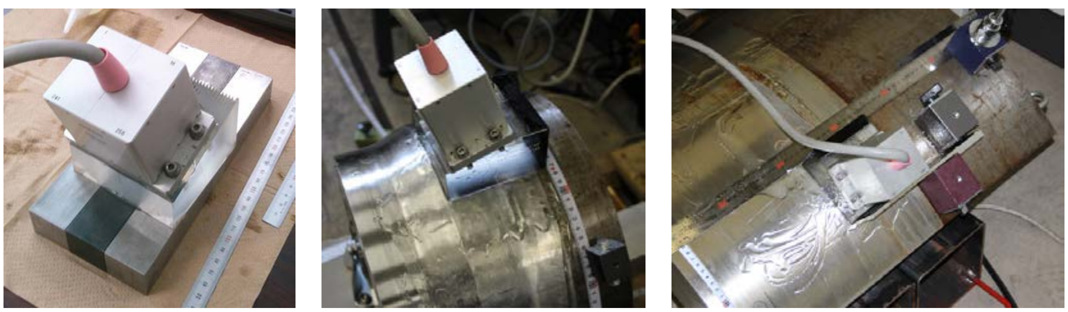

ENSI block   Small bore   Large bore

Figure E.12. Probe Placement

Figure E.13 shows the inspection conditions. The *x*, *y* and *z* coordinates are defined as shown in Figure E.13 (this definition does not always correspond with the coordinates of a specimen). Because the locations and sizes of the defects are disclosed, the transducer is placed as the “central beam axis” bumps on the defect plane (the plane that includes a defect surface such as a crack face) at the distance ℓ from the incident point. Here the “central beam axis” means the central beam axis when all the transducer elements are regarded as one transducer element. After the ultrasonic signals for every transmitter-receiver combination are recorded, three-dimensional SAFT data is generated based on the principle explained in Section E.2.1. The center point of the area where the data is generated is the point at the distance ℓ from the incident point along the center beam axis. The size of the *y*-*z* cross-section of the area is determined by the length *a* in the direction parallel to the central beam axis and the length *b* in the direction perpendicular to the central beam axis. Table E.3 shows the values ℓ, *a* and *b* determined for each specimen. The length of the area in the *x* direction is fixed to 40 mm.

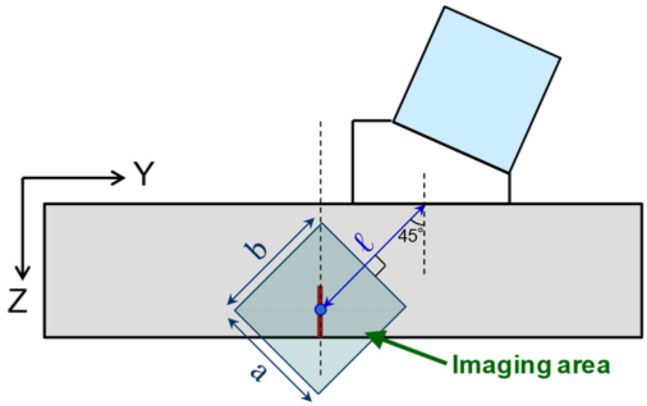

(a) Cross-sectional view

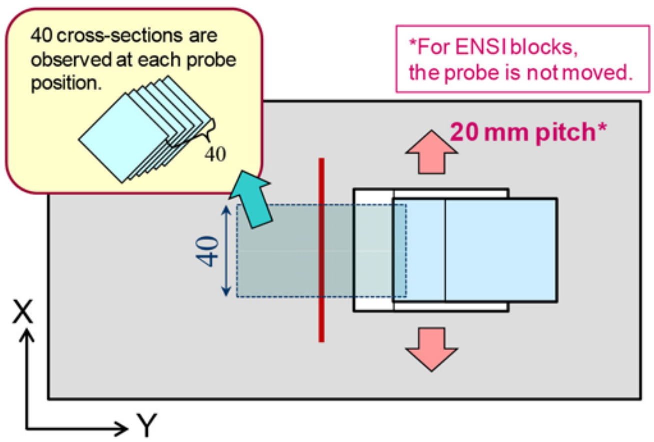

(b) Top view

Figure E.13. Inspection Conditions

Table E.3. Parameters for Imaging Range

	ℓ (mm)	***a* (mm)**	***b* (mm)**
ENSI Block	42.5	45	50
Large bore pipe specimen	80	100	120
Small bore pipe specimen	43	80	70

From the three-dimensional SAFT data, two-dimensional SAFT images are constructed on several cross-sections to examine the inside of the specimen. At one position of the transducer, SAFT images are constructed on 40 *y-z* cross-sections (20 cross-sections on either side of the center section) at 1-mm pitch in the *x* direction. If the SAFT images obtained at one transducer position are insufficient for evaluating a whole defect, the transducer is moved along the longer direction of the defect with a 20-mm pitch, and the SAFT images are obtained at each position. Also, when the images are not clear enough to evaluate a defect, the transducer is moved forward toward the defect to obtain better images.

When an axial defect on a pipe specimen is evaluated, a specimen surface has a curvature in the incident direction as shown in Figure E.14. The transducer is placed with this curvature taken into consideration. However, the *x*, *y* and *z* coordinates of the data acquisition software for this measurement are the same relative to the transducer as the transducer is placed on a flat plate. Because the PARENT protocol prescribes, for the pipe specimens, the *x* and *y* coordinates go along the outer surface of the specimen and the *z* coordinate is perpendicular to the outer surface of the specimen, the prescribed coordinates become inclined with increasing distance from the transducer in the circumferential direction, which causes an error between these two coordinate systems. As a result, although the true *z* direction is perpendicular to the outer surface of a pipe specimen, a defect perpendicular to the outer surface of the pipe specimen is considered to be inclined with respect to the *z* direction of the coordinate system of the data acquisition software when the specimen surface has a curvature in the incident direction. In this case, the *z* component of the defect size is shortened.

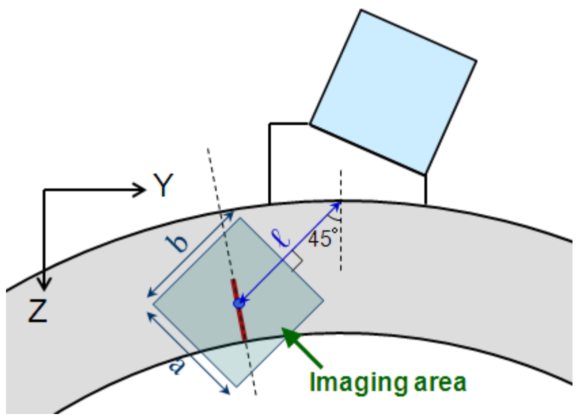

Figure E.14. Inspection Conditions for Axial Defect of Pipe Specimens

Let us consider the error due to the above-mentioned problem. The central angle of the arc between the incident point and the defect plane is given by

$$\theta = \arctan\left(\frac{\ell}{\sqrt{2}\,r_{\mathrm{OD}} - \ell}\right),$$

where ℓ is the distance between the incident point and the defect plane along the center beam axis, and r_{OD} is the outer radius of the pipe specimen. If the true *z* component of the defect size is *d*, the *z* component shown by the data acquisition software is $d \cos\theta$, and then the difference between them is $d\,(1\text{-}\cos\theta)$, which is the percentage of the true *z* component. This percentage is 1% for the large bore pipe specimens and 3.5% for the small bore pipe specimens. In this inspection, this error is less than 1 mm. Therefore, any correction is not made for this error in this inspection.

If bottom echoes are not obtained in the measurement, the bottom surface is assumed to be the level at the depth equal to the pipe wall thickness below the incident point. However, when the inner surface of the specimen has a curvature in the incident direction, the *z* coordinate of the inner surface is not constant along the incident direction in the coordinate system of the data acquisition software. Then, this causes an error if bottom echoes are not obtained in the measurement because the *z* component of the defect size is obtained by the difference of the *z* coordinates between the tip of the defect and the assumed bottom surface. Let r_{ID} be the inner radius of the pipe specimen. The *z* coordinate of the inner surface where the defect is located is lower than that of the assumed bottom surface by the distance r_{ID} $(1\text{-}\cos\theta)$. Therefore, the *z* component of the defect size is shortened due to this gap. In this inspection, any correction is not made for this gap either.

E.2.4 Data Analysis

After the acquisition of the three-dimensional SAFT data, the defect profile is derived from SAFT images. Figure E.15 shows the accumulated images on *x-y* (C-scan), *y-z* (B-scan) and *z-x* (D-scan) planes that are obtained by adding up values of the SAFT data along the direction perpendicular to each plane. In these images, the *z-x* plane corresponds to the defect plane (this coordinate system corresponds to that of a specimen only when the defect extends in the circumferential direction). In the image on the *z-x* plane, the strong indications a little below the center are induced by the corner echoes, and the weak indications that shape the elliptical outline above the center are formed by the defect tip echoes.

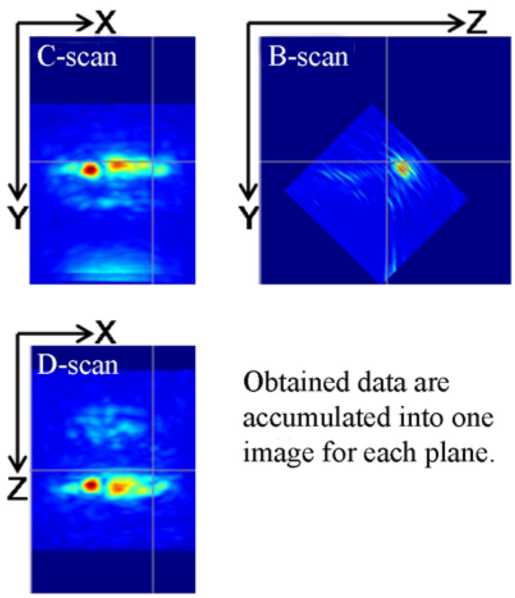

Figure E.15. Accumulated Images Obtained by Merging SAFT Images (when the defect extends in the circumferential direction)

Figure E.16 shows the derivation of defect profile. The left image of Figure E.16 is obtained by binarizing the accumulated image on the *z-x* plane with the noise level used as the threshold. The noise level is determined from a set of the SAFT images. This binarized image represents the defect shape. The SAFT images on the *y-z* plane are closely examined one by one to locate the tip and corner echo positions as coordinate values, which results in the right graph in Figure E.16. In this process, a significant indication is distinguished from a strong noise by considering the positional relation between the corner indications and the tip indications, the continuity of indications, and the tendency for indications to follow the movement of the transducer. The defect depth and length are determined from these results. In this data analysis, an indication that cannot be characterized as a noise on systematic criteria is evaluated as a significant indication even if that indication obviously seems to be a noise because its positional relation is unlikely for a defect.

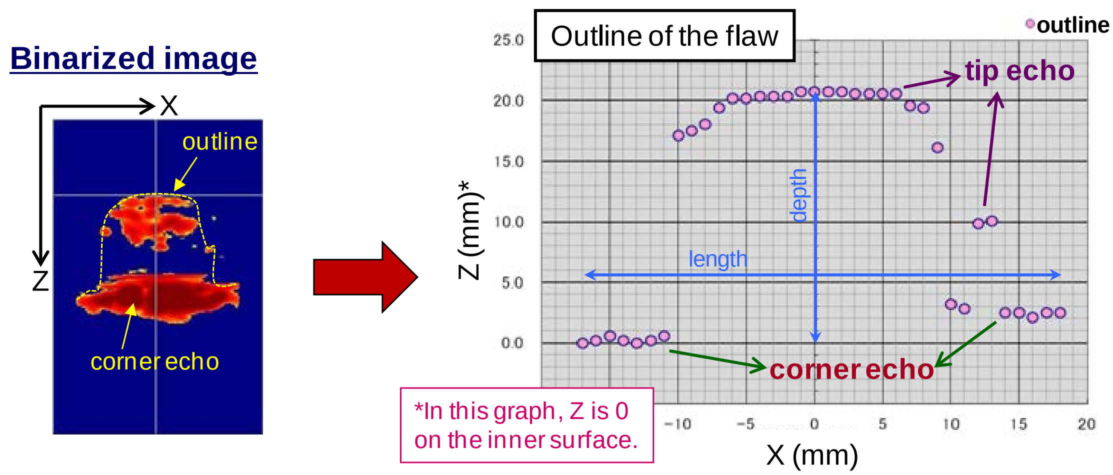

Figure E.16. Derivation of Defect Profile

If strong indications are found around the bottom surface just below defect tip indications, that defect is considered as a surface-breaking defect. The point of the peak value in the indications around the bottom surface is taken as the representative point of the bottom surface. A point in the tip indications is selected as the defect apex in such a way that the distance in the *z* direction between this point and the representative point of the bottom surface is maximized. The depth of a defect is defined by this distance in the *z* direction. When indications are not obtained around the bottom surface and only tip indications are obtained, the bottom surface is determined as the level at the depth equal to the pipe wall thickness below the incident point.

To obtain the defect length, each end of a defect is determined as the point where the amplitude of an indication around the bottom surface becomes less than the noise level. When indications spread over a wide range around the bottom surface and it is difficult to determine the ends of the indications, the point where the distance from the bottom surface first becomes less than 1 mm is taken as an end of the defect. When no indication is found around the bottom surface, it is decided that the defect length cannot be obtained.

On a data sheet of the round robin test, the position and the dimensions of a defect is reported as the *x*, *y* and *z* coordinates that describe a defect area, which is the smallest cuboid that can contain the defect. When a defect area is set up from a measurement result, a defect area is considered as a two-dimensional rectangular area perpendicular to the *x*-*y* plane, parallel to the longer direction of the defect and including the defect apex. The edges of the defect area are determined by the defect apex and both ends of the defect.

As mentioned in Section E.2.3, a defect is inspected from both sides of the defect. To report the *x*, *y* and *z* coordinates of a defect area, the measurement results for both sides of the defect should be combined. From the two measurement results, two defect areas are obtained for each defect. If the perpendicular distance between the two defect areas is less than or equal to 10 mm, the conclusive defect area is reported as the smallest cuboid that contains the two defect areas. If the perpendicular distance is greater than 10 mm but the tip indications of these measurement results intersect with each other, the two defect areas are treated as one conclusive defect area and its range in the direction perpendicular to the two defect areas is made ±5 mm from the middle point of the two defect areas. Besides, if the above-mentioned conditions are not satisfied but any special reason is found such as profile symmetry of both sides and correlation of the distributions of indications, the conclusive defect area is reported in the same manner as the above second case. In the other cases, the two defect areas are considered to be caused by independent defects and each area is individually reported as a conclusive defect area.

E.2.5 Team's Assessment of the Technique Based on the Round Robin Test Results

Whereas phased array ultrasonic testing has a low accuracy for crack depth sizing at a steep slope of the crack profile, 3D SAFT can obtain the overall profile of the crack and an accurate depth estimate even at such a steep part.

Although the specimens P1 and P37 include internal cracks, it is difficult to catch an indication of the lower end of an internal crack because strong indications around the bottom surface obscure weak indications due to the lower end of an internal crack. Therefore, it had to be considered that the lower end of an internal crack reaches the bottom surface.

In this round robin test, since the defects exists in the nickel-based alloy welds and several specimens have about 80 mm-thick walls, ultrasonic testing results are subject to strong attenuation. 3D SAFT has difficulty generating high-amplitude ultrasonic waves and sometimes cannot even detect a defect because 3D SAFT uses a transducer that consists of many small transducer elements. Therefore, the results show low detectability of the defects especially for measuring the axial defects, which require ultrasonic waves to travel a long distance inside weld metal. Meanwhile, 3D SAFT obtained the approximate profiles of the detected defects and can be expected to estimate the profile of a defect in a nickel-based alloy weld unless ultrasonic attenuation causes a significant problem. Although the results of the defect profile estimation cannot be evaluated for lack of the information of the true profiles, most of the sizing errors are acceptable and it is considered that 3D SAFT provided reliable defect profile estimation.

E.3 Subharmonic Phased Array for Crack Evaluation, Technique ID 6-SHPA1, 6-SHPA2, 6-SHPA3, 6-SHPA4

E.3.1 Overview

Crack can be detected by ultrasound if cracks are open, since ultrasound is strongly scattered by the crack. However, if cracks are closed because of compressive residual stress and/or the oxide films generated between crack faces, ultrasonic inspection can cause the underestimation or nondetection of cracks since ultrasound penetrates through the closed crack. To detect and measure defects, a crack imaging method, subharmonic phased array for crack evaluation (SPACE) was used. SPACE is on the basis of the subharmonic generation by short-burst waves and the phased array algorithm with frequency filtering. There are two types of SPACE. One is SAW SPACE which uses surface acoustic wave (SAW), where the array transducer is positioned on the crack opening side through a wedge designed to generate SAW. SAW SPACE is used to detect defects and measure their lengths. The other one is Bulk SPACE which uses bulk longitudinal wave, where the array transducer is positioned on the opposite of crack opening side. Bulk SPACE is used to measure the depths of defects.

E.3.2 Principle

The schematic of SAW SPACE is shown in Figure E.17. SAW SPACE uses a surface acoustic wave (SAW). A PZT array transducer with a wedge was used to generate intense ultrasound by focusing. The phased array equipment is MultiX LF (produced by M2M). Each element of the PZT array transducer was excited by a three-cycle burst of a frequency of 3.5 MHz with 150 V following a delay law for transmission focusing. The scatterings of fundamental and subharmonic waves occur at the open and closed parts of defects, respectively. The scattered waves received by the PZT array transducer are analog-to-digital converted. Subsequently, they are digitally filtered at fundamental and subharmonic frequencies, where the sampling frequency was 50 MS/s. After their phased shift following the delay law for reception focusing, they are summed. Finally, the root-mean-square (RMS) value is calculated as the intensity at a focal point. This process is repeated over a scan area with a step to create images. The image is created in sequence for each transmission focal point. The images for all transmission focal points can be merged. The fundamental array (FA) and subharmonic array (SA) images obtained can indicate the open and closed parts of cracks, respectively.

The schematic of Bulk SPACE is shown in Figure E.18. A PZT array transducer was used to generate and receive ultrasound by focusing. The phased array equipment are MultiX LF (produced by M2M) and PAL (produced by KrautKramer). Each element of the PZT array transducer was excited by a three-cycle burst with 150 V following a delay law for transmission focusing. We selected the input frequency of 2 MHz, 5 MHz, and 7 MHz, depending on specimens. The scattering of fundamental and subharmonic waves occur at the open and closed parts of defects, respectively. The scattered waves received by the PZT array transducer are analog-to-digital converted. Subsequently, they are digitally filtered at fundamental and subharmonic frequencies. After their phased shift following the delay law for reception focusing, they are summed. Finally, the root-mean-square (RMS) value is calculated as the intensity at a focal point. This process is repeated over a scan area with a step to create images. The image is created in sequence for each transmission focal point. The images for all transmission focal points can be merged. The FA and SA images obtained can indicate the open and closed parts of cracks, respectively.

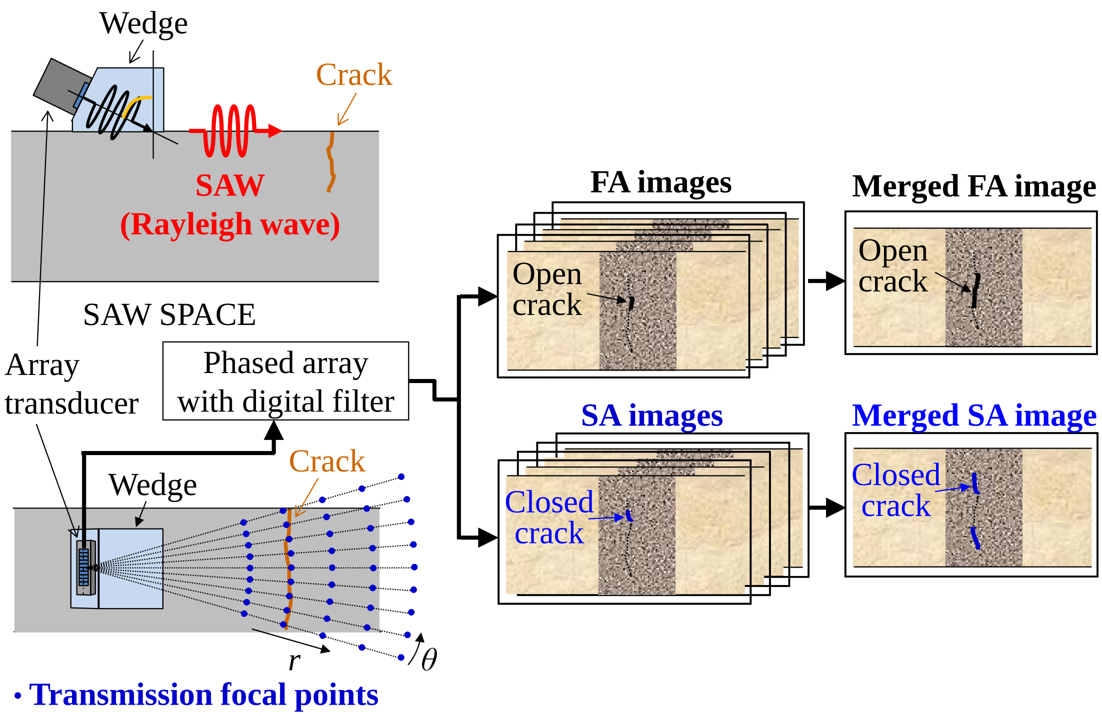

Figure E.17. Schematic of SAW SPACE

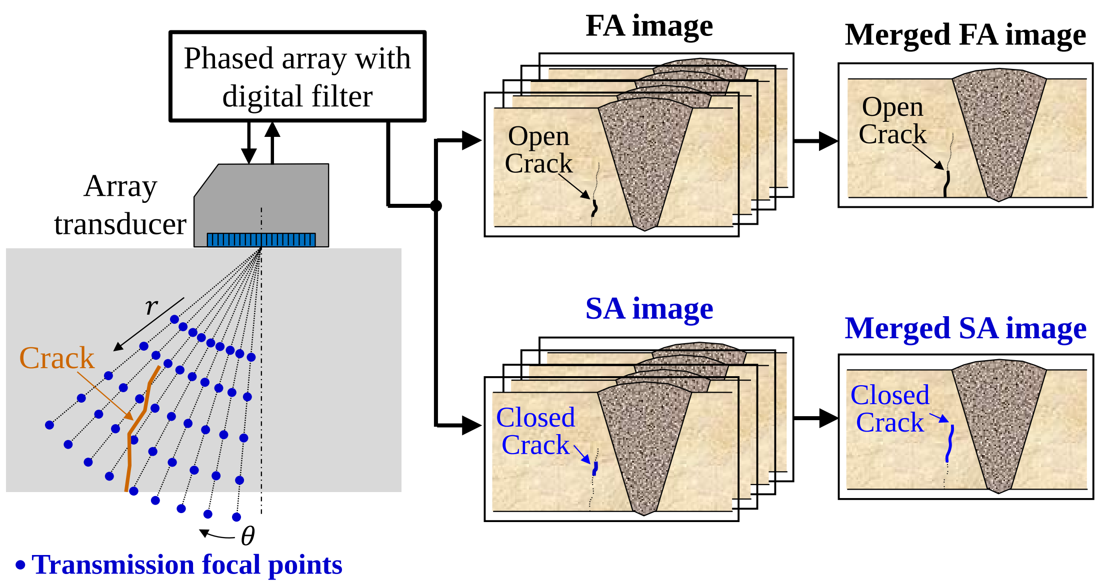

Figure E.18. Schematic of Bulk SPACE

E.3.3 Procedure and Technique

We selected four techniques, which are SHPA01, SHPA02, SHPA03, and SHPA04 as follows:

- [SHPA0]
  - FA image (5 MHz) of Bulk SPACE
  - Phased array apparatus: PAL produced by KrautKramer
  - Probe: PZT array transducer (5 MHz, 32 el, 0.5 mm pitch, 10 mm width) produced by Imasonic
  - Input frequency: 5 MHz
  - Input voltage: 100 V
  - Scanning condition:
    - Focus on transmission: depth=15 mm–45 mm (3.5-mm step), θ=10° ~60° (1° step)
    - Focus on reception: depth=15 mm–45 mm (3.5-mm step), θ=10° ~60° (1° step)
- [SHPA1]
  - FA image (2 MHz) of Bulk SPACE
  - Phased array hardware: PAL (produced by KrautKramer)
  - Probe: PZT array transducer (2 MHz, 32 el, 0.5 mm pitch, 10 mm width) produced by JapanProbe
  - Input frequency: 2 MHz
  - Input voltage: 100 V
  - Scanning condition:
    - Focus on transmission: depth=15 mm–45 mm (3.5-mm step), θ=10° ~60° (1° step)
    - Focus on reception: depth=15 mm–45 mm (3.5-mm step), θ=10° ~60° (1° step)
- [SHPA2]
  - SA image (3.5 MHz) of Bulk SPACE (f/2)
  - Phased Array Hardware: MultiX-LF produced by M2M
  - Probe: PZT array transducer (5 MHz, 32 el, 0.5 mm pitch, 10 mm width) produced by Imasonic
  - Input frequency: 7 MHz
  - Input voltage: 150 V
  - Scanning condition:
    - Focus on transmission: r=14 mm–42 mm (7-mm step), θ=6°–65° (1° step)
    - Focus on reception: 0.5-mm step

- [SHPA3]
  - FA image (3.5 MHz) of SAW SPACE
  - Phased array hardware: MultiX-LF produced by M2M
  - Probe: PZT Array transducer (5 MHz, 32 el, 0.5 mm pitch, 10 mm width) produced by Imasonic
  - Input frequency: 3.5 MHz
  - Input voltage: 100 V
  - Scanning condition:
    - Focus on transmission: r=39.5 mm, θ=−14°~15° (1° step)
    - Focus on reception: r=39.5 mm, θ=−14°~15° (1° step)

E.3.4 Self Assessment of the Technique Based on the Round Robin Test Results

In this measurement, we used flat PZT array transducer because the curvature of the specimen is not so large. On the other hand, our techniques can be applied to specimens with a large curvature by using flexible array transducer or a shoe conformable to the curvature with a delay law under the consideration of curvature.

Specimens P1, P4, P28-P32 were measured by subharmonic phased array for crack evaluation (SPACE). As a result, most cracks were visualized in FA images, suggesting that they were open. On the other hand, hipped EDM (P4, Nos. 1 and 2) were visualized in SA images, suggesting that they were closed. Thus, it was proved that SPACE was capable to detect all the cracks of each specimen, and to measure their lengths and depths. In addition, the importance of the subharmonic waves with lower frequency than the incident wave was verified to detect and measure closed defects in highly attenuating objects with coarse grains or textures.

E.4 Large Amplitude Excitation Subharmonic UT, Technique ID 18-LASH1, 18-LASH2

E.4.1 Overview of LASH Technique

LASH (Large Amplitude Subharmonic) technique develops to combine with a SPACE measurement system as shown in Figure E.19. When larger amplitude ultrasound is incident to the crack subharmonic wave sometime generate at the crack. For the imaging of these subharmonic images, commercial phased array system is applied using aperture synthesis processing and additional digital filter. However amplitude of transmitted ultrasound is limited because larger voltage burst wave of SPACE will be damage to the usual transducers. Thus, LASH technique is expected to break this limitation of SPACE in industrial inspection.

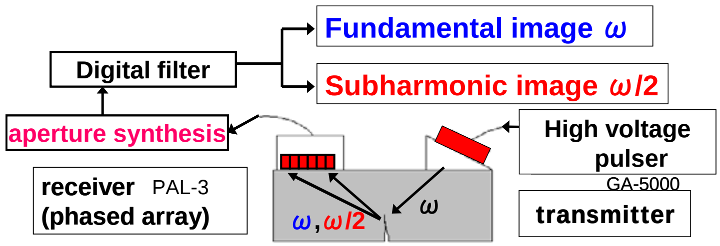

Figure E.19. Schematic Diagram of Basic SPACE System

The schematic diagram of LASH (Lager amplitude SPACE) system is shown in Figure E.20. Only the ultrasonic transmission components were improved from usual SPACE. We must be focus whether the LASH system has an advantage in crack tip echo identification of low S/N ratio for conventional SPACE system or not.

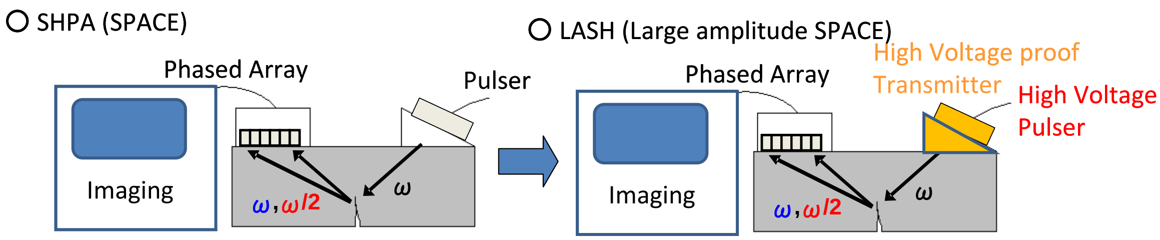

Figure E.20. Schematic Diagram of Improved LASH System

For the high voltage excitation of SPACE without any damage in transducer, the structure of transducer must improve to proof up to 2000 V excitation as shown in Figure E.21. Since the fabricated temperature of process is 600 ℃ which is higher than the Curie point of the PZT, re-polarization process with the DC voltage of 1000 V/mm during 30 minutes at 200 ℃ in silicon oil bath is applied after the fabrication of the transducer. We have developed two techniques of high voltage pulser (include the transformer coil system) and laminated transducer system as the LASH techniques. In this study high voltage pulser up to 1000V excitation was used for the large amplitude ultrasound transmission. We call tech ID 18-0 for 400 V excitation LASH measurement system which is as same excitation voltage as conventional SPACE measurement, and tech ID 18-1 for high voltage excitation LASH measurement system.

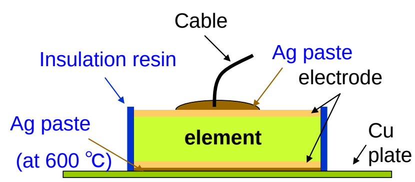

Figure E.21. Improvement for High Voltage Transducer

In comparison of the spatial resolution with conventional inspection imaging and the SPACE, our SPACE system applied here is a laboratory system which used 32 element phased array and 8 bit RF signals for subharmonic imaging by aperture synthesis improving the old commercial phased array system. Therefore, obtained images may be inferior to the one by modern phased array systems (e.g., 128 element and 10 bit) in measurement sensitivity or in spatial resolution. However the most important point here is whether the SPACE technique has an advantage in crack tip echo identification or not in case that the estimated crack tip show lower S/N ratio in conventional inspections. If the advantage of SPACE can be found for even some of the cracks, higher resolution and sensitivity can be improved by replacing the old phased array system of present SPACE to the modern commercial phased array system in future.

E.4.2 Inspection Procedures for Open Specimens

Since all the positions of cracks in each our measurement specimens were open, we positioned the transducers to given crack positions and only the detectability of crack tips were investigated using LASH. In these measurements, single B-scope was measured by aperture synthesis procedures with LASH system.

Furthermore only for the cracks in which crack tips can be clearly observed in subharmonic B-scope images, three dimensional B-scope images were measured using the encoder system with 1.3 mm pitch as shown in Figure E.22 to estimate of the three dimensional crack shape. Reconstruction of the three dimensional B-Scope images was made at the parallel positions along the weld line. Since this scanning equipment with encoder also fabricated for laboratory use, fairly good image can be obtained for flat surface specimen of P-28 ～ P-32, however significant measurement can't be made for large curved surface specimens of P-1 and P-12. Thus, B-scan image at the center position of each given crack position was measured as a standard inspection data and a three dimension image with encoder system obtained as an optional one in this report.

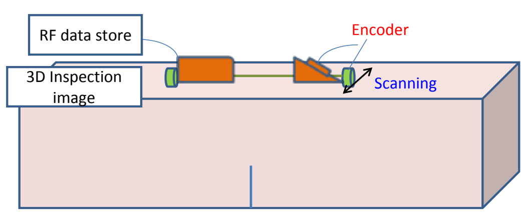

Figure E.22. Three Dimensional Inspection with Encoder

E.4.3 Experimental Results

E.4.3.1 Small Flat Specimen

Representative B-scan images at the center of given crack position of P28 specimen were shown in Figure E.23. Left image was a fundamental 5 MHz image (correspond to conventional inspection of linear ultrasound) and right one was a subharmonic 2.5MHz image. Red line shows a position of a back surface and black dot line shows a crack tip from the given crack position.

B-scan images for specimen P30, P31 and P32 were shown in Figures E.24–E.26. All the images were obtained by 1000 V excitation which expected to obtained the highest S/N ratio of crack tip echo comparing to the one by standard 400 V excitation of conventional SPACE.

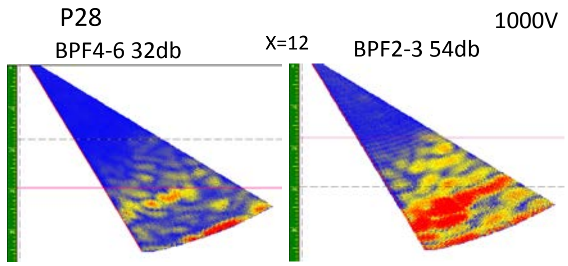

Figure E.23. B-Scope Image of P28 Specimen

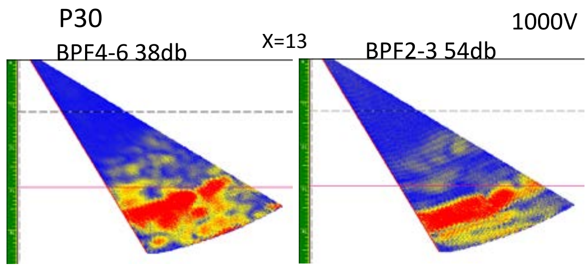

Figure E.24. B-Scope Image of P30 Specimen

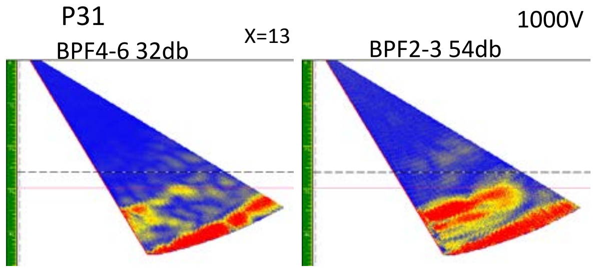

Figure E.25. B-Scope Image of P31 Specimen

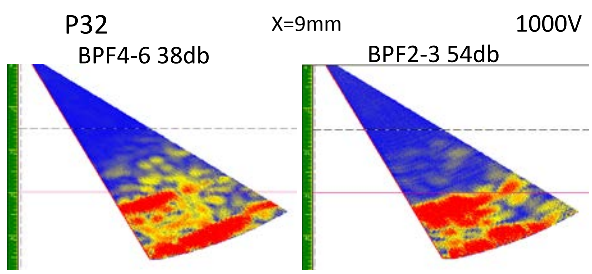

Figure E.26. B-Scope Image of P32 Specimen

Measurement condition of amplitude and applied band path filter for each imaging were described in top of each figure. All the obtained images of specimen P28, P30, P31 and P32 show low S/N ratio in crack tip echo detection due to the large backscattering from microstructure around the welding area. Only in P28 image in Figure E.23, crack tip could be detected especially in right subharmonic image. However in all the specimens crack tip cannot be clearly detected both by linear and nonlinear ultrasound measurement.

B-scan images for specimen of P29 for the excited voltage of 400V, 700V and 1000V were shown in Figure E.27(a), (b), (c).

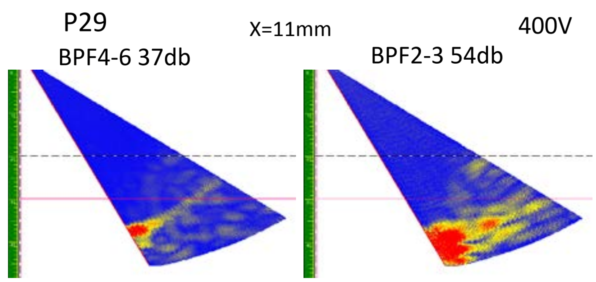

(a) 400V Excitation

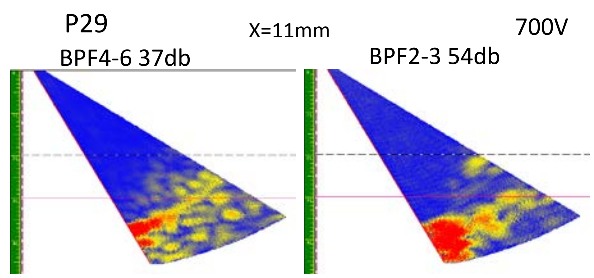

(b) 700V Excitation

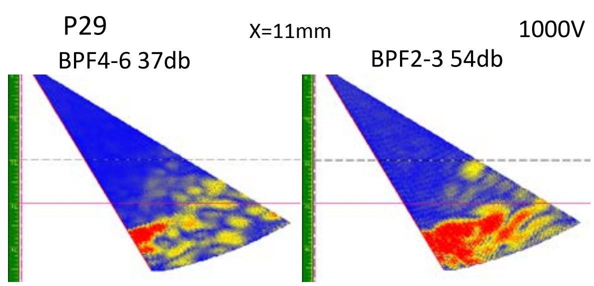

(c) 1000V Excitation

Figure E.27. B-Scope Image of P29 Specimen

Comparing with the fundamental left images, crack tip echo could be obtained clearly in subharmonic right images for all excitation voltage and S/N ratio and the detectability of crack tip echo were increasing according to the excitation voltage. In fundamental linear images of left one, any crack tip echoes could not be detected due to large backscattering noise. For the detection of the crack tip in P29 specimen, thus, especially LASH technique was extremely effective. Since we can clearly detect the crack tip echo for P28 and P29 specimens, three dimensional imaging procedures using encoder were applied. Sample of the results were shown in Figure E.28. Upper one was 3D view and lower one was cross-section view. Left one was fundamental images and right one was subharmoinic images.

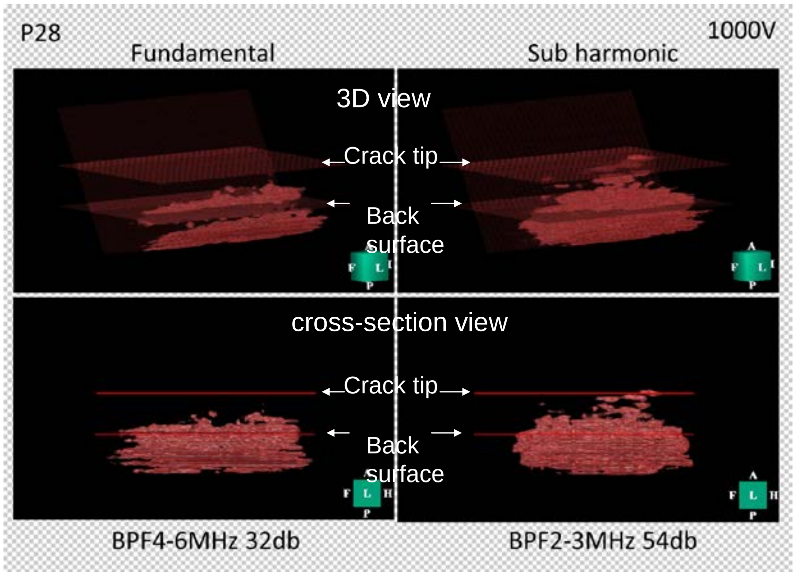

Figure E.28. Three-D View and Cross-section View of P29 Specimen with 1000V Excitation

Hatchings in 3D images were the given positions of crack tip and back surface. Though we show the 3D images only for the specimens P28 andP-29 in this report, significant crack tip could not be obtained because of large scattering noise in other 3D images for other specimens.

E.4.3.2 Large Specimens

Though we tried to detect the cracks of BMI specimens, the curved specimen surface and large thickness of the specimen did not match our measurement setup because our system had been developed in laboratory use for a flat and small specimen.

Representative B-scan images at the center of the given position of SCC in P12 specimen with 1000V excitation were shown in Figure E.29.

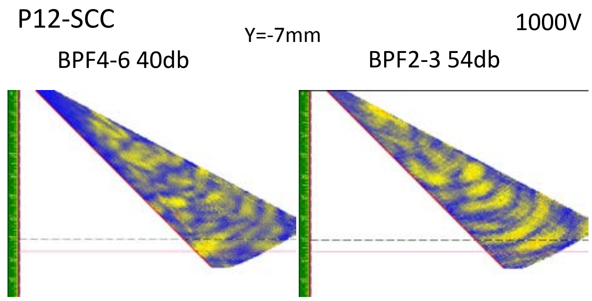

Figure E.29. B-Scope Image of SCC in P12 Specimen

Both in left fundamental image and right subharmonic image, crack tip cannot be detected due to the extremely large scattering noise. This might be caused by the bad couplant condition due to the curved surface and to the large thickness of the specimen P12. For the comparison, B-scan images of EDM notch in specimen P12 with 1000V excitation with no filter were shown in Figure E.30.

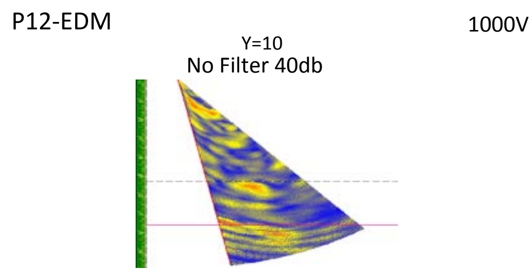

Figure E.30. B-Scope Image of EDM Notch in P12 Specimen

Though EDM notch tip could be recognized at the given position of dotted line due to the large amplitude of tip echo, extremely large scattering echoes were also observed. B-scan images of flaws 1, 3, 4 in specimen P1 are shown in Figure E.31(a), (b), (c). All the images were obtained by 1000 V excitation which expected as higher S/N ratio of flaw tip echo.

Since the thickness of the specimen P1 was thinner than specimen P12, scattering noises from microstructures were lower than one of P12 specimen. However, both in left fundamental image and right subharmonic image, crack tip echo cannot be detected for the flaw-1, 3, 4. B-scan images of flaw 2 in specimen P1 with the excited voltage of 400V, 700V and 1000V are shown in Figure E.32(a), (b), (c).

Since Flaw-2 show lower scattering noise than one of other flaws, crack tip echo might be detected extremely in higher voltage subharmonic images using LASH technique. However S/N ratio of flaw tip echo was not enough and further improvement of the measurement setup especially for curved surface specimen will be expected.

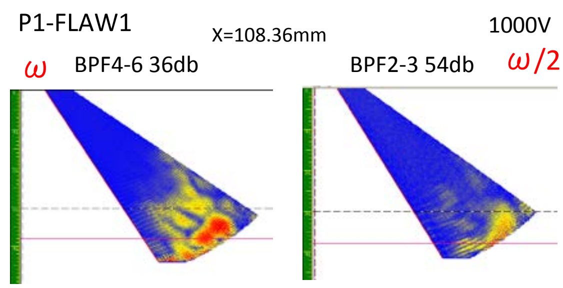

(a) Flaw 1

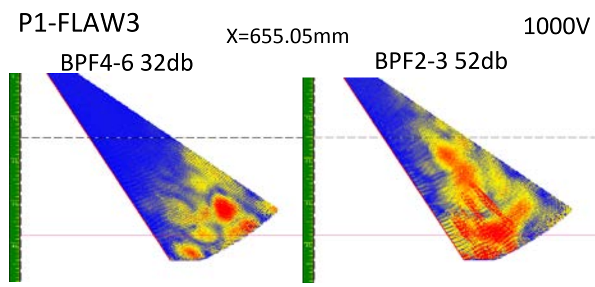

(b) Flaw 3

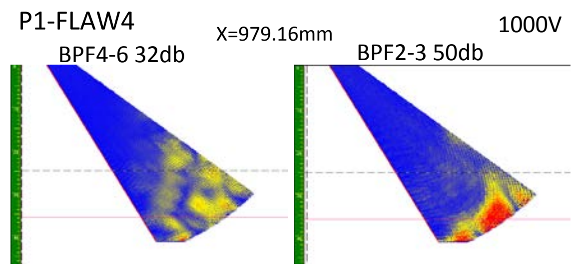

(c) Flaw 4

Figure E.31. B-Scope Images of Flaws in P1 Specimen

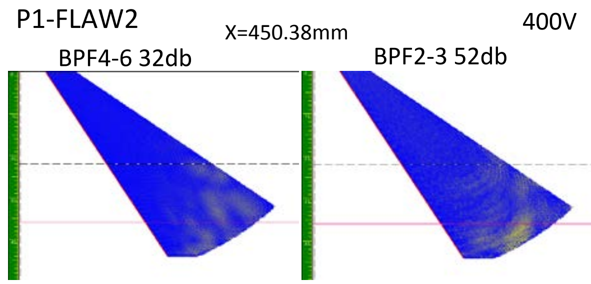

(a) 400V Excitation

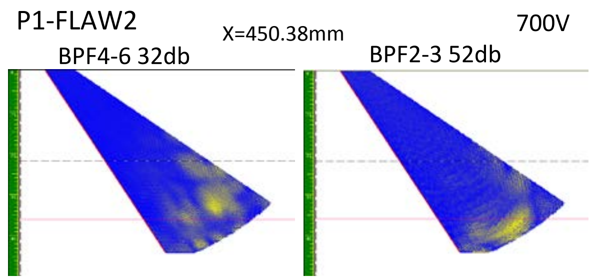

(b) 700V Excitation

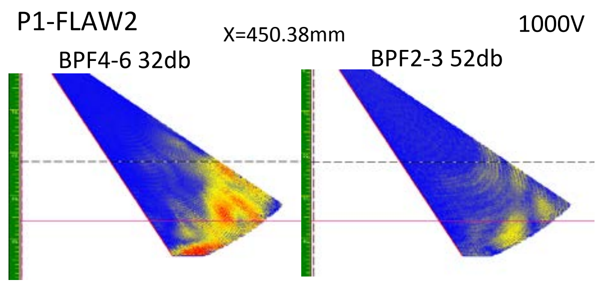

(c) 1000V Excitation

Figure E.32. B-Scope Images of Flaw 2 in P1 Specimen

E.4.4 Assessment of LASH Technique for the Round Robin Test

We applied LASH techniques with high voltage SPACE of nonlinear imaging inspection system up to 1000 V excitation to the five small and two large DMW specimens and obtained following conclusions.

1. About the crack in small specimen P-28, 29 and the Flaw-2 in large specimen, LASH technique up to 1000V was effective for the detection of the flaw tip echo comparing with the conventional linear ultrasound technique and conventional SPACE technique.
2. However an improvement of the measurement setup especially for couplant to curved surface specimen will be required. Larger amplitude ultrasonic incident and the improvement of the S/N ratio in subharmonic inspection image will also be required.

E.5 Higher Harmonic UT, Technique ID 27-HHUT1, 27-HHUT2, 27-HHUT3

E.5.1 Overview

Higher harmonic ultrasonic testing (HHUT) detects waveform distortion of the ultrasonic waves scattered at cracks or SCC in comparison with the incident sinusoidal tone-burst wave as higher harmonic amplitudes. Different from the conventional UT based on the acoustic impedance difference, HHUT is free from the grain boundary scattering noise, therefore it can detect closed cracks and SCC with high S/N ratio.

We apply an immersion higher harmonic imaging technique (HHIT) for detecting cracks and SCC.

E.5.2 Principle of Higher Harmonic UT and Higher Harmonic Imaging

E.5.2.1 Waveform Distortion and Harmonic Generation

Ultrasonic propagation across cracks and SCC in metals could be modeled as shown in Figure E.33. The cracked face has high stiffness for compressive stress, however, it has far lower stiffness in tensile stress. When a sine burst wave is sent for a cracked face, the transmitted wave across the face is severely deformed. The fast Fourier transformation (FFT) of the transmitted wave has many higher harmonics in frequency domain as shown in Figure E.34. By using an analog high pass filter with appropriate cut-off frequency, we could extract desired higher harmonics.

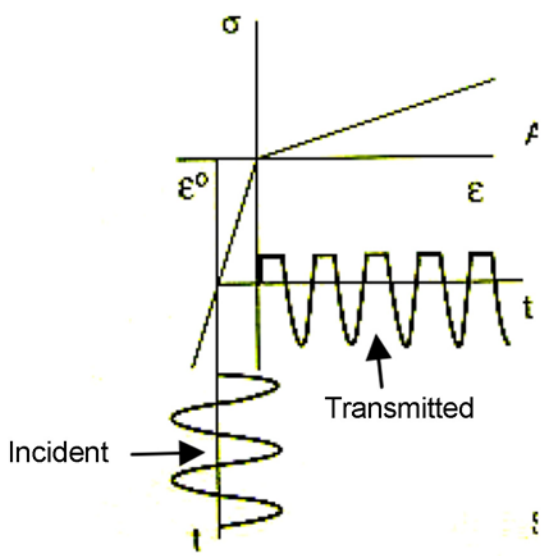

Figure E.33. Waveform Distortion of the Incident Sine Wave at Crack Face

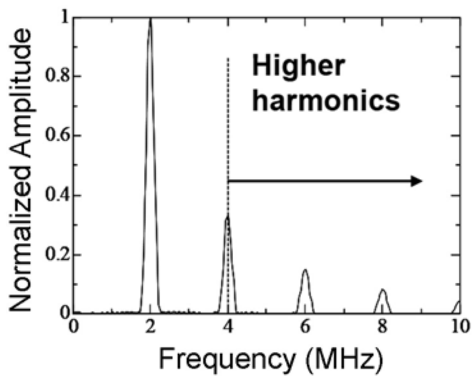

Figure E.34. Extraction of Higher Harmonics Using Analog High Pass Filter

E.5.2.2 Immersion Higher Harmonic Imaging of Cracks and SCCs

The higher harmonic imaging system is composed of a sine burst wave pulser, a focused transducer, an in-plane scanning unit, analog high pass filters, an A/D wave memory and imaging software. The burst wave pulser, RITEC RPR-4000, transmits high power sinusoidal wave with low noise of harmonics. The higher harmonic waveforms scattered at cracks or SCC are extracted by using the analog high pass filter and stored in the wave memory and the harmonic amplitude is mapped on X-Y plane.

The main units of the imaging system are shown in Figures E.35–E.37. For angular incidence, the transducer is mounted on the attachment shown in E.37.

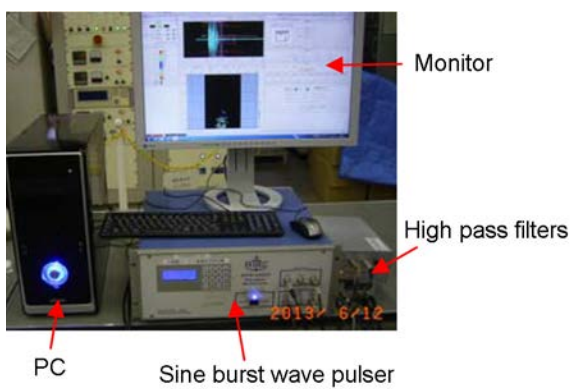

Figure E.35. Higher Harmonic Imaging System

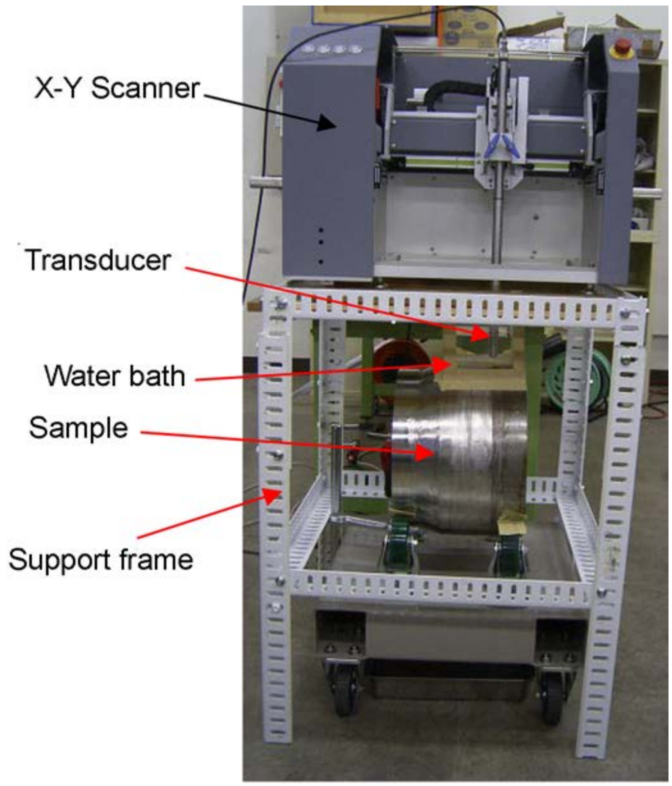

Figure E.36. Measurement Setup for Normal Incidence

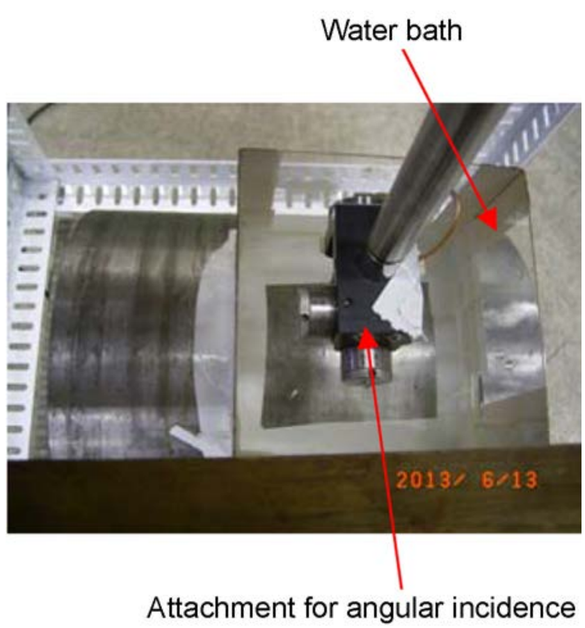

Figure E.37. Measurement Setup for Angular Incidence

Examples images of crack or SCC are shown in Figures E.38 and E.39. These images are constructed by using imaging software of InsightScan and InsightAnalysis. The C-scan images in Figures E.38 and E.39 are the best images of crack or SCC corresponding to the slice gates shown in Figure E.40.

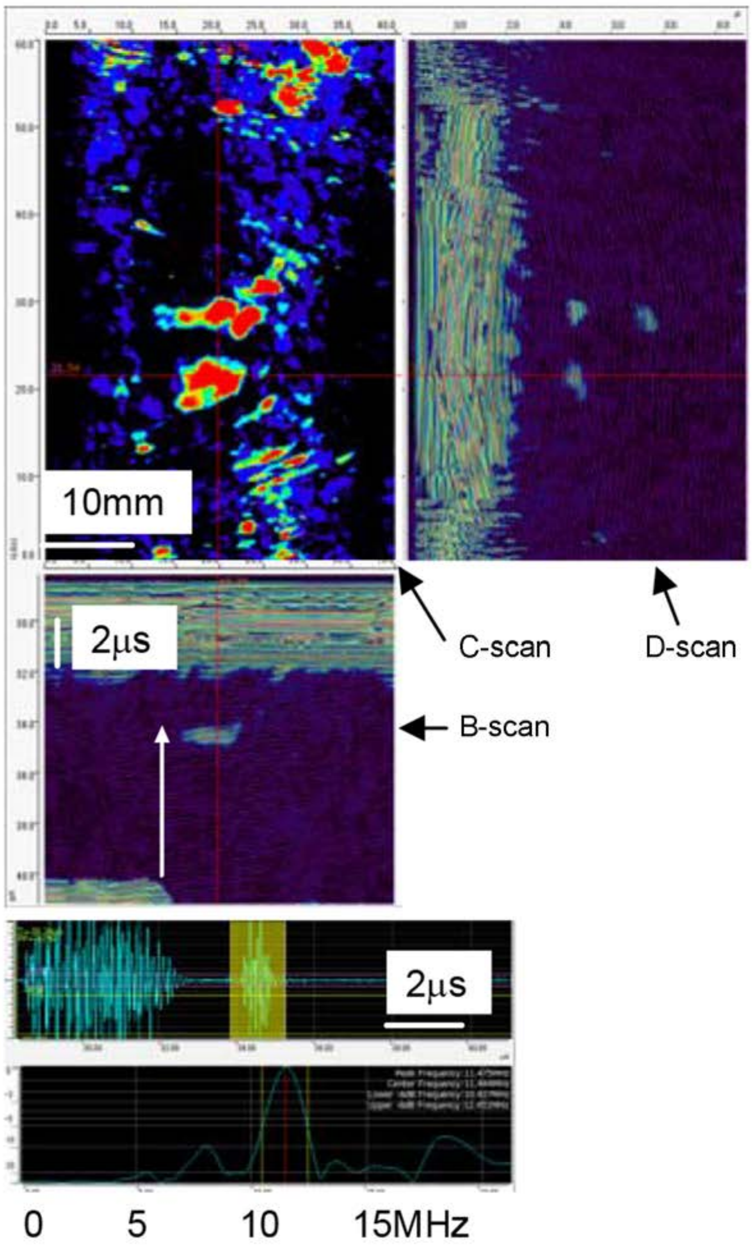

Figure E.38. Example of C-, B-, and D-scan Images, Waveforms and FFT of Normal Incidence

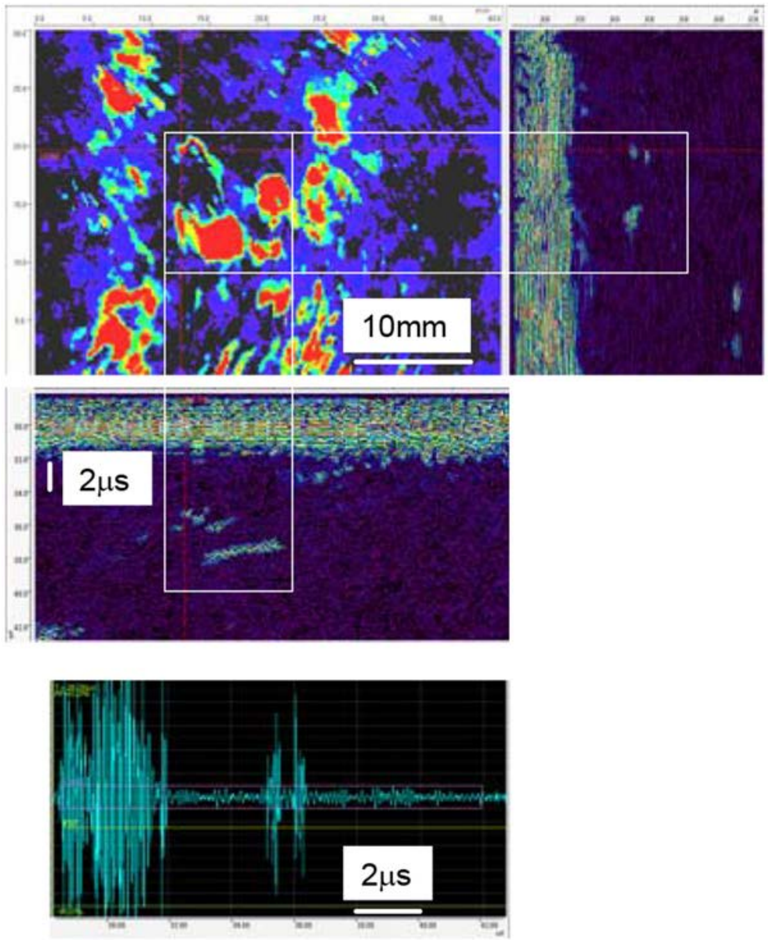

Figure E.39. Example of C-, B-, and D-scan Images and Waveforms of Angular Incidence

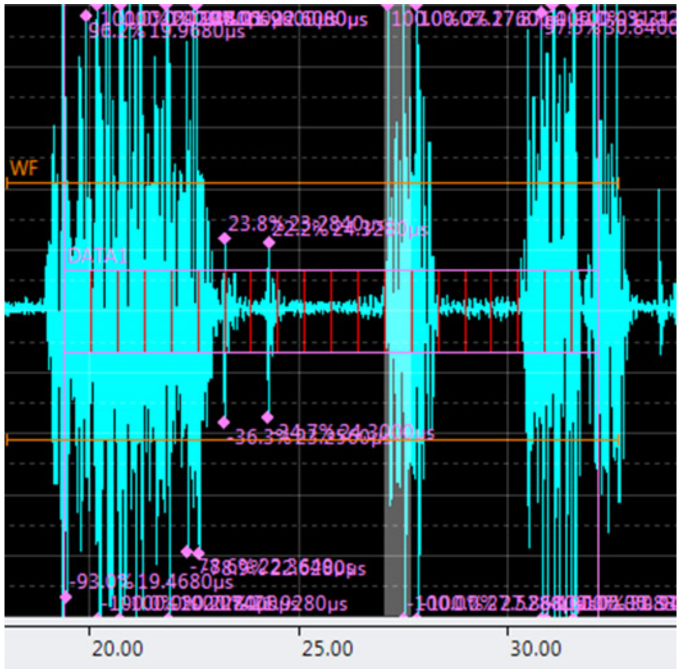

Figure E.40. Slice of Gates for C-scan

The B- and D-scan images show the horizontal and vertical cross-section along the horizontal and vertical red line in the C-scan image. The waveform at the cross point of the horizontal and vertical red lines is shown.

In this in-plane X-Y scanning, as shown in Figure E.41, the ultrasonic beam is deflected away from the focus depending on the incident point. Thus the length of circumferential crack or SCC is underestimated.

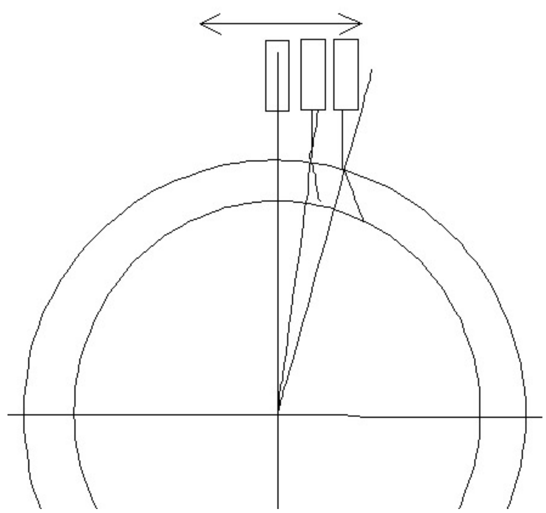

Figure E.41. Beam Deflection by In-plane Scanning

E.5.3 Inspection Technique by Normal Incidence

E.5.3.1 Setting

- Transducer: Frequency 5 MHz, Focal length 76 mm, element diameter 9.6 mm
- Transmission: 4 MHz, 3 cycle, 240V
- High-pass filter: 8 MHz
- Receiver gain: around 54 dB with 8 MHz high-pass filter
- Angle of incidence: 0 (normal)

E.5.3.2 Imaging

- Scan pitch 0.25 mm (X, Y)
- Slice gate for C-scan (20 division)
- Scanning velocity : 20-30 mm/s
- Display: C, B & D
- Imaging higher harmonic: 3rd harmonic (12 MHz)

E.5.3.3 Calibration

- No calibration because of no suitable calibration blocks for HHUT.

E.5.4 Inspection Technique by 5-degree Angular Incidence

E.5.4.1 Setting

- Transducer: Frequency 5 MHz, Focal length 76 mm, element diameter 9.6 mm
- Transmission: 4 MHz, 3 cycle, 240V
- High-pass filter: 8 MHz
- Receiver gain: around 54 dB with 8 MHz high-pass filter
- Angle of incidence: 5 degree for cylinders.

E.5.4.2 Imaging

- Scan pitch 0.25 mm (X, Y)
- Slice gate for C-scan (20 division)
- Scanning velocity : 20-30 mm/s
- Display: C, B & D
- Imaging higher harmonic: 3rd harmonic (12 MHz)

E.5.4.3 Calibration

- No calibration because of no suitable calibration blocks for HHUT.

E.5.5 Inspection Technique by 2-degree Angular Incidence for Rectangular Blocks

E.5.5.1 Setting

- Transducer: Frequency 5 MHz, Focal length 76 mm, element diameter 9.6 mm
- Transmission: 3.5 MHz, 2 cycle, 240V
- High-pass filter: 10 MHz
- Receiver gain: around 58 dB with 10 MHz high-pass filter
- Angle of incidence: 2 degree

E.5.5.2 Imaging

- Scan pitch 0.25 mm (X, Y)
- Slice gate for C-scan (20 division)
- Scanning velocity: 20-30 mm/s
- Display: C, B & D
- Imaging higher harmonic: 3rd harmonic (10.5 MHz)

E.5.5.3 Calibration

- No calibration because of no suitable calibration blocks for HHUT.

	Pipe	**Square Block**
Frequency of burst waves	4	3.5
Cycles of burst waves	3	2
Frequency of high-pass filter	8 MHz	10 MHz
Angle of incidence	0 or 5 degree	2 degree

E.6 Orthogonal Coil Array Eddy Current, Technique 16-ECT1

E.6.1 Overview

Eddy Current Testing (ECT) is one of nondestructive testing methods using electromagnetic interaction and has high detectability for surface breaking cracks. A test object should be made of a conductive material. ECT is performed with a probe that consists of a single or multiple coils. When a probe is placed on the surface of a test object and an alternating current is applied to a coil of the probe, a magnetic field is induced around the coil (this process is called *excitation*). This magnetic field penetrates into the surface of the test object and generates a circulating current, which is called eddy current, in the test object. If a defect exists in the test object, the defect interferes with this current flow. Then, a coil of the probe can detect a change of the magnetic field caused by this current flow and show where the defect exists (this process is called *detection*).

An ECT array probe has several coils so as to inspect a wider area at once.

E.6.2 Equipment

The equipment used in this inspection is a commercial ECT system that consists of an inspection instrument R/D Tech MS5800 and a ZETEC ECT array probe (E342024D). Figure E.42 shows the appearance of this ECT array probe. This ECT array probe has 24 coil elements aligned in two rows. Each of 24 output channels of the system outputs ECT signals obtained with the corresponding coil element. Figure E.43 shows the coil layout of this ECT array probe. Each coil element is 3 mm-wide orthogonal coils that are formed by two coils vertically standing on the contact surface and orthogonal to each other. According to the specification, the center-to-center distance of the two coil rows is 6.65 mm, and the intervals of coils in a row are 4.89 mm. The system employs the impedance (IMP) mode in which both coils of a coil element are used for both excitation and detection, and the transmit-receive (TR) mode in which one coil is used for excitation and the other is used for detection. Because preliminary experiments showed the IMP mode provided better results than the TR mode, only the IMP mode is used in this inspection. The excitation frequency is set to 200 kHz.

Figure E.42. ECT Array Probe

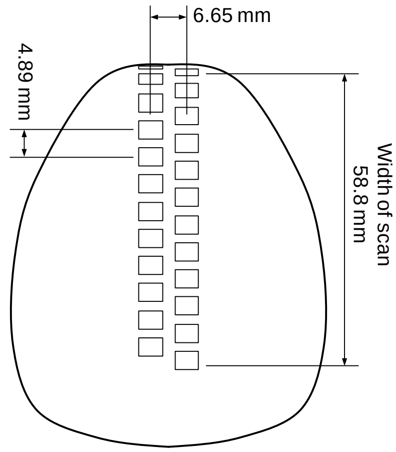

Figure E.43. Coil Layout of ECT Array Probe

E.6.3 Data Acquisition

The ECT array probe is placed on the inner surface of a test block in such a way that the coil rows are perpendicular to the weld line of the test block. The probe is moved along the weld line to inspect the surface of an area around the weld line (Figure E.44). In this round-robin test, the length of the coil rows can cover the whole areas where the defects exist with one line or one circle of movement.

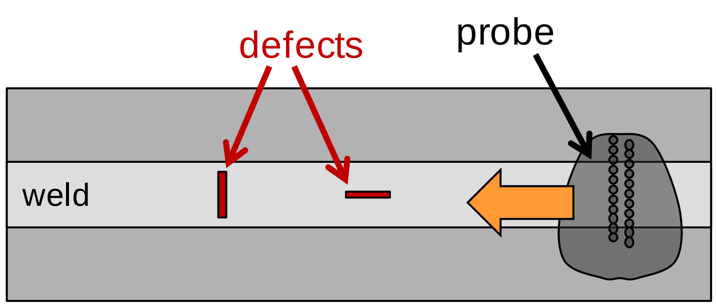

Figure E.44. Scanning Procedure

For the pipe test blocks, while the probe is fixed to have contact with the inner surface of a test block, the test block is rotated on a rotating rack to make the probe scan an area around the weld line (Figure E.45). The wire end of a wire encoder is attached to the outer surface of a pipe test block so as to acquire the probe position (Figure E.46).

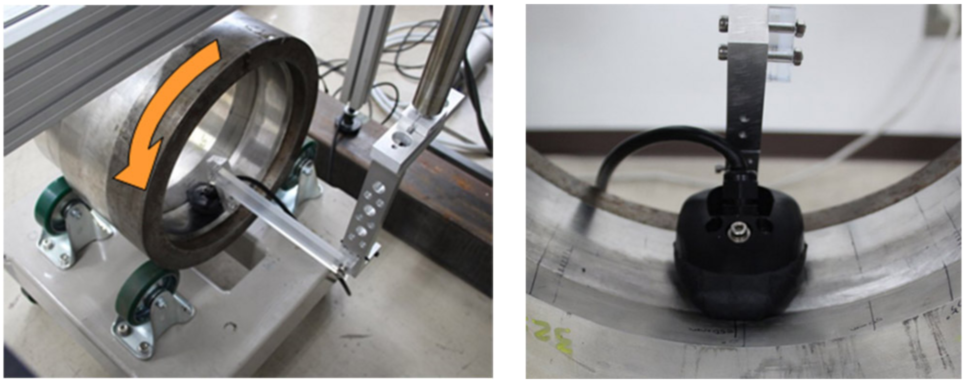

Figure E.45. Probe Placement on Pipe Test Blocks

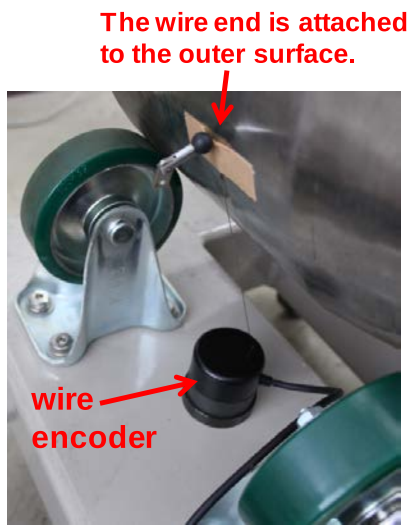

Figure E.46. Wire Encoder Attached to Pipe Test Blocks

For the BMI test blocks, a test block is placed on a turntable, and the probe is fixed on an inspected surface of a test block in such a way that the front edge of the probe touches the tube in the center of the test block. Then, the test block is rotated on the turntable to make the probe scan an area around the weld line (Figure E.47). The wire end of a wire encoder is attached to the outer edge of the turntable to acquire the moving distance of the outer edge of the turntable. Since the diameter of the turntable is 400 mm, the rotation angle is obtained by dividing this moving distance by 200 mm.

For the rectangular test blocks, since the inspected surface is flat, an electric scanner is used to make the probe scan the inspected surface (Figure E.48). Only for these test blocks, the probe is placed on a test block in such a way that the coil rows are parallel to the weld line and moved across the weld line because the rectangular test blocks are elongated in the direction perpendicular to the weld line. Figure E.48shows two blocks are placed together. The right block is placed for positioning the probe.

Figure E.47. Probe Placement on BMI Test Block

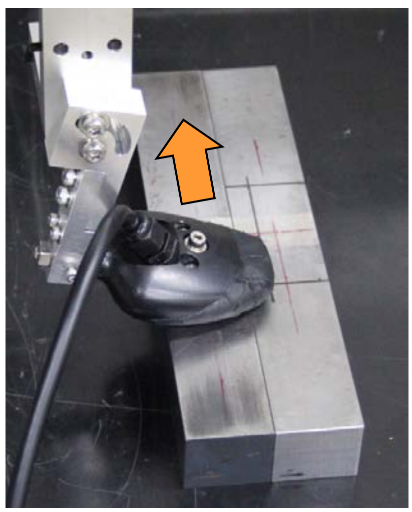

Figure E.48. Probe Placement on Rectangular Test Blocks

E.6.4 Signal Processing

Since the pipe and BMI test blocks are rotated manually, the intervals of the points to sample ECT signals are not constant. To analyze ECT signals smoothly, ECT signals at regular intervals are calculated from the measured ECT signals by using linear interpolation. In this inspection, these intervals are set to 0.1 mm.

Figure E.49 shows distributions of signal amplitude obtained by inspecting a reference block with the equipment explained above. The reference block has four narrow slits that are made by wire electrical discharge machining (EDM) across the full width of the block. The depths of these EDM slits are 1 mm, 2 mm, 3 mm and 4 mm from the left. As shown in Figure E.49(a), raw signals often include noises mainly due to the contact condition between the probe and the inspected surface. The differences in the contact conditions among the coil elements give rise to noises that make stripes in a signal distribution. To reduce noises, the following noise reduction methods are applied. Note that ECT signals are alternating current (AC) signals and have two components (V_x, V_y) that can provide signal amplitudes and signal phases.

E.6.4.1 Average Noise Reduction

A signal is regarded as a noise according to the following criteria.

1. The beginning of a signal sequence

   The signals at N_{av} points from the beginning of a signal sequence of each channel are always regarded as noises.

2. Small signals

   A signal the amplitude of which is less than V_{th} is regarded as a noise.

3. Signals similar to the average of recent noises

   A signal is regarded as a noise when the magnitude of the difference between this signal and the average of the noises at the previous N_{av} points is less than V_{th}.

   When this average of the noises is calculated, the noise at a point where the signal is not regarded as a noise is defined as the average of the noises at the previous N_{av} points at that point.

4. Signals similar to the interim average of noises

   A signal is regarded as a noise when the magnitude of the difference between this signal and the interim average of the noises at the points preceding that point is less than V_{th}.

   When this average of the noises is calculated, the noise at a point where the signal is not regarded as a noise is defined as the average of the noises at the previous N_{av} points at that point.

Then, the average of the noises at the previous N_{av} points is subtracted from an ECT signal at each point. At the N_{av} points from the beginning of a signal sequence, the interim average of the noises at the preceding points is subtracted from an ECT signal at each point.

The difference of the material properties between base metal and weld metal causes a significant change of an ECT signal when the probe is moved across the border between them. Because the rectangular test blocks P28, P29, P30, P31, P32, P38 and P42 have a defect in the welded part, only a small part around the defect is analyzed for these test blocks to focus on the welded part and avoid picking up indications due to a material difference. However, in the case of P38, the defect exists on the border of base metal and weld metal, and the area preceding the defect is base metal. Therefore, the average noise reduction is applied backward to a sequence of ECT signals for P38.

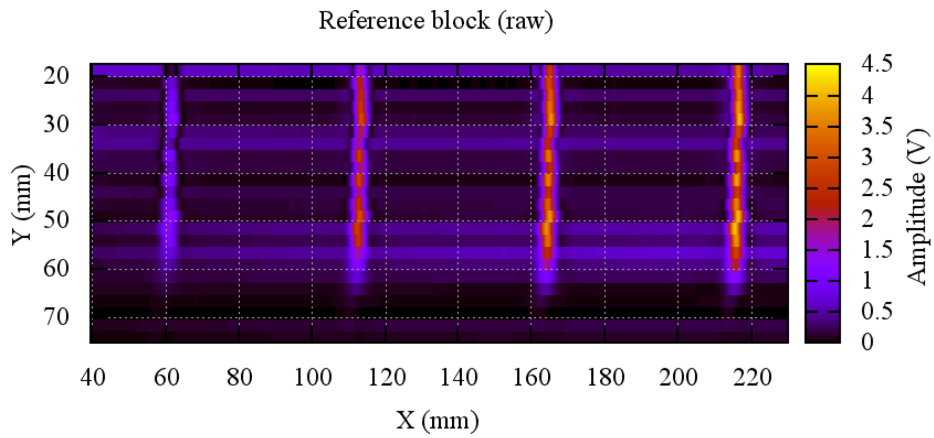

(a) Raw signals.

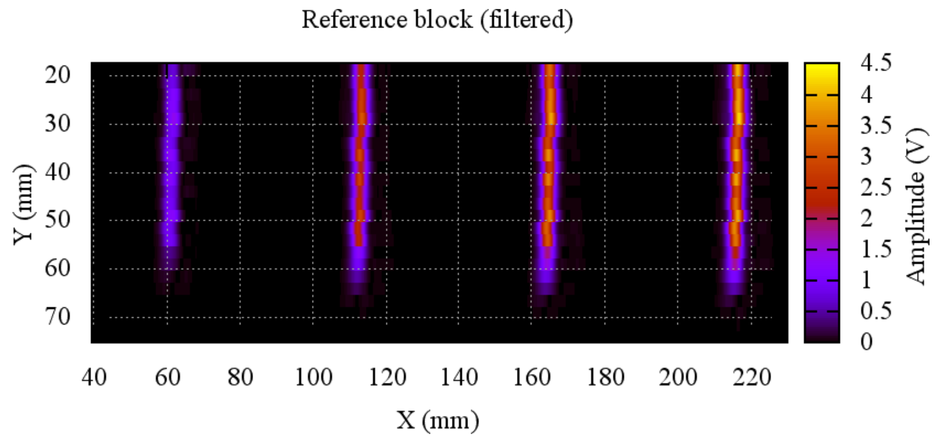

(b) Signals after average noise reduction is applied.

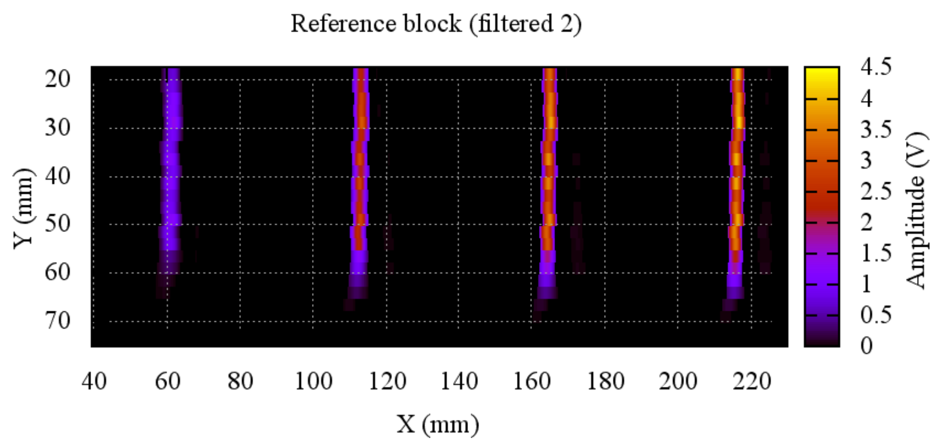

(c) Signals after phase filter is applied.

Figure E.49. Distributions of Signal Amplitude

E.6.4.2 Phase Filter

If noises cannot be eliminated enough by the average noise reduction, a phase filter is applied.

When the excitation frequency is 200 kHz, the signal phase of an indication of a crack parallel to the coil rows tends to have a value around 130°, and the signal phase of an indication of a crack perpendicular to the coil rows tends to have a value around −50°. Then, to detect a crack parallel to the coil rows, the ECT signals are removed at the points where the signal phases are out of the range [100°, 160°]. Also, to detect a crack perpendicular to the coil rows, the ECT signals are removed at the points where the signal phases are out of the range [−80°, −20°].

The above-mentioned noise reduction methods are applied and the parameters are set as follows.

Test Block	Average Noise Reduction	Phase Filter
P1	N_{av}=50, V_{th}=0.2 V	Not applied
P4	N_{av}=50, V_{th}=0.1 V	Not applied
P5, P7, P41	N_{av}=25, V_{th}=0.3 V	Not applied
P12	N_{av}=25, V_{th}=0.3 V	Applied
P28, P29, P30, P31, P32, P38, P42	N_{av}=25, V_{th}=0.3 V	Applied

E.6.5 Data Analysis

A defect indication is defined as a continuous region where the signal amplitude is more than or equal to 0.1 V and the maximum signal amplitude of the region is more than or equal to 0.5 V. If the minimum gap of two defect indications is less than or equal to 5 mm, these two defect indications are treated as one defect indication.

If the aspect ratio of a defect indication is more than or equal to 1.5, the defect is considered as an axial or circumferential defect. An axial or circumferential defect is defined as a defect that goes through the point of the maximum amplitude of the indication, has a length in the axial or circumferential direction and does not have a width. The length of an axial or circumferential defect is set to the length of the defect indication in the axial or circumferential direction, respectively. If the aspect ratio is less than 1.5, the size of a defect is answered as the minimum rectangle that can include the defect indication. In any case, the defect depth is not evaluated.

Furthermore, the length of two adjacent axial or circumferential defects is determined according to ASME Boiler & Pressure Vessel Code Section XI IWA-3400.

A preliminary experiment shows the maximum signal amplitude of an indication of a subsurface EDM slit is about 0.2 V although the distance between the inspected surface and the top of the slit is less than 0.5 mm. Then, all detected indications are considered as surface-breaking defects.

E.6.6 Team's Assessment of the Technique Based on the Round Robin Test Results

Except the defects of the BMI test block P7, all the defects of the inspected test blocks were detected. From this result, it can be said that these defects can be sufficiently detected with a commercial ECT system. For the defect of P7, more detailed analysis is required to clarify the exact cause of the detection failure and verify whether these weld solidification cracks are appropriate to simulate PWSCC.

Although most of the defect indications are sufficiently clear, reducing more noises in the signals provides more accurate information to discriminate and evaluate defects. More study is expected to find a more appropriate way to place the probe and an effective signal processing method.

E.7 Advanced Eddy Current, Technique ID 33-AECT1

E.7.1 Overview

Eddy current testing (ECT) is an analysis using electromagnetic induction whereby flaws in conductive materials can be detected. A pancake coil carrying current is placed near the test specimen. When an alternating current is supplied to the coil, the magnetic field is changed through interaction between the specimen and the eddy current generated near the surface of the specimen. Variations in the phase and amplitude of the eddy current can be detected using a receiver coil.

A differential probe is used that easily distinguishes signals from a flaw and background noise, because the flaw detection signal features a characteristic loop. However, the drawback is that this signal is hard to detect by simple scanning and placement of the detection coils. The signal is only significant when the pair of coils scans in a direction perpendicular to the longitudinal direction of the flaw. In contrast, if the scan is parallel, the flaw signal is weaker.

The probe used in the present method has four detection coils which are arranged inside one exciting coil. Hence, both perpendicular and parallel defect signals can be obtained irrespective of scanning direction of the probe over the flaw. Moreover, the technique is robust against lift-off noise.

In this study, the detection performance and sizing performance of the length are evaluated using the multi-probe.

E.7.2 Principle of Advanced ECT Method (Multi-probe)

E.7.2.1 Overview and Operating Principle of the Multi-probe for ECT

Figure E.50 shows a schematic of the coil arrangement of the multi-probe. The multi-probe has four detection coils which are arranged inside a circular exciting coil. The detection coils are labeled 1–4 in a clockwise sense; coils 1 and 3 are aligned perpendicular to the scanning direction, whereas coils 2 and 4 are aligned parallel. Irrespective of scan direction, it is possible to obtain flaw signals parallel, perpendicular, and at 45° to the scanning direction by taking differences in the detection signals of pairs of coils.

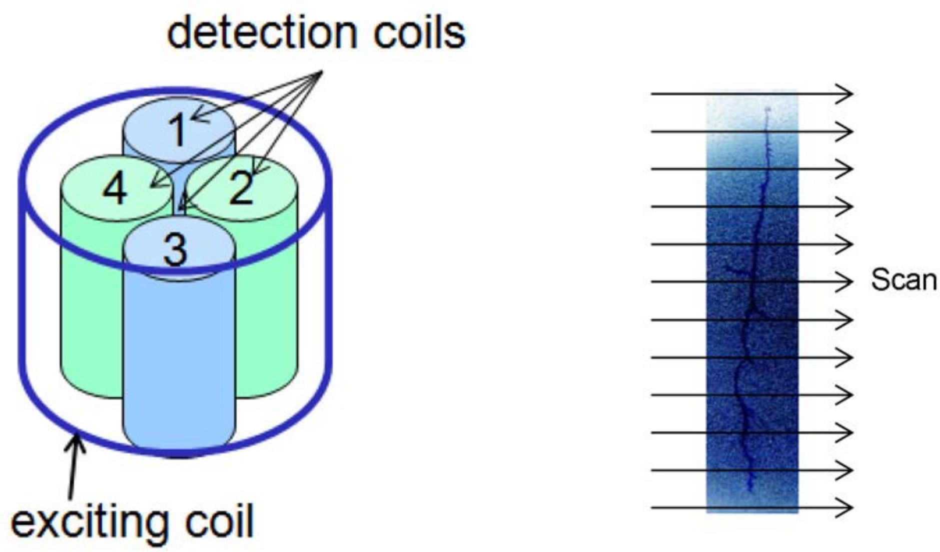

Figure E.50. Overview of the Coil Arrangement and Scanning Procedure of the Multi-probe

An example of a measurement of thermal fatigue specimen is presented. Figure E.51 shows the dye-test results of a crack resulting from thermal fatigue. Figure E.52 shows the detection signal obtained from each of the detection coils. Additionally, Figure E.53 shows the amplitude of the differential signal of coil pairings 1-2, 1-3, 1-4, and 2-4. The flaw can be evaluated in detail based on these defect signals. Branching cracks are seen in Figure E.51 and can also be inspected.

Figure E.51. Results of a Dye Test of a Crack Produced by Thermal Fatigue

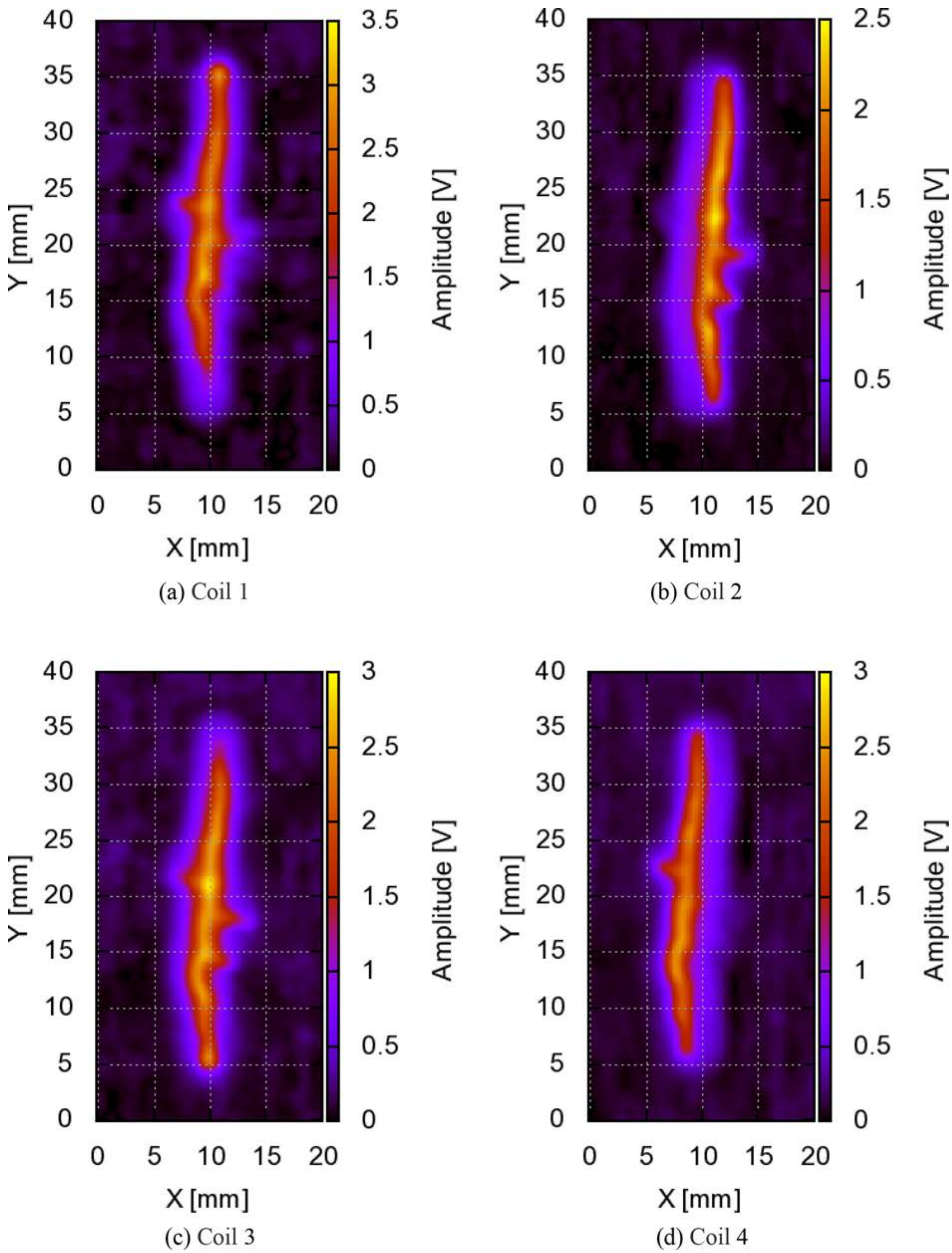

Figure E.52. ECT Signals from Detection Coils 1–4

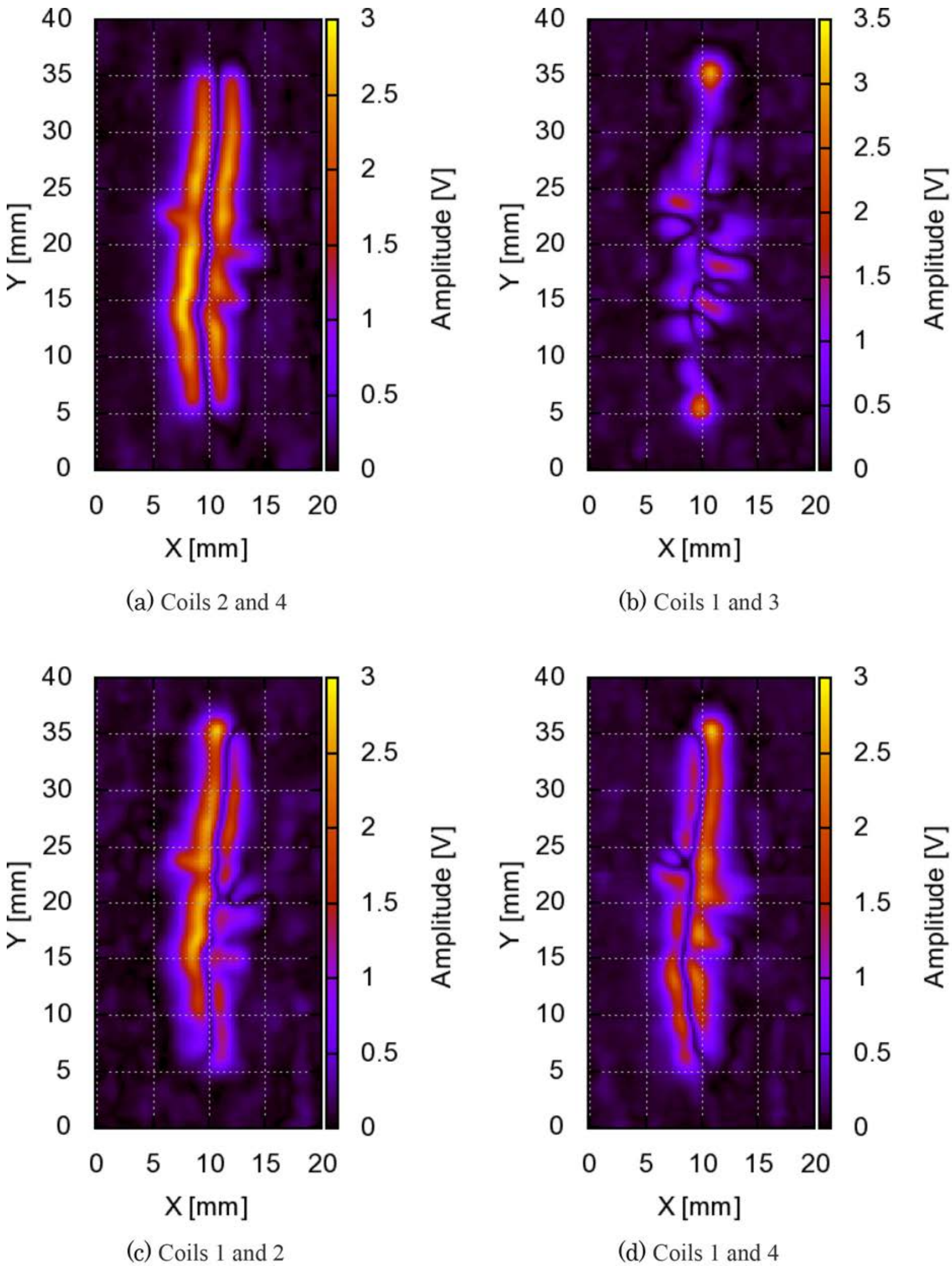

Figure E.53. Differential Signals from the Various Coil Pairings

E.7.2.2 ECT System with the Multi-probe

Figure E.54 shows a schematic diagram of the ECT system. The ECT was conducted with an ECT multi-channel flaw detector (48CH flaw detector, Aswan Electronics Co., Ltd., Osaka, Japan), multi probe, motorized XY stage or rotation stage, stage controller, and a DAQ pad or data logger. The multi-probe is of differential-type consisting of five pancake coils, one excitation coil and four detection coils. The excitation coil with 100 turns has an outer diameter of 5 mm, an inner diameter of 4.2 mm, and a height of 5 mm. The detection coils, each with 300 turns, have an outer diameter of 1.5 mm, an inner diameter of 0.7 mm, and a height of 1.3 mm. The test frequency in this study is 100 kHz.

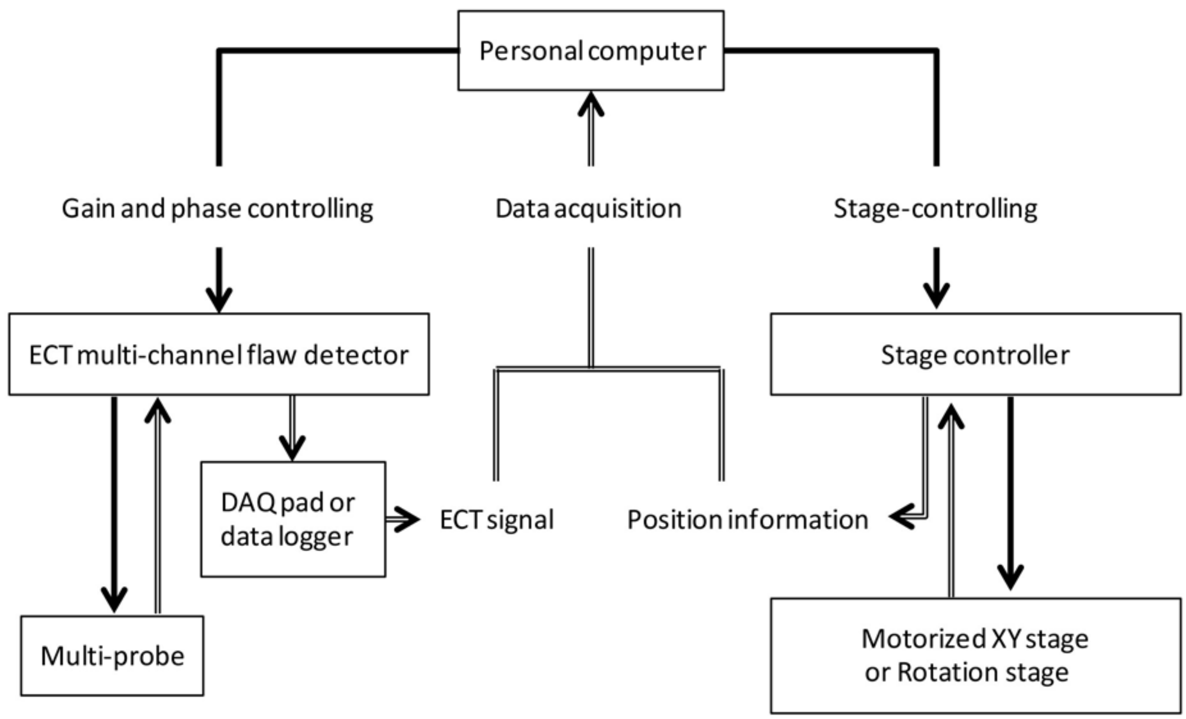

Figure E.54. Results of a Dye Test of a Crack Produced by Thermal Fatigue

E.7.2.3 Scanning Method and Data Collection Method

The motorized XY stage or the rotation stage is used in conducting probe scans. The motorized XY stage is used in taking measurements of various specimens labeled Test Blocks P28, P29, P30, P31, P32, P38, P42, P46, and P12. The rotation stage is used in taking measurements of Test Blocks P37, P41, P5, and P7. When using the motorized XY stage, analog signals from the flaw detector are converted into digital signals by the DAQ pad to be stored as data on the PC. When using the rotation stage, the detection signals are recorded on the PC using a data logger.

E.7.2.4 Calibration of ECT Signal

Calibrations were conducted so that the EC signals from a 2-dimensional slit with depth of 1 mm and width of 0.33 mm have an amplitude of 1 V and a phase of 90°. The four detector coils are calibrated in the same way. The specimen material is Inconel 600; its dimensions are 20 mm in thickness, 200 mm in length, and 75 mm in width.

Figure E.55 shows the calibrated signal of the four detection coils. Figure E.56 shows the differential signal of coil pairs 1-3 and 2-4. These differential signals feature a characteristic figure-of-eight shape with an angle of inclination of nearly 90°.

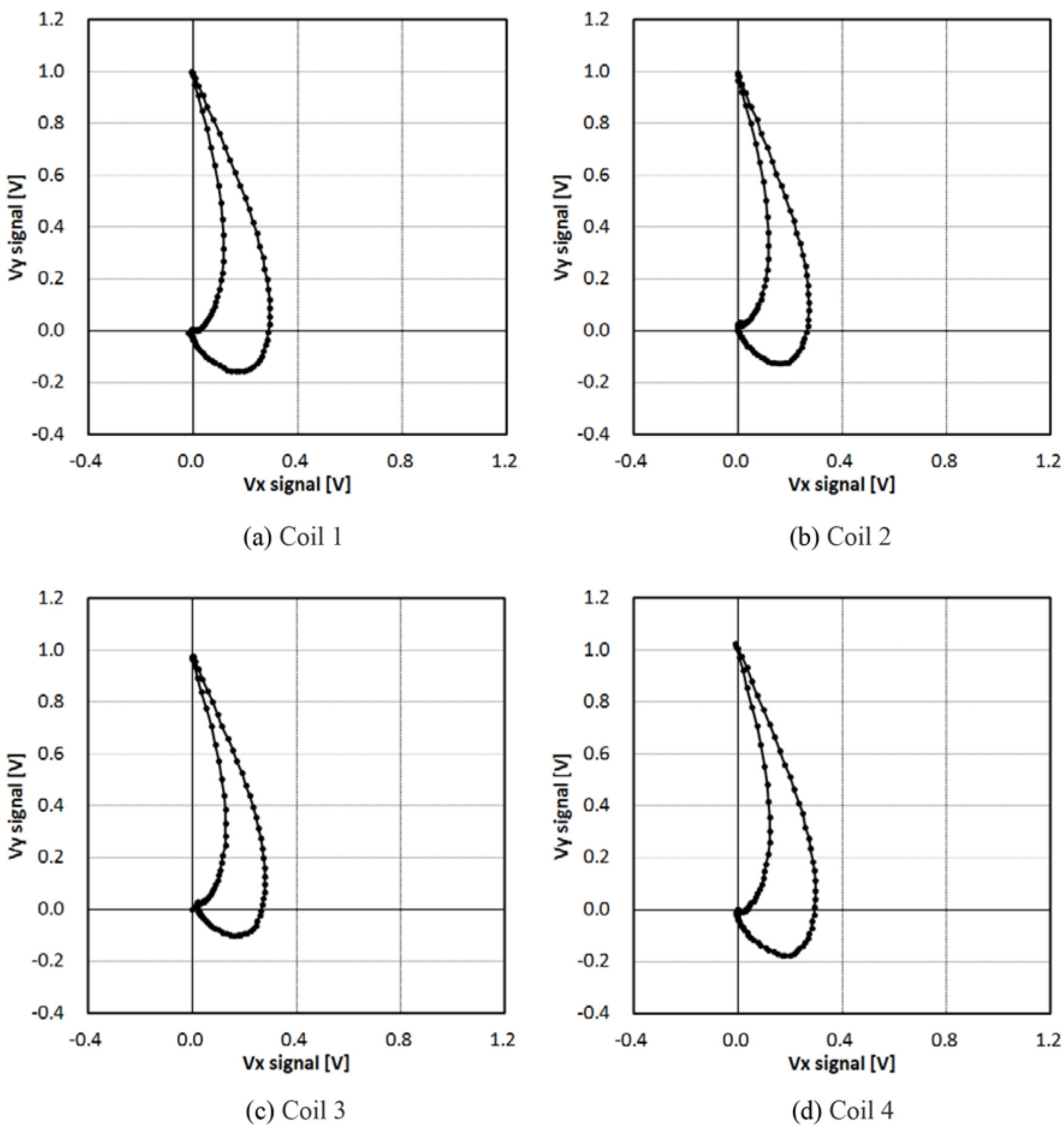

Figure E.55. Calibrated Signals from the Four Detection Coils

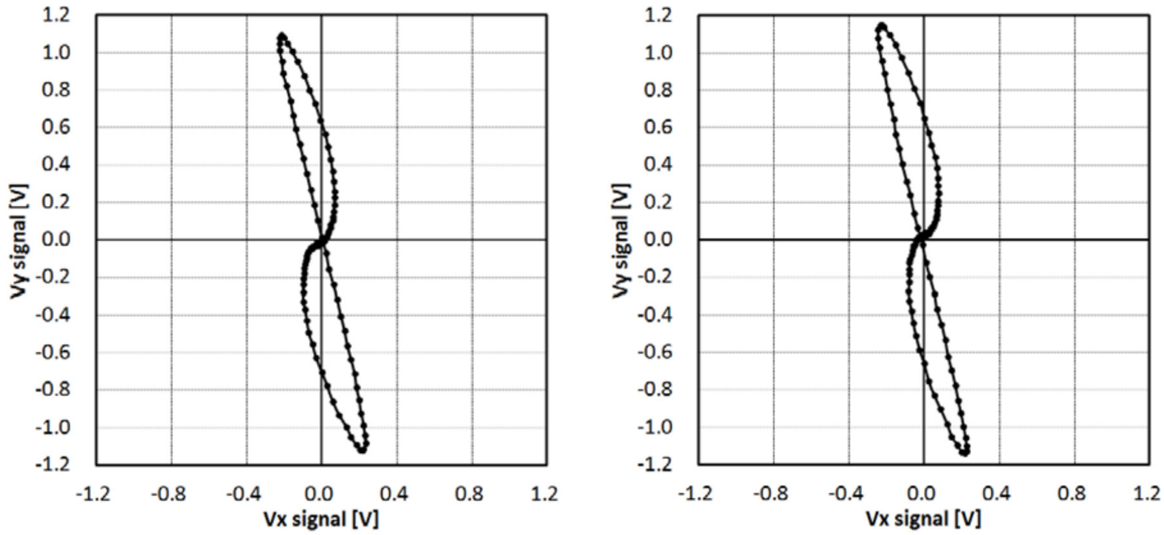

(a) Coil pairing 1 and 3

(b) Coil pairing 2 and 4

Figure E.56. Differential Signals from the Multi-coil

For this study we prepared type-316 stainless-steel plate specimens each etched with a 2-dimensional slit of width 0.2 mm but various depths of 1.0, 2.0, 3.0 or 5.0 mm, as illustrated in Figure E.57. Figure E.58 shows the results of measurements of these slits using the multi-probe. These results show that the amplitude varies with slit depth, but the phase does not change significantly.

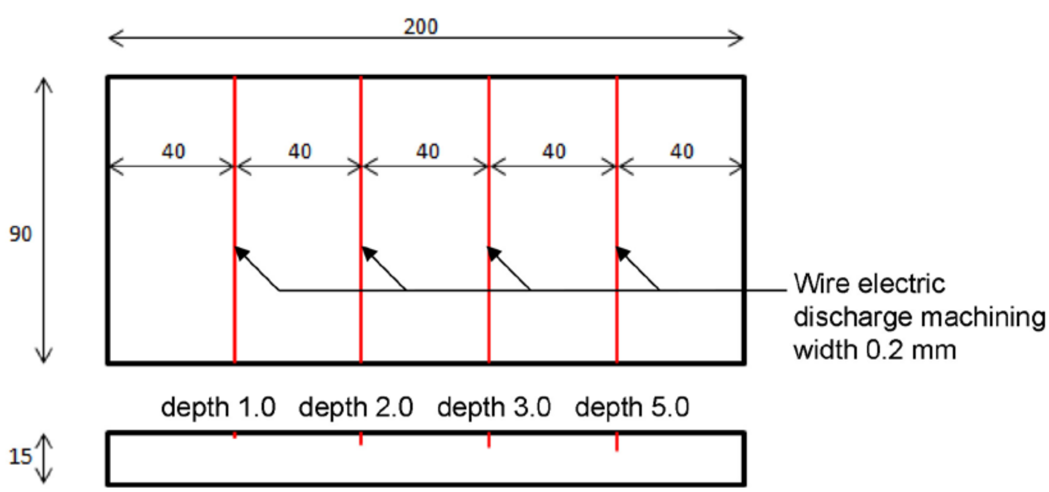

Figure E.57. Dimensions of the Type-316 Stainless Steel Plate Specimen

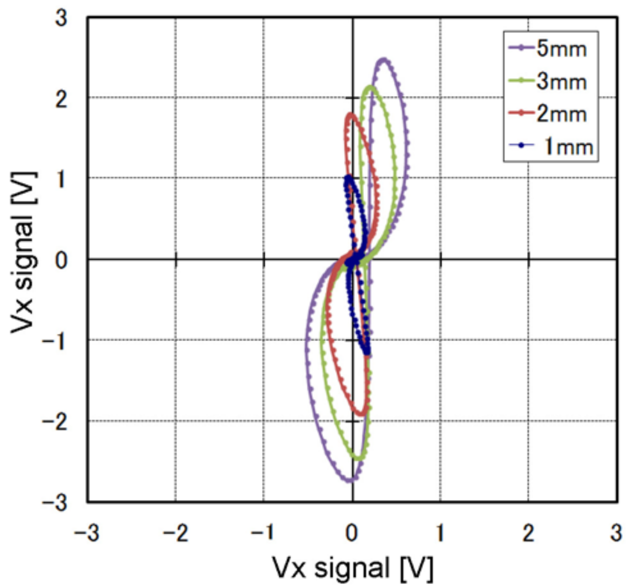

Figure E.58. ECT Signals from Slits of Various Depths

E.7.2.5 Signal Processing Method

Figure E.60 shows the Vy and Vx signals of Test Block P28 obtained by scanning from +22.5 to −22.5 mm along the X-axis direction about the center (Y=0). The signal change in position at 10 mm and −10mm on the the X-axis are influences from the boundary of the weld and the base metal. The defect signal is the signal change about X=0 mm. Figure E.61 shows a typical Lissajous waveform. In particular, Figure E.61(a) is a Lissajous waveform of the detection signal along the X-axis from −22.5 mm to 25 mm. The large amplitude signal that is inclined at 30° is a signal change resulting from influences from the weld. Figure E.61(b) shows an enlargement of the Lissajous waveform corresponding to the flaw. This signal is characteristic of a flaw signal with its angle of inclination at nearly 90°. The amplitude at the center of the Lissajous waveform will not necessarily be 0 V because of influences of lift-off and the weld. Hence, the phase is calculated as the inclination of the changing signal between steps of the scan. The phase θ is calculated from the inclination between the (Vx,Vy) signal of the n^{th} and $(n+1)^{th}$ turning points,

$$\theta = ATAN\left[\left(Vy_{(n+1)} - Vy_{(n)}\right) \Big/ \left(Vx_{(n+1)} - Vx_{(n)}\right) \right],$$

where $Vx_{(n)}$ and $Vy_{(n)}$ are the values of (Vx,Vy) of the n^{th} turning point. Figure E.62 shows the phase results calculated using the amplitude and a threshold of 80–110°. The phase of 80–110° near X=1 mm confirms the presence of a flaw at this position.

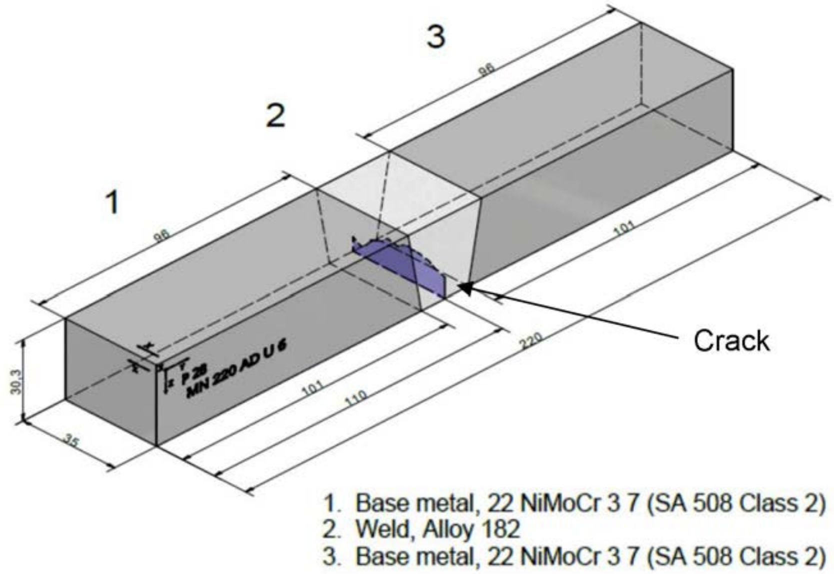

Figure E.59. Composition and Dimensions of Test Block P28

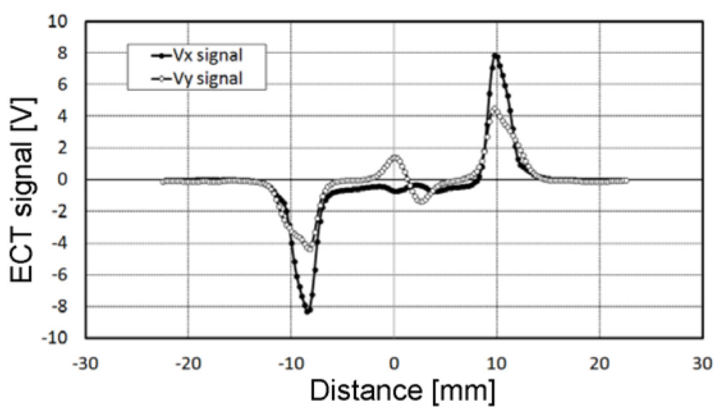

Figure E.60. ECT Signals Vx, Vy of Test Block P28 on Y=0

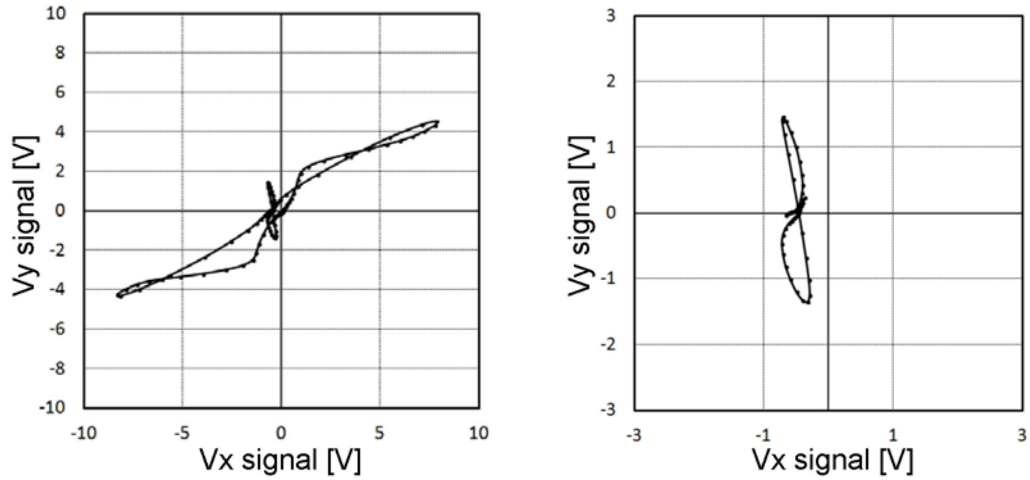

(a) On X-axis from −22.5 to +22.5 (b) On X-axis from −5 to +5

Figure E.61. Lissajous Waveform of Test Block P28 on Y=0

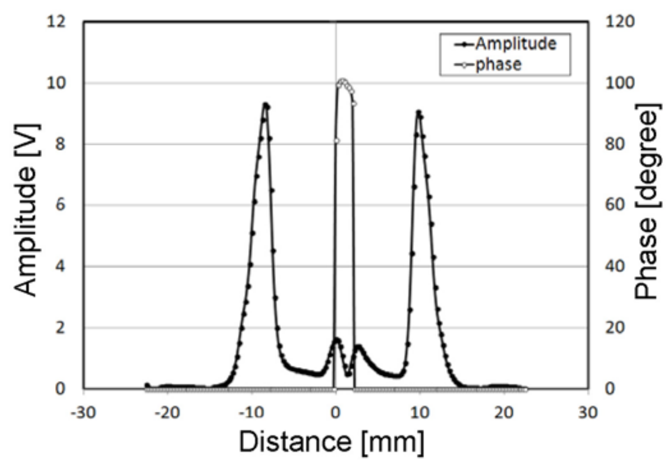

Figure E.62. Amplitude and Phase of Test Block P28 on Y=0

Figure E.63 shows a C-scan display of Test Block P28. Specifically, Figure E.63(a) gives the amplitude of the flaw signal which is smaller than the noise signal from the boundary of the base material and welds, Figure E.63(b) gives the phase of the signal, and Figure E.63(c) displays the results from the analysis. The threshold for the amplitude is set so that the absolute value of the difference between Vy(n+1) and Vy(n) is more than 0.1V, whereas that of the phase is set at 80–110°. The threshold of amplitude is 25% or more of amplitude which is determined from the calibration signal and the scan pitch. Additionally, if the significant value does not appear continuously three times or more, the phase is 0°. The flaw, colored orange in Figure E.63(c), has a length determined from the result of the analysis.

The length of the flaw is evaluated based on the signal disappearance instructions length from the analysis result. If the plural defects are adjacent and intermittent, the length is determined by ASME XI IWA-3400 “Linear flaws detected by surface or volumetric examinations.”

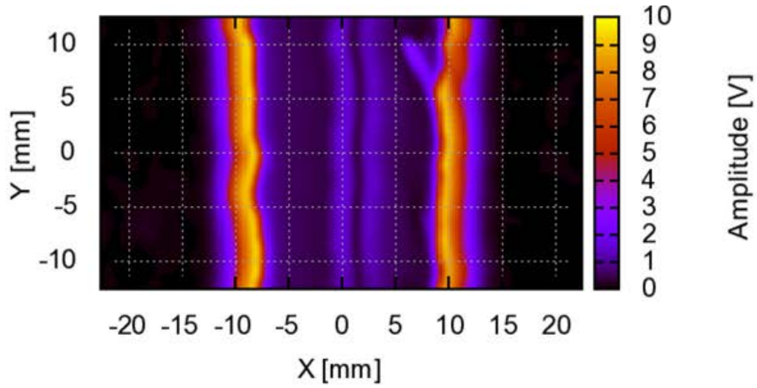

(a) Amplitude of ECT signal of Test Block P28

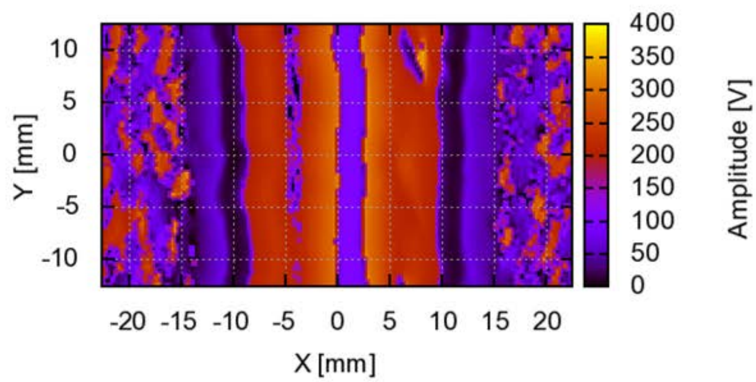

(b) Phase of ECT signal of Test Block P28

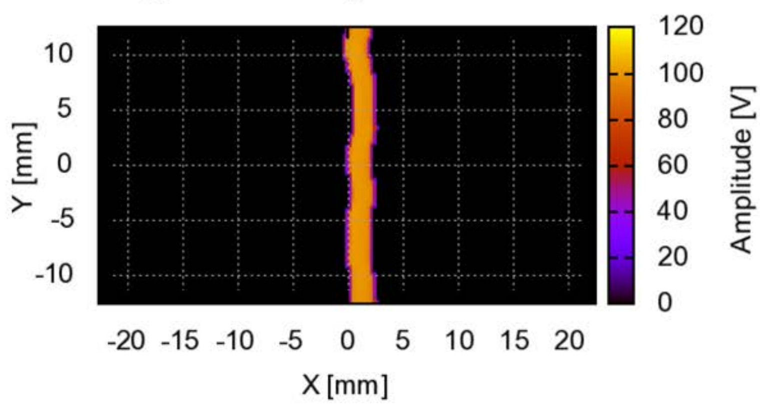

(c) Phase of the flaw

Figure E.63. C-scan Display of Test Block P28

E.7.3 Inspection Method for the Test Blocks of P28, P29, P30, P31, P32, P38, P42, P46, and P12

Figure E.64 shows experimental setup for ENSI-Blocks. The motorized XY stage is used in scanning the probe over Test Blocks P28–P32, P38, P42, P46, and P12. At each measurement point, the probe measures the ECT signal recorded along with the scanning position information and stored on the PC. The scan is taken at intervals of 0.25 mm in both X and Y directions.

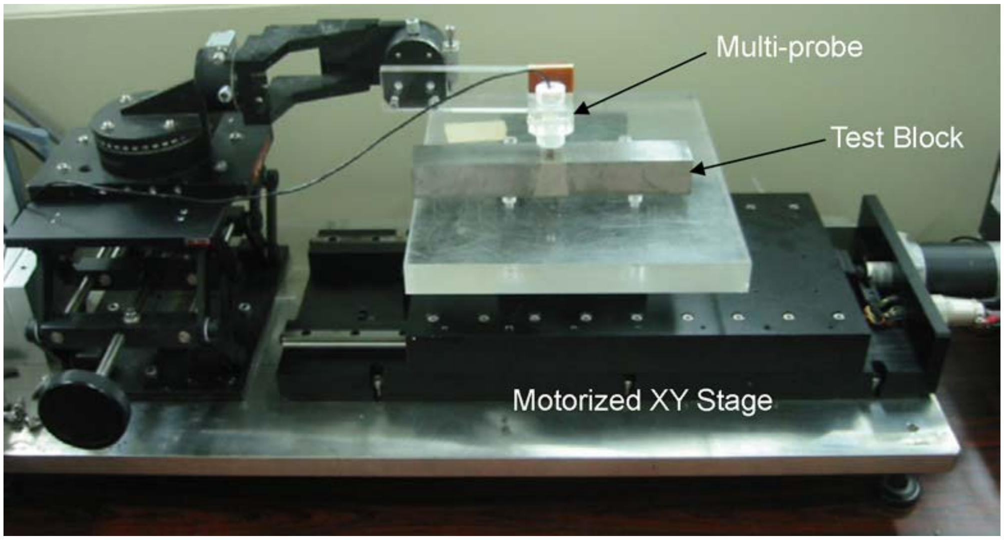

Figure E.64. Experimental Setup for ENSI-Blocks

E.7.4 Inspection Method for the Test Blocks of P37, and P41

Figure E.65 shows experimental setup for Small DMW P41 using rotation stage. The rotation stage is used to scan the probe for Test Blocks P37 and P41. The probe is scanned over the inner surface of the pipe in conducting the flaw detection test, as shown in Figure E.66. The measuring angle and rotational speed of the rotation stage are controlled by the stage controller. The Y-axis positioning of the probe is performed manually using a feed screw. The ECT signal and time measurements are collected using the data logger. The measurement position (measurement angle) is calculated from the angular speed of the rotation stage and the elapsed time. Finally, the angular measurement is converted to a distance from an origin 0 on the outer peripheral.

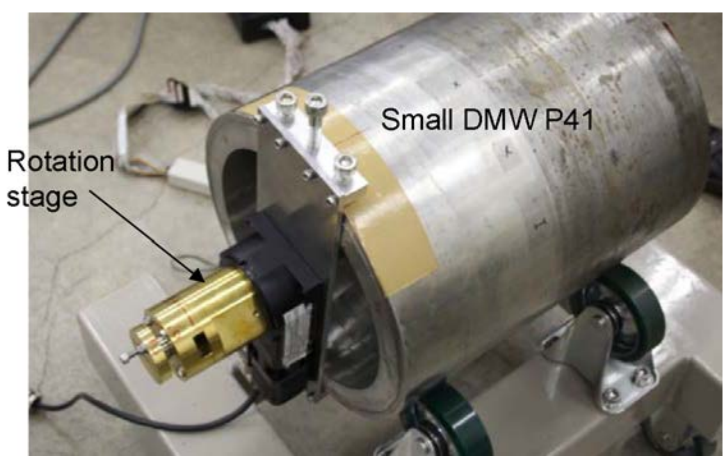

Figure E.65. Experimental Setup for Small DMW P41 Using Rotation Stage

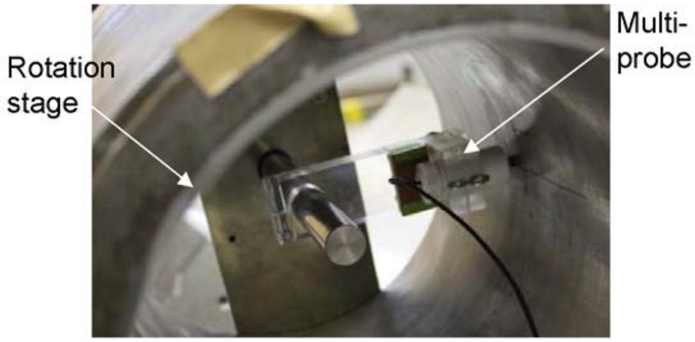

Figure E.66. Photo of Multi-probe Inside the Pipe

E.7.5 Inspection Method for the Test Blocks of P5, and P7

Figure E.67 shows experimental setup for Small DMW P41 using rotation stage. The rotation stage is used to scan the probe over Test Blocks P5 and P7 (BMI; Bottom Mounted Instrumentation) to perform flaw detection around the pipe, as shown in Figure E.68. The measuring procedure is the same as in Procedure-2. The ECT signal and elapsed time measurements are recorded using the data logger. The measurement position (measurement angle) is calculated from the angular speed of the rotation stage and elapsed time measurements.

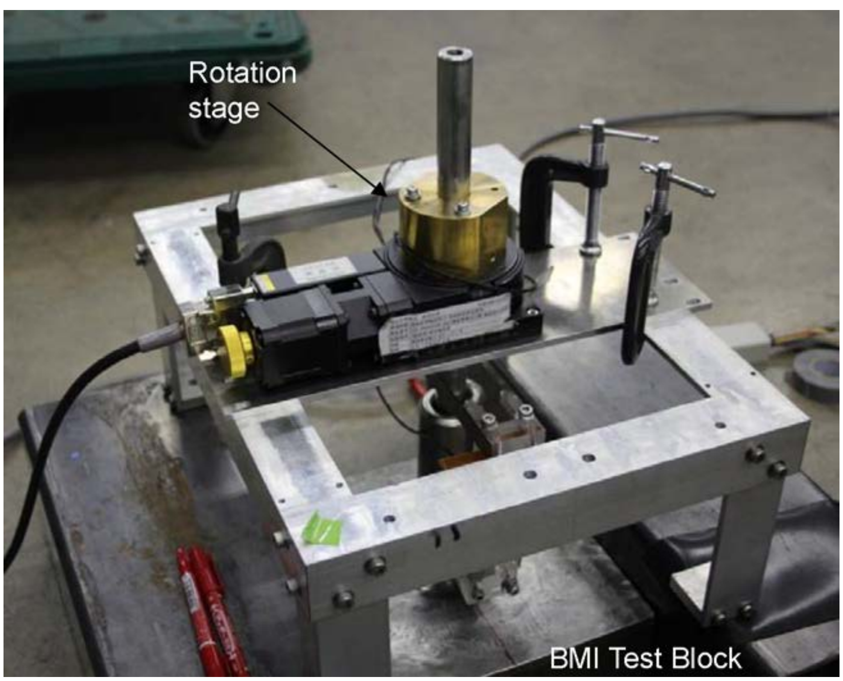

Figure E.67. Experimental Setup for BMI Using Rotation Stage

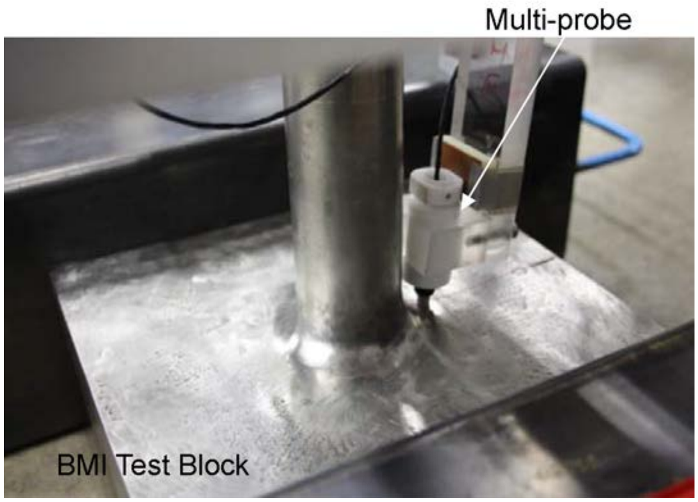

Figure E.68. Status of Multi-probe

E.7.6 Team's Assessment of the Technique, Based on the Round Robin Test Results

1. What is the purpose and advantage of the emerging technique (what problem was it developed to solve?)?

- The present probe consists of differential receivers and an exciter surrounding receivers, and this configuration allows high detectability to small cracks according to the experience obtained by the team. In addition, the receiving unit of the probe has two pairs of differential coils which are aligned perpendicular to each other. Using two sets of differential signals, the probe can detect and evaluate flaws having various directions without rotating the probe. Moreover, the technique is robust against lift-off noise.

2. Provide a brief assessment of the results of your testing, specifically regarding the ability of the technique to detect and size (length/depth) flaws?

- Small Test Blocks (P28, P29, P30, P31, P32, P38, P42, P46), DMW Test Blocks (P12, P37, P41) and BMI Test Blocks (P5, P7) were evaluated using the multi-probe for eddy current testing.
- The flaws located in the weld could be detected, and the length values were evaluated with relatively good accuracy.
- However, the signals of flaws lying on the bond of welds include the large amount of noise and length sizing for these flaws did not work well. In the cased of closed flaws, the detectability is low.

3. Were there any problems/issues that limited application of the technique to the test blocks?

- How often was the technique usable to its full extent (for example, could the technique only be applied to the flat ENSI test blocks, but not to curved surfaces?)?
  - In the case of manual inspection of BMI, due to the curvature of welds of penetrating pipes, it is difficult to keep constant inclinations, which lead large noises of measurements.

- If there were limitations of the technique, please provide your ideas about how these limitations may be overcome in the future.
  - It is necessary to apply a scanner which automatically positions the probe keeping the inclination with respect to the weld lines.

E.8 Controlled Excitation Eddy Current, Technique ID 5-CEECT1

E.8.1 Overview

The technique applied is based on eddy current inspection. The uniqueness of the technique is that it would enable to evaluate the depth of deep flaws more quantitatively than conventional eddy current testing.

The physics in action of the technique, which is illustrated in Figure E.69, is basically identical that of conventional eddy current testing. That is, the technique emits an alternating magnetic field to conductive media to induce eddy currents, and senses the magnetic fields that the induced eddy currents generate in order to detect and evaluate a flaw. Measurements are carried out on the surface where a flaw opens, and signals are obtained as a function of the position of a probe. The amplitude and the phase of the signals are used to estimate the position, surface length, and the depth of a flaw. The uniqueness stems from the use of a probe consisting of vertical exciters and a horizontal detector situated away from the exciters. The physical background of the technique is explained in Yusa et al. (2011) together with several experimental validations.

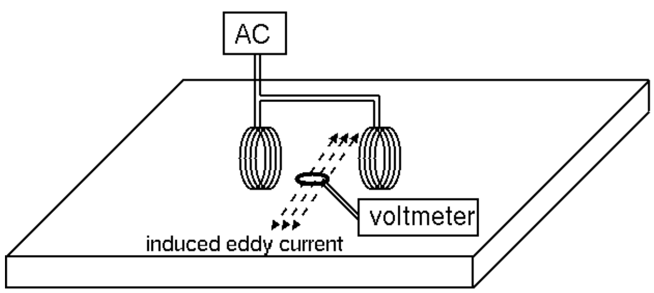

Figure E.69. Physics in Action

Signals obtained through the technique are maximized above the edges of a flaw, which can be used to estimate the position and the surface length of the flaw. The depth of a flaw is evaluated on the basis of the relation between the phase of a signal and the depth of a flaw obtained through experiments or numerical simulations conducted to gather signals due to artificial slits with known depths. Whereas these approaches are basically same with those used in conventional eddy current testing, the technique has such advantage that the phase of signals changes clearly with the depth of a flaw even though the flaw is several times deeper than the depth of penetration as depicted in Figure E.70.

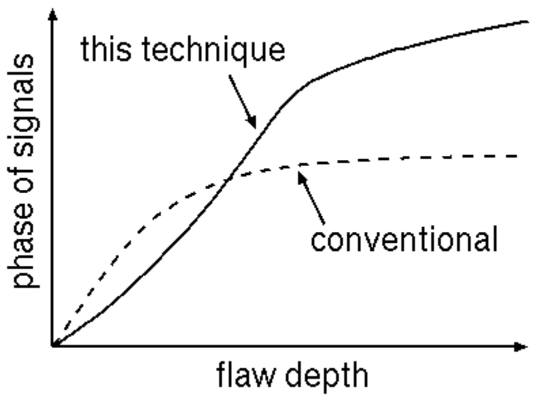

Figure E.70. The Advantage of the Technique

One of the largest problems about the technique is that the effect of flaw parameters on measured signals is not fully revealed. Whereas earlier studies have confirmed the depth of a flaw affects signals significantly, they have also revealed that the length of a flaw has a large effect on signals. This implies that the technique is sensitive to the cross-sectional profile of a flaw much more than conventional eddy current testing, and it is likely that sophisticated inversion is needed to quantitatively evaluate the depth of a flaw. The studies revealed that the technique cannot show advantage over conventional eddy current testing if the surface length of a flaw is shorter than approximately 20 mm, whose physical background has not been fully revealed yet. An exciting frequency of 50 kHz has been used in earlier studies; no quantitative evaluation on the effect of frequency has been conducted so far. Consequently, the limitation of the technique in flaw evaluation has not been clarified. Another practical drawback is that the probe used for the technique is much larger those used for the conventional eddy current testing. This makes it difficult to scan non-flat surfaces.

E.8.2 NDE Equipment Used to Implement the Technique

The schematic diagram of the equipment is illustrated in Figure E.71. An AC current is supplied to the exciter to induce eddy currents inside the target, and signals are measured by a lock-in amplifier. The signals are gathered by a PC through an A/D converter. Important pieces of equipment are listed below.

- Function synthesizer (WF1974, NF Corporation)
  - The function synthesizer generates sinusoidal voltage to excite the exciter. The frequency and the amplitude of the voltage in this experiment were 50 kHz and 15Vpp, respectively.
- Bipoler amplifier (HSA4051, NF Corporation)
  - The bipolar amplifier was used to amplify the voltage generated by the function synthesizer and to feed sufficiently large exciting current to the exciters. The amplification in this experiment was set to 40 times.
- Oscilloscope (1001B, Tektronix, Inc.)
  - The oscilloscope monitored the exciting current by measuring the voltage of the shunt resistance to measure the amplitude of exciting current and to confirm that the current exhibits no obvious distortion.

- Lock-in amplifier (LI5640, NF Corporation)
  - The lock-in amplifier was used to measure detector signals. The voltage of the shunt resistance, which was measured by the oscilloscope, was used as reference signals. The lock-in amplifier displayed both in-phase and quadrature components of the signals, and output them as DC signals ranging ±10V.
- A/D converter (NR-500, Keyence Japan)
  - The A/D converter was used to convert the output of the lock-in amplifier, which is in analog, into digital signals that can be recorded by the PC connected with the A/D converter with USB.
- PC
  - The PC, which is an ordinary PC with Windows 7, recorded the data using dedicated data logger software, Wave Logger (Keyence Japan).

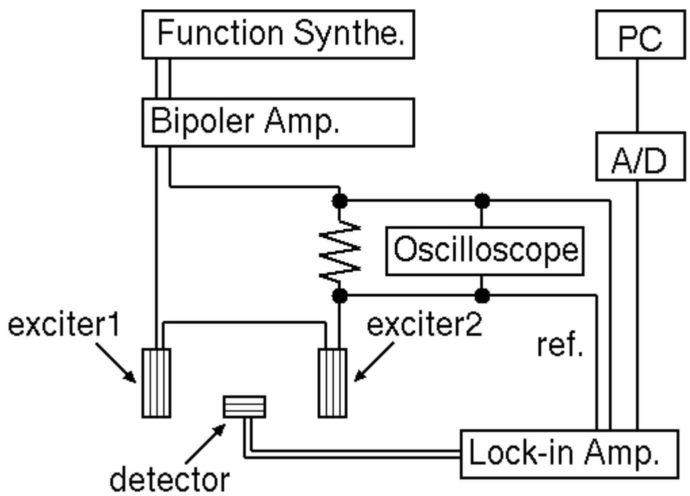

Figure E.71. Connection Diagram

Probe utilized is shown in Figure E.72. The probe had two vertical exciters and one horizontal detector. The two vertical exciters generate magnetic fields with the same polarity, which induces a directional eddy current directly below the detector. The distance between the exciters was set to either 54 or 12 mm. Note that the technique requires situating the detector away from the exciters in order that measured signals changes clearly with the depth of a flaw. Therefore, when the distance is 12 mm, the measurements become basically same with conventional eddy current testing, and signals measured are used only to detect flaws.

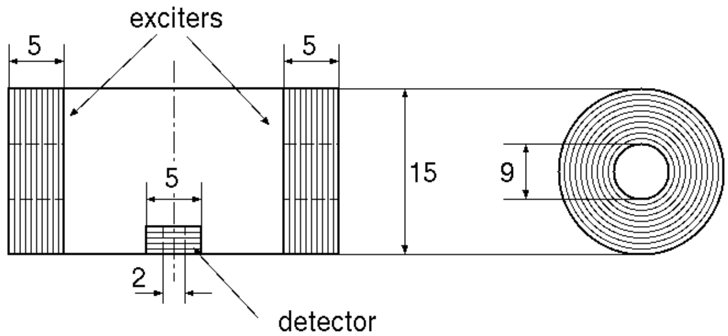

Figure E.72. Probe

E.8.3 Data Acquisition Process/Parameters

- Automated or manual: manual
- Encoded or not: no
- Access surface on test blocks: surfaces where the flaw opens
- Data acquisition speed: 10 kHz

Details are given in the reports.

E.8.4 Signal Processing Performed on the Acquired Data

There is no signal processing performed on the data.

E.8.5 Acquired Data Analysis Process for the Technique

Signals due to a flaw are distinguished from noise on the basis of the fact that a flaw should provide two signal maximums whose phases are opposite to each other as illustrated in Figure E.73. It should be noted however, this assumes that a flaw has a symmetric boundary profile. It is likely that this approach does not work well if a flaw has an extremely complicated boundary profile.

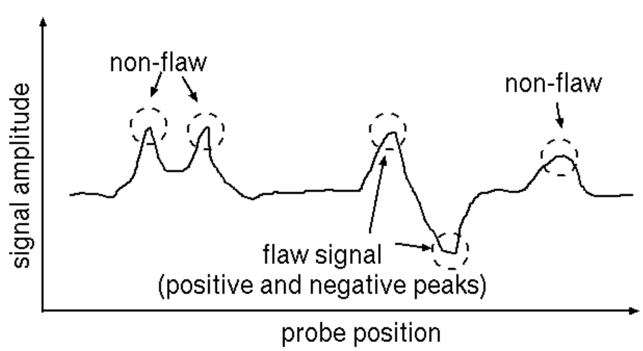

Figure E.73. Distinguishing Flaw/Non-flaw Signals

The depth of a flaw is evaluated on the basis of the phase of measured signals, as mentioned above. More specifically, the trajectory of the measured signals is displayed on two-dimensional plane to evaluate the phase of the signals, θ, as shown in Figure E.74. Then, the depth of a flaw is estimated using a calibration curve obtained through experiments or numerical simulations conducted to gather signals due to artificial slits with known depths.

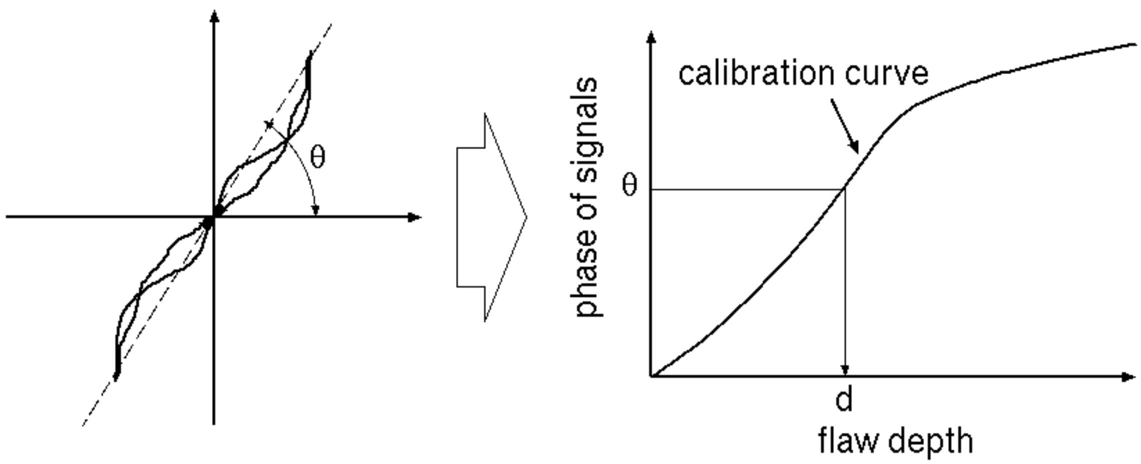

Figure E.74. Evaluating the Depth of a Flaw

E.8.6 Team's Assessment of the Technique, based on the Round Robin Test Results

The technique was developed to overcome that conventional eddy current does not provide clear information about the depth of flaws due to the skin effect. Whereas studies conducted so far in laboratories using flat plate specimens have demonstrated the effectiveness of the technique, it was not possible to size the flaws used in the round robin test. Furthermore, not all the flaws were clearly detected using the technique. Problems that limited the application of the technique to the test blocks are as follows.

1. Low signal-to-noise ratio due to the welds

- The welds caused relatively large noise, which made it difficult to evaluate signals to size the flaws. More quantitative information about the position of probe, which would be obtained using stages, would enable signal processing to enhance signal-to-noise ratio by taking consideration of the spatial distribution of measured signals.

2. Difficulty in inspecting curved surfaces

- Since the probe needs to be large, inspecting surface with a curvature led to a large lift-off and small signal amplitude.

E.9 Microwave Near-field Microscope, Technique ID 28-MM1, 28-MM2

E.9.1 Overview

Microwave is an electromagnetic wave having a frequency from 300 MHz to 300 GHz. It has an advantage of propagating well in air. Therefore, a coupling medium is not necessary when nondestructive inspection is carried out. Microwave induces a current on the crack surface, when microwave irradiates a metal surface where a crack is present. Therefore, a conductor loss is created due to the current flowing on the crack surface. This feature enables us to detect cracks on the metal surface.

An open-ended coaxial line sensor which supports transverse electromagnetic (TEM) waves without cutoff frequency for the fundamental TEM mode was used because the operating frequency band can be broad, and it is possible to decrease the size of aperture for increasing the spatial resolution. A network analyzer was used to generate a continuous wave signal which was fed to the open-ended coaxial line sensor and to measure the amplitude of the reflection coefficient. The amplitude of the reflection coefficient was used to evaluate the depth of a crack.

E.9.2 Principle of Microwave Near-field Microscope Technique

E.9.2.1 Open-ended Coaxial Line Sensor

Figure E.75 shows the distribution of the electric field at the sensor aperture. For the fundamental TEM mode, the electric field is only in the radial direction between inner and outer conductors.

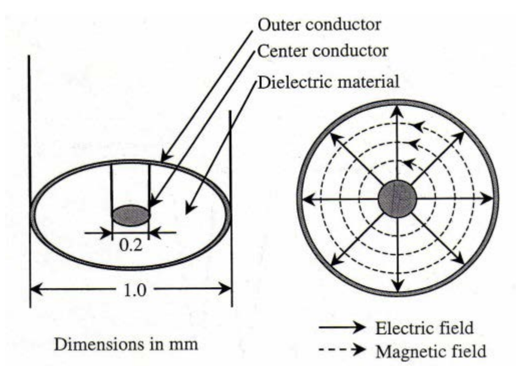

Figure E.75. Distribution of the Electric Field at the Sensor Aperture

The microwave is irradiated from sensor to sample. We detect the crack from the reflection of wave. Figure E.76 shows the amplitude of the reflected wave measured by scanning a crack in a sample at the frequency of 110 GHz. The shape of graph indicates the result of the interaction of the microwave with the crack. When the crack is located between the inner and outer conductors under the sensor, the sum of the components of the electric field that is perpendicular to the crack takes its maximum value, thereby the conductor loss reaches the maximum value. Therefore, the value of amplitude shows the largest decrease. However, when the crack is located under the center of the sensor, no conductor loss will be generated, since the elected field is parallel to the crack. Moreover, two decreased peaks of the value of amplitude can be obtained as shown in Figure E.76, since the crack passes twice between the inner and outer conductors under the sensor. Consequently, a W-shaped characteristic signal was obtained. Hence, the average of the two peaks, P_1 and P_2 shown in Figure E.76, was used to calculate the amplitude difference ΔA.

$$\Delta A = \frac{P_1 + P_2}{2} \tag{E.1}$$

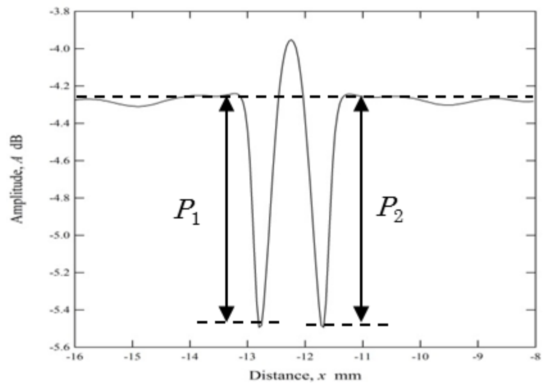

Figure E.76. Amplitude of Reflected Wave Measured by Scanning a Crack

E.9.2.2 Evaluation of Crack Depth

The depth of a crack is evaluated based on microwave propagation theory. Crack is modeled as a parallel plate waveguide. Equation for evaluating the depth of the crack is obtained by considering the relationship between the crack depth and reflection coefficient as

$$d = \frac{\Delta A}{40(\log_{10} e)\alpha_{\mathrm{M}}} \tag{E.2}$$

where, α_M is a constant depending on the crack shape and sensor dimension.

E.9.3 Experimental Procedure for P1, P4, P12, P21, P23, P24, and P41

E.9.3.1 Data Acquisition

The photograph of a vector network analyzer is shown in Figure E.77. The frequency band of the vector network analyzer used for manual measurement is possible to propagate microwave from 10 MHz to 67 GHz. In this experiment, the test was performed with the frequency of 67 GHz. The sensor used for manual measurement in which an open-ended coaxial line was fixed by encasing in epoxy resin was shown in Figure E.78. The amplitude difference was obtained by scanning a crack perpendicular to the crack length direction. The measurement was carried out in manual raster scanning. Direction of scanning was perpendicular to the crack direction. A crack was measured with the scan pitch of 33 points/sec.

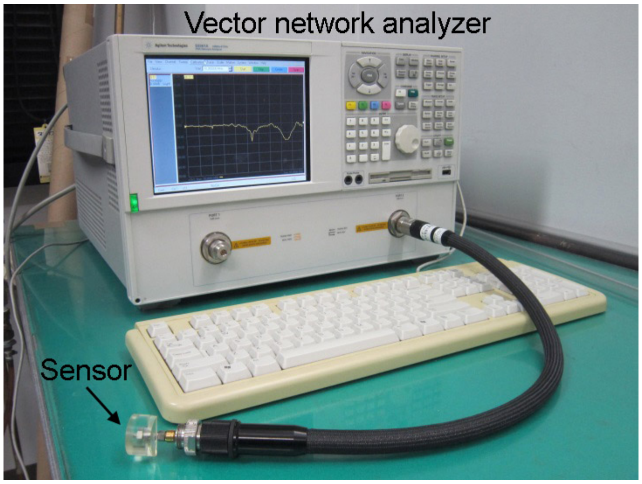

Figure E.77. Photograph of Vector Network Analyzer and Sensor

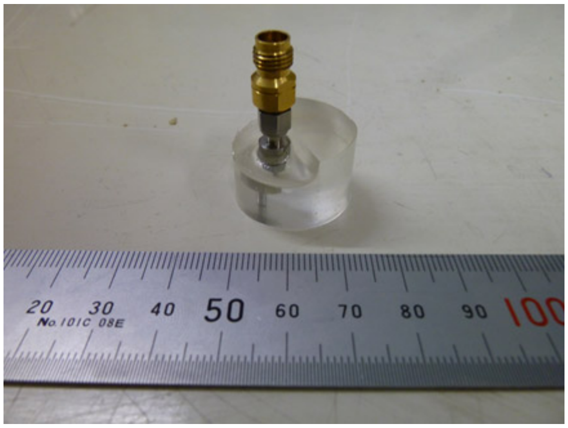

Figure E.78. Photograph of Open-ended Coaxial Line Sensor

E.9.3.2 Signal Processing and Evaluation

The graph like Figure E.76 can be drawn from the data obtained by scanning the crack. Based on the graph, the average value of the two peaks was determined and the crack depth was evaluated by substituting the value in Equation (E.2).

E.9.4 Experimental Procedure for P28, P29, P30, P31 and P32

E.9.4.1 Data Acquisition

Experimental method and principle are based on the above measurement. The photograph of the microwave microscope is shown in Figure E.79. A network analyzer, which is designed to process the amplitude and phase of the transmitted and reflected waves from the network, was used to generate a continuous wave signal which is fed to an open-ended coaxial line sensor. The photograph of open-ended coaxial line sensor is shown in Figure E.80. The operating frequency was 110 GHz, the standoff distance between the sensor and the sample was 60 μm. The measurements were carried out in automated raster scanning and scan direction pitch is 0.04 mm and step direction pitch is 1 mm.

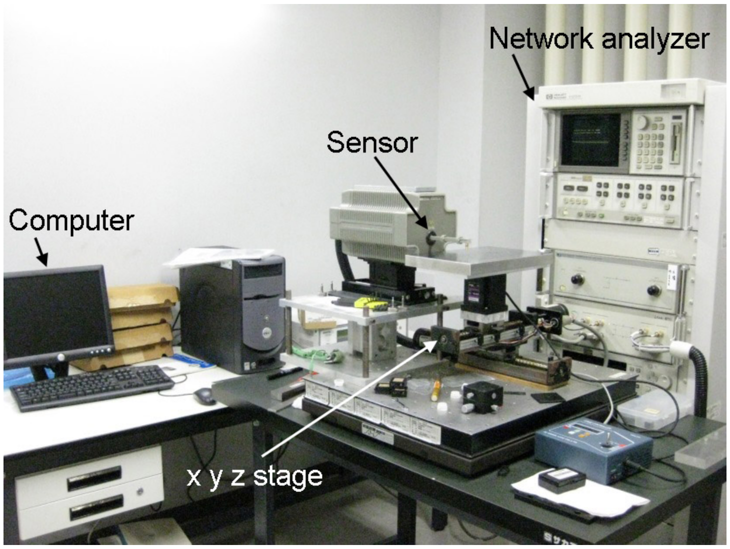

Figure E.79. Photograph of Microwave Microscope

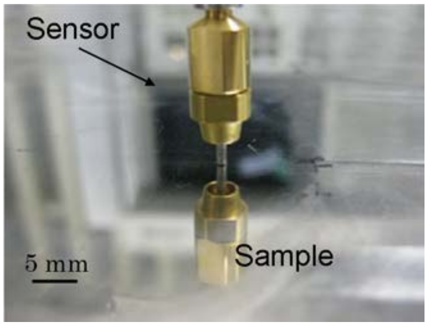

Figure E.80. Photograph of Open-ended Coaxial Line Sensor

E.9.4.2 Signal Processing and Evaluation

The measured amplitude of reflected wave was imaged as C-scan, and the crack length on the sample surface was measured. In addition, at the position of maximum amplitude difference, the crack depth was evaluated by substituting it in Equation (E.2).

E.9.5 Team's Assessment of the Technique, Based on the Round Robin Test Results

E.9.5.1 The Purpose and Advantage of the Emerging Technique

Microwave has an advantage of propagating well in air. Therefore, a coupling medium is not necessary when nondestructive inspection is carried out. In addition, open-ended coaxial line sensor supports transverse electromagnetic (TEM) waves without cutoff frequency for the fundamental TEM mode. Therefore, the operating frequency band can be broad, and it is possible to decrease the size of aperture for increasing the spatial resolution.

E.9.5.2 A Brief Assessment of the Results of the Testing

EDM slits on the curved surface can be detected, and the cracks length can be evaluated correctly. However, fatigue cracks could not be detected. The evaluation of the depth is impossible in both. Some cracks in flat ENSI test blocks can be detected, and the cracks length can be evaluated, but the others could not be detected.

E.9.5.3 Limitation of the Technique to the Test Block

On the curved surface, the technique only could be applied to EDM slits. And, it is difficult to scan rough surface. So, it cannot be applied to cracks on welding part. Since microwave has high sensitivity, it is susceptible to surface roughness, i.e., standoff distance between a sensor and a sample surface. Therefore, in advance, it should be considered to remove the noise by measuring the surface shape with a laser displacement meter.

E.10 References

Ishida H and J Kitasaka. 2013. "Development of a Phased Array TOFD UT Method to Measure the Depth of SCCs in Dissimilar Metal Weld." In *9th International Conference on NDE in Relation to Structural Integrity for Nuclear and Pressurized Components*, pp. 754-762. May 22-24, 2012, Seattle, Washington. NDT.net, Rheintalstr, Germany. http://www.ndt.net/article/jrc-nde2012/papers/120.pdf.

Karasawa H, T Ikeda, S Matsumoto, T Hamajima and H Isobe. 2009. "3D-SAFT Ultrasonic Inspection Equipment "Matrixeye™"." In *Proceedings of the Seventh International Conference on NDE in Relation to Structural Integrity for Nuclear and Pressurised Components*, pp. 669-683. May 12-14, 2009, Yokohama, Japan. European Commission Joint Research Centre, Luxembourg. http://www.ndt.net/article/jrc-nde2009/papers/97.pdf.

Komura I and T Furukawa. 2010. "Improvement of SCC Depth Sizing Capability by 3D-SAFT UT Method in Ni Alloy Weld." In *Proceedings of the Eighth International Conference on NDE in Relation to Structural Integrity for Nuclear and Pressurised Components*, pp. 831-837. September 29-October 1, 2010, Berlin, Germany. European Commission Joint Research Centre, Luxembourg.

Yusa N, Y Sakai and H Hashizume. 2011. "An Eddy Current Probe Suitable to Gain Information about the Depth of Near-side Flaws Much Deeper than the Depth of Penetration." *NDT & E International* 44:121-130.

Pacific Northwest
NATIONAL LABORATORY

Proudly Operated by Battelle *Since 1965*

902 Battelle Boulevard
P.O. Box 999
Richland, WA 99352
1-888-375-PNNL (7665)

www.pnnl.gov

Prepared for the U.S. Nuclear Regulatory Commission
under a Related Services Agreement with the U.S. Department of Energy
CONTRACT DE-AC05-76RL01830

U.S. DEPARTMENT OF ENERGY